June 2024 Vol:10 Issue:2 Haziran 2024 Cilt:10 Sayı 2

T.C.
ÇANAKKALE ONSEKİZ MART ÜNİVERSİTESİ
LİSANSÜSTÜ EĞİTİM ENSTİTÜSÜ

CANAKKALE ONSEKİZ MART UNIVERSITY JOURNAL OF ADVANCED RESEARCH IN NATURAL AND APPLIED SCIENCES

ISSN 2757-5195

Journal of Advanced Research in Natural and Applied Sciences

e-ISSN: 2757-5195

Volume 10 / Issue 2

Cilt 10 / Sayı 2

2024-Haziran/June

Yayımcı / Publisher: Çanakkale Onsekiz Mart Üniversitesi

Rektör / Rector: Prof. Dr. R. Cüneyt ERENOĞLU

Dil Editörü / Language Editor

Doç. Dr. Mehmet YILDIZ

Mizanpaj Editörü / Layout Editor

Burak ARSLAN

Yayın Editörü / Production Editor

Deniz FİDAN

Önsöz:

Journal of Advanced Research in Natural and Applied Sciences Dergisi Fen, Mühendislik, Doğa ve Temel bilimler alanlarında daha önce yayımlanmamış orijinal araştırma makalesi, derleme yazılar, teknik not türünde araştırmaları yayınlayan ulusal ve uluslararası indekslerde taranan, hakemli ve bilimsel bir dergidir. Journal of Advanced Research in Natural and Applied Sciences Dergisi Mart, Haziran, Eylül, Aralık olmak üzere yılda dört sayı yayınlanacaktır. Tr-Dizin'de taranan Journal of Advanced Research in Natural and Applied Sciences Dergisi'nin 10. cilt 2. sayısında 18 adet araştırma makalesi yayına kabul edilmiştir.

	TÜBİTAK TR DİZİN tarafından taranmaktadır. Indexed by TR-DİZİN Database.
	TÜBİTAK-ULAKBİM DergiPark Akademik tarafından yayımlanmaktadır. Published by TÜBİTAK-ULAKBİM Turkish Journal Park Academic Database.
	CROSSREF® veri tabanı tarafından taranmakta ve makaleler DOI numarası ile yayımlanmaktadır. Indexed by CROSSREF® Database and articles are published with DOI number.
	SOBIAD, Scilit ve Academindex tarafından taranmaktadır. Indexed by SOBIAD, Scilit, and Academindex.

İletişim Adresi / Publisher Address

Çanakkale Onsekiz Mart Üniversitesi Lisansüstü Eğitim Enstitüsü

Terzioğlu Yerleşkesi Çanakkale (Sağlık Hizmetleri Meslek Yüksekokulu Binası)

Tel: 0286 218 05 23

Belgegeçer / Fax: 0286 218 05 24

E-posta / E-mail: jarnas.journal@gmail.com

Dergi Web Sayfası / Journal Home Page:

http://jarna.dergi.comu.edu.tr/

https://dergipark.org.tr/tr/pub/jarnas

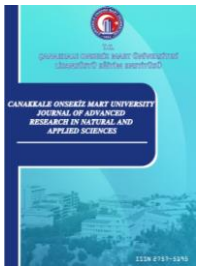

Çanakkale Onsekiz Mart University Journal of Advanced Research in Natural and Applied Sciences

Haziran (June) 2024 / Cilt (Volume) 10 / Sayı (Issue) 2 / e-ISSN 2757-5195

CONTENTS / İÇİNDEKİLER
(2024, 10:2)

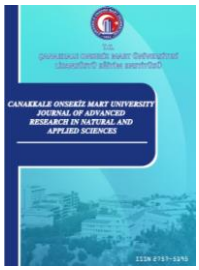

Çanakkale Onsekiz Mart University Journal of Advanced Research in Natural and Applied Sciences

Haziran (June) 2024 / Cilt (Volume) 10 / Sayı (Issue) 2 / e-ISSN 2757-5195

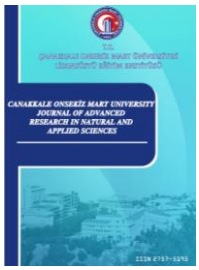

Çanakkale Onsekiz Mart University Journal of Advanced Research in Natural and Applied Sciences

Haziran (June) 2024 / Cilt (Volume) 10 / Sayı (Issue) 2 / e-ISSN 2757-5195

Çanakkale Onsekiz Mart University

Journal of Advanced Research in Natural and Applied Sciences

dergipark.org.tr/tr/pub/jarnas

Open Access

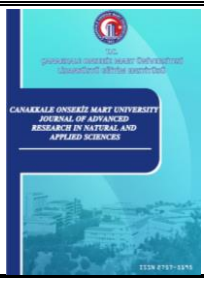

e-ISSN: 2757-5195 2024, Vol. 10, Issue 2, Pages: 243-251 doi.org/10.28979/jarnas.1381226

Uncovering the Hydrocracking Efficiency of Iron-Based Catalysts: A Novel Approach to Asphaltene Transformation in Iranian Heavy Oil

Kadir Yılmaz[1,3], Savaş Gürdal[2,3], Muzaffer Yaşar[3]

[1]Rectorate, Çanakkale Onsekiz Mart University, Çanakkale, Türkiye
[2]Science and Technology Application and Research Center, Çanakkale Onsekiz Mart University, Çanakkale, Türkiye
[3]Department of Chemical Engineering, Faculty of Engineering, İstanbul University-Cerrahpaşa, İstanbul, Türkiye

Article History

Received: 25 Oct 2023

Accepted: 13 Nov 2023

Published: 25 Jun 2024

Research Article

Abstract − In the quest for optimal asphaltene conversion, this study investigated a range of cost-effective and easily accessible catalyst precursors, targeting both high yields of lighter products and minimal coke formation. The hydrocracking experiments were conducted within a 10 ml bomb-type reactor equipped with a reciprocating stirrer operating at a reciprocation rate of 200 times per minute. The experiments were performed at a temperature of 425°C for a duration of 90 minutes, with an initial hydrogen pressure of 100 bar. The outcomes of each experiment were assessed in terms of liquid products, coke production and C5- gas products. To analyze the Iranian heavy asphaltene, Nuclear Magnetic Resonance (^{1}H NMR), Gel Permeation Chromatography (GPC) and elemental analysis were employed. Gas products were characterized using Gas Chromatography (GC). The investigation aimed to identify the catalyst precursor mixture that would maximize asphaltene conversion while minimizing coke production. A series of catalyst precursors, encompassing $FeSO_4 \cdot H_2O$, its binary mixtures with metal oxides (Fe_2O_3, Al_2O_3, CaO, SiO_2), and combinations of Fe_2O_3, Al_2O_3, and SiO_2 with elemental sulfur, were evaluated. The experimental results demonstrated that the toluene-soluble fraction (TSF), which includes the middle distillate portion, could be increased to a maximum of 56% while concurrently reducing the coke yield to 19%, down from the initial 36.9% when no precursor was used.

Keywords − *Asphaltene, hydrocracking, iron-based catalyst, optimization*

1. Introduction

The global energy landscape has long been shaped by the vast reservoirs of heavy oil blends, prominently featuring the Iranian Heavy Oil. Processed extensively in regions such as China, India, Japan, and the Mediterranean countries, this blend is characterized by its significant asphaltene content, a challenging component to refine due to its complex molecular structure and propensity to lead to coke formation [1].

In recent times, the shift towards heavier crude sources has been noted, with these sources containing a high concentration of contaminants like sulfur, nitrogen, metals, and asphaltenes, which significantly affect the quality of the residual oil post distillation [2]. Asphaltenes, in particular, pose a significant challenge in heavy oil refining due to their interference with hydroprocessing which is pivotal in achieving higher liquid oil yields [3].

One of the major challenges in refining heavy oils, particularly those high in asphaltenes, is their inherently low yield of valuable distillates. Asphaltenes are known for their high Conradson carbon residue value and the presence of heteroatoms that poison catalysts, making their effective conversion into low-boiling products

[1]kyilmaz@comu.edu.tr (Corresponding Author); [2]savas.gurdal@comu.edu.tr; [3]yasar@iuc.edu.tr

imperative yet challenging [4]. Historically, several methodologies have been tested to improve the cracking of asphaltenes, with catalytic hydrocracking standing out due to its efficiency. The increasing emphasis on refining heavy crude oil demands the development of novel upgrading techniques to produce high-value products. Both hydroconversion and thermal cracking have been recognized as pivotal processes for the distillation of heavy oil fractions and residues, specifically focusing on comprehending the molecular transformations of asphaltenic compounds subsequent to upgrading [5].

Recent studies have shown the promising results of various catalysts, such as NiMo/c-Al2O3, in enhancing the reactivity of asphaltenes [6]. Further adding to this body of work, [7] have demonstrated the efficacy of transition metal-based catalysts in the catalytic upgrading of heavy oil, suggesting that such catalysts could be particularly beneficial for the Iranian Heavy Oil context. The pivotal role of catalysts in heavy oil hydroprocessing is highlighted by the temperature-driven cracking reactions and the acidity of the catalyst support, both of which act as the primary drivers for the refining process [3]. However, the high cost of catalysts can be a limitation, as seen in methods like the catalytic oxidation reaction of asphaltene, where the cracking reaction rate was found to increase at temperatures above 180°C, albeit with a concurrent rise in coke generation rate [8].

Advancements in catalyst technology have led to the emergence of soluble dispersed catalysts. These catalysts display superior catalytic activity compared to finely powdered counterparts, primarily because of the in situ generation of exceedingly small active metal sites that boast high surface-area-to-volume ratios [9]. Recent technologies have reviewed the utilization of dispersed catalysts in heavy oil upgrading, shedding light on the advancements in catalyst systems that could potentially improve the hydrocracking process of heavy oils and asphaltenes. Furthermore, slurry-phase hydrocracking has gained attention, with the development of catalysts for this process undergoing two phases: homogeneous dispersed catalysts and heterogeneous solid powder catalysts. Homogeneous dispersed catalysts are subdivided into water-soluble dispersed catalysts and oil-soluble dispersed catalysts, each offering unique advantages for heavy oil hydrocracking [10].

Given the escalating demand for petroleum-derived products, the upgrading of heavier quality crude oil and petroleum residues is inevitable. [11] provide insights into the effectiveness of different ligand-based catalysts, which could be key to improving the upgrading process while maintaining cost-effectiveness. Hydroprocessing, a preferred process for heavy oil upgrading, is orchestrated with the presence of a catalyst, underscoring the vital role catalysts play in this process [12]. However, there remains significant scope for identifying and exploring alternative catalyst systems that are not only effective but also economically viable. In light of the growing scarcity of other energy sources, unconventional feedstocks like heavy vacuum residue (VR) have been explored for the production of high-value transportation fuels, and advancements in catalytic hydrocracking have been pivotal in enhancing the quality of these feedstocks [9,13].

In this context, iron-based catalysts present a compelling option. Drawing on the insights from [7] and [14], the present study explores the feasibility of using similar oil-soluble catalysts for Iranian Heavy Oil, aiming to improve the refining efficiency and quality of the end products. Iron, being abundant and relatively inexpensive, offers a sustainable alternative to more scarce and costly metals. Moreover, iron catalysts, especially in conjunction with other metal oxides, might provide unique catalytic properties that can boost asphaltene conversion rates and reduce coke formation.

A study showcased the use of ferrocene-based catalysts, including Magnetite (Fe_3O_4) and Iron Sulfide (FeS), which acted as active forms of catalysts to accelerate the hydrothermal conversion of heavy crude oil and its heavy fractions including resins and asphaltenes. These transformations were authenticated using X-ray

Diffraction (XRD), Scanning Electron Microscopy-Energy Dispersive X-ray Spectroscopy (SEM-EDX), and Mössbauer analyzing techniques [15,16]. In parallel, research by [16] delved into the potential of catalysts crafted from activated carbon amalgamated with iron. Their methodology either involved iron impregnation onto the carbon, subsequently transforming it into iron sulfide in situ, or combining it with pyrite. When subjected to semi-batch autoclave hydrocracking tests under modest hydrogen pressures (7–10 MPa), these catalysts showcased a commendable capability in curbing coke formation during vacuum residue hydrocracking. In a different study, another inquiry focused on the nuances of asphaltene conversion, specifically with 10 wt.% Fe catalysts, characterized by average pore diameters oscillating between 4.5–15 nm. Findings indicated that conversion escalated with pore diameter expansion up to 12 nm, approximating a 70% conversion rate. Beyond this threshold, the rate plateaued. Moreover, maltene yield seemed to be intrinsically tied to pore diameter, with an apex yield of 40% being observed in the 12–15 nm range [17]. Amplifying the scope of enhancing thermal recovery efficiencies, [18] embarked on a study aimed at the catalytic hydrothermal treatment of heavy oil. Their objective was to pare down the presence of dense constituents such as resins and asphaltenes. This research leaned on the use of an iron tallate catalyst during a hydrothermal simulation executed on a bituminous sandstone sample sourced from the Ashal'cha reservoir.

Despite the various strides made in employing iron-based catalysts for asphaltene hydrocracking, the literature still presents a gap in understanding the nuanced behavior and performance metrics of these catalysts, particularly in the context of Iranian Heavy Oil. The majority of the studies focus on generic heavy oils or different types of crude, which may have distinct compositional and reactive properties compared to Iranian Heavy Oil. The specific exploration of $FeSO_4.H_2O$ and its binary mixtures with metal oxides (Fe_2O_3, Al_2O_3, CaO, SiO_2) alongside combinations with elementary sulfur in the hydrocracking reactions has been scant. This creates an avenue for a detailed investigation to fathom the synergies between these materials and the asphaltene content in Iranian Heavy Oil. Furthermore, the precise impact of these catalyst systems on the yield of valuable distillates and the mitigation of coke formation remains to be thoroughly elucidated. The extant literature also lacks a systematic comparison of the performance metrics of these iron-based catalyst systems relative to other metallic and non-metallic catalysts under similar operational conditions. This underscores the imperativeness of the present study, which aims to bridge these knowledge gaps through a meticulous exploration of the performance of specified iron-based catalysts in the hydrocracking of asphaltenes derived from Iranian Heavy Oil. Through this endeavor, the study aspires to unveil new insights that could potentially revolutionize the refining practices for heavy oils rich in asphaltenes, thereby contributing to the broader endeavor of enhancing the efficiency and sustainability of heavy oil processing. Furthermore, [14] highlight the importance of continued research into in-situ upgrading and catalysis, which is especially pertinent for the types of heavy oils addressed in this study.

The present study delves deep into the performance of iron-based catalysts, specifically $FeSO_4.H_2O$, its binary mixtures with metal oxides (Al_2O_3, Fe_2O_3, SiO_2,CaO) and combinations with elementary sulfur, in the hydrocracking reactions of asphaltenes derived from Iranian Heavy Oil. Through a systematic exploration, the study aims to identify the potential of these catalysts in transforming the refining landscape of heavy oils rich in asphaltenes.

2. Materials and Methods

2.1. Resid Analysis

The feedstock employed for the slurry phase hydrocracking reactions in this study was sourced from TUPRAS and consisted of Iranian heavy vacuum residue (VR). This vacuum residue was derived during the processing of 100% Iranian Heavy crude oil, specifically originating from ASRFO and HVGO according to ASTM D1160, with a 95% cut point temperature at 550 °C. The VR exhibited a specific gravity of 1045.0 Kg/m^3 at 15 °C, corresponding to an API gravity of 3.9 as per EN-ISO-3675 standards.

2.2. Asphaltenes Isolation

The feedstock utilized in this investigation was Iranian Heavy Vacuum Residue (IHVR) acquired from TUPRAS. Notably, IHVR exhibited a pour point above room temperature, necessitating pre-treatment in an oven at 120 °C for 30 minutes to enhance its flowability. Following this, the residue was subjected to a precipitation process by combining it with n-heptane at a weight ratio of 1/40, after preheating. The emerging mixture was stirred at 60°C and subsequently cooled with consistent stirring for six hours. Post-stirring, the solution was kept overnight, leading up to a filtration step. The filtrate was then processed to extract maltenes by evaporating the n-heptane. For the isolation of asphaltene, the technique of Soxhlet extraction was employed.

In total, ten separate experiments were conducted to obtain asphaltene from Iranian heavy vacuum residue, yielding asphaltene content variations ranging from 13% to 13.5%. The comprehensive analysis of these experiments revealed that the average asphaltene content for Iranian heavy oil residue stands at approximately 13.28%.

2.3. Materials

For the catalyst experiments, high-purity chemicals were utilized. These comprised 99.5% $FeSO_4 \cdot 7H_2O$ and 99% Al_2O_3 from Merck. Additionally, >99% Fe_2O_3, 98% CaO, and 99% SiO_2 were procured from Sigma-Aldrich. Elemental sulfur with a purity of 99.8% was sourced from TUPRAS for the studies. In assessing the coke yield, reagents of elevated purity, like 99% n-heptane and >99.5% carbon disulfide from Merck, and >99.7% toluene from Sigma-Aldrich, were employed. For molecular weight assessments, 99% tetrahydrofuran, obtained from Merck, was used. Soxhlet extraction was conducted using cellulose cartridges measuring 28x80 mm provided by Macherey Nagel.

2.4. Structural Analysis

Elemental characterization was performed using the Thermo Finnigan Flash EA 1112 Series Elemental Analyzer. In this procedure, helium served as the carrier gas, while a 2 mg sample was combusted in the presence of oxygen at 1000 °C. The outcomes from this analysis are detailed in Table 1.

Table 1. Iranian asphaltene analysis

Elemental Analysis	C (%)	H (%)	S (%)	N (%)	O (%)
	75.52	7.39	4,86	1.18	1,05
GPC Analysis	Mn (g/mol)			Mw (g/mol)	
	1422			3826	
SARA Analysis	Saturates (%)	Aromatic (%)	Resin (%)	Asphaltene (%)	
	25	45	17	13	

For molecular weight assessments, the Agilent 1200 series Gel Permeation Chromatography (GPC) instrument was employed. A Zorbax column measuring 300 x 7.5 mm, packed with mixed gel, was employed, and refractive index detection was utilized. Tetrahydrofuran served as both the solvent and carrier phase, and the analysis involved injecting 20 µl of the sample at a volumetric rate of 1 ml/min, as detailed in Table 1.

For the ^{1}H-NMR analysis, a Varian UNITY INOVA 500MHz NMR spectrometer was utilized. A 0.5 ml solution of chloroform (CDCl3) was employed as the solvent for dissolving 5 mg of the IRHV sample, as shown in Figure 1.

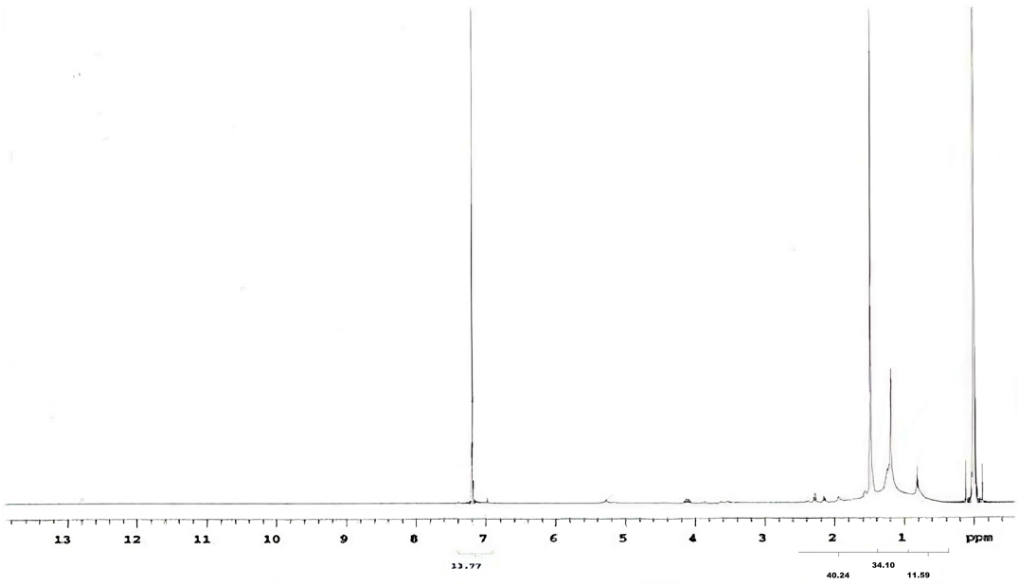

Figure 1. ^{1}H-NMR analysis of Iranian asphaltene

2.5. Methods

2.5.1. Pre-treatment

$FeSO_4 \cdot 7H_2O$ underwent a drying procedure for an hour at 120 °C in an oven. Following this, the metal oxides and $FeSO_4 \cdot 7H_2O$ were combined in a 1:1 weight ratio and transferred to a Retsch PM 400 ball mill for blending. After approximately 20 minutes of milling, the mixtures were subjected to sieving via a Retsch AS 450 analytical sieve shaker. Catalyst precursor materials that were within the 50-325 mesh size range, corresponding to 45 microns to 300 microns, were preserved in sealed desiccators for subsequent use in hydrocracking reactions. Additionally, elemental sulfur was milled using the Retsch PM 400 ball mill.

2.5.2. Reactors

The hydrocracking reactions were conducted within 10 ml batch tubing bomb reactors, each consisting of two distinct sections. The upper section was equipped with a D-Pro high-pressure needle valve, linked to 1/4 inch stainless steel Swagelok tube fittings. For effective mixing of the reaction contents, a metal ball with a diameter of 9.5 mm was placed inside the reactor, achieving a stirring speed of 200 rpm.

2.5.3. Reactions Procedure

The reactors were conventionally loaded with 0.5 g of Iranian heavy oil asphaltene along with 0.025 grams of catalyst precursors. Before commencing the reaction, the reactor was subjected to a purging procedure,

consisting of five cycles alternating between nitrogen and hydrogen. Following this, the reactor was pressurized with hydrogen to reach 100 bars and the shut-off valve was secured. Subsequently, the complete reactor setup was submerged in a Yigitsan fluidized sand bath pre-set at 425°C.

Once the reaction had proceeded for 90 minutes, the reactor was promptly removed from the sand bath and rapidly cooled by immersing it in cold water for about 10 minutes. After this rapid cooling, the reactor setup was left to stabilize at ambient temperature for around 30 minutes.

Precise measurements of the reactor's weight were undertaken, and gas yield was ascertained upon opening the high-pressure needle valve, followed by re-weighing. The gas products underwent analysis using Gas Chromatography. A Soxhlet extraction was performed employing 28x80 mm cellulose cartridges, utilizing toluene as the extracting solvent. The residual solid, comprising both coke and the catalyst, was weighed. The toluene-soluble fraction was computed by deducing the weights of the gas and solid residues from the starting weight of the reaction mixture.

3. Results and Discussion

3.1. Structural Analysis Results

The spectral analysis reveals distinctive regions associated with various structural elements. The area encompassing chemical shifts up to 1 ppm is indicative of approximately 11.57% methyl groups. Within the range of 1 to 1.7 ppm, the spectrum reflects a substantial presence of methylene branching, accounting for approximately 34.1% of the structural composition. Furthermore, the region spanning from 2.1 to 2.4 ppm suggests the prevalence of α-methyl branching, constituting approximately 40.56% of the structural features. Signals within the chemical shift range of 2.4 to 3.5 ppm correspond to the presence of CH and CH_2 methylene groups proximate to aromatic ring structures. In the higher chemical shift region, specifically between 7 and 8 ppm, signals correspond to the existence of two and three-ringed structural motifs.

3.2. Catalyst Performance Results

The mixing ratios of the precursors used in the study are shown in Table 2. Table 3 provides a comprehensive overview of the masses of reactants and the percentages of products. This encompasses the initial mass of the mixture containing resid and catalyst precursors, the amount of H_2 consumed, and the weight percentages of the resultant coke, gas, and the toluene-soluble fraction (TSF) products. It is noteworthy that the utilization of the $FeSO_4 \cdot H_2O+SiO_2$ mixture as a catalyst precursor yields the lowest coke yield, with a noteworthy achievement of a 10% coke yield.

Table 2. Mixing ratios of the precursors

Reaction No	Precursor Used	Asphaltene (g)	Asphaltene / Precursor	Precursor (g)
1	Without precursor	0.5	-	-
2	$FeSO_4.H_2O$	0.5	20	$FeSO_4.H_2O$:0.025
3	$FeSO_4.H_2O+Fe_2O_3$	0.5	20	$FeSO_4.H_2O$:0.0125; Fe_2O_3:0.0125
4	$FeSO_4.H_2O+Al_2O_3$	0.5	20	$FeSO_4.H_2O$:0.0125; Al_2O_3:0.0125
5	$FeSO_4.H_2O$+CaO	0.5	20	$FeSO_4.H_2O$:0.0125; CaO:0.0125
6	$FeSO_4.H_2O+SiO_2$	0.5	20	$FeSO_4.H_2O$:0.0125; SiO_2:0.0125
7	$Fe_2O_3+Al_2O_3$+S	1.0	10	Fe_2O_3:0.02; Al_2O_3:0.02; S:0.06
8	$Fe_2O_3+Al_2O_3+SiO_2$+S	1.0	10	Fe_2O_3:0.025; Al_2O_3:0.025; SiO_2:0.025; S:0.025
9	Maltene+Fe_2O_3+S	1.0	10	Maltene:1.00; Fe_2O_3:0.02; S:0.08

Table 3. Asphaltene slurry hydrocracking reactions products

Reaction No	Precursor Used	Asphaltene + Precursor Mass (g)	H_2 mass (g)	Coke (%)	Gas (%)	TSF (%)
1	Without precursor	0.500	0.140	36.9	11.0	52.1
2	$FeSO_4.H_2O$	0.525	0.140	33.0	30.0	37.0
3	$FeSO_4.H_2O+Fe_2O_3$	0.525	0.120	25.1	26.0	48.9
4	$FeSO_4.H_2O+Al_2O_3$	0.525	0.130	36.5	44.3	19.2
5	$FeSO_4.H_2O+CaO$	0.525	0.140	25.4	53.0	21.6
6	$FeSO_4.H_2O+SiO_2$	0.525	0.100	23.0	62.5	14.5
7	$Fe_2O_3+Al_2O_3+S$	1.100	0.130	27.0	41.0	32.0
8	$Fe_2O_3+Al_2O_3+SiO_2+S$	1.100	0.140	19.0	25.0	56.0
9	$Maltene+Fe_2O_3+S$	2.100	0.140	37.3	54.1	8.6

The existing literature provides accounts of hydrocracking reactions involving heavy oil fractions that transpire under diverse sets of conditions. These conditions encompass a wide spectrum of temperature, pressure, and residence time, and the reactions are typically carried out using catalysts like $NiMo/Al_2O_3$, $CoMo/Al_2O_3$, and NiW/SiO_2-Al_2O_3 in tubular fixed-bed reactors or continuous stirred-tank reactors (CSTRs). The range of hydrocracking temperatures investigated spans from 340 to 500°C, while the associated pressures have been explored within the range of 70 to 125 bars. Moreover, the residence times have been observed to range from 10 minutes to 3 hours.

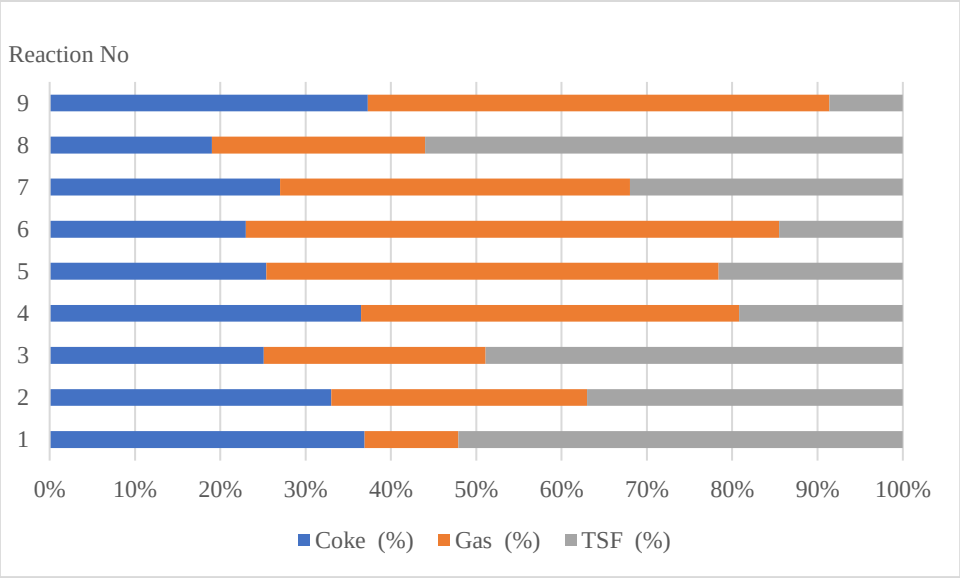

Figure 2. Slurry hydrocracking reactions products

In many commercial hydrocracking facilities, the primary feedstock is HVGO, and the heavier components of the crude oil often remain uncracked. In this research, asphaltene derived from Iranian heavy oil residue was subjected to experimentation within a laboratory-scale batch slurry reactor. The primary objective was to identify the most efficient, cost-effective, and easily prepared catalyst. Several precursor options were explored, including $FeSO_4 \cdot H_2O$, its binary mixtures with metal oxides (Fe_2O_3, Al_2O_3, CaO, SiO_2), and combinations of Fe_2O_3, Al_2O_3, and SiO_2 with elemental sulfur. The slurry hydrocracking reactions products are shown in Figure 2. The resulting product mixture was systematically separated into its gas, liquid, and solid components, and the yields of each product category were quantified individually. Remarkably, the lowest coke yield was achieved when using $Fe_2O_3+Al_2O_3+SiO_2+S$ as a precursor.

In typical commercial hydrocracking processes, the focus is on producing middle distillate products such as kerosene and diesel from HVGO, and coke formation is rarely observed during these reactions. In the context of residue cracking, however, coke formation poses a significant challenge due to its potential to obstruct

reactor systems, even though it is the least valuable product. Asphaltene, as a primary constituent, is recognized as a key factor contributing to coke formation. Consequently, the primary aim of this study was to minimize coke formation, while the secondary goal was to maximize the yield of middle distillate fractions. The experimental results demonstrated that the toluene-soluble fraction (TSF), which includes the middle distillate portion, can be increased to a maximum of 56% while concurrently reducing the coke yield to 19%, down from the initial 36.9% when no precursor was used.

4. Conclusion

In exploring the hydrocracking of asphaltenes from Iranian heavy oil residue, this research illuminated the profound impact of precursors on both product yield and the reduction of by-products, specifically coke. Using a lab-scale batch slurry reactor, the experimentation shed light on the advantages of strategically choosing and combining precursors. Remarkably, the combination of Fe_2O_3, Al_2O_3, SiO_2, and elemental sulfur yielded the most optimal results, minimizing coke formation to a significant degree. Given the inherent challenges associated with coke, which can hinder reactor operations and offers limited economic returns, this outcome is particularly noteworthy. Furthermore, the study also highlighted the potential to elevate the yield of the toluene-soluble fraction (TSF), which includes the desired middle distillate fractions. The peak achievement was a boost in TSF to an impressive 56%, while simultaneously slashing the coke yield from its initial 36.9% (without precursor) to 19%. These findings, therefore, not only further the understanding of asphaltene hydrocracking dynamics but also suggest a potential pathway to optimizing commercial hydrocracking processes, emphasizing the judicious choice of catalysts and precursors.

Author Contributions

The first and second authors conducted statistical evaluations, gathered the data, and authored the manuscript. The third author formulated and planned the analysis. This paper is derived from the second author's master's thesis, supervised by the third author.

Conflicts of Interest

All the authors declare no conflict of interest.

Acknowledgement

This word was supported by the Scientific Research Projects Coordination Unit of Istanbul University-Cerrahpaşa, Grant number: 22746.

References

[1] A. Kitous, Z. Vrontisi, B. Saveyn, T. Vandyck, *Impact of low oil prices on the EU economy*, JRC Technical Reports (2015) EUR 27537 EN.

[2] A. Marafi, H. Albazzaz, M. S. Rana, *Hydroprocessing of heavy residual oil: Opportunities and challenges*, Catalysis Today 329 (2019) 125–134.

[3] M. T. Nguyen, D. L. T. Nguyen, C. Xia, T. B. Nguyen, M. Shokouhimehr, S. S. Sana, A. N. Grace, M. Aghbashlo, M. Tabatabaei, C. Sonne, S. Y. Kim, S. S. Lam, Q. V. Le, *Recent advances in asphaltene transformation in heavy oil hydroprocessing: Progress, challenges, and future perspectives,* Fuel Processing Technology 213 (2021) 106681.

[4] M. Yasar, D. M. Trauth, M. T. Klein, *Asphaltene and resid pyrolysis. 2. The effect of reaction environment on pathways and selectivities*, Energy & Fuels 15 (2001) 504–509.

[5] M. L. Chacón-Patiño, C. Blanco-Tirado, J. A. Orrego-Ruiz, A. Gómez-Escudero, M. Y. Combariza, *Tracing the compositional changes of asphaltenes after hydroconversion and thermal cracking processes by high-resolution mass spectrometry*, Energy & Fuels 29 (10) (2015) 6330–6341.

[6] Y. Zhao, Y. Yu, *Kinetics of asphaltene thermal cracking and catalytic hydrocracking*, Fuel Processing Technology 92 (2010) 977–982.

[7] M. A. Suwaid, M. A. Varfolomeev, A. A. Al-Muntaser, C. Yuan, V. L. Starshinova, A. Zinnatullin, F. G. Vagizov, I. Z. Rakhmatullin, D. A. Emelianov, A. E. Chemodanov, *In-situ catalytic upgrading of heavy oil using oil-soluble transition metal-based catalysts*, Fuel 281 (2020) 118753.

[8] H. Yang, H. Yang, X. Yan, *Low-Temperature oxidation of heavy oil asphaltene with and without catalyst*, Molecules 27 (2022) 7075.

[9] T. A. Al-Attas, S. A. Ali, M. H. Zahir, Q. G. Xiong, S. A. AlBogami, Z. O. Malaibari, S. A. Razzak, M. M. Hossain, *Recent advances in heavy oil upgrading using dispersed catalysts*, Energy Fuels 33 (9) (2019) 7917−7949.

[10] S. Zhang, D. Liu, W. Deng, G. Que, *A review of slurry-phase hydrocracking heavy oil technology*, Energy & Fuels 21 (6) (2007) 3057–3062.

[11] M. A. Suwaid, M. A. Varfolomeev, A. A. Al-Muntaser, N. I. Abdaljalil, R. Djimasbe, N. O. Rodionov, A. Zinnatullin, F. G. Vagizov, *Using the oil-soluble copper-based catalysts with different organic ligands for in-situ catalytic upgrading of heavy oil*, Fuel 312 (2022) 12291.

[12] C. T. Tye, *Catalysts for hydroprocessing of heavy oils and petroleum residues*, in: R. M. Gounder (Ed.), Processing of Heavy Crude Oils - Challenges and Opportunities, IntechOpen, 2019, Ch. 13.

[13] R. Sahu, B. J. Song, J. S. Im, Y. P. Jeon, C. W. Lee, *A review of recent advances in catalytic hydrocracking of heavy residues*, Journal of Industrial and Engineering Chemistry 27 (2015) 12–24.

[14] A. V. Vakhin, M. A. Khelkhal, A. L. Maksimov, *Special Issue "Heavy Oil In Situ Upgrading and Catalysis"*, Catalysts 13 (1) (2023) 99.

[15] A. N. Mikhailova, A. A. Al-Muntaser, M. A. Suwaid, R. R. Zairov, I. T. Kadhim, R. Djimasbe, A. Dovzhenko, I. A. Bezkishko, A. Zinnatullin, D. A. Emelianov, R. S. Umarkulyevna, F. G. Vagizov, C. Yuan, M. A. Varfolomeev, *Ferrocene-based catalysts for in-situ hydrothermal upgrading of heavy crude oil: Synthesis and application*, Fuel 348 (2023) 128585.

[16] H. Fukuyama, S. Terai, *An active carbon catalyst prevents coke formation from asphaltenes during the hydrocracking of vacuum residue*, Petroleum Science and Technology 25 (1-2) (2007) 231–240.

[17] E. Bjambajav, Y. Ohtsuka, *Hydrocracking of asphaltene with metal catalysts supported on SBA-15*, Applied Catalysis A: General 252 (1) (2003) 193–204.

[18] S. A. Sitnov, I. I. Mukhamatdinov, D. A. Feoktistov, Y. V. Onishchenko, V. A. Sudakov, M. I. Amerkhanov, A. V. Vakhin, *Underground upgrading of the heavy crude oil in content-saturated sandstone with aquathermolysis in the presence of an iron based catalyst*, Catalysts 11 (2021) 1255.

Çanakkale Onsekiz Mart University

Journal of Advanced Research in Natural and Applied Sciences

dergipark.org.tr/tr/pub/jarnas

Open Access

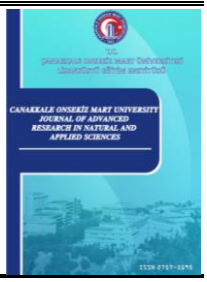

e-ISSN: 2757-5195 2024, Vol. 10, Issue 2, Pages: 252-271 doi.org/10.28979/jarnas.1337409

Evaluation of Blockchain Technology for Supply Chains using an Integrated Fuzzy Cognitive Map-QFD Methodology

Ayça Maden[1], Sadettin Emre Alptekin[2]

[1]Department of Industrial Engineering, Faculty of Engineering, Beykent University, İstanbul, Türkiye
[1]Department of Industrial Engineering, Faculty of Engineering, Galatasaray University, İstanbul, Türkiye

Article History
Received: 03 Aug 2023
Accepted: 14 Nov 2023
Published: 25 Jun 2024

Research Article

Abstract − The rapid advancement of technology has made it imperative for supply chains to adapt to the changing landscape. Blockchain technology holds immense potential to transform supply chain processes, but the challenge lies in identifying the most suitable blockchain characteristics to meet the various performance indicators of a supply chain. To overcome this challenge, this study aims to prioritize the most critical blockchain characteristics in a supply chain. The study adopts a two-stage Quality Function Deployment (QFD) methodology to rank blockchain characteristics based on supply chain and software requirements. The methodology evaluates the supply chain performance indicators using the Supply Chain Operations Reference (SCOR) model and software needs using the International Organization for Standardization (ISO) software quality characteristics. After determining the problematic SCOR and ISO software-related metrics, the study utilizes the QFD Stage 1 to obtain the weights of ISO software characteristics and employs the Fuzzy Cognitive Map (FCM) to determine the most crucial blockchain characteristics for QFD Stage 2. The results of this study show that the top priorities for blockchain characteristics in a supply chain are smart contract functionality, privacy, transaction per second, tokenization, security, permissioned network, scalability, cost, modularity, and licensing, in order of importance.

Keywords − *Blockchain, fuzzy cognitive map, fuzzy QFD, supply chain management*

1. Introduction

Supply chains must adapt their operations to fulfil the demands of their customers, which requires a harmonized approach that encompasses various processes, such as design, manufacturing, logistics, marketing, and more [1]. Technology serves as a crucial tool in advancing business processes [2]. As a novel technology, blockchain promises to disrupt the traditional methods of handling transactions and managing organizational processes [3]. By redesigning business processes to fully leverage the benefits of blockchain, organizations can attain greater efficiency [4]. To this end, it is important to thoroughly examine the blockchain characteristics relevant to supply chain processes. These characteristics encompass complex architectural, permission-related, and consensus-based elements that must be considered from multiple perspectives within the context of supply chains.

This study aims to prioritize the most significant blockchain technology characteristics for a supply chain. By utilizing a combination of supply chain and software-related metrics and problems, we employed an integrated FCM-QFD methodology in our examination. The integration of FCM into the QFD process reflects the complex relationships and trade-offs between blockchain characteristics. The processes within the supply chain are largely automated, thus requiring an increased focus on software to thoroughly address any supply

[1]aycamaden@beykent.edu.tr (Corresponding Author); [2]alptekin@gsu.edu.tr

chain-related problems. The current state of software characteristics and metrics within the supply chain is not well-defined, and utilizing organization-specific, non-standard quality frameworks, metrics, and models may pose difficulties in comparability [5]. Therefore, the problematic software quality characteristics were determined through the use of ISO/IEC 25010 [6] and ISO/IEC 25012 [7] standard quality characteristics in the supply chain.

Evaluating different dimensions of supply chain performance is crucial for the effective evaluation of blockchain technology. This is because supply chains are complex systems that encompass multiple processes, actors, and technologies. By using a range of performance metrics, supply chains can ensure that their technology evaluation is aligned with their specific goals and priorities. One of the key benefits of evaluating multiple performance dimensions is that it provides a more comprehensive view of the strengths and weaknesses of blockchain in the supply chain context. Studies on the application of blockchain technology in supply chain management have largely focused on a single dimension of performance, such as sustainability. For example, Bai and Sarkis [8] proposed a framework for sustainable supply chain transparency using hesitant fuzzy sets and regret theory. Yousefi and Tosarkani [9] evaluated the impact of blockchain technology on sustainable supply chain performance. Yadav et al. [10] evaluated the drivers of sustainable food security in India through blockchain technology, and Zkik et al. [11] evaluated the barriers and enablers of adopting blockchain for sustainable performance in e-enabled agriculture supply chains. Zhang and Song [12] evaluated the sustainability risks associated with blockchain adoption in sustainable supply chains. In the field of food supply chains, the impact of blockchain technology on performance has been explored, but with a limited focus on specific performance indicators [13]. Stranieri et al. [13] addressed this gap by evaluating the impact of blockchain technology on food supply chains in an exploratory manner. Kshetri [14] analyzed the mechanisms by which blockchain technology can support supply chain objectives, particularly regarding the roles of IoT in blockchain-based solutions and the degree of blockchain deployment for identity validation. The study also examined the potential impact of blockchain on primary supply chain management objectives such as cost, quality, speed, dependability, risk reduction, sustainability, and flexibility.

One of the key benefits of using standard characteristics and metrics is that they provide a common language and understanding for supply chain stakeholders. This promotes better communication and collaboration across the supply chain, leading to improved decision-making and increased operational efficiency. Furthermore, the use of standardized metrics facilitates benchmarking and enables organizations to identify best practices and opportunities for improvement. By providing a common language and consistent framework for performance evaluation, these standards support better communication, collaboration, and decision-making across the supply chain. Evaluating both supply chain metrics and software metrics is crucial in the assessment of blockchain technology in supply chains. Instead of evaluating them in isolation, it is important to take a holistic approach that considers both sets of metrics in a unified manner. This allows for a more comprehensive understanding of the interplay between the different metrics, leading to a more nuanced evaluation of the technology. The literature lacks studies that examine both supply chain and software performance indicators simultaneously through the application of standardized metrics and characteristics. In this study, the proposed methodology that integrates FCM and Fuzzy QFD evaluates a range of software issues and supply chain performance indicators. The indicators of the SCOR model and ISO quality models benefited.

The rest of the paper is organized as follows: Section 2 reviews the literature, and Section 3 outlines the methodology. Section 4 explains the application procedure, and Section 5 presents the conclusion.

2. Literature Review

2.1. Blockchain Technology and Supply Chain Management

Blockchain revolutionizes business models in many fields, particularly in logistics and supply chain management [8,14]. Blockchain applications improve the monitoring and screening performance of suppliers and provide verification claims about their products [15]. In supply chain activities, communication problem is generally intense [14]. This is precisely an issue satisfied thanks to blockchain technology in supply chains [14]. Numerous studies have been conducted on the topic of blockchain and supply chain management. Kamble et al. [16] identified key enablers of blockchain technology for supply chain applications using a combination of Interpretive Structural Modelling (ISM) and Decision-Making Trial and Evaluation Laboratory (DEMATEL) methods. The authors found that traceability was the most important reason for companies to adopt blockchain in agriculture supply chains. Korpela et al. [17] examined the disruptive potential of blockchain in digital supply chains, using QFD to translate integration requirements into system functionalities. Erol et al. [18] evaluated blockchain technology applicability in sustainable supply chains using an integrated method combining Fuzzy Stepwise Weight Assessment Ratio Analysis (SWARA), Complex Proportional Assessment (COPRAS), Evaluation based on Distance from Average Solution (EDAS) and COPELAND methods.

The utilization of standard software tools and performance metrics in evaluating blockchain technology for supply chains is important for its wider adoption. This is crucial because the use of standard metrics and tools will allow for comparison across different studies and applications of blockchain in supply chains, which will lead to a better understanding of its impact and how to optimize its implementation. The domain-independent software quality model ISO/IEC 25010 [6] helps ensure that the evaluation is based on widely accepted and recognized standards, which will increase the reliability and validity of the results. This will also encourage wider adoption of blockchain technology in supply chains as it demonstrates its potential benefits and helps address challenges. The choice of blockchain technology and its specific characteristics should align with the requirements and goals of the application in consideration of the trade-offs between performance, security, and scalability [19]. Trade-off analysis between blockchain characteristics is important for supply chains as it helps them make informed decisions about the implementation of blockchain technology. This analysis enables them to optimize their supply chain processes, improving efficiency, transparency, and security while also reducing costs. In a highly competitive business environment, the ability to effectively evaluate and manage the trade-offs between blockchain characteristics can give a supply chain a significant advantage, allowing it to remain competitive and respond effectively to changes in the market.

Evaluating the trade-offs between different blockchain characteristics is crucial for supply chain management. This is because blockchain is a complex technology that has a range of features, each of which may have different implications for the supply chain. For example, the transparency and security benefits of blockchain may come at the cost of scalability or data privacy. It is important to understand these trade-offs when evaluating the potential of blockchain for supply chain improvement. This helps organizations to identify the most appropriate use cases for blockchain, as well as the specific features and configurations that are best suited to their needs. For instance, a supply chain that prioritizes traceability and security may be better suited to a permissioned blockchain, which allows for the controlled sharing of data, while a supply chain that places greater emphasis on efficiency and scalability may be better suited to a more decentralized blockchain architecture. In literature, limited studies on the impact of blockchain on supply chain performance dimensions exist, with a narrow focus on specific supply chain performance indicators. Additionally, the current literature

on the intersection of supply chain and blockchain often uses domain-specific software characteristics, hindering comparison between different software systems. Most of the studies on blockchain characteristics do not deal with trade-offs between blockchain characteristics. A literature review of blockchain technology and supply chains is shown in Table 1 (N/A is an abbreviation for Not Available, and A is an abbreviation for Available).

Table 1. A brief literature review of blockchain technology and supply chains

Study	Supply Chain Performance	Focus area on Blockchain	Methods and Tools	Area	Blockchain Trade-offs	Standard Metrics/Features
[14]	Cost, speed, dependability, risk reduction, sustainability, flexibility	Supply chain management objectives	Multiple-case studies	Logistics, insurance etc.	N/A	N/A
[20]	N/A	Challenges in blockchain adoption	Grey-DEMATEL, fuzzy Delphi, WASPAS	Manufacturing	N/A	N/A
[8]	Sustainable supply chain transparency	A supply chain transparency and sustainability	Integrated hesitant fuzzy set and regret theory	N/A	N/A	N/A
[21]	Circular economy	Circular economy adoption barriers	QFD, Hesitant Fuzzy Linguistic Term Sets (HFLTS)	N/A	N/A	N/A
[9]	Sustainability	Blockchain benefits	Analytical hierarchical process	N/A	N/A	N/A
[22]	Sustainable food security	Blockchain drivers	Total Interpretive Structural Modelling, Fuzzy MICMAC, Fuzzy DEMATEL	Agriculture	N/A	N/A
[23]	Overall Supply Chain Performance	Blockchain-enabled supply chain	Simulation	N/A	N/A	N/A
[11]	Sustainability	Blockchain barriers	(CoCoSo) and (CRITIC), Pythagorean fuzzy sets	Agriculture	N/A	N/A
[24]	Sustainability	Blockchain barriers and enablers	Pythagorean Fuzzy sets (PFS), Cumulative Prospect Theory (CPT), and VIKOR	N/A	N/A	N/A
[25]	Efficiency, flexibility, responsiveness, food quality, and transparency of supply chains	Blockchain impact on agri-food supply chain performance	Case Study	Manufacturing	N/A	N/A
[26]	N/A	Blockchain barriers	Best worst method (BWM)	N/A	N/A	N/A
[16]	Sustainability	Blockchain enablers	Interpretive Structural Modelling (ISM), DEMATEL	Agriculture	N/A	N/A
[13]	Supply chain risks	Blockchain-enabled supply chain	Fuzzy analytical hierarchical processing (F-AHP)	Agri-food	N/A	N/A
[27]	Effective digital supply chain	Blockchain barriers	House of Quality, Intuitionistic fuzzy sets, Incomplete preferences	Food supply chain	N/A	N/A
[18]	Sustainability	Blockchain benefits	Fuzzy SWARA-COPRAS-EDAS and COPELAND	Agriculture	N/A	N/A
[28]	Sustainability	Sustainability risk assessment of blockchain adoption	Best-Worst Method (BWM), CoCoSo	Pharmaceutical, Fast moving consumer goods, Precious metals and automotive	N/A	N/A
[29]	N/A	Blockchain readiness	FCM, Fuzzy best–worst method (FBWM)	N/A	A	N/A
[12]	Sustainable supply chain	Blockchain adoption enablers	Network theory, FCM, Fuzzy data envelopment analysis	N/A	A	N/A
[30]	Cost, customer demand etc.	Blockchain's impact on the supply chain	Hesitant fuzzy cognitive map (HFCM), Probabilistic-linguistic fuzzy cognitive map (PL-FCM), Rough set cognitive map (RS-CM)	N/A	A	N/A

2.2. Blockchain Technology and Supply Chain Management

Blockchain technology is renowned for its complex characteristics, including its architectural design, permission types, and consensus mechanisms, making it challenging to comprehend and assess. Multiple studies have been conducted on evaluating blockchain characteristics through the application of Multi-Criteria Decision-Making (MCDM) methods. Maden and Alptekin [31] employed the use of Fuzzy DEMATEL to identify and evaluate the critical factors driving blockchain adoption in the logistics sector, based on the needs

of the company. As per the experts' assessments, the most significant factors influencing the adoption of blockchain technology, in order of priority were: cryptocurrency, instant money transfer, privacy, real-time processing, smart contract, security, authentication, transparency, immutability, traceability, distributed ledger, reduced delays, and peer-to-peer networks. Orji et al. [32] proposed a technology-organization-environment (TOE) structure for the critical factors that impact the successful adoption of blockchain in the freight logistics industry and prioritized them using the Analytic Network Process (ANP). They concluded that the three most important factors affecting blockchain technology adoption in the freight logistics sector are: the availability of specific blockchain tools, infrastructural facilities, and government policy and support.

Zarour et al. [33] conducted a study to evaluate the impact of various blockchain frameworks in healthcare management by gathering expert evaluations. They used Fuzzy ANP to determine the weights of the blockchain criteria and applied the Fuzzy TOPSIS method to evaluate blockchain alternatives. Tang et al. [34] conducted an extensive evaluation of public blockchains using the TOPSIS method to rank alternative public blockchains and the entropy method to calculate the weight of indicators. Garriga et al. [35] presented a conceptual framework aimed at supporting software architects, developers, and decision-makers in selecting the appropriate blockchain technology. They validated the framework through architectural trade-off analysis to evaluate real-world blockchain case studies. Farshidi et al. [36] proposed a decision framework for blockchain platform selection, modelling it as an MCDM problem and using the ISO/IEC 25010 [6] as a standard set of quality attributes. This domain-independent software quality model provides reference points for software systems. Mingxiao et al. [37] reviewed the fundamental principles and characteristics of blockchain consensus algorithms.

Decentralization is a crucial aspect of blockchain technology [38]. However, the decentralized nature of blockchain can hinder its performance concerning throughput and latency [39]. Immutability refers to the inability to alter or modify a thing over time, or for it to remain unchanged for a specific period [16]. The chain of cryptographic hashes connecting blocks in the blockchain ensures immutability for historical transactions [40]. However, practical challenges may arise in real-world blockchain systems, such as disputed transactions, wrong addresses, private key loss or disclosure, data entry errors, and unexpected changes to assets tokenized on the blockchain [40]. Advances in cryptography and computer science enable secure, encrypted operation of data-based applications through techniques like zero-knowledge proofs, homomorphic encryption, secure multiparty computation, and trusted execution environments [41]. These technologies are often utilized in blockchain-based use cases to maintain an audit trail of transactions between users [41]. However, businesses may not want to share data on public ledgers, or certain data may not be made public due to GDPR (General Data Protection Regulation) protections [42].

Blockchain is a decentralized database that is highly tamper-resistant, designed to operate in extreme byzantine environments, and has a dominant design target of security [43,44]. It has scalability limits, such as the size of data, transaction processing rate, and latency of data transmission [19]. Smart contracts and cryptographic tokens are used to digitize assets and currencies in blockchain [16,45]. Deciding which data and computation to keep on-chain or off-chain can affect the blockchain's scalability and performance [46,47]. Off-chain data storage can provide more computation power, data storage, and lower costs [19,46]. Cryptographic tokens can only be accessed with a private key and can only be signed by that key [45].

In a permissioned blockchain, only authorized participants can take part in network operations with their revealed identity [48]. Permissionless blockchains have a large network size with low transaction capacity, while permissioned blockchains have a small network size with high transaction capacity [48]. The consensus algorithm is crucial in maintaining the security and efficiency of blockchains [37] as it is used to agree on the

value of data among many nodes in a distributed framework [49]. TPS (Transactions Per Second) measures the speed of the platform or network in processing transactions, while block time or latency refers to the delay in approving transactions and adding them to a block [49]. The block is then joined to the blockchain [49]. A double-spending attack occurs when the same amount of money is attempted to be spent multiple times [49]. After inspecting the literature in detail, the architecture, permission type, consensus mechanism, and other characteristics of blockchain were summarized in Table 2.

Table 2. Blockchain characteristics

Architectural	Decentralization [35,38]
	Immutability [19]
	Privacy [35,41]
	Security [35,36,43,50,51]
	Performance & Scalability [19,35,51]
	Cost [35,51]
	Smart contract functionality [16,35,52]
	On-chain transactions [36,47]
	Off-chain transactions [36,47]
	Tokenization [36,45]
Permission Type	Permissioned blockchain [36,45,51]
	Permissionless blockchain [36,45,51]
	Governance [45]
	Participation [36,45]
	Transparency [45]
	Network size [45]
	Transaction capacity [19,45]
Consensus Mechanism	Transaction per second (TPS) [37,53,54]
	Verification speed/Block verification time [37,54]
	Double spending [54]
	Throughput [37,53,54]
	Adversary tolerance (Fault tolerance) [37,53,54]
Other Features	Blockchain data structure [19,39]
	Non-blockchain data structure [39]
	Enterprise system integration [36,55]
	API support [51,55]
	Popularity [36,51]
	Licensing [51,55]
	Community support [51,55]
	Modularity [55]
	Ease of use [51,55]

In the literature, studies related to blockchain have generally focused on the consensus mechanism or architectural characteristics of blockchain. However, with this study, we have summarized blockchain characteristics more comprehensively, as shown in Table 2. This is because the evaluation of blockchain technology in supply chains requires the assessment of other diverse characteristics such as enterprise system integration and ease of use.

The trade-off between performance and security can be managed by choosing the appropriate consensus mechanism, network architecture, and permission type [37]. Some consensus mechanisms, such as Proof of Work (PoW), require a lot of computational resources and can lead to high energy consumption, which can hinder performance [48]. It is also important to consider scalability in blockchain applications as more users and transactions can increase the latency and overhead of the system [42]. The scalability can be improved by

implementing techniques such as sharding, where the network is divided into smaller components to handle transactions in parallel [35]. The choice of blockchain technology and its specific characteristics should align with the requirements and goals of the application in consideration of the trade-offs between performance, security, and scalability [19].

3. Materials and Methods

In this study, we employed an integrated FCM-QFD methodology to evaluate supply chain-related and software-related problems. To accomplish this, we leveraged the SCOR) a modelling approach to address the vague and imprecise process and metric definitions commonly present in a typical supply chain scenario. The SCOR model enabled us to identify the problematic performance metrics for an engineer-to-order supply chain. For software-related problems, we relied on ISO standards to determine the problematic quality characteristics. After determining the problematic SCOR performance metrics and software characteristics, we utilized them in QFD Stage 1 to obtain the weights of technical characteristics.

The blockchain technology characteristics were gathered from the literature, specifically for use in the supply chain context (refer to Table 2). At this stage, we used FCM to determine the most critical blockchain characteristics, as it can showcase both positive and negative relationships between these characteristics. Subsequently, we calculated the QFD Stage 2 correlations and combined the results with those obtained from FCM to obtain the QFD Stage 2 technical characteristics' weights. The cross-functional and multi-staged structure of QFD allowed us to reflect both supply chain and software-related problems in the evaluation process of blockchain characteristics. The methodology we proposed is depicted in Figure 1.

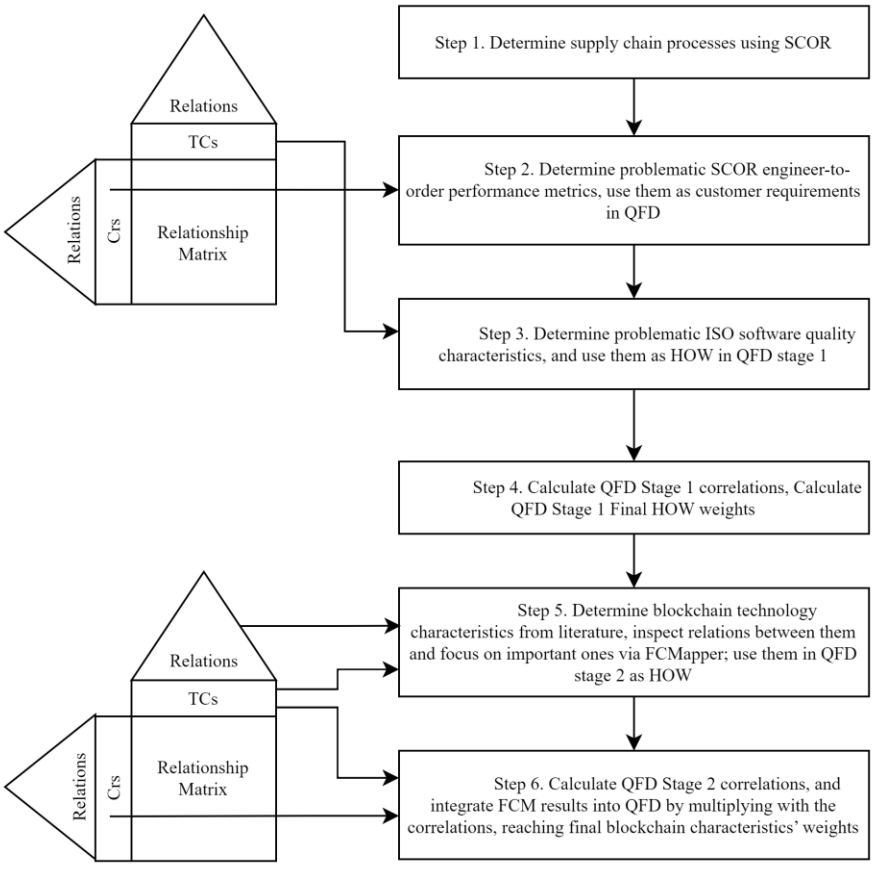

Figure 1. Methodology of the study

3.1. Models and Standards

3.1.1. SCOR Model and Performance Metrics

The Supply Chain Operations Reference (SCOR) is a widely recognized reference model that classifies business processes based on six fundamental management processes, including plan, source, make, deliver, return, and enable [56]. It consists of four levels, with the first level defining the scope and content, the second level dividing management processes into process alternatives (e.g., make-to-stock, make-to-order, engineer-to-order), and the third level serving as the basis for describing the supply chain performance metrics [57].

SCOR's performance component consists of two parts: performance attributes and metrics. A performance attribute is comprised of metrics used to describe a strategy [56], while typical SCOR metrics include reliability, responsiveness, agility, cost, and assets. The choice of supply chain performance metrics can be made using a process-based approach that takes into consideration the specific characteristics of a project and the requirements of stakeholders [57]. In this study, the SCOR 11.0 model [56] was utilized.

3.1.2. Software Quality Models

The software engineering domain contains a variety of quality models, including McCall's [58] (McCall et al., 1977), Boehm's [59], FURPS [60], Dromey's [61], and ISO 25010 [6]. Additionally, there exist several frameworks and procedures that enable the assessment of software architecture suited for specific purposes. In this study, we utilized ISO 25010 due to it being the most recent quality model constructed on an international agreement.

3.1.3. SQuaRE Standards Family

The Software Quality Requirements and Evaluation (SQuaRE) framework comprise three quality models that provide a comprehensive evaluation of software systems: quality in use, product quality, and data quality. The quality-in-use model, as described in ISO/IEC 25010 [6], evaluates both computer systems and software products in actual use. The product quality model, as described by Nakai et al. [5], assesses the extent to which critical software requirements such as performance, usability, and maintainability are met. The data quality model, as defined by ISO/IEC 25012 [7], evaluates how well the data meets the needs specified by the product owner. The data quality characteristics are divided into two categories: inherent data quality and system-dependent data quality.

In this study, we utilized all three SQuaRE quality models to conduct a broad evaluation of existing supply chain software systems. Our findings revealed that incorporating ISO data product quality characteristics into the evaluation proved beneficial when considering data-related concerns such as data cybersecurity and compliance with the General Data Protection Regulation (GDPR) data protection law.

3.2. Methods

3.2.1. Fuzzy Quality Function Deployment (QFD)

The objective of a House of Quality (HOQ) is to determine the relative importance of design requirements based on the perceived importance of customer needs and the correlation between customer requirements and design requirements [62]. QFD has been widely applied in various fields, including software systems, production, supply chain, service, and communication. QFD, a cross-disciplinary process involving teams

from design engineering, manufacturing engineering, marketing, and others, has found widespread application in sectors such as software systems, production, supply chain, service, and communication [63,64]. It serves as a potent tool in development activities, particularly when addressing quality concerns [65]. As a quality management method, QFD undergoes continuous challenges, refinements, and developments, akin to other techniques within the quality management toolkit [66].

Unlike conventional quality frameworks that aim to minimize negative quality in the product, QFD centers on maximizing positive quality by incorporating customer requirements into product design from the conceptual phase [65]. The competitive advantage of QFD lies in its structured implementation of strategic concepts [67]. The protection of customers' voices ensures that customer requirements remain unaltered during the development phase, thereby safeguarding the voice of the customer in the design features [67]. In this study, QFD has been employed in conjunction with fuzzy expressions at various QFD stages.

3.2.2. Fuzzy Cognitive Map (FCM)

The FCMs (Fuzzy Cognitive Maps) are robust but simple tools that utilize fuzzy logic to model dynamic networks [68]. The original cognitive maps considered the values of concepts and connection matrices to be negative, positive, or neutral. Kosko [69] built upon this study by incorporating fuzzy causality into the directed edges and concepts. Various MCDM methods such as ANP, DEMATEL, and FCM can demonstrate relationships between concepts [70]. However, FCM has the advantage of being able to display both positive and negative relationships between criteria. The steps of the technique are as follows [71]:

Step 1: Aggregation of fuzzy weights of the attributes. The arithmetic mean of the fuzzy weights taken from decision-makers is computed as:

$$\widetilde{w}_p = \frac{\sum_i^s \widetilde{w}_{pi}}{\mathrm{s}}, p \in \{1,2,3,\cdots,n\} \tag{3.1}$$

The $\widetilde{w}_{pi}$ values represent the aggregated fuzzy weights.

Step 2: Normalization of the crisp weight vector. The centroid method is usually preferred because of its simplicity. This method is applied using the following formula,

$$\mathrm{Centroid}(\tilde{A}) = \frac{l+m+u}{3} \tag{3.2}$$

The normalized crisp weight vector (nw_p), is computed using (3.3),

$$nw_p = \frac{w_p}{\sum_{i=1}^n w_i} \tag{3.3}$$

The FCMs are versatile tools that can be easily adapted by adding new concepts and relationships or by altering the weight of causal linkages [72]. Furthermore, FCM models can be made more manageable by simplifying them. Homenda et al. [73] analyzed the effects of removing weak relationships or concepts a posteriori. As a result, the map can be pruned iteratively by eliminating weights weaker than thresholds of 0.2, 0.4, and 0.6. Weights that fall below these threshold values can be considered insignificant and set to zero, indicating the absence of relationships. In our study, we pruned the map by removing weights weaker than a threshold of 0.5. This helped simplify the FCM model, as larger maps are challenging to interpret and apply.

3.2.2.1. Establishing FCM Structure

As the first step, initial concept values are determined using the normalized weight vector as in (3.4) [71]:

$$\left(C_{MA_1}^{t=0} \quad ..C_{MA_p}^{t=0}.. \quad C_{MA_n}^{t=0}\right) = \left(nw_1 ..nw_p ..nw_n\right) \tag{3.4}$$

where $C_{MA_i}^{t=0}$ is the concept value of the *i*th main attribute when t = 0.

Then, fuzzy influence matrices, which are taken from a group of decision-makers are aggregated,

$$\tilde{e}_{ji}^{MA} = \frac{\sum_{u=1}^{s} \tilde{e}_{jiu}^{MA}}{S} \tag{3.5}$$

where $\tilde{e}_{ji}^{MA}$ shows the aggregated fuzzy influence matrix of the main attributes. Finally, aggregated fuzzy weights are defuzzified, and the aggregated crisp influence matrix e_{ji}^{MA} is calculated.

3.2.2.2. Simulating FCMs and Obtaining the Final Weights

After establishing the FCM structure, first, the parameters of the activation function are specified. Different activation (threshold) functions can be utilized for this purpose. In this study, the sigmoidal function was chosen for its ability to produce outcome values ranging from 0 to 1, which can be used as criteria weights without any additional transformation. During the FCM simulation process, the dynamic behavior of the relationships is determined using (3.6).

$$C_{MA_i}^{t+1} = f\left(C_{MA_i}^{t} + \sum_{\substack{j=1 \\ j=1}}^{n} e_{ji}^{MA} \times C_{MA_j}^{t}\right) \tag{3.6}$$

where $C_{MA_i}^{t}$ is the concept value of the *i*th main attribute at time *t*.

Next, the steady-state concept values are normalized, and the final steady-state weights of the primary attributes are determined:

$$w_i = \frac{C_{MA_i}}{\sum_{i=1}^{n} C_{MA_i}} \tag{3.7}$$

The final step of the process is to calculate the crisp weights. It is an open-licensed Excel macro developed by Michael Bachhofer and Martin Wildenberg [74]. In this study, the FCM method provided a means to prioritize the most important characteristics of blockchain technology, and also evaluate the trade-offs between different characteristics through the use of FCM analysis.

3.3. Application

The purpose of this study is to prioritize the most important blockchain characteristics to be implemented in the supply chain of a case company. The case company utilizes state-of-the-art technology and industry expertise to support global mechanical and plant engineering projects. Through cutting-edge technology, it provides customer-specific integrated automation solutions, offering a comprehensive range of products and services required by the industry. Moreover, the company's experts offer unique services and resources

throughout the project lifecycle, from design to project realization. The company is committed to delivering customer-specific products with precise timing, quality, and quantity while emphasizing cost efficiency. Given the diverse nature of customer demands, the company strives to ensure diversity in all aspects. Unfortunately, the company fell short of its performance targets in the procurement processes, where challenges were particularly pronounced. To address the issues the company faces, we propose using blockchain technology as a solution. The prioritization of blockchain characteristics will be based on the company's strategy, which is centered around reliability, responsiveness, cost, and agility. The study's results will help the company make informed decisions about which blockchain characteristics to implement in its supply chain to achieve its performance targets.

To prioritize the blockchain characteristics for the company's supply chain, it would be helpful to first assess the current challenges and pain points in the procurement process. This could include issues with transparency, traceability, and collaboration between different supply chain partners. Once these issues have been identified, the most relevant blockchain characteristics can be prioritized based on their ability to address the specific problems at hand. For example, if the issue is a lack of trust between supply chain partners, then a blockchain with strong security and privacy features would be more important. If the issue is a lack of transparency and traceability, then a blockchain with robust data sharing and tracking capability would be more critical. In addition, factors such as scalability, cost-effectiveness, and ease of integration with existing systems should also be considered.

To prioritize blockchain characteristics for the supply chain, this study analyzed software-related issues by conducting an application study in the company. The company experienced issues such as security breaches, responsiveness problems, and compliance issues. The study conducted an interview-based discovery with stakeholders such as the company, customers, procurement personnel, and software developers to gather information. Each time, an assessment was carried out by a committee comprising three experts who have significant experience within the supply chain, each with more than five years of expertise. For the QFD Stage 1, the evaluation committee consists of a customer representative, a procurement personnel, and a software developer. For QFD Stage 2, the committee comprises three software stakeholders from the supply chain. These distinct committees have been formed due to the requirement for different expertise for each QFD stage. The methodology followed the steps outlined in Figure 1. In Step 1, we determined the supply chain processes using SCOR. For the case supply chain, the engineer-to-order approach is chosen. In Step 2, we determined the problematic engineer-to-order performance metrics. The metrics' representation values include RS (Responsiveness), CO (Cost), AG (Agility), and RL (Reliability). Among these metrics, the problematic six metrics are identified as Select Supplier and Negotiate Cycle Time (RS.3.125), Percent of the Orders/Lines Received Defect Free (RL.3.19), Sourcing Automation Cost (CO.3.006), Identify Sources of Supply Cycle Time (RS.3.35), Material Risk, and Compliance Cost (CO.3.012), and Demand sourcing-supplier constraints (AG.3.46). These metrics were used in QFD Stage 1 as customer requirements.

In Step 3, considering the supply chain's software problems, we evaluated the supply chain's existing software systems using all three quality models of the SQuaRE. We used ISO/IEC 25022 (Measurement of quality in use), ISO/IEC 25023 (Measurement of system and software product quality), and ISO/IEC 25024 (Measurement of data quality) to define and quantitatively evaluate the quality measures. Considering the measures and related performance gaps from their targets, the identified problematic software product quality, quality in use, and data quality sub-characteristics are summarized in Table 3.

Table 3. Problematic product quality, quality in use and data quality sub-characteristics

Sub-characteristics	Measures
Time behaviour	*Mean response time, Response time adequacy, Mean turnaround time, Turn-around time adequacy, Mean throughput
Resource Utilization	*Mean processor utilization, Mean memory utilization, Mean I/O devices utilization, Bandwidth utilization
Fault tolerance	*Failure avoidance, Redundancy of components, Mean fault notification time
Confidentiality	*Access controllability, Data encryption correctness, Strength of cryptographic algorithms
Compliance	*Regulatory compliance due to technology
Modularity	*Coupling components
Modifiability	*Modification correctness
Functional Completeness	*Functional correctness

The determined problematic 8 software characteristics were: resource utilization, time behavior, fault tolerance, confidentiality, compliance, modularity, modifiability, and functional completeness, respectively. These characteristics were used in QFD Stage 1 as technical characteristics. In Step 4, we calculated QFD Stage 1 correlations.

The determined SCOR Level 3 metrics of AG.3.46, CO.3.006, CO.3.012, RS.3.35, RS.3.125, and RL.3.19 were used, respectively, in the customer requirements part of QFD Stage 1. Aggregated evaluations of decision-makers using the 6 SCOR metrics and 8 ISO characteristics can be seen in Table 4. After the aggregation, we multiplied the SCOR metrics' weights with the aggregated correlation values. The normalized QFD Stage 1 final HOW weights of ISO characteristics can be seen in Table 5.

Table 4. Aggregated evaluations of decision-makers

	1	2	3	4	5	6	7	8
1	0.600	0.600	0.300	0.900	0.300	0.300	0.300	0.900
2	0.800	0.500	0.400	0.500	0.600	0.600	0.500	0.800
3	0.400	0.400	0.300	0.900	0.400	0.300	0.300	0.900
4	0.600	0600	0.500	0.500	0.600	0.600	0.500	0.600
5	0.800	0.800	0.500	0.500	0.500	0.600	0.600	0.600
6	0.500	0.500	0.400	0.600	0.500	0.500	0.500	0.500

Table 5. Normalized QFD Stage 1 final HOW weights of ISO characteristics

1	2	3	4	5	6	7	8
0.146	0.130	0.096	0.116	0.087	0.137	0.128	0.159

In Step 5, we determined blockchain characteristics and found the most significant ones using FCM. After inspecting the literature, we summarized 31 blockchain characteristics, including blockchain data structure, non-blockchain data, permissioned network, permissionless network, smart contract functionality, privacy, off-chain transactions, on-chain transactions, security, TPS, cost, community support, scripting language, governance, scalability, cryptocurrency support, tokenization, licensing, popularity, enterprise system integration, ease of use, modularity, API support, adversary fault tolerance, verification speed, block time, double spending, transparency, network size, transaction capacity, and participation, respectively. We inspected positive and negative relationships between these 31 blockchain characteristics.

In evaluating the positive and negative relationships between blockchain design requirements, we considered both the legal and architectural characteristics of blockchain technology. For example, the inability to delete data under GDPR laws was seen as a major barrier to the adoption of blockchain technology in the supply chain. Hence, on-chain transactions may limit privacy in the supply chain, especially when legal issues are significant. Permissioned blockchains, with their identity-shown characteristics and efficient network management, were seen as a more suitable solution compared to permissionless blockchains.

After determining the relations between blockchain characteristics as shown in Table 6, we aggregated and defuzzified the fuzzy influence matrix. Steady-state concept values were reached in 9 iterations using the FCMapper, as presented in Table 7. In Table 7, columns indicate blockchain characteristics, while rows indicate iterations. The final normalized weights of the blockchain characteristics can be seen in Table 8.

Table 6. Positive and negative relations between blockchain characteristics

Relation Type	**Relation Pair**
Positive relations	1-8;1-16;1-24;1-26;3-6;3-9;3-14;4-28;4-29;4-31;5-11;5-13;5-17;7-2;7-6;7-15;8-1;8-9;9-14;9-18;10-25;10-26;13-5;14-3;14-4;14-6;14-7;14-9;14-12;15-10;15-30;16-11;16-17;16-19;18-21;20-22;20-23;22-6;22-21;23-20;24-9;25-10;25-26;29-31
Negative relations	1-15;3-28;3-29;3-30;3-31;4-6;4-9;4-14;4-30;6-28;7-9;8-6;8-15;9-27;9-28;14-28;18-11;24-27;28-6

Table 7. Steady-state concept values

	1	2	3	4	5	6	7	8	9	10	11	12	13	14	15	16
1	0.750	0.750	0.832	0.750	0.846	0.858	0.750	0.750	0.968	0.917	0.900	0.750	0.750	0.711	0.832	0.750
2	0.695	0.695	0.779	0.695	0.797	0.840	0.695	0.695	0.943	0.882	0.863	0.695	0.697	0.666	0.783	0.695
3	0.682	0.682	0.765	0.682	0.783	0.836	0.682	0.682	0.935	0.870	0.850	0.682	0.685	0.658	0.768	0.682
4	0.679	0.679	0.761	0.679	0.780	0.835	0.679	0.679	0.932	0.867	0.846	0.679	0.682	0.657	0.764	0.679
5	0.679	0.679	0.760	0.678	0.779	0.835	0.678	0.679	0.932	0.866	0.845	0.678	0.681	0.656	0.763	0.679
6	0.678	0.678	0.760	0.678	0.778	0.834	0.678	0.678	0.932	0.866	0.845	0.678	0.681	0.656	0.763	0.678
7	0.678	0.678	0.760	0.678	0.778	0.834	0.678	0.678	0.932	0.866	0.845	0.678	0.681	0.656	0.763	0.678
8	0.678	0.678	0.760	0.678	0.778	0.834	0.678	0.678	0.932	0.866	0.845	0.678	0.681	0.656	0.763	0.678
9	0.678	0.678	0.760	0.678	0.778	0.834	0.678	0.678	0.932	0.866	0.845	0.678	0.681	0.656	0.763	0.678

	17	18	19	20	21	22	23	24	25	26	27	28	29	30	31
1	0.917	0.832	0.750	0.731	0.750	0.769	0.750	0.750	0.750	0.750	0.450	0.500	0.769	0.550	0.622
2	0.882	0.804	0.695	0.675	0.696	0.714	0.695	0.695	0.699	0.695	0.359	0.400	0.703	0.481	0.548
3	0.871	0.797	0.682	0.663	0.683	0.700	0.682	0.682	0.687	0.682	0.349	0.383	0.686	0.473	0.536
4	0.867	0.795	0.679	0.660	0.680	0.697	0.679	0.679	0.684	0.679	0.349	0.381	0.682	0.473	0.534
5	0.866	0.795	0.679	0.659	0.679	0.696	0.678	0.679	0.684	0.679	0.350	0.381	0.681	0.473	0.534
6	0.866	0.795	0.678	0.659	0.679	0.696	0.678	0.678	0.684	0.679	0.351	0.381	0.681	0.474	0.534
7	0.866	0.795	0.678	0.659	0.679	0.696	0.678	0.678	0.684	0.679	0.351	0.381	0.681	0.474	0.534
8	0.866	0.795	0.678	0.659	0.679	0.696	0.678	0.678	0.684	0.678	0.351	0.381	0.681	0.474	0.534
9	0.866	0.795	0.678	0.659	0.679	0.696	0.678	0.678	0.684	0.678	0.351	0.381	0.681	0.474	0.534

Table 8. Normalized weights of the blockchain characteristics

1	2	3	4	5	6	7	8	9	10	11	12	13	14	15	16
0.0317	0.0317	0.0356	0.0317	0.0364	0.0390	0.0317	0.0317	0.0436	0.0405	0.0395	0.0317	0.0319	0.0307	0.0357	0.0317

17	18	19	20	21	22	23	24	25	26	27	28	29	30	31
0.0405	0.0372	0.0317	0.0308	0.0318	0.0326	0.0317	0.0317	0.0320	0.0317	0.0164	0.0178	0.0319	0.0222	0.0250

Table 9. Steady-state concept values

	1	2	3	4	5	6	7	8	9	10
1	0.731	0.731	0.917	0.858	0.818	0.668	0.731	0.870	0.832	0.731
2	0.675	0.675	0.874	0.809	0.766	0.603	0.675	0.822	0.794	0.675
3	0.663	0.663	0.860	0.794	0.751	0.590	0.663	0.807	0.782	0.663
4	0.660	0.660	0.857	0.790	0.747	0.588	0.660	0.803	0.779	0.660
5	0.659	0.659	0.856	0.789	0.746	0.588	0.659	0.802	0.778	0.659
6	0.659	0.659	0.856	0.789	0.746	0.588	0.659	0.801	0.777	0.659
7	0.659	0.659	0.855	0.788	0.746	0.588	0.659	0.801	0.777	0.659
8	0.659	0.659	0.855	0.788	0.746	0.588	0.659	0.801	0.777	0.659

Table 10. Normalized weights of the blockchain characteristics

1	2	3	4	5	6	7	8	9	10
0.092	0.092	0.119	0.110	0.104	0.082	0.092	0.111	0.108	0.092

Table 11. QFD Stage 2 defuzzified correlation values

	1	2	3	4	5	6	7	8	9	10
1	0.400	0.600	0.400	0.400	0.700	0.900	0.600	0.400	0.600	0.200
2	0.800	0.700	0.200	0.200	0.900	0.600	0.700	0.400	0.200	0.200
3	0.300	0.900	0.800	0.800	0.500	0.500	0.500	0.600	0.100	0.100
4	0.500	0.800	0.900	0.900	0.500	0.500	0.500	0.800	0.100	0.100
5	0.600	0.800	0.800	0.800	0.500	0.500	0.500	0.400	0.200	0.200
6	0.600	0.600	0.500	0.500	0.600	0.600	0.600	0.400	0.200	0.900
7	0.900	0.700	0.400	0.300	0.700	0.700	0.900	0.400	0.200	0.600
8	0.500	0.900	0.400	0.400	0.200	0.200	0.300	0.800	0.100	0.300

Table 12. Normalized QFD Stage 2 HOW weights without cognitive map effect

1	2	3	4	5	6	7	8	9	10
0.112	0.144	0.101	0.098	0.111	0.109	0.111	0.103	0.043	0.066

Table 13. Final QFD Stage 2 HOW weights with cognitive map effect

1	2	3	4	5	6	7	8	9	10
0.104	0.133	0.121	0.109	0.116	0.090	0.103	0.115	0.047	0.061

4. Results and Discussion

After obtaining the steady-state concept values for the 31 blockchain characteristics, we calculated their normalized weights by dividing each characteristic value by the total of the steady-state values. These weights were used to prioritize the 10 blockchain characteristics. The characteristics with a normalized weight equal to or greater than the average value (0.0322) were considered for further analysis. The 10 prioritized characteristics were: permissioned network, smart contract functionality, privacy, security, TPS, cost, scalability, tokenization, licensing, and modularity, respectively.

To further understand the inter-relationships between these characteristics, we used FCMapper with the previously determined aggregated relationships. Using the same aggregated relationships of blockchain characteristics, we activated the 10 characteristics by setting the other characteristics' values to 0 in FCMapper. The steady-state concept values for these characteristics can be seen in Table 9, and their normalized weights are listed in Table 10.

In Step 6, we calculated QFD Stage 2 correlations and integrated the FCM results into QFD by multiplying them with the correlations. After taking the fuzzy correlation values of three decision-makers in QFD Stage 2, we defuzzified them. QFD Stage 2 defuzzified correlation values can be seen in Table 11. After calculating the final QFD Stage 1 HOWs' weights, we used them in QFD Stage 2 as new customer requirements. After finding the QFD Stage 2 defuzzified correlation values, we multiplied them using the values obtained through QFD Stage 1 final weight. Here, the result of this multiplication does not include relationships between blockchain characteristics. Normalized QFD Stage 2 HOW weights without and with FCM effect can be seen in Tables 12 and 13, respectively.

In summary, we used a combination of QFD and FCM to prioritize and rank the most important blockchain characteristics for supply chain use. Considering the values in Table 13, this multiplication increased the QFD Stage 2 weights of privacy, security, TPS, tokenization, and licensing. However, the multiplication decreased the weights of permissioned network, smart contract functionality, cost, scalability, and modularity. Seeing

Table 13, the most important blockchain characteristics are, in the order of priority: smart contract functionality, privacy, TPS, tokenization, security, permissioned network, scalability, cost, modularity, and licensing. The current and alternative technologies can be compared against these characteristics to determine their suitability for supply chain use.

5. Conclusion

Evaluating both supply chain and software metrics in a unified approach is crucial for assessing blockchain technology in supply chains. In the existing literature, there are few comprehensive investigations into the influence of blockchain on various dimensions of supply chain performance, primarily concentrating on specific performance indicators. In this study, an attempt is made to explore the diverse impact of blockchain technology on various supply chain performances, aiming to address the existing gap in the literature. Moreover, the present body of literature examining the convergence of supply chain and blockchain frequently relies on software characteristics specific to certain domains, making it challenging to compare different software systems. In this study, an effort has been made to fill the relevant gap in the literature by utilizing standardized performance metrics. Thanks to the use of these standardized metrics, blockchain technology will become more comprehensible and comparable with different technologies. Many studies on blockchain characteristics also neglect to address the trade-offs that may exist between these characteristics. The objective of this research is to determine the key characteristics of blockchain technology that hold the utmost importance for a supply chain. Our approach involves the integration of supply chain and software-related metrics and issues, employing a unified FCM-QFD methodology for analysis. The incorporation of FCM into the QFD process is indicative of the intricate relationships and trade-offs inherent in blockchain characteristics. Examining the trade-offs among the characteristics of blockchain technology could contribute to a better understanding of this technology by supply chains. In this study, the integration of FCM and QFD provided a comprehensive evaluation of the performance metrics, resulting in a prioritized list of blockchain characteristics. The use of FCM allowed for a thorough evaluation of the complex relationships and trade-offs between blockchain characteristics, considering stakeholders' differing opinions. With the advancement of blockchain technology, the characteristics may become outdated, and future studies may need to consider new trade-offs arising from changes in blockchain structure or regulations like GDP.

The evaluation of multiple performance dimensions in supply chains is of paramount importance when assessing blockchain technology. It is crucial to employ a diverse set of performance metrics that align with the specific goals and objectives of the supply chain. Standardized characteristics and metrics offer several benefits for supply chain stakeholders. Firstly, they provide a shared language and understanding, promoting better communication and collaboration. Secondly, standardized metrics allow for benchmarking and identifying best practices and areas for improvement, leading to better decision-making and operational efficiency. In this study, the SCOR modelling approach was used to address ambiguous and indistinct process and metric definitions in supply chain scenarios. To evaluate software-related issues, ISO standards were used to determine essential quality characteristics.

While this study assessed KPIs in the context of the overall projects of the case company, it is advisable to update and modify KPIs dynamically in response to changes in the business environment. Our evaluation of performance metrics primarily considered their understandability, measurability, and unambiguity. However, a more comprehensive evaluation can be achieved by examining criteria such as specificity, relevancy, verifiability, and comparability. Utilizing a Multi-Criteria Decision Making (MCDM) method can help weigh these criteria for the selection of appropriate performance metrics.

Although the linguistic evaluations in the created committees were conducted by three stakeholders each, the competence of the stakeholders in their respective fields deemed this number sufficient. However, increasing the number of stakeholders could lead to more reliable results. In addition to this, quality models enable the consideration of characteristics that hold significance for various stakeholders, including system integrators, acquirers, software developers, users, and more. In our case study, the software stakeholders were primarily software developers, who possessed expertise in software product quality, data product quality, and quality in use. However, it is crucial to involve all types of stakeholders, ranging from software developers to end-users, in the process of determining the quality characteristics that should be incorporated into a system.

Our study acknowledges the presence of uncertainty due to subjectivity in human judgments. The determination of the increase or decrease in SCOR performance metrics relied on subjective judgments, introducing uncertainty. Our future research will delve into a more detailed examination of the extent to which metrics deviate from their target values, employing data-driven modelling for a more accurate analysis.

Various blockchain characteristics were summarized to demonstrate the wide range of specific use cases in a supply chain context. The use of a threshold value for prioritizing characteristics in the FCM may not be necessary if fewer characteristics are considered, and different threshold values can be used for comparison purposes. This research primarily concentrated on assessing the procurement process. In future studies, we intend to expand our evaluations to encompass various processes beyond procurement. Additionally, our assessments will incorporate supply chain metrics from different companies within the case supply chain. Because the performance assessment of a supply chain necessitates the joint evaluation of performance metrics coming from various functions of multiple companies.

Author Contributions

The second author conceived and designed the analysis. The first author collected data and performed the analysis. This paper is derived from the first author's doctoral dissertation supervised by the second author. They all read and approved the final version of the paper.

Conflicts of Interest

All the authors declare no conflict of interest.

References

[1] Y. D. Hwang, Y. C. Lin, J. Lyu Jr, *The performance evaluation of SCOR sourcing process—The case study of Taiwan's TFT-LCD industry*, International Journal of Production Economics 115 (2) (2008) 411–423.

[2] I. Bashir, Mastering Blockchain, Packt Publishing, Birmingham, 2017.

[3] J. Mendling, I. Weber, W. V. D. Aalst, J. V. Brocke, C. Cabanillas, F. Daniel, S. Debois, C. D. Ciccio, M. Dumas, S. Dustdar, A. Gal, L. García-Bañuelos, G. Governatori, R. Hull, M. L. Rosa, H. Leopold, F. Leymann, J. Recker, M. Reichert, H. A. Reijers, S. Rinderle-Ma, A. Solti, M. Rosemann, S. Schulte, M. P. Singh, T. Slaats, M. Staples, B. Weber, M. Weidlich, M. Weske, X. Xu, L. Zhu, *Blockchains for business process management-challenges and opportunities*, ACM Transactions on Management Information Systems (TMIS) 9 (1) (2018) 1–16.

[4] F. Milani, L. Garcia-Banuelos, *Blockchain and principles of business process re-engineering for process innovation* (2018) 15 pages, https://doi.org/10.48550/arXiv.1806.03054.

[5] H. Nakai, N. Tsuda, K. Honda, H. Washizaki, Y. Fukazawa, *A SQuaRE-based software quality evaluation framework and its case study*, in: A. Alphones, R. Gupta, M. Ong (Eds.), IEEE Region 10 Conference (TENCON), Singapore, 2016, pp. 3704–3707.

[6] ISO/IEC 25010, Systems and software engineering – Systems and software quality requirements and evaluation (SQuaRE) – System and software quality models, 2011.

[7] ISO/IEC 25012, Systems and software quality requirements and evaluation (SQuaRE) – Data quality model, 2008.

[8] C. Bai, J. Sarkis, *A supply chain transparency and sustainability technology appraisal model for blockchain technology*, International Journal of Production Research 58 (7) (2020) 2142–2162.

[9] S. Yousefi, B. M. Tosarkani, *An analytical approach for evaluating the impact of blockchain technology on sustainable supply chain performance*, International Journal of Production Economics 246 (2022) 108429.

[10] V. S. Yadav, A. R. Singh, R. D. Raut, N. Cheikhrouhou, *Blockchain drivers to achieve sustainable food security in the Indian context*, Annals of Operations Research 327 (2023) 211–249.

[11] K. Zkik, A. Belhadi, S. A. Rehman Khan, S. S. Kamble, M. Oudani, F. E. Touriki, *Exploration of barriers and enablers of blockchain adoption for sustainable performance: implications for e-enabled agriculture supply chains*, International Journal of Logistics Research and Applications 26 (11) (2023) 1498–1535.

[12] F. Zhang, W. Song, *Sustainability risk assessment of blockchain adoption in the sustainable supply chain: An integrated method*, Computers & Industrial Engineering 171 (2022) 108378.

[13] S. Stranieri, F. Riccardi, M. P. Meuwissen, C. Soregaroli, *Exploring the impact of blockchain on the performance of agri-food supply chains*, Food Control 119 (2021) 107495.

[14] N. Kshetri, *1 Blockchain's roles in meeting key supply chain management objectives*, International Journal of Information Management 39 (2018) 80–89.

[15] Q. Zhu, M. Kouhizadeh, *Blockchain technology, supply chain information, and strategic product deletion management*, IEEE Engineering Management Review 47 (1) (2019) 36–44.

[16] S. S. Kamble, A. Gunasekaran, R. Sharma, *Modeling the blockchain enabled traceability in agriculture supply chain*, International Journal of Information Management 52 (2020) 101967.

[17] K. Korpela, J. Hallikas, T. Dahlberg, *Digital supply chain transformation toward blockchain integration*, Proceedings of the 50th Hawaii International Conference on System Sciences, Hawaii, 2017, 4182–4191.

[18] I. Erol, I. M. Ar, I. Peker, *Scrutinizing blockchain applicability in sustainable supply chains through an integrated fuzzy multi-criteria decision-making framework*, Applied Soft Computing 116 (2022) 108331.

[19] X. Xu, I. Weber, M. Staples, L. Zhu, J. Bosch, L. Bass, C. Pautasso, P. Rimba, *A taxonomy of blockchain-based systems for architecture design*, 2017 IEEE International Conference on Software Architecture (ICSA), Gothenburg, 2017, 243–252.

[20] K. Karuppiah, B. Sankaranarayanan, S. M. Ali, *A decision-aid model for evaluating challenges to blockchain adoption in supply chains*, International Journal of Logistics Research and Applications 26 (3) (2023) 257–278.

[21] I. Erol, I. M. Ar, I. Peker, C. Searcy, *Alleviating the impact of the Barriers to circular economy adoption through blockchain: An investigation using an integrated MCDM-based QFD with hesitant fuzzy linguistic term sets*, Computers & Industrial Engineering 165 (2022) 107962.

[22] A. A. Mukherjee, R. K. Singh, R. Mishra, S. Bag, *Application of blockchain technology for sustainability development in agricultural supply chain: Justification framework*, Operations Management Research 15 (2022) 46-61.

[23] C. Ozturk, A. Yildizbasi, *Barriers to implementation of blockchain into supply chain management using an integrated multi-criteria decision-making method: A numerical example*, Soft Computing 24 (19) (2020) 14771-14789.

[24] F. Longo, L. Nicoletti, A. Padovano, G. d'Atri, M. Forte, *Blockchain-enabled supply chain: An experimental study*, Computers & Industrial Engineering 136 (2019) 57–69.

[25] X. Han, P. Rani, *Evaluate the barriers of blockchain technology adoption in sustainable supply chain management in the manufacturing sector using a novel Pythagorean fuzzy-CRITIC-CoCoSo approach*, Operations Management Research 15 (3-4) (2022) 725–742.

[26] A. Budak, V. Çoban, *Evaluation of the impact of blockchain technology on supply chain using cognitive maps*, Expert Systems with Applications 184 (2021) 115455.

[27] S. Khan, M. K. Kaushik, R. Kumar, W. Khan, *Investigating the barriers of blockchain technology integrated food supply chain: A BWM approach*, Benchmarking: An International Journal 30 (3) (2022) 713–735.

[28] S. Dua, M. G. Sharma, V. Mishra, S. D. Kulkarni, *Modelling perceived risk in blockchain-enabled supply chain utilizing fuzzy-AHP*, Journal of Global Operations and Strategic Sourcing 16 (1) (2023) 161–177.

[29] M. Irannezhad, S. Shokouhyar, S. Ahmadi, E. I. Papageorgiou, *An integrated FCM-FBWM approach to assess and manage the readiness for blockchain incorporation in the supply chain*, Applied Soft Computing 112 (2021) 107832.

[30] G. Büyüközkan, G. Tüfekçi, D. Uztürk, *Evaluating Blockchain requirements for effective digital supply chain management*, International Journal of Production Economics 242 (2021) 108309.

[31] A. Maden, E. Alptekin, *Evaluation of factors affecting the decision to adopt blockchain technology: A logistics company case study using Fuzzy DEMATEL*, Journal of Intelligent & Fuzzy Systems 39 (5) (2020) 6279–6291.

[32] I. J. Orji, S. Kusi-Sarpong, S. Huang, D. Vazquez-Brust, *Evaluating the factors that influence blockchain adoption in the freight logistics industry*, Transportation Research Part E: Logistics and Transportation Review 141 (2020) 102025.

[33] M. Zarour, M. T. J. Ansari, M. Alenezi, A. K. Sarkar, M. Faizan, A. Agrawal, R. Kumar, R. A. Khan, *Evaluating the impact of blockchain models for secure and trustworthy electronic healthcare records*, IEEE Access 8 (2020) 157959–157973.

[34] H. Tang, Y. Shi, P. Dong, *Public blockchain evaluation using entropy and TOPSIS*, Expert Systems with Applications 117 (2019) 204–210.

[35] M. Garriga, S. Dalla Palma, M. Arias, A. De Renzis, R. Pareschi, D. Andrew Tamburri, *Blockchain and cryptocurrencies: A classification and comparison of architecture drivers*, Concurrency and Computation: Practice and Experience 33 (8) (2021) e5992.

[36] S. Farshidi, S. Jansen, S. España, J. Verkleij, *Decision support for blockchain platform selection: Three industry case studies*, IEEE Transactions on Engineering Management 67 (4) (2020) 1109–1128.

[37] D. Mingxiao, M. Xiaofeng, Z. Zhe, W. Xiangwei, C. Qijun, *A review on consensus algorithm of blockchain*, in: A. Basu (Ed.), IEEE international conference on Systems, Man, and Cybernetics (SMC), Banff, 2017, 2567–2572.

[38] E. Bellini, Y. Iraqi, E. Damiani, *Blockchain-based distributed trust and reputation management systems: A survey*, IEEE Access 8 (2020) 21127–21151.

[39] C. Fan, S. Ghaemi, H. Khazaei, P. Musilek, *Performance evaluation of blockchain systems: A systematic survey*, IEEE Access 8 (2020) 126927–126950.

[40] S. K. Lo, X. Xu, Y. K. Chiam, Q. Lu, *Evaluating suitability of applying blockchain*, in: J. Zhao, B. Xu (Eds.), 22nd International Conference on Engineering of Complex Computer Systems (ICECCS), Fukuoka, 2017, 158–161.

[41] T. Lyons, L. Courcelas, Blockchain Use Cases in Health Care (2020), https://blockchain-observatory.ec.europa.eu/publications/blockchain-use-cases-healthcare_en, Accessed 3 Aug 2023.

[42] J. J. Hunhevicz, D. M. Hall, *Do you need a blockchain in construction? Use case categories and decision framework for DLT design options*, Advanced Engineering Informatics 45 (2020) 101094.

[43] S. Raval, Decentralized applications: Harnessing Bitcoin's blockchain technology, O'Reilly Media, Inc, 2016.

[44] A. Shahaab, B. Lidgey, C. Hewage, I. Khan, *Applicability and appropriateness of distributed ledgers consensus protocols in public and private sectors: A systematic review*, IEEE Access 7 (2019) 43622-43636.

[45] S. Voshmgir, Token economy: How blockchains and smart contracts revolutionize the economy, BlockchainHub Berlin, 2019.

[46] H. Y. Paik, X. Xu, H. D. Bandara, S. U. Lee, S. K. Lo, *Analysis of data management in blockchain-based systems: From architecture to governance*, IEEE Access 7 (2019) 186091-186107.

[47] X. Xu, C. Pautasso, L. Zhu, V. Gramoli, A. Ponomarev, A. B. Tran, S. Chen, *The blockchain as a software connector*, 13th Working IEEE/IFIP Conference on Software Architecture (WICSA), Venice, 2016, 182–191.

[48] Y. Xiao, N. Zhang, W. Lou, Y. T. Hou, *A survey of distributed consensus protocols for blockchain networks*, IEEE Communications Surveys & Tutorials 22 (2) (2020) 1432–1465.

[49] S. M. H. Bamakan, A. Motavali, A. B. Bondarti, *A survey of blockchain consensus algorithms performance evaluation criteria*, Expert Systems with Applications 154 (2020) 113385.

[50] J. Zou, B. Ye, L. Qu, Y. Wang, M. A. Orgun, L. Li, *A proof-of-trust consensus protocol for enhancing accountability in crowdsourcing services*, IEEE Transactions on Services Computing 12 (3) (2018) 429–445.

[51] S. Nanayakkara, M. N. N. Rodrigo, S. Perera, G. T. Weerasuriya, A. A. Hijazi, *A methodology for selection of a Blockchain platform to develop an enterprise system*, Journal of Industrial Information Integration 23 (2021) 100215.

[52] W. Viriyasitavat, D. Hoonsopon, *Blockchain characteristics and consensus in modern business processes*, Journal of Industrial Information Integration 13 (2019) 32–39.

[53] B. Xu, D. Luthra, Z. Cole, N. Blakely, EOS: An Architectural, Performance, and Economic Analysis (2018), https://blog.bitmex.com/wp-content/uploads/2018/11/eos-test-report.pdf, Accessed 3 Aug 2023.

[54] S. J. Alsunaidi, F. A. Alhaidari, *A survey of consensus algorithms for blockchain technology*, International Conference on Computer and Information Sciences (ICCIS), Aljouf, 2019, 1–6.

[55] M. Gord, J. Holek, Blockchain for Enterprises (2019), https://www.whatmatrix.com/comparison/Blockchain-for-Enterprise, Accessed 3 Aug 2023.

[56] APICS. Supply Chain Operations Reference Model (Revision 11.0) (2015), https://docs.huihoo.com/scm/supply-chain-operations-reference-model-r11.0.pdf, Accessed 3 Aug 2023.

[57] J. C. Cheng, K. H. Law, H. Bjornsson, A. Jones, R. D. Sriram, *Modeling and monitoring of construction supply chains*, Advanced Engineering Informatics 24 (4) (2010) 435–455.

[58] J. A. McCall, P. K. Richards, G. F. Walters, Factors in Software Quality (RADC TR-77-369) (1977),

https://apps.dtic.mil/sti/pdfs/ADA049014.pdf, Accessed 3 Aug 2023.

[59] B. W. Boehm, Characteristics of software quality, North-Holland Publishing Company, 1978.

[60] R. B. Grady, Practical software metrics for project management and process improvement, Prentice-Hall, Englewood Cliffs, 1992.

[61] R. G. Dromey, *Cornering the chimera [software quality]*, IEEE Software 13 (1) (1996) 33–43.

[62] C. Temponi, J. Yen, W. A. Tiao, *House of quality: A fuzzy logic-based requirements analysis*, European Journal of Operational Research 117 (2) (1999) 340–354.

[63] E. Haktanır, C. Kahraman, *A novel interval-valued Pythagorean fuzzy QFD method and its application to solar photovoltaic technology development*, Computers & Industrial Engineering 132 (2019) 361–372.

[64] S. Ç. Onar, G. Büyüközkan, B. Öztayşi, C. Kahraman, *A new hesitant fuzzy QFD approach: An application to computer workstation selection*, Applied Soft Computing 46 (2016) 1–16.

[65] N. O. Erdil, O. M. Arani, *Quality function deployment: More than a design tool*, International Journal of Quality and Service Sciences 11 (2) (2019) 142–166.

[66] Z. Iqbal, N. P. Grigg, *Enhancing voice of customer prioritisation in QFD by integrating the competitor matrix*, International Journal of Productivity and Performance Management 70 (1) (2020) 217–229.

[67] P. G. Brown, *QFD: Echoing the voice of the customer*, At&T Technical Journal 70 (2) (1991) 18–32.

[68] E. I. Papageorgiou, D. K. Iakovidis, *Towards the construction of intuitionistic fuzzy cognitive maps for medical decision making*, 9th International Conference on Information Technology and Applications in Biomedicine, Cyprus, 2009, 1–4.

[69] B. Kosko, *Fuzzy cognitive maps*, International Journal of Man-Machine Studies 24 (1) (1986) 65–75.

[70] S. Shokouhyar, N. Pahlevani, F. M. M. Sadeghi, *Scenario analysis of smart, sustainable supply chain on the basis of a fuzzy cognitive map*, Management Research Review 43 (4) (2019) 463–496.

[71] A. Baykasoğlu, İ. Gölcük, *Alpha-cut based fuzzy cognitive maps with applications in decision-making*, Computers & Industrial Engineering 152 (2021) 107007.

[72] A. Jetter, W. Schweinfort, *Building scenarios with fuzzy cognitive maps: An exploratory study of solar energy*, Futures 43 (1) (2011) 52–66.

[73] W. Homenda, A. Jastrzebska, W. Pedrycz, *Time series modeling with fuzzy cognitive maps: Simplification strategies. IFIP International Conference on Computer Information Systems and Industrial Management*, Springer, Berlin, Heidelberg, 2015, 409–420.

[74] FCMapper, FCMapper - Fuzzy Cognitive Mapping Software Solution, http://www.fcmappers.net/joomla/, Accessed 3 Aug 2023.

Çanakkale Onsekiz Mart University

Journal of Advanced Research in Natural and Applied Sciences

dergipark.org.tr/tr/pub/jarnas

Open Access

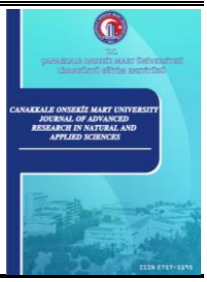

e-ISSN: 2757-5195 2024, Vol. 10, Issue 2, Pages: 272-284 doi.org/10.28979/jarnas.1350766

Optical and Electrical Characterization of Crystallized M:WO_3 (Cu, Fe, Ni) Films in Acidic Medium

Emin Yakar[1], Irmak Karaduman Er[2], Fatma Sarf[3]

[1]Department of Materials Science and Engineering, Faculty of Engineering, Çanakkale Onsekiz Mart University, Çanakkale, Türkiye
[2]Department of Medical Services and Techniques, Eldivan Medical Services Vocational School, Çankırı Karatekin University, Çankırı, Türkiye
[3]Çan Vocational School, Çanakkale Onsekiz Mart University, Çanakkale, Türkiye

Article History

Received: 27 Aug 2023

Accepted: 21 Nov 2023

Published: 25 Jun 2024

Research Article

Abstract − Pure and metal (M) doped [copper (Cu), nickel (Ni) and iron (Fe)] WO_3 films have been produced on In:SnO_2 (ITO) slides by using facile chemical bath deposition and then annealed at 500 ºC for 2 h. Structural, morphological, electrical and optical properties of the produced WO_3-based films were examined. Monoclinic WO_3 phase were observed in all the samples, and the peak intensities were decreased by metal inclusion with heterogeneous film growth on ITO substrate. Slight shifts from defect related emission peaks (blue and green) were observed in metal-substituted WO_3 samples from PL study. An optical band gap was observed to decrease in M:WO_3 samples. The surface resistance values were significantly reduced by metal additives compared to its pure counterpart, especially by the inclusion of nickel ions in WO_3. The results indicated that nucleus growth and thereby impurity/defect-related surfaces had a serious effect on the optical and electrical properties of M:WO_3 films.

Keywords − *Chemical bath deposition, electrical, optical, WO_3 film*

1. Introduction

In the past decade, metal oxide semiconductor structures of all dimensions (0D, 1D, 2D and 3D) have been often studied to use in many technological fields such as gas sensors [1], supercapacitors [2], solar cells [3] and magnetic memory devices [4]. Thanks to their numerous advantages, they have been proposed as an alternative to silicon-based technology. Regardless of the technological field in which it is used, properties of metal oxides such as low cost, abundance in nature, simple production, high chemical stability and versatile approach have stood out [5]. In order to find their advanced applications, it is important to understand these materials by conducting extensive research. Improvement in the using field is mostly achieved by low concentration of elements or oxygen vacancy doping [6] and hetero-/homojunction construction with adding C-based material [7] which have a high impact on the crystal growth and surface forms.

As an unique metal oxide material, tungsten trioxide (WO_3) has an oxygen-deficient n-type wide band gap of around 2.6-3 eV, high work function, enhanced specific surface area and the fast recombination of photogenerated electron-hole pairs of WO_3 [8,9]. The compounds between tungsten and oxygen are quite numerous and complex. For example, in fully oxidized tungsten oxide compounds, W metal gets +6 valency and forms 4 octahedrons with oxygen.

With its gradually improving optical and electrical properties, different type WO_3 structures (nanorods,

[1]eyakar@comu.edu.tr (Corresponding Author); [2]irmakkaradumaner@karatekin.edu.tr; [3]fatmaozutok@comu.edu.tr

nonosheets, thin films) were synthesized for a variety of applications such as photodedectors [10], organic light emitting diodes [11], electrochromic devices [12], and optoelectronic devices [13]. The choice of WO_3 production method is so important to obtain desired structures.

Among the thin film production methods, the chemical bath deposition provides the ability to be applied to large surfaces and allows the production of the necessary topographic, physical and crystallographic structures by making the necessary deposition optimization (solution type, precursor molarity, working temperature and etc.) [14]. Through the homogeneous or heterogeneous growth process could be controlled, the final product could be easily fabricated. For example, $H_2C_2O_4$ was used as a growth controller to regulate the growth process of the H_2WO_4 film formed on FTO substrate. Hence, three steps were proposed for homogeneous nanosheet WO_3 thin film growth by controlling the reactants amount [15].

It has been stated that film quality (adherency, thickness, homogeneous surface etc.) is mostly dependent on film production, which significantly affects the film growth process in many studies [16]. Among chemical type film production techniques (dip coating, chemical vapor deposition, spin coating etc.) chemical bath deposition is so attractive with its simplicity, no set-up and ability to expand to large surfaces

There are a lot of studies realized about hetero-atom doped WO_3 films [17]. In solar cell applications, element-doped WO_3 could promoting photocatalytic activity by extending the solar light response range and inhibiting the recombination of photogenerated charge carriers [18]. As a gas sensor sensing layer, 1 wt% Pt:WO_3 sensor exhibited quite low detection limit of 100 ppb at optimum operating temperature of 160 °C [19]. Binary metal components were dispersed into each other, which contributed to promoting the metal/metal electron interaction and adjusting the physicochemical properties of mixed metal oxides, according to transition metal doped WO_3 mixed oxides study of Chen et.al [20].

In this paper, we discuss the metal inclusion (Cu, Fe and Ni) effect on the electrical and optical properties of WO_3 films depending on changing surface morphology and lattice structure.

2. Materials and Methods

In this study, facile chemical bath deposition was used to produce M:WO_3 films and detailed production stages was explained in our previous study [21]. The chemicals used in the preparation of films were of high quality and purity (Sigma Aldrich, 99.9 %). Tungsten and metal sources were sodium tungsten dihydrate, nickel acetate tetrahydrate, iron chloride hexahydrate and copper acetate dihydrate.

All WO_3 films were coated on to In:SnO_2 (ITO) substrates after standard substrate cleaning. In 100 ml distilled water, homogenous aqueous solutions were obtained under Table 1 conditions to obtain different type metal doped WO_3 films. Complex agent (HCl) was added drop by drop and pH was kept constant throughout the experiment. Films were prepared in harsh acidic medium unlike a similar study to observe film growth process [22]. The pH value of the solution was 2 at room temperature. Finally, all films were annealed in air furnace under Table 1 condition.

Structural and morphological properties were investigated by X-ray powder diffraction (XRD; Rigaku Smart Lab x-ray diffractometer; CuKα radiation; 45 kV; 40 mA; step size 0.013º) and scanning electron microscopy (SEM; JEOL JSM- 7100F; Au-Pd ratio of 80-20 %), respectively. WO_3 thin films with and without additives coated on IDT, whose properties will be determined, were fixed on an aluminum substrate with 1×3 cm dimensions and 1 mm thickness. Thin films fixed on the aluminum substrate are placed in the measuring cell made of aluminum. The electrical contacts between the sample and the measuring cell are made using liquid

silver. The thickness was estimated by the weight difference method which is given our previous study [23]. The thickness of WO_3, Ni-doped WO_3, Fe-doped WO_3 and Cu-doped WO_3 were calculated as 800 nm, 500 nm, 600 nm and 930 nm, respectively.

Table 1. Deposition parameters of WO_3 films

Parameters	Values
pH	2
Working temperature	70±5 °C
Bath time	15 min.
Annealing temperature	500 °C
Annealing time	2 h

3. Results and Discussion

Figure 1 shown the 3D-AFM topography of synthesized WO_3 samples. It is clearly seen that the surface roughness has increased with nickel inclusion. Surface roughness (root-mean-square (rms)) values were 93.8-142 nm range for produced samples. Thick and heterogenous distribution particle on the substrate by metal inclusion indicates that the attraction force between the different metal atoms might increase and agglomerative or cluster forms might be occurs.

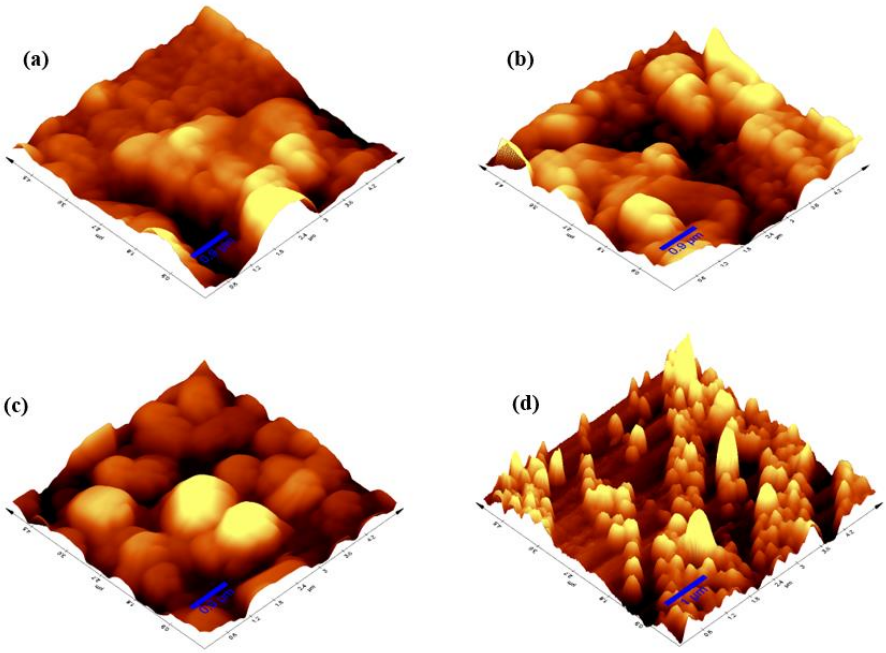

Figure 1. The AFM images of WO_3 (a), Cu:WO_3 (b), Fe:WO_3 (c) and Ni: WO_3(d)

Figure 2 depicted the x-ray diffraction peaks of WO_3 samples. Characteristic three monoclinic WO_3 polycrystalline phase peaks of (001), (020) and (200) were seen according to JCPDS Card No: 43-1035 [24]. ITO-based peak and W-related peak are observed in the 2θ= 65-70 and 2θ= 45°-50° range, respectively due to less crystal nuclei in harsh acidic medium and low adhesion of coating film on ITO [21,25]. The material with the significant change crystallization is the WO_3 sample with nickel included due to heterogeneous growth (caused by low dissolution of Ni-source) on ITO surface. The crystalline size were calculated by Debye-Scherrer equation from the below formula;

$$D = \frac{k\lambda}{\beta \cos\theta} \tag{3.1}$$

In Equation (3.1.), k is a numerical factor frequently referred to as the crystallite-shape factor, λ is the wavelength of the X-rays, β is the width (full-width at half-maximum) of the X-ray diffraction peak in radians and θ is the Bragg angle. The average crystalline size of the produced samples was calculated according to the preferred orientation of (110). The average crystalline size of samples was calculated 136, 133, 87 and 16 nm for pure WO_3, Fe:WO_3, Cu:WO_3 and Ni.WO_3, respectively. Apart from the peaks related to the substrate and tungsten, no second phase has been found. It indicates that metal atoms were placed in the host WO_3 structure however defects have enormous effect on the host lattice with shifting of typical WO_3 peaks which may be attributed to the development of additional growth centers by metal inclusion [26, 27]. Ionic radius of W^{6+}, Cu^{2+}, Fe^{2+} and Ni^{2+} are 62 nm [28], 73 nm [29], 64 nm [28], and 69 nm [24], ionic radius of selected metal atoms is higher than tungsten ionic radius. This may cause it difficult to replacement of W-M ions and thereby lattice damage increases.

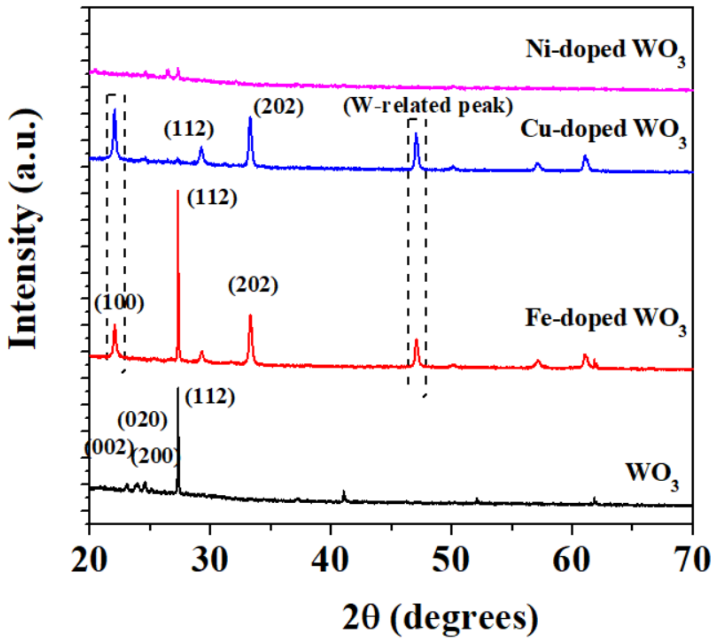

Figure 2. The x-ray diffraction (XRD) peak analysis of the produced pure and M:WO_3 films

To study the influence of defects in WO_3 host lattice photoluminescence (PL) was performed and PL spectra is deconvoluted into multi peaks with using Gaussian fitting. Figure 3 shows the PL analysis of pure and M:WO_3 films. A series of peaks are detected at 428, 427,429, 523, 560 and 687 nm which may be attributed to surface defects. It is clear that these emissions may be predicted by the recombination of free excitons [30]. Furthermore, it is interesting to find that the intensity of light in the range of 510-687 nm changes with the hetero-crystal growth. Blue emission peak at around 428 nm and green emission peak approximately at 523 nm were observed in pure WO_3, which correlated to similar studies [27]. Emission peaks broadening and shifting were observed in metal included WO_3 samples (especially in Ni:WO_3 sample) due to recombination of electron-hole pairs attributed to oxygen vacancies, self-trapped excitons states and surface defects/states [31,32].The PL peak intensity of WO_3 is increased by copper inclusion with a similar crystal structure of host WO_3.

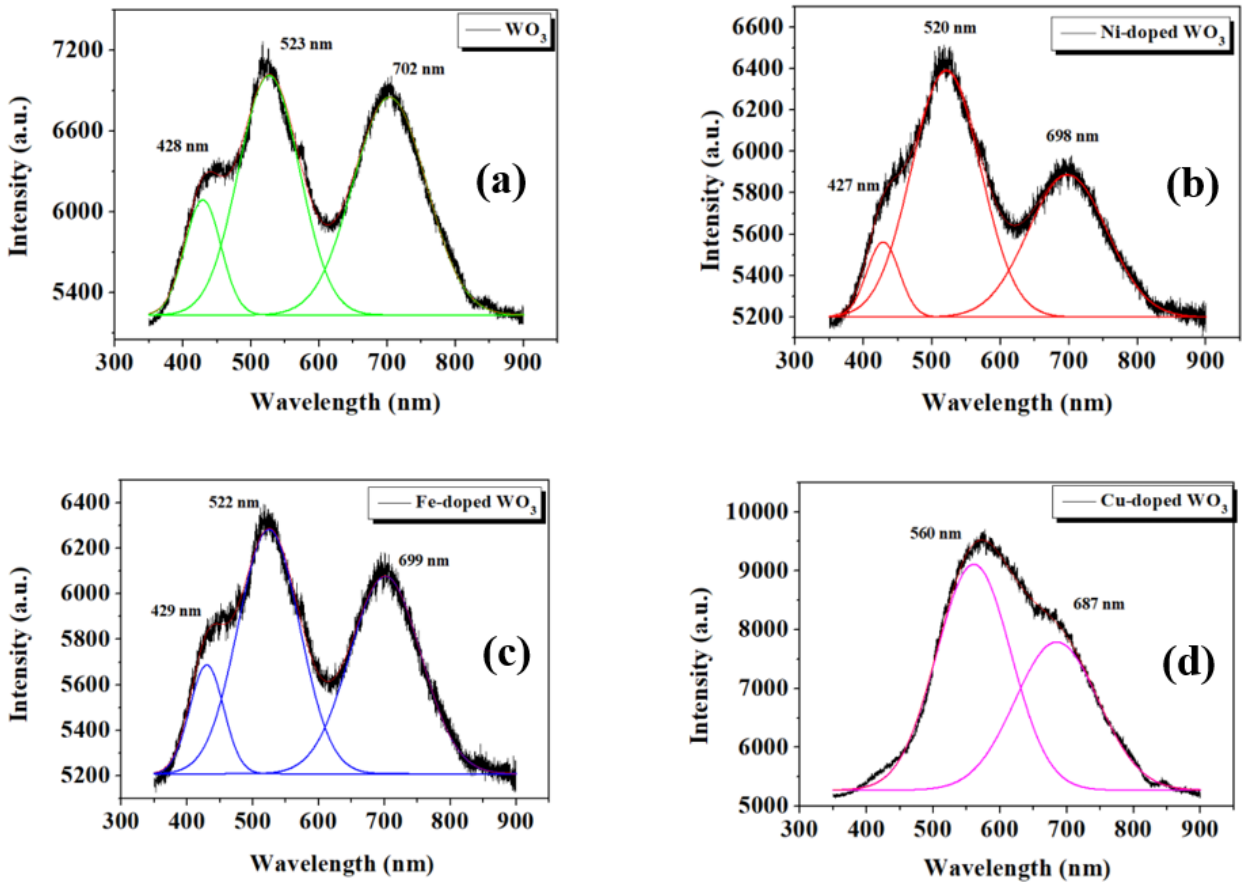

Figure 3. The PL analysis of WO_3 (a), Ni: WO_3 (b), Fe:WO_3 (c) and Cu:WO_3 (d)

Figure 4 and Figure 5 exhibited the UV-Vis spectra in the 200-800 nm range and the optical band gap of the samples, respectively. The broad optical absorption band in the optical transmittance spectrum of the deposited WO_3 film is attributed to the presence of tungsten (W^{4+}) ions [33]. It is clear that optical parameters have been affected by film thickness, surface topography, crystal quality etc. Optical band edge shifted higher wavelength by iron inclusion and defect-related second optical absorption edge was observed in WO_3, Ni:WO_3 and Cu:WO_3. The low crystal quality in the WO_3 host lattice and the metal-tungsten interstitial location may be the reason why pure WO_3 changes its optical character.

The optical band gap estimated by extrapolating the straight-line portion of the $(\alpha h\nu)^2$ vs $h\nu$ plot for WO_3 samples. The optical band gap was calculated by using the below Tauc plot [34, 35]:

$$\alpha = \frac{A(h\upsilon - E_g)^n}{h\vartheta} \tag{3.2}$$

where A is a constant and n is an index for allowed direct and non-direct transitions are 1/2 and 2, respectively. In our study, the band gap of both undoped and doped TiO_2 films were obtained by considering the direct (1/2) transition since it is more favorable for anatase TiO_2 according to the reported studies of Reddy et.al. [34] and Devi et.al. [35].

The thickness was estimated by the weight difference method which is given our previous study [23]. The thickness of WO_3, Ni-doped WO_3, Fe-doped WO_3 and Cu-doped WO_3 were calculated as 800 nm, 500 nm, 600 nm and 930 nm, respectively.

The optical band gap of WO_3, Ni:WO_3, Fe:WO_3 and Cu:WO_3 were calculated 2.92 eV, 2.79 eV, 2.87 eV and 2.78 eV, respectively. Optical band gap decrease was shown by metal inclusion which correlated to change of crystalline size [36, 37]. Metal inclusion of pure WO_3 may cause lattice damage which induces the defect energy levels below the conduction band causes the decrease of optical band gap [38]. In our previous study, the indirect bandgap energies of the nickel doped WO_3 films were found as 3.36 eV-2.74 eV range with using different type nickel precursors and optical band gap decrease was also observed as in this study [36].

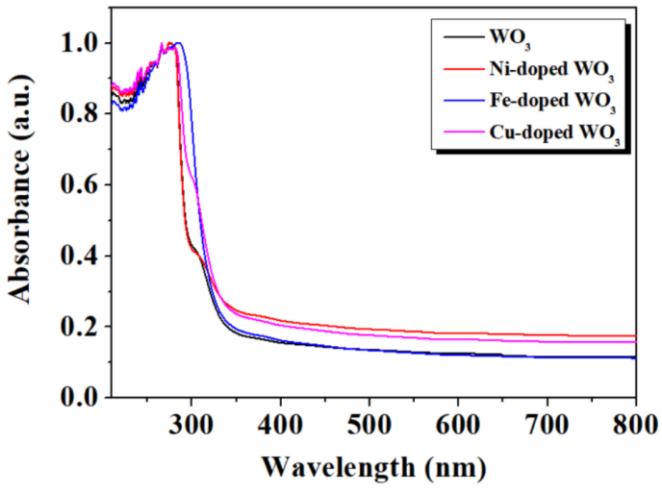

Figure 4. UV-Vis spectra of pure WO_3 and M:WO_3 films

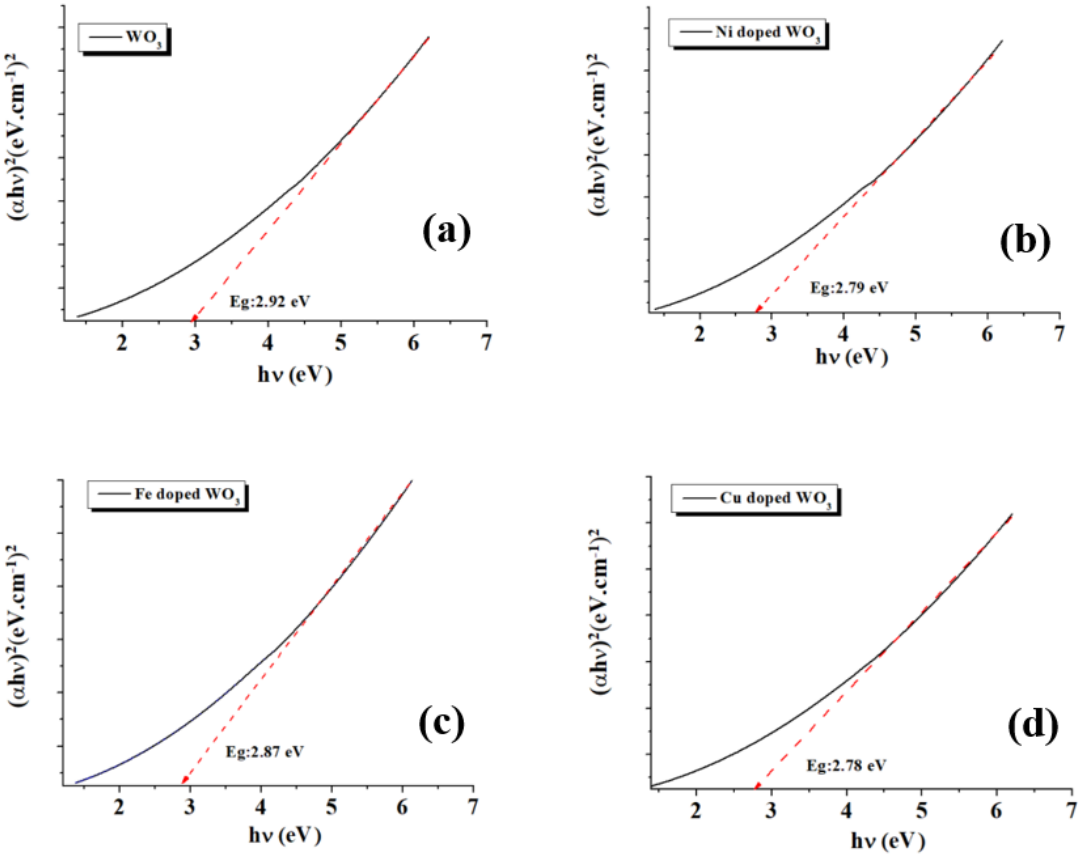

Figure 5. The optical band gap of WO_3 (a), Ni:WO_3 (b), Fe:WO_3 (c) and Cu:WO_3(d)

Other optical parameters are extinction coefficient and refractive index of WO_3, Ni:WO_3, Fe:WO_3 and Cu:WO_3 were exhibited in Figure 6 and 7, respectively. The extinction coefficient (k) is calculated as the below equation [39, 40]:

$$k = \frac{\alpha}{4\pi} \tag{3.3}$$

where α is the absorption coefficient. Figure 6 gives the k values of samples. The refractive index of the films were calculated as in the below equation [41, 42]:

$$n = \left(\frac{1+R}{1-R}\right) + \sqrt{\left(\frac{4R}{(1-R)^2} - k^2\right)} \tag{3.4}$$

where R is reflectance, and k is the extinction coefficient. These graphs exhibited that suggests a decrease in optical density with metal addition in WO_3 [43].

The dielectric constant was estimated by the below equations [42]:

$$\varepsilon = \varepsilon_r - i\varepsilon_i \tag{3.5}$$

$$\varepsilon_r = n^2 - k^2 \tag{3.6}$$

$$\varepsilon_i = 2nk \tag{3.7}$$

$$\tan\delta = \frac{\varepsilon_i}{\varepsilon_r} \tag{3.8}$$

where n is refractive index, and k is the extinction coefficient.

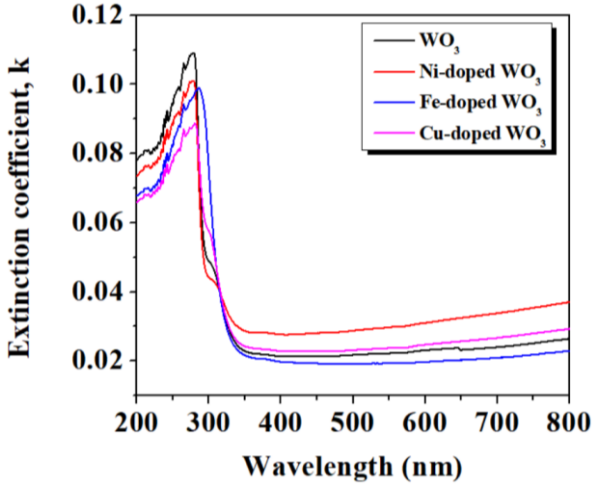

Figure 6. The extinction coefficient of pure WO_3 and M:WO_3 films

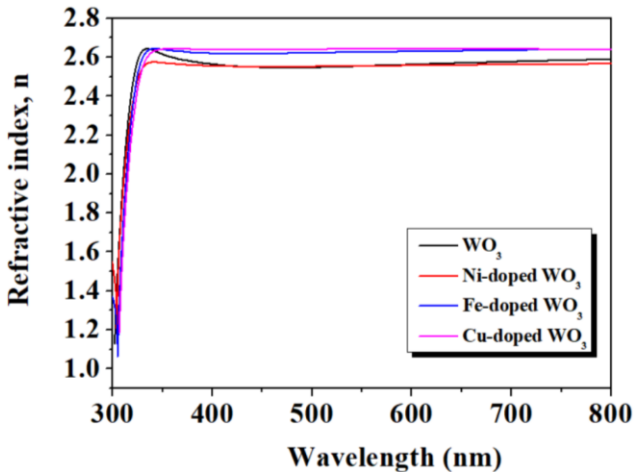

Figure 7. The refractive index of pure WO_3 and M:WO_3 films

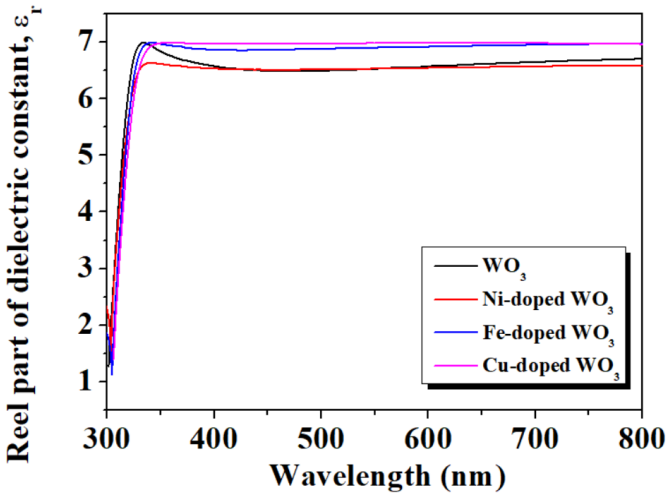

Figure 8. The reel part of dielectric constant of pure WO_3 and M:WO_3 films

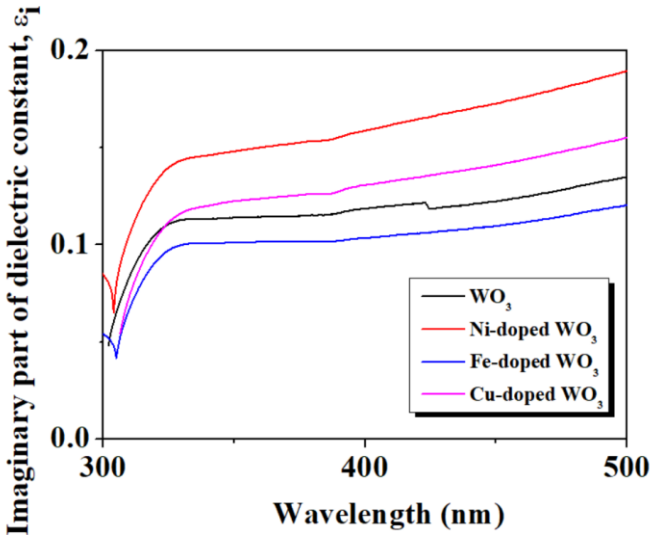

Figure 9. The imaginary part of dielectric constant of pure WO_3 and M:WO_3 films

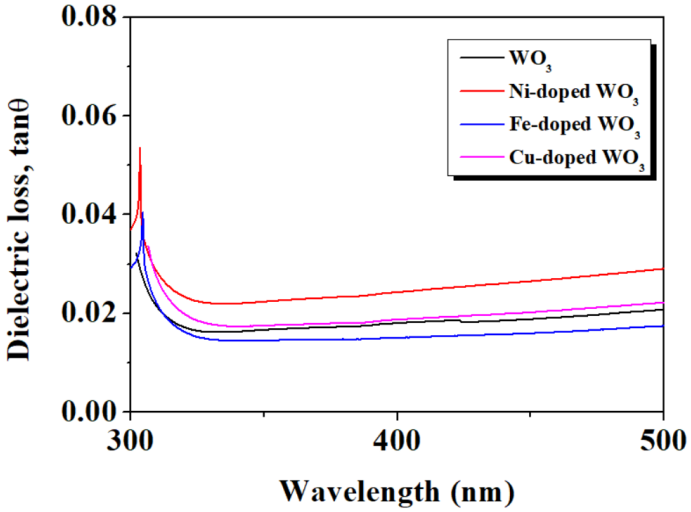

Figure 10. Dielectric loss of pure WO_3 and M:WO_3 films

The optical dielectric constant values were calculated as 6.49 , 6.51, 6.88 and 6.97 for WO_3, Ni:WO_3,Fe:WO_3 and Cu:WO_3 at the wavelength of 500 nm, respectively. From these results, the real and imaginary parts of the dielectric constant follow different patterns and the values of ε_1 are higher than those of ε_2 parts [44]. The least loss was calculated for the Fe:WO_3 sample. The dielectric constant change with hv indicates that there are complex chemical interactions dependent on the solution solubility in the investigated samples.

The current-voltage (I-V) characteristics of pure WO_3 and M:WO_3 films shown at room temperature in Figure 11. The direct current (DC) electrical characterization of each prepared pure WO_3 and M:WO_3 films was realized by measuring current-voltage (I-V) values between 0 and +2 V range. I–V curves of all samples are linear, as shown in Fig. 11 which indicates the formation of ohmic contacts between the coated films and Ag electrodes although low adhesion between ITO/coated M:WO_3. Some metal atoms are incorporated into the WO_3 films during the doping process and might form small metal clusters in the WO_3 lattice, as shown in AFM images. The conductivity of a transition metal oxide can be changed through the dopant impurity levels of electrons [23]. The resistance of samples were given in Figure 12 and calculated as 221 kΩ, 91.9 kΩ, 130 kΩ and 170 kΩ for WO_3, Ni:WO_3, Fe:WO_3 and Cu:WO_3, respectively. This slightly decrease (except for Ni:WO_3 samples) of resistance was observed by metal substitution due to the stoichiometry variation and crystal quality [45]. Since the thickness of the films is more than 100 nm, the electrical properties are independent of the film thickness, and other transmission mechanisms need to be taken into account to account for the current results [46].

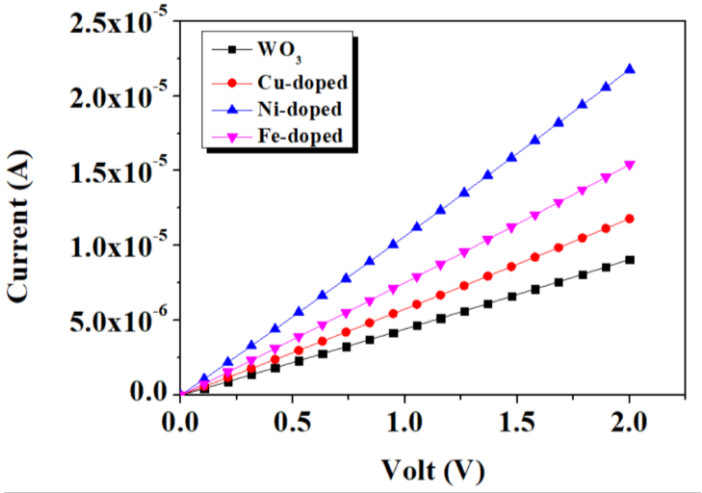

Figure 11. The current-voltage characteristics of pure WO_3 and M:WO_3 films

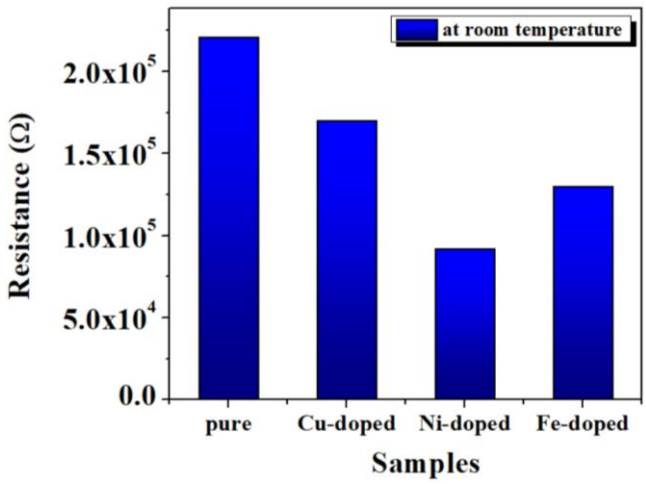

Figure 12. The resistance values of pure WO_3 and M:WO_3 films

4. Conclusion

In this study, we investigated the pure and M:WO_3 (M:Cu, Fe,Ni) films with using facile chemical bath deposition in (pH=2) acidic medium. Effect of the metal substitution on the structural, optical and electrical properties of the produced WO_3 films is studied. Structural analysis results show that all films have typical monoclinic WO_3 phase however crystal quality is low in harsh acidic medium. Optical parameters (optical absorption, emission peaks, optical band gap, optical dielectric constant) shown that the band–band transition and localized states which were produced by defects and the oxygen vacancies in metal substituted tungsten films. I-V character was linear and decrease of electrical resistance was recorded in M:WO_3 films. Each metal doping has had a different effect on both optical and electrical properties, which is due to different surface defects and lattice placement. These results shown that M:WO_3 films are proper for opto-electronic device applications.

Author Contributions

The first and third authors made experimental part. The first author designed the characterization. The second author collected data, performed the analysis, and wrote the paper with support from the third author. They all read and approved the final version of the paper.

Conflicts of Interest

All the authors declare no conflict of interest.

References

[1] N. Goel, K. Kunal, A. Kushwaha, M. Kumar, *Metal oxide semiconductors for gas sensing*, Engineering Reports 5 (6) (2023) e12604.

[2] S. A. Beknalkar, A. M. Teli, J. C. Shin, *Current innovations and future prospects of metal oxide elecrospun materials for supercapacitor technology: A review*, Journal of Materials Science & Technology 166 (2023) 208–233.

[3] K. Valadi, S. Gharibi, R. Taheri-Ledari, *Metal oxide electron transport materials for perovskite solar cells: A review*, *Environmental Chemistry Letters* 19 (2021) 2185–2207.

[4] M. Zhou, S. Wang, M. Qiu, B. Hu, G. Wang, Y. Lu, *Recent advances in the removal of U(VI) by magnetic metal oxides*, Journal of Molecular Liquids 385 (2023) 122295.

[5] S. Masroor, *Chapter 4 - Basics of metal oxides: properties and applications*, Inorganic Anticorrosive Materials (2022) 85-94.

[6] M. Tang, J. Shanga, Y. Zhang, *Oxygen vacancy and doping atom effect on electronic structure and optical properties of Cd_2SnO_4*, RSC Advances 8 (2) (2018) 640–646.

[7] F. Özütok, E. Yakar, *Optical and electrochemical properties of PB-ZnO and PB-ZnO/MWCNT nanocomposite films deposited by chemical bath*, Journal of New Materials for Electrochemical Systems 21 (2) (2018) 119–126.

[8] B. Zhang, Z. An, M. Li, L.-H. Guo, *Synthesis, functionalization and photoelectrochemical immunosensing application of WO_3-based semiconductor materials*, TrAC Trends in Analytical Chemistry 165 (2023) 117149.

[9] M. Razzaq, M. J. Khan, Z. Imran, M. Ahmad, S. Rasool, M. Rehan, S. Iqbal, M. A. R. Anjum, S.

Mehboob, M. Saifullah, *Enhanced electrochemical performance of WO3 thin films prepared from polyvinyl alcohol-modified nanoparticle ink*, Solid State Communications 397 (2023) 116246.

[10] M. Ikram, S. Rasheed, A. M. Afzal, N. A. Shad, Y. Javed, A. Mohyuddin, T. Alomayri, M. M. Sajid, A. Almahri, D. Hussain, *Ultrasensitive V doped WO_3 1D nanorods heterojunction photodetector with pronounced photosensing activities*, Journal of Alloys and Compounds 909 (2022) 164753.

[11] K. Sutanto, N. R. Al Amin, C.-H. Chen, D. Luo, C. Chen, S. Biring, C. Lee, S. Liu, *Vacuum deposited WO_3/Al/Al:Ag anode for efficient red organic light-emitting diodes*, Organic Electronics 103 (2022) 106454.

[12] J. Y. Zheng, Q. Sun, J. Cui, X. Yu, S. Li, L. Zhang, S. Jiang, W. Ma, R. Ma, *Review on recent progress in WO3-based electrochromic films: preparation methods and performance enhancement strategies*, Nanoscale 15 (1) (2023) 63–79.

[13] Z. Xin-Ping, L. Gao, H. Zhang, Y. Peng, X. Zhang, Q. Wang, H. Zhang, *Defect Engineering of Ultrathin WO3 Nanosheets: Implications for Nonlinear Optoelectronic Devices*, ACS Applied Nano Materials 5 (1) (2022) 1169–1177.

[14] R. A. Phokojoe, S. V. Motloung, T. E. Motaung, M. A. Kebede, H. C. Swart, L. F. Koao, *Effect of annealing time on copper selenide thin films prepared by chemical bath deposition*, Physica B: Condensed Matter 666 (2023) 415112.

[15] Z. Yao, P. Li, X. Liu, *Growth regulation of WO_3 film by H2C2O4 during chemical bath deposition*, Journal of Crystal Growth 601 (2023) 126947.

[16] F. Sarf, I. Karaduman, A. Ajjaq, E. Yakar, A. O. Çağırtekin, S. Acar, *Varying electrical and dielectric properties of Ni:SnO2 films by MWCNTs and GNPs coating*, Physica Scripta 97 (2) (2022) 25805-25815.

[17] Ü. Ö. A. Arıer, *Effects of doping ratios on the electrochromic features of WO3-VO2 nano-composite films*, Optik 262 (2022) 169195.

[18] X. Dong, Y. Wei, J. Gao, X. Liu, L. Zhang, Y. Tong, Y. Lu, *Efficient charge transfer over Cu-doped hexagonal WO_3 nanocomposites for rapid photochromic response*, Journal of Photochemistry and Photobiology A: Chemistry 425 (2022) 113716.

[19] H. Liu, J. Zhou, L. Yu, Q. Wang, B. Liu, P. Li, Y. Zhang, *High-sensitivity SO_2 Gas Sensor based on noble metal doped WO_3*, nanomaterials, International Journal of Electrochemical Science 16 (12) (2021) 211240.

[20] Z. Chen, J. Li, S. Wang, J. Zhao, J. Liu, J. Shen, C. Qi, P. Yang, *Structure-property-performance relationship of transition metal doped WO3 mixed oxides for catalytic degradation of organic pollutants*, Chemosphere 316 (2023) 137797.

[21] O. E. Gülen, E. Yakar, F. Sarf, *Investigation of microstructural and intrinsic defect states of facile synthesized WO3 film*, Bilge International Journal of Science and Technology Research 6 (1) (2022) 16–19.

[22] J. Velevska, N. Stojanov, M. Pecovska-Gjorgjevich, M. Najdoski, *Electrochromism in tungsten oxide thin films prepared by chemical bath deposition*, Journal of Electrochemical Science and Engineering 7 (1) (2017) 27–37.

[23] I. Karaduman Er, S. Uysal, A. Ateş, S. Acar, *Some sol–gel processing parameters effect on the properties of dip coated TiO_2 thin films*, *J Mater Sci: Mater Electron* 34 (2023) Article Number 1512 19 pages.

[24] H. Lincy P. C. J. Prabakar, S. J. Gnanamuthu, I. J. D. Ebenezar, *Ammonia sensing performance of Ni doped-WO3 nano particles prepared by simple hydrothermal method at room temperature*, Materials Today: Proceedings 80 (2) (2023) 958-964.

[25] C. Lu, M. H. Hon, C. Kuan, I. Leu, *Preparation of WO3 nanorods by a hydrothermal method for electrochromic device*, Japanese Journal of Applied Physics 53 (2014) 06JG08 1–5.

[26] R. Solarska, A. Królikowska, J. Augustyński, Silver nanoparticle induced photocurrent enhancement at WO3 photoanodes. Angewandte Chemie International Edition 49 (43) (2010) 7980-3.

[27] V. S. Kavitha, V. Biju, K. G. Gopchandran, R. Praveena, C. K. Jayasankar, W. Mekprasart, K. Boonyarattanakalin, W. Pecharapa, V. P. M. Pillai, *Tailoring the emission behavior of WO_3 thin films by Eu^{3+} Ions for light-emitting applications*, Nanomaterials 13 (1) (2023) 7.

[28] M. F. Al-Kuhaili, Q. A. Drmosh, *Investigating the structural and optoelectronic properties of co-sputtered Fe-doped WO_3 thin films and their suitability for photocatalytic applications*, Materials Chemistry and Physics 281 (2022) 125897.

[29] H. Liyanaarachchi, C. Thambiliyagodage, C. Liyanaarachchi, U. Samarakoon, *Efficient photocatalysis of Cu doped TiO_2/g-C_3N_4 for the photodegradation of methylene blue*, Arabian Journal of Chemistry 16 (6) (2023) 104749.

[30] A. Lushchik, M. Kirm, Ch. Lushchik, I. Martinson, H. Zimmerer, *Luminescence of free and self-trapped excitons in wide-gap oxides*, Journal of Luminescence 87 (2000) 232–234.

[31] P. Kumar, M. Singh, G. B. Reddy, *Core–shell WO_3–WS_2 nanostructured thin films via plasma assisted sublimation and sulfurization*, ACS Applied Nano Materials 2 (3) (2019) 1691–1703.

[32] T. Kuechle, S. Klimmer, M. Lapteva, T. Hamzayev, A. George, A. Turchanin, T. Fritz, C. Ronning, M. Gruenewald, G. Soavi, *Tuning exciton recombination rates in doped transition metal dichalcogenides*, Optical Materials: X 12 (2021) 100097.

[33] Y. S. Zou, Y. C. Zhang, D. Lou, H. P. Wang, L. Gu, Y. H. Dong, K. Dou, X. F. Song, H. B. Zeng, *Structural and optical properties of WO_3 films deposited by pulsed laser deposition*, Journal of Alloys and Compounds 583 (2014) 465–470.

[34] K. M. Reddy, S. V. Manorama, A. R. Reddy, *Bandgap studies on anatase titanium dioxide nanoparticles*, Materials Chemistry and Physics 78 (1) (2003) 239–245.

[35] M. Devi, M. R. Panigrahi, *Synthesis and characterization of Mg doped TiO_2 thin film for solar cell application,* International Journal of Engineering & Applied Sciences 7 (2015) 1–7.

[36] I. Karaduman Er, F. Sarf, E. Yakar, *Investigation of H_2S gas sensing performance of Ni:WO_3 films at room temperature: nickel precursor effect*, *Journal of Materials Science: Materials in Electronics* 33 (2022) 3397–3410.

[37] Deepika, D. Gupta, V. Chauhan, S. K. Sharma, S. Kumar, R. Kumar, *Effect of gamma irradiation induced modifications in tungsten oxide thin films and their potential applications,* Indian Journal of Engineering and Materials Sciences 30 (3) (2023) 409–415.

[38] D. Gupta, V. Chauhan, A. Mahajan, R. Gupta, S. A. Ali, R. Kumar, *Influence of gamma radiation on optical, structural and surface morphological properties of WO_3 thin films grown by RF sputtering*, Radiation Physics and Chemistry 2022 (2022) 110554.

[39] R. Suresh, V. Ponnuswamy, R. Mariappan, *Influence of mole concentration on the optical properties of nebulized spray coated CeO_2 thin films*, Journal Optics 44 (2015) 203–209.

[40] M. N. Solovan, P. D. Maryanchuk, V. V. Brus, O. A. Parfenyuk, *Electrical and Optical Properties of TiO_2 and TiO_2: Fe thin films*, Inorganic Materials 48 (10) (2012) 1026–1032.

[41] A.-S. Gadallah, M. M. El-Nahass, *Structural, Optical Constants and Photoluminescence of ZnO Thin Films Grown by Sol-Gel Spin Coating*, Advances in Condensed Matter Physics 2013 (2013) Article ID 234546 11 pages.

[42] S. Tekin, I. Karaduman Er, *The structural, morphological, optical and gas-sensing properties of Mn_3O_4 thin films grown by successive ionic layer adsorption and reaction technique*, Journal of Materials Science: Materials in Electronics 33 (2022) 14519–14534.

[43] A. Rydosz, K. Dyndał, K. Kollbek, W. Andrysiewicz, M. Sitarz, K. Marszałek, *Structure and optical properties of the WO_3 thin films deposited by the GLAD magnetron sputtering technique*, Vacuum 177 (2020) 109378.

[44] E. M. Ngigi, P. S. Nomngongo, J. C. Ngila, *Synthesis and application of Fe-doped WO_3 nanoparticles for photocatalytic degradation of methylparaben using visible–light radiation and H_2O_2,* Catalysis Letters 149 (2019) 49–60.

[45] V. V. Ganbavle, G. L. Agawane, A. V. Moholkar, J. H. Kim, K. Y. Rajpure, *Structural, Optical, Electrical, and Dielectric Properties of the Spray-Deposited WO_3 Thin Films*, Journal of Materials Engineering and Performance 23 (2014) 1204–1213.

[46] M. Regragui, V. Jousseaume, M. Addou, A. Outzourhit, J. C. Bernéde, B. El Idrissi, *Electrical and optical properties of WO_3 thin films*, Thin Solid Films, 397 (1–2) (2001) 238-243.

Çanakkale Onsekiz Mart University

Journal of Advanced Research in Natural and Applied Sciences

dergipark.org.tr/tr/pub/jarnas

Open Access

e-ISSN: 2757-5195 2024, Vol. 10, Issue 2, Pages: 285-299 doi.org/10.28979/jarnas.1377362

Dolgu Barajlarda Çekme Çatlaklarının Duvarına Etkiyen Gerilmelerin Fiziksel Olarak Modellenmesi

Sadettin Topçu[1], Hasan Tosun[2]

[1]Kütahya Dumlupınar Üniversitesi, Kütahya Teknik Bilimler Meslek Yüksek Okulu, İnşaat Bölümü, Kütahya, Türkiye
[2]Mudanya Üniversitesi, Rektörlük, Bursa, Türkiye

Makale Tarihçesi
Gönderim: 17 Ekim 2023
Kabul: 20 Aralık 2023
Yayım: 25 Haziran 2023

Araştırma Makalesi

Öz – Dolgu barajların güvenliği, inşaatında kullanılan malzemelerin su akımıyla taşınması olarak tanımlanan içsel erozyon ile tehdit edilmektedir. Özellikle geçirimsiz perde inşaatında kullanılan kil zeminlerde gelişen çekme çatlaklarında oluşan içsel erozyon türlerinden olan kaçak erozyon, çekme çatlağının derinliği ve genişliği ile ilgili hidrolik parametrelerle kontrol edilir. Ek olarak kil zeminin içsel erozyon direncini kapsayan malzeme özellikleri de göz önünde tutulur. Bu çalışmada bu kontrol faktörlerine ilave olarak çatlama sonrası çatlak duvarlarında gelişen gerilme koşullarının da dikkate alınabilmesi için dolgu barajlardaki çatlak mekanizmasından faydalanılarak yeni bir yaklaşım üretilmiştir. Bu yaklaşımın da laboratuvar koşullarında fiziksel olarak modellenebilmesi için nümerik analiz yardımıyla yeni bir test cihazı; Modifiye Edilmiş Gerilme Kontrollü Üç Eksenli Test Cihazı (MGÜET), tanımlanmıştır. Duvarları tam düşey ve tam yatayda olan çekme çatlaklarının çatlama sonrası duvarlarında toplam gerilme esasında oluşan asal gerilme koşulları, bu test cihazıyla laboratuvar koşullarında oluşturulabilmiştir. Dolgu barajlarda gelişen çekme çatlakları, silindirik zemin örneğinde oluşturulan dairesel bir delik ile modellenmiştir. Böylece, içi boş silindirik cisimlerin mekaniğinden faydalanılarak çekme çatlaklarının çatlama sonrası duvar gerilmeleri, dairesel deliğin duvarında gelişen gerilmeler ile açıklanabilmektedir.

Anahtar Kelimeler – *Çatlak, dolgu baraj, içsel erozyon, ansys workbench, üç eksenli gerilme*

Physical Modelling of Stresses Affecting the Walls of Tensile Cracks in Embankment Dams

[1]Department of Construction, Kütahya Technical Sciences Vocational School, Kütahya Dumlupınar University, Kütahya, Türkiye
[2]Rectorate, Mudanya University, Bursa, Türkiye

Article History
Received: 17 Oct 2023
Accepted: 20 Dec 2023
Published: 25 Jun 2024

Research Article

Abstract – The safety of embankment dams is threatened by internal erosion, defined as the transporting materials used in their construction by water flow. One of the types of internal erosion, such as Concentrated Leak Erosion that occurs in tension cracks that develop in clay soils used in impervious zone construction, is controlled by hydraulic parameters related to the depth and width of the tension crack. Also, material properties, including the clay soil's internal erosion resistance, are considered. This study produced a new approach by utilizing the crack mechanism in an embankment dam to evaluate the stress conditions developing in the crack walls after cracking. To physically model this approach under laboratory conditions, a new test equipment was designed with the help of numerical analysis, i.e., Modified Stress Control Triaxial Equipment (MSCTE). The principal stress conditions occurring based on total stress in the post-cracking walls of tensile cracks with fully vertical and fully horizontal walls could be created under laboratory conditions with this test equipment. Tensile cracks developing in embankment dams were modeled with a circular hole formed in a cylindrical soil sample. Thus, by utilizing the mechanics of hollow cylindrical materials, the post-cracking wall stresses of tensile cracks can be explained by the stresses developing on the wall of the circular hole.

Keywords – *Crack, embankment dam, internal erosion, ansys workbench, triaxial stress*

[1]sadettin.topcu@dpu.edu.tr (Corresponding Author); [2]hasantosun26@gmail.com

1. Giriş

Dolgu barajlarda meydana gelen çatlaklar, bu toprak yapıların kısa ve uzun dönemli güvenliğini tehdit eden en önemli faktörlerden biridir. Dolgu barajlarda Lowe'a [1] göre genel olarak dört tip çatlak gelişir: enine çatlak, yatay çatlak, boyuna çatlak ve kuruma çatlakları (Şekil 1). Dolgu barajların göçmesine neden olarak ön plana çıkan çatlaklar ise memba-mansap doğrultusunda uzanıp rezervuardaki su seviyesinin altında kalan enine ve yatay çatlaklardır. Enine çatlaklarda çatlak duvarları düşey düzlemde iken yatay çatlaklarda ise çatlak duvarları yatay düzlem boyunca uzanır [2]. Dolgu barajların göçme mekanizmalarından biri olan "İçsel erozyon" kısaca dolgu inşaatında kullanılan malzemelerin sızma ve basınçlı boru akımları etkisiyle taşınması olarak tanımlanır. Yıkılan dolgu barajların %30~50'si içsel erozyon mekanizması sonucu göçmüştür [3]. İçsel erozyonun memba-mansap doğrultusunda uzanan bu çatlaklarda gelişen biçimine "kaçak erozyonu" adı verilir. Kaçak erozyonunda çatlak duvarlarındaki kohezyonlu malzeme basınçlı boru akımının etkisiyle aşınarak barajın mansabına doğru taşınır [4]. Eğer dolgu barajın çekirdeğinde kullanılan ince daneli malzeme USBR [5] ve ICOLD'da [6] belirtilen partikül tutulma, drenaj ve boşluksuz derecelendirme kriterlerine uygun bir granüler filtre ile korunursa kaçak erozyon başlangıç aşamasında durdurulur. Bu granüler filtre koruması yoksa kaçak erozyon gelişerek barajın gediklenerek göçmesine neden olur. Buna örnek olarak, homojen dolgu tipinde inşa edilen Teton Barajı'nın 5 Haziran 1976 tarihinde göçmesi gösterilebilir [7].

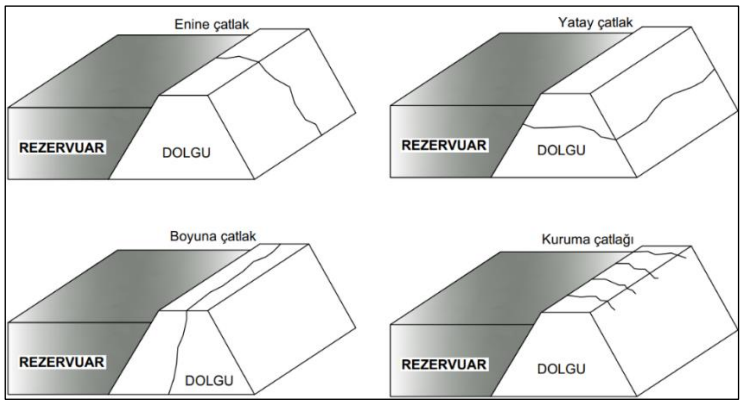

Şekil 1. Dolgu barajlarda görülen çatlak tipleri

Dolgu barajlarda çatlak mekanizmasını tetikleyen etkenler iki başlık halinde toplanabilir: 1) Gerilme nedenli oluşan çatlaklar, 2) Malzeme kaynaklı oluşan çatlaklar. Gerilme nedenli oluşan çatlaklar; farklı oturma, zayıf sıkıştırma, hareketli yükler, hidrolik çatlama ve sismik hareketlerden dolayı gelişebilir. Dolgu barajlar, nihai oturmalarının % 80-90'ını inşaat aşamasında tamamlar [8]. Bu nihai oturmaların tamamlanması esnasında barajın inşa edildiği vadi yamaçlarının dik ve dike yakın olması, baraj temelinin yerleştirildiği taban profilinin basamaklı veya temelin farklı dayanıma sahip malzemelerden oluşması durumunda farklı oturmalardan kaynaklı enine çatlaklar gelişebilmektedir [9]. Yine farklı oturma etkisiyle gerilme nedenli enine çatlaklar, baraj temel tabanının yüzey profilindeki süreksizliklerin çıkıntı şeklinde, dolgu yüksekliğinin % 3~5'ini aşacak uzunluklara sahip olması durumunda da oluşabilmektedir [10]. Bunun yanında dar tipte inşa edilmiş zonlu dolgu barajlarda, kil çekirdeğin kuru tarafta zayıf sıkıştırılması ve çekirdek genişliğinin dolgunun yüksekliğinin dörtte birinden küçük olması durumunda da gerilme nedenli çatlakların oluşabileceği belirlenmiştir [11].

Yukarıda da anlatıldığı gibi gerilme nedenli çatlakları tetikleyen faktörler olarak; dolgunun geometrisi, dolgunun inşa edildiği vadinin geometrisi ve dolguda geçirimsiz perde oluşturmak için kullanılan ince daneli zeminlerin çekme dayanımlarının düşük olması gösterilebilir. Dolgu barajlarda boyuna kemerlenme sonucunda enine çatlaklar, enine kemerlenme sonucunda ise yatay çatlaklar oluşabilmektedir [2]. Bu çatlaklar

çoğu zaman hidrolik çatlama işleminin katkısıyla da oluşabilmektedir [12]. Gövde içerisine sızan suyun hidrostatik basıncıyla memba-mansap doğrultusunda uzanan mevcut çatlağın ilerlemesi veya hidrostatik su basıncıyla dolgu içerisindeki düşük gerilme zonlarında gelişen çatlama mekanizmasına "hidrolik çatlama" adı verilir [13]. Deprem kaynaklı gelişen çatlakların büyük çoğunluğu boyuna çatlaklardır. Çok az vakada nedeni bilinmemekle birlikte memba-mansap doğrultusunda uzanan çatlaklar gözlemlenmiştir [14].

Memba-mansap doğrultusunda uzanan çatlakların malzeme kaynaklı olmasının esası, geçirimsiz perdede kullanılan ince daneli zeminlerin yoğurulma kabiliyeti ile ilişkilendirilir. Dolgu inşaatında kullanılan ince daneli zeminlerin plastisite indeksinin (PI) 15'ten küçük ve dane çaplarının 0.002 mm ve 1.20 mm arasında olması çatlak oluşma riskini arttırmaktadır [15]. Yine Londe'ye [16] göre, dolgunun sıkıştırma su muhtevası ve plastisite indeksi enine çatlakların gelişmesinde ön plana çıkan iki önemli faktör olarak değerlendirilmiştir. Dolguda kullanılan ince daneli zeminlerin çatlama potansiyelinin azaltılabilmesi için genel olarak bu zeminlerin ıslak tarafta sıkıştırılması önerilmektedir. Bunun yanında birçok dolgu baraj tasarım rehberi geçirimsiz perdeyi oluşturacak zeminin plastisite indeksinin 14~15'ten büyük olmasını istemektedir.

Dolgu barajlarda kaçak erozyonu sonucu göçmeye varan durumlarla karşılaşılmasına neden olan memba-mansap doğrultusundaki çatlaklar için son yıllarda yapılan çalışmalar, sismik ve statik koşullarda gelişen çatlağın oluştuğu derinlik ile çatlağın genişliği arasındaki ilişkiye yoğunlaşmıştır [9,17]. Bunun yanında nümerik modellemeler yardımıyla bu çatlakların derinliğini, konumunu ve genişliğini belirleyen yaklaşımlarda vardır [18]. Daha önceki çalışmaların özellikle çatlak derinliği ve genişliği konularına eğilmesinin sebebi, kaçak erozyonunun başlamasına ve gelişmesine neden olan hidrolik parametrelerin (hidrolik eğim, akımın hızı vs.,) bu verilerle hesaplanabilmesidir. Kaçak erozyonunun başlamasına etki eden faktörler, malzemelerin içsel erozyon direnci ve akımın hidrolik parametreleridir. Kohezyonlu zeminlerin içsel erozyon direncini; kuru yoğunluk-su muhtevası [19], sıkıştırma enerjisi [20], plastisite indeksi-likit limit [21] gibi fiziksel ve geoteknik karakteristikler etkilemektedir. Bunlara ilaveten, bu çalışmada; enine ve yatay çatlakların duvarlarında gelişen gerilmelerin de kaçak erozyon mekanizmasına etki eden bir faktör olduğu düşünülerek bu çatlakların duvarlarında çatlama sonrası oluşabilecek gerilmeleri belirleyecek yeni bir yaklaşım geliştirilmiştir. Bu yaklaşımla belirlenen gerilme şartlarını laboratuvar koşullarında modellemek için yeni bir test cihazı tanımlanmıştır.

2. Materyal ve Yöntem

Dolgu barajlardaki enine-yatay çatlakların duvarlarında oluşan gerilme koşullarının belirlenmesi ve modellenmesinde Coulomb tarafından geliştirilen sürtünme kanununun, Otto Mohr tarafından bulunan ve Mohr daireleri ile birleştirilerek zeminlere uygulandığı Mohr-Coulomb teorisi kullanılmıştır. Mohr-Coulomb teorisinde kesme gerilmelerinin sıfır olduğu doğrultudaki normal gerilmelere asal gerilmeler adı verilir. Dolgu barajlarda maksimum asal gerilmeler (σ_1) yerçekimi doğrultusunda; ortanca asal gerilmeler (σ_2) baraj aksı doğrultusunda; minimum asal gerilmeler (σ_3) ise baraj aksına dik doğrultuda yani memba-mansap doğrultusunda gelişirler (Şekil 2). Mohr-Coulomb'da zeminlerin kesme yenilmesi; minimum ve maksimum asal gerilmeleri birleştiren yarım daire ve zeminlerin kesme dayanımı parametreleri olan kesişim kohezyon (c) ve içsel sürtünme açısı (ϕ) değeriyle belirlenen kesme yenilmesi zarfı tarafından kontrol edilir. Ortanca asal gerilmelerin zeminlerin yenilmesine bir etkisi yoktur [22].

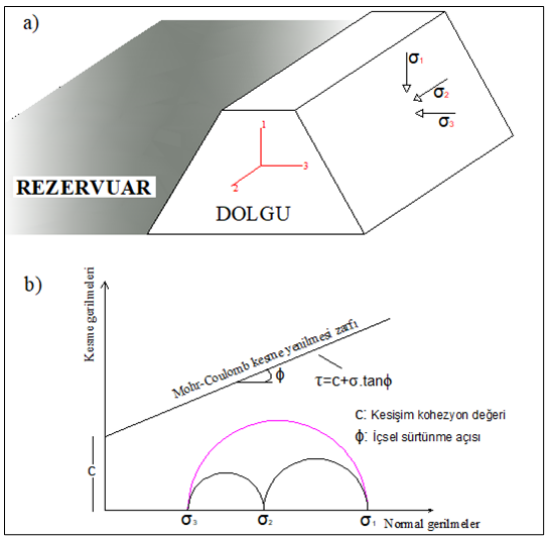

Şekil 2. a) Dolgu barajlarda oluşan asal gerilmeler b) Mohr-Coulomb teorisi

2.1. Dolgu Barajlarda Çatlak Mekanizması ve Çekme Yenilmesi

Dolgu barajlarda çatlaklar, barajın geçirimsiz perdesinde kullanılan ince daneli zeminler için gerilme temelinde çekme ve kesme çatlakları olmak üzere iki farklı şekilde gelişir. Çekme çatlaklarının gelişebilmesi için zeminin çekme dayanımının; kesme çatlaklarının gelişebilmesi için ise kesme dayanımının yenilmesi gerekir. Truscott'a [23] göre kesme yenilmesinde çekme yenilmesinde olduğu gibi suyun akabileceği bir kanalcık oluşmaz. Kesme yenilmesinde genelde örselenmiş, suyun geçişine kapalı bir göçme düzlemi oluşur. Bu nedenle dolgu barajlarda kaçak erozyonu için çekme yenilmesi sonucu oluşan çekme çatlaklarının oluş mekanizması daha kritiktir. Lambe [24], ince daneli zeminlerde kesme ve çekme yenilmeleri için Şekil 3' deki gerilme izlerini tanımlamıştır.

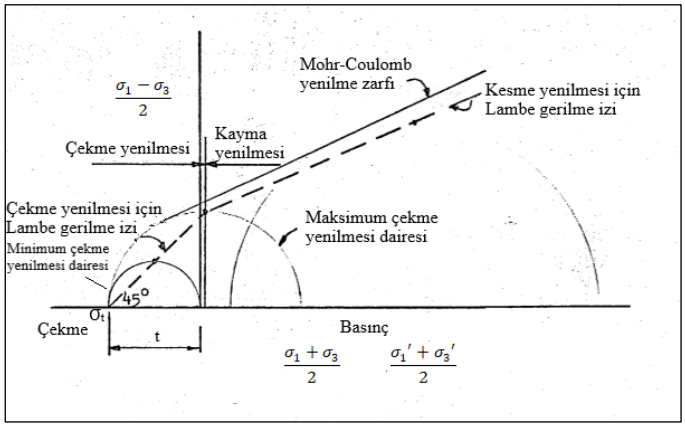

Şekil 3. Kesme ve çekme yenilmeleri için gerilme izi [24]

Maksimum çekme yenilmesi dairesinde çevre basıncı sıfırdan büyüktür. Bishop ve Garga [25] çevre basıncının sıfırdan büyük olması durumunda da killerde çekme yenilmesinin oluşabileceğini ifade etmişlerdir. Çekme yenilmesi için Lambe gerilme izi, zeminlerin çekme dayanımından (σ_t) başlayıp minimum çekme yenilmesi dairesini oluşturan asal gerilmelerin ortalamasından geçerek maksimum çekme yenilmesi dairesini oluşturan asal gerilmelerin ortalamasında sonlanmıştır. Minimum çekme yenilmesi dairesinin çapı, t ile gösterilmektedir. Zeminlerin çekme dayanımı olan, σ_{te} ise ihmal edilebilecek düzeyde çok düşüktür [26]. Bu nedenle minimum asal gerilmelerin çekme gerilmeleri halinde etkimesi durumunda da muhazafakar bir yaklaşımla çekme çatlaklarının oluşabileceği kabul edilebilir. Dolguda kretten daha derinlere doğru gidildikçe enine ve boyuna kemerlenme etkisiyle düşük gerilme zonları oluşabilir. Diğer bir ifade ile düşey gerilmelerin azalmasıyla da

zeminlerin kesişim kohezyon değerine bağlı olarak çekme çatlakları oluşabilir. Fell vd. [9] dolgu barajların içsel erozyona bağlı göçmelerinin olasılıksal olarak tahmin edilmesinde dikkate alınan enine çatlakların derinliklerini hidrolik çatlamalar hariç kret seviyesinden 10 m ile sınırlandırmışlardır. Bu derinliğin altında meydana gelen enine çatlakların içsel erozyon açısından bir problem ortaya çıkarmayacağını belirtmişlerdir. Truscott [23], [24]'te verilen gerilme izlerinden yola çıkarak bir dolgu barajda meydana gelecek çekme çatlakları için oluşması gereken gerilme izlerini Şekil 4 'de göstermiştir.

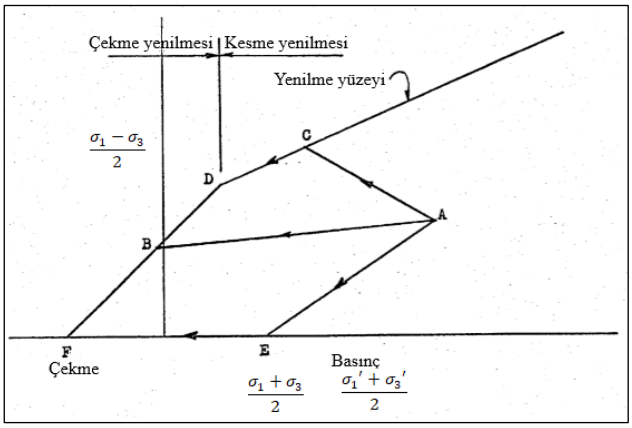

Şekil 4. Çekme çatlaklarının oluşmasına neden olan gerilme izleri [23]

Zeminin başlangıç gerilme koşulları A noktasındadır. Çekme çatlaklarının oluşabilmesi için ACD, AB ve AEF gibi üç farklı gerilme izi oluşabilir. ACD gerilme izinde önce kesme yenilmesi oluşur. Daha sonra ortalama asal gerilmelerin azalmasıyla çekme çatlağı oluşur. AB gerilme izinde direk çekme çatlağı meydana gelir. AEF gerilme izinde önce; maksimum ve minimum asal gerilmelerin farkı sıfır olur (E noktası) ve daha sonra ortalama asal gerilmelerin değeri azalarak F noktasında çekme çatlağı gerçekleşir. Böyle bir durum teorikte mümkündür fakat pratikte gerçekleşmesi mümkün değildir. D noktası kesme ve çekme yenilme düzlemlerini ayıran noktadır. D noktasının yerini zeminlerin kesişim kohezyon değeri belirler. D noktasının pozitif yönde orijinden uzaklaşması kesme yenilmesi potansiyelini azaltırken çekme yenilmesi potansiyelini arttırır. D noktası toplam gerilme koşullarında orijinden uzaklaşır; efektif gerilme koşullarında ise orijine yaklaşır (Şekil 5). Bundan dolayı dolgu inşaatı sırasında ve hemen sonrasında toplam gerilme koşulları hâkim olduğu için çekme çatlağının oluşma potansiyeli daha yüksektir. Barajın işletme sırasında ise zamanla konsolidasyon olayının gerçekleşmesiyle efektif gerilme koşulları geçerli olacağı için çekme çatlaklarının oluşma potansiyeli oldukça azalmaktadır.

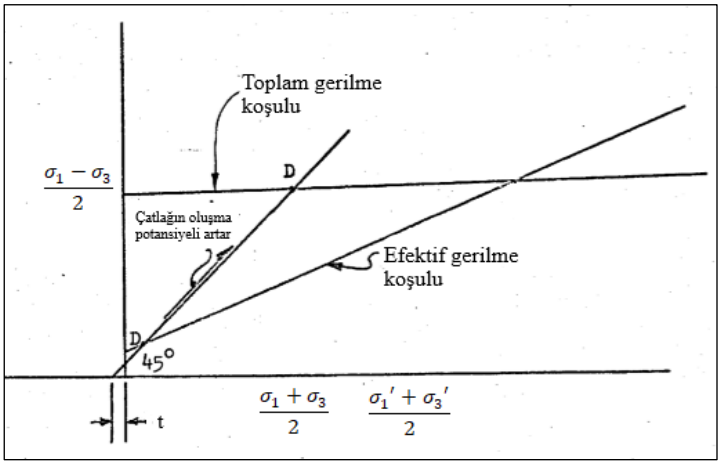

Şekil 5. Çekme çatlağının toplam ve efektif gerilme koşullarına göre oluşma potansiyeli [23]

3. Bulgular ve Tartışma

3.1. Çatlak Duvarlarındaki Asal Gerilmelerin Modellenmesi

Üç eksenli gerilme koşullarında çekme çatlaklarının oluştuğu gerilme koşulları ve çatlak doğrultularının çekme gerilmesinin düzlemi ile yaptıkları açılar Şekil 6'da verilmiştir.

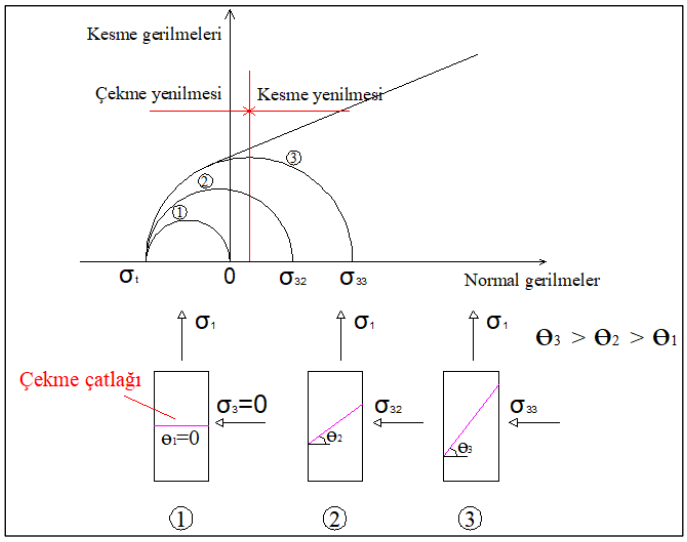

Şekil 6. Üç eksenli gerilme koşullarında çekme çatlağının oluştuğu gerilme koşulları

Bir dolgu barajda kret civarında düşey gerilmeler çok küçük olduğu için 1 nolu çekme yenilmesi dairesi oluşabilir. Dolguda derinlik arttıkça düşey gerilmeler arttığı için sırası ile 2 ve 3 nolu çekme yenilmesi dairesi ile gösterilen memba-mansap doğrultusunda uzanan diyagonal çekme çatlakları görülebilir. Çatlak duvarlarında oluşan asal gerilmelerin basitçe belirlenebilmesi için bu çalışmada Θ=0° durumu göz önünde tutulmuştur. Buna göre; dolgu barajlarda çatlak duvarları, sırasıyla tam düşeyde ve tam yatayda oluşan enine ve yatay çatlakların oluşması esnasındaki çatlak duvarlarına etki eden gerilmeler Şekil 7'de gösterilmiştir.

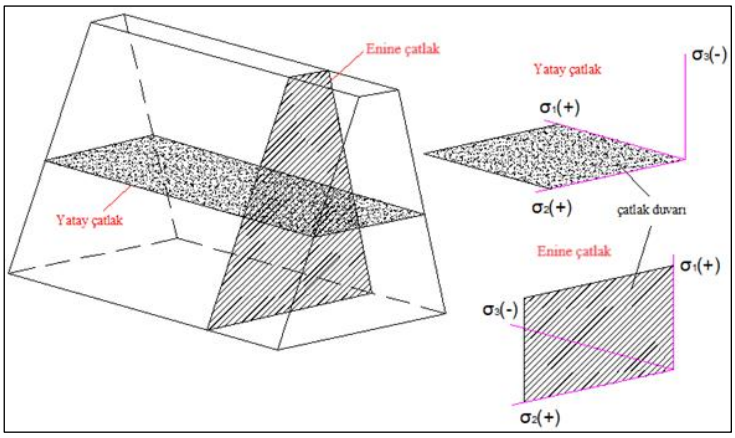

Şekil 7. Dolgu barajlarda Θ=0° durumu için çatlak oluşması esnasındaki çatlakların duvarlarına etki eden gerilmeler

Dolgu barajlarda maksimum asal gerilmeler düşey düzlemde; ortanca asal gerilmeler baraj aksı düzleminde; minimum asal gerilmeler ise baraj aksına dik doğrultuda memba-mansap doğrultusunda gelişirler. Θ=0° durumu için, çatlak duvarları yatayda olan yatay çatlakların gelişebilmesi için düşey gerilmelerin; çatlak duvarları düşeyde olan enine çatlakların gelişebilmesi için ise baraj aksı doğrultusunda etki eden gerilmelerin çekme gerilmesi halinde etkimesi gerekir. Bu yönlerdeki gerilmeler; çekme gerilmeleri halinde etkiyince doğal olarak minimum asal gerilmeler olur. Diğer iki yönde etkiyen gerilmeler ise büyüklüklerine göre maksimum

ve ortanca gerilmeler halini alır. Her iki çatlakta da akım doğrultusunda duvarlara etki eden gerilmeler memba-mansap doğrultusundaki ortanca asal gerilmelerdir. Çatlak duvarında, akım doğrultusuna dik etki eden gerilmeler ise yatay çatlakta baraj aksı doğrultusundaki gerilmelerdir. Enine çatlakta ise yerçekimi yönünde etkiyen gerilmelerdir. Bu gerilmeler çatlama esnasında maksimum asal gerilmeler olur. Truscott'a [23] göre çatlaklar aniden gelişir ve çatlak çevresindeki gerilme koşulları çatlak oluşmadan önceki durumuna geri dönmeye çalışır. Bununla birlikte Sanchez vd. [27] çatlağın oluşmasına neden olan çekme gerilmelerinin, çatlak oluştuktan sonra çatlak açıklığına ve duvarına basınç gerilmeleri halinde etkiyerek çatlağın kapanmasına (iyileşmesine) neden olabileceğini ifade etmişlerdir. Buna göre, enine ve yatay çatlakların oluşması esnasındaki ve sonrasındaki çatlak duvarlarına etki eden gerilme koşulları Şekil 8'de gösterilmiştir.

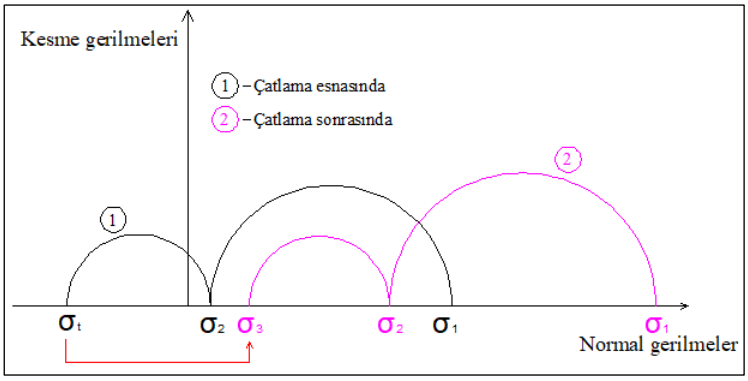

Şekil 8. Çatlakların duvarında çatlama esnasında ve sonrasında oluşan gerilme koşulları

Çatlama sonrasında yatay çatlaklarda, düşey yönde çekme gerilmeleri halinde etkiyen gerilmeler çatlak duvarına basınç olarak etkiyen minimum asal gerilmeler olur. Akıma dik doğrultuda baraj aksı doğrultusunda etkiyen gerilmeler ise maksimum asal gerilmeler olur. Akım doğrultusunda etkiyen gerilmeler ise ortanca gerilmelerdir. Enine çatlaklarda ise baraj aksı doğrultusunda çekme gerilmeleri halinde etkiyen gerilmeler, basınç olarak etkiyen minimum asal gerilmeler olur. Yatay çatlaklarda olduğu gibi akıma dik doğrultuda etkiyen düşey gerilmeler maksimum asal gerilme; akım doğrultusunda etkiyen gerilmeler ise ortanca gerilmeler olur. Her iki çatlak türü için çatlama sonrası çatlak duvarlarına etkiyen asal gerilmelerin oryantasyonu birbirinin aynısı olur.

Bu çalışmada yukarıda anlatılanlar doğrultusunda; dolguda memba-mansap doğrultusunda uzanan çatlakların çatlama sonrasında duvarlarında gelişen asal gerilmeler, laboratuvar koşullarında fiziksel bir modele dönüştürülebilmesi için silindirik bir zemin örneğinde çatlağın dairesel bir delik olduğu kabulüyle Şekil 9'da olduğu gibi sunulmuştur. İçi boş silindirik bir cisme, eksenel ve çevre basınçları uygulandığında delik duvarında eksenel, teğetsel ve radyal gerilmeler oluşur [28]. Buna göre fiziksel modelde delik duvarındaki maksimum asal gerilmeler, teğetsel gerilme (σ_t); ortanca asal gerilmeler, eksenel gerilme (σ_a) ve minimum asal gerilmeler radyal gerilme (σ_r) olmaktadır.

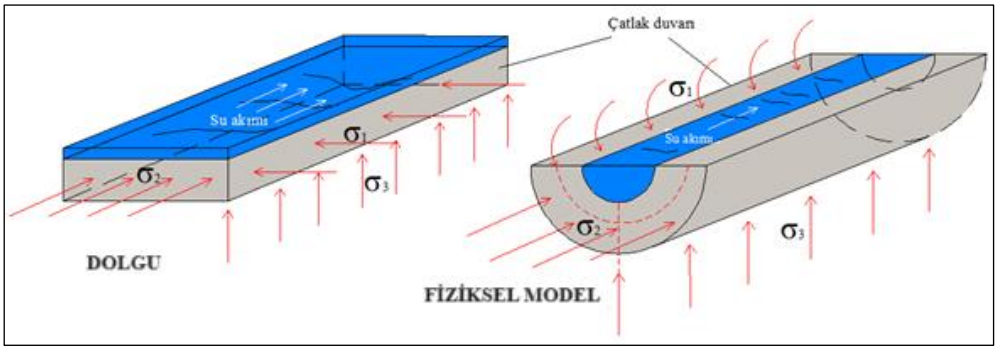

Şekil 9. Dolguda ve fiziksel modellemede çatlak duvarlarında gelişen asal gerilmeler

3.2. Yeni Test Cihazının Tanımlanması

Bir önceki bölümde çatlak duvarı için anlatılan asal gerilme koşullarının; laboratuvar koşullarında anlamlı, kullanılabilir ve uyumlu bir fiziksel modele dönüştürülebilmesi için Modifiye Edilmiş Gerilme Kontrollü Üç Eksenli Test Cihazı (MGÜET) geliştirilmiştir (Şekil 10).

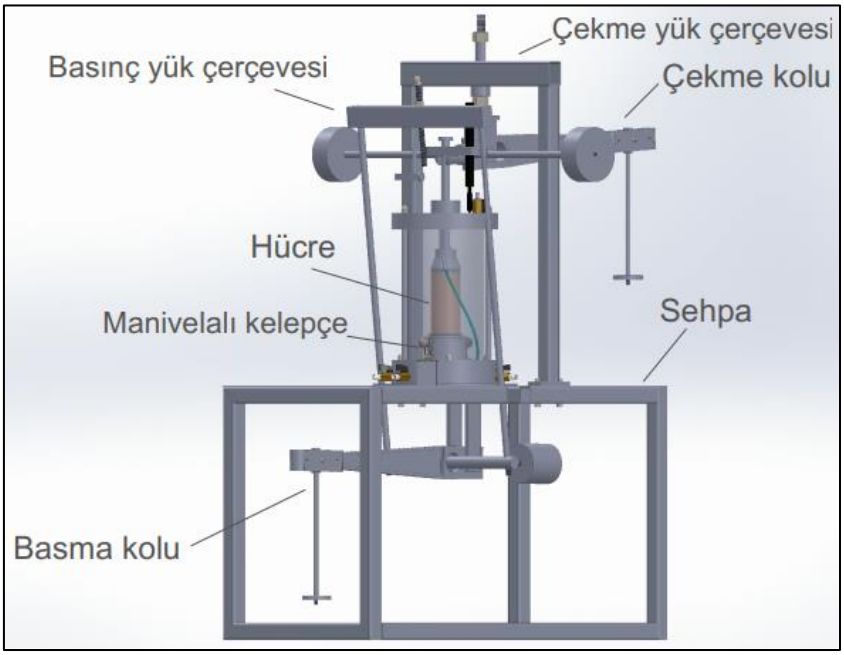

Şekil 10. Modifiye edilmiş gerilme kontrollü üç eksenli test cihazı (MGÜET)

Modifiye Edilmiş Gerilme Kontrollü Üç Eksenli Test Cihazında zemin örneklerinde çevre basıncı oluşturmak için Yağ/su Sabit Basınç Ünitesi kullanılmıştır. Analog manometreye sahip, 1700 kPa'ya kadar çevre basıncı oluşturabilecek bir Yağ/su sabit basınç ünitesi kullanılmıştır. Çevre basıncı aynı zamanda kalibre edilmiş basınç transmitter ile data logger aracılığıyla ölçülmüştür. Zemin örneğine uygulanan üç eksenli yüklemeler sonucunda örnekte oluşan eksenel şekil değiştirmeler yine data logger yardımıyla deplasman transdüseri ile monitörden takip edilmiştir. MGÜET ile zemin örneğine çevre basıncı yanında eksenel doğrultuda hem çekme gerilmeleri hem de basınç gerilmeleri uygulanabilmektedir. Çekme kuvvetleri; çekme kolu ile 1:5 oranında, basınç kuvvetleri ise basınç kolu ile 1:10 oranında büyütülerek zemin örneğine aktarılmaktadır. Cihaz, basınç gerilmeleri için 50-300 kPa ve çekme gerilmeleri için ise 25-150 kPa aralıklarında çalışabilecek şekilde kalibrasyon işlemine tabi tutulmuştur. Yükleme esnasında hücrenin stabil ve hareketsiz halde kalması için hücre, iki adet manivelalı kelepçe ile alt tablaya sabitlenebilmektedir. Hücre, 70 veya 100 mm çaplı silindirik örnekler için kullanılabilen üç eksenli deney hücresidir (Şekil 11). Hücre, 1000 kPa hidrostatik basınca dayanıklı kalabilecek pleksiglas malzemeden üretilmiştir. Hücrenin üzerine oturtulduğu alt tablada dört ve hücrenin üst kısmında bir adet olmak üzere toplamda beş adet vana vardır. Bu vanalardan giriş ve çıkış vanaları zemin örneğinde oluşturulan deliğe gönderilen su akımının hücreye giriş ve çıkış yaptığı noktalarda yer almaktadır. Zemin örneğinde çevre basıncı oluşturmak için hücre içerisine suyun dolumu/boşaltımı, besleme/boşaltma vanası ile yapılmaktadır. Zemin örneğine Yağ/su sabit basınç ünitesinde oluşturulan çevre basıncı, çevre basıncı vanasıyla verilmekte ve örneğe çevre basıncı verilmeden hücre içerisinde bulunan hava da, hava alma vanasıyla dışarıya atılmaktadır.

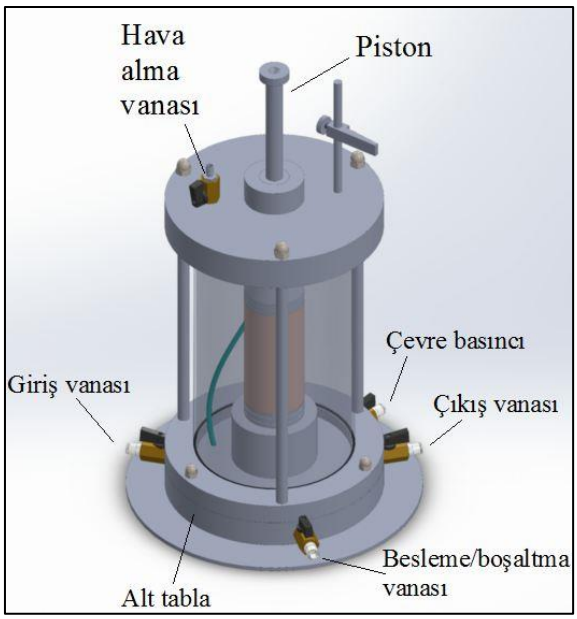

Şekil 11. Deney hücresi

Modifiye Edilmiş Gerilme Kontrollü Üç Eksenli Test Cihazı'nda yüklemeye maruz bırakılacak zemin örnekleri içi boş silindirik bir şekilde hazırlanmaktadır. Çatlak olarak kabul edilen dairesel deliğin çapı 2 mm ve akımın geçtiği bu dairesel deliğin uzunluğu 115 mm'dir. Deliğe akımın verilebilmesi için 25 mm uzunluğa ve sırasıyla 6 ve 14 mm, iç ve dış çapa sahip bir nozül yuvası bırakılmıştır. Böylelikle içi boş silindirik modelin çapı 70 mm ve toplam yüksekliği de 140 mm olarak dikkate alınmıştır (Şekil 12). Dolgu barajlarda çekme gerilmeleri esasındaki çatlama mekanizmasının, toplam gerilme koşullarında ve kısmi doygunluk şartlarında gelişmesinden dolayı boşluk suyu basıncı ölçümlerinin alınmasına gerek duyulmamıştır. Bu nedenle, çalışma kapsamında yapılan tüm önermelerin "toplam gerilme" esasında yapıldığı belirtilmelidir.

Şekil 12. Zemin örneği

Giriş vanasından alınan su akımının hücredeki çevre basıncından etkilenmemesi için, su akımı et kalınlığı fazla ve malzemesi sert plastik bir boru yardımıyla üst adaptörden nozüle, oradan da zemin örneğinde oluşturulan deliğe aktarılır (Şekil 13). Zemin örneğine çevre basıncı altında uygulanan eksenel yüklerin, eksiksiz bir şekilde örneğe aktarılmasına dikkat edilmiş ve pistonun, üst adaptör ile birleşiminde kilitleme aparatı kullanılmıştır. Kilitleme aparatının üzerinde pistonun anahtar gibi tek bir yönde girebileceği bir yuva vardır. Bu yuvaya giren piston sağa veya sola 90^0 kadar çevrildiğinde tam bir kilitlenme sağlanmaktadır.

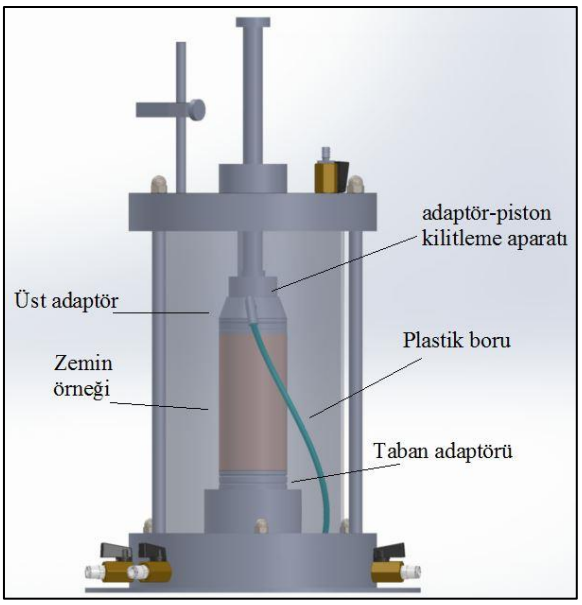

Şekil 13. Hücre içerisindeki zemin örneğinin görüntüsü

Geliştirilen yeni test cihazıyla zemin örneklerinde sadece çevre basıncı etkisi altında izotropik yükleme koşulları, çevre basıncıyla birlikte çekme ve basınç kollarına konulacak ağırlık ile de sırasıyla anizotropik-genleşme ve anizotropik-sıkışma yükleme koşulları oluşturulabilmektedir. Bu yükleme koşulları altında içi boş silindirik zemin örneğinde delik duvarındaki asal gerilmeleri belirlemek için ANSYS v14. Programının Workbench modülü kullanılmış ve asal gerilmeler sonlu elemanlar yöntemiyle nümerik olarak üç boyutlu modelleme ile belirlenmiştir [29]. Fiziksel model altında, Tablo 1'deki seçilen yükleme koşulları için dört farklı zemin örneğindeki eksenel şekil değiştirmeler ölçülmüştür. σ_{1d}: Eksenel basınç. σ_{3d}: Çevre basıncı.

Tablo 1. Yükleme koşulları

Yükleme no.	σ_{1d} (kPa)	σ_{3d} (kPa)	Yükleme koşulu
1	66.7	100	Anizotropik-genleşme
2	100	100	İzotropik
3	150	100	Anizotropik-sıkışma

Lineer-elastik malzeme modeli kabulüyle, üç farklı yükleme koşulu altında dört farklı zemin örneğinin elastisite modüllerini hesaplamak için anizotropik yüklemelerde [30]'da ve izotropik yüklemede ise [31]'de verilen yaklaşım kullanılmıştır (Tablo 2).

Tablo 2. Nümerik modellemelerde kullanılan elastisite modülleri

Yük.no.	Elastisite Modülü, E, (kPa)			
	Afyon-1	Afyon-2	Çatören Brj.	Kunduzlar Brj.
1	10122	17254	9514	8495
2	20896	13333	18421	14894
3	12500	13514	15576	16234

Zemin örneklerinde poisson oranı, anizotropik yüklemeler için suya doygunluk derecesine bağlı olarak Oh ve Vanapalli'ye [32] göre 0.47; izotropik yükleme için ise 0 olarak dikkate alınmıştır. Nozül yuvasının sınır koşulları, silindirik mesnet ile tanımlanmıştır. Nozülün, örnek ile temas ettiği yüzeylerin teğeti ve normali yönündeki hareketi kısıtlanmıştır. Örneğin alt yüzeyi, tüm doğrultularda deplasman ve dönmelere karşı da sınırlandırılmıştır. 130763 düğüm noktası ve 94051 dört üçgen yüzlü (tetrahedron) elemanlardan oluşan geometrik model (Şekil 14), ortalama çarpıklık ölçütüne (n=0.239) göre mükemmel kalitede oluşturulmuştur [33].

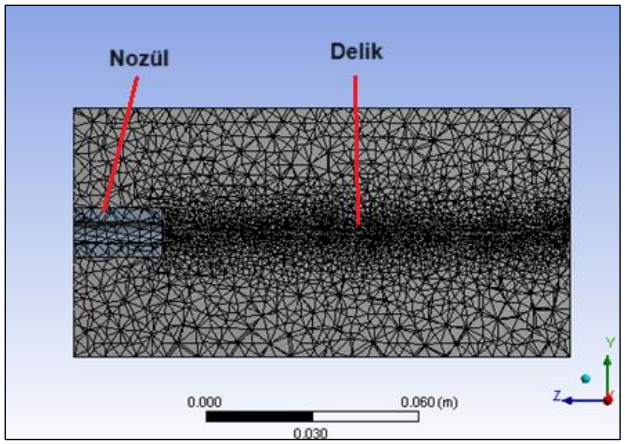

Şekil 14. Geometrik modelin boykesiti

Gerçekleştirilen analizler sonucunda seçilen üç farklı yükleme koşulunda dört faklı zemin örneği için elde edilen eksenel şekil değiştirmeler, fiziksel modelde ölçülenler ile birbirine yakındır (Şekil 15). Özellikle izotropik yükleme koşulları için tüm örneklerde nümerik analiz sonucu elde edilen şekil değiştirmeler ve deney esnasında ölçülen şekil değiştirmeler aynıdır. Buna rağmen özellikle anizotropik-genleşme yüklemesi için bu değerlerin farklılık arz ettiği görülmüştür. Bu farklılık ise anizotropik-sıkışma yüklemesi için daha az gerçekleşmiştir.

Nümerik analizlerde asal gerilmelerin delik uzunluğu boyunca değişkenlik gösterdiği belirlenmiştir (Şekil 16-18). Bunun nedeni olarak nozül kalınlığı dışında kalıp, gerilmelerin etkiyemediği delik üst yüzey kısmının varlığı gösterilebilir. Çatlağın dairesel bir delik olarak kabul edilmesiyle modellenen asal gerilme koşulları (bkz. şekil 9) beklendiği gibi tüm yükleme koşullarında gerçekleşmiştir. Delik duvarına etki eden teğetsel gerilmeler maksimum asal gerilme; eksenel gerilmeler ortanca asal gerilme; radyal gerilmeler ise minimum asal gerilmeler olmuştur. Anizotropik-genleşme yükleme koşulu için eksenel ve radyal gerilmeler birbirine yakın iken, anizotropik-sıkışma yüklemesinde ise teğetsel ve eksenel gerilmeler birbirine yakın elde edilmiştir. Anizotropik-genleşme yüklemesinde deliğin nozül tarafındaki kısmında radyal gerilmeler çok küçük değerlerde de olsa çekme gerilmeleri halinde etkimektedir. İzotropik yükleme koşulunda eksenel ve radyal gerilmeler deliğin bu kısmında yine çekme gerilmeleri halinde etkidiği görülmüştür. Anizotropik-sıkışma yükleme koşulunda ise tüm gerilme değerleri deliğin nozül tarafındaki bölümünde çekme gerilmeleri halinde etkimektedir.

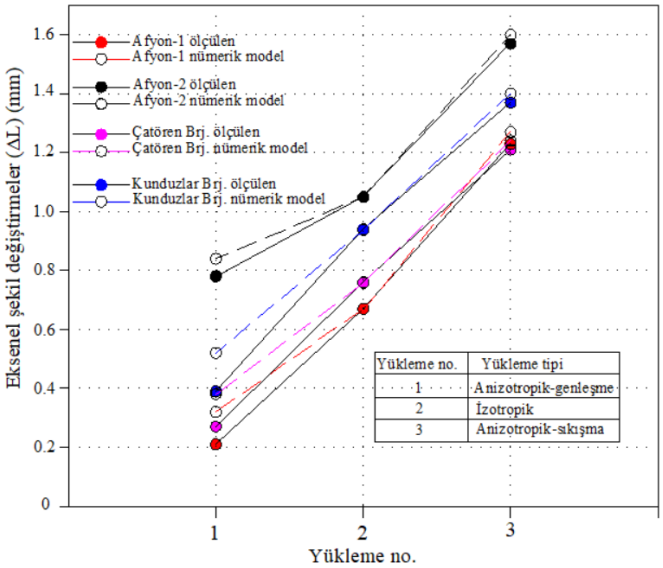

Şekil 15. Deney sırasında ölçülen ve nümerik modellemede belirlenen eksenel şekil değiştirmeler

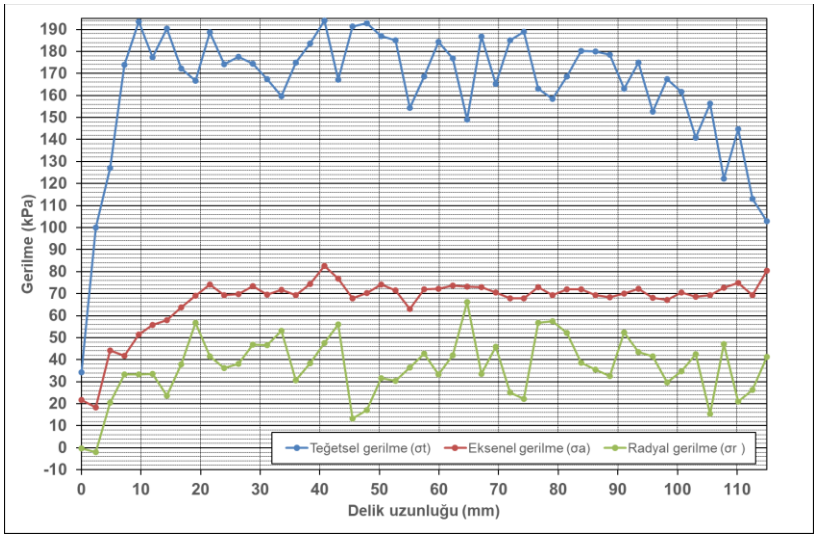

Şekil 16. Yükleme no.1 için nümerik analizde delik duvarı boyunca oluşan gerilmeler

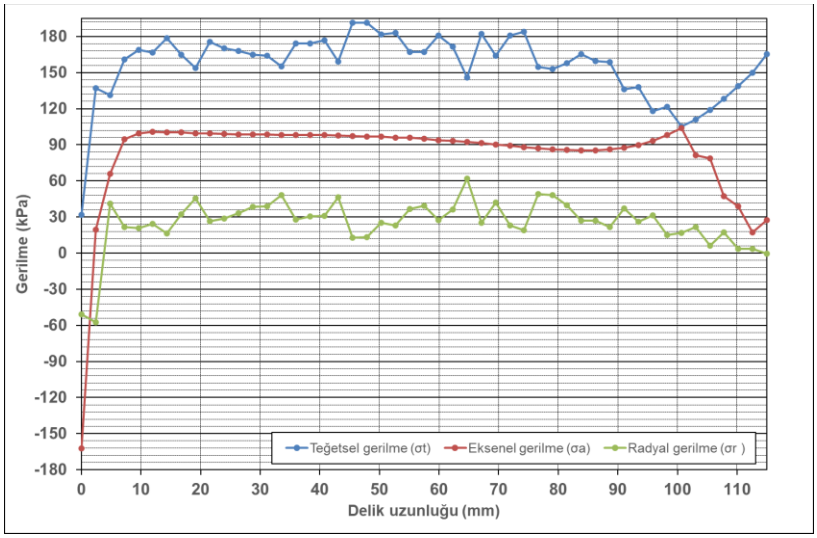

Şekil 17. Yükleme no.2 için nümerik analizde delik duvarı boyunca oluşan gerilmeler

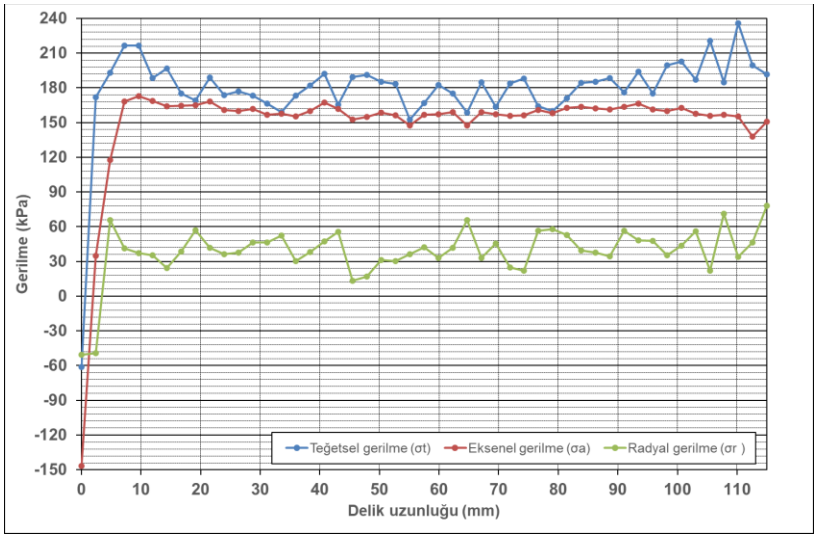

Şekil 18. Yükleme no.3 için nümerik analizde delik duvarı boyunca oluşan gerilmeler

4. Sonuçlar

Bu çalışmada; dolgu barajlarda çekme çatlağı olarak gelişen yatay ve enine çatlakların, çatlama sonrası duvarlarında oluşan asal gerilmeler yeni bir yaklaşımla belirlenerek, bu gerilmelerin nümerik analiz desteğiyle laboratuvar koşullarında fiziksel bir modele dönüştürülmesi için yeni bir test ekipmanı olan Modifiye Edilmiş Gerilme Kontrollü Üç Eksenli Test Cihazı (MGÜET) başarıyla tanımlanmıştır.

Çalışmadan çıkarılan sonuçlar ve öneriler özetlenmiştir: Dolgu barajlarda geçirimsiz perde olarak kullanılan kil zeminlerde içsel erozyona neden olarak göçmeye neden olacak çatlakları, silindirik zemin örneklerinde oluşturulan dairesel bir delikle modellemek mümkün olmaktadır. Çatlama sonrası çatlak duvarlarında oluşan asal gerilme koşulları ile laboratuvarda geliştirilen cihazda yüklenen zemin örneklerindeki deliğin duvarlarında gelişen asal gerilme koşulları aynı olmaktadır. Bu durumun nümerik analiz ile de sağlaması yapılmıştır. Yeni geliştirilen test cihazında izotropik, anizotropik-genleşme ve anizotropik-sıkışma yükleme koşulları; geleneksel üç eksenli test cihazındaki deplasman kontrollü yerine gerilme kontrollü bir şekilde oluşturulabilir. İzotropik yükleme koşullarında silindirik örneklerin eksenel ve radyal şekil değiştirmeleri birbirine eşit olduğundan enkesit alanları değişmemektedir. Bu nedenle bu yükleme koşulu için poisson oranı 0 olarak dikkate alınmalıdır. Yüklenen zemin örneklerindeki delikten geçirilecek su akımının hidrolik yükü, yüksekliği ayarlanabilir taşırma kabıyla veya manometreli pompaj ile basınçlandırılarak sağlanabilir.

Yazar Katkıları

Tüm yazarlar bu çalışmaya eşit katkı sağlamıştır. Tüm yazarlar makalenin son halini okuyup onaylamıştır.

Çıkar Çatışması

Yazarlar hiçbir çıkar çatışması olmadığını beyan etmektedir.

Kaynaklar

[1] J. Lowe, *Recent development in the design and construction of earth and rockfill dams*, 10th International Congress on Large Dams, Montreal, Canada, 1970, pp. 11–23.

[2] S. Topçu, *Kil çekirdekli kaya dolgu barajlarda hidrolik çatlama potansiyelinin tahmin edilmesi*, DSİ Teknik Bülten 125 (2017) 1–7.

[3] M. Foster, R. Fell, M. Spannagle, *The statistics of embankment dam failures and accidents*, Canadian Geotechnical Journal 37 (5) (2000) 1000–1024.

[4] S. Topçu, *Comparative analysis of internal erosion behaviour for fine grained soils under different stress state*, Doctoral Dissertation Eskişehir Osmangazi University (2021) Eskişehir.

[5] United States of Burea of Reclamation (USBR), Design Standard No. 13. Embankment Dams, Protective Filters (2011), https://www.usbr.gov/tsc/techreferences/designstandards-datacollectionguides/finalds-pdfs/DS13-5.pdf, Accessed 17 Oct 2023.

[6] International Comission of Large Dams (ICOLD), Bulletin No. 95: Embankment Dams: Granular Filters and Drains – Review and Recommendations, Paris, 1994.

[7] H. Tosun, S. Topçu, Toprak Dolgu Barajlarda Hidrolik Çatlama, *Uluslararası Katılımlı IV. Ulusal Baraj Güvenliği Sempozyumu*, Elazığ, 2014, pp. 519–530.

[8] G. Hunter *The deformation behaviour of embankment dams and landslides in natural and constructed soil slopes*, Doctoral Dissertation The Universty of New South Wales (2003) Australia.

[9] R. Fell, M. A. Foster, J. Cyganiewicz, G. L. Sills, N. D. Vroman, R. R. Davidson, Risk analysis for dam safety: a unified method for estimating probabilities of failure of embankment dams by ınternal erosion and piping, URS Australia, Sdyney, 2008.

[10] Norwegian Geotechnical Institute (NGI), Jukla Sekundaerdam Lkkaasjer,Reparasjober,Pavisning av erosjonskanaler Gjennom Tetningskjernen, Internal Report 53600-1, Oslo, 1984.

[11] H. Bui, R. Fell, C. Song, Two and Three Dimensional Numerical Modelling of the Potential for Cracking of Embankment Dams during Construction, UNICIV Report 426, The Universty of New South Wales (2004) Sydney.

[12] J. G. Zhu, J. J. Wang, *Investigation to arching action and hydraulic fracturing of core rock-fill dam*, Proceedings of the 4th International Conference on Dam Engineering New Developments in Dam Engineering, Nanjing, 2004, pp. 1171–1180.

[13] J. J. Wang, Hydraulic Fracturing in Earth-Rock Fill Dam, Water Publication of China, China, 2012.

[14] S. Pells, R. Fell, Damage and Cracking of Embankment Dams by Earthquakes and the Implications for Internal Erosion and Piping, University of New South Wales, 2002.

[15] J. L. Shrerard, Influence of Soil Properties and Construction Methods on the Performance of Homogeneous Earth Dams, USBR Tech Memo No.645, Denver, 1953.

[16] P. Londe, La fissuration des Noveaux.Proc. 10th ICOLD, Montreal, vol. IV, 1970.

[17] F. C. Fong, W. J. Bennett, *Transverse cracking in earth dams due to earthquakes*, Proc. Western Regional Conference, American Society of State Dam Safety Officials, Red Lodge, 1995.

[18] K. He, C. Song, R. Fell, *Numerical modelling of transverse cracking in embankment dams*, Computers and Geotechnics 132 (2021) 104028.

[19] V. N. Nguyen, J. R. Courivaud, P. Pinettes, H. Souli, J. M. Fleureau, *Using an improved jet-erosion test to study the influence of soil parameters on the erosion of a silty soil*, Journal of Hydraulic Engineering 143 (8) (2017) 04017018.

[20] B. Burns, G. S. Ghataora, *Internal erosion of kaolin*, in A. J. Puppala, N. Hudyma, W. J. Likos (Eds.), Problematic Soils and Rocks and In Situ Characterization, Colorado, 2007, 1–8.

[21] H. J. Gibbs, *A Study of erosion and tractive force characteristics in relation to soil mechanics properties*, U. S. Department of Interior, Bureau of Reclamation, Colorado, Report No. EM-643, 1962.

[22] M. A. Tekinsoy, Zeminlerde kırılma ve denge (Mukavemet'de odömetre tekniği), Şırnak Üniversitesi Yayınları, Şırnak, 2018.

[23] E. G. Truscott, *Behaviour of embankmemnt dams*, Doctoral Dissertation University of London (1977) London.

[24] W. T. Lambe, *Stress path method*, ASCE Journal of the Soil Mechanics and Foundations Division 93 (6) (1967) 309–331.

[25] A. W. Bishop, V. K. Garga, *Drained tension tests on London clay*, Geotechnique 19 (2) (1969) 309–313.

[26] F. H. Kulhawy, T. M. Gurtowski, *Load transfer and hydraulic fracturing in zoned dams*, ASCE Journal of the Geotechnical Engineering Division 102 (9) (1976) 963–974.

[27] R. L. Sanchez, A. I. Strutynsky, M. L. Silver, *Evaluation of the erosion potential of embankment core materials using the laboratory triaxial erosion test procedure (No. WES/TR/GL-83-4)*, Army Engineer Waterways Experiment Station Vicksburg Ms Geotechnical Lab, 1983.

[28] W. Fairbairn, Two lectures, on the construction of boilers, and on boiler explosions, with the means of prevention: Delivered before the Leeds' Mechanics' Institution, April 23 and 24, 1851: also a paper on

the consumption of fuel and prevention of smoke, read before the British association for the advancement of science, Simpkin, Marshall, and Co., 1851.

[29] T. Stolarski, Y. Nakasone, S. Yoshimoto, Engineering analysis with ANSYS software, Butterworth-Heinemann, 2018.

[30] M. H. Farzin, R. J. Krizek, R. B. Corotis, *Evaluation of modulus and poisson's ratio from triaxial tests*, Transportation Research Record 537 (1975) 69–80.

[31] J. L. Briaud, *Introduction to soil moduli*, Geotechnical News 19 (2) (2001) 54–58.

[32] W. T. Oh, S. K. Vanapalli, *Relationship between Poisson's ratio and soil suction for unsaturated soils*, 5th Asia-Pacific Conference on Unsaturated Soils Bangkok, Thailand, 2011, 239–245.

[33] M. Ozen, *Mesh Metric Spectrum Quality, California*, Journal of Physics of Fluid 48 (2012) 236–267.

Çanakkale Onsekiz Mart University

Journal of Advanced Research in Natural and Applied Sciences

dergipark.org.tr/tr/pub/jarnas

Open Access

e-ISSN: 2757-5195 2024, Vol. 10, Issue 2, Pages: 300-311 doi.org/10.28979/jarnas.1392427

Ağır Hizmet Araçlarının Gürültü Kalkanı Parçasının Akustik ve Mekanik Dayanım Performansının İncelenmesi

İbrahim Aydın[1], Sena Arslan[2], Merve Çalışkan Akduman[3], Dilara Çay[4], Öznur İskender[5]

[1,2,3,4,5]Formfleks Otomotiv Yan Sanayi ve Ticaret A.Ş., Bursa, Türkiye

Makale Tarihçesi

Gönderim: 17 Kasım 2023

Kabul: 30 Ocak 2024

Yayım: 25 Haziran 2024

Araştırma Makalesi

Öz – Kamyon, tır gibi ağır hizmet araçlarında en çok gürültü üreten yapı olan motor odasında oluşan ısı ve sesin izole edilmesi için bu yapının yakına yalıtım malzemesi olarak gürültü kalkanı konumlandırılmaktadır. Bu çalışmada, ağır hizmet araçlarında gürültü kalkanı olarak kullanılmak üzere, ses ve ısı üreten yapıya bakacak yönde konumlandırılan alt katmanda taş yünü, gürültü kalkanı parçasının mukavemet ve akustik performansını arttırmakla görevli üst katmanda PP/GF, GF/EP, GF/PET, Karbon/EP, fenolik keçe ve yapıştırıcı malzeme olarak PE film kullanılarak düz kalıpta, 190 °C sıcaklıkta ve 110 bar basınç altında kompozit sandviç yapılar oluşturulmuş ve bu yapıların empedans tüpünde ses yutum katsayıları ölçülerek akustik performansları birbiriyle karşılaştırılmıştır. Akustik performans test sonuçları incelendiğinde, ses yutum katsayısı (α) 1 değerine en yakın olan kompozit sandviç yapının dıştan içe doğru iki kaplama telası arasında PP/GF, PE film, taş yünü içeren malzeme kompozisyonu 1 olduğu tespit edilmiştir. Kalınlığın akustik performansa ve mukavemete etkisini incelemek üzere, en iyi akustik performansı gösteren malzeme kompozisyonu 1 ile 10 mm, 20 mm ve 30 mm kalınlıklarında üretilen numunelere akustik performans ve 3 nokta eğilme testleri uygulanmıştır. Elde edilen verilerden kalınlık arttıkça ses yutum kapasitesinin ve eğilme dayanımının arttığı tespit edilmiştir.

Anahtar Kelimeler – *Akustik, gürültü kalkanı, kompozit, mekanik dayanım, yalıtım malzemesi*

Investigation of Acoustic and Mechanical Strength Performance of the Noise Shield Part of Heavy-Duty Vehicles

[1,2,3,4,5]Formfleks Otomotiv Yan Sanayi ve Ticaret A.Ş., Bursa, Türkiye

Article History

Received: 17 Nov 2023

Accepted: 30 Jan 2023

Published: 25 Jun 2024

Research Article

Abstract – The motor compartment is the primary source of noise production in heavy-duty vehicles such as trucks and trailers due to the heat and sound generated. A noise shield is positioned in close proximity as insulation material to isolate these effects. This study specifically focuses on the use of insulation materials as a noise shield in heavy-duty vehicles. The lower layer addressing the structure producing heat and sound includes rock wool. The upper layer, responsible for enhancing strength and acoustic performance, consists of various materials, such as PP/GF, GF/EP, GF/PET, Carbon/EP, phenolic felt, and PE film as an adhesive material. These materials have been carefully selected to ensure optimal performance and meet the highest quality standards. Composite sandwich structures were created using these materials in a flat mold at a temperature of 190°C and a pressure of 110 bars. The acoustic performance of these structures was compared by measuring their sound absorption coefficients in an impedance tube. Upon examining the results of the acoustic performance tests, it was determined that Composition 1, including PP/GF, PE film, and rock wool between the two outer layers, had the sound absorption coefficient (α) closest to 1. To investigate the impact of thickness on both acoustic performance and strength, acoustic performance, and 3-point bending tests were conducted on samples produced with the best-performing material composition 1 at thicknesses of 10 mm, 20 mm, and 30 mm. The data obtained showed that as the thickness increased, so did the sound absorption capacity and bending strength.

Keywords – *Acoustic, composite, insulation material, mechanical strength, noise shield*

[1]ibrahim.aydin@ff-rd.com; [2]sena.arslan@ff-rd.com; [3]merve.akduman@ff-rd.com; [4]dilara.cay@ff-rd.com; [5]oznur.iskender@ff-rd.com (Corresponding Author)

1. Giriş

Enerjinin sıvı, katı veya gaz ortamda transferi esnasında oluşturduğu mekanik titreşimler ses olarak adlandırılmaktadır [1]. Titreşim enerjiye dönüşür ve dalgalar halinde yayılır. Ses dalgalarına akustik dalgalar da denmektedir. Ses dalgaları mekanik ve boyuna dalgalardır. Bir saniyede oluşan ses dalgası sayısına, frekans denmekte olup, birimi Hertz (Hz)'tir [2]. Gürültü, temel olarak titreşim halindeki bir parçanın meydana getirdiği istenmeyen ses olarak bilinmektedir. Gürültü, ses başlığı altında değerlendirildiğinde ise bir anlam vermeyen, belli bir ses seviyesini aşan durumlarda kullanılır. Bu açıdan bakıldığında, istenmeyen seviyelere ulaşmış sesler gürültü olarak değerlendirilmektedir. Örneğin yüksek devirlerde kullanılan bir binek araç "gürültü" olarak algılanabilir. Kuş ötmesi, matkap sesi, yoldan gelen traktör sesi veya havaalanına yakın bir bölgede duyulan helikopter sesi de "gürültü" olarak değerlendirilebilir [3]. Gürültüyü kontrol etmek ve gürültü kaynağını engellemek üzerine araştırmalar yapan bilim dalı akustiktir [2].

Taşıtlarda gürültü kontrolü, gürültüyü oluşturan kaynakların fazla olması ve gürültü yayılım yollarının çeşitliliği nedeniyle çözümü zor akustik bir problemdir. Ses ve titreşimlerin taşıtın bütün gövdesi ve donanımları üzerinden yayılabilmesinden dolayı öncelikle taşıttaki gürültü kaynakları belirlenmelidir [4]. Taşıtların sebep oldukları gürültüler dış ve iç gürültü olarak iki başlık altında incelenebilmektedir. Taşıt içerisindeki konfor ve rahatı iç gürültü etkilerken, taşıtın çevreye verdiği rahatsızlığın ana sebebi dış gürültüdür [5].

Araçlarda iç gürültünün en önemli kaynağı motordur. İçten yanmalı motorlarda gürültü genel olarak mekanik gürültü, yanma gürültüsü ve yardımcı ekipmanlardan kaynaklanan gürültüler olarak üç ana başlık altında toplanabilmektedir. Çeşitli operasyon koşullarında, motor komponentlerinin motor gürültüsüne katkısı motor çeşidine bağlıdır [6]. Kamyonlarda da kullanılan V-6 motorundaki gürültü kaynaklarının frekans aralıkları incelendiğinde, yanma gürültüsünün 500-8000Hz olduğu tespit edilmiştir [7]. Motor yüzeyinden yayılan gürültü mekanizması incelendiğinde ise motor yanma gürültüsünün 500-5000Hz aralığında etkin olduğu görülmüştür [8]. Ancak bir insan 20-10000Hz arasındaki sesleri duymakta iken (kişiye ve yaşa göre değişir) esas olarak 1000-4000Hz arasını daha çok duymaktadır [9].

Otomotiv sektöründe, gürültü, titreşim ve konfor (NVH), araçların özellikle de otomobillerin ve kamyonların gürültü ve titreşim özelliklerinin incelenmesi ve değiştirilmesidir. Araç içerisindeki sürücü ve yolcuların yaşadığı gürültü ve titreşimle iç NVH ilgilenirken dış NVH, büyük ölçüde araç tarafından yayılan gürültüyle ilgilenmekte ve araçtan dış ortama yayılan gürültülerin testlerini içermektedir [10].

Bahsedilen tüm bu değişkenler tasarlanıp üretilen aracın kabin içi ve kabin dışında NVH açısından rekabetçi olmasını sağlayan en temel özelliklerdir. Son yıllarda otomotiv sektöründe artan rekabet ve gelişen teknoloji ile otomotiv firmaları Ar-Ge departmanları içerisinde barındırdıkları araç mühendisliği ekipleriyle bu konu üzerine ciddi çalışmalar yürütülmektedir [11].

Malzemelerin ses emme verimliliğini değerlendirmek için yaygın olarak kullanılan nicelik, soğurulan enerjinin gelen enerjiye oranı olarak tanımlanan ses yutum katsayısıdır ve α ile temsil edilmektedir. Akustik enerji tamamen emilebiliyorsa, $\alpha=1$'dir [12]. Araç kabinlerinde gürültü seviyesini azaltmak üzere, farklı malzeme kompozisyonları ile konumlandırılacakları alana özel yalıtım parçaları kullanılmaktadır. Araç içi gürültü kontrolünde kullanılan bu yalıtım parçalarının da ses yutum katsayısının olabildiğince 1'e yaklaşması beklenmektedir. Aracın çevreye yaydığı ses düzeyinin azaltılmasında kullanılan yalıtım parçalarından biri de gürültü kalkanıdır. Gürültü kalkanı, aracın ses üreten yapısı olan motoru en azından kısmen saracak şekilde düzenlenmiş, akustik izolasyon malzemesidir. Esas olarak ses üreten yapıya bakacak şekilde düzenlenmiş

birinci yüzey, ses üreten yapıdan uzağa bakacak şekilde düzenlenmiş ve zıt konumlandırılmış ikinci bir yüzey içermektedir [13]. Gelişen teknoloji ile araçlarda ağırlık artışı sağlamadan ses ve ısı gelen yapılardan yayılan gürültü ve ısıyı izole etmek üzere kullanılan gürültü kalkanının üretiminde de kompozit malzemeler kullanılmaya başlanmıştır. Üretiminde kompozit malzemelerin kullanıldığı ürünlerin ağırlık, rijitlik, aşınma dayanımı, kırılma tokluğu, yüksek sıcaklık özellikleri, yorulma dayanımı, korozyon dayanımı, ısıl ve akustik iletkenlik, fiyat ve estetik görünüm gibi özellikleri geliştirilebilmektedir [14].

Mineral katkılı malzemeler ve elyaflarla takviye edilmiş polimer malzemelerin akustik performans ve mekanik özelliklerinin incelenmesine yönelik literatürde çeşitli çalışmalar yer almaktadır. Otomotivde ses yutum malzemeleri ile ilgili farklı kalınlık, akış direnci ve yüzey yoğunluğuna sahip malzemelerin incelenmesi sonucunda, ince malzemelerde iyi yutum sağlanabilmesi için kalın örneklere göre daha belirgin bir akış direncine sahip olunması gerekliliği bildirilmiştir [15]. Gözenekli lifli malzemelerin ses yutma özelliklerinin araştırıldığı bir çalışmada, farklı kalınlıklarda, farklı yoğunluklara sahip cam yünü ve taş yünü numunelerinin ses yutma katsayıları ölçülmüş, numune kalınlığının artması ile ses yutma kapasitesinin arttırılabileceği tespit edilmiştir [16]. Cam elyaf takviyeli epoksi kompozit plakaların darbe davranışına plaka kalınlığının etkisinin incelendiği çalışmada, plaka kalınlığının artması ile kompozit plakanın darbe dayanımının arttığı sonucuna varılmıştır [17].

Bu çalışmada, kamyon, tır vb. gibi ağır hizmet araçlarının motor bölgelerinde ortaya çıkan ses ve yüksek sıcaklığın ortamlar arası geçişini engellemek üzere, ses ve ısı üreten yapıyı en azından kısmen örtecek şekilde konumlandırılan, yüksek mukavemet, düşük ağırlık, dayanıklılık, yanmazlık gibi özelliklerin yanı sıra düşük maliyetli bir malzeme kompozisyonuna sahip gürültü kalkanı elde edilmesine yönelik öncelikle malzeme kompozisyonları üzerine çalışmalar gerçekleştirilmiştir. Malzeme kompozisyonları belirlenirken; araç motor bölgesinde kullanılabilecek izolasyon malzemelerine ait test şartnameleri, maliyet, akustik ve NVH ihtiyaçları gibi durumlar bir arada düşünülmüştür. Akabinde malzeme kompozisyonları düz kalıplarda formlanarak sandviç panel formunda prototip üretimler gerçekleştirilmiştir. Elde edilen prototiplerin ses yutum katsayıları ölçülerek birbiri ile karşılaştırılmıştır. En iyi akustik performansa sahip malzeme kompozisyonu belirlenerek farklı kalınlıklarda prototip ürün üretimi gerçekleştirilmiş ve ürünlerin eğilme gerilmesi ölçümleri gerçekleştirilmiştir.

2. Materyal ve Yöntem

2.1. Malzeme Kompozisyonunun Geliştirilmesi

Son yıllarda havacılık, otomotiv ve gemi sanayinde yaygın olarak kullanılmakta olan ve kullanım alanları da her geçen gün artan kompozit malzemeler, diğer izo-tropik malzemelere (çelik, alüminyum vb.) kıyasla daha yüksek eğilme rijitliği, yüksek termal yalıtım, düşük özgül ağırlık, kolay tamir edilebilme gibi eşsiz özelliklere sahiptirler [18]. Çalışmada, yüksek mukavemet, düşük ağırlık, dayanıklılık, yanmazlık gibi özelliklerin yanı sıra düşük maliyetli bir gürültü kalkanı parçası elde etmek üzere sandviç panel formunda farklı malzeme kompozisyonu seçimleri gerçekleştirilmiştir. Malzeme kompozisyonları belirlenirken; araç motor bölgesinde kullanılabilecek izolasyon malzemelerine ait test şartnameleri, maliyet, akustik ve NVH ihtiyaçları gibi durumlar bir arada düşünülmüştür. Gürültü kalkanı parçasının üretiminde kullanılmak üzere seçilen alternatif malzeme kompozisyonları tablo 1'de verilmiştir.

Tablo 1. Malzeme kompozisyonları (MK)

	İçerik					
MK 1	%5,1 Kaplama telası	%42,0 PP/GF	%1,8 PE Film	%46,0 Taş Yünü	%5,1 Kaplama telası	
MK2	%4,0 Kaplama telası	%35,0 PP/GF	%0,5 PE Film	%18,5 GF/EP	%38,0 Taş yünü	%4,0 Kaplama telası
MK 3	%3,0 Kaplama telası	%28,0 Fenolik keçe	%28,0 PP/GF	%0,5 PE Film	%6,5 Karbon/EP	%31,0 Taş yünü %3,0 Kaplama telası
MK 4	%4,5 Kaplama telası	%39,0 PP/GF	%1,0 PE Film	%8,0 Karbon/EP	%43,0 Taş yünü	%4,5 Kaplama telası
MK 5	%3,0Kaplama telası	%26,5 PP/GF	%1,0 PE Film	37,50 GF/PET	%29,0 Taş yünü	%3,0 Kaplama telası

2.2. Prototip Ürünlerin Hazırlanması

Tablo-1'de verilen malzeme kompozisyonları kullanılarak düz kalıpta 190 °C sıcaklıkta ve 110 bar basınç altında sandviç panel formunda prototip ürün üretimleri gerçekleştirilmiştir. Üretimlerde, elde edilecek prototip ürün kalınlığına etki eden ve kalıp üzerine yerleştirilen stoperlerin kalınlıkları ve kalıplama süreleri değiştirilerek 12 adet prototip ürün üretimi gerçekleştirilmiştir. Prototip ürün üretiminde kullanılan malzeme kompozisyonları, proses parametreleri ve stoper kalınlıkları tablo 2'de verilmiştir.

Tablo 2. Malzeme kompozisyonları, proses parametreleri ve stoper kalınlıkları

Numune numarası	Malzeme kompozisyonu	Kalıp sıcaklığı (C°)	Kalıp basıncı (Bar)	Stoper Kalınlığı (mm)	Kalıplama Süresi (dk)
1	Malzeme kompozisyonu 1	190	110	20	3
2	Malzeme kompozisyonu 1	190	110	15	4
3	Malzeme kompozisyonu 1	190	110	7.5	5
4	Malzeme kompozisyonu 2	190	110	7.5	5
5	Malzeme kompozisyonu 2	190	110	7.5	4
6	Malzeme kompozisyonu 4	190	110	7.5	4
7	Malzeme kompozisyonu 3	190	110	7.5	4
8	Malzeme kompozisyonu 4	190	110	7.5	3
9	Malzeme kompozisyonu 5	190	110	7.5	2
10	Malzeme kompozisyonu 1	190	110	25	3
11	Malzeme kompozisyonu 1	190	110	30	3
12	Malzeme kompozisyonu 1	190	110	40	3

Sandviç panel formunda üretilen tüm prototip ürünlerde, ses ve ısı üreten yapıya bakacak yönde konumlandırılan alt katmanda 1200 kg/m^3 dansiteye sahip taş yünü kullanılmıştır. Ses ve ısı üreten yapıya uzak yönde konumlandırılan, gürültü kalkanı parçasının mukavemetini ve akustik performansını arttırmakla görevli olan üst katmanda ise ağırlıklı olarak 1100 kg/m^3 dansiteye sahip PP/GF (cam elyaf katkılı polipropilen) kullanılmıştır. Malzeme kompozisyonu 3'te diğer kompozisyonlardan farklı olarak PP/GF üzerinde 1100 kg/m^3 dansiteye sahip fenolik keçe kullanılmıştır. Alt ve üst katman arasında ise malzeme kompozisyonu 1'den farklı olarak 580 kg/m^3 dansiteye sahip GF/EP (cam elyaf takviyeli epoksi), Sheet Molding Compound (SMC) yöntemi ile üretilmiş 1550 kg/m^3 dansiteye sahip GF/PET (cam elyaf takviyeli polyester) ve 245 kg/m^3 dansiteye sahip karbon/EP (karbon elyaf takviyeli epoksi) kullanılmıştır. Çalışma kapsamında üretilen prototip ürünlerde en az 2 kat olacak şekilde yapıştırıcı malzeme olarak PE film kullanımı tercih edilmiştir. Prototip ürünlerin en dış katmanını oluşturan kaplama telası ise, piyasada PANOX® ticari ismi ile bilinen, alev geciktirici özelliğe haiz %50 karbon içerikli NW kumaştan mamul olup, 130 kg/m^3 dansiteye sahiptir.

2.3. Empedans (Kundt) Tüpü Ölçümleri

Ses yutma katsayısı ölçümlerinde kullanılan yaygın metot, empedans tüpünde yapılan ses şiddeti ölçümleridir. Ses yutma katsayısı, basit olarak emilen dalganın kaynaktan gelen dalgaya oranı olarak tanımlanmaktadır [19].

Empedans tüpü içerisine yerleştirilen 30-100 mm boyutlarındaki numunenin ses yutum katsayısı ve ses iletim kaybı değerleri numune üzerine yerleştirilen mikrofonlar yardımıyla ölçülmektedir [20].

Kamyon, tır vb. gibi ağır hizmet araçlarının motor bölgelerinde ses izolasyonu sağlamak ve motor bölgesinden gelen yüksek sıcaklığın izole edilmesini sağlamak amacıyla öncelikle 5 farklı malzeme kompozisyonu belirlenmiş olup, kalıp sıcaklığı ve basıncı sabit tutularak farklı kalıplama süreleri uygulanarak 9 adet prototip numune elde edilmiş ve bu ürünlerin akustik performans testleri, TS EN ISO 10534-2 standardına uygun olarak Formfleks Ar-Ge laboratuvarında yer alan empedans tüpü (Şekil 1) ile 250~6300Hz ölçüm aralığında gerçekleştirilmiştir. En iyi akustik performansı gösteren malzeme kompozisyonu ile hazırlanan 3 farklı kalınlıkta numunenin ses yutum katsayıları ölçülerek kalınlığın akustik performansa etkisi ayrıca incelenmiştir. Literatürde Kundt tüpü olarak da adlandırılan empedans tüpü, Alman fizikçi August Kundt tarafından bir gaz veya katı çubuktaki ses hızını ölçmek amacıyla icat edilen deneysel bir akustik cihazdır [21].

Şekil 1. Empedans tüpleri

2.4. Eğilme Testi

Eğilme testi, malzemenin mekanik özelliklerini incelemek üzere, aynı malzeme kompozisyonuna sahip 3 farklı kalınlıkta (10 mm, 20 mm, 30 mm) üretilen her bir prototip numuneden (Şekil 2) 80*10 mm boyutlarında 5 set test numunesi kesilmiş ve ISO 178 standardı kapsamında, test parametreleri hedef bükme mesafesi 20 mm, test hızı 20 mm/dakika olacak şekilde, Formfleks Ar-Ge laboratuvarında yer alan 5 kN kapasiteli çekme basma test makinesi ile gerçekleştirilmiştir (Şekil 3).

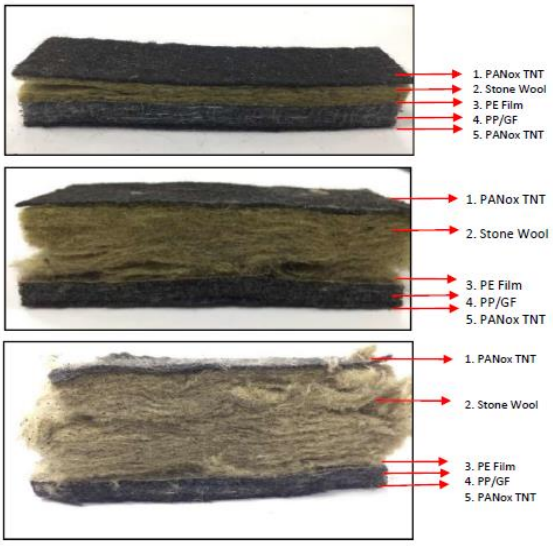

Şekil 2. Farklı kalınlıkta prototip numuneler

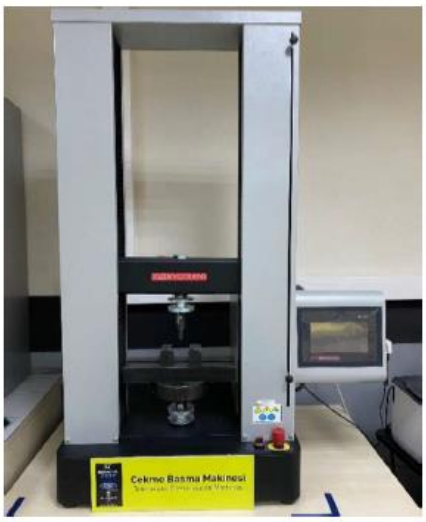

Şekil 3. Çekme basma test makinesi

3. Bulgular ve Tartışma

3.1. Akustik Performans Test Sonuçları

Aynı proses parametreleri (190 °C, 110 bar, 5 dakika) ve stoper kalınlığı (7.5 mm) kullanılarak malzeme kompozisyonu 1 ile prototip numune 3, malzeme kompozisyonu 2 ile de prototip numune 4 elde edilmiştir. Malzeme kompozisyonu 1 ve 2 ile elde edilen prototip numune 3 ve 4'ün ana matrisi aynı iken kompozisyon 2'de ses ve ısı üreten yapıya bakan katmanda kullanılan taş yünü altında ek olarak GF/EP kullanımı söz konusudur. Şekil 4'te prototip numune 3 ve numune 4'e ait ses yutum katsayısı-frekans grafiği verilmiştir. Her iki numuneye ait ses yutum katsayısı-frekans grafiği incelendiğinde; ses yutum katsayısının prototip numune 3'ün 400-2500Hz frekans aralığında daha iyi bir performans sergilediği gözlenmiştir.

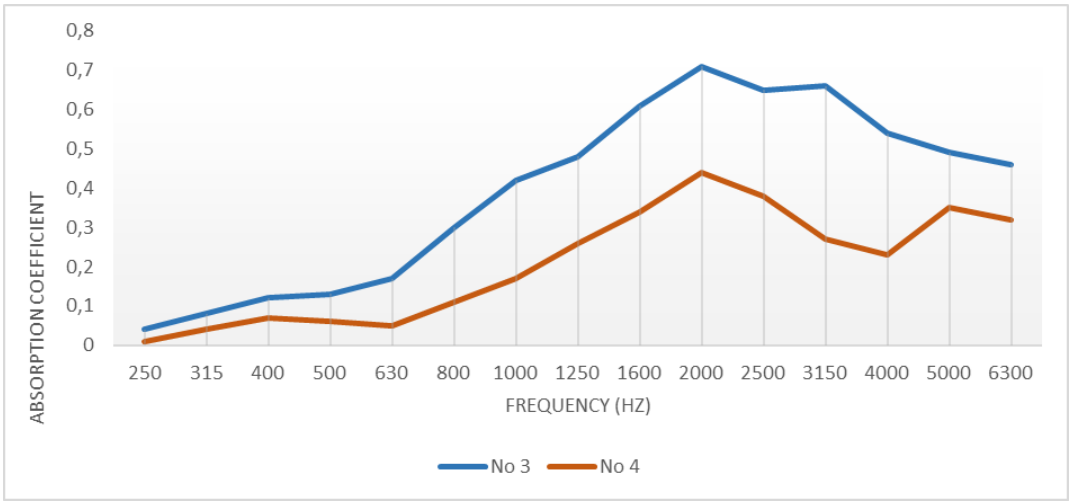

Şekil 4. Prototip numune 3 ve 4'e ait ses yutum katsayısı-frekans grafiği

Şekil 5'te prototip numune 6 ve 7'ye ait ses yutum katsayısı-frekans grafiği verilmiştir. Aynı proses parametreleri (190 °C, 110 bar, 4 dakika) ve stoper kalınlığı (7.5 mm) kullanılarak malzeme kompozisyonu 4 ile prototip numune 6, malzeme kompozisyonu 3 ile de prototip numune 7 elde edilmiştir. Malzeme kompozisyonu 4 ve 3 ile elde edilen prototip numune 6 ve 7'nin ana matrisi farklıdır. Bu malzemelerin ses absorpsiyonu üzerindeki etkisi incelendiğinde, prototip numune 6 ve 7 düşük frekanslarda benzer performansı

gösterirken, fenolik keçenin kullanıldığı prototip numune 7 yüksek frekanslarda daha iyi bir performans göstermiştir. Bunun nedeni, keçe malzemenin poroz yapısından kaynaklandığı düşünülmektedir. Cam elyaf malzeme, sahip olduğu yüksek mukavemet, hafiflik, esneklik, dayanıklılık, stabilite, ısıya, kimyasala ve neme karşı direnç gibi üstün özellikleri ile otomotiv üreticileri tarafından sıklıkla tercih edilmektedir [22]. Absorpsiyon katsayısı düşük olan malzemelerin iletim (bariyer) özelliğinin daha iyi olduğu görülmektedir. Otomotiv sektöründe, cam elyaf genel olarak bariyer görevi özelliği istenen malzemelerde kullanılmakta olup, elde edilen sonuçlarda bu bulguyu doğrular niteliktedir.

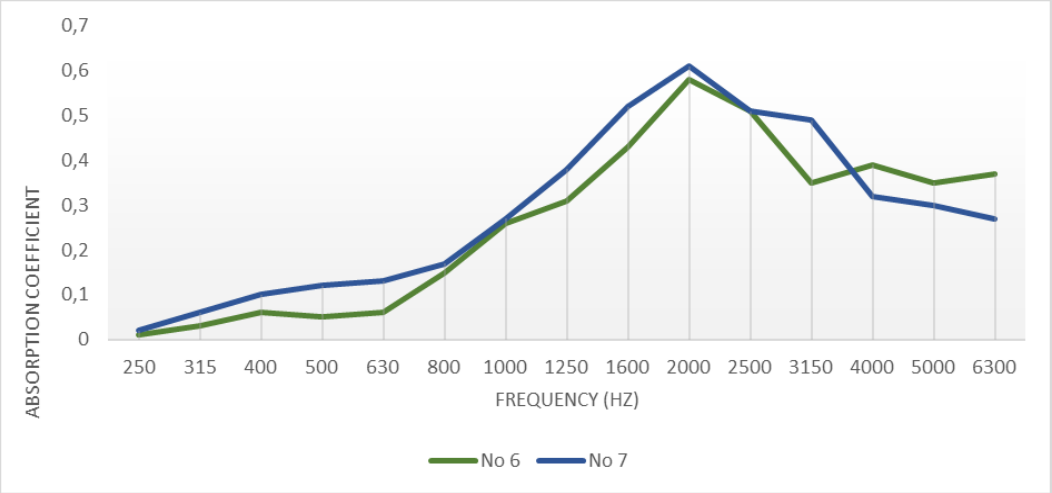

Şekil 5. Prototip numune 6 ve 7'ye ait ses yutum katsayısı-frekans grafiği

PP/GF rijitlik ve akustik isterleri karşılayan bir malzemedir. Malzeme kompozisyonu 2 ile üretilen prototip numune 5, malzeme kompozisyonu 4 ile elde edilen prototip numune 6 ve malzeme kompozisyonu 5 ile elde edilen prototip numune 9'a ait ses yutum katsayısı-frekans grafiği incelendiğinde prototip numune 6'nın 2000Hz ve üzerinde akustik performansının diğer iki numuneye göre daha iyi olduğu gözlenmektedir. Bunun nedeninin yapısında epoksi reçine ve karbon bulunması olduğu düşünülmektedir. Epoksi reçineler iki karbon ve bir oksijen atomundan oluşan üçlü halkanın bulunduğu epoksi gurubuyla tanımlanır. Epoksi gurubu diğer moleküllerle olan bağlanma noktasıdır ve elyaf yüzeyi gibi katı yüzeyler üzerinde yüksek adhezyon özelliğine sahiptir [23]. Adezyon özelliği, epoksi malzemenin daha mukavim olmasını, fiziksel yapısının daha poroz olmasını sağlamaktadır ve bunun da ses absorpsiyon katsayısının daha iyi çıkmasının bir sebebi olduğu düşünülmektedir. Şekil 6'da prototip numune 5, 6 ve 9'a ait ses yutum katsayısı-frekans grafiği verilmiştir.

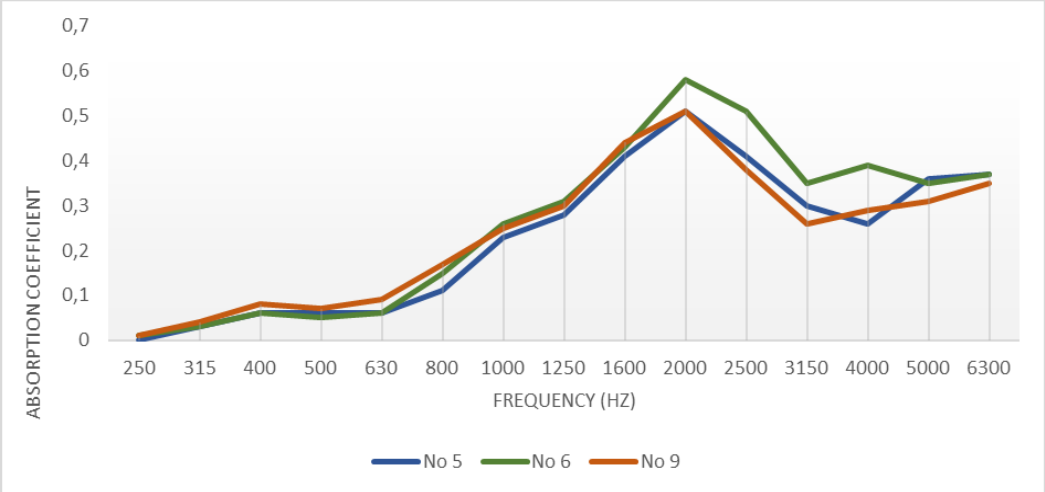

Şekil 6. Prototip numune 5, 6 ve 9'a ait ses yutum katsayısı-frekans grafiği

Çalışma kapsamında üretilen tüm prototip numunelere ait ses yutum katsayısı-frekans grafiği incelendiğinde ise, malzeme kompozisyonu 1 ile elde edilen prototip numunelerin 2000-4000Hz arasında akustik hedef olan ses yutum katsayısı α=1 değerine en yakın sonucu verdiği görülmektedir. Bunun nedeninin bileşenlerin bağ yapılarının kompozit yapı içerisinde birbiri ile sağladığı uyum olduğu düşünülmektedir. Malzeme kompozisyonu 1 içerisinde sağlanan yapıya katılan her bir yeni bileşenin ses absorpsiyonu kötü yönde etkilediği gözlenmiştir. Bu prototip numunelere ait empedans tüpü test sonuçları Tablo 3'te, ses yutum katsayısı-frekans grafiği ise Şekil 7'de verilmiştir.

Tablo 3. Prototip numunelere ait empedans tüpü test sonuçları

Frequency [Hz]	No 1	No 2	No 3	No 4	No 5	No 6	No 7	No 8	No 9
250	0.03	0.01	0.04	0.01	0	0.01	0.02	0.01	0.01
315	0.06	0.04	0.08	0.04	0.03	0.03	0.06	0.03	0.04
400	0.11	0.07	0.12	0.07	0.06	0.06	0.1	0.04	0.08
500	0.14	0.1	0.13	0.06	0.06	0.05	0.12	0.05	0.07
630	0.19	0.12	0.17	0.05	0.06	0.06	0.13	0.09	0.09
800	0.27	0.19	0.3	0.11	0.11	0.15	0.17	0.18	0.17
1000	0.38	0.29	0.42	0.17	0.23	0.26	0.27	0.25	0.25
1250	0.53	0.4	0.48	0.26	0.28	0.31	0.38	0.31	0.3
1600	0.68	0.54	0.61	0.34	0.41	0.43	0.52	0.44	0.44
2000	0.82	0.66	0.71	0.44	0.51	0.58	0.61	0.58	0.51
2500	0.92	0.73	0.65	0.38	0.41	0.51	0.51	0.6	0.38
3150	0.97	0.88	0.66	0.27	0.3	0.35	0.49	0.47	0.26
4000	0.98	0.92	0.54	0.23	0.26	0.39	0.32	0.4	0.29
5000	0.94	0.93	0.49	0.35	0.36	0.35	0.3	0.46	0.31
6300	0.91	0.92	0.46	0.32	0.37	0.37	0.27	0.51	0.35

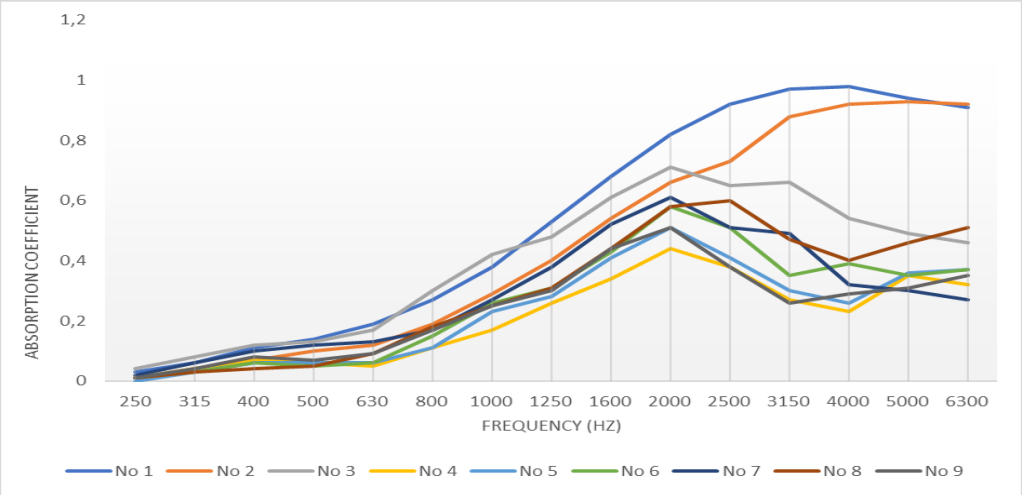

Şekil 7. Prototip numunelere ait ses yutum katsayısı-frekans grafiği

Kalınlığın akustik performansa etkisini incelemek üzere, en iyi akustik performansı gösteren malzeme kompozisyonu 1 ile hazırlanan farklı kalınlıklara sahip prototip numunelerin ses yutum katsayıları ölçülerek incelenmiştir. Tablo 4'te malzeme kompozisyonu 1 için kalınlık değişimine bağlı empedans tüpü test sonuçları, Şekil 8'de ise malzeme kompozisyonu 1 ile farklı kalınlıklarda üretilen prototip numunelerin ses yutum katsayısı-frekans grafiği verilmiştir. Söz konusu grafikten anlaşılacağı üzere, kalınlık arttıkça

malzemenin ses absorplama özelliği artmıştır. Bunun nedeni ses dalgalarının şiddetinin her bir katmanda azalmasıdır. Kalınlığın artması ile sesin kat ettiği mesafe artacaktır.

Tablo 4. Malzeme kompozisyonu 1 için kalınlık değişimine bağlı empedans tüpü test sonuçları

Frequency [Hz]	No 10	No 11	No 12
160	0	0.02	0.05
200	0.01	0.08	0.12
250	0.04	0.16	0.2
315	0.09	0.28	0.31
400	0.16	0.42	0.44
500	0.2	0.49	0.5
630	0.26	0.56	0.57
800	0.38	0.71	0.7
1000	0.51	0.84	0.82
1250	0.65	0.92	0.92
1600	0.76	0,97	0.97
2000	0.85	0.98	1
2500	0.93	0.95	0.99
3150	0.98	0.9	0.96
4000	0.98	0.85	0.94
5000	0.95	0.9	0.98
6300	0.94	0.96	1

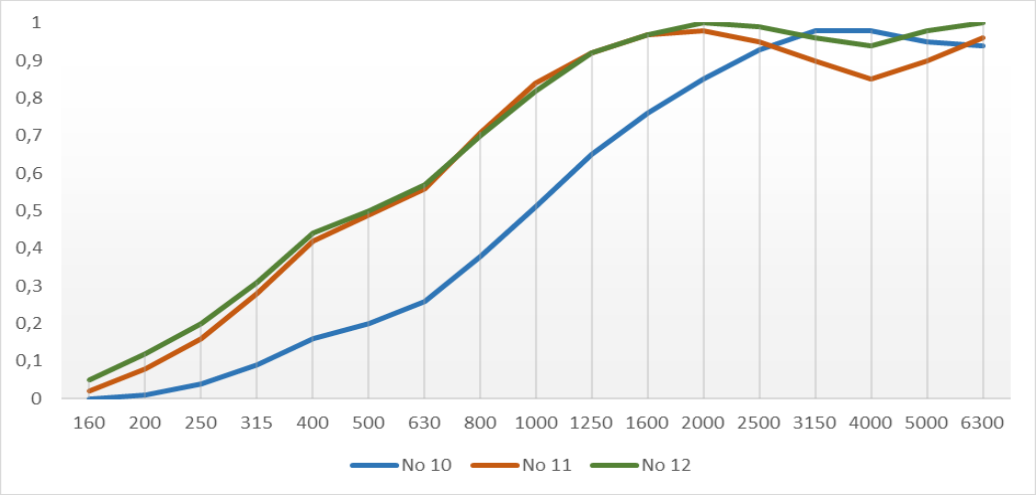

Şekil 8. Malzeme kompozisyonu 1 ile farklı kalınlıklarda üretilen prototip numunelerin ses yutum katsayısı-frekans grafiği

3.2. Eğilme Test Sonuçları

Çalışma kapsamında kalınlığın ses üzerindeki etkisini incelemek üzere, uzunlamasına yatay bir pozisyonda destekler üzerine konumlandırılan test numunelerinin tam ortasına test süresince artan değerlerde kuvvet uygulanmış ve her bir numune için elde edilen Fmax (maksimum kuvvet) değerleri Şekil 9'da Fmax kuvvetlerine karşılık gelen eğilme gerilmesi değerleri ise Şekil 10'da verilmiştir. Tablo 5'te farklı

kalınlıklardaki test numunelerin eğilme test sonuçlarına ait ortalama Fmax ve ortalama eğilme gerilmesi değerleri ayrıca verilmiştir.

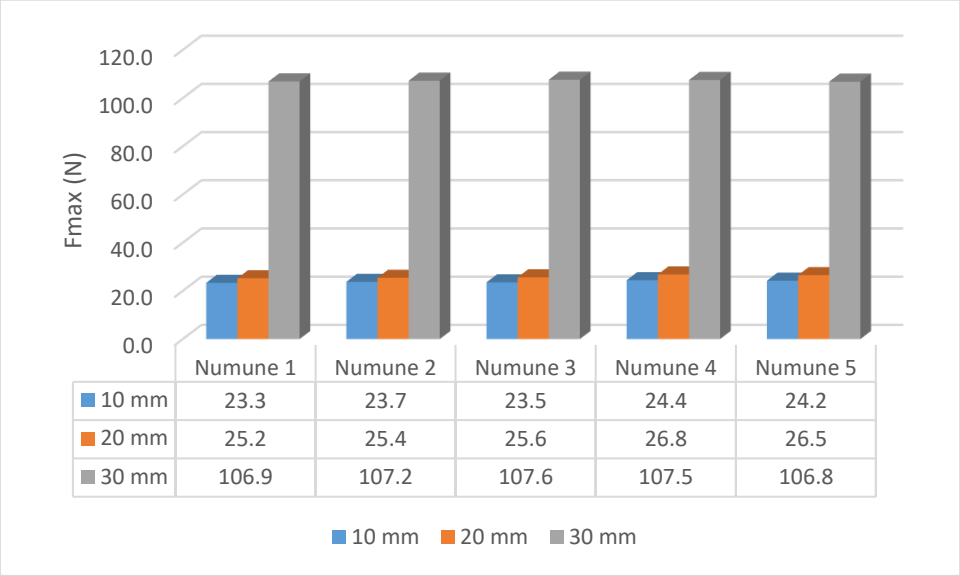

Şekil 9. Farklı kalınlıklardaki test numunelerinin Fmax grafiği

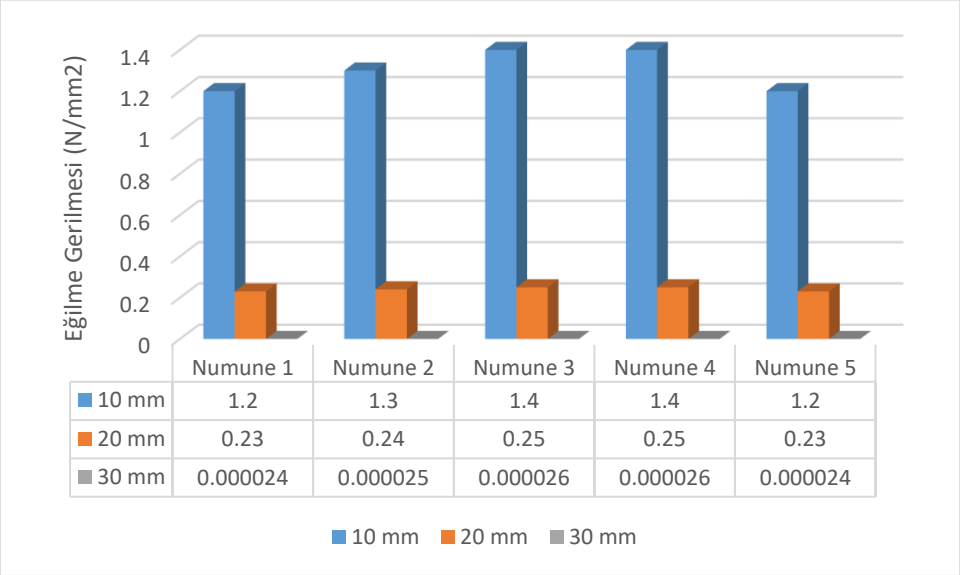

Şekil 10. Farklı kalınlıklardaki test numunelerinin eğilme gerilmesi grafiği

Tablo 5. Farklı kalınlıklardaki test numunelerin eğilme test sonuçlarına ait ortalama Fmax ve ortalama eğilme gerilmesi sonuçları

Kalınlık (mm)	Uygulanan maksimum kuvvet (N)	Eğilme gerilmesi (N/mm^2)
10	23.8	1.3
20	25.9	0.24
30	107.2	$2.5x10^{-5}$

3 nokta eğilme testi sonucunda, test numunelerinde herhangi bir kırılma ya da kopma yaşanmadığı ve buna ek olarak kalınlık arttıkça malzemenin yük dayanımının arttığı gözlenmiştir. Bu da motor bölgesinde kullanılacak olan parçanın darbelere karşı dayanıklı olmasını sağlayacaktır. Çalışma sonucunda elde edilen sonuçlar

literatür ile uyumludur. Kompozit tabaka kalınlığının artmasıyla darbe direncinin arttığı literatürde belirtilmiştir [24].

4. Sonuçlar

Bu çalışmada, ağır hizmet araçlarında gürültü kalkanı olarak kullanılmak üzere, ses ve ısı üreten yapıya bakacak yönde konumlandırılan alt katmanda taş yünü, gürültü kalkanı parçasının mukavemet ve akustik performansını arttırmakla görevli üst katmanda PP/GF, GF/EP, GF/PET, Karbon/EP, fenolik ve yapıştırıcı malzeme olarak PE film kullanılarak düz kalıpta, 190 °C sıcaklıkta ve 110 bar basınç altında kompozit sandviç yapılar oluşturulmuş ve bu yapıların empedans tüpünde ses yutum katsayıları ölçülerek akustik performansları birbiriyle karşılaştırılmıştır. Akustik performans test sonuçları incelendiğinde, ses yutum katsayısı (α) 1 değerine en yakın olan kompozit sandviç yapının dıştan içe doğru iki kaplama telası arasında PP/GF, PE film, taş yünü içeren malzeme kompozisyonu 1 olduğu tespit edilmiştir. Kalınlığın akustik performansa ve mukavemete etkisini incelemek üzere, en iyi akustik performansı gösteren malzeme kompozisyonu 1 ile 10 mm, 20 mm ve 30 mm kalınlıklarında üretilen numunelere akustik performans ve 3 nokta eğilme testleri uygulanmıştır. Elde edilen verilerden kalınlık arttıkça ses yutum kapasitesinin ve mukavemetinin arttığı tespit edilmiştir. Yapılan bu çalışmada, motorlu araçlarda kullanılan gürültü kalkanı parçasının geliştirilmesinde uzmanlara destek olacak malzeme kompozisyonları ortaya koyulmuş olup, gelecekte farklı malzeme kompozisyonları ile NVH alanında çalışmak isteyen uzmanlara yol göstereceği bir düşünülmektedir.

Yazar Katkıları

Tüm yazarlar bu çalışmaya eşit katkı sağlamıştır. Tüm yazarlar makalenin son halini okuyup onaylamıştır.

Çıkar Çatışması

Yazarlar hiçbir çıkar çatışması olmadığını beyan etmektedir.

Kaynaklar

[1] E. Karaman, *Recognition of vehicle models from engine sounds*, Master's Thesis Akdeniz University (2018) Antalya.

[2] E. N. Keskin, *Investigation the surface and acoustic properties of polyurethanes produced with different monomer mixing ratios*, Master's Thesis Bursa Uludağ University (2023) Bursa.

[3] P. Mallick, Materials, design and manufacturing for lightweight vehicles, 2nd Edition, Woodhead Publishing, 2021.

[4] N. Aktürk, O. Akdemir, İ. Üzkurt, *Environmental noise caused by traffic lights timing and traffic volume*, Journal of the Faculty of Engineering and Architecture of Gazi University 18 (1) (2003) 71–78.

[5] D. R. Raichel, The science and applications of acoustics, 2nd Edition, Springer, Berlin, 2006.

[6] E. Boztepe, *Investigation of relation between acoustic properties and heat conduction in automotive interior trim materials*, Master's Thesis Bursa Uludağ University (2018) Bursa.

[7] G. Shen, Vehicle noise, vibration, and sound quality, Warendale, Pensnsylvania, 2012.

[8] B. M. Spessert, H. S. Kochanowski, *Diesel engine noise emission*, in: K. Mollenhauer, H. Tschoeke (Eds.), Handbook of Diesel Engines, Springer, Berlin, Heidelberg, 2010, Ch. 16, pp. 487–504.

[9] P. B. Metinoğlu, *Effect of material and design in noise shields used in trucks*, Master's Thesis İstanbul

Technical University (2014) İstanbul.

[10] M. A. Balcı, *Research of the effect of engine beauty covers on vehicle's interior and exterior noises*, Master's Thesis Ege Üniversitesi (2022) İzmir.

[11] X. Wang, Vehicle noise and vibration refinement, Woodhead Publishing, Cambridge, 2010.

[12] M. Tuzla, *Structural optimization of automobile upper components*, Master's Thesis Bursa Uludağ Üniversitesi (2022) Bursa.

[13] F. A. Presezniak, L. Sofia, A Noise Shield Arrangement Comporising a Thermally Conductive Element – European Patent Application (EP4046875A1) (2021), https://worldwide.espacenet.com/patent/search/family/074672147/publication/EP4046875A1?q=EP4046875A1, Accessed 17 Nov 2023.

[14] Y. Ulcay, M. Akyol, R. Gemci, *Investigation of different cure methods on the interfacial strength of polymer based fiber reinforced composites*, Uludağ University Journal of The Faculty of Engineering and Architecture 7 (1) (2002) 93–116.

[15] A. Zent, J. T. Long, *Automotive sound absorbing material survey results*, Society of Automotive Engineering Noise and Vibration Conference and Exhibition, Illinois, 2007.

[16] C. N. Wang, J. H. Torng, *Experimental study of the absorption characteristics of some porous fibrous materials*, Applied Acoustics 62 (4) (2001) 447–459.

[17] Ü. Esendemir, A. Y. Caner, *Experimental investigations on the impact behavior of laminated composite materials*, Süleyman Demirel University Journal of Natural and Applied Sciences 22 (1) (2018) 207–215.

[18] O. Özdemir, H. Kandaş, *Thickness and temperature effects on the impact behavior of glass fiber reinforced polypropylene composites*, Journal of Textiles and Engineer 25 (110) (2018) 103–112.

[19] İ. Aydın, *Measurement of sound absorption coefficients on the automotive isolation materials and determining the optimum material thickness*, Master's Thesis Gazi Üniversity (2008) Ankara.

[20] T. Doğru, *Investigation of relation between acoustic properties and heat conduction in automotive interior trim materials*, Master's Thesis Bursa Uludağ Üniversity (2020) Bursa.

[21] A. Kundt, *Acoustic experiments*, The London, Edinburgh and Dublin Philosophical Magazine and Journal of Science 35 (4) (1866) 41–48.

[22] İ. Kocaoğlu, Otomotiv Sektöründe Kompozit Malzeme Kullanımı (2021), https://kalkinmaguncesi.izka.org.tr/index.php/2021/06/17/otomotiv-sektorunde-kompozit-malzeme-kullanimi/, Accessed 17 Nov 2023.

[23] M. Tanoğlu, M. Toğulga, *Kompozit malzemeler ve jeotermal uygulamaları*, Jeotermal Enerji Semineri (2005) 407–419.

[24] W. A. de Morais, S. N. Monteiro, J. R. M. d'Almeida, *Effect of the laminate thickness on the composite strength to repeated low energy impacts*, Composite Structures 70 (2005) 223–228.

Çanakkale Onsekiz Mart University

Journal of Advanced Research in Natural and Applied Sciences

dergipark.org.tr/tr/pub/jarnas

Open Access

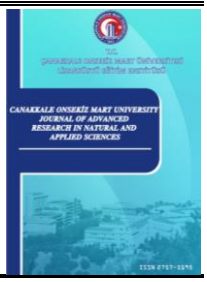

e-ISSN: 2757-5195 2024, Vol. 10, Issue 2, Pages: 312-328 doi.org/10.28979/jarnas.1392427

Machine Learning-Based Classification of Turkish Music for Mood-Driven Selection

Nazime Tokgöz[1], Ali Değirmenci[2], Ömer Karal[3]

[1,2,3]Department of Electrical and Electronics Engineering, Faculty of Engineering, Ankara Yıldırım Beyazıt University, Ankara, Türkiye

Article History

Received: 06 Oct 2023

Accepted: 01 Feb 2024

Published: 25 Jun 2024

Research Article

Abstract − Music holds a significant role in our daily lives, and its impact on emotions has been a focal point of research across various disciplines, including psychology, sociology, and statistics. Ongoing studies continue to explore this intriguing relationship. With advancing technology, the ability to choose from a diverse range of music has expanded. Recent trends highlight a growing preference for searching for music based on emotional attributes rather than individual preferences or genres. The act of selecting music based on emotional states is important on both a universal and cultural level. This study seeks to employ machine learning-based methods to classify four different music genres using a minimal set of features. The objective is to facilitate the process of choosing Turkish music according to one's mood. The classification methods employed include Decision Tree, Random Forest (RF), Support Vector Machines (SVM), and k-Nearest Neighbor, coupled with the Mutual Information (MI) feature selection algorithm. Experimental results reveal that, with all features considered in the dataset, RF achieved the highest accuracy at 0.8098. However, when the MI algorithm was applied, SVM exhibited the best accuracy at 0.8068. Considering both memory consumption and accuracy, the RF method emerges as a favorable choice for selecting Turkish music based on emotional states. This research not only advances our understanding of the interaction between music and emotions but also provides practical insights for individuals who want to shape their music according to their emotional preferences.

Keywords − *Classification, emotions, feature selection, music genres, mutual information*

1. Introduction

Music, an integral part of our daily lives, transcends cultural and linguistic boundaries, serving various purposes with its universal language and structure. From melodies heard in the womb, comforting lullabies sung as a baby, to songs shared during school days, music plays an important role in shaping our experiences and emotions [1, 2].

Often referred to as the "food of the soul," music possesses the transformative power to influence a person's emotional state in response to external stimuli. Recent years have seen music increasingly used in meditation practices and subliminal suggestions, emphasizing the potential impact of music on psychological health. [3]. The suggestive power of music holds particular significance in therapeutic contexts, where repetition enhances the acceptance of suggestions, with music serving as a carrier of hidden messages. The choice of songs and lyrics can wield a profound influence on emotions, whether intentional or not, eliciting calming, instructive, exhilarating, or even angering effects based on musical type and rhythm. People usually make predictions about what will happen next while listening to music. This causes music to be processed in the brain as action, emotion, and learning [4]. The emotional and calming effects of music have been evidenced in diverse settings,

[1]n.tokgoz@ankarad.com; [2]alidegirmenci@ybu.edu.tr; [3]omerkaral@ybu.edu.tr (Corresponding Author)

from studies involving pregnant women to those conducted before and during surgical procedures [5].

With music's profound impact on individual moods and its listening by large audiences, there has been a growing inclination for people to choose music aligned with their emotional states. This desire has prompted the need to develop methods for selecting or measuring the change in emotion based on music selection [6].

In recent years, numerous studies have been conducted around the world exploring the intersection of music and emotions. Fritz et al. recorded individuals' facial expressions while listening to music and then segmented their moods into three basic emotional states: happy, sad, and scared [7]. Mahadik et al. focused on classifying music selections based on facial emotion expressions, including emotions such as happy, angry, sad, neutral, surprised, and afraid, and then recommending music that aligned with the identified emotion [8]. Durahim et al. developed a model to automatically detect perceived emotion from song lyrics with the help of machine learning algorithms [9]. Er and Aydilek pioneered a novel music emotion recognition method, employing deep learning techniques on pre-trained deep networks, diverging from frequently utilized machine learning methods [10]. The optimal result, determined through VGG-16 in the Fc7 layer, yielded an accuracy of 89.2%. Chaudhary et al. proposed three distinct Music Emotion Classification Systems (MECS), with the first two utilizing Convolutional Neural Network (CNN) and the last employing Support Vector Machine (SVM) [11]. The song database was categorized into four, eight, and sixteen classes, achieving accuracies of 91%, 88%, and 86% in three experiments for the first MECS model. Quasim et al. introduced an Emotion-Based Music Recommendation and Classification Framework (EMRCF), achieving 96.12% accuracy with high precision in classifying songs based on individuals' interpersonal teams, incorporating memory and emotion [12]. Su et al. proposed a music recognition method combining Deep Learning (DL) and SVM, demonstrating its superiority over other audio-based music emotion tagging methods based on results obtained from the CAL500 dataset [13]. Pandrea et al. conducted experimental studies on a novel emotion detection approach, presenting a language-aware end-to-end architecture (SincNet) model that learns to label emotions in music with lyrics in three different languages, achieving 71% accuracy on the Turkish Emotion dataset [14]. Ciborowski et al. introduced an emotion model predicting nine emotional states, with color assignments based on the color theory in film, achieving the best result with the Inception V3 method with a minimal Mean Squared Error (MSE) of 0.0542% [15]. Huang et al. developed an end-to-end Attention-based Deep Feature Fusion (ADFF) technique for music emotion recognition, achieving relative improvements of 10.43% and 4.82% in valence [16]. Zhang et al. employed VGGish and SVM methods together for emotion classification, obtaining the highest success with 66.98% accuracy [17].

In the realm of machine learning, feature selection is crucial for revealing the most descriptive features (k features) while minimizing generalization error. This process significantly influences the performance of machine learning models, as an excess of features can extend training times, reduce interpretability, and potentially lead to overfitting. Due to overfitting, the model success may be high in the training but low in the test data.

The Turkish Music Emotion data set in Er and Aydilek used in our study has been the focus of some studies in the literature [10]. Moldovan developed the Binary Horse Optimization Algorithm (BHOA), a bio-inspired feature selection method that can be used for different classification techniques. The performance of BHOA was evaluated via six machine learning methods (Logistic Regression (LR), k-Nearest Neighbors (kNN), Decision Tree (DT), Random Forest (RF), Gradient Boosted Tree (GBT), and SVM) on nine different datasets, including the Turkish Music Emotion dataset [18]. The datasets were randomly split into 80% (training) and 20% (testing) sets, and the results from BHOA were compared with the binary particle swarm optimization, binary gray wolf optimizer, and binary crow search optimization algorithms. Experimental results showed that

the developed BHOA showed promising performance when compared with alternative optimization algorithms. Pandrea et al. applied the SincNet architecture to Mandarin, English, and Turkish music emotion datasets with in-dataset and mixed dataset setups [14]. The accuracy achieved within the scope of Turkish Music Emotion data was reported as 63%. Feng et al. proposed the FESVM method, which is SVM and feature generation-based ensemble learning [19]. New features are produced from the classification probabilities obtained from the basic classifiers, and hyperparameter optimization is carried out with 5-fold cross-validation, using 70% of the datasets for training and 30% for testing. The accuracy of the FESVM method on the Turkish Emotion dataset is reported as 81.5%. Compared with the results obtained in our study, the combination of our proposed MI feature selection method and RF machine learning algorithm achieved an accuracy of 80.75% using only 20 features. This shows that the method we present is more convenient in terms of both memory and speed.

In this research, the Turkish Music dataset from Er and Aydilek served as the foundation for selecting music based on individual moods or gauging the emotional shifts prompted by specific music choices [10]. To achieve this objective, four distinct machine-learning algorithms were employed: DT, kNN, RF, and SVM. Diverging from conventional practices, the dataset was not partitioned into fixed proportions for training and testing; instead, the k-fold cross-validation method was adopted to enhance reliability and observe the impact of each sample. To optimize the performance of kNN, RF, and SVM methods, meticulous investigations into method-specific hyperparameters were conducted. The grid search method was utilized to identify hyperparameters that yielded the highest scores. Subsequently, the importance of each feature was assessed through the Mutual Information (MI) feature selection algorithm. Machine learning models were trained using subsets of data, with features ranked from the highest to the lowest mutual information score. This approach aimed to achieve optimal performance by utilizing the minimum number of features. Experimental results indicated that the RF method outperformed others in both feature selection and without feature selection. The RF method achieved the highest accuracy score of 81% when considering all features in the dataset. Impressively, even with only 20 features, the accuracy remained high at 80.75%. Notably, thanks to the MIFS algorithm, a comparable level of accuracy was attained using only 40% of the features in the dataset. This highlights the effectiveness of feature selection techniques in optimizing the performance of machine learning models.

The subsequent sections of this study are outlined as follows: In Section 2, detailed presentation of the materials used, and the methodologies employed is provided. Section 3 delves into the outcomes of the study and engages in a comprehensive discussion. The MI feature selection algorithm, instrumental in identifying descriptive features within the dataset, is introduced. Additionally, the machine learning methods employed for music emotion classification are explicated, paving the way for an in-depth exploration of the results. Section 4 encompasses a thorough examination of the metrics employed to evaluate the performance of machine learning methods in Turkish music emotion classification. This includes an analysis of both machine learning methods and the feature selection technique, shedding light on the experimental results. The final section encapsulates the conclusions drawn from the study and outlines potential avenues for future research. It provides a succinct summary of the key findings and offers insights into areas where further exploration and refinement could enhance the understanding and application of machine learning in the context of Turkish music emotion classification.

2. Materials and Methods

In this study, Turkish music emotion datasets were used from the UCI machine learning repository. The dataset, structured as a discrete model, comprises four distinct classes representing basic emotional states, namely happy, sad, angry, and relaxed. To create the dataset, verbal, and non-verbal music from diverse genres of Turkish music were carefully selected. The database includes a total of 100 music pieces, ensuring an equal distribution of samples across each emotional class. The original dataset has 400 samples, each lasting 30 seconds [10]. For feature extraction, the MIR toolbox was utilized to analyze the emotional content within musical signals. Various features, including mel frequency cepstral coefficients, chromagram, tempo, and spectral and harmonic features, were extracted. This comprehensive feature extraction process aimed to provide a nuanced examination of the emotional nuances embedded in the Turkish music samples.

2.1. Methods

Within the framework of this study, a comparative analysis is conducted on four distinct machine learning methods employed to classify emotions within the Turkish music emotion dataset. Additionally, feature selection is integrated into the methodology to pinpoint the most informative features, as explained by Çakır et al. [20]. The following subsections provide details regarding the specific machine learning methods and feature selection techniques, ensuring a comprehensive understanding of the methodology employed in the study. This rigorous approach aims to enhance the interpretability and effectiveness of the machine learning models developed for emotion classification in Turkish music.

2.1.1. Mutual Information (MI)

The dependency or measure of shared information between two random variables is defined as MI. The definition of entropy can be defined by the concept given by Shannon [21].

$$H(A) := -\sum_{x} p(a)\log_2\big(p(a)\big) \tag{2.1}$$

(2.1) gives the uncertainty associated with the random variable A. In feature selection, the focus is on maximizing the information shared between the target and feature variables.

The joint entropy value, defined by (2.2), quantifies the uncertainty present in two random discrete variables, like A and B, simultaneously.

$$\begin{aligned} H(B\backslash A) &= -\sum_{a\in A}\sum_{b\in B} p(a,b)\log_2 p(b\backslash a) \\ H(A,B) &= -\sum_{a\in A}\sum_{b\in B} p(a,b)\log_2 p(a,b) \end{aligned} \tag{2.2}$$

When the specific value of A is denoted as "a" and the specific value of B is "b", the probability of these values occurring together, denoted as $p(a,b)$, is taken into account. The expression $p(a,b)\log_2 p(a,b)$ is defined to be 0 if $p(a,b)=0$. The value of joint entropy varies based on the dependence between A and B. If A and B are completely dependent, then the joint entropy is at its minimum, whereas it reaches its maximum when they are entirely independent.

Conditional entropy measures the uncertainty of B when the value of A is known and is mathematically defined as follows (2.3):

$$H(B\backslash A) = -\sum_{a\in A}\sum_{b\in B} p(a,b)\log_2 p(b\backslash a) \tag{2.3}$$

Entropy serves as a metric to quantify the information that one variable contains about another. MI is defined as the relative entropy between joint distributions, as outlined by Gonzalez-Lopez et al. [22]. The product distribution is depicted in (2.4):

$$MI(A;B) = \sum_{a\in A}\sum_{b\in B} p(a,b)\log\left(\frac{p(a,b)}{p(a),p(b)}\right) \tag{2.4}$$

$$MI(A,B) = H(B) - H(B|A)$$

$$MI(A,B) = H(A) - H(A|B) \tag{2.5}$$

$$MI(A,B) = H(A) + H(B) - H(A,B)$$

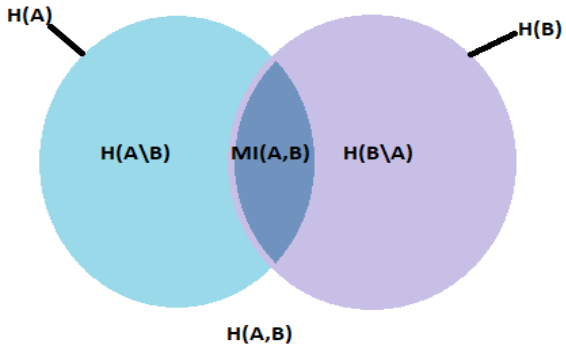

Figure 1. Venn diagram illustrating the entropy and MI relationships between two correlated variables (A and B)

An algorithm is used to determine maximum of MI. There is a subset of features initialized with a feature, denoted by the S matrix, and features are sequentially added to this subset one by one Zhang et al. [23].

$$j = \underset{j\notin S}{\operatorname{argmax}}\, MI\left(Y_S \cup x^j; t\right) \tag{2.6}$$

(2.6) is also employed for the selection of the initial feature. The chosen features are treated as independent. Once the increase in MI reaches its peak, the addition of new features is stopped. When the increase in MI is highest, adding new features is stopped. This methodology facilitates the reduction of feature dimensionality [24].

2.1.2. k-Nearest Neighbour (kNN)

The kNN is a straightforward yet widely used machine learning technique that has demonstrated success across various fields. Its application extends to diverse data types such as free text, images, audio, and video. In the kNN approach, a database is searched for identifying items most similar to a given query item, with similarity

determined by a defined distance function. Each item in the database is associated with a label (class), and the primary goal of the algorithm is to determine the class of a new state [25].

kNN relies on two user-defined hyperparameters: the number of nearest neighbors (k) and the choice of distance functions. The parameter k indicates the number of nearest neighbor samples considered to determine the class of the query sample within the dataset. Distance functions play an important role in measuring the distance between samples, significantly affecting the performance of the kNN classifier. Commonly used distance metrics include Euclidean distance and Manhattan distance in the kNN technique. Optimizing these hyperparameters is essential for achieving optimal performance across different datasets.

2.1.2.1. Euclidean Distance

The Euclidean distance, widely used in machine learning, shows the distance between points on a straight line. Computing the distance between two points is based on the Pythagorean theorem. Euclidean distance is determined by taking the square root of the sum of squared difference between two vectors. Mathematically, the Euclidean distance is defined as:

$$d_{Euclidean}(x_1, x_2) = \left(\sum_{k=1}^{n} (x_{1i} - x_{2i})^2 \right)^{\frac{1}{2}} \tag{2.7}$$

where $d_{Euclidean}$ is the Euclidean distance between the two samples, x_1 and x_2 represent the two samples whose distances are to be calculated and i is the features in these samples, and n is equal to the number of features in the dataset.

2.1.2.2. Manhattan Distance

The Manhattan distance, also known as city block distance or taxi-cab distance, expresses the absolute difference of the coordinates of x and y objects in D space [26]. Mathematically, Manhattan distance is given by

$$d_{Manhattan}(x_1, x_2) = \sum_{k=1}^{n} |x_{1i} - x_{2i}| \tag{2.8}$$

A visualization of the Euclidean and Manhattan distances employed for determining nearest neighbors for 2D data is given in Figure 2.

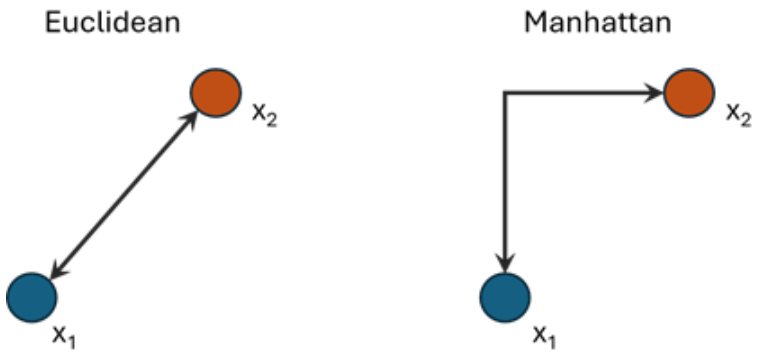

Figure 2. Distance computation with Euclidean and Manhattan metrics in 2D data

2.1.3. Decision Tree (DT)

The DT method is the process of classifying each observation, starting from the root node to the leaves, assigning a "Yes" or "No" outcome based on specific situation. A splitting condition is applied to each node to produce homogeneous subsets. The best split conditions can be selected this way. Impurity measurement is performed for each split state to select the split condition with the lowest impurity value. Various indices such as Gini index, Information gain, gain ratio and misclassification rate have been proposed in the literature to measure the impurity value of a split condition. This study will specifically investigate the effect of Gini index and information gain on classification [27]. The structure of the decision tree is shown in Figure 3.

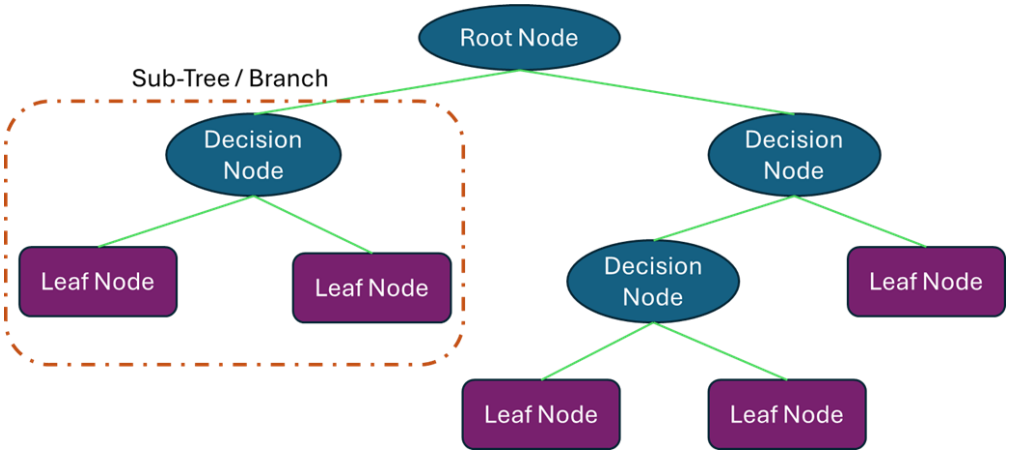

Figure 3. Structural representation of Decision Tree

2.1.3.1. Gini Index

Consider a learning example denoted as $L = \{(x_1, c_1), (x_2, c_2), \cdots, (x_i, c_j)\}$ where $x_1, x_2, \cdots, x_i$ represents an observation vector, and $c_1, c_2, \cdots, c_j$ are the class labels. x_i is a vector of input variables. The division conditions depend on one of these variables. Let p_i denote the probability that a random beam belongs to class c_i [28]. After p_i can be measured as (2.9):

$$p_i = \frac{C_i}{L} \tag{2.9}$$

The Gini index serves as a metric to demonstrate the purity of a class. In the process of determining purity, dataset is initially divided with respect to a specific characteristic, and the resulting clusters' purity improves with a well-executed division. If we denote L as a dataset with J different class labels, the Gini index is computed by (2.10) [29].

$$Gini(L) = 1 - \sum_{i=1}^{j} p_i^2 \tag{2.10}$$

where p_i is relative frequency if class i in L. If the dataset is divided by attribute A into two subsets L_1 and L_2 with dimensions N_1 and N_2 respectively, Gini is computed as (2.11):

$$Gini_A(L) = \frac{N_1}{N} Gini(L_1) + \frac{N_2}{N} Gini(L_2) \tag{2.11}$$

Reduction in impurity computed as (2.12):

$$\Delta Gini(A) = Gini(L) - Gini_A(L) \tag{2.12}$$

2.1.3.2. Entropy

Information gain is based on entropy, a measure of impurity or randomness in a dataset [30]. Homogeneous subsets within a dataset imply no impurity or randomness. If all measurements in the subsets belong to a one class, the entropy value for the dataset will be 0. The computation involves summing the probability of each label and the log probability of the same label, denoted by (2.13):

$$Entropy(L) = -\sum_{i=1}^{j} p_i \log_2(p_i) \tag{2.13}$$

For a dataset with one class label, p_i will be 1 and $\log_2(p_i)$ is 0. If the dataset is homogeneous, entropy is zero. As uncertainty, impurity and mixing ratio increase, the entropy value also increases [31].

2.1.4. Random forest (RF)

RF algorithm aims to increase the classification accuracy by employing multiple decision trees during the classification process. It incorporates several hyperparameters that control the structure of each tree for example, the minimum node size for node division. In addition, it influences the overall structure and size of the forest including the number of trees, and the level of randomness presented in the model [32].

The number of trees in a forest is a parameter that cannot be adjusted in the classical sense but needs to be set high enough. For certain error metrics, out-of-bag error curves (somewhat) are observed from time to time, increasing with the number of trees. The rate of convergence, and therefore the number of trees required to achieve optimum performance, depends on the characteristics of the dataset.

Oshiro et al. and Probst and Boulesteix using multiple datasets empirically show that the most remarkable performance improvement usually occurs with the initial 100 trees [33, 34]. The convergence speed of RF relies on both the dataset's characteristics and the hyperparameters. A lower sample size, higher node size values, and smaller input values lead to fewer correlated trees. Since these trees are different from each other, they are expected to provide better predictions. Based on this fact, it is thought that convergence can be achieved by using more trees [32]. Moreover, the level of tree depth also affects the computation rate. The complexity of each decision tree is controlled by the maximum tree depth. The computational cost increases with increasing tree depth. The optimal depth depends on other forest parameters and data characteristics. Error can be reduced by ensuring appropriate depth. High depth may lead to overfitting. Increasing the depth too much reduces the prediction stability. The highest stability will be achieved by using shallow trees, but too much shallowness renders the model inadequate [35].

In the experiment, the training data was divided into random subsets and results were obtained for each subset. Subsequently, all the results were combined, and a majority voting approach was applied. Eventually, a result was obtained. The process of the random forest is depicted in Figure 4.

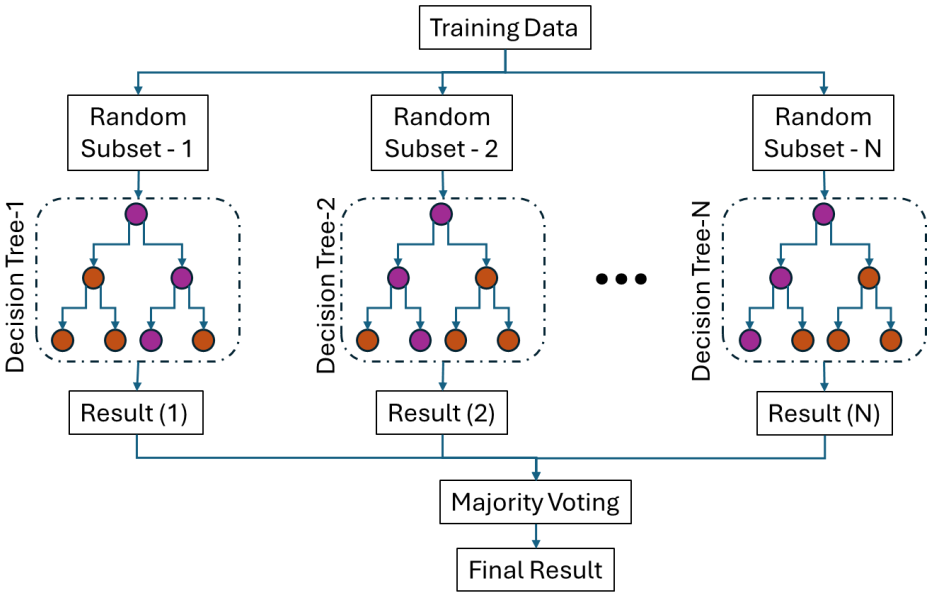

Figure 4. Graphical representation of Random Forest

2.1.5. Support Vector Machine (SVM)

The SVM are a non-parametric statistical learning method that operates in a supervised manner without making any assumptions about the data distribution. Initially introduced by Vapnik and his group in the 1970s, SVM operates on a kernel-based algorithm, typically defining a singular boundary between classes. It divides a dataset into predefined classes using training data. SVM determines the optimal hyperplane to be able to make a separate number of classifications. To maximize separation, it uses support vectors that are closest to the decision boundary of the training sample [36].

The linear separable SVM separates the training sample dataset samples of different categories in sample space where a training sample set is M with the appropriate dividing hyperplane.

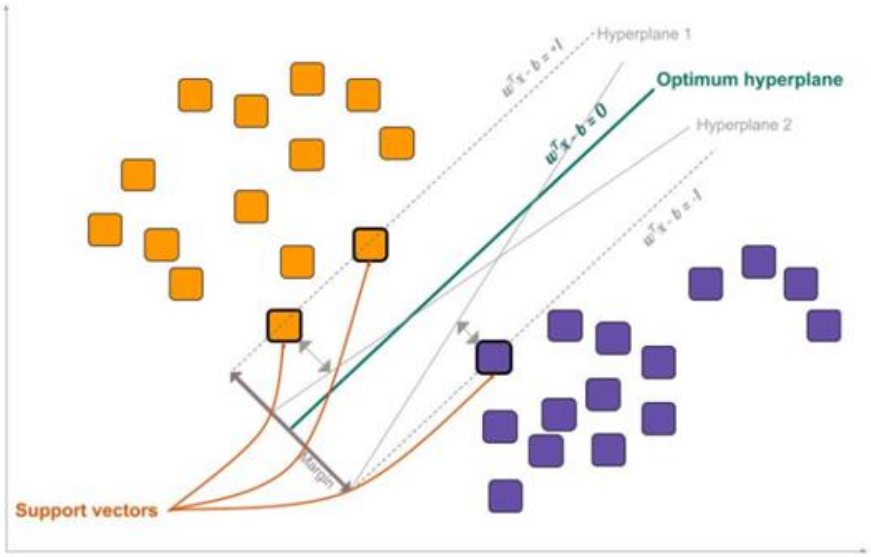

Figure 5. Linear SVM model

In the sample space, the following (2.14) is used to calculate the maximum interval, which expresses the division of the hyperplane.

$$\boldsymbol{w}^T x + b = 0 \tag{2.14}$$

where, **w** is a weight vector and *b* is a bias term. If the hyperplane can classify the samples correctly [37], then it verifies the following (2.15)

$$\begin{aligned} w^t x_i + b \geq 1, \quad & y = 1 \\ w^t x_i + b \leq -1, \quad & y = -1 \end{aligned} \tag{2.15}$$

The aim of the SVM model is to find optimally the **w** and *b* values. Thus, the hyperplane separates the data and maximizes the margin $\frac{2}{\|w\|}$. The linear SVM model is shown in Figure 5.

3. Results and Discussion

3.1. Performance Metrics

Performance metrics are utilized to assess the performance of machine learning methods. Studies in the literature have generally focused on binary classification problems in which there are only two classes. In binary classification problems 2×2 confusion matrix is generated but as the number of classes increases the dimension of the confusion matrix changes the $N \times N$ where N is the number of classes in the dataset. Consequently, the performance metrics derived from the confusion matrix undergo adjustments. The confusion matrix for *N* number of classes in shown in Table 1. i^{th} row j^{th} column in the confusion matrix corresponds to the element of C_{ij}. C_{ij} denotes the number of instances classified as C_j by the machine learning model from instances whose true class is C_i. The confusion matrix for multi-class classification is shown in Table 1.

Table 1. Confusion matrix for multi-class classification

		Predicted Class		
		C_1	$\cdots C_j \cdots$	C_N
Actual Class	C_1	C_{11}	C_{1j}	C_{1N}
	⋮		⋮	
	C_i	C_{i1}	$\cdots C_{ij} \cdots$	C_{iN}
	⋮		⋮	
	C_N	C_{N1}	C_{Nj}	C_{NN}

- True Positive (TP): The actual class is C_i, and it is predicted as C_j where $i = j$.
- False Positive (FP): value for a i^{th} class is the sum of the values in j^{th} column except C_{ij} where $i = j$
- False Negative (FN): value for a i^{th} class is the sum of the values in i^{th} row except C_{ij} where $i = j$
- True Negative (TN): equals to the sum of all the values in confusion matrix except for i^{th} row j^{th} column values where $i = j$

Performance metrics derived from the confusion matrix, provide valuable insights into the effectiveness of machine learning models in multi-class classification scenarios. Some commonly used metrics for multi-class classification include accuracy, micro average precision (MAP), micro average recall (MAR) and macro average F1-score.

Accuracy: measures the correct classification performance of the model. It is calculated as the ratio of the sum of all correctly classified samples to the number of samples in the dataset. It is defined as

$$Accuracy = \frac{\sum_{i=1}^{N} C_{ii}}{\sum_{i=1}^{N}\sum_{j=1}^{N} C_{ij}} \tag{3.1}$$

Macro average precision (MAP): MAP equals the average of precisions for each class in the dataset. It is defined as

$$MAP = \frac{1}{N}\sum_{i=1}^{N}\frac{C_{ii}}{C_{.i}}$$

where

$$C_{.i} = \sum_{j=1}^{N} C_{ji}, \quad \forall i \in \{1, \cdots, N\} \tag{3.2}$$

Macro average recall (MAR): The MAR is computed by averaging the recalls for each class in the dataset. It is given as

$$MAR = \frac{1}{N}\sum_{i=1}^{N}\frac{C_{ii}}{C_{i.}}$$

where

$$C_{i.} = \sum_{j=1}^{N} C_{ij}, \quad \forall i \in \{1, \cdots, N\} \tag{3.3}$$

Macro F1-Score combines the MAP, MAR metrics into a single performance metric, and is equal to their harmonic mean. Macro F1-score combines is evaluated by

$$MacroF1 - Score = \frac{1}{N}\sum_{i=1}^{N}\frac{2\frac{C_{ii}}{C_{.i}}\frac{C_{ii}}{C_{i.}}}{\frac{C_{ii}}{C_{.i}} + \frac{C_{ii}}{C_{i.}}} \tag{3.4}$$

3.2. Experimental Results

Emotions in Turkish music is predicted by four different machine learning methods: kNN, DT, RF, and SVM. Because these methods take user-defined hyperparameters, their performance is affected by hyperparameter settings. To optimize the performance and achieve the highest accuracy in these algorithms, a grid search approach is employed to identify the most proper hyperparameter values. The specific hyperparameters and their respective ranges for each algorithm are detailed in Table 2. Furthermore, *k*-fold cross validation technique is performed instead of a simple train-test split to measure the performance of the benchmarked methods. This approach ensures that all samples in the dataset are used for both training and testing the model, leading to more robust and reliable results.

In the conducted experiments, the *k* value of the *k*-fold cross method was chosen as 5, and the process is iterated 10 times. The average 5-fold cross validation results of the benchmarked methods with the specified hyperparameters are visually presented in Figure 6 (a)-(d).

Table 2. Benchmarked classification methods, method specific hyperparameters and range of values

Method	Hyperparameter	Value
k Nearest Neighbor	Number of nearest neighbor	3, 4, 5, … , 30
Decision Tree	Criterion	"gini", "entropy"
	max_depth	1, 2, … , 20
	min_samples_split	2, 3, … , 17
Random Forest	Criterion	"gini", "entropy"
	max_depth	1, 2, … , 32
	number of trees	2^0, 2^1, … , 2^1
Support Vector Machines	Kernel	"linear", "poly", "rbf", "sigmoid"
	Cost	2^{-4}, 2^{-13}, … , 2^{14}
	Gamma	2^{-12}, 2^{-9}, … , 2^5
	Degree	1, 2, … , 19

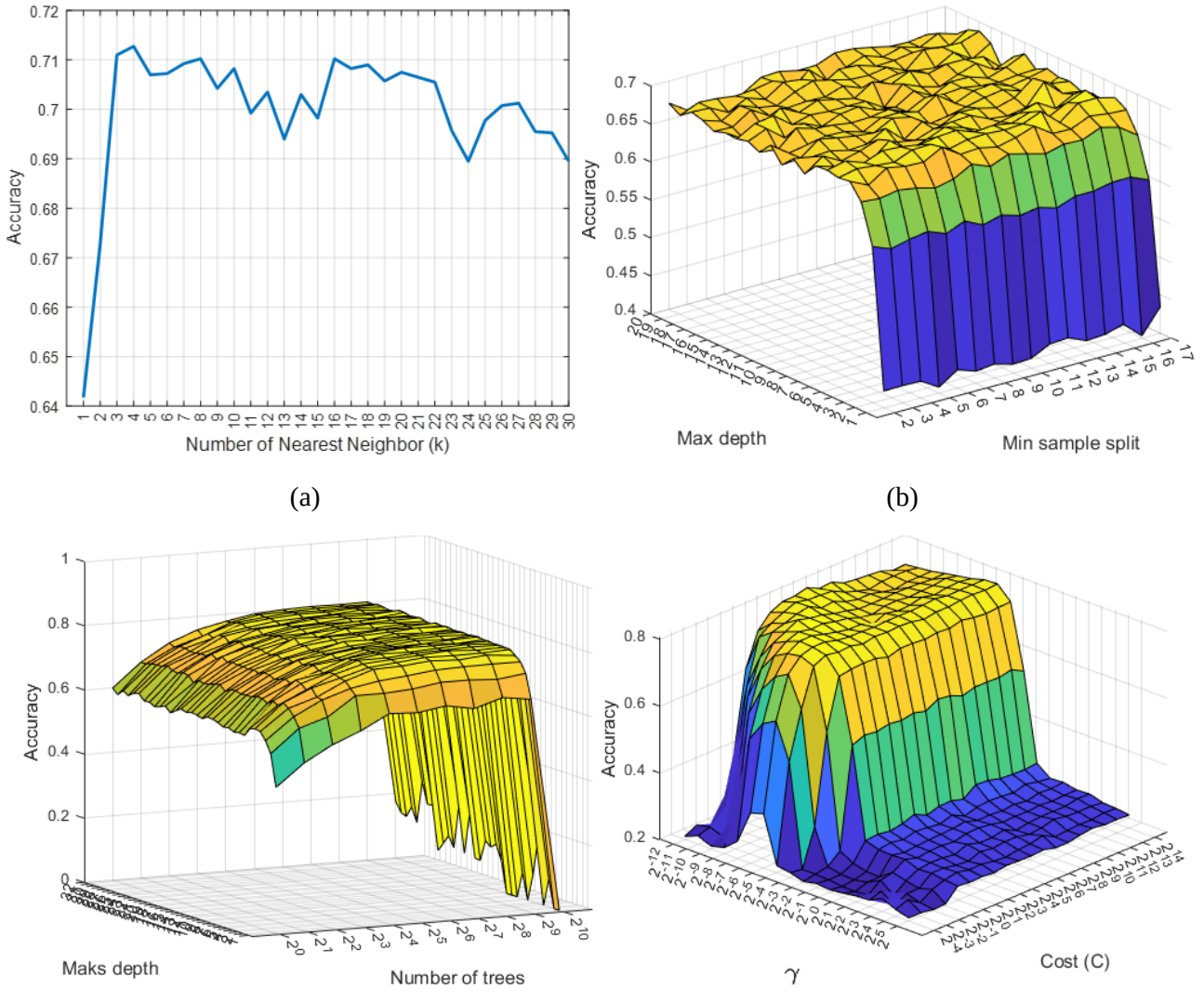

(a) (b) (c) (d)

Figure 6. Accuracy results of the benchmarked methods (a) kNN, (b) Decision Tree, (c) Random Forest, (d) Support Vector Machines

In Figure 6 (a), the results of the kNN algorithm for varying *k* values are presented. The kNN achieves maximum accuracy 71.48% with *k = 4*. In cases where the *k* value is greater than 4, the results exhibit

fluctuations with an example being $k = 16$, where the accuracy value 71.03% is quite close to the highest value. The results are very similar except for $k = 1$. The results of the DT algorithm concerning the *min_sample_split* and *max_depth* hyperparameters are displayed in Figure 6 (b). The effect of the *min_sample_split* hyperparameter is notably limited, while the results are significantly affected when the *max_depth* hyperparameter is less than 3. The performance of the RF method, considering the *max_depth* and the number of trees hyperparameters, is illustrated in Figure 6 (c). "Gini" and "entropy", which are the splitting node criterion for the RF method, are examined, and since Gini outperformed, its results are shown. Similar observations to the results in DT can be made for the RF method, as changing the number of trees hyperparameter has little effect on the results. Accuracy is significantly reduced when the *max_depth* hyperparameter is greater than 2^{10}. At values where the *max_depth* hyperparameter values begin to drop from 2^4, the accuracy of the RF decreases. In SVM, four different kernels are evaluated with the specified hyperparameter setting, but only the radial-based kernel (RBF) results are shown in Figure 6 (d), as it yields the highest accuracy. The accuracy of SVM with RBF kernel decreases when the gamma value is greater than 2^{-4} and a decrease is also observed when the C value falls below 2^{-1}.

3.2.1. Feature Selection

To identify the most prominent features the MI feature selection method is applied to the Turkish music emotion dataset. The subsets of the dataset are formed based on the features ranked from the highest to the lowest in terms of prominence. Benchmark methods are then applied to these subsets to determine the best performing method using the least number of features. The hyperparameters of the benchmarked methods with the highest accuracy scores were determined in the previous subsection. The performance of these methods is assessed using four different performance metrics: accuracy, precision, recall, and f1-score is illustrated in Figure 7 (a)-(d).

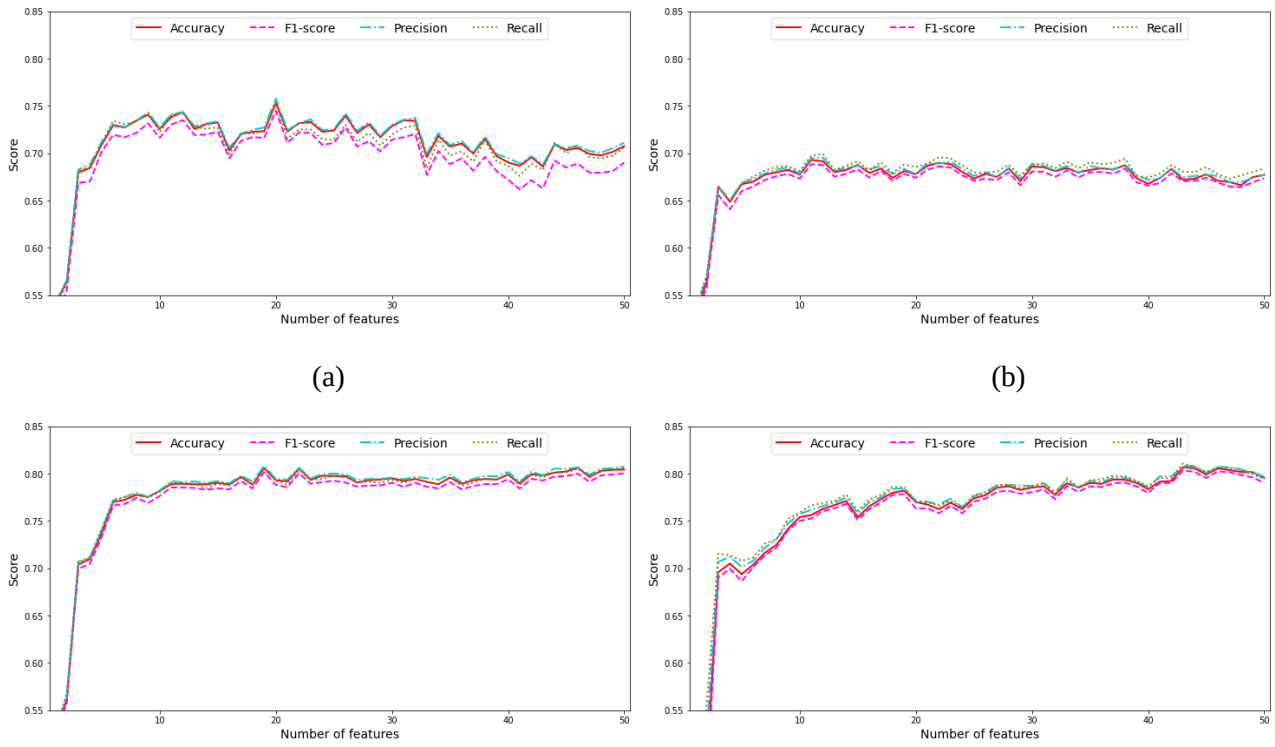

Figure 7. Performance results of the compared methods depending on the increasing number of features

The results of the kNN method are shown in Figure 7 (a). For kNN, the highest accuracy (75.33%) is obtained when the number of features is equal to 19. However, with 12 features, an accuracy (74.35%) score is attained. Comparing the results using features 4 through 51, the variation between the highest (0.7533) and lowest (0.6845) results is 10.05%. Figure 7 (b) illustrates the performance results of the DT method. The optimal accuracy in DT (0.6930) is obtained with 11 features. When considering features between 5 and 50, the accuracy scores of DT vary between 0.6663 and 0.6930. Figure 7 (c) presents the results of the RF method. As can be seen in the Figure 7 (c), the performance using fewer features in the RF method was not superior to the performance using all features. Considering the trade-off between the number of features and accuracy, the optimum number of features will be 19. This is because the accuracy when using the 19 features with the highest MI score (0.8058) is very close to the accuracy when using all features in the dataset (0.8098). Additionally, the accuracy of models created with more than 15 subsets of features consistently remains above 0.7900. Figure 7 (d) depicts the result of the SVM method. Although SVM results may fluctuate depending on the number of features, there is a general tendency for increased performance as the number of features rises. The highest accuracy (0.8068) in SVM is achieved with 43 features.

The accuracy results of the comparative methods with the specified hyperparameters, using both all features in the dataset and a subset of the features, are given in Table 3. The Table also shows in parentheses the number of features used for the corresponding accuracy values. Feature selection leads to enhanced performance in the kNN and SVM methods, while DT and RF methods experience a decline in performance. Notably, in kNN method, a performance increase over 5% is observed when utilizing only 40% of features. Conversely, in the DT method, there is a minimal loss of less than 0.5% in accuracy with the using of approximately 20% of the features. Similar observations can be made for the RF method, where a loss in performance of less than 0.5% is maintained while using less than 40% of the features. The highest accuracy value (0.8068) was achieved when the MI method is combined with the SVM method; but this success needs the utilization of more than 80% of the features. While the accuracy of SVM+MI (0.8068) slightly surpasses RF+MI (0.8058) by only 0.001, RF+MI uses less than 40% fewer features compared to SVM+MI. Considering the experimental results, RF+MI is the best choice when trying to optimize both accuracy and memory usage efficiency.

Table 3. Accuracy results of the benchmarked method with/ without feature selection

Methods	Hyperparameters	All features	Mutual Information
k Nearest Neighbor	k = 4	0.7128	0.7533 (20)
Decision Tree	Criterion = “gini” min_samp_split = 15 maks_depth = 8	0.6958	0.6930 (11)
Random Forest	Criterion = “gini” maks_depth = 17 number of trees = 2^8	0.8098	0.8058 (19)
Support Vector Machines	Kernel = “rbf” C = 2^2 $\gamma = 2^{-9}$	0.8065	0.8068 (43)

4. Conclusion

In this study, four distinct machine learning algorithms – kNN, DT, RF, and SVM – were applied to determine the emotions from the Turkish music. A rigorous examination of method-specific hyperparameters was conducted, revealing that the RF method, utilizing hyperparameters such as node *splitting criterion = “Gini”*, *number of trees = 28*, and *max_depth = 10*, achieved the highest accuracy (0.8118) when using all features in the dataset, which includes 50 features.

To identify the most descriptive features in the dataset, the MI feature selection algorithm was employed. Comparative analyses were then conducted on subsets of the dataset, using the hyperparameters obtaining the highest accuracy with all features. In this way, it is aimed to achieve a success rate comparable to or higher than the result when all features were used, while using fewer features. The adoption of fewer features not only led to decreased memory consumption but also resulted in processing time.

The SVM method, when coupled with MI feature selection, gave the best results despite utilizing a large number of features. Conversely using the RF method with feature selection, yielded very close results, but with significantly fewer features. As a result, RF+MI emerges as the optimal choice considering both memory usage efficiency and accuracy. This is evidenced by a marginal drop-in success rate of 0.5% compared to using all features and using 60% fewer features.

Future studies may investigate model interpretation methods to elucidate the interpretability of these models. Additionally, different feature selection techniques can be explored to identify the most salient features in the dataset.

Author Contributions

The first author performed supervision, literature review, investigation, verification, arrangement. The first, second, and third authors devised the main conceptual ideas and developed the theoretical framework. The second author performed the experiment and statistical analyses. The third author reviewed and edited the paper. All authors read and approved the final version of the paper.

Conflicts of Interest

All the authors declare no conflict of interest.

References

[1] C. Ji, J. Zhao, Q. Nie, S. Wang, *The role and outcomes of music therapy during pregnancy: a systematic review of randomized controlled trials*, Journal of Psychosomatic Obstetrics & Gynecology 45 (1) (2024) 2291635 10 pages.

[2] G. Leslie, A. Ghandeharioun, D. Zhou, R. W. Picard, *Engineering music to slow breathing and invite relaxed physiology*, 8th international conference on Affective Computing and Intelligent Interaction (ACII), Cambridge, 2019, pp.1–7.

[3] M. Umbrello, T. Sorrenti, G. Mistraletti, P. Formenti, D. Chiumello, S. Terzoni, *Music therapy reduces stress and anxiety in critically ill patients: a systematic review of randomized clinical trials*, Minerva Anestesiologica 85 (8) (2019) 886–898.

[4] P. Vuust, O. A. Heggli, K. J. Friston, M. L. Kringelbach, *Music in the brain*, Nature Reviews Neuroscience 23 (5) (2022) 287–305.

[5] B. M. O. Shimada, M. A. Cabral, V. O. Silva, G. C. Vagetti, *Interventions among pregnant women in the field of music therapy: A systematic review*, Revista Brasileira de Ginecologia e Obstetrícia/RBGO Gynecology and Obstetrics 43 (05) (2021) 403–413.

[6] D. Han, Y. Kong, J. Han, G. Wang, *A survey of music emotion recognition*, Frontiers of Computer Science 16 (6) (2022) 166335 11 pages.

[7] T. Fritz, S. Jentschke, N. Gosselin, D. Sammler, I. Peretz, R. Turner, A. D. Friederici, S. Koelsch, *Universal recognition of three basic emotions in music*, Current Biology 19 (7) (2009) 573–576.

[8] A. Mahadik, S. Milgir, J. Patel, V. B. Jagan, V. Kavathekar, *Mood based music recommendation system*, International Journal of Engineering Research & Technology (IJERT) 10 (6) (2021) 553–559.

[9] A. O. Durahim, A. C. Setirek, B. B. Özel, H. Kebapci, *Music emotion classification for Turkish songs using lyrics*, Pamukkale University Journal of Engineering Sciences 24 (2) (2018) 292–301.

[10] M. B. Er, I. B. Aydilek, *Music emotion recognition by using chroma spectrogram and deep visual features*, International Journal of Computational Intelligence Systems 12 (2) (2019) 1622–1634.

[11] D. Chaudhary, N. P. Singh, S. Singh, *Development of music emotion classification system using convolution neural network*, International Journal of Speech Technology 24 (2021) 571–580.

[12] M. T. Quasim, E. H. Alkhammash, M. A. Khan, M. Hadjouni, *RETRACTED ARTICLE: Emotion-based music recommendation and classification using machine learning with IoT Framework*, Soft Computing 25 (18) (2021) 12249–12260.

[13] J. H. Su, T. P. Hong, Y. H. Hsieh, S. M. Li, *Effective music emotion recognition by segment-based progressive learning*, 2020 IEEE International Conference on Systems, Man, and Cybernetics, Toronto, 2020, pp. 3072–3076.

[14] A. G. Pandrea, J. S. Gómez Cañón, H. Boyer, *Cross-dataset music emotion recognition: an end-to-end approach*, in: J. Cumming, J. H. Lee, B. McFee, M. Schedl, J. Devaney, C. McKey, E. Zangerle, T de Reuse (Eds.), 21st International Society for Music Information Retrieval Conference, Québec, 2020, 2 pages.

[15] T. Ciborowski, S. Reginis, D. Weber, A. Kurowski, B. Kostek, *Classifying emotions in film music—A deep learning approach*, Electronics 10 (23) (2021) 2955 22 pages.

[16] Z. Huang, S. Ji, Z. Hu, C. Cai, J. Luo, X. Yang, *ADFF: Attention based deep feature fusion approach for music emotion recognition* (2022) 5 pages, https://doi.org/10.48550/arXiv.2204.05649.

[17] K. Zhang, X. Wu, R. Tang, Q. Huang, C. Yang, H. Zhang, *The JinYue database for huqin music emotion, scene and imagery recognition*, in: L. O' Conner (Ed.), In 2021 IEEE 4th International Conference on Multimedia Information Processing and Retrieval (MIPR), Tokyo, 2021, pp. 314–319.

[18] D. Moldovan, *Binary horse optimization algorithm for feature selection*, Algorithms 15 (5) (2022) 156 27 pages.

[19] W. Feng, J. Gou, Z. Fan, X. Chen, *An ensemble machine learning approach for classification tasks using feature generation*, Connection Science 35 (1) (2023) 2231168 23 pages.

[20] M. Çakır, A. Degirmenci, O. Karal, *Exploring the behavioural factors of cervical cancer using ANOVA and machine learning techniques*, in: J. Filipe, A. Ghosh, R. O. Prates, B. Horizonte, L. Zhou (Eds.), International Conference on Science, Engineering Management and Information Technology, Ankara, 2022, pp. 249–260.

[21] H. Li, B. Wan, D. Chu, R. Wang, G. Ma, J. Fu, Z. Xiao, *Progressive geological modeling and uncertainty analysis using machine learning*, ISPRS International Journal of Geo-Information 12 (3) (2023) 97 19 pages.

[22] J. Gonzalez-Lopez, S. Ventura, A. Cano, *Distributed multi-label feature selection using individual mutual information measures*, Knowledge-Based Systems 188 (2020) 105052 13 pages.

[23] P. Zhang, G. Liu, J. Song, *MFSJMI: Multi-label feature selection considering join mutual information and interaction weight*, Pattern Recognition 138 (2023) 109378.

[24] J. R. Vergara, P. A. Estévez, *A review of feature selection methods based on mutual information*, Neural Computing and Applications 24 (2014) 175–186.

[25] A. Degirmenci, O. Karal, *iMCOD: Incremental multi-class outlier detection model in data streams*,

Knowledge-Based Systems 258 (2022) 109950.

[26] R. Suwanda, Z. Syahputra, E. M. Zamzami, *Analysis of Euclidean distance and Manhattan distance in the K-means algorithm for variations number of centroid K*, Journal of Physics: Conference Series 1566 (1) (2020) 012058 6 pages.

[27] A. N. Karaoglu, H. Caglar, A. Degirmenci, O. Karal, *Performance improvement with decision tree in predicting heart failure*, 6th International Conference on Computer Science and Engineering (UBMK), Ankara, 2021, 781–784.

[28] S. Tangirala, *Evaluating the impact of GINI index and information gain on classification using decision tree classifier algorithm*, International Journal of Advanced Computer Science and Applications 11 (2) (2020) 612–619.

[29] M. A. Bouke, A. Abdullah, S. H. ALshatebi, M. T. Abdullah, H. El Atigh, *An intelligent DDoS attack detection tree-based model using Gini index feature selection method*, Microprocessors and Microsystems 98 (2023) 104823.

[30] S. Yao, Y. Wu, F. Akter, *An introduction to artificial intelligence and machine learning*, in: F. Akter, N. Emptage, F. Engert, M. S. Berger (Eds.), Neuroscience for Neurosurgeons, Cambridge University Press, 2023, Ch. 9, pp.146–157.

[31] R. Mirzaeian, R. Nopour, Z. Asghari Varzaneh, M. Shafiee, M. Shanbehzadeh, H. Kazemi-Arpanahi, *Which are best for successful aging prediction? Bagging, boosting, or simple machine learning algorithms?*, Biomedical Engineering Online 22 (1) (2023) 85 25 pages.

[32] M. Apaydın, M. Yumuş, A. Değirmenci, Ö. Karal, *Evaluation of air temperature with machine learning regression methods using Seoul City meteorological data*, Pamukkale Üniversitesi Mühendislik Bilimleri Dergisi 28 (5) (2022) 737–747.

[33] T. M. Oshiro, P. S. Perez, J. A. Baranauskas, *How many trees in a random forest?*, in: P. Perner (Ed.), Machine Learning and Data Mining in Pattern Recognition: 8th International Conference, Berlin, 2012, 154–168.

[34] P. Probst, A. L. Boulesteix, *To tune or not to tune the number of trees in random forest*, The Journal of Machine Learning Research 18 (1) (2017) 6673–6690.

[35] C. B. Liu, B. P. Chamberlain, D. A. Little, Â. Cardoso, *Generalising random forest parameter optimisation to include stability and cost*, in: M. Ceci, J. Hollmén, L. Todorovski, C. Vens, S. Džeroski (Eds.), Machine Learning and Knowledge Discovery in Databases: European Conference, Skopje, 2017, 102–113.

[36] M. Muttaqi, A. Degirmenci, O. Karal, *US accent recognition using machine learning methods*, Innovations in Intelligent Systems and Applications Conference (ASYU), Antalya, 2022, 1–6.

[37] M. Sheykhmousa, M. Mahdianpari, H. Ghanbari, F. Mohammadimanesh, P. Ghamisi, S. Homayouni, *Support vector machine versus random forest for remote sensing image classification: A meta-analysis and systematic review*, IEEE Journal of Selected Topics in Applied Earth Observations and Remote Sensing, 13 (2020) 6308–6325.

Çanakkale Onsekiz Mart University

Journal of Advanced Research in Natural and Applied Sciences

dergipark.org.tr/tr/pub/jarnas

Open Access

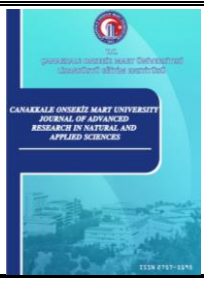

e-ISSN: 2757-5195 2024, Vol. 10, Issue 2, Pages: 329-336 doi.org/10.28979/jarnas.1405595

Hydrothermal Synthesis of CuO Nanoparticles: Tailoring Morphology and Particle Size Variations for Enhanced Properties

Gürkan Akarken[1], Uğur Cengiz[2], Tijen Ennil Bektaş[3]

[1,2]Energy Resources Application and Research Center, Çanakkale Onsekiz Mart University, Çanakkale, Türkiye

[2,3]Department of Chemical Engineering, Faculty of Engineering, Çanakkale Onsekiz Mart University, Çanakkale, Türkiye

Article History

Received: 15 Dec 2023

Accepted: 02 Feb 2024

Published: 25 Jun 2024

Research Article

Abstract − Transition metal oxides, particularly copper oxides, have garnered significant attention due to their intriguing photochemical, photomagnetic, photo-thermal, and photoconductive properties. Among these, CuO stands out as a p-type semiconductor having narrow bandgap energy ranges from 1.2 to 2 eV, finding versatile applications such as gas sensing, magnetic storage, solar energy conversion, photocatalysis, supercapacitors, field-emission emitters, and optical switches. Additionally, it serves as a crucial component in materials designed for lithium-ion electrodes. In this study, five different CuO nanoparticles were synthesized by simple and cost-effective hydrothermal method with various reaction temperatures and times in a teflon lined stainless steel autoclave. Copper (II) chloride dihydrate was used as copper source in this process. Various characterization techniques were conducted including X-ray powder diffraction (XRD), Raman spectroscopy, and transmitting electron microscopy (TEM). The effect of temperature and time on synthesis process was characterized and discussed. TEM images show that particle size of CuO increase with the temperature and reaction time. First reaction had the smallest particle sizes (mostly around 9-11 nm). This can be attributed to its lowest reaction temperature and shortest reaction time. For the other reactions, two of them accumulate around 19-35 nm and two around 27-45 nm range. However, the rise in the particle's diameters is not directly proportional to temperature and time. As a result, CuO nanoparticles have been produced with simple method for the market. It can be produced in large quantities for heat exchangers, gas sensing, magnetic storage, solar energy conversion, photocatalysts, supercapacitors, etc.

Keywords − *CuO, nanoparticle, hydrothermal, particle size*

1. Introduction

Transition metal oxides are a significant characteristic of semiconductors that have been extensively ex-plored due to their unique features for possible applications [1]. Copper oxides are one type of transition metal oxide that have gained a lot of interest because of their fascinating photochemical, photomagnetic, photo-thermal and photoconductive characteristics. Cu_2O and CuO are two examples of the several stoichiometries and phases that copper oxides (CuxO) may exist in, have narrow bandgap energy ranges from 1.2 to 2 eV. CuO is a p-type semiconducting material has many different ap-plications including gas sensing, magnetic storage, solar energy conversion, photocatalysts, supercapacitors [2-4] , field emission emitters, photocatalysts, optical switches, and materials for lithium-ion electrodes [5]. In addition, it is essential for a variety of chemical reactions, including oxidation of carbon monoxide, hydrocarbons, fine compounds, the degradation of nitrous oxides and the selective catalytic reduction of nitric oxide with ammonia [6, 7].

These various applications have led to appear numerous chemical routes to synthesize CuO such as sol-gel for

[1]gurkanakarken@gmail.com.tr (Corresponding Author); [2]ucengiz@comu.edu.tr; [3]ennilbektas@comu.edu.tr

more complex and high-tech methods, solid-state reaction, precipitation-stripping, alkoxide-based synthesis, sonochemical production, microwave irradiation and precipitation-pyrolysis [8, 9]. Moreover, thermal oxidation [10], hydrolysis [11], solvothermal [12], microemulsion system [13] and the hydrothermal method are also in use for synthesizing CuO particles.

The synthesis of nanomaterials using hydrothermal method may occur at temperatures ranging from ambient temperature to extremely high temperatures. Hydrothermal technique has several advantages comparing the other methods. For instance, low-pressure or high-pressure circumstances can be used to control the size and shape development of the materials, based on the vapor pressure of the primary component in the reaction. Hydrothermal synthesis allows for the production of nanomaterials with well-controlled compositions due to liquid phase or multistage chemical processes [14] . Nanomaterials which are unstable at high temperatures can be produced by this method. High vapor pressure nanomaterials can be produced using the hydrothermal technique with the least amount of material loss [15]. This method also stands out as a convenient approach for copper oxide synthesis, yielding nanoparticles characterized by exceptional dispersibility, strong crystallinity, high purity, and distinct morphologies of varying dimensions [16, 17].

Recently, there has been extensive research into the controlled shaping of various nanostructures, as the physical and chemical properties of nanocrystals are strongly influenced by factors such as sizes, shapes, compositions, and structures. This paper describes the hydrothermal synthesis of CuO nanostructures in the presence of sodium hydroxide (NaOH), utilizing a simple and surfactant-free technique. The study explores the effects of hydrothermal temperature, and time on crystal growth, and shape through simple and cheap hydrothermal method with integration of heat and time parameters.

2. Materials and Methods

All of the compounds utilized in this work were analytical grade and did not require any additional purification. Copper (II) chloride dihydrate ($CuCl_2 \bullet 2H_2O$, ≥99% purity), NaOH (≥99% purity), ethanol (CH_3CH_2OH, 99,8%) and distilled water were used in the experiments for preparing and cleaning samples. $CuCl_2 \bullet 2H_2O$ were supplied by Merck, sodium hydroxide was purchased from Interlab and absolute technical grade ethanol supplied by Panceac.

CuO nanoparticles synthesized by simple hydrothermal method. Synthesis procedure adapted from Wang and his co-workers' published paper [3]. Different sized and shaped nanoparticles were obtained by changing the reaction parameters such as time and temperature. Nanoparticles were formed by thermal decomposition of $CuCl_2 \bullet 2H_2O$ and precipitation in aqueous solution. The preparation procedure was started with dissolving of $CuCl_2 \bullet 2H_2O$ in distilled water, 0,01 mol $CuCl_2 \bullet 2H_2O$ dissolved in 25 ml distilled water and stirred for 15 minutes at room temperature. After that 20 ml of 1mol/L NaOH solution was slowly added to this solution in 20 minutes under the continuous magnetic stirring. Stirring was kept on extra 10 minutes more after adding NaOH solution to obtain homogenous mixing. Afterward, solution was transferred to teflon lined stainless steel autoclave for hydrothermal process. Autoclave was transferred to hot air oven for various temperatures and times as given in Table 1. Finally black colored CuO nanoparticles were collected and washed several times with ethanol and distilled water (Figure 1). As a last step of the process particles were dried in oven for 24 hours at 65 ^{o}C. All the samples produced with the same method but with particular experimental conditions (Table 1) and characterized with several techniques.

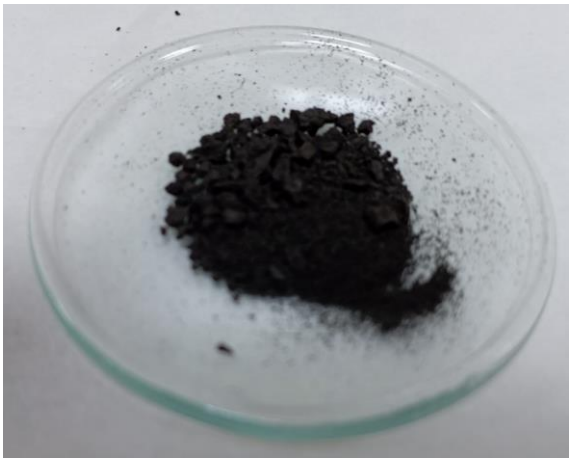

Figure 1. Successfully synthesized CuO nanoparticles after washing and drying procedures

Table 1. Temperature and time parameters of hydrothermal reactions

Sample	Temperature (°C)	Time (h)
1	110	2
2	150	2
3	190	2
4	110	4
5	110	6

2.1. Characterizations

Produced CuO nanoparticles were characterized using Malvern Panalytical model X-ray powder diffraction (XRD) with a scanning angle range of 2θ = 5-80, and a scanning rate of 0.02° per minute, utilizing Cu-Kα radiation (Figure 2). For the further structural analyse CuO nanoparticles were characterized using a Witec Alpha model 300RA Raman spectrometer (Figure 3). The particle size analyses of the samples were conducted using a JEOL JEM-1400 transmitting electron microscope (TEM). Nanoparticles should be clean for to get clear TEM images. Particles have washed multiple times with ethanol and water. Synthesized particles pounded in a mortar to obtain smaller grains for sample preparation. CuO nanoparticles do not need any conductive coating because of their conductivity. The percentage distributions of nanoparticles in the nano size range were analyzed from TEM images (Figure 4).

3. Results and Discussion

Crystal structure of the first CuO nanoparticle is given in Figure 2. The exceptional crystalline quality of the particles is shown by the strong and sharp diffraction peaks. Primary diffraction peaks corresponding to the (002) and (111) planes were observed at 2θ values of 35.57 and 38.75, respectively. Additionally, other diffraction peaks such as (110), (202), (020), (202), (113), (022), (220), and (311) are also visible. The (002) and (111) peaks are the most prominent, indicating that the growth model of CuO crystals occurs predominantly along the (002) and (111) planes. These peaks are correlated with previous studies [3, 18].

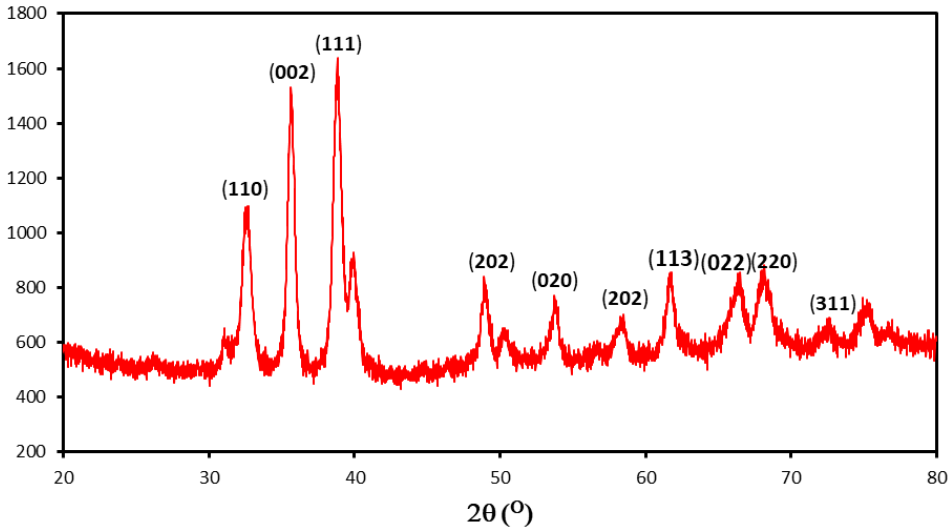

Figure 2. XRD pattern of first CuO nanoparticle synthesized at 110 °C in 2 hours

Figure 3 shows first CuO nanoparticles Raman spectra. A popular optical method for identifying deformations, structural problems, and defect chemistry in materials is Raman spectroscopy. CuO is a p-type semiconductor with a monoclinic structure belonging to the C^6_{2h} (c^2/c) space group [19]. This space group has twelve vibrational modes at the center, including three normal acoustic modes ($A_u + 2B_u$), six infrared active modes ($3A_u + 3B_u$) and three Raman active modes ($A_g + 2B_g$) at peaks 294, 332, 626 cm-1 [20]. The peak at 294 cm^{-1}, corresponding to the monoclinic phase of CuO, belongs to the A_g mode, and the peaks at 332 and 626 cm^{-1} belong to the B_g modes and matches the previously reported data [21].

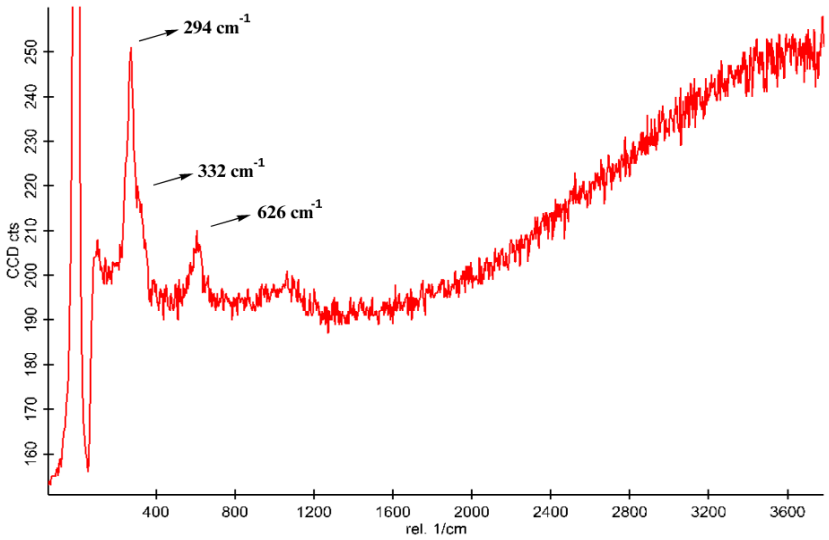

Figure 3. Raman spectrum of CuO nanoparticles synthesized at 110 °C in 2 hours

TEM images are given in Table 2. Spherical-shaped nanoparticles are more common in first and second synthesis. Hydrothermal reaction times were the same (2 hours) for the first 3 synthesis, but reaction temperatures were different (Table 1). It is obvious that spherical-shaped nanoparticle numbers decreased and became more polyhedron-like structures as the temperature elevated. The temperature had great impact on the accretion of CuO nanostructures. The precursor's disintegration and CuO's expansion all increased with rising temperatures. Because the nanocrystals tended to orient the crystal lattices in the direction of growth at higher temperatures. The thermal movement of the molecules in the elements for growth accelerated and subsequently sped up the formation of the crystal cores [22].

For the fourth and fifth synthesis, reaction temperatures kept constant and reaction times were changed comparing the first synthesis. It's seen that nanoparticle shapes became more plate-like unlikely the first synthesized nanoparticles. This was also observed by Janene et al. They investigated the effect of different reaction times and synthesized CuO nanoplates with 2 to 24 hours reaction times [23].

Table 2. TEM images of five different CuO nanoparticles synthesized at different temperatures and reaction time

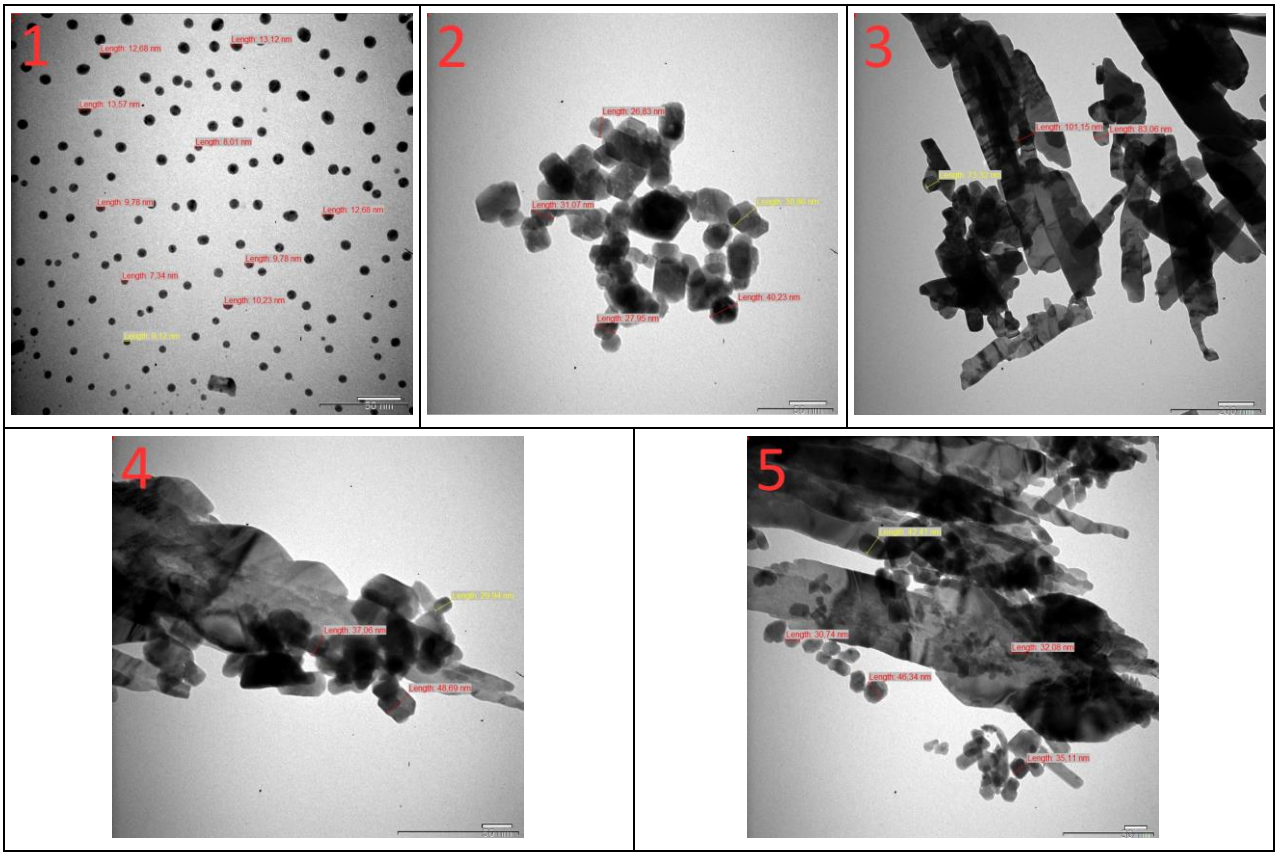

Particle size distributions of synthesized nanoparticles are given in Figure 4. Particle size measurements were conducted via ImageJ on TEM images including Table 2 and more images. First reaction has the smallest particle sizes (mostly around 9-11 nm). This can be attributed to its lowest reaction temperature and shortest reaction time [24].

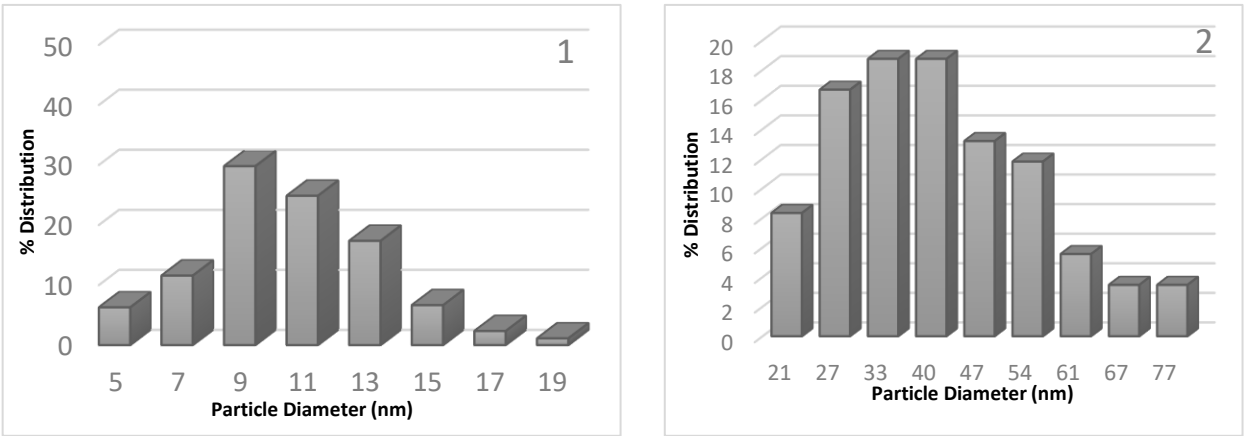

Figure 4. Particle size distributions of CuO nanoparticles synthesized at different temperatures and reaction time

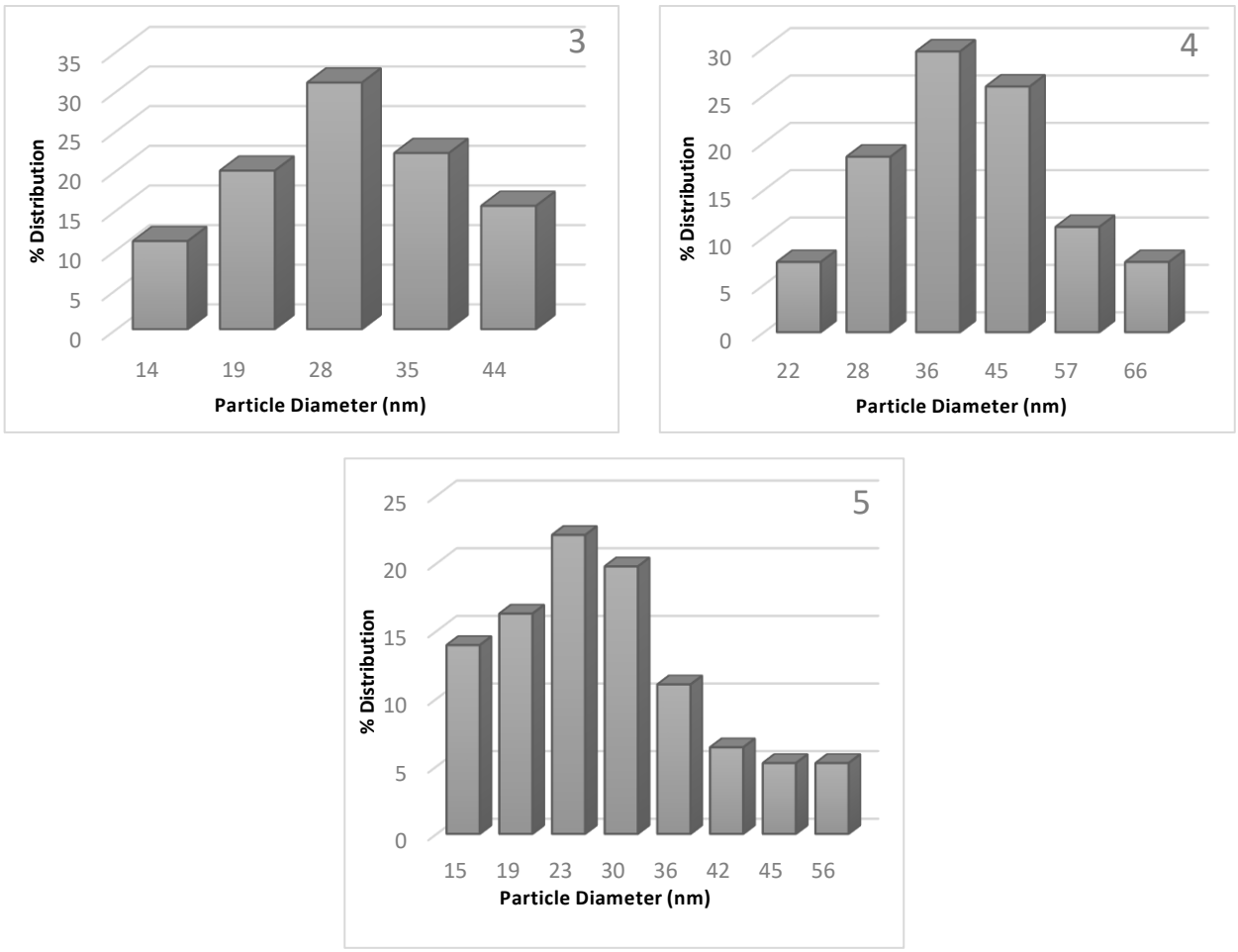

Figure 4. (Continued) Particle size distributions of CuO nanoparticles synthesized at different temperatures and reaction time

During hydrothermal treatment, uniform heating within the reaction system significantly impacts the morphology of CuO nanoparticles. The morphological characteristics of these nanoparticles are intricately tied to both temperature and partial pressure inside the autoclave throughout the synthesis process. Furthermore, the morphology of CuO nanocrystals is influenced by temperature and reaction time. Incomplete reactions occur at lower temperatures, while at higher temperatures, reduction of CuO takes place, aligning with findings reported by other researchers [25-27].

4. Conclusion

The ultimate goal of this study was to produce CuO nanoparticles practically for the market. CuO nanoparticles were successfully synthesized via simple hydrothermal method with several reaction temperatures and times. Copper (II) chloride dihydrate was used as copper source. Various characterization techniques were conducted including XRD, Raman spectroscopy and TEM. First synthesis was more spherical-shaped comparing the other four reactions, they had more rod-like structures. TEM images show that particle size of CuO increase with the temperature and reaction time. However, rise in the particle's diameters are not directly proportional to temperature and time. Finally, CuO nanoparticles have produced with simple method for the market. It can be produced in large quantities for heat exchangers, gas sensing, magnetic storage, solar energy conversion, photocatalysts, supercapacitors etc.

Author Contributions

All the authors equally contributed to this work. They all read and approved the final version of the paper.

Conflicts of Interest

All the authors declare no conflict of interest.

References

[1] C. Xu, Y. Liu, G. Xu, G. Wang, *Preparation and characterization of CuO nanorods by thermal decomposition of CuC2O4 precursor*, Materials Research Bulletin 37 (14) (2002) 2365-2372.

[2] A. Aslani, V. Oroojpour, *CO gas sensing of CuO nanostructures, synthesized by an assisted solvothermal wet chemical route*, Physica B: Condensed Matter 406 (2) (2011) 144–149.

[3] Y. Q. Wang, D. Wang, B. Yan, Y. Chen, C. Song, *Fabrication of diverse CuO nanostructures via hydrothermal method and their photocatalytic properties*, Journal of Materials Science-Materials in Electronics 27 (7) (2016) 6918–6924.

[4] M. -J. Song, S. W. Hwang, D. Whang, *Non-enzymatic electrochemical CuO nanoflowers sensor for hydrogen peroxide detection*, Talanta 80 (5) (2010) 1648–1652.

[5] T. H. Nguyen, T. L. Nguyen, T. D. Thuy Ung, Q. L. Nguyen, *Synthesis and characterization of nano-CuO and CuO/TiO2 photocatalysts*, Advances in Natural Sciences: Nanoscience and Nanotechnology 4 (2) (2013) 025002 6 pages.

[6] C. L. Carnes, J. Stipp, K. J. Klabunde, J. Bonevich, *Synthesis, characterization, and adsorption studies of nanocrystalline copper oxide and nickel oxide*, Langmuir 18 (4) (2002) 1352–1359.

[7] W. Wang, Y. Zhan, X. Wang, Y. Liu, C. Zheng, G. Wang, *Synthesis and characterization of CuO nanowhiskers by a novel one-step, solid-state reaction in the presence of a nonionic surfactant*, Materials Research Bulletin 37 (6) (2002) 1093–1100.

[8] J. Pike, S. W. Chan, F. Zhang, X. Wang, J. Hanson, *Formation of stable Cu_2O from reduction of CuO nanoparticles*, Applied Catalysis A: General 303 (2) (2006) 273–277.

[9] K. Zhou, R. Wang, B. Xu, Y. Li, *Synthesis, characterization and catalytic properties of CuO nanocrystals with various shapes*, Nanotechnology 17 (15) (2006) 3939 5 pages.

[10] J. T. Chen, F. Zhang, J. Wang, G. A. Zhang, B. B. Miao, X. Y. Fan, D. Yan, P. X. Yan, *CuO nanowires synthesized by thermal oxidation route*, Journal of Alloys and Compounds 454 (1-2) (2008) 268–273.

[11] J. Zhu, H. Bi, Y. Wang, X. Wang, L. Lu, *Synthesis of flower-like CuO nanostructures via a simple hydrolysis route*, Materials Letters 61 (30) (2007) 5236–5238.

[12] X. Tang, L. Ren, L. Sun, W. Tian, M. Cao, C. Hu, *A solvothermal route to Cu2O nanocubes and Cu nanoparticle*, Chemical Research in Chinese Universities 22 (5) (2006) 547–551.

[13] D. Han, H. Yang, C. Zhu, F. Wang, *Controlled synthesis of CuO nanoparticles using TritonX-100-based water-in-oil reverse micelles* Powder Technology 185 (3) (2008) 286–290.

[14] P. Basnet, S. Chatterjee, *Structure-directing property and growth mechanism induced by capping agents in nanostructured ZnO during hydrothermal synthesis—A systematic review*, Nano-Structures & Nano-Objects 22 (2020) 100426.

[15] Y. X. Gan, A. H. Jayatissa, Z. Yu, X. Chen, M. Li, *Hydrothermal synthesis of nanomaterials*, Journal of Nanomaterials 2020 (2020) Article ID 8917013 3 pages.

[16] Q. Yang, Z. Lu, J. Liu, X. Lei, Z. Chang, L. Luo, X. Sun, *Metal oxide and hydroxide nanoarrays: Hydrothermal synthesis and applications as supercapacitors and nanocatalysts*, Progress in Natural Science: Materials International 23 (4) (2013) 351–366.

[17] W. Shi, S. Song, H. Zhang, *Hydrothermal synthetic strategies of inorganic semiconducting nanostructures*, Chemical Society Reviews 42 (13) (2013) 5714–5743.

[18] L. L Feng, R. Wang, Y. Zhang, S. Ji, Y. Chuan, W. Zhang, *In situ XRD observation of CuO anode phase conversion in lithium-ion batteries*, Journal of Materials Science 54 (2) (2019) 1520–1528.

[19] S. Al-Amri, M. S. Ansari, S. Rafique, M. Aldhahri, S. Rahimuddin, A. Azam, A. Memic, *Ni doped CuO nanoparticles: Structural and optical characterizations*, Current Nanoscience 11 (2) (2015) 191–197.

[20] V. K. Gupta, R. Chandra, I. Tyagi, M. Verma, *Removal of hexavalent chromium ions using CuO nanoparticles for water purification applications*, Journal of Colloid and Interface Science 478 (2016) 54–62.

[21] Q. Yu, H. Huang, R. Chen, P. Wang, H. Yang, M. Gao, X. Peng, Z. Ye, *Synthesis of CuO nanowalnuts and nanoribbons from aqueous solution and their catalytic and electrochemical properties*, Nanoscale 4 (8) (2012) 2613–2620.

[22] S. Sabbaghi, H. Orojlou, M. R. Parvizi, R. Saboori, M. Sahooli, *Effect of temperature and time on morphology of CuO nanoparticle during synthesis*, International Journal of Nano Dimension 3 (1) (2012) 69–73.

[23] F. Janene, H. Dhaouadi, L. Arfaoui, N. Etteyeb, D. Touati, *Nanoplate-like CuO: hydrothermal synthesis, characterization, and electrochemical properties*, Ionics 22 (8) (2016) 1395–1403.

[24] M. Outokesh, M. Hosseinpour, S. J. Ahmadi, T. Mousavand, S. Sadjadi, W. Soltanian, *Hydrothermal synthesis of CuO nanoparticles: Study on effects of operational conditions on yield, purity, and size of the nanoparticles*, Industrial & Engineering Chemistry Research 50 (6) (2011) 3540–3554.

[25] R. A. Köppel, C. Stöcker, A. Baiker, *Copper-and silver–zirconia aerogels: preparation, structural properties and catalytic behavior in methanol synthesis from carbon dioxide*, Journal of Catalysis, 179 (2) (1998) 515–527.

[26] M. P. Neupane, Y. K. Kim, I. S. Park, K. A. Kim, M. H. Lee, T. S. Bae, *Temperature driven morphological changes of hydrothermally prepared copper oxide nanoparticles*, Surface and Interface Analysis 41 (3) (2009) 259–263.

[27] T. Jiang, Y. Wang, D. Meng, X. Wu, J. Wang, J. Chen, *Controllable fabrication of CuO nanostructure by hydrothermal method and its properties*, Applied Surface Science 311 (2014) 602–608.

Çanakkale Onsekiz Mart University

Journal of Advanced Research in Natural and Applied Sciences

dergipark.org.tr/tr/pub/jarnas

Open Access

e-ISSN: 2757-5195 2024, Vol. 10, Issue 2, Pages: 337-349 doi.org/10.28979/jarnas.1342983

Analysis of the Impact of Demographic Characteristics and Business Conditions on Employee Job Satisfaction

Fatma Betül Bağlan[1], Umut Hulusi İnan[2], Hüseyin Başlıgil[3]

[1,3]Department of Industrial Engineering, Faculty of Engineering and Architecture, İstanbul Esenyurt University, İstanbul, Türkiye
[2]Department of Industrial Engineering, Faculty of Engineering and Architecture, İstanbul Gelişim University, İstanbul, Türkiye

Article History

Received: 14 Aug 2023

Accepted: 06 Feb 2024

Published: 25 Jun 2024

Research Article

Abstract − Job satisfaction is an important concept in terms of productivity and continuity of enterprises. The decrease in the job satisfaction level of the employees may cause many problems such as slowing down the work and low productivity. In this study, the surveys conducted on 150 employees from 52 sectors were evaluated with the SMART-PLS 3 package program, and the effect of perceptions on business conditions (economic, ergonomic, internal communication, workload level, and career opportunities) on job satisfaction was examined. The topic addressed in the study, the classification of organizational conditions and the methodology employed, contributes to the literature. As a result of the analyses, it was determined that the perceptions of internal communication and career opportunities affect the level of job satisfaction of the employees. In the continuation of the study, the effect of the demographic characteristics of the employees on these perceptions was examined by using the SPSS 22 statistical program. This examination revealed that the gender affected the perception of internal communication and the education level the perception of career opportunities.

Keywords − *Job satisfaction, partial least squares structural equation modelling (PLS-SEM), statistics*

1. Introduction

The happiness that arises as a result of the fulfillment of needs or desires is defined as reaching the satisfaction of the heart. It is defined as a reaction of employees' feelings about their jobs [1]. Job satisfaction, in other words, is how the employee feels towards the job, has a decisive role in the attitudes of the employees towards the job [2].

The concept of job satisfaction emerged in the 1920s, and its importance was understood in the 1940s. From past to present, various definitions of job satisfaction have been made. Lawler [3] said that job satisfaction is measured by the difference between employees' expectations from the job and what they get from the job. Locke [4] defined job satisfaction as the emotional response of an employee to his or her job. Schultz and Schultz and Schultz [5] stated that job satisfaction is a quality measure of working life. Soysal et al. [6] defined job satisfaction as the feelings that emerge as a result of the work experience of the employees. According to Kasimati [7], job satisfaction is the emotional reactions of employees to different aspects of their jobs, the degree of liking and disliking their job.

The concept of job satisfaction is an important term in terms of productivity and continuity of enterprises. With the industrial revolution, the Classical Management approach was accepted by the organizations, and the humanitarian elements began to be ignored. With the Neo-classical approach that emerged in the following

[1]fatmabetulbaglan@esenyurt.edu.tr (Corresponding Author); [2]uhinan@gelisim.edu.tr; [3]huseyinbasligil@esenyurt.edu.tr

process, this shortcoming in the classical management approach was eliminated. According to this approach, one of the most important elements in the production processes of organizations is human, and it is not possible for an employee who is dissatisfied with his work to contribute to the effectiveness and efficiency of the organization [8]. It is inevitable that the standard conditions of an enterprise with low job satisfaction level of its employees may deteriorate. The decrease in the job satisfaction levels of the employees can cause many problems such as slowing down the work and low productivity. The effective and productive work of their employees are largely related to their high job satisfaction level [9].

In today's intensely competitive environment, businesses must be able to use their resources effectively and efficiently in order to survive. One of the most important of these resources is human, i.e. employees. Job satisfaction has an impact on employee performance, while employee performance has an impact on business productivity. Ali et al. [10] stated that the success and sustainability of organizations depend on their employees and their attitudes towards their works they do.

For many years, researchers have been examining the factors affecting job satisfaction. Demirel and Özçınar [2] examined the effect of organizational citizenship behavior on job satisfaction, İşcan and Sayın [11] analyzed the relationship between organizational justice, job satisfaction and organizational trust, Julseth et al. [12] studied the relationship between job satisfaction of patrol officers and their capacity to perceive problems, Bayramlık et al. [8] investigated the effect of person-organization fit on job satisfaction, Neubert and Halbesleben [13], the effect of psychological factors on organizational outcomes such as job satisfaction and organizational commitment, Kardaş and Şencan [14] tested the effect of five factor personality traits on job satisfaction, Şenol and Öngel [15] assessed the effect of internal marketing practices on job satisfaction, and Akçakanat et al. [16] examined the effect of job love on job satisfaction. Örücü et al. [17] listed the factors affecting job satisfaction, which is a very important organizational concept, as follows:

- Organizational
- Cultural
- Environmental
- Individual or group related factors

Organizational factors, such as economic conditions, are thought to positively or negatively influence individuals' job satisfaction [18]. Locke [19] introduces the value theory and emphasizes that one of the key factors of satisfaction is salary.

Ergonomic conditions refer to environmental factors within the organization, such as temperature, light levels, cleanliness, etc. It is believed that maintaining good ergonomic conditions in workplaces, where individuals spend a significant part of their day, positively affects job satisfaction [20].

Internal communication within the organization is another organizational factor believed to impact job satisfaction [21]. It is known that adopting an open communication policy towards employees contributes to the creation of a positive atmosphere within the organization, thereby assisting employees in managing their work more efficiently [22].

Workload level can be considered as an organizational factor. Parmaksız et al. [23] suggested that workload distribution should be fair to form employees' perceptions of organizational justice. Keser and Yılmaz [24] stated that employees' workload levels contribute to burnout.

Tetik et al. [25] mentioned that giving importance to employees' career development will enhance organizational success. It is believed that employees who are aware that successful performance will be

rewarded by advancing in their careers will have higher levels of job satisfaction.

There are numerous studies examining the direct impact of demographic characteristics on job satisfaction [26-28]. The results of these studies indicate that factors such as gender, age, education level, and years of work experience have an impact on job satisfaction.

In this study, business conditions were discussed for the first time under 5 headings as economic conditions, ergonomic conditions, internal communication, workload level, and career opportunities, and the effects of employees' perceptions of these conditions on job satisfaction were analyzed. Following this, in contrast to analyses focusing on the direct impact of job satisfaction in the literature, an examination was conducted to determine whether individuals' demographic characteristics have an influence on perceptions of organizational conditions. Figure 1 shows the structural model established in the first step of the research.

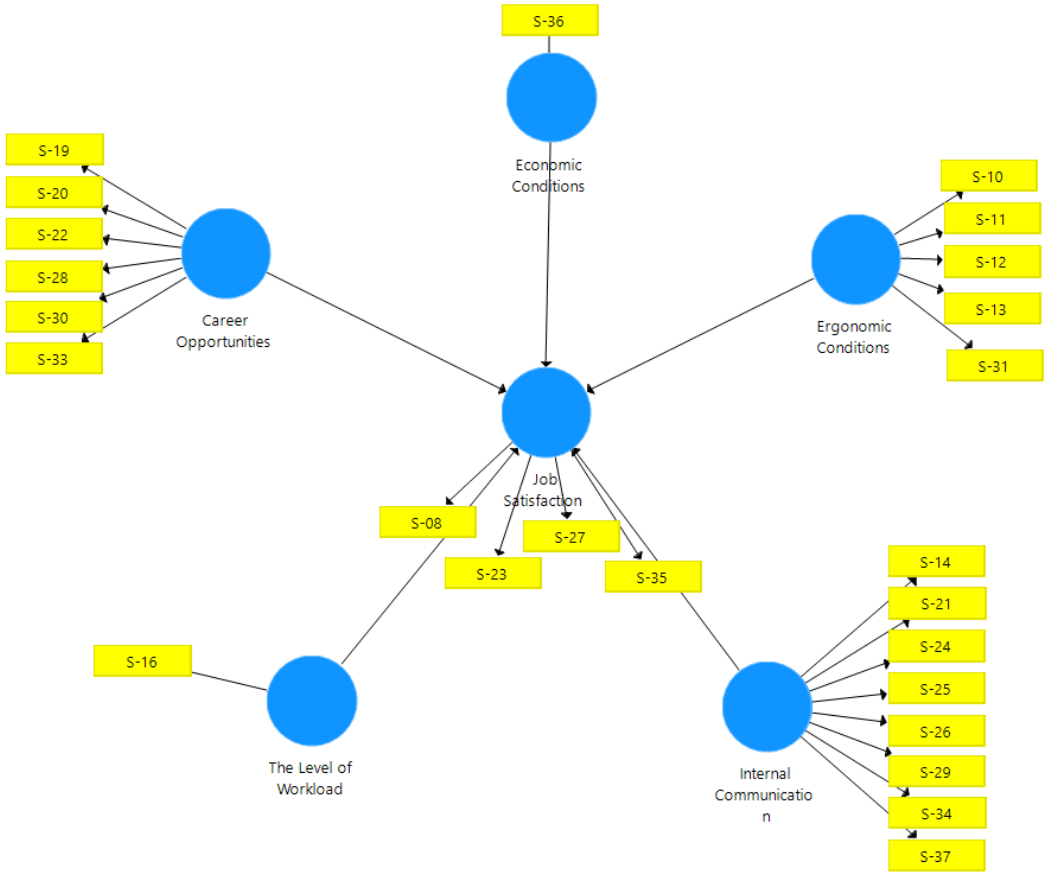

Figure 1. Structural model of the research

The research hypotheses established to measure the effect of business conditions on the job satisfaction of employees are given in Table 1.

Table 1. Research hypotheses

H1	Economic conditions affect the job satisfaction level of employees.
H2	Ergonomic conditions affect the job satisfaction level of employees.
H3	Internal communication affects the job satisfaction level of employees.
H4	The level of workload affects the job satisfaction level of the employees.
H5	Career opportunities affect the job satisfaction level of employees.

2. Materials and Methods

In this study, the impact of organizational conditions on job satisfaction levels of sector employees will be examined.

2.1. Sampling, Data Collection

The data were collected through a questionnaire (Annex-1), and the sample of the study consists of employees from 52 sectors. In the first part of the questionnaire, there were questions about the demographic characteristics of the employees. In the second part of the questionnaire, the suggestion was presented to measure the job satisfaction level of the employees, the communication within the enterprise, the workload level of the employees, the career opportunities in the workplace, and the economic and ergonomic conditions of the workplace. The propositions were asked to be evaluated according to a 5-point Likert Scale. A total of 150 survey results were evaluated in the study. A simple random sampling method was employed in the research, and data were collected through face-to-face and electronic surveys. The fact that Cronbach Alpha values exceeded 0.80 indicates the reliability of the research model.

2.2. Analysis of Data

In order to test the hypotheses established in the first step of the study, Partial Least Squares Structural Equation Modeling (KEKK-YEM) and Smart PLS 3 package programs, a second generation statistical software, were used to test the reliability, validity and hypothesis of the data.

KEKK-SEM is a modeling technique used for modeling complex multivariate relationships between observed and latent variables. KEKK-YEM, which is mostly preferred in exploratory research, was first discussed by Wold [29] and subsequently developed by Löhmöller [30]. KEKK-SEM does not require the assumption of normality compared to other methods, can provide accurate results even in small sample sizes, and can make successful measurements in complex models [31]. Many alternative KEKK-YEM software packages (VisualPLS, PLS-GUI, PLS-Graph) have been developed since the 1980s. The KEKK-YEM analysis in this study was carried out with the Smart PLS 3 package program. PLS, which is one of the most popular methods in data analysis today, is a variance-based structural equation modeling method [32-34]. During the evaluation of the measurement model, which is the first stage of KEKK-SEM, reliability and validity analyzes of the theoretically constructed model were carried out, and during the evaluation of the structural model, which is the second stage, a path analysis was conducted in which the established hypotheses were tested.

SPSS 22 statistical program was used to test the hypotheses established in the second step of the research. Normality test, Pearson Correlation coefficient, regression analysis, t test and ANOVA test were used. Post Hoc-LSD test was performed to detect the groups that differed in the comparisons of more than one group. The obtained data were analyzed at the 5% significance level ($p<0.05$).

3. Findings

3.1. Demographic Features

Demographic findings of the research sample are summarized in Table 2. Of the participating employees in the research, 54.7% are male, and 45.3% are female. 69.4% of the participants have received education at least

at the undergraduate level, and 73.3% have been in the workforce for at least 5 years. 65.3% of the participants are married, and 30.7% are single, with 50% falling within the age range of 25-35.

Table 2. Demographic characteristics of the research sample

Demographic Feature		Frequency	Percentage	Demographic Feature		Frequency	Percentage
Age	18-25	11	7.3	**Marital Status**	Single	46	30.7
	26-35	75	50.0		Married	98	65.3
	36-45	45	30.0		Divorced	6	4.0
	46-55	11	7.3		Total	150	100.0
	56-65	8	5.3	**Education**	Primary-Secondary School	11	7.3
	65+	0	0		High School	22	14.7
	Total	150	100.0		Associate Degree	13	8.7
Working Year	1-5	40	26.7		Licence	67	44.7
	6-10	36	24.0		Graduate	37	24.7
	11-15	30	20.0		Total	150	100.0
	16-20	22	14.7	**Gender**	Women	68	45.3
	21+	22	14.7		Man	82	54.7
	Total	150	100.0		Total	150	100.0

3.2. Evaluation of Hypotheses with Partial Least Squares Structural Equation Modeling (KEKK-YEM)

Before testing the established research hypotheses, the validity and reliability analyzes of the measurement model were made. Since the factor load of 5 factors was insufficient (<0.6) in the measurement model, which was initially created with 30 factors and 6 variables, the measurement model was established with 25 factors and 6 variables. The results of the analysis performed with the Smart PLS 3 program are given in Table 3.

Table 3. Measurement model results

Factor/ Variable	Factor Load	T-value	R^2	Cronbach Alpha	Composite Reliability	Rho_A	AVE
Economic Conditions				1.000	1.000	1.000	1.000
S-36	1.000						
Ergonomic Conditions				0.807	0.865	0.816	0.562
S-10	0.685	9.313					
S-11	0.737	9.162					
S-12	0.841	17.163					
S-13	0.766	13.572					
S-31	0.711	12.592					
Internal Communication				0.921	0.936	0.927	0.684
S-14	0.775	18.660					
S-21	0.874	38.510					
S-24	0.848	33.442					
S-25	0.691	9.716					
S-26	0.742	11.516					
S-29	0.820	23.527					
S-34	0.870	31.876					
S-37	0.801	22.469					

Table 3. (Continued) Measurement model results

Factor/ Variable	Factor Load	T-value	R^2	Cronbach Alpha	Composite Reliability	Rho_A	AVE
The Level of Workload				1.000	1.000	1.000	1.000
S-16	1.000						
Career Opportunities				0.849	0.889	0.852	0.572
S-19	0.710	12.794					
S-20	0.811	20.607					
S-22	0.714	11.181					
S-28	0.714	11.836					
S-30	0.858	28.457					
S-33	0.718	11.862					
Work Satisfaction			0.762	0.817	0.880	0.835	0.649
S-8	0.750	17.047					
S-23	0.714	12.484					
S-27	0.861	27.693					
S-35	0.884	36.738					

Although the majority of researchers argue that factor loadings should be 0.70 and above [35], there are also researchers who accept values in the range of 0.60-0.70 [36]. When the factor loads of the model established in this study were examined, it is seen that the factor loads of all propositions were above 0.60. In order to measure research reliability, Cronbach's Alpha internal consistency values, Composite Reliability (CR) values and Rho_A values should be examined [37, 38]. CR values higher than 0.80 indicate that the research model is reliable [39]. Cronbach's Alpha and Rho_A values higher than 0.60 are considered sufficient for model reliability [40]. Looking at Table 3, the minimum CR value is 0.886, the minimum Cronbach's Alpha value is 0.807, and the mini-candle Rho_A value is 0.816. According to these results, the structural model of the research is reliable. Another indicator that should be examined in order to analyze the explanatory power and stability of the structural model is the R2 value. If the R2 value is greater than 0.75, the model has the ability to predict power [41]. The R2 value of job satisfaction in the research model is 0.762, which indicates that the model has a high predictive/explanatory power.

In order to measure the discriminant validity of the model, HTMT (Heterotrait-Monotrait Ratio) and Fornell-Larcker values should be examined. HTMT values express the ratio of the mean of the correlations of the expressions of all variables to the geometric mean of the correlations of the expressions of the same variable [42] and should be less than 1.0 [43]. The HTMT values of the variables in the research model are given in Table 4. All values less than 1.0 indicate that the model has discriminant validity.

Table 4. HTMT values for discriminant validity

	Economic Conditions	Ergonomic Conditions	Career Opportunities	Work Satisfaction	The Level of Workload	Internal Communication
Economic Conditions						
Ergonomic Conditions	**0.522**					
Career Opportunities	0.680	**0.814**				
Work Satisfaction	0.623	0.794	**0.978**			
The Level of Workload	0.223	0.115	0.166	**0.209**		
Internal Communication	0.643	0.831	0.957	0.973	**0.227**	

According to Fornell and Larcker [44], the square roots of the AVE values of the model should be higher than the correlations between the structures in the research [42]. The values given in bold in Table 5 are the square roots of the model's AVE values. The fact that these values are higher than the correlation coefficients between the constructs shows that the validity values of the model are appropriate.

Table 5. Fornell Larcker values for discriminant validity

	Economic Conditions	Ergonomic Conditions	Career Opportunities	Work Satisfaction	The Level of Workload	Internal Communication
Economic Conditions	**1.000**					
Ergonomic Conditions	0.487	**0.750**				
Career Opportunities	0.623	0.711	**0.756**			
Work Satisfaction	0.572	0.666	0.794	**0.806**		
The Level of Workload	0.223	0.081	0.154	0.164	**1.000**	
Internal Communication	0.621	0.731	0.751	0.802	0.202	**0.805**

In the Table 6, path coefficients, sample averages, standard deviations, t-test values and p values of the hypotheses tested in the study model are given. In order to evaluate the significance of the KEKK path coefficients by bootstrapping, 1000 sub-samples were taken from the sample, and t and p values for the hypotheses were calculated. In the analysis, the threshold t-test value was evaluated as 1.96 for 95% significance level ($p \leq 0.05$) [45].

Table 6. Analysis results of the structural model

Hypothesis	Path Coefficient	Sample Mean	Standard Deviation	T Value	P Value	Conclusion
H1	0.013	0.019	0.068	0.190	0.849	Rejection
H2	0.023	0.039	0.075	0.303	0.762	Rejection
H3	0.547	0.537	0.147	3.716	0.000	**Acceptance**
H4	-0.004	-0.006	0.054	0.076	0.940	Rejection
H5	0.333	0.328	0.114	2.913	0.004	**Acceptance**

According to the results of the analysis, H3 and H5 hypotheses were accepted, while H1, H2, and H4 hypotheses were rejected. The order of the accepted hypotheses according to their importance is given in Table 7.

Table 7. Values related to accepted hypotheses

Hypothesis	Serial Number	Path Coefficient	Serial Number	Sample Mean	Serial Number	Standard Deviation	Serial Number	T Value	Serial Number	P Value
H3	1	0.547	1	0.537	1	0.147	1	3.716	2	0.000
H5	2	0.333	2	0.328	2	0.114	2	2.913	1	0.004

When Table 7 is examined, it is seen that the effect of H3 hypothesis, that is, internal communication, on job satisfaction, is higher than the H5 hypothesis, that is, career opportunities, according to all other indicators except the P value indicator.

3.3. Examining the Effects of Employees' Demographic Characteristics on Perceptions of Internal Communication and Career Opportunities

In the previous stage, it was concluded that the perceptions of the employees about internal communication and career opportunities had an effect on their job satisfaction. In this stage, it was analyzed whether the demographic characteristics of the employees have an effect on these two perceptions. In this stage of the study, the formulated hypotheses are as follows:

H2.1. The demographic characteristics of employees influence their perceptions of internal communication.

H2.2. The demographic characteristics of employees influence their perceptions of career opportunities.

First of all, normality test was applied to assess the normality of the data. The normality of the data was determined by looking at the Skewness and Kurtosis values. Normality test results are given in Table 8.

Table 8. Results of normality test of data

	Skewness	Kurtosis
Internal Communication	-0.174	-0.149
Career Opportunities	0.225	-0.584

When we look at the Skewness and Kurtosis values, it is seen that they are in the range of ±1, that is, the data are normally distributed. The analyzes regarding the effect of gender, age, education, working year and marital status of the employees on their perceptions of internal communication and career opportunities are given in Tables 9-17. In cases where there are two groups, the t test was applied, and in cases where there were more than two groups, the ANOVA test was applied. Post Hoc-LSD test was used to obtain different groups.

Table 9. T-test results regarding the effect of gender factor on variables

Variables	Groups	N	X	ss	t-test	
					sd	p
Internal Communication	Women	68	3.21	0.75	148	**0.032**
	Man	82	3.49	0.82		
Career Opportunities	Women	68	2.83	0.89	148	0.081
	Man	82	3.08	0.88		

When Table 9 is examined, it is seen that employees' perceptions of Career Opportunities do not show a significant gender difference ($p>0.05$). Moreover, it is seen that the perceptions of Internal Communication indicate a significant gender difference ($p<0.05$). However, the perceptions of male employees are more positive than those of female employees.

Table 10. Results of homogeneity test of variances regarding the effect of age factor on variables

		Sum of Squares	df	Mean Square	F	Sig.
Internal Communication	Between Groups	1,422	4	0,354	0,550	0,699
	Within Groups	93,762	145	0,647		
	Total	95,184	149			
Career Opportunities	Between Groups	3,683	4	0,921	1,164	0,329
	Within Groups	114,673	145	0,791		
	Total	118,357	149			

When the Tables 10 and 11 are examined, it is seen that the variances are homogeneously distributed. It is seen that the perceptions of the employees towards Internal Communication and Career Opportunities do not point out a significant age difference ($p>0.05$).

Table 12. Results of homogeneity test of variances regarding the effect of education factor on variables

	Levene Test	df1	df2	p Value
Internal Communication	0,660	4	145	0,621
Career Opportunities	3,110	4	145	**0,017**

Table 13. ANOVA test results regarding the effect of education factor on variables

		Sum of Squares	df	Mean Square	F	Sig.
Internal Communication	Between Groups	3,898	4	0,975	1,548	0,191
	Within Groups	91,286	145	0,630		
	Total	95,184	149			
Career Opportunities	Between Groups	10,052	4	2,513	3,364	**0,011**
	Within Groups	108,305	145	0,747		
	Total	118,357	149			

When the Tables 12 and 13 are examined, it is seen that the variances do not show a significant difference according to the education level of the employees' perceptions of Internal Communication ($p>0.05$). It is seen that their perceptions of Career Opportunities show a significant difference according to their educational status ($p<0.05$).

Table 14. Results of the homogeneity test of variances regarding the effect of the working year factor on the variables

	Levene Test	df1	df2	p Value
Internal Communication	1,118	4	145	0,319
Career Opportunities	2,105	4	145	0,083

Table 15. ANOVA test results regarding the effect of the working year factor on the variables

		Sum of Squares	df	Mean Square	F	Sig.
Internal Communication	Between Groups	0,420	4	0,105	0,160	0,958
	Within Groups	94,764	145	0,654		
	Total	95,184	149			
Career Opportunities	Between Groups	2,627	4	0,657	0,823	0,513
	Within Groups	115,730	145	0,798		
	Total	118,357	149			

When Tables 14 and 15 are examined, it is seen that the variances are homogeneously distributed. It is seen that the perceptions of the employees towards Internal Communication and Career Opportunities do not show a significant difference according to their working years ($p>0.05$).

Table 16. The Results of homogeneity test of variances regarding the effect of marital status factor on variables

	Levene Test	df1	df2	p Value
Internal Communication	0,369	2	147	0,692
Career Opportunities	0,469	2	147	0,627

Table 17. ANOVA test results regarding the effect of marital status factor on variables

		Sum of Squares	df	Mean Square	F	Sig.
Internal Communication	Between Groups	0,320	2	0,160	0,248	0,781
	Within Groups	94,864	147	0,645		
	Total	95,184	149			
Career Opportunities	Between Groups	0,932	2	0,466	0,584	0,559
	Within Groups	117,424	147	0,799		
	Total	118,357	149			

When Tables 16 and 17 are examined, it is seen that the variances are homogeneously distributed. It is seen that the perceptions of the employees towards Internal Communication and Career Opportunities do not show a significant difference according to marital status ($p>0.05$).

In this step of the study, it was determined that only the perceptions of development opportunities suggested a significant difference according to the level of education ($p<0.05$). Post-Hoc test was performed to analysis this difference. According to the test results, the employees with primary education had a higher perception of development opportunities than the employees with graduate degrees.

4. Conclusion

In this study, the effect of demographic characteristics of employees and business conditions on job satisfaction was analyzed. First of all, the effect of business conditions under 5 headings on the level of job satisfaction was analyzed. These hypotheses established within the scope of the research were tested with Partial Least Squares Structural Equation Modeling (PLSSEM) and a second-generation statistical software, the Smart PLS 3 package program. While 3 of the 5 hypotheses subject to the analysis were rejected, 2 were accepted. The results of the hypotheses are given below:

H1: It has not been determined that economic conditions have an effect on the level of job satisfaction of the employees. Locke [19] posit theories suggesting that economic conditions, as one of the organizational factors, have an impact on job satisfaction. In this study, the deviation from these theories is considered to stem from sample differences, leading to contrasting results.

H2: It has not been determined that ergonomic conditions have an effect on the level of job satisfaction of the employees. According to Telman and Ünsal [20], improving the ergonomic conditions of employees who spend a significant portion of their days in the workplace positively influences their job satisfaction. However, the conducted study did not yield results supporting this idea.

H3: It has been determined that the level of internal communication has a positive effect on the job satisfaction level of the employees. It has been observed that the job satisfaction of the employees who think that the communication within the enterprise is at a high level is higher. Sabuncuoğlu and Tüz [22] stated that internal communication positively influences employees. Yeşilyurt and Koçak [21] found that internal communication is an organizational factor affecting job satisfaction. The results obtained in our study are consistent with previous research, supporting these findings.

H4: It has not been determined that the level of workload has an effect on the level of job satisfaction of the employees. The literature indicates a relationship between workload levels and employees' perceptions of organizational justice [23] as well as their levels of burnout [24]. However, according to the results of our study, a relationship between workload levels and the job satisfaction levels of employees could not be identified.

H5: It has been determined that career opportunities have a positive effect on the level of job satisfaction of employees. It has been observed that the job satisfaction of the employees who think that the career opportunities offered to them in the businesses they work are at a high level. The obtained results align with the literature [25].

In the continuation of the study, it was analyzed whether the demographic characteristics of the employees had an effect on the perceptions of the H3 and H5 hypotheses, which were accepted as a result of the KEKK-YEM analysis. SPSS 22 statistical program was used for this analysis. According to the results of the analysis, 2 effects were determined.

- It has been determined that the gender factor had an effect on the perception of internal communication. It has been observed that female employees had more positive perceptions than male employees. Karakaya and Sancı [46], in their study focusing on occupational health and safety specialists, found no significant difference in internal, external, and overall satisfaction levels based on gender. Although not directly addressed in our study, it can be inferred that this observation may be due to the inherent emotional nature of women and the importance of communication for them. Indeed, Kırel [47], Hulin and Smith [48], and Sauser and York [49] have suggested the influence of gender on job satisfaction in their studies. While the results of this study do not directly address it, they indirectly support the presence of such an effect.

- It has been determined that the education level factor had an effect on the perception of career opportunities. It has been observed that employees with low education levels had a higher perception of career opportunity compared to other employees. This result may be considered as an indicator of the importance that enterprises attach to the training and development of their employees. According to the findings of Gürkan et al. [26], employees with lower educational levels have higher job satisfaction levels. Although a direct impact on this aspect was not explicitly investigated in our study, the indirectly observed effect aligns with the literature.

The topic addressed in the study, the classification of organizational conditions and the methodology employed, contributes to the literature. In the future, more precise results may be obtained by performing similar analyzes on samples that are higher in number or limited in terms of sector.

Author Contributions

The first author made a literature review and statistical analysis and wrote the study. The second author collected the data, designed the study methodology and translated it into English. The third author planned and designed the methodology of the study. They all read and approved the final version of the paper.

Conflicts of Interest

All the authors declare no conflict of interest.

References

[1] C. Kahya, *Does cynicism affect job performance? The mediating effect of job* satisfaction, Global Journal of Economics and Business Studies 2 (3) (2013) 34–46.

[2] Y. Demirel, M. Y. Özçınar, *Örgütsel vatandaşlık davranışının iş tatmini üzerine etkisi: farklı sektörlere yönelik bir araştırma*, İktisadi ve İdari Bilimler Dergisi 23 (1) (2009) 129–145.

[3] E. E. Lawler, Motivation in work organisations, Monterey, 1973.

[4] E. A. Locke, *What is job satisfaction?*, Organizational Behavior and Human Performance 4 (4) (1969) 309–336.

[5] D. P. Schultz, S. E. Schultz, Pschology and work today: An introduction to industrial and organizational psychology, 1st Edition, Routledge, 1998.

[6] A. Soysal, P. Öke, F. Yağar, M. Tunç, A*n analysis of the levels organizational communication and job satisfaction: Example of a private hospital*, The Journal of Selcuk University Social Sciences Institute 37 (2017) 243–253.

[7] M. Kasimati, *Job satisfaction and turnover under the effect of person organization fit in Albanian public organizations,* Journal for East European Management Studies 16 (4) (2011) 315–337.

[8] H. Bayramlık, M. E. Bayık, G. Güney, *The effects of job satisfaction on personorganization fit: A research on the employees of heavy equipment machinery sector*, Science Journal of Turkish Military Academy 25 (2) (2015) 1–28.

[9] Ö. Bozkurt, İ. Bozkurt, *A field study on job satisfaction effecting internal factors in education sector*, Doğuş University Journal 9 (1) (2008) 1–18.

[10] S. A. M. Ali, N. A. Said, S. D. A. Kader, D. S. Ab Latif, R. Munap, *Hackman and Oldham's job characteristics model to job satisfaction*, Procedia-Social and Behavioral Sciences 129 (2014) 46–52.

[11] Ö. F. İşcan, U. Sayın, *Örgütsel adalet, iş tatmini ve örgütsel güven arasındaki ilişki.* Atatürk Üniversitesi İktisadi ve İdari Bilimler Dergisi, 24 (4) (2010) 195–216.

[12] J. Julseth, J. Ruiz, D. Hummer, *Municipal police officer job satisfaction in Pennsylvania: A study of organisational development in small police departments*, International Journal of Police Science and Management 13 (3) (2011) 243–254.

[13] M. J. Neubert, K. Halbesleben, *Called to commitment: an examination of relationships between spiritual calling, job satisfaction, and organizational commitment*, Journal of Business Ethics 132 (4) (2015) 859–

872.

[14] S. Kardaş, H. Şencan, *The effect of five factor personality on business satisfaction*, İstanbul Ticaret Üniversitesi Sosyal Bilimler Dergisi 17 (33) (2018) 287–299.

[15] Ş. Şenol, V. Öngel, *The effect of internal marketing practices on employees' job satisfaction and the mediating role of organizational justice*, The Academic Elegance 6 (12) (2019) 445–475.

[16] T. Akçakanat, T. Erhan, H. H. Uzunbacak, *The effect of calling on job satisfaction: The mediator role of flow experience*, İzmir Kâtip Çelebi University Faculty of Economics and Administrative Sciences 2 (1) (2019) 80–95.

[17] E. Örücü, S. Yumuşak, Y. Bozkır, *Job Satisfaction and its Determinants for Individuals Who Works in The Banking Sector in Quality Management Perspective*, Celal Bayar Üniversitesi İktisadi ve İdari Bilimler Fakültesi Yönetim ve Ekonomi Dergisi 13 (1) (2006) 39–51.

[18] M. M. Grunberg, *Job Satisfaction*, Unvin Brothers Ltd., London, 167 (1976).

[19] E. A. Locke, *The nature and causes of job satisfaction*, in: M. D. Dunnette (Ed.), Handbook of Industrial and Organizational Psychology, 1, 1996, 1297–1343.

[20] N. Telman, P. Ünsal, Çalışan memnuniyeti, Epsilon Yayınları, (2004) 14–28.

[21] H. Yeşilyurt, N. Koçak, *The analysis of relationship between job satisfaction and organizational citizenship behavior in the hotels*, Dokuz Eylul University The Journal of Graduate School of Social Sciences 16 (2) (2014) 303–324.

[22] Z. Sabuncuoğlu, M. Tüz, Örgütsel psikoloji, Ezgi Kitabevi, Bursa, 1995.

[23] A. Parmaksız, T. Ersöz, T. Özseven, F. Ersöz, *Evaluation of Job Satisfaction, Job Stress and Ergonomic Conditions of Employees at Workplace*, Gaziosmanpaşa Journal of Scientific Research (8) (2013) 82–99.

[24] A. Keser, G. Yılmaz, *Workload, burnout, and job satisfaction among call center employees*, Journal of Social Policy Conferences 66-67 (2014) 1–13.

[25] S. Tetik, G. Uçar, B. Yalçın, *Örgütlerde İş Tatminini Etkileyen Etmenler ve Emniyet Mensupları ile Yapılan Alan Araştırması*. Verimlilik Dergisi 1 (2008) 79–105.

[26] H. Gürkan, C. Barut, O. Ünsel, E. Aybal, *Examination of the relationship between demographic variables and job satisfaction: Implementation of Bitlis tourism sector employees*, Journal of Bitlis Eren University Institute of Social Sciences 6 (2) (2017) 130–157.

[27] N. Elibüyük, S. Güney, *Examination of job satisfaction levels of employees by demographic variables*, Anadolu Bil Meslek Yüksekokulu Dergisi, 15 (58) (2020) 171–192.

[28] B. Heybeli, B. Kayıhan, Y. Tepeli, *Resarch on the levels of job satisfactions of certified public accountants according to demographic variables: The sample of Muğla*, Afyon Kocatepe Journal of Economics and Administrative Sciences 16 (2) (2014) 155–165.

[29] H. Wold, *Soft modeling: The basic design and some extensions*, in: K. G. Jöreskog, H. Wold (Eds.), Systems Under Indirect Observations, Amsterdam, Part I, 1982, pp. 1–54.

[30] J. B. Lomoller, Latent variable path modeling with partial least squares, Physica-Verlag, Heidelberg, 1989.

[31] J. Henseler, C. M. Ringle, R. R. Sinkovics, *The use of partial least squares path modeling in international marketing*, in: R. R. Sinkovics, P. N. Ghauri (Eds.) New Challenges to International Marketing (Advances in International Marketing, Vol. 20), Emerald Group Publishing Limited, Bingley, (2009) pp. 277–319.

[32] F. B. Bağlan, U. İ. İnan, H. Başlıgil, *Analysis of the effect of heavy industry workers' demographic*

characteristics on their life quality, Mehmet Akif Ersoy University Journal of Social Sciences Institute (35) (2022) 1–13.

[33] P. Singkheeprapha, Z. A. Jumani, S. Sukhabot, *Is Islamic brand attitudes Thai Muslims' buying behavioural intentions: A quantitative analysis using Smart-PLS*, Journal of Islamic Marketing 13 (11) (2021).

[34] X. Xu, K. Xue, L. Wang, D. Gürsoy, Z. Song, *Effects of costumer-to-customer social interactions in virtual travel communities on brand attachment: the mediating role of social well-being*, Tourism Management Perspectives 38 (2021) 100790.

[35] J. F. Hair, G. T. M. Hult, C. Ringle, M. Sarstedt, *A primer on partial least squares structural equation modeling (PLS-SEM)*, Sage Publications, (2016).

[36] W. W. Chin, *How to write up and report PLS analyses*, in: V. Esposito Vinzi, W. Chin, J. Henseler, H. Wang (Eds.) Handbook of Partial Least Squares, Springer Handbooks of Computational Statistics, Springer, Berlin, Heidelberg, 2010, Ch. 28, pp. 655–690.

[37] R. P. Bagozzi, Y. Yi, *On the evaluation of structural equation models*, Journal of Academy of Marketing Science 16 (1) (1998) 74–94.

[38] K. K. K. Wong, *Partial least structural equation modeling (PLS-SEM) techniques using smart PLS*, Marketing Bulletin 24 (1) (2013) 1–32.

[39] J. C. Nunnally, I. H. Bernstein, Psychometric theory, Mc Graw-Hill, New York, 1994.

[40] Y. Terzi, *Anket, güvenilirlik-geçerlilik analizi ders notları* (2019), Ondokuz Mayıs Üniversitesi Fen-Edebiyat Fakültesi.

[41] Ö. Çark, A. Marşap, *The factors affecting benefits of enterprise resource planning system from user perception*, Third Sector Social Economic Review 54 (2) (2019) 992–1013.

[42] H. Çetiner, Ö. Yayla, *The effect of activity commitment on life satisfaction and quality of life: A research about cyclists*, Pamukkale University Journal of Social Sciences Institute 42 (2021) 209–222.

[43] A. G. Karababa, *The organizational role of social support perceived by women employees, on job and life satisfaction, and the conflict of family-family life and family-work life*, Doctoral Dissertation Hasan Kalyoncu University (2021) Gaziantep.

[44] C. Fornell, D. F. Larcker, *Structural equation models with unobservable variables and measurement error: Algebra and statistics*, Journal of Marketing Research 18 (3) (1981) 328–388.

[45] J. F. Hair, C. M. Ringle, M. Sarstedt, *PLS-SEM: Undeed a silver bullet*, The Journal of Marketing Theory and Practice 19 (2) (2011) 139–152.

[46] A. Karakaya, V. Sancı, *A Study on Job Satisfaction of Occupational Safety Experts: The Black Sea Region Case*, Karabük Üniversitesi Sosyal Bilimler Enstitüsü Dergisi 7 (1) (2017) 1–13.

[47] A. Ç. Kırel, *Esnek Çalışma Saatleri Uygulamasında Cinsiyet, İş Tatmini ve İş Bağlılığı İlişkisi.* İstanbul Üniversitesi İşletme Fakültesi Dergisi, 28 (2) (1999) 115–136.

[48] C. L. Hulin, P. C. Smith, *Sex differences in job satisfaction*, Journal of Applied Psychology 48 (2) (1964) 88–92.

[49] W. I. Sauser, C. M. York, *Sex differences in job satisfaction: A Re-Examination*, Personnel Psychology, 31 (3) (1978) 537–547.

Çanakkale Onsekiz Mart University

Journal of Advanced Research in Natural and Applied Sciences

dergipark.org.tr/tr/pub/jarnas

Open Access

e-ISSN: 2757-5195 2024, Vol. 10, Issue 2, Pages: 350-366 doi.org/10.28979/jarnas.1384800

Betonarme Çerçeve ve Kolonlarda İtme Analizi

Aydın Özkarabulut[1], Hasan Orhun Köksal[2]

[1]Çanakkale Onsekiz Mart Üniversitesi, Lisansüstü Eğitim Enstitüsü, İnşaat Mühendisliği Anabilim Dalı, Çanakkale, Türkiye
[2]Çanakkale Onsekiz Mart Üniversitesi, Mühendislik Fakültesi, İnşaat Mühendisliği Bölümü, Çanakkale, Türkiye

Makale Tarihçesi
Gönderim: 01 Kasım 2023
Kabul: 06 Şubat 2024
Yayım: 25 Haziran 2024

Araştırma Makalesi

Abstract − Bu makale, 1950'lerden bu yana betonarme çerçeve ve kolonların karmaşık davranışlarının modellenmesine yönelik devam eden deneysel ve analitik çalışmaların, günümüz yönetmeliklerindeki statik itme analizlerine olan etkileri üzerine odaklanmıştır. Bu noktada yapı elemanlarının moment eğrilik ilişkilerinin analizlere gerçekçi bir şekilde yansıtılması, davranışı belirleyici nitelik taşımaktadır. Bu çalışmada, Koksal-Erdogan tarafından önerilen çok eksenli basınç altındaki beton davranış modeli kullanılarak geliştirilen bir program aracılığıyla elde edilen moment-eğrilik ilişkileri, analizlerde kullanılmıştır. Geliştirilen yapısal analiz programı ise, tek açıklıklı ve tek katlı boş betonarme çerçeve ile ankastre tekil kolonların deneysel olarak belirlenmiş davranışlarını tahmin etmekte kullanılmıştır. Yapılan analizlerin sonucunda, deney çerçeve ve kolonlarına ait yatay deplasmanlar ve kuvvetlerin, Koksal-Erdogan modeli ile birlikte karşılaştırmalı bir şekilde Mander modelinden elde edilen moment-eğrilik diyagramları kullanılarak başarıyla tahmin edilebildiği belirlenmiştir. Makalede ayrıca, Mander modeli ile Koksal-Erdogan modeli arasında gerilme-şekildeğiştirme ilişkileri bakımından da karşılaştırmalar yapılmış ve sonuçların oldukça uyumlu olduğu ancak Koksal-Erdogan modelinin biraz daha düşük gerilme değerleri verdiği belirtilmiştir. Geliştirilen moment-eğrilik programının geçerliliğini göstermek amacıyla, literatürde bulunan SEMAp programıyla bazı karşılaştırmalar yapılmış ve iki program arasında benzer sonuçlar elde edildiği belirlenmiştir. Koksal ve Mander modellerine göre incelenen kolonlar ve çerçeve için elde edilen iç kuvvet şekil değiştirme tahminlerinin, deney sonuçlarıyla uyumlu olduğu gözlenmiştir.

Anahtar Kelimeler − *Bünyesel modeller, itme analizi, moment-eğrilik, sargılı beton*

Pushover Analysis in Reinforced Concrete Frames and Columns

[1]Department of Civil Engineering, School of Graduate Studies, Çanakkale Onsekiz Mart University, Çanakkale, Türkiye
[2]Department of Civil Engineering, Faculty of Engineering, Çanakkale Onsekiz Mart University, Çanakkale, Türkiye

Article History
Received: 01 Nov 2023
Accepted: 06 Feb 2024
Published: 25 Jun 2024

Research Article

Abstract − This article focuses on the effects of ongoing experimental and analytical studies on modeling the complex behavior of reinforced concrete frames and columns since the 1950s on the static pushover analyses in today's regulations. At this point, realistic consideration of the moment-curvature relationships of the structural elements in the analysis is decisive. In the study, moment-curvature relationships obtained through a program developed using the multi-axial compressive concrete behavior model proposed by Koksal-Erdogan were used in the analyses. The developed structural analysis program was used to predict the experimentally determined behavior of single-span and single-storey bare frame and fixed single columns. As a result of the analyses, it is found that the horizontal displacements and forces of the experimental frame and columns could be successfully predicted using the moment-curvature diagrams obtained from the Mander model, in a comparative manner with Koksal-Erdogan model. In the article, comparisons were also made between the Mander model and the Koksal-Erdogan model in terms of stress-strain relations, and it was stated that the results were quite similar to each other, but the Koksal-Erdogan model gave slightly lower stress values. In order to demonstrate the validity of the developed moment-curvature program, some comparisons were made with the SEMAp program found in the literature, and it was determined that similar results were obtained between the two programs. It was observed

[1]22414957001@ogr.comu.edu.tr (Corresponding Author); [2]hokoksal@comu.edu.tr

that the internal force strain predictions obtained for the columns and frame examined according to the Koksal and Mander models agreed with the experimental results.

Keywords − *Constitutive models, pushover analysis, moment-curvature, confined concrete*

1. Giriş

Betonarme elemanların doğrusal olmayan davranışları ve modellenmesi ile ilgili araştırmaların başlangıcı 1950'li yıllara kadar uzanmaktadır. Modelleme çalışmalarındaki ilerleme, bilgisayar teknolojilerinin gelişimine bağlı olarak artmıştır [1-4]. Beton, özellikle çok eksenli basınç altında doğrusal olmayan davranış gösteren bir yapı malzemesidir. Çekme altında ise çatlaklar oluşmakta ve çatlak yüzeyleri boyunca taşınan kuvvetlerden dolayı beton davranışı daha da karışık bir hale gelmektedir. Bu nedenle, tasarım amaçlı kesit hesaplarında genellikle betonun çekme dayanımına ulaştıktan sonraki davranışı ihmal edilmektedir.

Beton yıllar içinde sırasıyla doğrusal elastik, doğrusal olmayan elastik, elasto-plastik teoriler kullanılarak modellenirken; donatı çeliği homojen yapısından ötürü pekleşmeli elasto-plastik malzeme olarak tanımlanmıştır. 1970li yıllarla birlikte betonda doğrusal olmayan davranışın en önemli nedenlerinden olan çatlak oluşumu ve modellenmesi için de pek çok farklı model ileri sürülmüştür [5, 6]. Hasar modeli yaklaşımı, betonda oluşan hasarı belirli bir yüzdeyle ifade etmeye çalışan, bu açıdan günümüzdeki etkin eğilme rijitliği kavramına benzetilebilecek bir teorik modellemeyi de betonun bünyesel modelleme çalışmalarına dahil etmiştir [7,8]. Ülkemizde ise 1985 yılında taşıma gücü yönteminin kullanılmasıyla birlikte beton basınç dayanımının tam kapasitesi dikkate alınarak davranışa uygun daha gerçekçi tasarımlar yapılmaya başlanmıştır. Deprem etkisindeki yapı tasarımı bakımından ise 2007 yılı deprem yönetmeliğinin kullanıma girmesi ile statik itme analizleri yardımıyla yapının son sınır durumuna yanal ötelemeler ile ulaşacağı kabulünden yola çıkılarak kapasite ve deplasman talebi kavramları betonarme yapı tasarımına dahil edilmiştir. Taşıma gücü yaklaşımında son sınır durumların belirlenmesi ancak beton için kullanılacak kırılma modelleri ile mümkün olmaktadır. Bu teorik modellerin en kapsamlılarından ve bilinenlerinden olan Willam-Warnke [9] modeli, daha sonraki yıllarda Mander vd. [10] tarafından beton için önerilen analitik bünyesel bağıntıların geliştirilmesinde kullanılmıştır. Söz konusu model TBDY 2018 kapsamında çok eksenli basınç etkisindeki beton gerilme birim şekil değiştirme ilişkilerinin elde edilmesi amacıyla önerilmektedir.

Başlangıçta üç boyutlu gerilme ve birim şekil değiştirme uzaylarında geliştirilen doğrusal olmayan analitik modellerin beton için kullanımının bireysel betonarme elemanlar dışında pek mümkün olamaması, araştırmacıları daha basite indirgenmiş pratik yaklaşımlar geliştirmeye yönlendirmiştir. Mander, Saatçioğlu-Razvi ve Sheikh-Uzumeri gibi sargılı beton modelleri bu soruna çözüm üretmek amacıyla geliştirilen sayısal modellerden en bilinenleridir [10-12]. Bu çalışmalarda, eksenel basınç etkisindeki bir betonarme kolon, etriyeler ve/veya başka yanal kuşatma mekanizmaları tarafından uygulanan basınç etkileriyle birlikte tek bir çubuk eleman olarak düşünülmüş ve bu çubuk elemana ait eksenel gerilme deformasyon ilişkileri elde edilmeye çalışılmıştır. Bir başka ifade ile üç boyutlu gerilme ve şekil değiştirme uzayında gerçekleşen yüklemeler ve gerilmeler betonarme eleman modellenmesinde tek bir boyuta indirgenmiştir. Benzer yaklaşım, yüklemeler boyunca sürekli bir değişkenlik gösteren eğilme davranış ve rijitliğinin yapısal analizlerde modellenmesinde eğilme davranışının karakteristik bazı noktaları için doğrusal kısımlara bölünerek tasarıma dahil edilmesinde de kullanılmıştır [13, 14].

Yukarıda belirtilen tüm bu çalışmalara paralel olarak iki boyutlu ve üç boyutlu doğrusal olmayan sonlu eleman analizlerinin betonarme elemanlarda kullanılması ve bünyesel modellerin geliştirilmesi çalışmalarına devam edilmiştir [15]. Ancak sonlu eleman analizlerinin karmaşıklığı ve bilgisayar bakımından ağır yükü Mander vd. [10] tarafından önerilen model türü basitleştirilmiş yaklaşımlara olan ilgiyi giderek arttırmıştır. Günümüzde

söz konusu modeller itme analizlerinde ve moment-eğrilik ilişkilerinin tanımlanmasında sıklıkla kullanılmaktadır. Burada unutulmaması gereken nokta, elemanın akma momentine ulaşmasıyla birlikte TBDY'ye [16] göre doğrusal olmayan bütün davranışın elemanların uçlarında tanımlanan sonlu plastik şekil değiştirme bölgelerinde yığılı plastik davranış modeli biçiminde modellenmesi durumudur. Aynı yönetmelik, kolon ve kirişlerde plastik mafsalların kolon-kiriş birleşim bölgesinin hemen dışına bir başka deyişle elemanların net açıklıklarının uçlarına konulabileceğini de belirtmektedir. Bu şekildeki bir modelleme yaklaşımında, yükleme sırasında eleman boyunca gerçekleşecek çatlak yüzeyleri arası agrega kenetlenmesi, donatının kaldıraç etkisi ile çatlaklar arasında kalan sağlam betonun elemanın doğrusal olmayan davranışına olan tüm katkısı ihmal edilmektedir. Yönetmelikteki başka bir belirsizlik ise uçlarındaki plastik mafsallar arasında kalan uzunluk boyunca kolon ve kirişler için kullanılması istenilen etkin kesit rijitliği bağıntısının sadece akma momenti ve akma dönmesine dayandırılmış olmasıdır. Bu nedenle literatürde üç veya daha çok doğrusal parçaya ayrılmış moment-eğrilik ilişkilerinin kullanıldığı çalışmalar da bulunmaktadır [17]. Mafsallar elemanın iki ucunda aynı anda oluşamayacağı gibi başlangıç durumundan akmaya kadar olan tüm eleman davranışı için de böylesi genel bir eğilme rijitliği önerilmesinin gerçekçi olmayacağı ve sadece kaba bir tahminden öteye geçemeyeceği açıktır. İki ucunda akma momentine ulaşmasından sonra uçlarda tanımlanan mafsallar vasıtasıyla elemanın daha fazla eğilme momenti almasına izin verilmemekte, doğal olarak bu modellemeyle eleman çekme ya da basınç çubuğuna dönüşmektedir. Bu türden bir modellemenin, çerçeve ya da kolonun gerçek davranışına göre son derece basitleştirilmiş bir yaklaşım olduğu unutulmamalıdır.

Bu çalışmada betonun çok eksenli basınç altındaki davranışının modellenmesinde Koksal-Erdogan [18] ileri sürdüğü yeni bir model moment-eğrilik ilişkilerinin elde edilmesinde kullanılmıştır [18, 19]. Deneysel olarak sonuçları mevcut betonarme çerçeve ve tekil kolonların itme analizleri, bu model kullanılarak gerçekleştirilmiştir. Sonuçlar Mander modeliyle de karşılaştırmalı olarak verilmiştir.

2. Materyal ve Yöntem

Koksal-Erdogan [18] modeli, yüksek dayanımlı beton sınıfları için önerilmiş ve bu makale kapsamında normal beton dayanım sınıfları için de uygulanmıştır. Mander ve Koksal sargılı beton modelleri kullanılarak moment-eğrilik ilişkilerinin elde edilebilmesi için Python programlama dilinde yazılım geliştirilmiştir. Ayrıca, betonarme düzlem çerçevelerin yapısal analizlerini matris deplasman metodunu kullanarak gerçekleştiren başka bir Python yazılımı geliştirilerek araştırma kapsamında kullanılmıştır.

2.1. Koksal-Erdogan Sargılı Beton Modeli

Türkiye Bina Deprem Yönetmeliği [16] de önerilen Mander sargılı beton modeli, etriye ve çiroz gibi donatılar tarafından oluşturulan pasif kuşatma basınçlarını dikkate almaktadır. Bu ve benzeri modellere temel olan eksenel kısalma ve yanal şekil değiştirme değerlerinin deneysel olarak ölçüldüğü bölge, kolon yarı yüksekliğinde kabuk beton üzerinde yer alan ON orta noktalarıdır. Ancak bu kısım, etriyelere yakın beton kesit üzerinde olduğundan, ölçülen şekil değiştirme ve hesaplanan gerilme değerleri kolon kesitinin tümüne olduğu gibi aktarılamamaktadır. Araştırmacılar bu gerçekten yola çıkarak önerdikleri yanal kuşatma basıncı değerlerinde azaltmaya gitmişlerdir [11]. Mevcut tüm modellerde her ne kadar kuşatma basıncının çekirdek betonu çevreleyen yüzeydeki dağılımı temel alınsa da aslında çekirdek betonun tamamına yayılan ve özellikle en büyük basınç gerilmeleri etkisindeki kolon iç bölgesine doğru azalan bir gerilme durumu mevcuttur.

Bu durumda kolon eksenel dayanımı ile eşleşen yanal kuşatma basıncı değerleri, Şekil 1'de gösterilen kolon kenar orta noktası ON'de ölçülen değerler yerine daha iç bölgede yer alan bir MN noktasında belirlenmelidir.

Koksal-Erdogan [18] modelinde, bu gerçekliği temel alarak çekirdek betonun içindeki MN kısımda oluşan ortalama kuşatma gerilmesinin hesaplanması için bağıntılar önerilmiştir. Bu bağıntılarda kuşatma basıncı, etriye kol sayısı ile doğru orantılı bir şekilde iç bölgeye olan etkisini arttırmaktadır. Bu şekilde bulunacak beton çekirdeği temsil eden bir hacim üzerindeki en küçük kuşatma basıncı değeri, kritik yanal kuşatma basıncı olarak dikkate alınmaktadır. Böylece kuşatılmış beton basınç dayanımı için, mühendislik açısından güvenli tarafta kalınmasını sağlayan sonuçlar hedeflenmiştir.

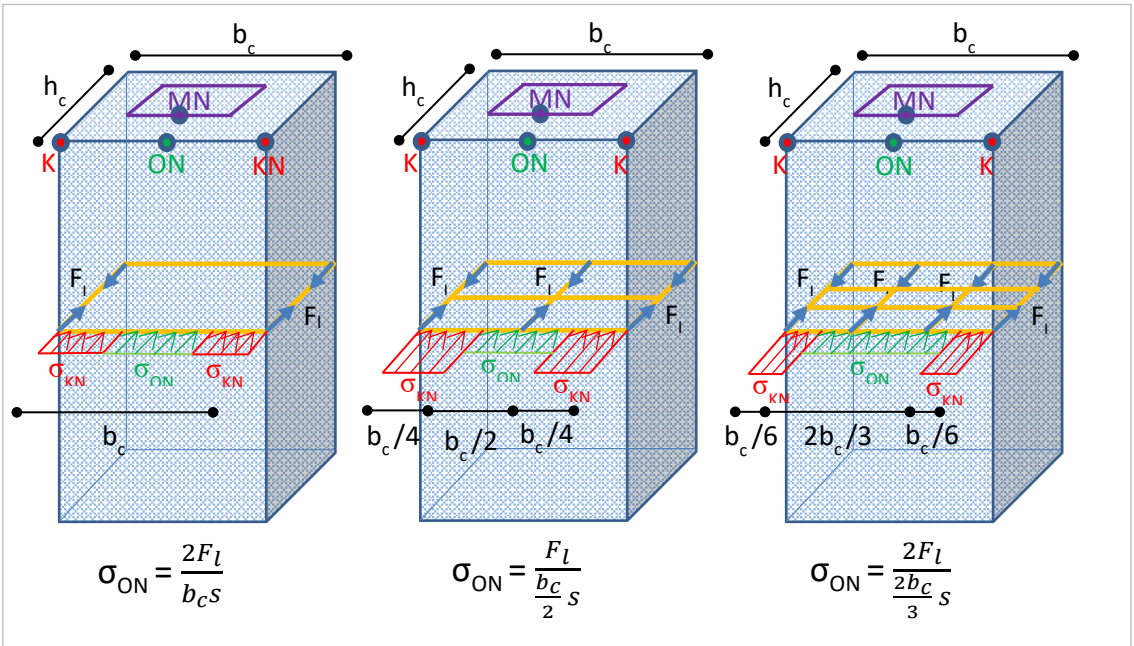

Şekil 1. Sargı donatısının her iki yönde 2, 3 ve 4 adet olması durumunda şematik gerilme dağılımı

Önerilen modelde, bir etriye kolunun beton çekirdek üzerinde oluşturacağı yanal basınç kuvveti, (2.1) ile bulunabilir [18].

$$F_l = \frac{\pi D^2}{4} f_{syh} \tag{2.1}$$

ON noktasına uygulanan gerilme, F_l kuvvetinin etki alanı dikkate alınarak Şekil 1'deki gibi (2.2) ile hesaplanabilir [18].

$$\sigma_{ON} = \frac{N F_l}{b_c\, s} \tag{2.2}$$

Denklem 2.1'deki D yanal donatı çapını, f_{syh} yanal donatı akma dayanımını; (2.2)'deki b_c çekirdek beton boyutunu, s ise yanal donatı aralığını göstermektedir. N ise etriye kolu sayısı n değerine bağlı olarak (2.3) ile bulunabilir [18].

$$\begin{aligned} n = 2 \; ise \; N = 2 \\ n > 2 \; ise \; N = n - 1 \end{aligned} \tag{2.3}$$

Mander modelinde olduğu gibi kuşatma gerilmelerindeki düzgün dağılımdan olan sapmayı yansıtacak şekilde, (2.4)'ten etkin sargılama basıncı katsayısı k_e hesaplanır [10].

$$k_e = \left(1 - \frac{\sum w_i^2}{6 b_c h_c}\right)\left(1 - \frac{s'}{2b_c}\right)\left(1 - \frac{s'}{2h_c}\right)\left(1 - \frac{A_{st}}{b_c\, h_c}\right)^{-1} \tag{2.4}$$

Ayrıca, Koksal-Erdogan [18] modelinde, sargılama basıncı için etriye kolu sayısına göre değişen k_r kat sayısı ile bir azaltma daha yapılarak MN iç noktası için yanal kuşatma basıncı değeri belirlenmektedir. Etriye kolu sayısı n' ye bağlı olarak bu katsayı, (2.5) kullanılarak elde edilebilir [18].

$$\begin{aligned} n = 2 \; ise \; k_r &= 4, \\ n = 3 \; ise \; k_r &= 3, \\ n = 4 \; ise \; k_r &= 2, \end{aligned} \tag{2.5}$$

Kuşatılmış beton dayanımı hesabında beton çekirdeği üzerindeki MN iç noktasında oluşacak azaltılmış kuşatma basıncı f_{ler} ise (2.6) ile bulunabilir [18].

$$\mathrm{f_{ler}} = \frac{k_e \, \sigma_{ON}}{k_r} \tag{2.6}$$

Tüm beton sınıfları için kuşatılmış beton basınç dayanımı f_{cc} ise (2.7)'de verilen basit ifade yardımı ile elde edilmektedir [18].

$$\mathrm{f_{cc}} = 7.84 \, f_{ler} + f'_{co} \tag{2.7}$$

Burada; f_{co} > 60 MPa veya 35 MPa < f_{co} < 60 MPa ve fsyh>1000 MPa ise f_{co}' = 0.85 f_{co} alınacaktır. Diğer durumlarda f_{co}' = f_{co} olarak dikkate alınabilir [18]. Sargılı beton gerilme-şekil değiştirme eğrisinin elde edilmesinde Saenz eğrisi kullanılmaktadır [20]:

$$\sigma_1 = \frac{\varepsilon_1 E_o}{1 + \left(\frac{E_o}{E_{sec}} - 2\right)\left(\frac{\varepsilon_1}{\varepsilon_{cc}}\right) + \left(\frac{\varepsilon_1}{\varepsilon_{cc}}\right)^2} \tag{2.8}$$

(2.8)'de yer alan E_o ve E_s, (2.9) ile elde edilmektedir [18].

$$\begin{aligned} \mathrm{E_o} &= 4750\sqrt{f_{co}} \\ \mathrm{E_{sec}} &= \frac{f_{cc}}{\varepsilon_{cc}} \\ \varepsilon_{\mathrm{cc}} &= \varepsilon_{\mathrm{co}} \left(1 + k_2 \frac{f_{ler}}{f_{cc}}\right) \end{aligned} \tag{2.9}$$

2.2. Mander Sargılı Beton Modeli

Mander sargılı beton modeli, ülkemizdeki deprem yönetmeliğinde yer alan ve oldukça yaygın olarak bilinen sayısal bir beton modelidir. Bu modelde etkin kuşatma basıncı, etriye sıklığının, boyuna donatıların ve kesit malzeme ve geometrisinin bir fonksiyonudur. Mander vd. [10] tarafından önerilen sargısız beton modelinin, yanal kuşatma mekanizmasının dikkate alınarak modifiye edilmiş halidir. Modelde kullanılan bağıntılar aşağıda verilmiştir. Sargılı beton basınç dayanımı f_{cc} ve maksimum gerilmeye karşılık gelen birim şekil değiştirme ε_{cc} sargısız durumdakine göre λ_c katsayısı ile arttırılma prensibine göre işlemektedir [10]. λ_c katsayısı, (2.10) ile bulunabilir [10].

$$\lambda_{\mathrm{c}} = 2.254 \sqrt{1 + \frac{7.94 \, f_e}{f_{co}}} - \frac{2 f_e}{f_{co}} - 1.254 \tag{2.10}$$

x ve y yönleri için etkin kuşatma gerilmeleri sırasıyla (2.11) ile elde edilmekteyken f_e ise iki yön için ortalama değer olarak alınmaktadır [10].

$$f_{ex} = \frac{A_{shx}}{sb} f_{syh} k_e$$
$$f_{ey} = \frac{A_{shy}}{sh} f_{syh} k_e \quad (2.11)$$

Çekirdek betonda gerilme-şekil değiştirme ilişkisi (2.12) ile elde edilmektedir [10].

$$\sigma_c = \frac{f_{cc}\, x\, r}{r - 1 + x^r} \quad (2.12)$$

(2.12)'de f_{cc} çekirdek betonda oluşması beklenen en büyük basınç gerilmesidir ve sargısız beton dayanımının λ_c katsayısıyla arttırılmış halidir. r ise (2.13) ile bulunabilir [10].

$$r = \frac{E_c}{E_c - E_{sec}}$$
$$E_c = 5000\sqrt{f_{co}}$$
$$E_{sec} = \frac{f_{cc}}{\varepsilon_{cc}} \quad (2.13)$$
$$\varepsilon_{cc} = \varepsilon_{co}\,[\,1 + 5\,(\lambda_c - 1)]$$

2.3. Moment Eğrilik Analizi Programı

Taşıyıcı sistem elemanlarının dış yükler altında nasıl davranacağının bilinmesi güvenilir tasarımlar yapabilmek için gereklidir. Moment eğrilik ilişkileri, eleman davranışı hakkında oldukça önemli bilgiler vermektedir. Bu önemli ilişki, laboratuvar ortamında tekrarlı yüklemeler yapılarak gerçekçi şekilde elde edilebilmektedir. Ancak bu deneyler, çoğu zaman oldukça masraflı ve zaman kaybına neden olabilen yöntemlerdir. Gelişen bilgisayar teknolojileri sayesinde, bu amaca yönelik geliştirilen yazılımlar, deney sonuçlarıyla oldukça uyumlu sonuçlar verebilmektedir. Bu çalışma kapsamında, Python programlama dili kullanılarak, betonarme elemanların moment eğrilik analizlerini gerçekleştiren bir yazılım geliştirilmiştir.

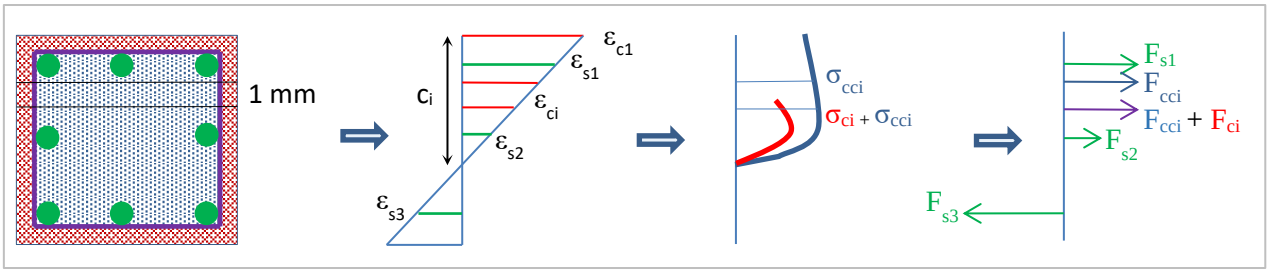

Şekil 2. Kesitin liflere ayrılması, şekil değiştirme dağılımının, gerilmelerin ve kuvvetlerin elde edilmesi

Daha sonra tarafsız eksen derinliği için varsayım yapılıp uygunluk denklemlerinden kesitteki şekil değiştirme dağılımı belirlenmektedir. Kesit, Şekil 3'deki gibi kabuk, çekirdek ve donatı olarak 3 kısma ayrılmaktadır [13].

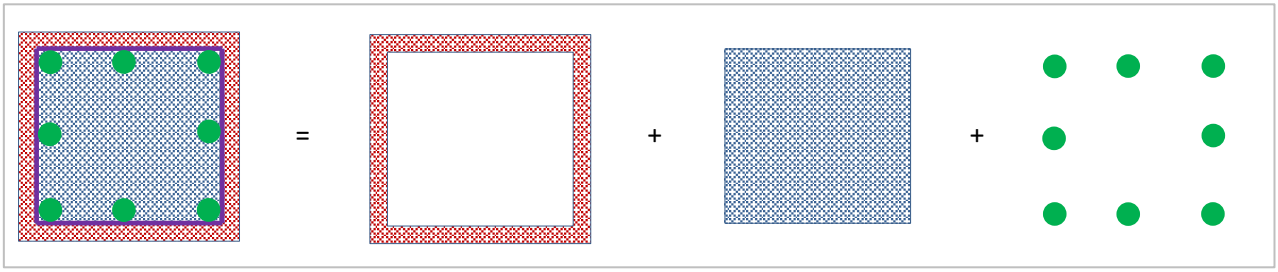

Şekil 3. Kesitin kabuk, çekirdek ve donatı olarak ayrılması

Şekil 2'deki birim şekil değiştirmelerden liflerdeki gerilmelere; gerilmelerden de iç kuvvete gidilmektedir. Dış ve iç kuvvet dengesi sağlanana kadar iteratif olarak tarafsız eksen derinliği değiştirilmektedir. Çekirdek betonun dışında kalan kısım için Hognestad modeli, çekirdek kısım için Mander veya Koksal modeli, donatı çeliği için ise Türkiye Bina Deprem Yönetmeliği 2018 de yer alan pekleşmenin dikkate alınabildiği model kullanılmaktadır. Bu üç ana kısımdan gelen etkiler süperpoze edilmektedir. Bağıl hata oranı olarak belirlenen 0.00001 değerinin altına düşüldüğünde ise o nokta için moment ve eğrilik değerleri hesaplanmaktadır.

2.4. Statik İtme Analizi Programı

Düzlem çerçeve olan her türlü taşıyıcı yapı sisteminin uç kuvvet ve deplasmanlarını hesaplamak amacıyla, matris deplasman yöntemi kullanılarak Python dilinde yapısal analiz programı geliştirilmiştir. Program, girilen nokta koordinatlarına göre taşıyıcı sistemi oluşturmakta ve eleman uzunluklarını, dönüşüm ve rijitlik matrislerini otomatik hesaplamaktadır. Daha sonra mesnet ve plastik mafsal şartları dikkate alınarak sistemdeki bilinmeyen deplasmanlar bulunmakta ve bu deplasmanlara göre uç kuvvetler elde edilmektedir. Program, plastik mafsalın oluşacağı elemanı, oluştuğu bölgeyi ve bu yatay yükü otomatik olarak bulmaktadır. Plastik mafsal oluşumundan sonra manuel olarak gerekli mesnet ve mafsal şartları tanımlanmaktadır. Her adımın sonunda deplasman ile kesme kuvvetleri kaydedilerek sistemin statik itme eğrisi çıkarılmaktadır.

3. Bulgular ve Tartışma

Bu bölümde Koksal-Erdogan [18] modeli kullanılarak elde edilen moment eğrilik analizlerinden faydalanılarak önce tekil kolonlar için iç kuvvet – deplasman ilişkisi tahmin edilmiştir. Daha sonra mevcut deney sonuçlarıyla kıyaslanmıştır. Aynı şekilde başka mevcut bir deneysel çalışmanın betonarme çerçeve için uygulandığı bir başka deneyin verileri kullanılmıştır.

3.1. Modelin Tekil Kolonlara Uygulanması

Bu çalışmada CH [21], Tip 1 ve Tip 2 [22] olmak üzere 3 adet betonarme kolonun deneysel verilerinden faydalanılmıştır. Öncelikle bu kolonların analitik moment eğrilik ilişkileri, geliştirilen program aracılığıyla elde edilmiştir. Daha sonra elde edilen verilere dayanarak, plastik mafsal teorisine göre kolonların deplasmanları ve oluşacak kuvvetler tahmin edilmiştir. Ayrıca Mander modeliyle kıyaslanmıştır.

Kolonlarda oluşacak elastik ve plastik dönmeler (3.1) ve (3.2) yardımıyla elde edilmiştir [23].

$$\theta_p = (\emptyset_u - \emptyset_y) l_p \tag{3.1}$$

$$\theta_e = 0.5(\emptyset_y) l \tag{3.2}$$

Burada Θ_p plastik dönme, Θ_e elastik dönme, l_p plastik mafsal boyu $\emptyset_u$ ve $\emptyset_y$ ise sırasıyla kesitin maksimum ve akma eğriliği, l ise kolon toplam boyudur. l_p kolon yüksekliğinin yarısı alınmıştır. Kolonlarda oluşacak toplam

deplasman ise yaklaşık olarak (3.3) kullanılarak elde edilebilir [23].

$$\Delta_t = \theta_e\left(\frac{2l}{3}\right) + \theta_p\left(l - \frac{l_p}{2}\right) \tag{3.3}$$

Bu çalışmada incelenen kolonlardan CH kolonunun net yüksekliği 1.5 m iken, Tip1 ve Tip2 kolonlarının yüksekliği 1.8 m dir [21,22]. Tablo 1 ve 2'de deney kolonları hakkında temel bilgiler; Şekil 4'te ise donatı yerleşimleri verilmiştir.

Tablo 1. Deney kolonlarının kesit ve geometrileri [21,22]

Kolon	b (cm)	h (cm)	Donatı Adeti / Çapı (mm)	Etriye Çapı (mm) / Aralığı (mm)
CH	50	50	12Ø25	Ø13/125
Tip 1	35	35	8Ø14	Ø8/165
Tip 2	35	35	8Ø14	Ø8/70

Tablo 2. Deney kolonları malzeme bilgileri [21,22]

Kolon	f_{ck} (MPa)	f_{sy} (MPa)	f_{su} (MPa)	f_{syh} (MPa)	E_s (MPa)	Eksenel Yük (kN)
CH	35	635	825	567	2E+05	1500
Tip 1	13	315	448	368	2E+05	318
Tip 2	25	454	604	469	2E+05	612

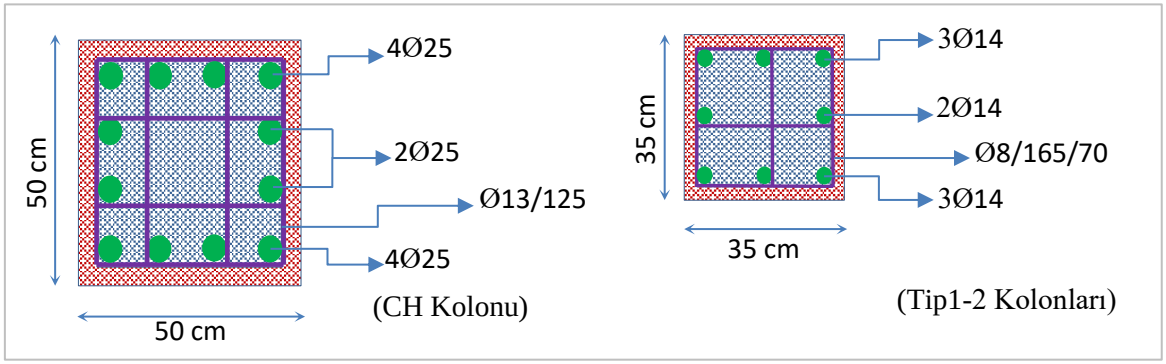

Şekil 4. CH ve Tip1-2 kolonu donatı şeması

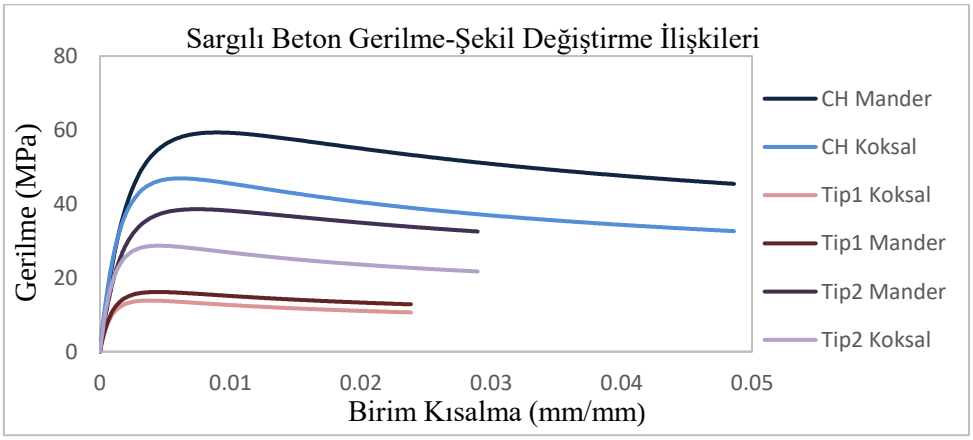

Şekil 5. Deney kolonlarının çekirdek beton için hesaplanan gerilme-şekil değiştirme ilişkileri

Şekil 5'te, Mander ve Köksal sargılı beton modellerine göre sargılı beton için hesaplanan gerilme-şekil değiştirme ilişkileri, kıyaslamalı olarak sunulmuştur. Görüldüğü üzere Köksal sargılı beton modeli, Mander sargılı beton modeline kıyasla, betonda daha düşük basınç gerilmelerinin oluşacağını öngörmektedir. Bunun

temel sebebi Köksal modelinin, sargı donatısının betonarme elemana uygulayacağı yanal kuşatma basıncını hesaplarken, Şekil 1'de gösterilen ON noktasını değil MN noktasını dikkate almasıdır. Böylelikle daha düşük yanal kuşatma basınç gerilmeleri elde edilmiş, dolayısıyla betonda oluşacak maksimum basınç gerilmelerinde bir miktar azalma olmuştur.

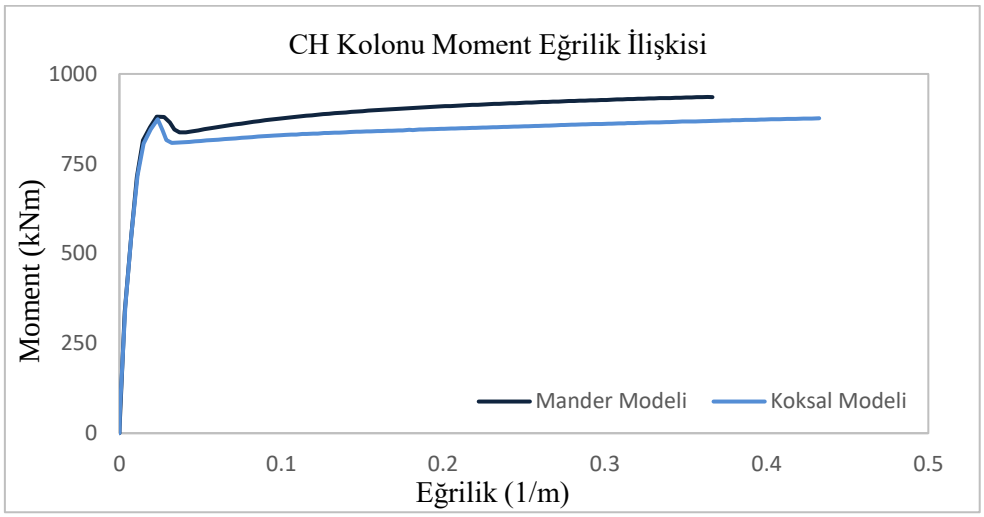

Şekil 6. CH kolonu moment-eğrilik grafiği

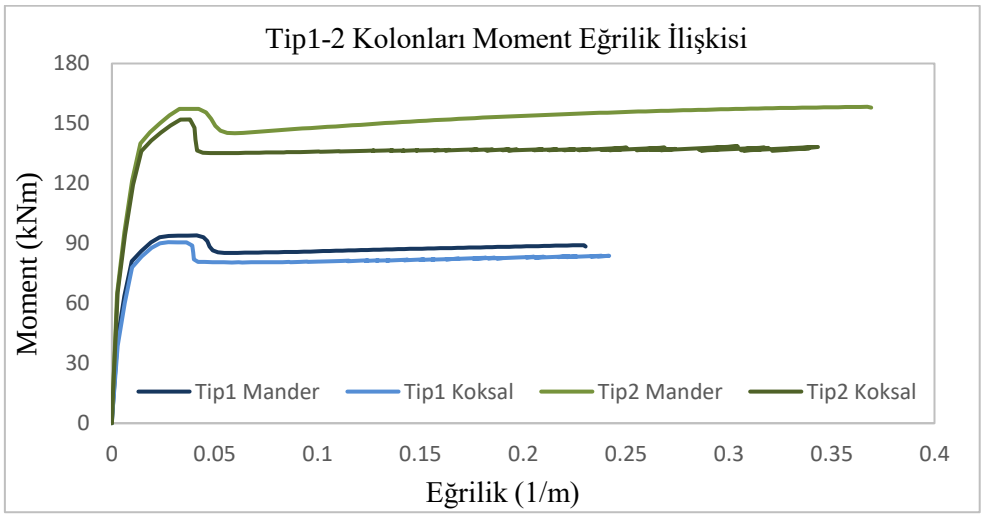

Şekil 7. Tip1-2 kolonu moment-eğrilik grafiği

Şekil 6 ve 7'de bu çalışma kapsamında geliştirilen yazılımdan elde edilen moment-eğrilik ilişkileri verilmiştir. Görüldüğü üzere Mander ve Köksal modellerinde, kesitin akma öncesi durumu için moment ve eğrilik açısından herhangi bir fark bulunmamaktadır. Ancak kesit akma kapasitesine ulaştıktan sonra Koksal modelinden elde edilen eğri, Mander modelinden elde edilen eğriye göre biraz daha aşağıda seyretmektedir. Bu farkın asıl nedeni kesitin akmasından sonra eğriliğin artmasına paralel olarak sargılı beton davranışının önem kazanmasıdır. Köksal modelinde sargılı beton kısmında daha düşük maksimum beton gerilmeleri elde edildiği için doğal olarak Mander modeline kıyasla daha düşük moment değerleri elde edilmektedir. Ayrıca kesitin ulaşabileceği maksimum eğrilik olan $Ø_u$ değerleri, her iki modelde de birbirine oldukça yakındır. Moment eğrilik ilişkilerinden elde edilen akma ($Ø_y$) ve maksimum eğrilikler ($Ø_u$) ile akma (M_y) ve maksimum momentler (M_u) Tablo 3'te verilmiştir.

Tablo 3. Akma ve göçme öncesi durumunda moment ve eğrilikler

Mander Modeli				
Kolon	M_y (kNm)	M_u (kNm)	$Ø_y$ (1/m)	$Ø_u$ (1/m)
CH	815.25	935.06	0.0146	0.367
Tip 1	81.11	88.48	0.0097	0.231
Tip 2	139.92	157.97	0.0138	0.369
Koksal Modeli				
Kolon	M_y (kNm)	M_u (kNm)	$Ø_y$ (1/m)	$Ø_u$ (1/m)
CH	806.63	876.63	0.0149	0.432
Tip 1	78.06	83.68	0.0098	0.238
Tip 2	136.16	138.17	0.0144	0.343

Tablo 4. Elastik, plastik ve toplam dönme ile yer değiştirmeler

Mander Modeli						
Kolon	$Θ_e$ (rad)	$Θ_p$(rad)	$Θ_t$ (rad)	$Δ_e$ (m)	$Δ_p$ (m)	$Δ_t$ (m)
CH	0.011	0.088	0.099	0.011	0.121	0.132
Tip 1	0.009	0.039	0.047	0.010	0.066	0.077
Tip 2	0.012	0.062	0.075	0.015	0.106	0.121
Koksal Modeli						
Kolon	$Θ_e$ (rad)	$Θ_p$(rad)	$Θ_t$ (rad)	$Δ_e$ (m)	$Δ_p$ (m)	$Δ_t$ (m)
CH	0.011	0.104	0.115	0.011	0.143	0.155
Tip 1	0.009	0.040	0.049	0.011	0.068	0.079
Tip 2	0.013	0.058	0.070	0.016	0.098	0.114

Tablo 4'te elastik ($Θ_e$) ve plastik ($Θ_p$) dönmeler ile deplasmanlar ($Δ_e$, $Δ_p$)verilmiştir. Bu değerler (3.1), (3.2) ve (3.3) kullanılarak hesaplanmıştır. $Θ_t$ ve $Δ_t$ ise toplam dönme ve deplasmanı temsil etmektedir.

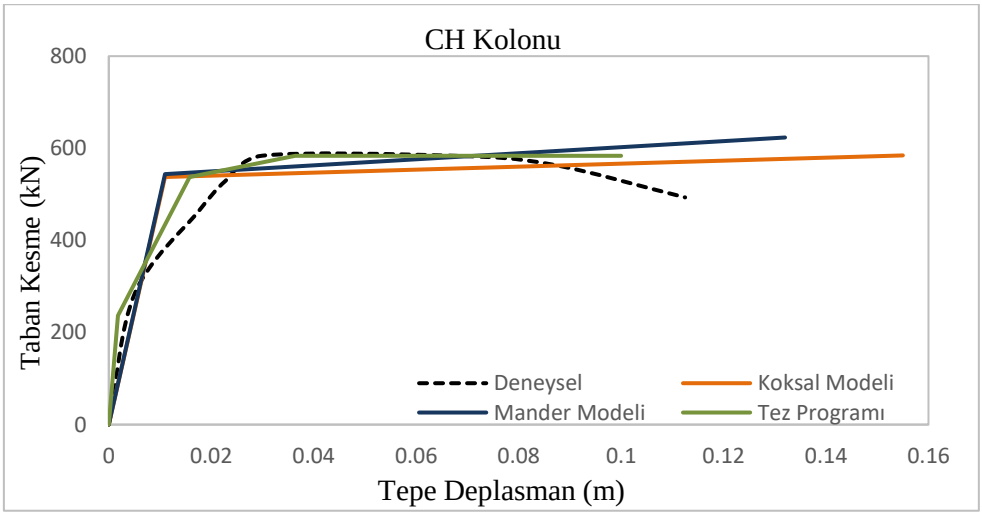

Şekil 8. CH kolonu analitik-deneysel iç kuvvet-deplasman ilişkisi

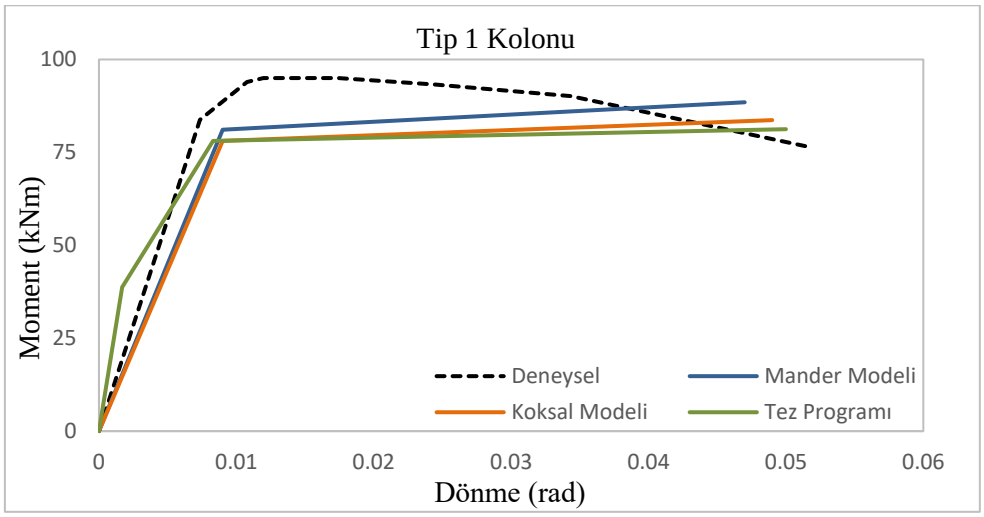

Şekil 9. Tip1 kolonu analitik-deneysel iç kuvvet-deplasman ilişkisi

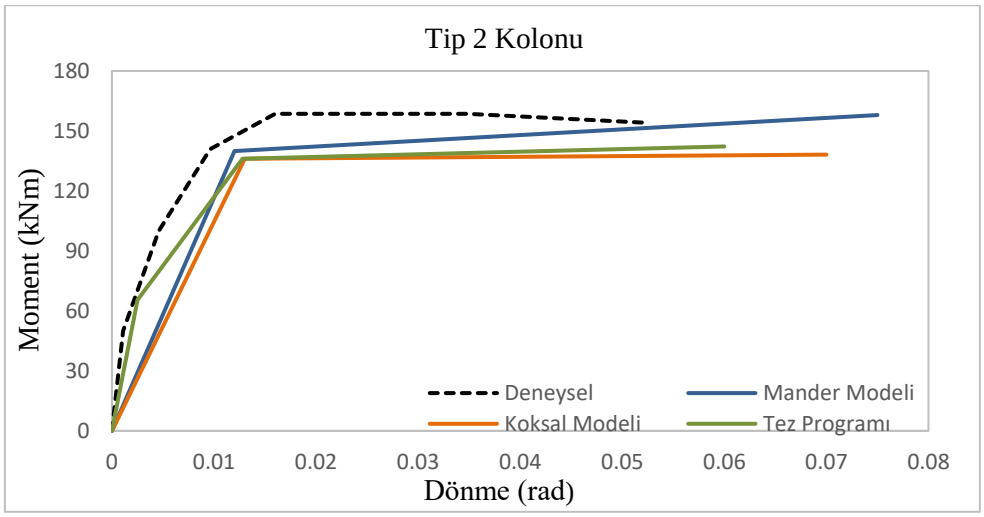

Şekil 10. Tip2 kolonu analitik-deneysel iç kuvvet-deplasman ilişkisi

Şekil 8, 9 ve 10'da gösterilen Mander ve Koksal modeli eğrileri, Tablo 4'deki değerleri temsil etmektedir. Tez programı eğrisi ise matris deplasman metodu kullanarak geliştirilen programdan elde edilen itme analizinin sonuçlarını göstermektedir. Bu programa, moment eğrilik ilişkisinden faydalanarak elde edilen eğilme rijitlikleri girilmiştir. Üç farklı bölge için eğilme rijitliği hesaplanmıştır. Bu bölgeler Şekil 11'de gösterilmiştir.

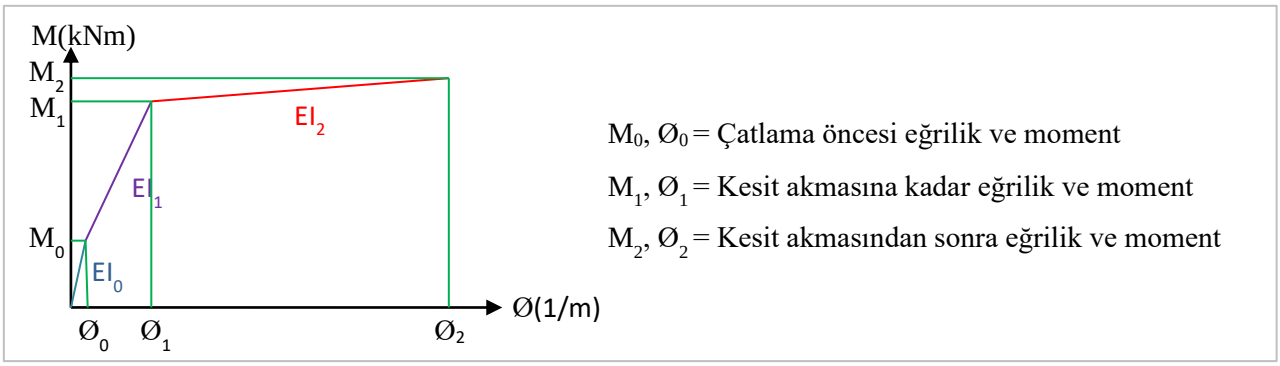

Şekil 11. Kolonların eğilme rijitliği hesaplanan bölgeleri

3.2. Modelin Düzlem Çerçeve Sisteme Uygulanması

Çalışmanın bu kısmında, Kim ve Yu tarafından test edilen betonarme bir çerçeve incelenmiştir [24]. Kim ve Yu yaptığı bu çalışmada, dolgu duvarların betonarme tek katlı tek açıklıklı bir taşıyıcı sistemin yatay yük taşıma performansına etkisini araştırmışlardır. Bu kapsamda, önerilen yeni sargılı beton modeli kullanılarak eleman kapasiteleri belirlenmiş ve analitik model kurularak yapı analiz edilmiştir. Elde edilen sonuçlar deney verileriyle kıyaslanmıştır. Deneyde kullanılan çerçevenin geometrisi Şekil 12'de verilmiştir. Bu deneyin sonuçları, Koksal-Erdogan [18] sargılı beton modeli kullanılarak yapılan statik itme analizi sonuçlarıyla kıyaslanmıştır. Elde edilen analitik sonuçların deney verileriyle uyumlu olduğu gösterilmiştir.

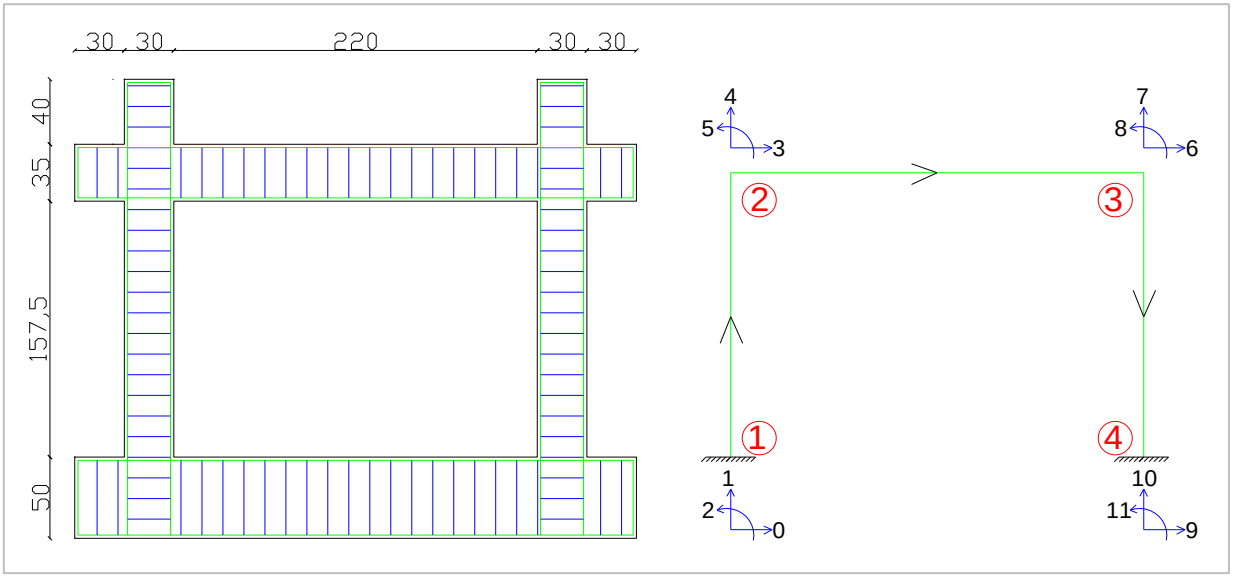

Şekil 12. Düzlem çerçevenin deneysel ve analitik modeli/serbestlik dereceleri

Şekil 12'de görüldüğü üzere deneye tabi tutulan düzlem betonarme çerçeve, tek katlı tek açıklıklı ve dolgu duvarsızdır. Kolonların boyutları 30x30 cm olup donatı düzenleri birbirinin aynısıdır. Kirişin boyutları ise 30x35 cm dir. Kolon net yüksekliği 1575 mm iken kiriş net açıklığı 2200 mm dir. Beton basınç dayanımı ise 36 MPa olup, boyuna donatının akma dayanımı 430 MPa 'dır.

Şekil 12'de analitik modelde görüleceği üzere başlangıçta 6 serbestlik derecesi vardır. Ancak her itme adımında plastik mafsal oluşacağı için serbestlik derecelerinde artış olmuştur. Akma dayanımına ulaşan kritik kesitlerin daha fazla yük alamayacağı kabulüyle eleman uçlarına mafsal konularak ilgili kesitlerin moment alması engellenmiştir.

Tablo 5'te elemanların kesit ve malzemelerin mekanik özellikleri, Şekil 13'te ise kolonların ve kirişin donatı planları verilmiştir.

Tablo 5. Eleman kesit ve malzeme mekanik özellikleri [24]

Eleman	b (cm)	h (cm)	Donatı Çapı (mm)		Etriye Çapı (mm) / Aralığı (mm)	
Kolon	30	30	8Ø16		Ø10/150	
Kiriş	30	35	8Ø16		Ø10/150	
Eleman	f_{ck} (MPa)	f_{sy} (MPa)	f_{su} (MPa)	f_{syh} (MPa)	E_s (MPa)	Eksenel Yük (kN)
Kolon	36	429	550	441	2E+05	0
Kiriş	36	429	550	441	2E+05	0

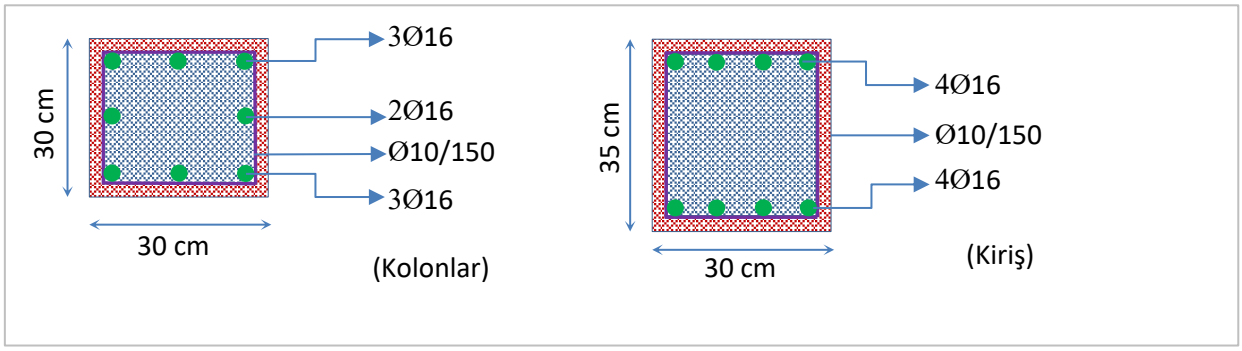

Şekil 13. Kolon ve kiriş donatı planı

Çerçeve elemanların sargılı beton için gerilme şekil değiştirme ilişkileri Şekil 14'te sunulmuştur. Bu eğrilerin çizilebilmesi için de ayrı bir Python programı geliştirilmiştir. Görüldüğü üzere Koksal-Erdogan [18] modeli, Mander modeline göre sargılı betonda daha düşük gerilmelerin oluşacağını öngörmektedir. Bu kısımda, Moment-eğrilik analiz programının test edilmesi açısından İnel vd. [14] tarafından geliştirilen programla karşılaştırmalar yapılmıştır.

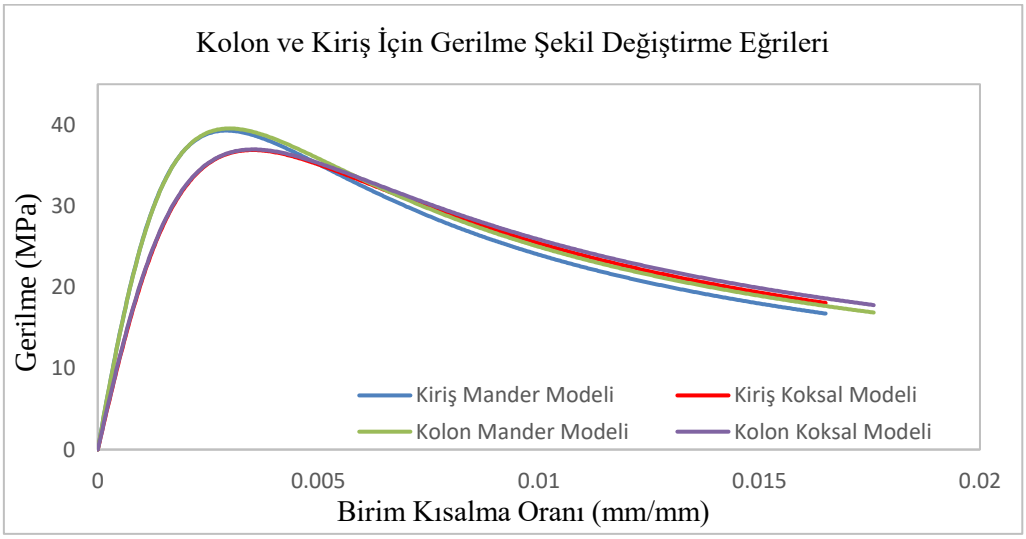

Şekil 14. Kolon ve kiriş için sargılı beton gerilme şekil değiştirme ilişkisi

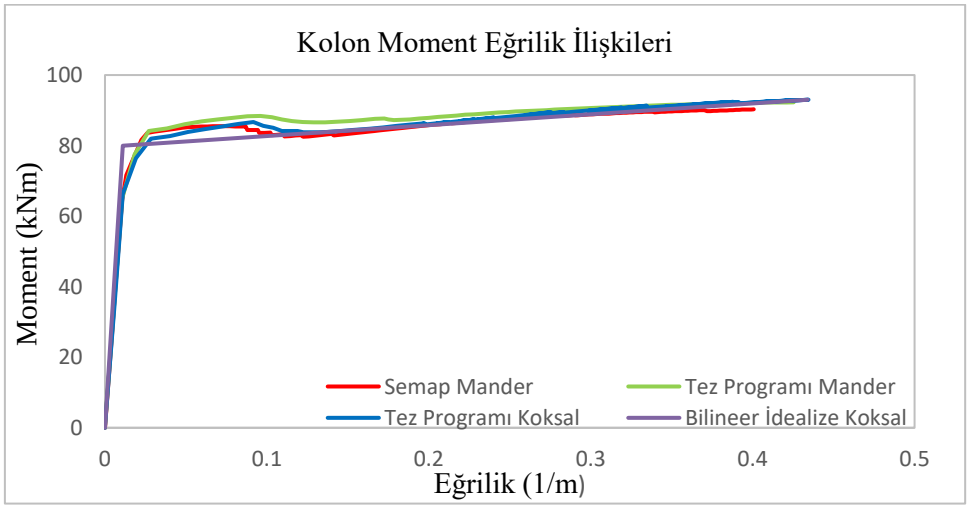

Şekil 15. Kolonların SEMAp ile kıyaslamalı moment eğrilik ilişkileri

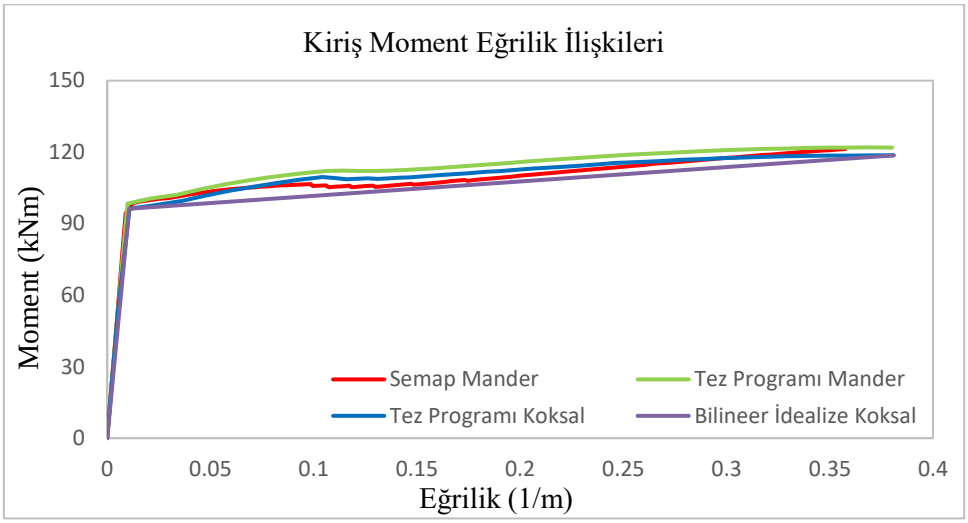

Şekil 16. Kiriş için SEMAp ile kıyaslamalı moment eğrilik ilişkileri

Sunulan betonarme çerçeve sistemde ilk yaklaşım olarak, Şekil 15 ve 16'da verilen ve bilineer olarak idealize edilen moment eğrilik ilişkisi grafiği verileri kullanılarak (3.4)'e göre etkin kesit rijitlikleri hesaplanmıştır [16]. Kesit akma dayanımına ulaştığında ise eleman uçlarına mafsal yerleştirilmiştir.

$$EI_e = \frac{M_y}{\theta_y}\frac{L_s}{3} \tag{3.4}$$

Burada M_y kesitin akma momentini, L_s kesme açıklığını, Θ_y ise etkin akma dönmesini temsil ederken, (3.5) ile elde edilmektedir [16]

$$\theta_y = \frac{\emptyset_y L_s}{3} + 0.0015\eta\left(1 + 1.5\frac{h}{L_s}\right) + \frac{\emptyset_y d_b f_{ye}}{8\sqrt{f_{ce}}} \tag{3.5}$$

(3.5)'te $\emptyset_y$ akma eğriliğini, h kesit yüksekliğini d_b ortalama donatı çapını f_{ye} ve f_{ce} beton ve donatının sırasıyla beklenen basınç ve akma dayanımlarını temsil etmekteyken, η kolon ve kirişler için 1 olarak dikkate alınmaktadır [16].

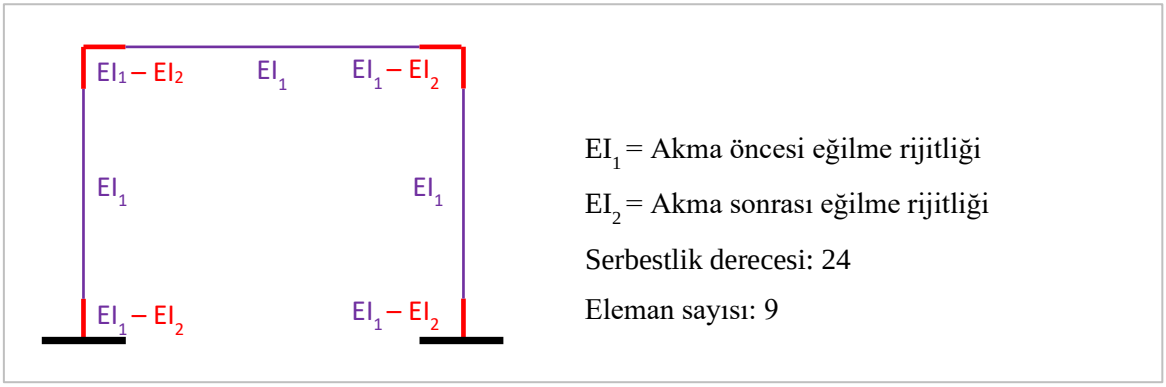

Şekil 17. Plasik mafsal uzunluğunca tanımlanan elemanlar

İkinci yaklaşım olarak ise Şekil 17'de gösterildiği gibi plastik mafsal uzunluğunda elemanlar yerleştirilmiş ve sistemdeki elemanların akma öncesi rijitlikleri (EI_1), bilineer moment eğrilik grafiklerinin birinci kısmının eğiminden hesaplanmıştır. Akma kapasitesine ulaşan elemanların rijitliği (EI_2) ise Şekil 15 ve 16'da gösterilen bilineer olarak idealize edilmiş eğrilerin ikinci kısmının eğimleri kullanılarak hesaplanmış ve bu rijitlikler programa girilerek itme analizi tekrarlanmıştır. Kullanılan kesit rijitlikleri, Tablo 6, 7 ve 8'de sunulmuştur.

Tablo 6. Akma öncesi ve sonrası idealize grafikten hesaplanan etkin kesit rijitliği katsayıları

Eleman	E (kN/m^2)	I (m^2)	EI (kNm^2)	EI$_1$ (kNm^2)	EI$_2$ (kNm^2)	EI$_1$/EI	EI$_2$/EI
Kolon	3.00E+07	0.000675	20250	7273.73	30.71	0.359	0.0015
Kiriş	3.00E+07	0.001072	32156	9000.94	60.31	0.280	0.0019

Tablo 7. Bilineer idealize moment eğrilik grafiğinde akma ve maksimum momentler ile eğrilikler

Eleman	M$_y$(kNm)	M$_u$(kNm)	Ø$_y$ (1/m)	Ø$_u$ (1/m)
Kolon	80	92.99	0.011	0.434
Kiriş	96.31	118.64	0.0108	0.381

Tablo 8. TBDY 2018'e göre kolon-kiriş için mafsal bilgileri ve hesaplanan etkin kesit rijitlikleri

Mafsal	Ø$_y$ (1/m)	L$_s$ (m)	h (m)	d$_b$ (m)	f$_{sy}$ (Mpa)	f$_{ck}$ (Mpa)	Θ$_y$ (rad)	EI$_e$ (kNm^2)
Kolon	0.011	0.7875	0.3	0.016	430	36	0.0083	3559.94
Kiriş	0.0108	1.1	0.35	0.016	430	36	0.0088	5023.19

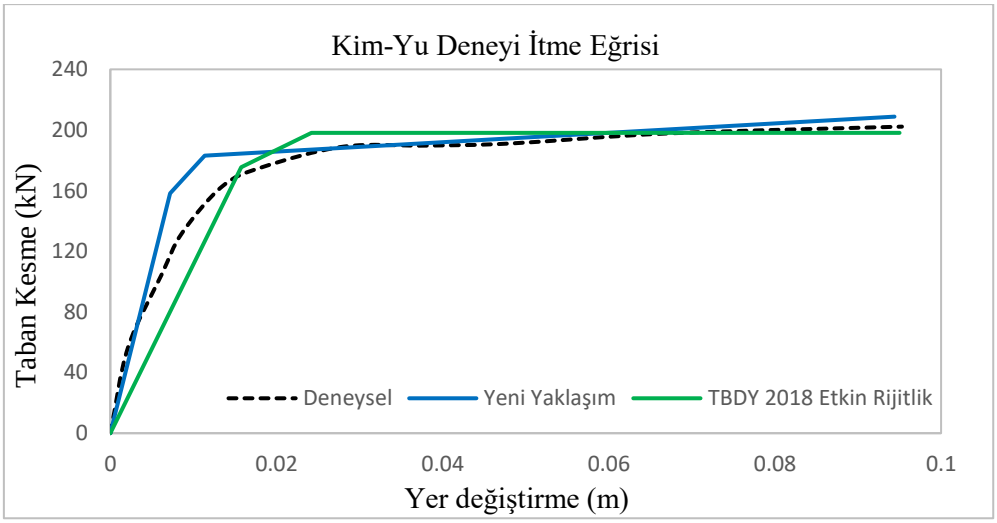

Şekil 18. Deneysel ve analitik itme eğrileri

Şekil 18'de görüldüğü üzere TBDY 2018'deki etkin kesit rijitlikleri ile analiz yapıldığında deneysel sonuçlara göre akma durumuna kadar olan davranışta, yanal ötelemelerin daha büyük olduğu görülmektedir. Bunun başlıca nedeni etkin kesit rijitiliğinin elemanın akma noktasına göre hesaplanması ve beton çatladıktan sonra bir eğilme rijitliği kullanılmasıdır. Bu çalışmada, Şekil 11'de açıklandığı gibi iki veya üç parçalı model kullanıldığında deneysel sonuçlara daha yakın değerler elde edildiği görülmüştür. Ancak moment eğrilik ilişkilerinden adım adım elde edilecek çok sayıda kesit rijitliklerinin kullanılması, gerçek davranışı belirlemede daha gerçekçi sonuçlar elde edilmesini sağlayacaktır.

4. Sonuçlar

Bu çalışmada, ülkemizde oldukça yaygın olarak bilinen ve TBDY 2018'de yer alan Mander modeli ile Köksal modeli arasında kıyaslamalar yapılmıştır. Sonuçların oldukça uyumlu olduğu ancak Köksal modelinin Mander modeline göre biraz daha düşük gerilme değerleri verdiği gözlenmiştir. Geliştirilen analitik moment eğrilik programının geçerliliğini göstermek amacıyla İnel vd. tarafından geliştirilen SEMAp programıyla kıyaslamalar yapılmış ve geliştirilen programla uyumlu sonuçlar elde edilmiştir.

Tekil kolonların analizleri için Acun ve Sucuoğlu [22] ile Eom vd. [21]'nin yaptığı çalışmalardan elde ettikleri deneysel veriler kullanılmış ve bu çalışmada seçilen analitik modellerle kıyaslamalar yapılmıştır. Koksal ve

Mander modellerinin kolonlar için uygulandığı 3 farklı analitik modelden edilen iç kuvvet şekil değiştirme tahminleri, deney sonuçlarıyla kıyaslandığında oldukça iyi sonuçların elde edildiği gözlenmiştir. Daha sonra Kim ve Yu [24]'nun çalışmasındaki tek katlı tek açıklı boş çerçeve yükleme deneyi için deneysel ve analitik sonuçlar kıyaslanmıştır. Bu çalışmada, TBDY 2018'de daha düşük eğilme riijitliği kullanılarak, akma noktasına kadar olan moment eğrilik değerleri için hem deneysel hem de bilineer modele göre daha büyük yanal deplasmanlar verdiği belirlenmiştir. Her üç durumda da en büyük yanal kuvvet açısından birbirine yakın değerler gözlenmiştir.

Taşıma gücü açısından en büyük yanal yükün gerek yönetmelik gerek bu çalışmadaki yaklaşımla çok yakın değerleri vermesi modellerin ve tasarımın güvenilirliği anlamına gelmez. Statik itme analizlerindeki bina performanslarının şekil değiştirme tabanlı olduğu unutulmamalıdır. Bu açıdan bakıldığında aynı yük değerine daha düşük bir rijitlikle ulaşılması betonarme bina kesit tasarımı açısından önemli farklar doğuracaktır. Bu noktanın irdelenmesi ve eğilme rijitliği değerlerinin modellemede yüke göre değişiminin dikkate alınması ileriki bir çalışmanın konusu olacaktır.

Yazar Katkıları

Birinci Yazar Python tabanlı programların geliştirilmesini ve analizlerin gerçekleştirilmesini, literatür araştırması yapılmasını, sonuçların raporlanmasını ve makalenin yazılmasını sağlamıştır. İkinci Yazar yeni sargılı beton modelinin kullanılmasını, analizlerin planlanmasını ve kontrolü gerçekleştirmiştir. Tüm yazarlar çalışmasın son hâlini okuyup onaylamıştır.

Çıkar Çatışması

Yazarlar hiçbir çıkar çatışması olmadığını beyan etmektedir.

Kaynaklar

[1] L. Cedolin, S. Dei Poli, Y. R. J. Crutzen, *Triaxial stress-strain relationship for concrete*, Journal of the Engineering Mechanics Division 103 (3) (1977) 423–439.

[2] E. Hognestad, A study of combined bending and axial load in reinforced concrete members, University of Illinois Bulletin, Urbana, 1951.

[3] H. Kupfer, H. Hisdorf, H. Rusch, *Behavior of concrete under biaxial stresses*, ACI Journal Proceedings 66 (8) (1969) 656–666.

[4] N. Ngo, A. Scordelis, *Finite element analysis of reinforced concrete beams*, ACI Journal Proceedings 64 (3) (1967) 152–163.

[5] P. Gambarova, C. Karakoc, *A new approach to the analysis of the confinement role in regularly cracked concrete elements*, 7th SMiRT Conference, Chicago, 1983, pp. 251–261.

[6] A. Hillerborg, M. Modéer, P. -E. Petersson, *Analysis of crack formation and crack growth in concrete by means of fracture mechanics and finite elements*, Cement and Concrete Research 6 (6) (1976) 773–781.

[7] B. Doran, H. O. Koksal, T. Turgay, *Nonlinear finite element modeling of rectangular/square concrete columns confined with FRP*, Materials & Design 30 (8) (2009) 3066–3075.

[8] J. Olivier, C. Miguel, S. Oller, *Isotropic damage models and smeared crack analysis of concrete*, in: N. Bićanić, H. Mang (Eds.), Austria: II International Conference on Computer Aided Analysis and Design of Concrete Structures, Zell Am See, 1990, 945–957.

[9] K. Willam, E. Warnke, *Constitutive model for the triaxial behaviour of concrete*, Structural Engineering Report 19 (1975) 1–30.

[10] J. B. Mander, M. J. N. Priestley, R. Park, *Observed stress-strain behavior of confined concrete*, Journal of Structural Engineering 114 (8) (1988) 1827–1849.

[11] S. A. Sheikh, S. M. Uzumeri, *Analytical model for concrete confinement in tied columns*, Journal of the Structural Division 108 (12) (1982) 2703–2722.

[12] M. Saatcioglu, S. R. Razvi, *Strength and ductility of confined concrete*, Journal of Structural Engineering 118 (6) (1992) 1590–1607.

[13] U. Ersoy, G. Özcebe, *Sarılmış Betonarme Kesitlerde Moment-Eğrilik İlişkisi Analitik Bir İrdeleme*, Teknik Dergi 9 (44) (1998) 1799–1827.

[14] M. İnel, H. Özmen, H. Bilgin, *Betonarme elemanların doğrusal ötesi davranışlarının bilgisayar ortamında modellenmesi*, Altıncı Ulusal Deprem Mühendisliği Konferansı, İstanbul, 2007, 207–216.

[15] H. O. Köksal, B. Doran, *Beton ve betonarme elemanlarda doğrusal olmayan oktahedral elastik ve plastik bağıntılar kullanılarak yapılan sonlu eleman uygulamaları*, *Teknik Dergi* 8 (38) (1997) 1445–1455.

[16] Afet ve Acil Durum Daire Başkanlığı, Türkiye Bina Deprem Yönetmeliği (2018), https://www.afad.gov.tr/kurumlar/afad.gov.tr/2309/files/TBDY_2018.pdf.

[17] A. Habibi, H. Moharrami, *Nonlinear sensitivity analysis of reinforced concrete frames*, Finite Elements in Analysis and Design 46 (7) (2010) 571–584.

[18] H. O. Koksal, A. Erdogan, *Stress–strain model for high-strength concrete tied columns under concentric compression*, Structures 32 (2021) 216–227.

[19] H. O. Koksal, *A failure criterion for RC members under triaxial compression*, Structural Engineering and Mechanics, 24 (2) (2006).137–154.

[20] P. Desayi, S. Krishnan, E*quation for the stress-strain curve of concrete*, ACI Journal Proceedings 61 (3) (1964) 345–350.

[21] T. -S. Eom, S. -M. Kang, H. -G. Park, T. -W. Choi, J.-M. Jin, *Cyclic loading test for reinforced concrete columns with continuous rectangular and polygonal hoops*, Engineering Structures 67 (2014) 39–49.

[22] B. Acun, H. Sucuoğlu, *Betonarme kolonların şekil değiştirme performans sınırlarının deneysel gözlemlerle değerlendirilmesi*, Teknik Dergi 22 (108) (2011) 5523–5541.

[23] Z. Celep, Deprem mühendisliğine giriş ve depreme dayanıklı yapı tasarımı, Beta Basım Yayım A.Ş., İstanbul, 2021.

[24] M. Kim, E. Yu, *Experimental study on lateral-load-resisting capacity of masonry-ınfilled reinforced concrete frames*, Applied Sciences 11 (21) (2021) 9950 17 pages.

Çanakkale Onsekiz Mart University

Journal of Advanced Research in Natural and Applied Sciences

dergipark.org.tr/tr/pub/jarnas

Open Access

e-ISSN: 2757-5195 2024, Vol. 10, Issue 2, Pages: 367-379 doi.org/10.28979/jarnas.1384800

Faz Değiştiren Malzeme Olarak Ötektik Su-Tuz Çözeltileri ile Soğutma Sistem Performansının Deneysel İncelenmesi

Berçem Kıran-Yıldırım[1], Gökçe Güner Karaali[2], Özgenur Yayla[3], Elif Yıldız[4], Ebru Mançuhan[5], Sibel Titiz-Sargut[6]

[1,2,3,4,5,6]Marmara Üniversitesi, Mühendislik Fakültesi, Kimya Mühendisliği Bölümü, İstanbul, Türkiye

Makale Tarihçesi

Gönderim: 04 Kasım 2023

Kabul: 08 Şubat 2024

Yayım: 25 Haziran 2024

Araştırma Makalesi

Öz − Ev-tipi buzdolapları yaygın kullanılan beyaz eşyalar arasında yer alması ve sürekli çalışmaları sebebiyle yüksek miktarda enerji tüketiminden sorumludurlar. Ev-tipi buzdolabının performansını incelemek için laboratuvar ölçekli bir soğutma sistemi ortalama 4°C sıcaklıkta faz değiştiren malzemesiz (FDM'siz) ve çeşitli FDM'lerle test edilmiştir. FDM olarak ötektik su-tuz çözeltilerinden dipotasyum hidrojenfosfat (K_2HPO_4) ve sodyum tiyosülfat ($Na_2S_2O_3$) çözeltileri farklı konsantrasyonlarda sisteme entegre edilmiştir. FDM'siz durumda %18,8 tespit edilen çalışma süresinin FDM olarak, uygun konsantrasyonlarda hazırlanan ötektik su-tuz çözeltileri ile azaldığı ortaya konulmuştur. FDM olarak ağırlıkça (ağ.) %2,0 K_2HPO_4 çözeltisi ile çalışma süresi (%) minimize edilmiştir. Çalışma süresi ağ. %2,0 K_2HPO_4 çözeltisi ile %11,1 olarak tespit edilmiştir. FDM'siz durumda sistemin 4 saatlik çalışma süresinde belirlenen toplam enerji tüketimi ağ. %2,0 K_2HPO_4 çözeltisi ile yaklaşık %46 oranında azaltılmıştır. Elektrik kesintisinin simüle edildiği durumda ise FDM'ler sisteme entegre edildiğinde kabin iç hava sıcaklığının ortam sıcaklığına (16°C) yükselme süresinin uzadığı ve maksimim olduğu durumda bu süresinin FDM'siz duruma göre yaklaşık 5 kat uzadığı belirlenmiştir. Tüm değerlendirmeler uygun FDM'nin ev-tipi buzdolaplarına entegrasyonun enerji tüketiminin azaltılmasında önemli rol oynacağı ortaya konulmuştur. Elektrik kesintisi periyodunda, kabin içindeki ürünlerin uzun süre bozunmadan muhafaza edilmesi FDM'lerin sistemlere entegrasyonunda sağlanacak diğer bir avantaj olacaktır.

Anahtar Kelimeler − *Ev-tipi buzdolabı, faz değiştiren malzemeler, soğutma sistem performansı, ötektik su-tuz çözeltileri*

Experimental Examination of Cooling System Performance with Eutectic Water-Salt Solutions as Phase Change Materials

[1,2,3,4,5,6]Department of Chemical Engineering, Faculty of Engineering, Marmara University, İstanbul, Türkiye

Article History

Received: 04 Nov 2023

Accepted: 08 Feb 2024

Published: 25 Jun 2024

Research Article

Abstract − Household refrigerators are responsible for a huge amount of energy consumption due to their widespread use as household appliances and continuous operation. A laboratory-scale cooling system was operated at an average temperature of 4°C to investigate the performance of a household refrigerator without phase change material (PCM) and with various PCMs. Dipotassium hydrogen phosphate (K_2HPO_4) and sodium thiosulfate ($Na_2S_2O_3$) solutions were integrated into the system at different concentrations as eutectic water-salt solution PCMs. It was revealed that the running time, determined to be 18.8% without PCM, decreased with the eutectic water-salt solutions prepared at suitable concentrations as PCMs. The running time (%) was minimized with 2.0 wt.% K_2HPO_4 solution. The running time was determined to be 11.1% with 2.0 wt.% K_2HPO_4 solution. The energy consumption was reduced by approximately 46% with 2.0 wt.% K_2HPO_4 solution than that of the case without PCM for a 4-hour operating period of the system. In the case of simulating a power failure, it was also determined that the time for reaching the cabin air temperature to ambient temperature (16°C) was prolonged with

[1]bercem.kiran@marmara.edu.tr (Corresponding Author); [2]gokcekaraali@gmail.com; [3]ozgenuryayla@marun.edu.tr; [4]elifyildiz21@marun.edu.tr; [5]emancuhan@marmara.edu.tr; [6]sibel.sargut@marmara.edu.tr

PCMs, and it was maximized to a value of approximately 5 times longer than that of the case without PCM. All evaluations indicate that the integration of suitable PCM into household refrigeration is of great importance in terms of reducing energy consumption. The integration of PCMs into systems will provide another advantage by ensuring the long-term preservation of products inside the cabinet during a power failure period.

Keywords − *Cooling system performance, eutectic water-salt solutions, household refrigerator, phase change materials*

1. Giriş

Ev-tipi buzdolaplarının günümüzde neredeyse her evde kullanılmaları ve sürekli çalışmaları göz önünde bulundurulduğunda önemli miktarda küresel enerjinin tüketiminden sorumlu oldukları bilinmektedir. Dünya çapında yaklaşık 1 milyar ev-tipi buzdolabı olduğu bilinmektedir [1]. Amerika Birleşik Devletleri (ABD)'de konut elektriğinin yaklaşık %14,0'ünün evlerde kullanılan buzdolaplarının tüketimine bağlı olduğu belirtilmiştir [2]. Malezya'da ise konut elektrik tüketiminin yaklaşık %26,0'sından buzdolapları-dondurucuların sorumluğu olduğu ortaya konulmuştur [3]. Bu sistemlerin her geçen gün kullanımının daha da yaygınlaşması göz önünde bulundurulduğunda enerji tüketimlerinin azaltılması hem enerji kaynaklarının korunması hem de enerji maliyetinin azaltılması açısından büyük önem taşımaktadır. Buzdolaplarının enerji tüketiminin bileşenlerinin verimliliğinden, ortam sıcaklığından, ürün yüklemesinden, kapı açılma sayısından, termostat ayar konumundan ve kompresör kapalı çevrimi sırasında soğutucu akışkan geçişinden etkilendiği belirtilmiştir [4]. Bu parametrelerin sistem enerji verimliliğine etkisini inceleyen farklı çalışmalar literatürde sunulmuştur. Liu vd. [5] yaptığı çalışmada, 10 saatlik çalışma periyodunda dondurucuyu her 40 dakikada bir defa, buzdolabı ünite kapağını ise her 12 dakikada bir defa 90° açıyla en az 5 saniye süre tutmak üzere açmışlardır. Bu durumun sistemde kapı açılmasının olmadığı duruma göre enerji tüketimini %10 arttırdığını ortaya koymuşlardır [5]. Buzdolabı bileşenleri dikkate alındığında ise, Bansal [6] laboratuvar ön testlerine göre değişken hızlı kompresörlerin kullanımının %40'a kadar enerji tasarrufu sağlama potansiyeline sahip olduğunu belirtmiştir. Ancak bu kompresörlerin geleneksel tek hızlı kompresörlere göre pahalı olduğu bilinmektedir.

Faz değiştiren malzemeler (FDM'ler) faz değişimleri esnasında büyük miktarda ısıyı depolayabilen ve serbest bırakabilen malzemelerdir [7]. Bu malzemelerin soğutma sistemlerine entegre edilmesi de alternatif enerji tasarrufu sağlama yollarından biridir. Literatürde FDM'lerin soğutma sistemlere entegrasyonun sağladığı avantajların incelenmesi ile ilgili çeşitli çalışmalar mevcuttur [8-10]. Bu çalışmalarda da görüleceği üzere FDM'lerin sistemlere entegre edilmesinde FDM'nin faz değişim sıcaklığı, kalınlığı, konumu ve miktarı gibi çeşitli parametreler göz önünde bulundurulmalıdır [7]. Pirvaram vd. [10] yaptığı çalışmada iki farklı faz değişim sıcaklığına sahip ötektik FDM'nin faz değişim sıcaklıklarının ve FDM miktarının ev-tipi dondurucunun enerji tüketimi ve sıcaklık dalgalanmalarına etkilerini incelemişlerdir. Toplam 6 rafa sahip ev-tipi buzdolabının üst 3 rafına yüksek faz değişim sıcaklığına sahip FDM yerleştirilirken, alt 3 rafına ise düşük faz değişim sıcaklığına sahip FDM yerleştirilmiştir. FDM'lerin birinin faz değişim sıcaklığı -18°C'de sabit tutulurken diğerinin faz değişim sıcaklığı -10°C'den -20°C'ye düşürülmesinin hem enerji tüketimini hem de sıcaklık dalgalanmasını azalttığı belirlenmiştir. Bu azalmanın hızının da FDM miktarından etkilendiği, belirli bir FDM miktarına kadar artışın olumlu etkilediği belirlenirken daha fazla artışın enerji tüketimini arttırdığı tespit edilmiştir. Sonuç olarak, enerji tüketiminin sisteme entegre edilen FDM'lerin faz değişim sıcaklığına ve miktarına oldukça bağlı olduğu tespit edilmiştir. Optimal değerlerin tespiti için, FDM-1 ve FDM-2 miktarı ve FDM-2'nin faz değişim sıcaklığı parametrelerini dikkate alarak yürüttüğü çalışmanın sonuçlarını merkezi kompozit tasarımına dayanan Yüzey Yanıt Metodu ile değerlendirilmiştir. Faz değişim sıcaklığı -18°C olan FDM'nin miktarının 1,97 kg iken diğer FDM'nin miktarı 1,57 kg iken -20°C faz değişim sıcaklığına sahip olduğu durumda enerji tüketim hızında azalmanın maksimize edildiği tespit edilmiştir [10].

Soğutma sistemlerinin çalışma koşullarına uygun FDM seçiminde belirtildiği gibi uygun faz değişim

sıcaklığına sahip olması en önemi parametrelerden biridir. FDM'ler organik ve inorganik olarak iki sınıfa ayrılabildiği gibi bu sınıflarda alt dal olarak bileşikler ve ötektikler olarak sınıflandırılabilmektedirler [11]. Ötektik FDM'ler iki veya daha fazla bileşenden oluştuğu için (organik-organik, inorganik-organik, inorganik-inorganik) [12] faz değişim sıcaklıkları bileşenlerin ağrılıkça konsantrasyonlarının değiştirilmesiyle ayarlanabilme avantajına sahiptirler. Su, FDM olarak yüksek gizli ısıya sahip olması, termofiziksel özelliklerinin bilinmesi ve kararlılığı göz önünde bulundurulduğunda dikkate değer bir malzemedir [13]. Ancak çalışma koşulları göz önünde bulundurulduğunda faz değişim sıcaklığı sebebiyle her sistem için suyun uygun olmadığı bilinmektedir. Bu sebeple suyun faz değişim sıcaklığının ayarlanabilmesi amacıyla su-tuz ötektik karışımları hazırlanmaktadır. Ötektik su-tuz çözeltilerinde tuz konsantrasyonun ayarlanmasıyla çalışma koşullarına uygun faz değişim sıcaklığına sahip FDM hazırlanabilmektedir. Kiran-Yildirim [9], yaptığı çalışmada ev-tipi buzdolabını simüle eden laboratuvar ölçekli bir soğutma sistemini FDM'siz ve FDM olarak su ve N_2SO_4 çözeltileri ile test etmiştir. FDM'siz duruma göre FDM olarak suyun entegre edildiği durumda enerji tasarrufunu maksimize eden uygun FDM miktarı 600 mL olarak belirlenmiştir. Ardından belirlenen miktarda farklı konsantrasyonlarda N_2SO_4 çözeltileri (ağ.%1,0-4,0) sisteme entegre edilmiştir. Enerji tasarrufunun sisteme ağ.%1,0 N_2SO4 çözeltisi entegre edildiğinde maksimize edildiği belirlenmiştir [9].

Bu çalışmamızda soğutma sistemlerinin enerji tüketimlerini incelemek için ev-tipi buzdolabının simüle edildiği laboratuvar ölçekli bir soğutma sistemi FDM'siz ve çeşitli FDM'lerle test edilmiştir. FDM olarak dipotasyum hidrojenfosfat (K_2HPO_4) ve sodyum tiyosülfat ($Na_2S_2O_3$) ötektik su-tuz çözeltileri farklı konsantrasyonları sisteme entegre edilmiştir. Ağırlıkça %36,8 K_2HPO_4 ve ağ.%30,0 $Na_2S_2O_3$ [14] ile hazırlanan ötektik su-tuz çözeltilerinin faz değişim sıcaklıkları ve gizli ısı değerleri sırasıyla -13,5℃ (198 kJ/kg) ve -11,0℃ (200 kJ/kg) olarak literatürde belirtilmiştir. Çalışmamızda kullanılan çözeltiler FDM olarak seçilirken faz değişim sıcaklıkları göz önünde bulundurulmuştur. FDM olarak ötektik su-tuz çözeltilerinin çalışma koşullarına uygun faz değişim sıcaklıklarının yanı sıra gizli ısı değeri, kinetik özellikleri vb. gibi özelliklerinin bileşik etkisi uygun FDM seçiminde dikkate alınması gerekmektedir. Malzemenin kinetik özellikleri olarak, sıvı fazda aşırı soğumanın önlenmesi için çekirdeklenme hızının ve ısının hızlı geri kazanımı için kristal büyüme hızının yüksek olması önemlidir [15-17].

Soğutma sistemi performansına FDM olarak ötektik su-tuz çözeltilerinin (ağ. %2-10 K_2HPO_4 ve $Na_2S_2O_3$ çözeltileri) etkilerini belirlemek için deneysel bir çalışma yapılmıştır. Deneysel çalışmanın amacı sistem performansını maksimize eden FDM'nin belirlenmesidir. Ayrıca, elektrik kesintisi esnasında sistem kabin iç hava sıcaklığının ortam sıcaklığına ulaşma süresini maksimize eden en uygun çözeltinin önerilmesidir. Böylece soğutma sistem performansı FDM'siz ve FDM'lerle çalışma ve elektrik kesintisi periyodu için ortaya konulacaktır.

2. Materyal ve Yöntem

Soğutma sistemlerinin enerji tüketimlerini incelemek için Şekil 1'de şematik gösterimi sunulan laboratuvar ölçekli bir soğutma sistemi [18] ev-tipi buzdolabını simüle edecek şekilde ortalama 4°C sıcaklık için FDM'siz ve FDM olarak çeşitli ötektik su-tuz çözeltilerinin sisteme entegre edildiği durumlar test edilmiştir.

Soğutma sistemi bir kabin (72 L) ve kabin iç sıcaklığının set edilen değerde çalışmasını sağlamak amacıyla temel bileşenler olarak bir evaporatör, bir kompresör, bir kondenser ve bir genleşme valfinden oluşmaktadır. Kabin iç hava sıcaklığı başta olmak üzere, tüm soğutma sistemi elemanlarının giriş ve çıkış noktalarında sıcaklık değerleri ölçülüp kaydedilmiştir. Güç tüketimi network analizörüyle ±1 doğrulukta ölçülmüştür.

Sistemde sirküle eden soğutucu akışkanın (R404A) kütlesel debisi ortalama 5,5 gram/saniye olarak ölçülmüştür. Test sisteminin kurulu olduğu ortam sıcaklığı klima kullanılarak 18°C'de sabit tutulmuştur.

FDM olarak, farklı konsantrasyonlarda (ağ.%2,0-ağ.%10,0) K_2HPO_4 ve $Na_2S_2O_3$ çözeltileri kullanılmıştır. Daha önce yapılan, FDM olarak distile suyun soğutma sistemine entegre edildiği bir çalışmada en uygun hacim 600 mL olarak belirlenmiştir. Dolayısıyla ötektik su-tuz çözeltileri hacimce 600 mL olarak hazırlanmıştır [9]. Alüminyum paketlere aktarılan çözeltiler -18°C'de çalışan bir dondurucuda yatay olarak dondurulmuştur. Hazırlanan donmuş çözelti paketleri soğutulan kabin içinde konumlandırılan evaporator yüzeyine entegre edilmiştir.

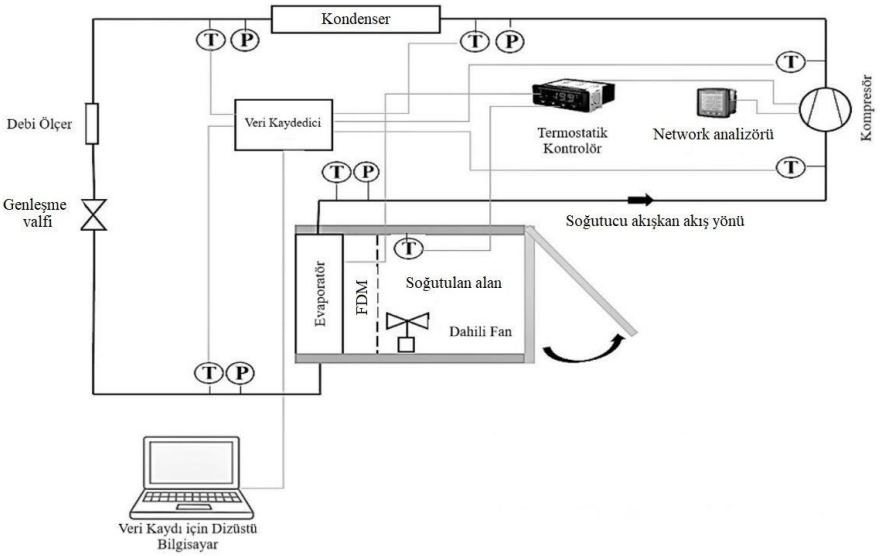

Şekil 1. Deney düzeneği

Sistemin kararlı rejime erişmesinden sonra veri kaydı alınmaya başlanmıştır. Çalışma periyodu esnasında tespit edilen bir döngüdeki kompresörün açık kalma süresi ($t_{açık}$, dakika) ve kapalı kalma süresi ($t_{kapalı}$, dakika) kullanılarak kompresör çalışma süresi yüzdesel olarak (2.1)'de sunulan denklem kullanılarak hesaplanmıştır.

$$\text{Çalışma Süresi } \% = \frac{t_{açık}}{t_{açık}+t_{kapalı}} \times 100 \tag{2.1}$$

Sistemin güç tüketim verileri anlık olarak kaydedilmiştir. Çalışma periyodu (4 saat) süresince toplam güç tüketim değerleri ($W(t)$, kJ) (2.2) kullanılarak hesaplanmıştır. Bu değerler kullanılarak ise enerji tasarrufu (%) değerleri (2.3) ile hesaplanmıştır.

$$W(t) = \int_{t=0\ saat}^{t=4\ saat} \dot{W}(t)dt \tag{2.2}$$

$$\text{Enerji Tasarrufu } \% = \frac{W_{FDM}-W}{W} \times 100 \tag{2.3}$$

FDM'siz ve FDM'li durumlarda toplam enerji tüketimi (kJ) sırasıyla W and W_{FDM} ile gösterilmektedir.

Çalışma periyodunun (4 saat) ardından elektrik kesintisi durumu da sistemde simüle edilmiştir. Elektrik kesintisi esnasında FDM'siz ve FDM'li durumlarda kabin iç hava sıcaklığının ortam sıcaklığı olan 18°C'ye ulaşma süreleri belirlenmiştir. Elde edilen verilerin değerlendirilmesinde kompresör çalışma süresini (%) minimize, enerji tasarrufunu maksimize eden ve elektrik kesintisi esnasında kabin iç hava sıcaklığının ortam sıcaklığına ulaşma süresini maksimize eden FDM, bu sistemlerde kullanılmak üzere önerilmiştir.

3. Bulgular ve Tartışma

Ev-tipi bir buzdolabının simüle edildiği laboratuvar ölçekli bir soğutma sistemi 8°C diferansiyel değeri (0°C - 8°C) ile ortalama 4°C'de FDM'siz ve ötektik su-tuz çözeltilerinin farklı konsantrasyonlarında hazırlanan FDM'lerle test edilmiştir. FDM olarak, K_2HPO_4 (ağ.%2,0-ağ.%10,0) ve $Na_2S_2O_3$ (ağ.%2,0-ağ.%10,0) çözeltileri kullanılmıştır. Sistemin çalışma periyodunda belirlenen verilerle çalışma süresi (%) ve toplam enerji tüketimi ve enerji tasarrufu (%) değerleri belirlenmiştir. Ardından elektrik kesintisi durumu simüle edilerek kabin iç hava sıcaklığının ortam sıcaklığına ulaşma süreleri tespit edilmiştir.

3.1. Kompresör Çalışma Süresi (%) Değerlerine FDM Entegrasyonun Etkisinin İncelenmesi

FDM'siz ve FDM olarak sırasıyla K_2HPO_4 (ağ.%2,0-ağ.%10,0) ve $Na_2S_2O_3$ (ağ.%2,0-ağ.%10,0) çözeltilerinin kullanıldığı durumlarda kabin iç hava sıcaklığının zamanla değişimi ilk 2 saatlik çalışma periyodu için Şekil 2'de sunulmuştur.

FDM'siz durumda toplam döngü sayısının 7,5 olduğu görülmektedir. Döngü sayısı ağ. %2,0 K_2HPO_4, ağ. %6,0 K_2HPO_4 ve ağ. %10,0 K_2HPO_4 çözeltileri sisteme entegre edildiğinde sırasıyla 4,4, 5,0 ve 5,7 değerlerine azalırken, ağ. %2,0 $Na_2S_2O_3$, ağ. %6,0 $Na_2S_2O_3$ ve ağ. %10,0 $Na_2S_2O_3$ çözeltileri ile sırasıyla 6,7, 5,5 ve 6,3 değerlerine azaldığı tespit edilmiştir. FDM'siz durumdaki toplam döngü sayısının sisteme entegre edilen tüm FDM'lerle azaldığı görülmektedir. Döngü sayının ağ. %2,0 K_2HPO_4 çözeltisi ile minimize edildiği belirlenmiştir.

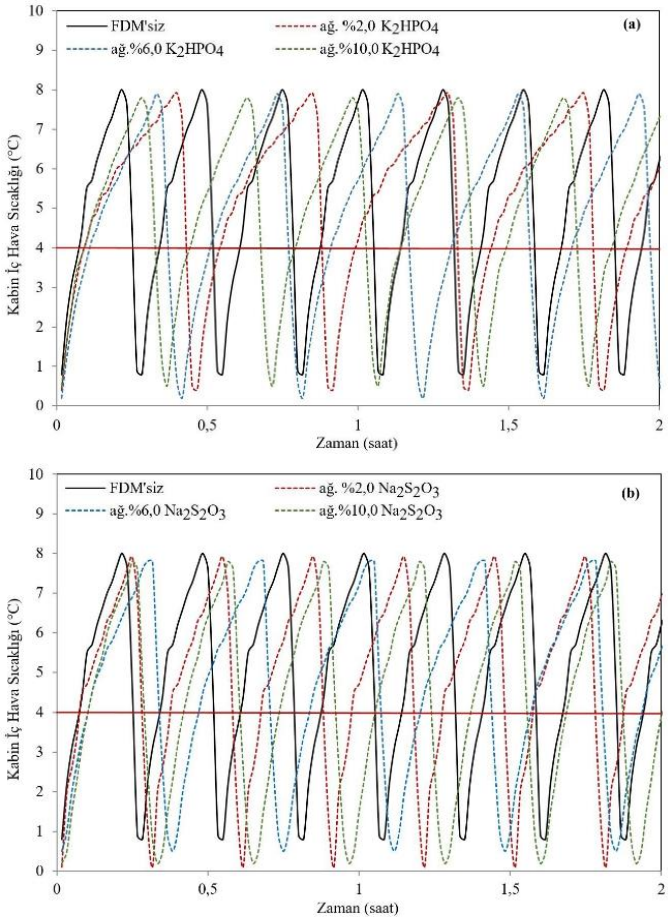

Şekil 2. FDM'siz ve FDM olarak (a) K_2HPO_4, (b) $Na_2S_2O_3$ çözeltileriyle kabin iç hava sıcaklığının zamanla değişimi (2 saat)

Şekil 2'de tespit edilen döngü sayısında ki azalma kompresörün kapalı kalma süresine ($t_{kapalı}$) bağlı olması kompresör çalışma süresinin (%) azalmasını sağlayacağı için enerji tasarrufu açısından önem taşımaktadır. Bu değerlendirmenin yapılabilmesi için kompresör açık ve kapalı kalma süreleri kullanılarak (2.1)'de sunulan denklem ile çalışma süresi (%) değerleri hesaplanmalıdır. Çalışma süresi (%) değerleri FDM'siz ve FDM'li durumlar için hesaplanmış ve Tablo 1'de sunulmuştur.

Tablo 1. FDM'siz ve FDM'li durumlarda kompresör çalışma süresi (%) değerleri

FDM	Konsantrasyon (ağ. %)	Açık Kalma Süresi, $t_{açık}$, (dakika)	Kapalı Kalma Süresi, $t_{kapalı}$, (dakika)	Bir Döngü Süresi (dakika)	Çalışma Süresi (%)
-	0	3	13	16	18,8
K_2HPO_4 Çözeltisi	**2,0**	**3**	**24**	**27**	**11,1**
	6,0	4	20	24	16,7
	10,0	4	17	21	19,0
$Na_2S_2O_3$ Çözeltisi	**2,0**	**3**	**15**	**18**	**16,7**
	6,0	4	18	22	18,2
	10,0	4	15	19	21,1

Tablo 1 incelendiğinde, FDM'li durumlarda döngü sayısında tespit edilen azalmanın FDM'lerin sisteme entegre edildiğidinde bir döngü süresinin uzaması ile ilişkili olduğu görülmektedir. Kapalı kalma süresinin literatürdeki çalışmalarda da tespit edildiği gibi tüm FDM'lerle uzadığı tespit edilmiştir. Ev-tipi buzdolabı performansını incelemek için literatürde evaporatör yüzeyine FDM entegre edilen iki tip buzdolabı ile deneysel bir çalışma yürütülmüştür. İki tip buzdolabında da FDM'siz duruma göre FDM entegrasyonuyla kompresör kapalı kalma süresinin önemli oranda uzadığı belirlenmiştir. Örneğin, suyun FDM olarak kullanıldığı buzdolabı 1 için, FDM'siz durumda 105 dakika olarak belirlenen kompresör kapalı kalma süresinin 215 dakikaya çıktığı belirlenmiştir [19]. Literatürde sunulan başka bir çalışmada ise, dikey bir içecek soğutucusunun soğutma performansı evaporatör yüzeyine FDM entegre edildiği durumda nümerik olarak incelenmiştir. FDM'siz durumda belirlenen kompresör açık ve kapalı kalma sürelerinin FDM'li durumlarda uzadığı ortaya konulmuştur. Ayrıca FDM kalınlığındaki artışın bu sürelerin uzamasını da arttırdığı tespit edilmiştir [20].

FDM olarak ağ. %2,0 K_2HPO_4 ve ağ. %2,0 $Na_2S_2O_3$ çözeltileri sisteme entegre edildiğinde FDM'siz durumda belirlenen kompresör açık kalma süresi (3 dakika) sabit kalırken kapalı kalma süresinin uzaması ile elde edildiği görülürken, diğer tüm FDM'lerle hem açık hem de kapalı kalma sürelerinin uzaması ile elde edildiği görülmektedir. Hem kapalı kalma hem de açık kalma sürelerinin uzaması döngü sayısını azaltmasına karşın, açık kalma süresinde uzamanın çalışma süresini (%) arttıracağı bilinmektedir. Örneğin, ağ. %10,0 K_2HPO_4 çözeltisi sisteme entegre edildiğinde de kompresör kapalı kalma süresinin uzadığı (17 dakika) görülmektedir. Ancak bu çözelti ile kompresör açık kalma süresinde de 1 dakikalık uzama olduğu belirlenmiştir. Sonuç olarak, döngü sayısındaki azalma beklenen bir durumdur. Ancak, kompresör açık kalma süresindeki uzama dikkate alındığında, sadece döngü sayısında tespit edilen azalma ile sistemde enerji tasarrufu sağlanabileceği söylenememektedir. Kompresör çalışma süresi FDM'siz durumda %18,8 olarak belirlenirken, bu çözelti ile artmış ve %19,0 olarak belirlenmiştir.

Çalışma süresi yüzdesinin uygun konsantrasyonda hazırlanan ötektik su-tuz çözeltilerinin FDM olarak kullanımıyla önemli oranda azaldığı tespit edilmiştir. FDM olarak ağ. %2,0 K_2HPO_4, ağ. %6,0 K_2HPO_4 ve ağ. %10,0 K_2HPO_4 çözeltilerinin sisteme entegre edilmesi durumunda sırasıyla %11,1, %16,7 ve %19,0 olarak belirlenirken, ağ. %2,0 $Na_2S_2O_3$, ağ. %6,0 $Na_2S_2O_3$ ve ağ. %10,0 $Na_2S_2O_3$ çözeltileri ile sırasıyla %16,7, %18,2 ve %21,1 olduğu tespit edilmiştir. Böylelikle, sisteme entegre edilen su-tuz çözeltilerinin uygun

konsantrasyonda hazırlanmasının önemi elde edilen verilerle ortaya konulmuştur. Çalışma süresi (%) değerinin ağ. %2,0 K_2HPO_4 çözeltisinin sisteme entegre edildiğinde minimize edildiği belirlenmiştir. Çalışma süresi FDM'siz duruma göre ağ. %2,0 K_2HPO_4 çözeltisi ile yaklaşık %41,0 azaldığı ortaya konulmuştur. Khan ve Afroz [21] ev-tipi bir buzdolabının performansını farklı termal yüklerde FDM'siz ve FDM'lerle deneysel olarak incelemiştir. FDM olarak iki farklı faz değişim sıcaklığına sahip (-5°C ve -10°C) ötektik çözeltiler kullanılmıştır. FDM'lerle bir döngüdeki ortalama kompresör çalışma süresinin FDM'siz duruma göre %5-30 azaldığı belirlenmiştir [21]. Literatürde sunulan başka bir çalışmada, ev-tipi bir buzdolabının performansı evaporatör yüzeyine FDM olarak etilen glikol entegre edildiği durumda test edilmiştir. Yapılan bu deneysel çalışmada da kompresör çalışma süresinin önemli oranda azaltıldığı belirlenmiştir. FDM'siz geleneksel buzdolabı ile kıyaslandığında bu oranın yüke bağlı olarak %17-20 aralığında değiştiği ortaya konulmuştur [22].

Kompresör çalışma süresinde belirlenen azalmanın sistemde enerji tasarrufu sağlayacağı bilinmektedir. (2.3)'teki enerji tasarrufu değerlerinin hesaplanabilmesi için (2.2)'de yer alan denklem kullanılarak FDM'siz ve FDM'li durumlarda toplam enerji tüketimi değerleri belirlenmelidir.

3.2. Enerji Tasarrufu (%) Değerlerine FDM Entegrasyonun Etkisinin İncelenmesi

FDM'siz ve farklı konsantrasyonlarda hazırlanan K_2HPO_4 ve $Na_2S_2O_3$ çözeltilerinin FDM olarak sisteme entegre edildiği durumlarda anlık kompresör güç tüketim verileri 2 saatlik çalışma periyodu için Şekil 3-(a) ve Şekil 3-(b)'de sunulmuştur.

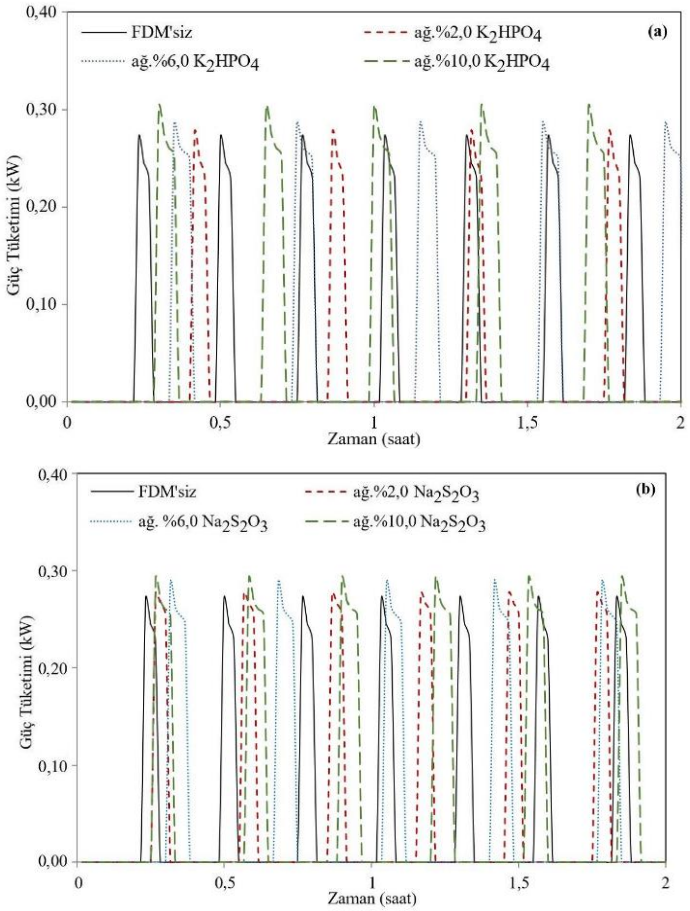

Şekil 3. FDM'siz ve FDM olarak (a) K_2HPO_4, (b) $Na_2S_2O_3$ çözeltileriyle kompresör güç tüketiminin zamanla değişimi (2 saat)

Şekil 3-(a) ve Şekil 3-(b) incelendiğinde, FDM'siz durumda güç tüketim değerleri 0,271 kW ile 0,229 kW arasında değişmektedir. Çeşitli FDM entegrasyonun bu değerleri arttırdığı görülmektedir. FDM olarak ağ. %2,0 K_2HPO_4, ağ. %6,0 K_2HPO_4 ve ağ. %10,0 K_2HPO_4 çözeltilerinin sisteme entegre edildiğinde maksimum ve minimum güç tüketim değerlerinin sırasıyla 0,276 kW-0,230 kW, 0,285 kW-0,250 kW ve 0,302 kW-0,253 kW aralığında değiştiği belirlenmiştir. Bu değerlerinin ağ. %2,0 $Na_2S_2O_3$, ağ. %6,0 $Na_2S_2O_3$ ve ağ. %10,0 $Na_2S_2O_3$ çözeltileri için 0,277 kW-0,255 kW, 0,288 kW-0,246 kW ve 0,292 kW-0,255 kW aralığında değiştiği gözlenmiştir. FDM'lerle anlık güç tüketim minimum ve maksimum değerlerinin ağ. %10,0 K_2HPO_4 ve ağ. %10,0 $Na_2S_2O_3$ çözeltileri ile maksimize edildiği görülmektedir. Sisteme ağ. %2,0 K_2HPO_4 çözeltisi sisteme entegre edildiğinde bu değerlerin minimize edildiği ve FDM'siz durumda belirlenen değerlere yakın olduğu görülmektedir.

Kompresör anlık güç tüketim değerleri ile (2.2) kullanılarak toplam güç tüketim değerleri FDM'siz ve FDM'li durumlarda hesaplanmıştır. Çalışma periyodu boyunca (4 saat) FDM'siz durumda toplam güç tüketim değeri 11,18 kJ iken ağ. %2,0 K_2HPO_4, ağ. %6,0 K_2HPO_4 ve ağ. %10,0 K_2HPO_4 çözeltileri ile ise sırasıyla 6,03 kJ, 10,54 kJ ve 11,99 kJ olarak bulunmuştur. Bu değer ağ. %2,0 $Na_2S_2O_3$, ağ. %6,0 $Na_2S_2O_3$ ve ağ. %10,0 $Na_2S_2O_3$ çözeltileri için ise sırasıyla, 10,37 kJ, 11,05 kJ ve 12,91 kJ olarak hesaplanmıştır. Toplam güç tüketim değerleri değerlendirildiğinde, çalışma süresinin (%) azaltıldığı durumlarda beklenildiği gibi sistemin toplam enerji tüketimi de azalmıştır. Dolayısıyla, çalışma süresinin minimize edildiği durum olan ağ. %2,0 K_2HPO_4 çözeltisinin sisteme entegre edilmesi durumunda toplam enerji tüketimi de 6,03 kJ değerine düşürülerek minimize edilmiştir. Çalışma süresi (%) değerinin FDM'siz durumdan fazla olduğu tespit edilen ağ. %10,0 K_2HPO_4 ve ağ. %10,0 $Na_2S_2O_3$ çözeltileri ile sistemde toplam güç tüketimi değerinin de önemli miktarda arttığı tespit edilmiştir.

FDM karışımını oluşturan bileşenlerin toplam enerji tüketimine etkisinin incelendiği farklı çalışmalar literatürde de sunulmuştur. Kiran-Yildirim [9] yaptığı çalışmada farklı konsantrasyonda (ağ.%1,0-ağ.%4,0) Na_2SO_4 çözeltilerinin enerji tasarrufuna etkisini incelemiştir. Elde edilen sonuçlar, ağ.%1,0 Na_2SO_4 çözeltisi sisteme entegre edildiğinde maksimum enerji tasarrufu elde edilirken artan konsantrasyonlarda avantaj sağlanamadığı tespit edilmiştir. Dolayısıyla, Kiran-Yildirim [9] tarafından yapılan çalışmada sistem enerji verimine uygun FDM seçiminin önemi ortaya konulmuştur.

Toplam enerji tüketim değerleri (2.3) dikkate alınarak enerji tasarrufu (%) hasaplamaları için kullanılmıştır. FDM'lerle hesaplanan enerji tasarrufu değerleri Tablo 2'de sunulmuştur.

Tablo 2. FDM'siz ve farklı FDM'lerle toplam enerji tüketimi ve enerji tasarrufu (%) değerleri

	FDM'siz	**%2,0 K_2HPO_4 /FDM**	**%6,0 K_2HPO_4 /FDM**	**%10,0 K_2HPO_4 /FDM**	**%2,0 $Na_2S_2O_3$ /FDM**	**%6,0 $Na_2S_2O_3$ /FDM**	**%10,0 $Na_2S_2O_3$ /FDM**
4 saat boyunca kompresör enerji tüketimi, (kJ)	11,18	**6,03**	10,54	11,99	**10,37**	11,05	12,91
4 saat boyunca toplam kompresör açık kalma süresi, (saat)	0,75	**0,44**	0,67	0,76	**0,67**	0,73	0,84
4 saat boyunca toplam kompresör kapalı kalma süresi, (saat)	3,25	**3,56**	3,33	3,24	**3,33**	3,27	3,16
Çalışma süresi (%)	18,8	**11,1**	16,7	19,0	**16,7**	18,2	21,1
Enerji Tasarrufu (%)	-	**-46,0**	-5,7	7,3	**-7,2**	-1,1	15,5

Tablo 2'den de görüldüğü üzere, FDM olarak ağ. %2,0 K_2HPO_4, ağ. %6,0 K_2HPO_4, ağ. %2,0 $Na_2S_2O_3$ ve ağ. %6,0 $Na_2S_2O_3$ çözeltileri ile sırasıyla %46,0, %5,7, %7,2 ve %1,1 enerji tasarrufu sağlandığı belirlenirken, ağ. %10,0 K_2HPO_4 ve ağ. %10,0 $Na_2S_2O_3$ çözeltilerinin toplam enerji tüketimini arttırdığı belirlenmiştir. Bu çalışmada belirlenen enerji tasarruf değerleri karşılaştırıldığında seçilen tuzlarla hazırlanan ötektik su-tuz çözeltilerinden FDM olarak en uygun çözeltinin ağ. %2,0 K_2HPO_4 çözeltisi olduğu belirlenmiştir.

3.3. Elektrik Kesintisi Periyoduna FDM Entegrasyonun Etkisi

Elektrik kesintisi durumu FDM'siz ve çeşitli FDM'lerle çalışma periyodunun ardından simüle edilmiştir. Elde edilen sonuçlar FDM'siz durumla kıyaslamalı olarak Şekil 4-(a) ve Şekil 4-(b)'de sunulmuştur.

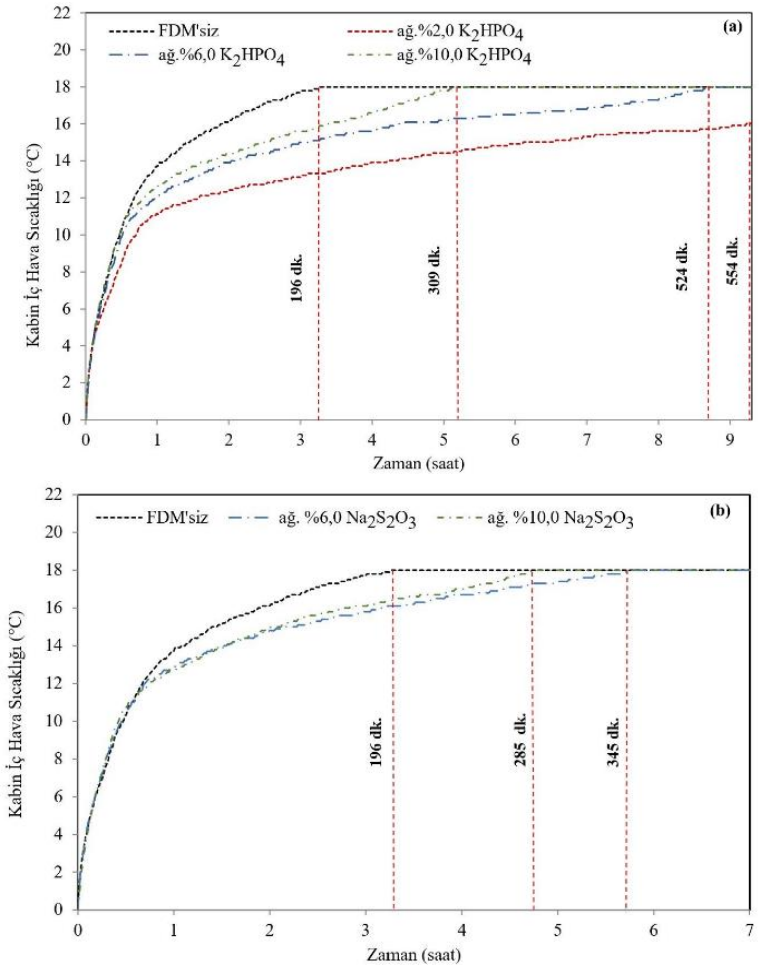

Şekil 4. Elektrik kesintisi periyodunda FDM'siz ve FDM'li (a) K_2HPO_4 ve (b) $Na_2S_2O_3$ çözeltili durumlarda kabin iç hava sıcaklığının zamanla değişimi

Şekil 4-(a) ve Şekil 4-(b) incelendiğinde, literatür çalışmaları ile benzer eğilimde sonuçlar elde edildiği, soğutma sistemine entegre edilen tüm FDM'lerin elektrik kesintisi esnasında kabin iç hava sıcaklığının ortam sıcaklığına (18°C) ulaşma süresini uzattığı görülmektedir. Literatürde elektrik kesintisi esnasında geleneksel buzdolabının kabin sıcaklığının 10°C altında 4 saat tutulabilirken FDM olarak etilen glikol kullanımı ile bu sürenin 16 saate çıktığı belirtilmiştir [22]. Ev-tipi buzdolabının FDM'siz ve FDM'lerle farklı termal yükler için performansının incelendiği deneysel başka bir çalışma ise, FDM olarak su ve bir ötektik karışım (faz değişim sıcaklığı: -3°C) kullanılmıştır. Elektrik kesintisi esnasında FDM'siz durumda 1-3 saat kesintisiz sistem çalışabiliyorken FDM ile bu sürenin 5-9 saate çıktığı öne sürülmüştür [13]. Khan vd. [23] yaptıkları çalışmada ise, ev-tipi bir buzdolabı kapağının açılması durumunda ve elektrik kesintisi esnasında FDM entegrasyonun sıcaklık dalgalanmasına etkisini incelemişlerdir. Sıcaklık dalgalanmasının FDM ile 3-5°C azaldığı ortaya

konulmuştur. Ayrıca elektrik kesintisi esnasında FDM'nin yaklaşık 2 saat kabin iç sıcaklığının düşük değerlerde tutulmasına olanak sağladığı belirtilmiştir [23].

Çalışmamız sonucunda da FDM'siz durumda kabin iç sıcaklığının ortam sıcaklığına (18°C) ulaşma süresi 196 dakika olarak belirlenmişken, sırasıyla sisteme ağ. %6,0 K_2HPO_4, ağ. %10,0 K_2HPO_4 ve ağ. %6,0 $Na_2S_2O_3$ ve ağ. %10,0 $Na_2S_2O_3$ çözeltileri entegre edildiğinde 524 dakika, 309 dakika, 345 dakika ve 285 dakika olduğu tespit edilmiştir. Sisteme ağ. %2,0 K_2HPO_4 çözeltisi entegre edildiğinde ise kabin iç hava sıcaklığının 16°C'ye ulaşma süresinin 554 dakika olduğu belirlenmiştir. Dolayısıyla bu sürenin ağ. %2,0 K_2HPO_4 çözeltisi ile maksimize edildiği görülmektedir.

3.4. Çalışma ve Elektrik Kesintisi Periyoduna FDM Entegrasyonun Etkisi

Her iki ötektik su-tuz çözeltilerinin farklı konsantrasyonları sisteme entegre edilmesi sonucu elde edilen kabin iç hava sıcaklığı değişimi ve toplam enerji tüketimleri değerlendirildiğinde ağ. %2,0 K_2HPO_4 çözeltilerinin FDM'ler arasında alternatif FDM olarak önerilebileceği görülmektedir. Bu FDM için kabin iç hava sıcaklığının ve enerji tüketiminin çalışma ve elektrik kesintisi periyotlarında zamanla değişimleri sırasıyla Şekil 5-a ve Şekil 5-b'de sunulmuştur.

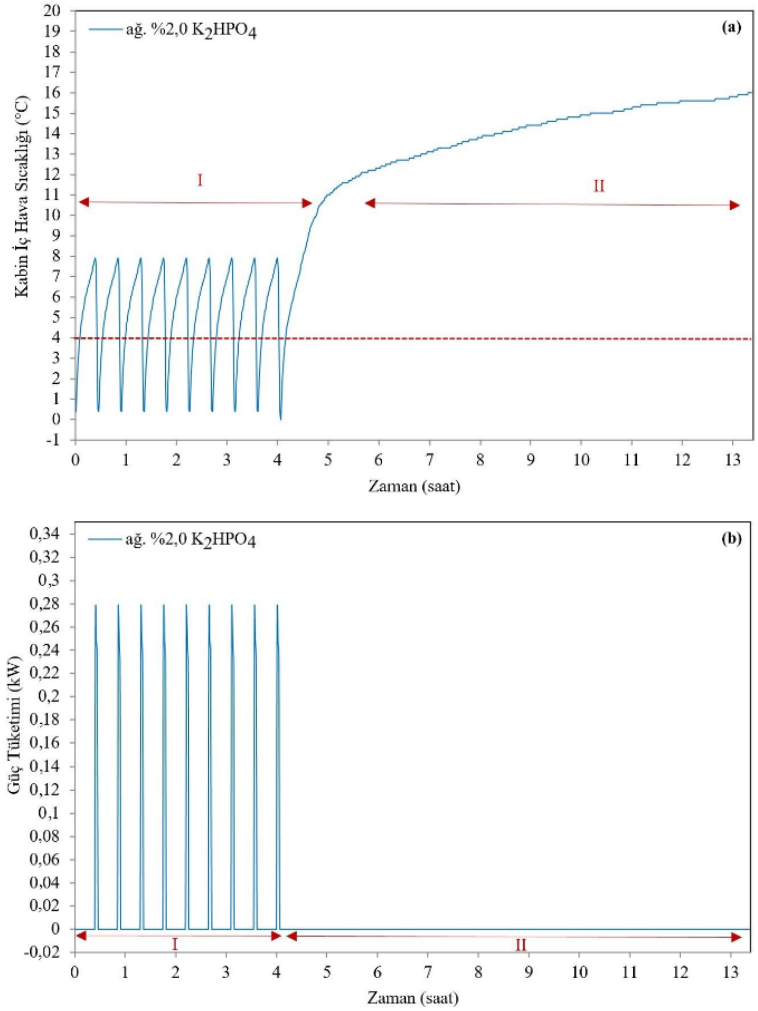

Şekil 5. FDM olarak ağ. %2.0 K_2HPO_4 çözeltisi sisteme entegre edildiğinde (a) kabin iç hava sıcaklığının ve (b) kompresör güç tüketiminin çalışma ve elektrik kesintisi periyodunda zamanla değişimi

Şekil 5-a incelendiğinde, sisteme FDM olarak ağ. %2,0 K_2HPO_4 çözeltisi entegre edildiği durumda, 4 saatlik çalışma periyodunda toplam döngü sayısının 8,9 olduğu görülmektedir. Döngü sayısının FDM'siz duruma

göre önemli ölçüde azaldığı belirlenmiştir. Her bir döngü incelendiğinde kapalı kalma süresinin uzun olduğu görülmektedir. Kompresör kapalı kalma süresinin 24 dakikaya uzaması sonucu, çalışma süresi %11,1 olarak belirlenmiştir. Bu durumda kompresörün çalışma sıklığının azaldığı ve dolayısıyla bu FDM entegrasyonuyla kompresörün yaşam ömrünün uzamasına katkı sağlanabileceği söylenebilmektedir.

Çalışma periyodunun ardından elektrik kesintisi periyodunda kabin iç hava sıcaklığının ağ. %2,0 K_2HPO_4 çözeltisi entegre edildiği durumda, 16°C'ye yaklaşık 9,2 saat sonunda ulaşılabildiği görülmüştür. FDM'siz durumda 16°C'ye yaklaşık 1,9 saatte ulaştığı dikkate alındığında, bu sürenin yaklaşık 5 katında çıktığı belirlenmiştir. Bu FDM ile elektrik kesintisi esnasında kabin iç hava sıcaklığının ani yükselişinin önüne gecilebileceği için kabin içinde ürünlerin uzun süre bozunmadan korunabileceği ortaya konulmuştur. Ayrıca Şekil 4-b incelendiğinde, güç tüketim verilerinin maksimum ve minimum değerlerinin sırasıyla 0,276 kW-0,230 kW arasında değiştiği görülmektedir. Toplam güç tüketiminin de FDM'siz duruma göre önemli ölçüde azaldığı tespit edilmiştir ve enerji tasarrufunun %46,0 olduğu belirlenmiştir. Dolayısıyla, ev-tipi buzdolabının simüle edildiği laboratuvar ölçekli soğutma sistemimize FDM olarak ağ. %2,0 K_2HPO_4 çözeltisinin entegre edilmesi durumunda önemli oranda enerji tasarrufu sağlandığı da tespit edilmiştir.

4. Sonuçlar

Soğutma sistemlerinin enerji tüketimlerini incelemek için ev-tipi buzdolabının simüle edildiği laboratuvar ölçekli bir soğutma sistemi FDM'siz ve FDM'lerle test edilmiştir. FDM olarak farklı konsantrasyonlarda hazırlanan K_2HPO_4 ve $Na_2S_2O_3$ çözeltileri kullanılmıştır. Sonuçlar aşağıda listelenmiştir.

- FDM'siz durumda %18,8 belirlenen çalışma süresi değeri, FDM'lerden ağ. %2,0 K_2HPO_4 ve ağ. %2,0 Na_2S_2O çözeltileri sisteme entegre edildiğinde sırasıyla %11,1 ve %16,7 değerlerine düşmüştür. Bu değeri minimize eden, dolayısıyla kompresör ömrünün korunmasına katkı sağlayacağı gibi sistemde enerji tasarrufunu maksimize edecek olan en uygun FDM'nin ağ. %2,0 K_2HPO_4 çözeltisi olduğu ortaya konulmuştur.
- Soğutma sisteminin çalışma periyodu boyunca toplam enerji tüketim değeri, FDM'siz durumda 11,18 kJ olarak belirlenirken, FDM olarak ağ. %2,0 K_2HPO_4 ve ağ. %2,0 Na_2S_2O çözeltileriyle sırasıyla 6,03 kJ ve 10,37 kJ değerlerine düşmüştür. Toplam enerji tüketiminin ağ. %2,0 K_2HPO_4 çözeltisi ile minimize edildiği, dolayısıyla enerji tasarrufunun maksimize edildiği belirlenmiştir. Enerji tasarrufu sisteme ağ. %2,0 K_2HPO_4 çözeltisi entegre edildiğinde %46,0 olarak tespit edilmiştir.
- Elektrik kesintisi esnasında kabin iç hava sıcaklığının ortam sıcaklığına (18°C) ulaşma süresi FDM'siz durumda 197 dakika (3,3 saat) iken, tüm FDM'lerle bu sürenin uzadığı belirlenmiştir. Bu sürenin ağ. %2,0 K_2HPO_4 çözeltisi ile maksimize edildiği, kabin iç hava sıcaklığının 16°C'ye ulaşma süresinin 554 dakika (9,2 saat) olduğu belirlenmiştir.

Tüm sonuçlar değerlendirildiğinde, ev-tipi buzdolabının simüle edildiği laboratuvar ölçekli bir soğutma sisteminde en iyi performansın FDM olarak ağ. %2,0 K_2HPO_4 çözeltisi ile elde edildiği ortaya konulmuştur. Günümüzde FDM'lerle ilgili pek çok araştırma ve geliştirme çalışması halen devam etmekte olup geliştirilen teknolojiler ticari ölçekte uygulanabilir durumdadır. Bu çalışmada önerilen FDM'de ev-tipi buzdolabı üreticileri tarafından yenilikçi tasarımlarla sisteme entegre edilebilir.

Yazar Katkıları

Birinci yazar deneysel çalışmanın planlanmasını ve tasarlanmasını, deneylerin yürütülmesini, elde edilen verilerin analiz edilmesini ve yorumlanmasını ve makalenin yazılmasını sağlamıştır. İkinci Üçüncü ve

Dördüncü Yazar deneysel çalışmaların yürütülmesini, verilerin toplanmasını ve sunulmasını sağlamıştır. Beşinci ve Altıncı Yazar deneysel verilerin analiz edilmesini ve yorumlanmasını sağlamıştır. Tüm yazarlar makalenin son halini okuyup onaylamıştır.

Çıkar Çatışması

Yazarlar hiçbir çıkar çatışması olmadığını beyan etmektedir.

Teşekkür

Bu çalışma 1919B012203087 Proje Numarasıyla TÜBİTAK Bilim İnsanı Destek Programları Başkanlığı (BİDEB) tarafından yürütülen, 2209-A Üniversite Öğrencileri Araştırma Projeleri Destekleme Programı kapsamında desteklenmiştir.

Kaynaklar

[1] D. Coulomb, *Refrigeration and cold chain serving the global food industry and creating a better future: two key IIR challenges for improved health and environment*, Trends in Food Science & Technology 19 (8) (2008) 413–417.

[2] Energy Information Administration (EIA), Residential Energy Consumption Survey (2001), https://www.eia.gov/consumption/residential/data/2001/index.php?view=consumption, Accesed 4 Nov 2023.

[3] T. M. I, Mahlia, H. H. Masjuki, R. Saidur, I. A. Choudhury, A. R. NoorLeha, *Projected electricity savings from implementing minimum energy efficiency standard for household refrigerators in Malaysia*, Energy 28 (7) (2003) 751–754.

[4] A. C. Marques, G. F. Davies, G. G. Maidment, J. A. Evans, I. D. Wood, *Novel design and performance enhancement of domestic refrigerators with thermal storage*, Applied Thermal Engineering 63 (2) (2014) 511–519.

[5] D. Y. Liu, W. R. Chang, J. Y. Lin, *Performance comparison with effect of door opening on variable and fixed frequency refrigerators/freezers*, Applied Thermal Engineering 24 (14-15) (2004) 2281–2292.

[6] P. K. Bansal, *Developing new test procedures for domestic refrigerators: harmonisation issues and future R&D needs—a review*, International Journal of Refrigeration 26 (7) (2003) 735–748.

[7] M. I. H. Khan, *Conventional refrigeration systems using phase change material: a review*, International Journal of Air-Conditioning and Refrigeration 24 (03) (2016) 1630007 16 pages.

[8] L. Abdolmaleki, S. M. Sadrameli, A. Pirvaram, *Application of environmental friendly and eutectic phase change materials for the efficiency enhancement of household freezers*, Renewable Energy 145 (2020) 233–241.

[9] B. Kiran Yildirim, *Performance evaluation of a laboratory-scale cooling system as a household refrigerator with phase change materials*, Energy Sources, Part A: Recovery, Utilization, and Environmental Effects 44 (3) (2022) 5852–5867.

[10] A. Pirvaram, S. M. Sadrameli, L. Abdolmaleki, *Optimization of energy consumption and temperature fluctuations for a household freezer using non-toxic and non-flammable eutectic phase change materials with a cascade arrangement*, International Journal of Energy Research 45 (2) (2021) 1775–1788.

[11] E. Oró, A. De Gracia, A. Castell, M. M. Farid, L. F. Cabeza, *Review on phase change materials (PCMs) for cold thermal energy storage applications*, Applied Energy 99 (2012) 513–533.

[12] W. Su, J. Darkwa, G. Kokogiannakis, *Review of solid–liquid phase change materials and their encapsulation technologies*, Renewable and Sustainable Energy Reviews 48 (2015) 373–391.

[13] K. Azzouz, D. Leducq, D. Gobin, *Enhancing the performance of household refrigerators with latent heat storage: An experimental investigation*, International Journal of Refrigeration 32 (7) (2009) 1634–1644.

[14] G. Li, Y. Hwang, R. Radermacher, H. H. Chun, *Review of cold storage materials for subzero applications*, *Energy* 51 (2013) 1–17.

[15] G. A. Lane, Solar heat storage: Volume I: Latent heat material, Boca Raton, CRC Press, 1983.

[16] H. P. Garg, S. C. Mullick, A. K. Bhargava, Solar thermal energy storage, D. Reidel Publishing Company, Dordecht, 1985.

[17] Y. Tek, *Synthesis, characterization and physicochemical properties of urea and thiourea-fatty acid condensation compounds*, Master's Thesis Tokat Gaziosmanpaşa Universiy (2009) Tokat.

[18] B. Kiran Yildirim, T. Noya, E. Mancuhan, S. Titiz Sargut, *Investigation of energy consumption for a PCM integrated laboratory scale cooling system: An experimental ctudy*, in: N. Yücel, R. Yumrutaş, M. S. Söylemez, M. Kanoğlu, Â. Atmaca, H. Yağlı (Eds.), 23rd Congress on Thermal Science and Technology with International Participation, 2021, Gaziantep, pp. 1002–1008.

[19] Y. Yusufoglu, T. Apaydin, S. Yilmaz, H. O. Paksoy, *Improving performance of household refrigerators by incorporating phase change materials*, International Journal of Refrigeration 57 (2015) 173–185.

[20] M. A. Ezan, E. O. Doganay, F. E. Yavuz, I. H. Tavman, *A numerical study on the usage of phase change material (PCM) to prolong compressor off period in a beverage cooler*, Energy Conversion And Management 142 (2017) 95–106.

[21] M. I. H. Khan, H. M. Afroz, *Effect of phase change material on compressor on-off cycling of a household refrigerator*, Science and Technology for the Built Environment 21 (4) (2015) 462–468.

[22] D. S. Niyaj, S. N. Sapali, *Performance evaluation of a domestic refrigerator with a thermal storage arrangement using propane as a refrigerant*, Energy Procedia 109 (2017) 34–39.

[23] I. H. Khan, H. M. Afroz, M. A. Karim, *Effect of PCM on temperature fluctuation during the door opening of a household refrigerator*, International Journal of Green Energy 14 (4) (2017) 379–384.

Çanakkale Onsekiz Mart University

Journal of Advanced Research in Natural and Applied Sciences

dergipark.org.tr/tr/pub/jarnas

Open Access

e-ISSN: 2757-5195 2024, Vol. 10, Issue 2, Pages: 380-398 doi.org/10.28979/jarnas.1327691

Üzüm Posasının Karbonizasyon Davranışının İncelenmesi

Feride Naime Türk[1]

[1]Çankırı Karatekin Üniversitesi, Merkez Araştırma Laboratuvarı Uygulama ve Araştırma Merkezi, Çankırı, Türkiye

Makale Tarihçesi

Gönderim: 14 Temmuz 2023

Kabul: 13 Şubat 2024

Yayım: 25 Haziran 2024

Araştırma Makalesi

Öz – Bu çalışmada üzüm posası hem inert hem de oksijenli atmosferlerde karbonizasyon davranışının incelenmesi amaçlanmıştır. Herhangi bir biyokütlenin torrefaksiyon koşullarında oluşturacağı ürünlerin miktarı, öncelikle biyokütlenin temel bileşenlerine bağlıdır. Çünkü temel bileşenlerin yapısal farklılıkları termal davranışlarının da farklı olmasına neden olmaktadır. Bu yüzden meydana gelen değişimlerin ve ortaya çıkan ürünlerin anlaşılması açısından şüphesiz oldukça önemlidir. Lignoselülozik maddelerin yapısında yaklaşık olarak %80 uçucu bileşen ve %20 sabit karbon bulundu. Karbonizasyon prosesi boyunca biyokütlenin elementsel oksijen oranı sıcaklıkla önemli oranda azaldı. 200-350˚C aralığında uçucu bileşenlerin bir kısmı biyokütleden ayrıldı ve böylece biyokütlenin yapısı daha sert ve kırılgan bir hale geldi. Büyük oranda hemiselülozların bozunması ve daha az oranda selüloz moleküllerinin bozunması suretiyle orijinal biyokütlenin fiber yapısı parçalandı. Bu durum biyokütle yapısının daha kırılgan bir hale gelmesine ve daha kolay öğütülmesine yardımcı olmaktadır. Uçucu bileşenler uzaklaştırıldıktan sonra biyokütlenin elementsel oksijen oranı azaldı ve buna bağlı olarak ısı değeri kademeli olarak 19 MJ. kg^{-1} den 21- 23 MJ. kg^{-1} değerine yükseldi.

Anahtar Kelimeler – *Karbonizasyon, torrefikasyon, kapalı sistem, ürün verimi, üzüm posası*

Investigation of Carbonization Behavior of Grape Pulp

[1]Central Research Laboratory Application and Research Center, Çankırı Karatekin University, Çankırı, Türkiye

Article History

Received: 14 Jul 2023

Accepted: 13 Feb 2024

Published: 25 Jun 2024

Research Article

Abstract – In this study, it was aimed to examine the carbonization behavior of grape pulp in both inert and oxygenated atmospheres. The number of products that any biomass will form under torrefaction conditions depending primarily on the basic components of the biomass because the structural differences of the basic components cause their thermal behavior to be different. Therefore, it is undoubtedly important to understand the changes that occur and the resulting products. Approximately 80% volatile components and 20% fixed carbon were found in the structure of lignocellulosic materials. During the carbonization process, the elemental oxygen content of the biomass decreased significantly with temperature. In the range of 200-350˚C, some of the volatile components separated from the biomass and thus the structure of the biomass became harder and more brittle. The fiber structure of the original biomass was broken down, largely by degradation of hemicelluloses and to a lesser extent by degradation of cellulose molecules. This helps the biomass structure become more fragile and grind more easily. After the volatile components were removed, the elemental oxygen content of the biomass decreased and accordingly the heat value gradually increased to 19 MJ. 21- 23 MJ from kg-1. increased to kg-1 values.

Keywords – *Carbonization, torrefaction, closed system, product yield, grape pulp*

1. Giriş

Dünya üzerindeki hızlı sanayileşme ve yaşam düzeyinin yükselmesi gibi çeşitli etkenler, günümüzde fosil yakıt kaynaklı enerji tüketimini artırmıştır. Bu durum, önemli oranlarda çevre ve hava kirliliğine yol açmıştır.

[1]feridenaimeturk@karatekin.edu.tr (Corresponding Author)

Yenilenebilir enerji kaynaklarının en önemli türlerinden biri olarak görülen biyokütle enerji kaynakları, kaynağa yönelik üretim teknolojilerinin iyi bilinmesi, çevre ile dostu olması, sürdürülebilir enerji üretimini, çevre yönetimini sağlaması ve kalkınmayı hedefleyen özellikleri ile tüm dünyada geniş bir uygulama alanı bulabilmiştir.

Biyokütle kullanışlı ve kolay sağlanabilen yenilenebilir bir enerji kaynağıdır. Biyokütle doğrudan yanma ile enerji üretiminde kullanılabilir. Ayrıca, çeşitli dönüşüm süreçleri uygulanarak, fosil yakıtların yerine kullanılabilen ekonomik olarak değerli katı, sıvı ve gaz yakıtlara da dönüştürülebilir. Isıl dönüşüm ile üretilen bu birincil ürünler genellikle hammaddeden daha çok kullanım alanına sahiptirler. Birincil ürünlerden daha sonra, hidrokarbon yakıtlar, güç, kimyasal maddeler gibi ikincil ürünler de elde edilebilir [1,2]. Katı biyokütlelere uygulanan birbirinden farklı ön işlemlerden birisi de karbonizasyon işlemidir. Karbonizasyon terimi, oksijensiz ortamda ılımlı piroliz anlamında kullanılmaktadır. Ham biyokütlelerin 200-300˚C aralığında inert gaz atmosferinde termal bozundurma amacıyla gerçekleştirilen bir ön işlemdir. Karbonizasyon esnasında, uçucu bazı organik maddelerin uzaklaştırılması ve reaktif hemiselüloz fraksiyonunun bozunması sağlanabilmektedir. Bu proses sayesinde farklı sıcaklıklarda bozunabilen bileşenlerden farklı yakıtlar elde edilebilme şansı doğacaktır [3].

Ham biyokütleler, bünyesinde hemiselüloz, selüloz ve lignin gibi bileşenleri bulundurur. Bu nedenle bu bileşenlerin termal bozunma özellikleri karbonizasyon performansını belirlemede önemli rol oynar. Ayrıca, karbonizasyon koşulları ham biokütlenin özelliklerine, uygulanan tekniğe, enerji yoğunluğu, öğütülebilirlik, peletlenebilirlik, nem oranı ve net ısı değeri gibi özelliklerden hangilerinin iyileştirilmek istendiğine bağlıdır. Günümüzde biyokütlelerin enerjilerinden yararlanmak amacıyla geliştirilmiş birçok karbonizasyon teknolojisi vardır. Karbonizasyon teknolojisine verilen önem son 5 yılda giderek artmıştır. Bu artış, biyokütlelerin özellikle ısı değerleri, yığın enerji yoğunluğu ve hidrofobluk yönünden kömüre benzer bir ürün elde edilmesinden kaynaklanmaktadır. Karbonizasyona uğratılmak suretiyle kavrulmuş ve enerji yoğunluğu artırılmış biyokütlelerin en olası kullanım yerleri; kömür ile biyokütlenin birlikte yakıldığı pulverize kömür enerji santralleri, kireç ocakları, çelik endüstrisi, küçük ve orta ölçekte çalışan biyokütle pelet yakıcıları ve sentez gazı üretimi olarak ifade edilebilmektedir [4].

Üzüm dünyada en çok üretilen ürünlerden biridir. Bu nedenle de çok miktarda üzüm posasının elde edilmesi mümkündür. Sonuç olarak üzüm, hatırı sayılır bir önem arz etmektedir. Ancak üzüm posası işlenmesi ve yeniden kullanılması hakkında yalnızca birkaç çalışma yapılmıştır. Yapılan çalışmalarda ise genellikle inert gaz atmosferinde deney gerçekleştirilmiş, oksijen ile işlem uygulaması çok az denenmiştir [5]. Üzüm posası ile yapılan bir karbonizasyon çalışmasında; çalışma koşulları 250˚C-300˚C ve 1 saat azot, karbondioksit ve hava karışımından oluşan süpürücü gaz karışımı olarak belirlenmiştir. Çalışmada ürün verimi ile katı ürün karakteristiği incelenmiştir. Yüksek sıcaklık kullanıldığında, süpürücü gazın niteliği önemli olmaksızın katı ürün özelliklerinin kömüre yaklaştığı gözlemlenmiştir. Ayrıca yüksek karbonizasyon sıcaklığı ve inert süpürücü gaz atmosferinde işlem görmüş örneğin tutuşma noktasının da yükseldiği görülmüştür. Taşıma ve depolama koşulları göz önüne alındığında ise, karbondioksitin azottan daha kullanışlı olduğu anlaşılmıştır [6]. Başka bir çalışmada, üzüm posası karbonizasyonu ve ham örneğin piroliz koşulları ile karşılaştırılmıştır. Sonuçta, karbonizasyona uğratılmış örnek, saf örneğe kıyasla kömüre daha fazla benzeyen ısıl özellikler göstermiştir. Ayrıca karbonizasyon sıvı ürününün, furan ve fenoller gibi yüksek miktarda kimyasal içerdiği belirlenmiştir. Katı ürünün fenolitik yağları ham örneğin piroliz katı ürününden daha yüksek miktarda hidrokarbon, fenoller içerirken düşük miktarda organik asit içerir. Bununla birlikte fenolitik yağların özellikleri karbonizasyon sıcaklıklarına bağlı olarak da değişmektedir. Yüksek verim ve sıvı ürün kalitesi bakımından en uygun karbonizasyon koşulları 275˚C ve 30 dakika olarak belirlenmiştir. Sonuçta karbonizasyon ön işlemi

ardından yapılan piroliz çalışmasında yüksek kaliteli sıvı ürün elde edilebileceği anlaşılmıştır [7]. Spiral (burgu) reaktörde yapılan bir başka karbonizasyon çalışmasında, 250-300˚C ve 10-60 dakika reaksiyon süresi koşulları uygulanmıştır. Ön işlem olarak karbonizasyon uygulandığında, sıvı ürünün ısıl değeri ve pH sının iyileştiği görülmüştür. Ancak, sıvı ürün verimliliğini iyileştirmek için karbonizasyon koşullarının da ciddi şekilde iyileştirilmesi gerekmektedir. Yapılan FTIR ve NMR analizleri ile sıvı ürün veriminin azalmasına, çapraz bağların ve char (kömürleşme) oluşumunun neden olabileceği anlaşılmıştır. Ayrıca gaz kromotografisi-kütle spektrometresi ile (GC-MS) asetik asit ve furfural miktarının karbonizasyon sıcaklığı ve kalma süresi ile azaldığı görülmüştür. Yapılan çalışma ile eğer çapraz bağlanma ve charlaşma azaltılırsa, karbonizasyon işleminin oldukça verimli hale geleceği sonucuna varılmıştır [8].

Günümüzde dünya üzerinde üzüm yetiştiriciliğinde en yüksek ekim alanı ile ilk sırayı İtalya almaktadır. Ardından ABD ve üçüncü olarak da Brezilya bulunmaktadır. Türkiye ise üzüme ayrılmış ekim alanı ile dünyada 5. sırada yer almaktadır [9]. Türkiye de üzüm, ekim alanları bakımından buğday ve arpadan sonra üçüncü sıradadır. Özellikle son yıllarda üzüm üretimine verilen önem artmış ve 2012 yılında ülkemiz üzüm üretiminde kendi kendine yeter hale gelmiştir. Türkiye İstatistik Kurumu (TUİK) verilerine göre, 2001 ve 2002 yıllarında 3 milyon ton civarında seyreden üzüm üretimi, 2015 yılında 6.4 milyon tona ulaşmıştır. Ülkemizde üzüm posası kullanım alanı oldukça geniştir. Ayrıca üzüm posası; gıda, tohumluk ve endüstriyel alanlarda da kullanıma sahiptir. Üzüm posası, elde edilen atıklar da pek çok alanda değerlendirilebilir. Bu tarımsal atığın miktarı göz önünde bulundurulduğunda, potansiyeli yüksek olabilecek nitelikte bir enerji kaynağı olarak değerlendirilmesi akılcı bir yol olarak görülebilir. Bu yüzden üzüm posası karbonizasyon sırasındaki davranışının incelenmesi bu doğrultuda atılacak adımların başlangıcını oluşturmaktadır [10-12].

Biyokütlelere örnek olarak, ağaçlar, mısır, buğday gibi özel olarak yetiştirilen bitkiler otlar, yosunlar, deniz algleri, organik çöpler, hayvan dışkıları verilebilir. Biyokütlenin tükenmez bir kaynak olması, genellikle tüm arazilerde yetiştirilebilmesi ve sosyoekonomik gelişmelere katkı sağlamış olması nedeniyle uygun ve önemli bir enerji kaynağı olarak görülmektedir. Canlı kütle ve dikili ürün olarak da bilinen biyokütle, çoğu kez bitkisel ve hayvansal olmak üzere ikiye ayrılır [13]. Güneş enerjisinin biyokütle enerjisine dönüşümü oldukça önemlidir. Bitkileri yalnızca besin kaynakları olarak değil, aynı zamanda tükenmez enerji kaynağı olarak da görmek mümkündür. Biyokütle enerji kaynakları arasında en çok bilinen, odundur. Ancak, bir odunun yetişmesi uzun yıllar almaktadır. Ayrıca ağaçların kesilmesi ile biyokütle elde edildiğinde, ormanların yok olmasına da yol açmaktadır. Bu nedenle enerji üretimi için kullanılacak biyokütlenin doğru bir şekilde belirlenmesi oldukça önemlidir [14-20].

Biyokütlenin fiziksel ve kimyasal özelliklerinde Torrefaksiyon işlemi önemli pozitif değişimleri sağlayan bir ön işlemdir. Torrefaksiyon işlemi inert ortamda ve düşük işletme hızında 200 ºC- 300 ºC gibi dar bir sıcaklık bandında yürütülen ve başlıca kömür ürünü elde etmek için uygulanan bir ısıl işlemdir. Lignoselülozik hemiselülozun büyük bir kısmı ilaveten selülozun ise belirli bir kısmı parçalanır. Bu proses işlemi süresince lignoselülozik biyokütlede dehidratasyon, deoksijenasyon ve dehidrojenasyon reaksiyonları etkinlikle meydana gelmektedir. Lignoselülozik biyokütlenin yapısındaki bu parçalanma onun öğütülebilirliği ayrıca reaktivitesini ve daha üniform bir yapı kazanmasını sağlar [21-22]. Aynı zamanda O/C ve H/C oranın azalması nedeni ile enerji yoğunluğu artmakta ve bu işlem ile Lignoselülozik biyokütle daha az hidrofolik hale gelmektedir. Ayrıca torrefaksiyon işlemi ile biyokütlede daha az uçucu madde kaldığından dolayı yanma sırasında daha az duman salınabilir ve nem içeriği azaldığından dolayı daha kolay tutuşabilir [16,23].

Bu nedenle; karbonizasyon işleminin üzüm posası enerji yoğunluğu, öğütülebilirliği gibi faktörlerin değişimlerinin değerlendirilmesi fazlasıyla gereklidir. Yerinde uygulanabilir tekniklerle yenilenebilir katı yakıt üretiminde değerlendirilme potansiyelinin bulunup bulunmadığının araştırılması da oldukça önemlidir. Bu

sayede, Türkiye'nin enerji yönünden dışa bağımlılığının azalmasında katkı sağlayıp sağlamayacağı anlaşılabilir. Tüm bu sebeplerden dolayı sunulan bu çalışmada üzüm posası hem inert hem de oksijenli atmosferlerde karbonizasyon davranışının incelenmesi amaçlanmıştır.

2. Materyal ve Yöntem

2.1. Örneklerin Hazırlanması

Üzüm posası örnekleri besicilik için yatak materyali hazırlayan Sakarya da bulunan bir fabrikadan sağlandı. Üzüm posası örnekleri, kâğıt üzerine konularak laboratuar koşullarında bir hafta süresince kurutulmaya bırakıldı. Ardından tam kuruluğun sağlanması için 105˚C lik etüvde bir saat bekletildi. Bu şekilde hazırlanan tanelerin tane büyüklüğüne göre çizilmiş dağılım toplamı ve dağılım yoğunluğu eğrileri Şekil 1 ve Şekil 2'de gösterilmektedir. Bu şekillerden örnek olarak kullanılan üzüm posasının ortalama tane büyüklüğünün 25.258 mm olduğu hesaplanmıştır. Karbonizasyon deneyi esnasında tane büyüklüğünün etkisinin incelenmesi için orta büyüklükte tanelerde kullanılmıştır. Orta büyüklükteki taneler için çizilmiş dağılım toplamı ve dağılım yoğunluğu eğrileri ise Şekil 3 ve Şekil 4'te gösterilmiş ve tane büyüklüğü 17.949 mm olarak hesaplanmıştır.

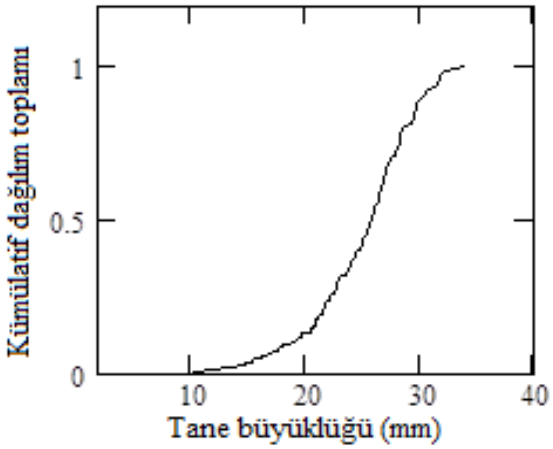

Şekil 1. İri tanelerin dağılım toplamı eğrisi

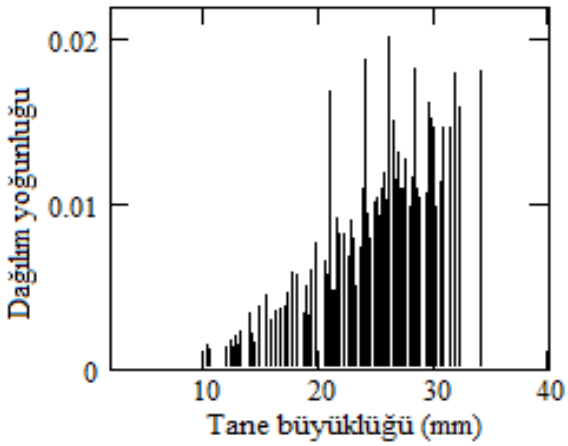

Şekil 2. İri taneler için dağılım yoğunluğu eğrisi

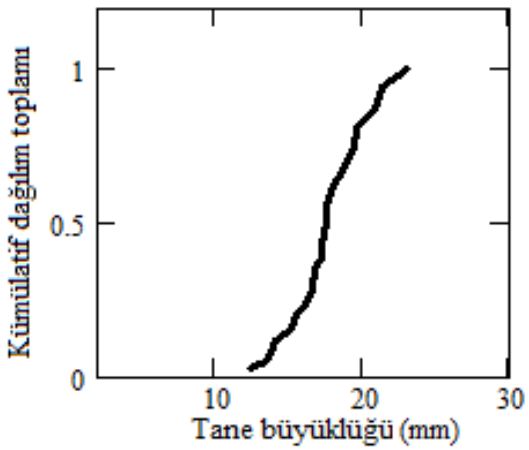

Şekil 3. Orta büyüklükteki taneler için dağılım toplamı eğrisi

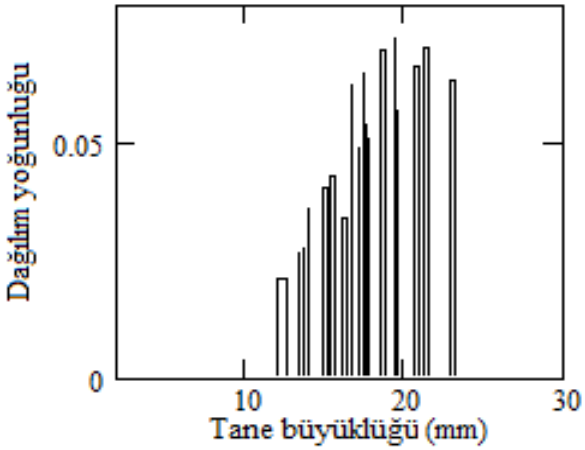

Şekil 4. Orta büyüklükteki taneler için dağılım yoğunluğu eğrisi

2.2. Örneklerin Kimyasal Bileşiminin Bulunması

2.2.1. Ekstrakte Edilebilir Materyal Miktarının Bulunması

Kurutulmuş örnekler, küçük hazneli yatay bıçaklı bir elektrikli öğütücü kullanılarak öğütüldü ve 50 mesh altına elendi. 50 meshin altına elendikten sonra analizlerde kullanılmak üzere kilitli poşetlere konuldu. İlk olarak örneklerin ekstrakte edilebilir materyal miktarını bulmak için Soxhlet ekstraksiyonu uygulandı. Bu amaçla benzen ve etanol karışımı; (2:1, h/h) 150 ml benzen ve 75 ml etanol kullanılarak ekstraktör balonu içerisine konuldu. Deneye başlamadan önce, süzgeç kâğıdına yaklaşık 12 gram öğütülmüş ham üzüm posası örneği tartılıp, zımba yardımıyla kapatılarak Soxhlet ekstraktörünün ekstraksiyon bölmesine konuldu. 4.5 saat süreyle ekstraksiyon sürdürüldü. Bu şekilde, üzüm posası ham örneklerinin bünyesinde bulunan, adi çözücülerde çözünebilen hidrofilik ve hidrofobik yapıdaki bileşenlerin bünyeden uzaklaştırılması sağlandı. Bu işlemin sonunda büyük oranda selüloz, hemiselüloz ve ligninden ibaret bir ürün elde edilmiş oldu. Deney sonunda çözelti ayrı olarak buzdolabında saklanırken, ekstraksiyon kartuşu 105˚C lik etüvde 1 saat kurutulduktan sonra tartıldı.

2.2.2. Ekstrakte Edilebilir Materyal Miktarının Bulunması

Hazne içerisindeki örnek kurutulduktan sonra, ekstraksiyon düzeneği hazırlandı. Bu örnek 500 ml hacmindeki balon içerisine boşaltılıp üzerine 200 ml dioksan: su (96: 4, h: h) eklendi. Manyetik karıştırıcılı ısıtıcı ile sıcaklığı 85˚C dolaylarında tutularak karıştırıldı bu şekilde iki saat ekstrakte edildi.

Ekstraksiyon işlemi tamamlandıktan sonra, katı kalıntı ve süzüntü süzgeç kâğıdı yardımıyla birbirinden ayrıldı. Süzüntü ayrı bir cam balonda toplandı ve S1 olarak adlandırıldı. Katı kalıntı ise ikinci kez tekrarlanacak olan ekstarksiyon işlemi için hazır hale getirildi. Katı kalıntı üzerine tekrar 200 ml dioksan su karışımı (96: 4, h: h) eklendi. 85˚C de ve 2 saat boyunca karıştırma devam ettirilerek ekstraksiyon işlemine devam edildi. İşlem sona erdiğinde yine bir süzgeç kâğıdı yardımıyla süzüldü süzüntüler, S1 süzüntü balonu içerisinde birleştirilip katı örnek ayrıldı.

Katı kalıntı son olarak 100 ml dioksan su ile (96: 4, h: h) yıkandı. Yıkama çözeltisi de S1 süzüntü kabının içerisine dâhil edilerek 500 ml süzüntü elde edilmiş oldu. Elde edilen bu süzüntüleri 60 ml ye deriştirmek için bir döner buharlaştırıcı kullanıldı. Bu sayede dioksan su karışımı geri kazanılarak değerlendirilmiş oldu. Elde edilen dioksan su daha sonraki deneylerde tekrar kullanıldı.

Döner buharlaştırıcıda süzüntü 60 ml ye kadar deriştirildiğinde işleme son verildi. Elde edilen derişik çözeltiye 180 ml % 96 lık etanol eklendi. Oluşan çökelek mavi bant süzgeç kâğıdı yardımıyla süzüldü ve süzgeç kâğıdı üzerinde kalan katı kalıntı hemiselülozların ilk kısmı olarak kaydedildi. Bu hemiselülozlara H1 ismi verildi.

100 ml dioksan su ile yıkama işleminin ardından süzüntüden ayrılan katı kalıntı ise 50˚C lik etüvde 1 saat kurutulmaya bırakıldı. Kurutulan bu katı kalıntıya (R1) adı verildi. R1 katı kalıntısı bu şekilde ekstraksiyon işleminin ikinci basamağına hazır hale getirildi.

İkinci kısım ekstraksiyon işlemi için oran 200 ml (50: 50, h: h) dioksan su olarak belirlendi. R1 katı kalıntısı ekstraksiyon balonuna konulup içerisine 200 ml çözelti eklenerek ekstraksiyon işlemine başlandı. 85˚C de 2 saat ekstraksiyon işlemi sürdürüldü. Ekstraksiyon işleminin ardından yine bir süzgeç kâğıdı yardımıyla katı kalıntı ve süzüntü birbirlerinden ayrıldı. Oluşturulan yeni süzüntü balonuna S2 adı verildi. Süzüntü saklanırken, katı kalıntı tekrar ekstraksiyon balonuna aktarıldı. Aynı oran kullanılarak ikinci kısım ekstraksiyon işlemi tekrarlandı. 85˚C, 2 saat ve 200 ml (50: 50, h: h) koşullarına bağlı kalındı. Ekstraksiyon işleminin sonucunda katı kalıntı ayrılıp, oluşan yeni süzüntü de S2 süzüntü balonunda dahil edildi. Bu ekstraksiyon işleminin sonucunda oluşan katı kalıntıya da R2 ismi verildi. R2 son olarak 100 ml dioksan su çözeltisi ile (50: 50, h: h) yıkandı. Yıkama çözeltisi de aynı S2 süzüntü balonuna eklendi. Sonunda R1 ve R2 katı kalıntılarının birleşiminden oluşan bir selüloz katı kütlesi elde edildi.

S2 olarak adlandırılan süzüntüler 40 ml ye deriştirilmek suretiyle ikinci kısım hemiselülozlar olan H2 elde edilmesi amaçlandı. Deriştirme, 45˚C de döner buharlaştırıcı kullanılarak gerçekleştirildi. 40 ml ye deriştirilmiş olan, S2 süzüntüsüne 120 ml %96 lık etanol çözeltisi ilave edildi. Oluşan çökelek mavi bant süzgeç kağıdı yardımıyla süzüldü ve süzgeç kağıdı üzerinde kalan katı kalıntı bu kez H2 hemiselülozlarını oluşturdu. Toplam hemiselüloz miktarı bu şekilde iki hemiselüloz süzüntüsü sonucu elde edilen katı kalıntılarının toplamından oluşturuldu. H1 ve H2 hemiselülozlarının katı kalıntılarından ayrılan süzüntüleri lignin tayini için kullanılmak üzere saklandı.

2.2.3. Ham ve İşlem Görmüş Örneklerin Analizleri

İşlem görmemiş ve karbonizasyona uğratılmış üzüm posasının analizinde -50 mesh örnekler kullanıldı. Tüm örneklerde 2 paralel deney yapılmıştır. Ham örneklerin nem tayininde Mettler LJ16 nem tayin cihazı kullanıldı. Karbonizasyona uğramış örneklerin (220˚C-10dk, 250˚C-10dk, 280˚C-10dk) uçucu madde tayini için yaklaşık 1 gram örnek tartılarak kapaklı ve önceden sabit tartıma getirilmiş porselen krozelere konuldu. Bu kroze 950˚C ye ısıtılmış kül fırınına konarak 7 dk beklendi. Çıkarılıp soğutulduktan sonra krozenin başlangıç ağırlığı ve son ağırlık arasındaki farktan uçucu madde miktarı hesaplandı (ASTM E 897-82). Krozeler uçucu madde

tayinin ardından 750˚C deki kül fırınında kapaksız olarak sabit tartıma gelene kadar bekletilerek kül tayini (ASTM D 1102-84) yapıldı. Sabit karbon yüzdesi aşağıdaki eşitlikle hesaplanmıştır.

$$\% \text{ Sabit karbon} = 100 - (\% \text{ Uçucu madde} + \% \text{ Nem} + \% \text{ Kül})$$

2.2.4. Deney Düzeneği

Karbonizasyon deneyleri, 2,9 cm iç, 3,5 cm dış çapında ve 20 cm yüksekliğinde pyrex cam, silindirik bir kamara (reaktör) içerisinde gerçekleştirildi. Deneyler, içerisinde direnç telleri bulunan ve uygun şekilde tasarlanmış refrakter tuğla ile döşenmiş silindirik bir ısıtma kamarası kullanılarak yapılmıştır. Reaktör fırına dikey şekilde yerleştirilip reaktörün üst kısmı 29/32 ölçüsünde rodajlı cam bir adaptör bulundurmaktadır. Kullanılan bu cam adaptör ile sisteme üst kısımdan azot girişi sağlandı. Fırının sıcaklık kontrolü, değişik voltaj transformatörü kullanılarak yapıldı. Fırın ile variak arasında bulunan sıcaklık ölçüm cihazı ile çalışılmak istenen sıcaklık belirlendi. Bu amaçla fırın içerisinde ortalama sıcaklığı temsil eden bölgeye bir K tipi termoçift yerleştirildi.

Karbonizasyon sırasında oluşan sıvı ürünü toplayabilmek için, 2,9 cm iç, 3,5 cm dış çapında ve 17,5 cm yüksekliğinde rodajlı cam sıvı ürün toplama kabı kullanıldı. Sıvı ürün toplama kabının üzerine iki deliğe sahip mantar tıpa takıldı ve Şekil 5'te görüldüğü gibi iki tuzaklı bir düzenek oluşturuldu. Bu sayede ilk tuzakta yoğunlaşamayan sıvı ürünlerin ikinci tuzakta yoğunlaşması sağlandı. Reaktör kamarası ve sıvı ürün toplama kabı birbirine 0.6 cm çapında 20 cm uzunluğunda cam boru ve 4 cm uzunluğunda silikon hortumun ile Şekil 5'te görüldüğü gibi bağlandı. Sıvı ürün toplama kabı, buz banyosu içerisine konuldu. Daha etkin bir soğuma sağlamak için, buz banyosuna bir miktar tuz eklendi.

Fırının sıcaklık kontrolü değişik voltaj transformatörü ile sağlandı. Ancak, termoçiftin sistem içerisinde bulunduğu konum ile örneklerin yerleştirildiği reaktör iç sıcaklığının aynı olup olmadığının anlaşılması için reaktörün dikey sıcaklık profili belirlendi. Bu sayede ölçülen sıcaklığın reaktör içindeki hangi sıcaklıklara karşılık geldiği belirlenmiştir. Bu işlem için sistem çalışır halde ve içi boşken, alt kısımdan 1 cm'lik aralıklarda termoçift reaktör içerisine sokuldu. Birer cm'lik artışlarla sıcaklık değerleri kaydedilip, örneğin yerleştirildiği yükseklik için sıcaklık ortalaması hesaplandı. Sistemin dikey sıcaklık profili Şekil 6'daki gibidir.

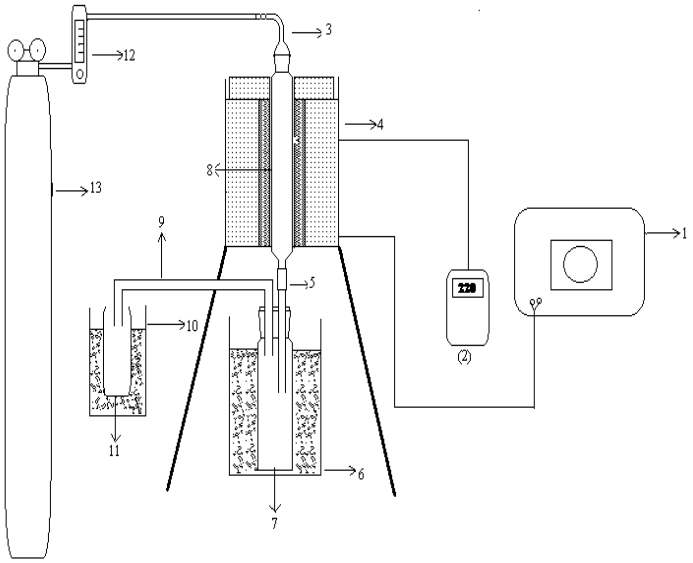

Şekil 5. Deney düzeneği, 1, değişken voltaj transformatörü; 2, sıcaklık ölçer; 3, adaptör; 4, fırın; 5, silikon hortum; 6-10, buz banyosu; 7, sıvı ürün toplama kabı; 8, reaktör; 9, sıvı ürün toplama tuzağı; 11, örnek tüpü; 12, rotametre; 13, süpürücü gaz

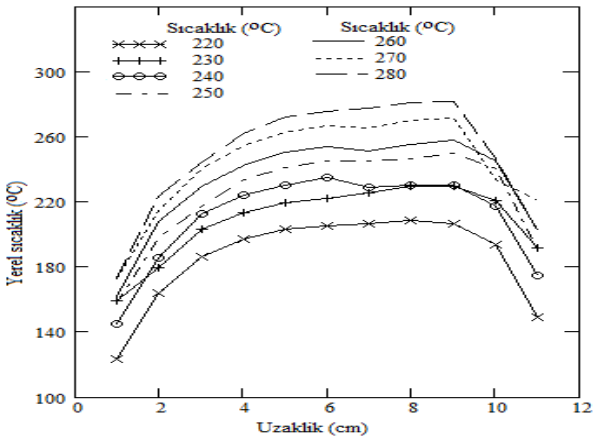

Şekil 6. Fırının dikey sıcaklık profilleri

Örneğin yerleştirildiği reaktörün 7 cm'lik uzunluğu içerisindeki ortalama sıcaklıklar Tablo 1'deki gibidir.

Tablo 1. 7 cm uzunluğundaki alanda ortalama sıcaklıklar

Sıcaklık (˚C)	220	230	240	250	260	270	280
Ortalama Sıcaklık	201.3	219.9	226.6	239.4	248.1	261	269.1

2.2.5. Deneyin Yapılışı

Karbonizasyon deneyine başlamadan önce boş reaktör, sıvı ürün toplama kabı ve sıvı ürünün konacağı cam örnek tüpü kapağı ile birlikte tartıldı. Sonra reaktör içerisine iri parçalı üzüm posası konulup deney öncesi tekrar tartıldı. Ağırlığı bilinen reaktör, fırın içerisine dikey şekilde yerleştirilip, üst kısmın cam adaptörü takıldı ve alt kısmın sıvı ürün toplama kabı ile bağlantısı yapıldı. Sıvı ürün toplama kabı buz banyosuna yerleştirildi. Sıvı ürün toplama kabı ile reaktör silikon hortumla birleştirildi. Sistem ısıtılmaya başlanmadan önce içerisinden 100 ml/dk akış hızında azot gazı geçirildi. Sonra sistem ısıtılmaya başlandı. Bu sırada sıcaklık sürekli olarak gözlendi. Sistem, istenilen sıcaklığa ulaşıncaya kadar hızlı bir şekilde ısıtılıp, istenen sıcaklıkta kalmaktadır. Sistem çalışılacak süre kadar bu sıcaklıkta bekletildikten sonra ısıtma sistemi kapatıldı. Sonra reaktör fırın içerisinden çıkartılıp soğumaya bırakıldı. Soğuma esnasında azot gazı geçişi devam ettirildi. Soğuma işlemi sonunda reaktörün üst kısmındaki adaptör çıkartıldı ve katı ürün (char) ile birlikte reaktör tekrar tartıldı. Sonra katı ürün ağzı kilitli poşetlerde muhafaza edildi. % katı ürün (%kü) verimi aşağıda verilen formülle hesaplandı.

$$\%\text{kü} = \frac{sR - bR}{dR - bR} \cdot 100 \qquad (2.1)$$

Burada bR: kamaranın boş ağırlığını, dR: kamaranın örnekle birlikte ağırlığını ve sR: kamaranın deney sonunda örnekle birlikte ağırlığını göstermektedir.

Sıvı ürün verimini belirlemek için, buz banyosu içerisindeki sıvı ürün toplama kabı oda koşullarına gelene kadar bekletildi. Sonra tartılıp ağırlığı kaydedildi. Reaktör içerisinde ve bağlantı borularında kalan sıvı ürünü de toplayabilmek için, 1,4 tetrahidrofuran çözücüsü kullanıldı. Bu sayede daha önceden ağırlığı bilinen örnek toplama kabı içerisinde sıvı ürün+çözücü biriktirilmiş oldu. Daha sonra örnek toplama kabı tartıldı ve ağırlığı kaydedildi. Örnek tüpü içerisinde bulunan sıvı ürün+çözücüden 1 ml lik pipet ile temsili örnek alınıp, boş ağırlığı bilinen aliminyum kap içerisine boşaltıldı. Oda koşullarında bir süre bekletildikten sonra çözücü

buharlaştırılarak kalan sıvı ürünün ağırlığı kaydedildi. % sıvı ürün (%sü) verimi aşağıda verilen formülle hesaplandı.

$$\%\text{sü} = \frac{(dS - bS) + \frac{csT - bT}{tC} \cdot kC}{dR - bR} \cdot 100 \tag{2.2}$$

Burada dS: sıvı ürün toplama kabının deney sonunda örnekle birlikte ağırlığını, bS: sıvı ürün toplama kabının boş ağırlığını, csT: örnek tüpünün çözücü ve sıvı ürün ile birlikte ağırlığını, bT: örnek tüpünün boş ağırlığını, kC: 1 ml' lik çözücü ve sıvı ürünün oda koşullarında bekletildikten sonra kalan ağırlığını ve tC: 1 ml' lik çözücü ve sıvı ürün ağırlığını göstermektedir.

Gaz ürün verimi ise daha önceden hesaplanmış olan katı ve sıvı ürün verim yüzdeleri toplamının 100'den çıkartılması ile bulundu. % gaz ürün verimi (%gü) aşağıda verilen formülle hesaplandı.

$$\%\text{gü} = 100 - \%\text{kü} - \%\text{sü} \tag{2.3}$$

Tüm deneyler, en az iki kez tekrarlanarak ortalaması alındı. Karbonizasyon sırasında çeşitli değişkenlerin ürün verimleri üzerindeki etkisi incelendi. Bu amaçla önce sıcaklığın ve Karbonizasyon süresinin daha sonra da süpürücü gaz bileşiminin ve tane büyüklüğünün etkileri ayrı ayrı ele alınmıştır.

3. Bulgular ve Tartışma

3.1. Deneylerde Kullanılan Üzüm Posasının Özellikleri

Karbonizasyon deneylerinde kullanılan üzüm posası örneklerinin kısa analiz, kesin analiz ve fiber analiz sonuçları Tablo 2'de verilmiştir.

Tablo 2. Üzüm posasının özellikleri

Kısa analiz (% kütle)				
Nem	Kül	Uçucu Madde		Sabit Karbon
5.7	2.9	74.64		16.76
Kesin Analiz (%kkt)				
%C	%H	%N	*%O	%S
65.4	2.3	4.6	26.5	1.2
Fiber Analiz				
Bileşen		Ağırlık ortalaması (%)		
EEM		12.7		
Selüloz		69.76		
Hemiselüloz		7.33		
Lignin		10.19		

*Farktan hesaplanmıştır.

Burada EEM, ekstrakte edilebilir materyali ifade etmektedir.

Yapılan kısa analizlerde üzüm posası diğer tarımsal atıklara göre, kül miktarının daha düşük, içerdiği nem miktarının kısmen yüksek olduğu görülmüştür. Fiber analiz için yapılan literatür taramasında selüloz oranının

ve lignin oranının uyumlu olduğu ancak hemiselüloz miktarının farklı olduğu gözlemlenmiştir. Bu durum, ekstraksiyon işlem basamaklarının daha farklı bir yöntem dahilin de bulunmasından kaynaklanmaktadır.

Biyokütle son zamanlarda bir enerji kaynağı olarak büyük ilgi görmüştür. Yenilenebilir ve karbon nötr bir enerji kaynağı olan biyokütlenin gelecekte enerji üretiminde önemli bir rol oynayacağı tahmin edilmektedir. Dünya toplam enerji tüketiminin yüzde onu ve toplam yenilenebilir enerjinin %78'i biyokütleden oluşmaktadır. Biyokütleler genel olarak odunsu ve odunsu olmayan malzeme türleri olarak sınıflandırılabilir. Odunsu biyokütleler genellikle ormancılık ve ağaç endüstrisinden elde edilirken, odunsu olmayan biyokütleler çoğunlukla tarımsal faaliyetlerden elde edilir. Çoğu biyokütle için, karmaşık bir matris oluşturan ana bitki bileşenlerini belirtmek için genel bir lignoselüloz terimi kullanılır. Örneğin, kara bitkilerinin odunsu dokuları, hücre duvarlarının ana bileşeni olarak selülozdan (%30-40), sırasıyla hemiselülozlardan (%25-35) ve ligninden (%12-30) oluşur. Bu yüzdeler farklı biyokütlelerin değişken bileşimlerini yansıtmaktadır. Bitki türlerinin ve çeşitlerinin çokluğu göz önüne alındığında, lignoselülozlar kendine özgü fiziksel ve kimyasal özelliklere sahip çok çeşitli materyaller içermektedir [24,25].

3.2. Karbonizasyon Deneylerinin Sonuçları

3.2.1. İnert Atmosferdeki Ürün Verimlerinin Zaman ve Sıcaklıkla Değişimi

220˚C de 100 ml/dk akış hızıyla saf azot atmosferinde gerçekleştirilen karbonizasyon deneylerinden elde edilen ürünlerin verimlerinin zamanla değişimi Tablo 3'te verilmektedir. Bu değerler aynı zamanda Şekil 7'de grafikle gösterilmektedir.

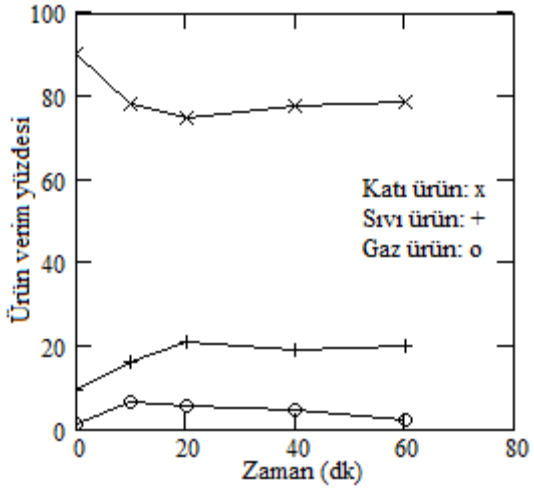

Şekil 7. 220˚C sıcaklıkta azot atmosferinde katı, sıvı ve gaz ürün yüzdelerinin zamanla değişimi

Tablo 3. 220˚C deki karbonizasyon deneylerinde ürün verimlerinin zamanla değişimi

Zaman (dk)	%Katı Ürün	%Sıvı Ürün	%Gaz Ürün
0	89.71	9.14	1.14
10	77.66	15.99	6.33
20	74.32	20.55	5.12
40	77.25	18.58	4.16
60	78.27	19.70	2.02

Şekil 7'de görüldüğü gibi 220˚C de ilk dakikalarda genel olarak tüm bozunmalar gerçekleşmiş olup, zaman ilerledikçe ürün verim yüzdelerinde fazla bir değişim gözlenmemektedir. İlk 20 dk boyunca, katı ürün verimi

azalırken, sıvı ürün veriminde artış olmaktadır ve gaz ürün verimi katı ve sıvı ürün verimlerine paralel şekilde değişmektedir.

250˚C de 100 ml/dk akış hızıyla saf azot atmosferinde gerçekleştirilen Karbonizasyon deneylerinden elde edilen ürünlerin verimlerinin zamanla değişimi Tablo 4'te verilmektedir. Bu değerler aynı zamanda Şekil 8'de grafikle gösterilmektedir.

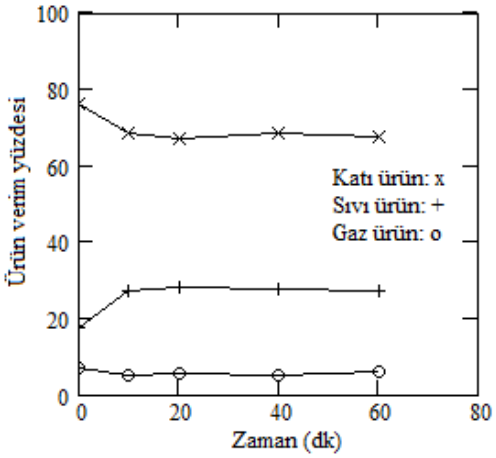

Şekil 8. 250˚C sıcaklıkta azot atmosferinde katı, sıvı ve gaz ürün yüzdelerinin zamanla değişimi

Tablo 4. 250˚C deki Karbonizasyon deneylerinde ürün verimlerinin zamanla değişimi

Zaman (dk)	%Katı Ürün	%Sıvı Ürün	%Gaz Ürün
0	75.82	17.40	6.76
10	68.12	27.09	4.78
20	66.90	27.99	5.10
40	68.24	27.17	4.57
60	67.47	26.82	5.70

250˚C de ilk 10 dakikada katı ürün verimi azalmış olup daha sonra yaklaşık olarak sabitlenmiştir. Sıvı ürün verimi ise ilk 10 dk artmış daha sonra sabitlenmiştir. Gaz ürün verimi Şekil 8'de görüldüğü gibi pek değişmemektedir. Katı ürün verimleri 220˚C ye göre daha düşüktür buna karşılık sıvı ürün verimi neredeyse üç kata kadar artmıştır. Gaz ürün verimleri 220 ˚C dekine göre çok farklı değildir.

280˚C de 100 ml/dk akış hızıyla saf azot atmosferinde gerçekleştirilen Karbonizasyon deneylerinden elde edilen ürünlerin verimlerinin zamanla değişimi Tablo 5'te verilmektedir. Bu değerler aynı zamanda Şekil 9'da grafikle gösterilmektedir.

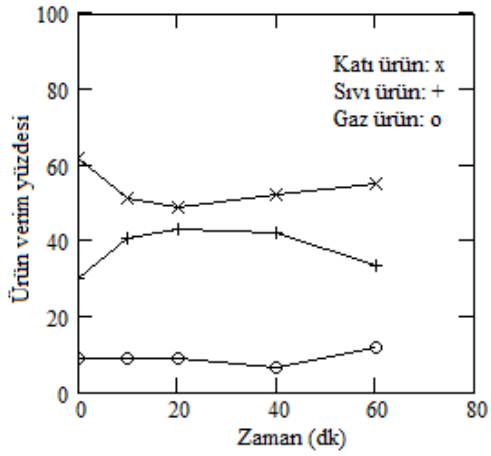

Şekil 9. 280˚C sıcaklıkta azot atmosferinde katı, sıvı ve gaz ürün yüzdelerinin zamanla değişimi

Tablo 5. 280˚C deki Karbonizasyon deneylerinde ürün verimlerinin zamanla değişimi

Zaman (dk)	%Katı Ürün	%Sıvı Ürün	%Gaz Ürün
0	61.50	29.70	8.79
10	50.85	40.32	8.82
20	48.67	42.27	8.54
40	52.03	41.82	6.14
60	54.92	33.32	11.75

280˚C de ilk 20 dakikada katı ürün verimi azalmış olup daha sonra belirgin şekilde artmaktadır. Sıvı ürün verimi, ilk 20 dakika boyunca artmıştır daha sonra hissedilir bir şekilde azalmaktadır. Gaz ürün verimi ise katı ve sıvı ürün verimlerinin değişimlerine paralel bir değişim göstermektedir. 40. dakikadan sonra şartlar sıvı ürünün aleyhine gelişmiştir.

3.3. Oksijenli Atmosferdeki Ürün Verimlerinin Değişimi

220˚C de değişik oranlarda oksijen bulunduran 100 ml/dk hızdaki süpürücü gaz ile 10 dakika sürdürülen Karbonizasyon deneylerinin sonuçları Tablo 6'da verilmektedir. Bu değerler aynı zamanda Şekil 10'da grafiklendirilmiştir.

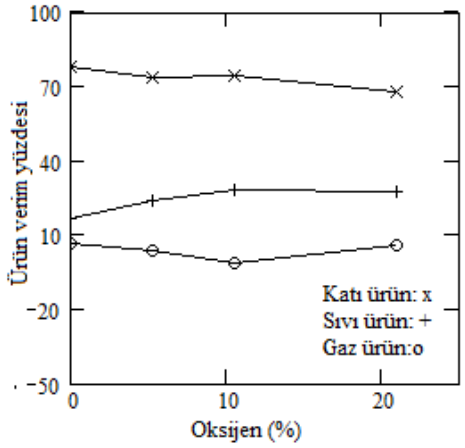

Şekil 10. 220˚C sıcaklıkta azot atmosferinde katı, sıvı ve gaz ürün verim yüzdelerinin oksijen yüzdesi değişimi

Tablo 6. 220˚C deki Karbonizasyon deneylerinde ürün verimlerinin oksijen yüzdesi değişimi

Oksijen yüzdesi	%Katı Ürün	%Sıvı Ürün	%Gaz Ürün
0	77.66	15.99	6.33
5.25	73.66	23.26	3.06
10.5	73.70	27.93	1.64
21	67.66	26.73	5.59

Deney boyunca oksijen miktarı arttığında katı ürün verimi belirgin şekilde azalmaktadır. Buna karşılık sıvı ürün verimi oksijen oranı ile birlikte neredeyse iki kata kadar artmaktadır. 220℃ sıcaklıkta azot yerine hava kullanıldığında, katı ürün veriminde bir miktar azalma olmakta buna karşılık sıvı ürün verimindeki artış bunu dengelemektedir. Sonuç da gaz ürün veriminin çok fazla değişim göstermemesidir. Torrefaksiyon terimi, oksijensiz ortamda piroliz anlamına gelmektedir. Ham biyokütlelerin 200-300˚C aralığında inert gaz atmosferinde termal bozundurma amacıyla gerçekleştirilen bir ön işlemdir. Torrefaksiyon esnasında, uçucu bazı organik maddelerin uzaklaştırılması ve reaktif hemiselüloz fraksiyonunun bozunması sağlanabilmektedir.

3.4. Hava Atmosferinde Yapılan Deneylerin Sonuçları

Üzüm posası ayrıca hafif (220˚C) karbonizasyon sıcaklığında, %100 hava atmosferinde ve 100 ml/dk akış hızındaki davranışı da incelenmiştir (Şekil 11 ve Tablo 7). Deneyler 0, 5 ve 10 dakikalarda yapılmıştır.

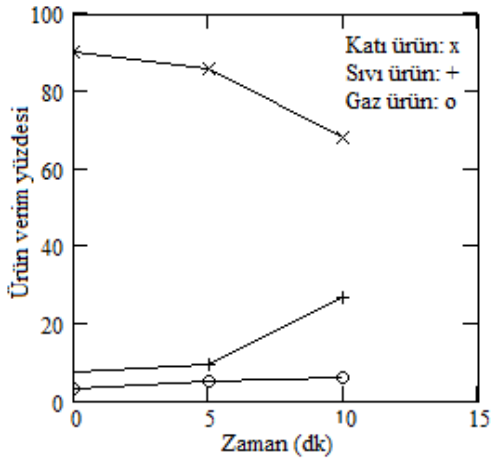

Şekil 11. 220˚C sıcaklıkta hava atmosferinde katı, sıvı ve gaz ürün verim yüzdelerinin zamanla değişimi

Tablo 7. 250˚C deki karbonizasyon deneylerinde ürün verimlerinin zamanla değişimi

Zaman (dk)	%Katı Ürün	%Sıvı Ürün	%Gaz Ürün
0	90.13	6.99	2.87
5	85.64	9.35	4.99
10	67.66	26.73	5.59

Hava ile çalışılan deneylerde sürenin uzaması ile katı ürün verimini belirgin şekilde azalmıştır. Bu durumun aksi şekilde sıvı ürün verimi aynı süre içerisinde keskin bir şekilde artmıştır. Gaz ürün verimi, katı ve sıvı ürün verimlerine bağlı şekilde değişkenlik göstermiştir.

3.5. Hava Atmosferinde Yapılan Deneylerin Sonuçları

Örneklerde, ısınma süresi boyunca ortaya çıkan değişimleri ortaya koymak amacıyla yürütülen deneylerdeki ürün verimlerinin sıcaklıkla değişimleri Tablo 8 ve Şekil 12'de verilmektedir.

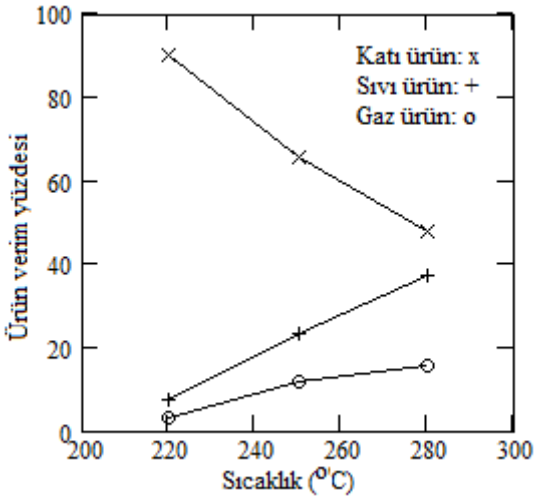

Şekil 12. Isınma süresi içinde hava atmosferinde katı, sıvı ve gaz ürün verim yüzdelerinin sıcaklıkla değişimi

Tablo 8. Isınma süresi içinde hava atmosferindeki karbonizasyon deneylerinde ürün verimlerinin sıcaklık ile değişimi

Sıcaklık (˚C)	%Katı Ürün	%Sıvı Ürün	%Gaz Ürün
220	90.13	6.99	2.87
250	65.61	22.85	11.53
280	47.50	36.99	15.50

Isınma süresi boyunca yapılan hava atmosferindeki deneylerde katı ürün verimi artan sıcaklıkla keskin bir şekilde azalmaktadır. Buna karşılık sıvı ürün verimi ise hızla artarken gaz ürün verimlerinin ise bu değişimlere paralellik göstermektedir.

3.6. Azot Atmosferinde Isınma Süresi Kadar Yürütülen Deneylerin Sonuçları

Örnekler karbonizasyon işlemine uğratılmadan önce, ısınma süresi boyunca olan değişimleri azot atmosferinde de incelenmiştir (Şekil 13 ve Tablo 9). Bu işlemler için hafif, orta ve şiddetli karbonizasyon sıcaklıkları ve 0. dakika koşulları kullanılmıştır.

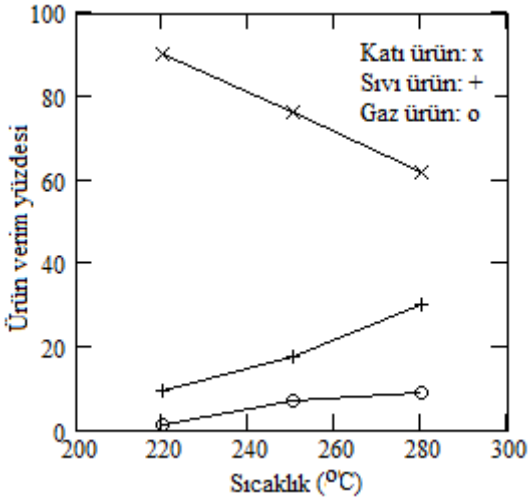

Şekil 13. Isınma süresi içinde azot atmosferinde katı, sıvı ve gaz ürün verim yüzdelerinin sıcaklıkla değişimi

Tablo 9. Isınma süresi içinde azot atmosferindeki karbonizasyon deneylerinde ürün verimlerinin sıcaklık ile değişimi

Sıcaklık (˚C)	%Katı Ürün	%Sıvı Ürün	%Gaz Ürün
220	89.71	9.14	1.14
250	75.82	17.40	6.67
280	61.50	29.70	8.79

Isınma süresi boyunca yapılan azot atmosferindeki deneylerde katı ürün veriminin artan sıcaklıkla belirgin şekilde azaldığı, sıvı ürün ve gaz ürün verimlerinin ise arttığı görülmüştür.

3.7. Ürün Verimlerine Tane Büyüklüğünün Etkisi

Karbonizasyon deneyleri esnasında olabildiğince iri tanelerden oluşmuş örnekler kullanılmıştır. Deneylerde 250˚C de ve 20 dakika karbonizasyon süresi için orta büyüklükte taneler ve küçük taneler kullanılmak suretiyle, tane büyüklüğünün ürün verimleri üzerine herhangi bir etkisinin olup olmadığı araştırılmıştır.

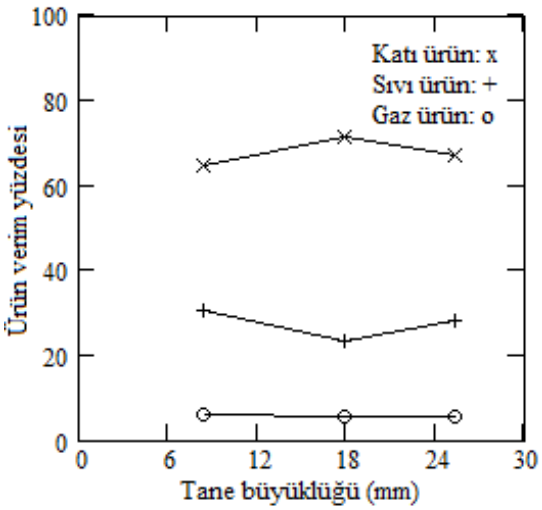

Şekil 14. 250˚C de azot atmosferinde katı, sıvı ve gaz ürün verim yüzdelerinin tane büyüklüğü ile değişimi

Tablo 10. 250˚C de azot atmosferindeki ürün verimlerinin tane büyüklüğü ile değişimi

Tane büyüklüğü (mm)	%Katı Ürün	%Sıvı Ürün	%Gaz Ürün
25.258	66.90	27.99	5.1
17.94	71.36	23.18	5.4
8.35	64.21	30.17	5.6

Şekil 14 ve Tablo 10'dan karbonizasyon ürün verimlerinin tane büyüklüğü ile değişimlerinin belirgin olmadığı ve aradaki farkların ortalamasının deneysel hata sınırları içerisinde sayılabildiği görülmektedir.

3.8. Karbonizasyondan Elde Edilen Katı Ürünlerin Özellikleri

10 dakika süreyle karbonizasyona uğratılmış charların kısa analiz sonuçları Tablo 11'de verilmektedir.

Tablo 11. İşlem görmüş örneklerin kısa analiz değerleri

Örnek	% Kül	% Uçucu Madde	% Sabit Karbon
220˚C	2.74	70.48	26.78
250˚C	3.53	66.38	30.09
280˚C	3.60	49.82	46.58

Sonuçlar değerlendirildiğinde kül miktarının, daha yüksek sıcaklıklarda oluşan örneklerde daha fazla olduğu görülmektedir. Ham örneklerde bulunan kül miktarı da yine işlem görmüş olan örneklerdekinden düşüktür. Uçucu maddeler ise sıcaklık arttıkça belirgin bir şekilde azalmaktadır. Ham örneklerde bu değer kısmen daha yüksektir. Sabit karbon miktarı ise kül ve uçucu madde miktarına paralel olarak değişmiştir.

3.9. Karbonizasyon Sonucu Elde Edilen Örneklerin Öğütülebilirliği

Örneklerin öğütülebilirlik deneyleri sonucu elde edilen kümülatif miktar kesri ve dağılım yoğunluğu eğrileri, Şekil 15 ve 16'da gösterilmektedir. Bu deneylerde saf azot atmosferinde 10 dakika süre ile gerçekleştirilen karbonizasyon işlemi sonucu elde edilen katı ürünler kullanılmıştır.

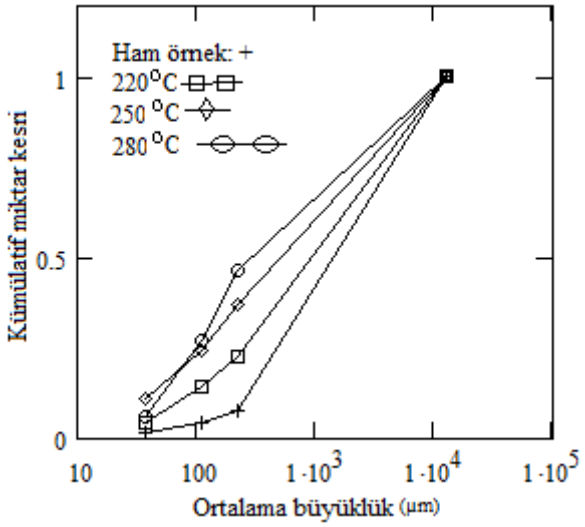

Şekil 15. Dağılım toplamı eğrisi

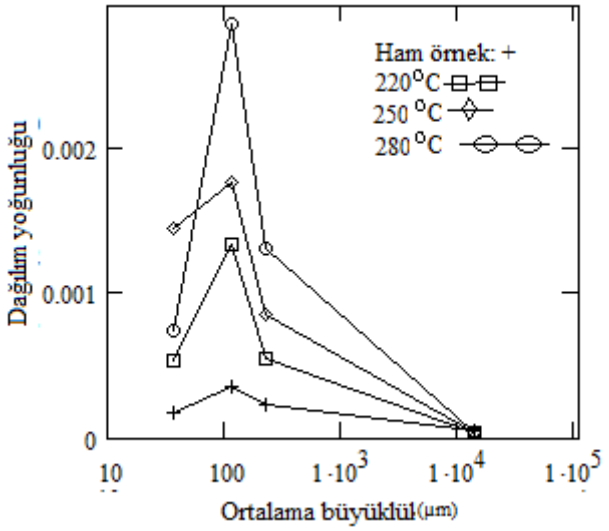

Şekil 16. Dağılım yoğunluğu eğrisi

Şekil 15'te görüldüğü gibi, sıcaklık arttıkça öğütme sonucu ortaya çıkan küçük tanelerin miktarlarının arttığı her iki grafikten de görülmektedir. Sıcaklık arttıkça tanelerin boyutunun arttığı net bir şekilde görülmektedir.

Biyokütle inert bir ortamda ısıtıldığında nem önce ayrışır, sonra ayrışmaya başlar. Uçucu maddeyi oluşturan bu bileşenler artan ısıtma sıcaklığının etkisiyle ayrılarak sıvı ve gaz ürünler oluşur. Artan proses sıcaklığı, biyokütlenin bozunma hızını artırarak katı ürün miktarının azalmasına, sıvı ve gaz ürün miktarının artmasına neden olur. Dolayısıyla katı ürün verimi, kavurma şiddetinin göstergesidir. Piroliz şiddeti arttıkça katı ürünün verimi düşer. Biyokütlenin içerdiği nem ve düşük molekül ağırlıklı uçucu bileşenler, düşük ve orta derecede kavurmanın meydana geldiği 220–250 °C sıcaklık aralığında ayrıştırılır. Biyokütlenin diğer bileşenleri olan selüloz ve ligninin deformasyon sıcaklıkları daha yüksek olduğundan, oluşan uçucu bileşenler bu sıcaklık aralığında hemiselülozun bozunması sonucu oluşur. 280 °C'de gerçekleştirilen yüksek kavurma işleminde hemiselülozların tamamı tükenmekte, hem de selüloz parçalanmaya başlamaktadır. Biyokütlede var olan lignin deformasyonu kademeli olarak ve 280-500 °C sıcaklık aralığında meydana geldiğinden, ligninin büyük bir kısmı bozunmadan katı ürün içerisinde kalır. Düşük kavurma koşullarında üretilen katı üründe işlem süresindeki artışın verimi etkilemediği ancak orta ve yüksek ısıtma işlemlerinde sürenin artmasıyla katı ürün

veriminin azaldığı tespit edilmiştir. Yüksek sıcaklıkta işlem süresinin arttırılması biyokütlenin bozulmaya devam etmesine neden olur [26,27].

Martin-Lara ve ark. zeytin ağacı budamalarının ezilmesinde de benzer sonuçlar bulmuşlardır. Kavurma sırasında maruz kalınan düşük sıcaklıklar nedeniyle, mineral maddenin yapısının ve miktarının bu işlemle değişmesi beklenmemektedir. Ayrıca inert atmosfer altında yapılan kavurma işleminde 200 °C'den sonra depolimerizasyon, dekarbonizasyon ve çatlama reaksiyonları oluşmaya başlar. 280 °C'de artan işlem süresi, bu reaksiyonların oluşmasına ve sabit karbon içeriğinin azalmasına neden olur [28].

4. Sonuçlar

Karbonizasyon işleminin üzüm posasına yerinde uygulanabilir tekniklerle yenilenebilir katı yakıt üretiminde değerlendirilme potansiyelinin bulunup bulunmadığının araştırılması da oldukça önemlidir. Bu sayede, Türkiye'nin enerji yönünden dışa bağımlılığının azalmasında katkı sağlayıp sağlamayacağı anlaşılabilir. Bu çalışmada üzüm posası hem inert hem de oksijenli atmosferlerde karbonizasyon davranışının incelenmesi amaçlandı.

Üzüm posasının artan torrefaksiyon sıcaklığı, süresi ile kömüre (char) benzeyen bir katı ürüne dönüştüğü tespit edildi. Torrefaksiyon şiddeti ve süresinin, oksitleyici ortamda katı ürün verimi üzerinde daha etkili olduğu belirlendi. Üzüm posasının oksitleyici ortamda katı ürün veriminin daha düşük olduğu torrefaksiyon sıcaklığı arttıkça arttığı tespit edilmiştir. İnert ortamda üzüm posasının kömür özelliğinde katı ürün elde etmek için, torrefaksiyon şartlarında kısa kalma süresinin, oksitleyici ortamda hafif torrefaksiyon şartlarında uzun kalma süresinin uygun olduğu belirlenmiştir.

İlave olarak ısınma süresi boyunca yapılan hava atmosferindeki deneylerde katı ürün verimi artan sıcaklıkla keskin bir şekilde azalmaktadır. Buna karşılık sıvı ürün verimi ise hızla artarken gaz ürün verimlerinin ise bu değişimlere paralellik göstermektedir.

Bazı torrefaksiyon teknolojilerinde odun tozu gibi küçük taneli hammaddeler işlenebiliyorken, bazılarıda iri taneler işlenebilmektedir. Ancak bu proseslerden çok azı geniş bir aralıktaki tane büyüklüklerini işleyebilmektedir. Bundan dolayı teknoloji seçimi hammadde özelliklerine dayanır veya torrefaksiyon öncesi aşırı iri materyali işlemek için boyut küçültme donanımı veya elek sistemleri gerekebilir. Bu faktörlerin hepsinin torrefaksiyon tesisi yatırım ve çalışma maliyeti üzerine etkisi vardır. Bu anlamda doğru teknolojiyi seçebilmek için ham maddenin özelliklerine ihtiyaç vardır. Yapılan çalşmalar sonucunda en iyi karbonizasyon sıcaklığı belirlendi.

Yazar Katkıları

Yazar makalenin son halini okuyup onaylamıştır.

Çıkar Çatışması

Yazar hiçbir çıkar çatışması olmadığını beyan etmektedir.

Kaynaklar

[1] W. Yan, T. C. Acharjee, C. J. Coronella, V. R. Vasquez, *Thermal pretreatment of lignocellulosic biomass*, Environmental Progress & Sustainable Energy 28 (3) (2009) 435–440.

[2] F. F. Felfli, C. A. Luengo, J. A. Suárez, P. A. Beatón, *Wood briquette torrefaction*, Energy for Sustainable Development 9 (3) (2005) 19–22.

[3] R. Harun, M. K. Danquah, G. M. Forde, *Microalgal biomass as a fermentation feedstock for bioethanol production*, Journal of Chemical Technology & Biotechnology 85 (2) (2010) 199–203.

[4] W.-H. Chen, Y.-J. Tu, H.-K. Sheen, *Impact of dilute acid pretreatment on the structure of bagasse for bioethanol production*, International Journal of Energy Research 34 (3) (2010) 265–274.

[5] W.-H. Chen, J.-C. Chen, C.-D. Tsai, T. L. Jiang, *Transient gasification and syngas formation from coal particles in a fixed-bed reactor*, International Journal of Energy Research 31 (9) (2007) 895–911.

[6] Y. Uemura, W. N. Omar, T. Tsutsui, S. B. Yusup, *Torrefaction of oil palm wastes*, Fuel 90 (8) (2011) 2585–2591.

[7] S. Ren, H. Lei, L. Wang, Q. Bu, S. Chen, J. Wu, J. Julson, R. Ruan, *The effects of torrefaction on compositions of bio-oil and syngas from biomass pyrolysis by microwave heating*, Bioresource Technology 135 (2013) 659–664.

[8] W. Chaiwat, I. Hasegawa, J. Kori, K. Mae, *Examination of degree of cross-linking for cellulose precursors pretreated with acid/hot water at low temperature*, Industrial & Engineering Chemistry Research 47 (16) (2008) 5948–5956.

[9] V. Repellin, A. Govin, M. Rolland, R. Guyonnet, *Modelling anhydrous weight loss of wood chips during torrefaction in a pilot kiln*, Biomass and Bioenergy 34 (5) (2010) 602–609.

[10] M. M. Küçük, A. Demirbaş, *Biomass conversion processes*, Energy Conversion and Management 38 (2) (1997) 151–165.

[11] R. C. Saxena, D. K. Adhikari, H. B. Goyal, *Biomass-based energy fuel through biochemical routes: A review*, Renewable and Sustainable Energy Reviews 13 (1) (2009) 167–178.

[12] L. Jiménez, F. González, *Study of the physical and chemical properties of lignocellulosic residues with a view to the production of fuels*, Fuel 70 (8) (1991) 947–950.

[13] S. Andrews, S. Aschmann, *Conservation issue brief resource effects of biomass energy production*. II. UNCCD, (2005), http://www.unccd.int/cop/reports/northmed/national/2002/.

[14] A. G. Dumanlı, İ. Gulyurtlu, Y. Yürüm, *Fuel supply chain analysis of Turkey*, Renewable and Sustainable Energy Reviews 11 (9) (2007) 2058–2082.

[15] H. Yang, R. Yan, H. Chen, D. H. Lee, C. Zheng, *Characteristics of hemicellulose, cellulose and lignin pyrolysis*, Fuel 86 (12-13) (2007) 1781–1788.

[16] A. Uslu, A. P. C. Faaij, P. C. A. Bergman, *Pre-treatment technologies, and their effect on international bioenergy supply chain logistics. Techno-economic evaluation of torrefaction, fast pyrolysis and pelletisation*, Energy 33 (8) (2008) 1206–1223.

[17] P. McKendry, *Energy production from biomass (part 1): Overview of biomass*, Bioresource Technology 83 (1) (2002) 37–46.

[18] A. Demirbaş, *Biomass resource facilities and biomass conversion processing for fuels and chemicals*, Energy Conversion and Management 42 (11) (2001) 1357–1378.

[19] A. Çağlar, A. Demirbaş, *Conversion of cotton cocoon shell to liquid products by supercritical fluid extraction and low pressure pyrolysis in the presence of alkalis*, Energy Conversion and Management 42 (9) (2001) 1095–1104.

[20] J. M. Encinar, F. J. Beltran, A. Ramiro, J. F. Gonzalez, *Pyrolysis/gasification of agricultural residues by carbon dioxide in the presence of different additives: Influence of variables*, Fuel Processing

Technology 55 (3) (1998) 219–233.

[21] W.-H. Chen, P.-C. Kuo, *A study on torrefaction of various biomass materials and its impact on lignocellulosic structure simulated by a thermogravimetry*, Energy, 35 (2010) 2580–2586.

[22] P. Rousset, L. Macedo, J. M. Commandré, A. Moreira, *Biomass torrefaction under different oxygen concentrations and its effect on the composition of the solid by-product*, Journal of Analytical and Applied Pyrolysis 96 (2012) 86–91.

[23] P. Basu, A. K. Sadhukhan, P. Gupta, S. Rao, A. Dhungana, B. Acharya, *An experimental and theoretical investigation on torrefaction of a large wet wood particle*, Bioresource Technology 159 (2014) 215–222.

[24] S. K. Satpathy, L. G. Tabil, V. Meda, S. N. Naik, R. Prasad, *Torrefaction of wheat and barley straw after microwave heating*, Fuel 124 (2014) 269–278.

[25] Q. V. Bach, Ø. Skreiberg, *Upgrading biomass fuels via wet torrefaction: A review and comparison with dry torrefaction*, Renewable and Sustainable Energy Reviews 54 (2016) 665–677.

[26] Y.-C. Chen, W.-H. Chen, B.-J. Lin, J.-S. Chang, H. C. Ong, *Fuel property variation of biomass undergoing torrefaction*, Energy Procedia 105 (2017) 108–112.

[27] W.-H. Chen, M.-Y. Huang, J.-S. Chang, C.-Y. Chen, W.-J. Lee, *An energy analysis of torrefaction for upgrading microalga residue as a solid fuel*, Bioresource Technology 185 (2015) 285–293.

[28] M. A. Martín-Lara, A. Ronda, M. C. Zamora, M. Calero, *Torrefaction of olive tree pruning: effect of operating conditions on solid product properties*, Fuel 202 (2017) 109–117.

Çanakkale Onsekiz Mart University

Journal of Advanced Research in Natural and Applied Sciences

dergipark.org.tr/tr/pub/jarnas

Open Access

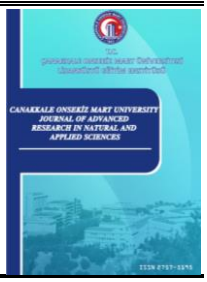

e-ISSN: 2757-5195 2024, Vol. 10, Issue 2, Pages: 399-414 doi.org/10.28979/jarnas.1404836

Experimental Investigation of Seawater for the Absorption of Carbon Dioxide from Ship Chimneys

İrem Koçyiğit Çapoğlu[1], Duygu Uysal[2], Özkan Murat Doğan[3], Bekir Zühtü Uysal[4]

[1,2,3,4]Department of Chemical Engineering, Faculty of Engineering, Gazi University, Ankara, Türkiye

Article History

Received: 15 Dec 2023

Accepted: 17 Feb 2024

Published: 25 Jun 2024

Research Article

Abstract − Carbon dioxide (CO_2) is the most important greenhouse gas that causes global warming. It is crucial to remove CO_2 from the atmosphere to combat climate change. It is believed that seawater could be a potential source for capturing CO_2, especially from ship chimneys and potentially high-concentration CO_2 emissions in coastal regions. In this study, the CO_2 absorption performance of sodium chloride (NaCl) solution as seawater, was investigated. The first phase of experiments was performed in a stirred cell at 91 kPa and 20°C. The total CO_2 absorption capacity ($molCO_2 \cdot L^{-1}$ solution) and dissolution rate ($mol \cdot s^{-1}$) of the solutions were determined by the pressure drop values occurring inside the cell. The experiments were conducted by preparing NaCl solutions at different concentrations (0-3.5 wt%). Additionally, 0.4% by volume calcium oxide (CaO) solution was added to NaCl solutions at different concentrations and its contribution to CO_2 absorption was examined. It was observed that there was a decrease in CO_2 absorption performance with the increase in salinity. However, it was determined that the addition of CaO to the NaCl solution had a positive effect on CO_2 absorption performance and increased the total CO_2 absorption capacity by 66%. The second phase of experiments was carried out in a falling film column. In these experiments, the liquid side individual physical mass transfer coefficients (k_L^0) were determined by the oxygen (O_2) desorption method for pure water and 3.5 wt% NaCl solution. Also, nonlinear regression analyses were performed, and correlations were developed for mass transfer coefficients.

Keywords − *Carbon dioxide, absorption, mass transfer coefficient, seawater, calcium oxide*

1. Introduction

Climate change resulting from global warming has become an important problem of today. The increase in carbon dioxide (CO_2) concentration in the atmosphere has a large share among the factors causing this problem. A large amount of CO_2 gas is released because of burning fossil fuels, especially for power and energy generation. The issue of CO_2 removal in the fight against climate change is noteworthy and emphasized on international platforms. According to the Intergovernmental Panel on Climate Change (IPCC), CO_2 emissions must reach net zero by 2050 with no or limited temperature rising [1]. In line with the 1.5°C temperature increase and net zero carbon targets set out on international platforms, it is necessary to increase the focus on renewable energy sources and reduce the use of fossil fuels [2, 3]. However, fossil fuels are still used because they are more economic. Also, fossil fuels are directly associated with excessive CO_2 emissions and other toxic gases such as SO_2, H_2S etc. [4, 5]. Therefore, it is important to implement CO_2 removal systems in the fight against climate change.

Ships produce sulfur oxide (SO_x), nitrogen oxide (NO_x), particulate matter and CO_2 emissions due to the fuel they consume in their power and propulsion systems. According to the International Maritime Organization

[1]iremkocyigit@gazi.edu.tr; [2]duysal@gazi.edu.tr (Corresponding Author); [3]mdogan@gazi.edu.tr; [4]bzuysal@gazi.edu.tr

(IMO), more than 80% of world trade is carried out by maritime transportation [6]. Maritime transport accounts for 30% of logistics sector emissions and approximately 2-3% of global CO2 [7]. Reducing CO2 emissions from ships is important in terms of climate change and environmental pollution.

Carbon capture, utilization, and storage systems (CCUS) are developed technologies [8]. There are three main systems to capture CO2: pre-combustion, post-combustion, and oxy-fuel combustion [9]. Also, there are many methods to capture CO2: absorption, adsorption, separation with membrane, cryogenic separation, etc. [10]. Among CO2 removal systems, CO2 capture via absorption method in post-combustion systems is one of the most well-known methods [11]. In post-combustion systems, CO2 is captured by organic solutions such as monoethanolamine (MEA), diethanolamine (DEA), etc. However, amine solutions have several drawbacks related to limited cyclic carbon dioxide loading capacity, degradation by oxygen, high equipment corrosion, and the operating cost is fairly high due to the high energy requirement for regeneration of the solution [12, 13]. The properties of the solutions used in the absorption process greatly affect the cost. These solutions are desired to have low energy costs, high CO2 selectivity, be environmentally friendly, and have low solution degradation and corrosion [14]. For this reason, efficient alternative solutions are being investigated. Some physical and chemical absorption solutions are widely studied academically and industrial for this purpose [15, 16].

In this study, it is contemplated that the utilization of seawater to capture CO2 from ship chimneys and processes with high CO2 emission potential, especially concentrated in the coastal region, will create a potential in terms of environmental impact and cost. The average seawater concentration is 3.5% by mass and most of it is sodium chloride (NaCl). Also, natural seawater is rich in Ca2+ and Mg2+ ions. The abundance of Ca2+ and Mg2+ ions in seawater facilitates a direct reaction with CO2, forming carbonate precipitates for effective CO2 absorption [17]. This integration combines CO2 capture with storage and advances the development of CCS (Carbon Capture and Storage) technology. However, the inherent capability of seawater for CO2 capture is constrained, prompting ongoing research efforts aimed at augmenting the absorption of CO2 in seawater. To increase the absorption capacity of seawater, researchers have examined the contributions of NH3, NH3-NH4Cl and organic amine solutions [18-20]. However, difficulties such as solution recovery and process complexity have emerged in these studies. Hence, it becomes imperative to explore suitable additives that can augment the CO2 capture capacity of seawater. The ideal additives should facilitate a straightforward process, yield effective absorption, be cost-effective, generate no by-products, and be environmentally friendly. In this context, it has been seen in the literature that there are studies in which steel slag (SS) with high calcium oxide and magnesium oxide content (~32–58% CaO and 3.9–10.0% MgO) is used as an additive material for CO2 capture [21, 22]. These additives have potential because of improved CO2 capture. Since these studies are limited and generally used as additives to fresh water, more research is needed.

This study investigated the CO2 absorption performance of NaCl solution as seawater and 0.4% v/v CaO + NaCl solution at different concentrations (0-3.5 wt%) in stirred cell. The addition of CaO to the NaCl solution had a positive effect on CO2 absorption performance and increased the total CO2 absorption capacity. This study was carried out at atmospheric pressure in Ankara (91 kPa) and ambient temperature (20oC). Also, second phase of experiments was carried out in a falling film column. The liquid side individual physical mass transfer coefficients (kL0) were determined by the oxygen (O2) desorption method for pure water and 3.5 wt% NaCl solution. Also, nonlinear regression analyses were performed, and correlations were developed for liquid side individual physical mass transfer coefficients.

2. Materials and Methods

In this study, experiments were carried out in two stages and the CO_2 absorption performance of sodium chloride (NaCl) solution as seawater was investigated. A stirred cell system was used to assess the CO_2 absorption performance of NaCl solutions. In stirred cell experiments, NaCl solutions were prepared in a range of low and high concentrations based on seawater salinity levels (0-3.5 wt%). Stirred cell experiments were carried out at 91 kPa pressure (atmospheric pressure in Ankara) and 20°C temperature. In falling film column experiments, liquid side individual physical mass transfer coefficients (k_L^0) were determined by the oxygen (O_2) desorption method for pure water and 3.5 wt% NaCl solutions. Falling film column experiments were carried out 91 kPa pressure (atmospheric pressure in Ankara) and 18°C temperature.

2.1. Stirred Cell Experiments

2.1.1. Experimental Set-Up

Experiments were carried out in a stirred cell system. The stirred cell is a known equipment for gas-liquid interaction systems [23, 24]. The stirred cell system operates on the principle of trapping the gas in the gas chamber and allowing it to be absorbed by the solution in the liquid reservoir. By observing the amount of gas absorbed by the solution and the pressure drop in the gas chamber, it is possible to determine how much gas has been absorbed. The schematic experimental set-up is shown in Figure 1.

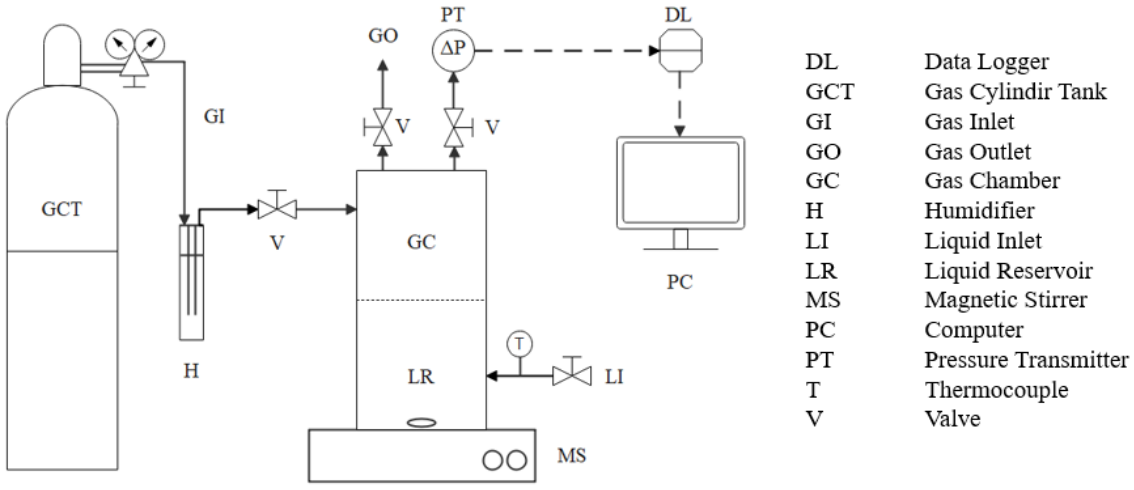

Figure 1. The stirred cell system

The stirred cell system consists of two parts, a gas chamber (0.5 L) and a liquid reservoir (0.4 L). The stirred cell is made of pyrex glass. The gas chamber has valves to which the gas inlet and outlet are connected. A CO_2 gas cylinder (>99.99%) is attached to the gas chamber. Before the gas was fed to the cell, the gas was passed through a humidifier to saturate the gas to water vapor. The absorption liquid is placed in the liquid reservoir. The two sections of the system are sealed together using a metal clamp. Throughout the experiments, the absorption liquid was stirred at a very low speed using a VELP SCIENTIFICA ARE model magnetic stirrer. The pressure drop in the cell was monitored using an HK Instruments DPT-R8 model differential pressure transmitter and recorded on the computer via the ORDEL UDL100 model data logger. Weight measurements were conducted using an analytical balance with an accuracy of ±0.1 mg.

2.1.2. Experimental Procedure

In the experiments, pure CO_2 gas flow was initially introduced into the stirred cell through the gas inlet to purge the air from the system. Subsequently, all valves were simultaneously closed, trapping the CO_2 gas in the gas chamber. Then, trapped CO_2 gas in the system was absorbed into the absorption solution. As CO_2 was absorbed, the pressure in the gas chamber gradually decreased until it stabilized at a constant value. Meanwhile, the absorption solution was stirred using a magnetic stirrer ensuring no vibration or vortex formation at the interface. This stirring served to prevent any potential mass transfer resistances that might occur at the liquid surface or in close proximity to it, providing homogeneity within the liquid. Additionally, the solution's temperature was continuously monitored by a thermocouple with an accuracy of ±0.2 K. During the experiments, the pressure in the gas chamber was recorded every second on the computer using a data logger and a differential pressure transmitter. While the pressure drop values initially increased over time in the stirred cell, they eventually stabilized. Subsequently, the total CO_2 absorption capacity and dissolution rate were calculated using the recorded data.

CO_2 dissolution in seawater occurs in a few steps. Dissolved CO_2 (in aqueous form as shown in (2.1)) in seawater converts to carbonic acid (H_2CO_3), carbonate (CO_3^-) and bicarbonate (HCO_3^-) ions as shown in (2.2)-(2.4), respectively. Then, carbonate (CO_3^-), Ca^{+2} and Na^{+2} ions in seawater form precipitation in solution as shown in (2.5) and (2.6).

$$CO_{2(g)} \leftrightarrow CO_{2(aq)} \tag{2.1}$$

$$CO_2 + H_2O \leftrightarrow H_2CO_3 \tag{2.2}$$

$$H_2CO_3 \leftrightarrow HCO_3^- + H^+ \tag{2.3}$$

$$HCO_3^- \leftrightarrow H^+ + CO_3^- \tag{2.4}$$

$$Ca^{2+} + CO_3^- \leftrightarrow CaCO_3 \tag{2.5}$$

$$Na^{2+} + CO_3^- \leftrightarrow NaCO_3 \tag{2.6}$$

2.1.3. Total CO_2 Absorption Capacity

To determine the pressure in the gas chamber, the ideal gas equation (shown in (2.7)) was used by correcting for real gases by using the compressibility factor [25].

$$PV_g = ZnRT \tag{2.7}$$

In this equation, P is the gas pressure [Pa] in the stirred cell gas chamber; V_g is the gas volume [m^3], Z is the compressibility factor [0.995], n is the mole of carbon dioxide gas [mol], R is the gas constant [8.314 $Pa{\cdot}m^3{\cdot}mol^{-1}{\cdot}K^{-1}$], T is the temperature [K]. The compressibility factor (Z) in the ideal gas equation was calculated by taking into account the composition of pure CO_2 gas passed through the humidifier. The compressibility factor (Z) according to the composition value of water-saturated CO_2 gas was calculated with the help of the Peng-Robinson model [26].

The pressure in the gas chamber of the stirred cell is equal to the difference between atmospheric pressure and pressure drop value which is shown in (2.8).

$$P = P_{atm} - \Delta P \tag{2.8}$$

The pressure drop values in the gas chamber were recorded on the computer via the differential pressure transmitter. Then these data were plotted against the time that is shown in Figure 2 as an example. The ordinate of the graph represents the pressure drop difference (ΔP) measured from the transmitter in Pa units, and the abscissa represents the time in seconds.

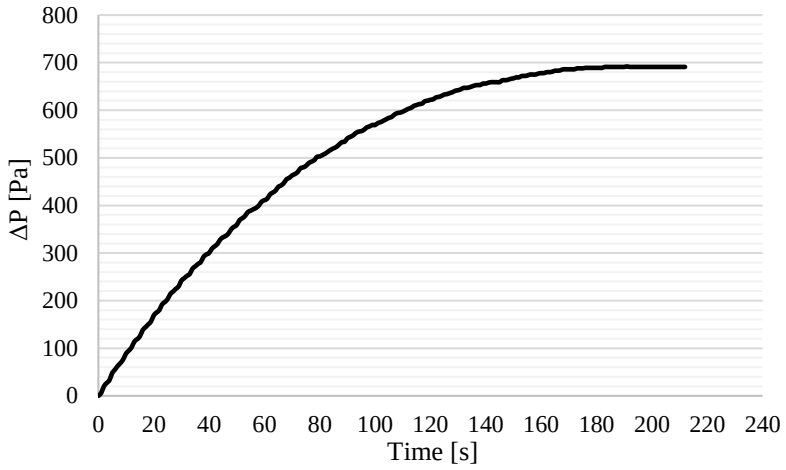

Figure 2. Increase in pressure drop (ΔP) in the gas chamber of the stirred cell with time

With the help of the pressure drop values fixed at the end of the experiment, the mole of CO_2 gas remaining in the gas chamber was calculated with (2.7). After that, by taking the difference between gas moles in the initial and final state, the amount of CO_2 absorbed into the unit volume of absorption liquid was determined [27].

2.1.4. Dissolution Rate

The dissolution rate experimental procedure is similar to the total CO_2 absorption capacity experiments but theoretically different. (2.9) is obtained by taking and arranging the differential of (2.7) [28].

$$dn = \frac{V_g}{ZRT} dP \tag{2.9}$$

Since the experiments are conducted as a function of time, the change of the expression obtained by (2.9) with time is shown in (2.10) [28].

$$w = \frac{dn}{dt} = \frac{V_g}{zRT} \frac{dP}{dt} \tag{2.10}$$

Here, w is the dissolution rate [mol·s^{-1}] of CO_2 in the absorption solutions. The part on the right side of the equation expresses the change in moles of CO_2 due to the absorption of CO_2 in the gas chamber into the absorption solutions over time.

The internal pressure in the gas chamber was determined with (2.8) and the internal pressure changing plot is shown in Figure 3. To determine the pressure change (dP/dt) over time, the slope of the first part of the graph, in which it proceeds linearly, was taken. Then, this value is used in Equations (2.10) and (2.11).

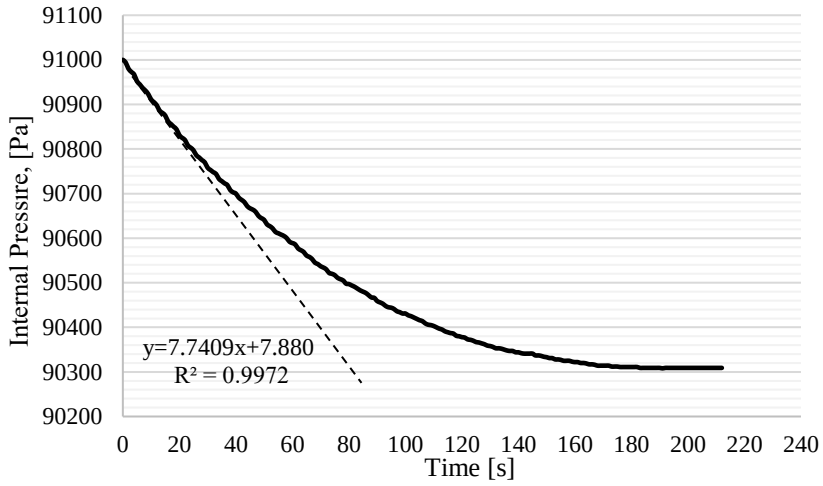

Figure 3. The change in the internal pressure (P) in the gas chamber of the stirred cell with time

The absorption occurred in the liquid reservoir volume (V_L), and the dissolution rate of CO_2 in the solution can be shown by (2.11) [28].

$$r = \frac{w}{V_L} = -\frac{1}{V_L}\frac{V_g}{zRT}\frac{dP}{dt} \tag{2.11}$$

Here, r is the rate of the absorption process relative to the total solution volume in the unit [$mol \cdot m^{-3} \cdot s^{-1}$], the slope read from the graph in the unit of dP/dt [$Pa\text{-}s^{-1}$] on the right side of the equation, V_L, solution volume [m^3], V_g, gas volume [m^3], T is the temperature in [K], R is the gas constant [8.314 $Pa \cdot m^3 \cdot mol^{-1} \cdot K^{-1}$].

2.2. Falling Film Column Experiments

2.2.1. Experimental Set-Up

Liquid side individual physical mass transfer coefficients (k_L^0) were determined by the O_2 desorption method in falling film column. O_2 desorption method is known in literature for determining k_L^0 [29, 30]. The falling film column used in the experiments is similar in concept with wetted wall columns. Wetted wall column are frequently used equipment in mass transfer studies because they are easy to design and provide a high mass transfer rate [31, 32]. The schematic falling film columns experimental set-up is shown in Figure 4.

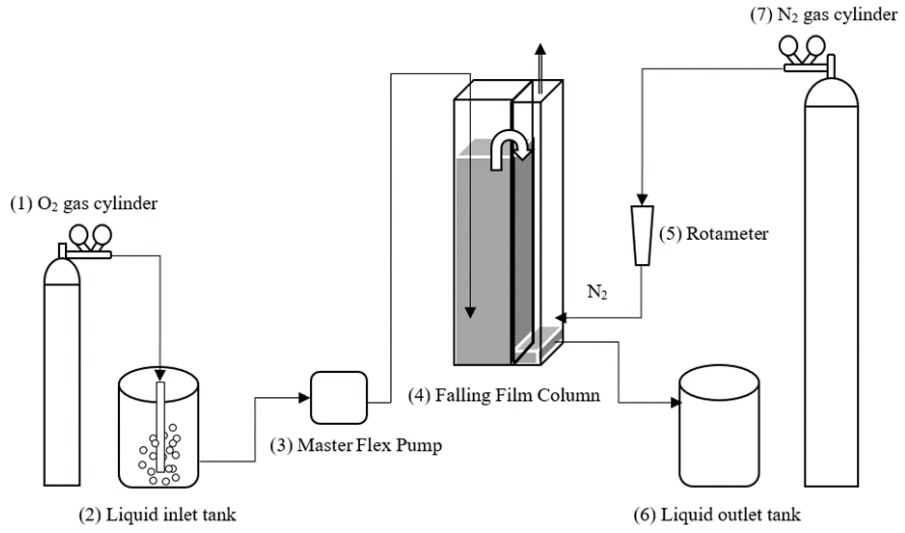

Figure 4. The falling film column system

The falling film column system consists of two different parts separated in the middle by a plate. The dimensions of the liquid chamber of the system are 55x200x60 mm and the dimensions of the gas chamber are 20x200x60 mm. The falling film column is made of plexiglass. To ensure smooth laminar flow over the plate in the middle, gas velocities are determined hydrodynamically as 0.0069, 0.0139, 0.0208, 0.0278, 0.0347 m·s^{-1} and liquid velocities 0.00606, 0.00808, 0.0101, 0.0121 m·s^{-1}. For the determination of the concentration of O_2 in the liquid inlet and outlet, a portative YSI Model 50B Dissolved Oxygen Meter was used.

2.2.2. Experimental Procedure

In the experiments, distilled water and sea water saturated with O_2 gas cylinder are fed to the system as liquid. During the laminar film flow over the middle plate, the dissolved oxygen in the liquid was desorbed into the nitrogen gas fed from the gas inlet of the system. During the experiments, three water samples for each gas velocity (into the 5 mL beakers) were obtained from the inlet and the outlet of the falling film column, and the concentration of O_2 in the liquid was measured instantaneously with a portative O_2 analyser. Experiments were carried out in 5 different gas and 4 different liquid velocities at 18°C temperature. Then, using the concentration of O_2 in the liquid, liquid side individual physical mass transfer coefficients were calculated.

2.2.3. Liquid Side Individual Physical Mass Transfer Coefficient

To determine the amount of O_2 passing from liquid to gas, the flux expression according to the two-resistance theory can be shown as (2.12).

$$\overline{N_A} = k_L^0 C_T (x_A - x_{A,i})_{LM} \tag{2.12}$$

where $\overline{N_A}$ is the average flux [kmol·m^{-2}·s^{-1}], k_L^0 is liquid side individual physical mass transfer coefficient [m·s^{-1}], C_T is the total concentration [kmol·m^{-3}], x_A [-] and $x_{A,i}$ are the mole fractions of liquid phase O_2 and the interfacial composition at the liquid side in equilibrium with the gas side O_2 composition, respectively.

If (2.12) is arranged, the liquid side individual physical mass transfer coefficients were calculated using (2.13).

$$k_L^0 = \frac{\overline{N_A}}{C_T(x_1 - x_2)}\, ln\frac{(x_1 - x_i)}{(x_2 - x_i)} \tag{2.13}$$

where x_1 and x_2 are the mole fractions of liquid phase O_2 at the inlet and outlet of the column, respectively. x_i value which is constant for the experimental temperature can be found in the literature, yet it was corrected for the ambient pressure [28]. According to both penetration and surface renewal theories in the literature, the mass transfer coefficient is directly proportional to the square root of the diffusion coefficient [33]. Therefore, the liquid side individual physical mass transfer coefficient of the CO_2 can be estimated using the correction factor as shown in (2.14) [33].

$$(\mathrm{k_L^0})_{\mathrm{CO_2}} = (\mathrm{k_L^0})_{\mathrm{O_2}} \sqrt{\frac{\mathrm{D_{CO_2-H_2O}}}{\mathrm{D_{O_2-H_2O}}}} \tag{2.14}$$

The diffusion coefficient of CO_2 in distilled water ($\mathrm{D_{CO_2-H_2O}}$) can be calculated as in (2.15) through the correlation developed by Versteeg and Van Swaaij, where the temperature is in [K] [34].

$$D_{CO_2-H_2O} = 2.35 \times 10^{-6} e^{-\frac{2119}{T}} \quad (2.15)$$

The diffusion coefficient of O_2 in water ($D_{O_2-H_2O}$) was calculated by the Wilke-Chang equation as shown in (2.16) [33].

$$D_{O_2-H_2O} = 1.17x10^{-13} \frac{\sqrt{\psi_B M_B} T}{\mu V_A^{0.6}} \quad (2.16)$$

where D_{AB} [$m^2 \cdot s^{-1}$] is diffusion coefficient, M_B [$kg \cdot kmol^{-1}$] is the molecular weight of the solvent, T [K] is temperature, V_A [$m^3 \cdot kmol^{-1}$] is the molar volume of solute at normal boiling temperature, μ [cp] is the viscosity of the solution and ψ_B [-] is association parameter for solvent B. Literature data from [35] were used for the diffusion coefficient of CO_2 in seawater at 18°C.

3. Results and Discussion

3.1. Total CO_2 Absorption Capacity and Dissolution Rate

As the result of stirred cell experiments, the dissolution rate (w), the rate of the absorption process relative to the total liquid volume (r), and the total CO_2 absorption capacity were calculated. All experiments were repeated 3 times and since the values are close to each other, the average values were determined for each solution. Firstly, 0-3.5 wt% NaCl experiments were carried out in stirred cell reactor. The results of the 0-3.5 wt% NaCl experiment are shown in Table 1.

Table 1. Experimental results of total CO_2 absorption capacity and dissolution rate for 0-3.5 wt% NaCl solutions

Solution	w* (mol/s)	r** (mol/m^3-s)	Total CO_2 absorption capacity (mol/L)
0 wt% NaCl (distilled-water)	2.90 x10^{-6}	0.0580	0.0048
0.5 wt% NaCl	2.70 x10^{-6}	0.0539	0.0046
1 wt% NaCl	2.65 x10^{-6}	0.0530	0.0045
1.5 wt% NaCl	2.61 x10^{-6}	0.0526	0.0044
2 wt% NaCl	2.58 x10^{-6}	0.0517	0.0040
2.5 wt % NaCl	2.48 x10^{-6}	0.0496	0.0040
3 wt % NaCl	2.43 x10^{-6}	0.0487	0.0039
3.5 wt % NaCl	2.42 x10^{-6}	0.0485	0.0038

*Dissolution rate

**The rate of the absorption process relative to the total liquid volume

The experimental results of the 0-3.5 wt% NaCl solutions are also shown in Figure 5 graphically.

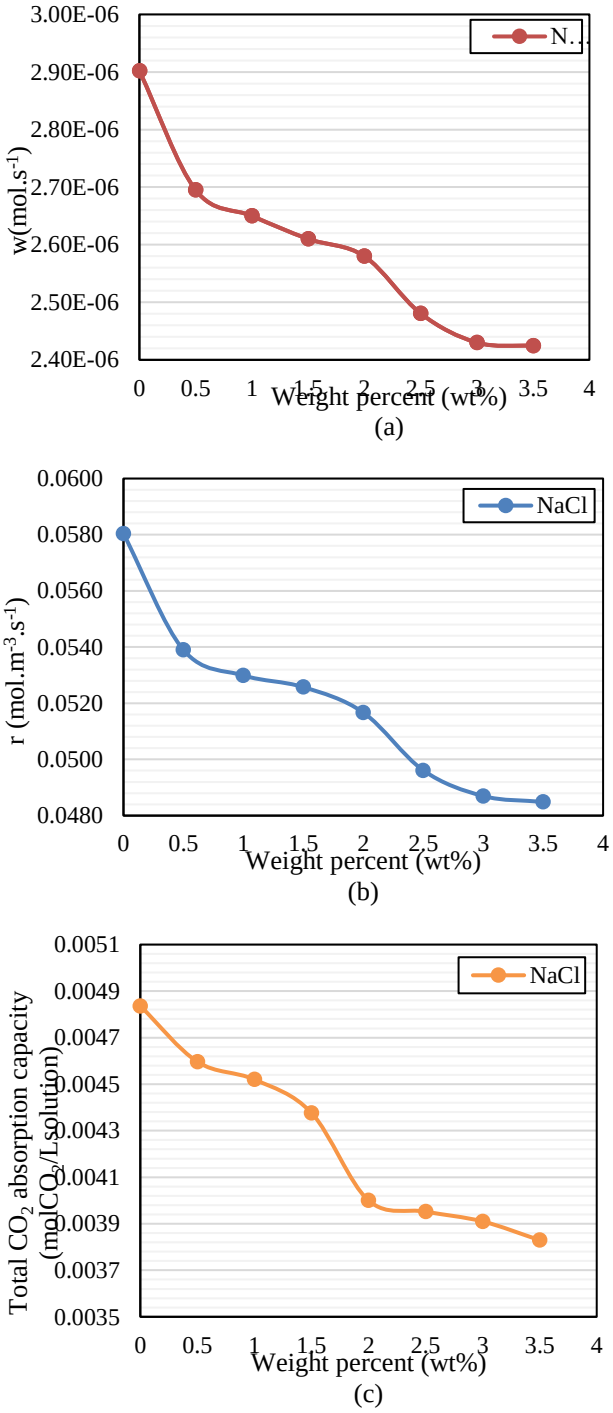

Figure 5. (a) The dissolution rate of CO_2 of 0-3.5 wt% NaCl solutions; (b) The rate of the absorption process relative to the total solution volume of 0-3.5 wt% NaCl solutions; (c) Total CO_2 absorption capacity of 0-3.5 wt% NaCl solutions

When Figure 5 is examined, the most striking result is the observation of a decreasing trend in absorption capacity and dissolution rate with increasing salinity. This result was compared with the literature and Li et al. [17] reported that Henry's constant increased and CO_2 solubility decreased with increasing salinity. Dissolved carbonate and bicarbonate ions in water will form more sodium carbonate in the presence of high salt concentration. For this reason, it can be said that there are more free carbonate and bicarbonate ions in water with lower salt concentrations. Therefore, it is an expected result that CO_2 absorption capacity decreases with increasing salinity.

Subsequently, the experiments were repeated by adding 0.4 v/v% CaO solution to 0-3.5 wt% NaCl solution. The results of the 0-3.5 wt% NaCl + 0.4 v/v% CaO solutions experiments are shown in Table 2.

Table 2. Experimental results of total CO_2 absorption capacity and dissolution rate for 0-3.5 wt% NaCl + 0.4 v/v% CaO solutions

Solution	w* (mol/s)	r** (mol/m^3-s)	Total CO_2 absorption capacity (mol/L)
0.5 wt% NaCl + 0.4 v/v% CaO	6.97 x10^{-6}	0.1395	0.01366
1 wt% NaCl + 0.4 v/v% CaO	6.67 x10^{-6}	0.1322	0.01345
1.5 wt% NaCl +0.4 v/v% CaO	6.54 x10^{-6}	0.1308	0.01293
2 wt% NaCl + 0.4 v/v% CaO	6.41 x10^{-6}	0.1281	0.01232
2.5 wt % NaCl + 0.4 v/v% CaO	6.15 x10^{-6}	0.1229	0.01161
3 wt % NaCl +0.4 v/v% CaO	5.20 x10^{-6}	0.0998	0.00890
3.5 wt % NaCl +0.4 v/v% CaO	4.82 x10^{-6}	0.0964	0.00830

*Dissolution rate

**The rate of the absorption process relative to the total liquid volume

The comparison results of the 0-3.5 wt% NaCl and 0-3.5 wt% NaCl + 0.4 v/v% CaO solutions are also shown in graphically Figure 6.

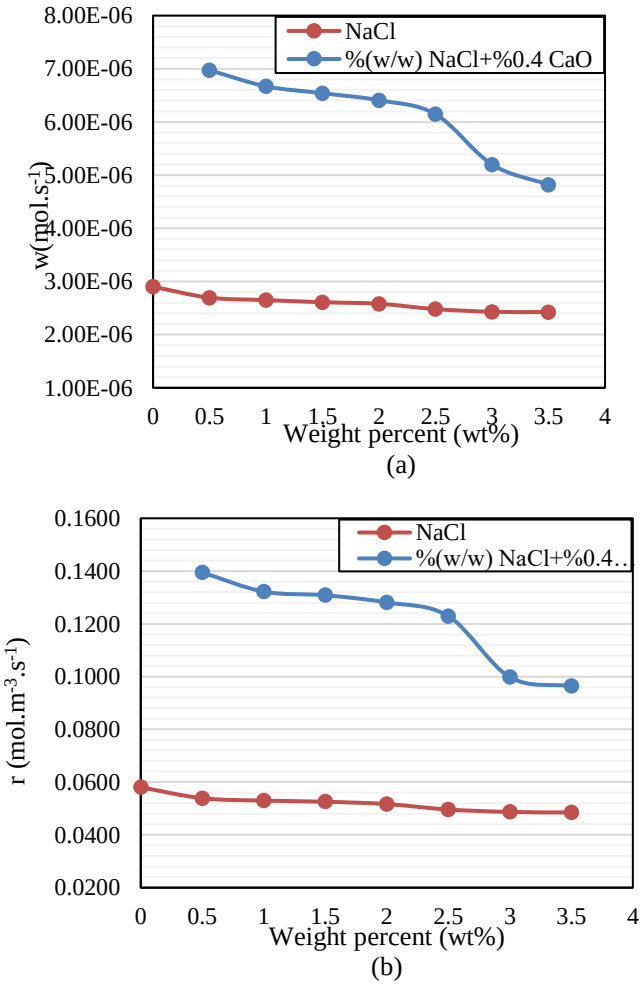

Figure 6. (a) The dissolution rate comparison of CO_2 of 0-3.5 wt% NaCl and 0-3.5 wt% NaCl + 0.4 v/v% CaO solutions; (b) The rate of the absorption process relative to the total solution volume comparison of 0-3.5 wt% NaCl and 0-3.5 wt% NaCl + 0.4 v/v% CaO solutions; (c) Total CO_2 absorption capacity comparison of 0-3.5 wt% NaCl and 0-3.5 wt% NaCl + 0.4 v/v% CaO solutions

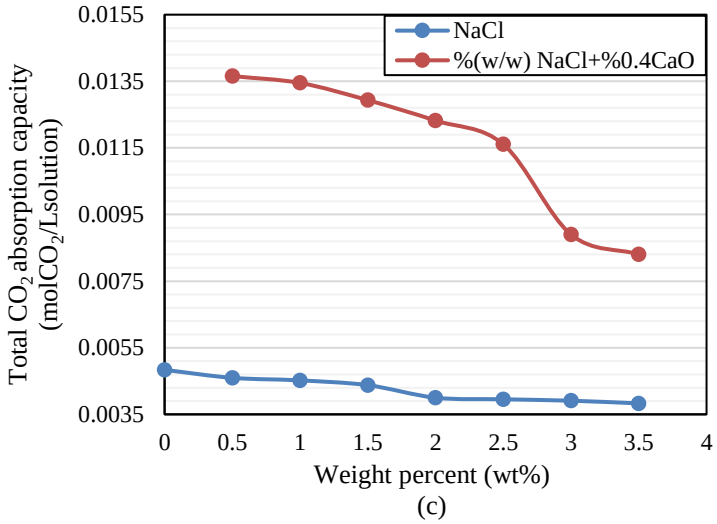

Figure 6. (Continued) (a) The dissolution rate comparison of CO_2 of 0-3.5 wt% NaCl and 0-3.5 wt% NaCl + 0.4 v/v% CaO solutions; (b) The rate of the absorption process relative to the total solution volume comparison of 0-3.5 wt% NaCl and 0-3.5 wt% NaCl + 0.4 v/v% CaO solutions; (c) Total CO_2 absorption capacity comparison of 0-3.5 wt% NaCl and 0-3.5 wt% NaCl + 0.4 v/v% CaO solutions

When Figure 6 is examined, it is clearly seen that CaO contribution to salty seawater has a positive effect. Seawater does not have the ability to form sufficient carbonate deposits itself. By dissolving in seawater, CaO increases the alkalinity of the water and increases the formation of carbonate and bicarbonate ions by promoting carbonic acid ionization in seawater. Increasing carbonate and bicarbonate ions also have a positive effect on CO_2 absorption potential. According to the results obtained, CaO addition increased the total CO_2 absorption capacity by 66%.

3.2. Liquid Side Individual Physical Mass Transfer Coefficient

As a result of falling film column experiments, liquid side individual physical mass transfer coefficients were calculated. The results of diffusion coefficient of CO_2 in distilled water and 3.5 wt% NaCl solution are shown in Table 3.

Table 3. Diffusion coefficients of distilled water, seawater and oxygen

$\mathbf{D_{CO_2-H_2O(distilled\ water)}}$ (m^2-s^{-1})	$\mathbf{D_{CO_2-H_2O(seawater)}}$ (m^2-s^{-1})	$\mathbf{D_{O_2-H_2O(distilled\ water)}}$ (m^2-s^{-1})	$\mathbf{D_{O_2-H_2O(seawater)}}$ (m^2-s^{-1})
1.617×10^{-9}	1.384×10^{-9}	2.780×10^{-9}	2.931×10^{-9}

The experimental results of the distilled water and 3.5 wt% NaCl solution with diffusion correction factor applied are shown in Figures 7 and 8, respectively.

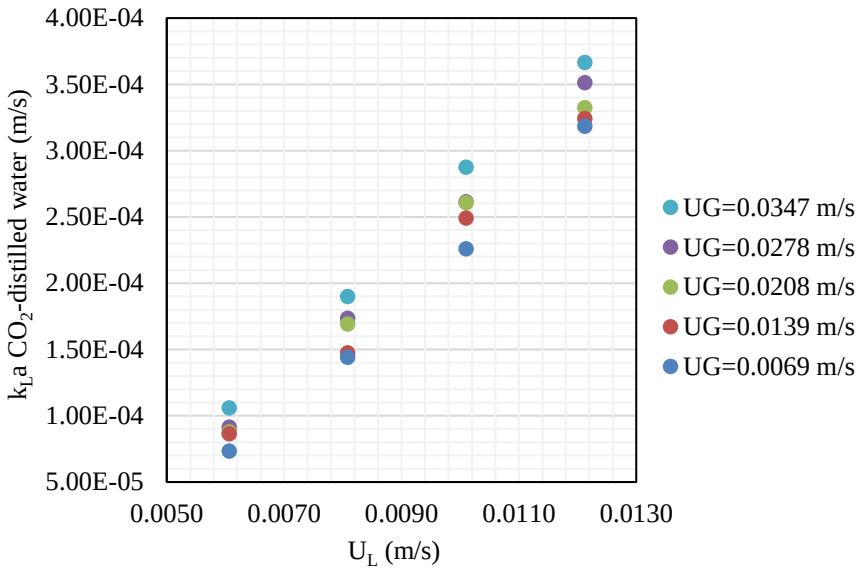

Figure 7. The liquid side individual physical mass transfer coefficients at different gas and liquid velocities by using oxygen desorption method-distilled water

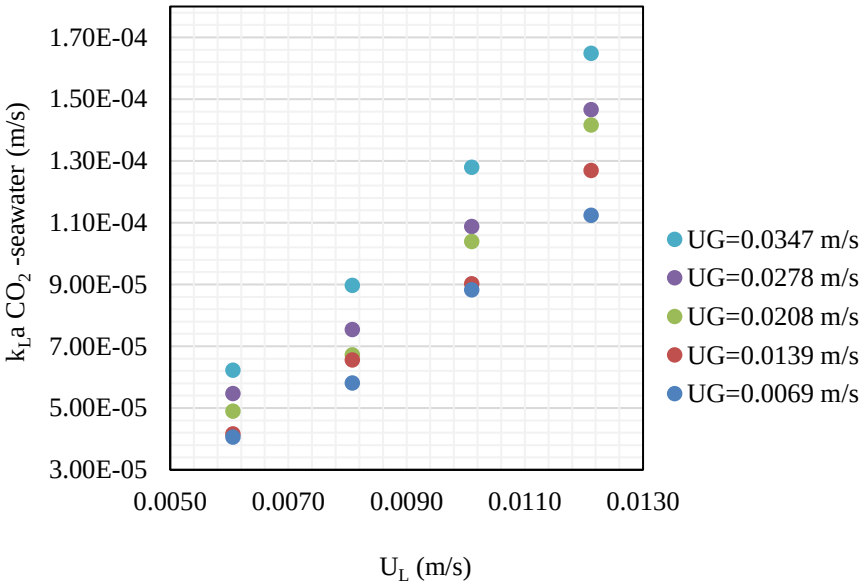

Figure 8. The liquid side individual physical mass transfer coefficients at different gas and liquid velocities by using oxygen desorption method-3.5 wt% NaCl solutions (as a seawater)

With the data obtained, the following correlation for the liquid side individual physical mass transfer coefficient of the CO_2 in water was developed with the nonlinear regression analysis and the regression coefficient was R^2=0.974.

$$k^0_{L\,(CO_2-distilled\ water)} = 1.230\ U_L^{1.829} U_G^{0.031} \tag{3.1}$$

With the data obtained, the following correlation for the liquid side individual physical mass transfer coefficient of the CO_2 in 3.5 wt% NaCl solution (as a seawater) was developed with the nonlinear regression analysis and the regression coefficient was R^2=0.904.

$$k_{L\,(CO_2-seawater)}^{0} = 0.153\ U_L^{1.543} U_G^{0.057} \tag{3.2}$$

As can be seen from the results, liquid side individual physical mass transfer coefficient correlations vary depending on both liquid and gas velocities. While the gas effect dominates at low liquid velocities, the liquid effect becomes dominant at high liquid velocities and the gas effect remains in the background. In this study, the liquid velocity operating range is higher than the gas velocity. Therefore, it is an expected result that the correlations are dependent on the liquid velocity. There are many k_L^0 correlations for distilled water in the literature and k_L^0 varies between 0.4-10x10^{-4} [m·s^{-1}] [28, 36, 37]. The results obtained from this study are in agreement with the literature. There are limited number of studies in the literature on the physical individual mass transfer coefficient of seawater. In their study, Cho & Choi [38] obtained k_L^0 in the range of 7.7-9.2x10^{-5} [m·s^{-1}] on average under 3-4 bar conditions. These results are similar to the results of this study in terms of order of magnitude.

4. Conclusion

In this study, experiments were carried out in two stages which are stirred cell and falling film column. In the stirred cell, the experiments were conducted at a concentration range of 0-3.5 wt% NaCl solutions and by adding CaO to NaCl solutions at the same concentration. When the experimental results were evaluated, it was observed that there was a decrease in CO_2 absorption performance as the salinity increased. When compared with the literature, it was seen that the study was in the same direction as the literature in terms of the effect of salinity. In the study, it was aimed to increase the CO_2 absorption capacity of the solution by adding CaO to the solution to increase the Ca^{+2} ion in the NaCl solution. As a result of the experiments, it was seen that adding CaO to NaCl solution had a positive effect on the results of total CO_2 absorption capacity (molCO_2·L^{-1} solution) and dissolution rate (mol·s^{-1}). When evaluated in terms of total CO_2 absorption capacity, it was determined that CaO-doped NaCl solutions absorbed CO_2 66% better than the pure NaCl solution. In the falling film column, the liquid side individual physical mass transfer coefficients (k_L^0) were determined by the oxygen (O_2) desorption method for pure water and 3.5 wt% NaCl solution. The results obtained were found to be compatible with the literature. Also, nonlinear regression analyses were performed, and correlations were developed for liquid side individual physical mass transfer coefficients.

Author Contributions

The first author collected data, performed the analysis, and wrote the paper. The second author conceived analysis, methodology, formal analysis, and review and edit of the paper. The third author also conceived the analysis and formal analysis. The fourth author designed the analysis and methodology. They all read and approved the final version of the paper.

Conflicts of Interest

All the authors declare no conflict of interest.

Acknowledgement

The authors would like to thank Hazel Sarıhan for her help in getting some experimental data for this study.

References

[1] IPCC, *Climate Change 2022: Impacts, Adaptation and Vulnerability*, in: H.-O. Pörtner, D. C. Roberts, M. Tignor, E. S. Poloczanska, K. Mintenbeck, A. Alegría, M. Craig, S. Langsdorf, S. Löschke, V. Möller, A. Okem, B. Rama (Eds.), Contribution of Working Group II to the Sixth Assessment Report of the Intergovernmental Panel on Climate Change, Switzerland, 2022, 35 pages.

[2] IPCC, *Global Warming of 1.5°C*, in: Masson-Delmotte, V., P. Zhai, H.-O. Pörtner, D. Roberts, J. Skea, P.R. Shukla, A. Pirani, W. Moufouma-Okia, C. Péan, R. Pidcock, S. Connors, J.B.R. Matthews, Y. Chen, X. Zhou, M.I. Gomis, E. Lonnoy, T. Maycock, M. Tignor, and T. Waterfield (Eds.) Intergovernmental Panel on Climate Change, Switzerland, 2018, pp. 541–562.

[3] H. Öztan, İ. Koçyiğit Çapoğlu, D. Uysal, Ö. M. Doğan, *A parametric study to optimize the temperature of hazelnut and walnut shell gasification for hydrogen and methane production*, Bioresource Technology Reports 23 (2023) 101581.

[4] Ö. Yörük, D. Uysal Zıraman, B. Z. Uysal, *Absorption of sulfur dioxide by iron(ii) hydroxide solution in a multiplate bubble column under magnetic field*, Chemical Engineering & Technology 44 (1) (2021) 1336–1342.

[5] Y. Yagizatli, B. Ulas, A. Sahin, İ. Ar, *Investigation of sulfonation reaction kinetics and effect of sulfonation degree on membrane characteristics for PEMFC performance*, Ionics 28 (5) (2022) 2323–2336.

[6] R. Baumler, M. C. Arce, A. Pazaver, *Quantification of influence and interest at IMO in Maritime Safety and Human Element matters*, Marine Policy 133 (2021) 104746 12 pages.

[7] H. Al Baroudi, A. Awoyomi, K. Patchigolla, K. Jonnalagadda, E. J. Anthony, *A review of large-scale CO_2 shipping and marine emissions management for carbon capture, utilisation and storage*, Applied Energy 287 (2021) 116510 42 pages.

[8] Z. Zhang, D. Huisingh, *Carbon dioxide storage schemes: Technology, assessment and deployment*, Journal of Cleaner Production 142 (2) (2017) 1055–1064.

[9] A. A. Olajire, *CO_2 capture and separation technologies for end-of-pipe applications–A review*, Energy 35 (6) (2010) 2610–2628.

[10] J. Buckingham, T. R. Reina, M. S. Duyar, *Recent advances in carbon dioxide capture for process intensification*, Carbon Capture Science & Technology 2 (95) (2022) 100031 19 pages.

[11] F. O. Ochedi, J. Yu, H. Yu, Y. Liu, A. Hussain, *Carbon dioxide capture using liquid absorption methods: a review*, Environmental Chemistry Letters 19 (2021) 77–109.

[12] S. Ahn, H. J. Song, J. W. Park, J. H. Lee, I. Y. Lee, K. R. Jang, *Characterization of metal corrosion by aqueous amino acid salts for the capture of CO_2*, Korean Journal of Chemical Engineering, 27 (5) (2010) 1576–1580.

[13] I. M. Bernhardsen, H. K. Knuutila, *A review of potential amine solvents for CO_2 absorption process: absorption capacity, cyclic capacity and pKa*, International Journal of Greenhouse Gas Control 61 (2017) 27–48.

[14] M. Wang, A. Lawal, P. Stephenson, J. Sidders, C. Ramshaw, *Post-combustion CO_2 capture with chemical absorption: A state-of-art review*, Chemical Engineering Research and Design 89 (9) (2011) 1609–1624.

[15] D. Uysal, Ö. M. Dogan, B. Z. Uysal, *Kinetics of absorption of carbon dioxide into sodium metaborate solution*, International Journal of Chemical Kinetics 49 (6) (2017) 377–386.

[16] G. Genç Çelikçi, D. Uysal, B. Z. Uysal, *Absorption of carbon dioxide into n-butanol and ethyl acetate in a column with structured packing*, Chemical Engineering & Technology 45 (8) (2022) 1489–1496.

[17] H. Li, Z. Tang, N. Li, L. Cui, X-Z. Mao, *Mechanism and process study on steel slag enhancement for CO_2 capture by seawater*, Applied Energy 276 (2020) 115515 14 pages.

[18] M. H. El-Naas, A. H. Al-Marzouqi, O. Chaalal, *A combined approach for the management of desalination reject brine and capture of CO_2*, Desalination 251 (1-3) (2010) 70–74.

[19] W. Wang, M. Hu, Y. Zheng, P. Wang, C. Ma, *CO_2 fixation in Ca^{2+}-/Mg^{2+}-rich aqueous solutions through enhanced carbonate precipitation*, Industrial & Engineering Chemistry Research 50 (13) (2011) 8333–8339.

[20] W. Wang, X. Liu, P. Wang, Y. Zheng, M. Wang, *Enhancement of CO_2 Mineralization in Ca^{2+}-/Mg^{2+}-rich aqueous solutions using insoluble amine*, Industrial & Engineering Chemistry Research 52 (23) (2013) 8028–8033.

[21] A. Said, H. -P. Mattila, M. Järvinen, R. Zevenhoven, *Production of precipitated calcium carbonate (PCC) from steelmaking slag for fixation of CO_2*, Applied Energy 112 (2013) 765–771.

[22] A. Said, T. Laukkanen, M. Järvinen, *Pilot-scale experimental work on carbon dioxide sequestration using steelmaking slag*, Applied Energy 177 (1) (2016) 602–611.

[23] L. Kucka, J. Richter, E. Y. Kenig, A. Górak, *Determination of gas–liquid reaction kinetics with a stirred cell reactor*, Separation & Purification Technology 31 (2) (2003) 163–175.

[24] J. Ying, D. A Eimer. D*etermination and measurements of mass transfer kinetics of co_2 in concentrated aqueous monoethanolamine solutions by a stirred cell*, Industrial & Engineering Chemistry Research 52 (7) (2013) 2548–2559.

[25] J. M. Smith, H. C. Van Ness, M. M. Abbott, M. T. Swihart, Introduction to chemical engineering thermodynamics, Mc Graw-Hill, New York, 2022.

[26] S. I. Sandler, Chemical, biochemical and engineering thermodynamics, 4th Edition, John Wiley & Sons Inc., New York, 2006.

[27] G. Genç Çelikçi, *Carbon dioxide capture in structured packing column with n-butanol and ethyl acetate*, Doctoral Dissertation Gazi University (2020) Ankara.

[28] D. Uysal, *Absorption of carbon dioxide into calcium acetate solution*, Doctoral Dissertation Gazi University (2016) Ankara.

[29] A. H. G. Cents, F. T. de Brujin, D. W. F. Brilman, G. F. Versteeg, *Validation of the Danckwerts-plot technique by simultaneous chemical absorption of CO_2 and physical desorption of O_2*, Chemical Engineering Science 60 (21) (2005) 5809–5818.

[30] A. Hoffmann, J. Maćkowiak, A. Gorak, M. Haas, J. M. Löning, T. Runowski, K. Hallenberger, *Standardization of mass transfer measurements: a basis for the description of absorption processes*, Chemical Engineering Research & Design 85 (1) (2007) 40–49.

[31] C. D. Park, T. Nosoko, *Three-dimensional wave dynamics on a falling film and associated mass transfer*, AIChe Journal 49 (11) (2003) 2715–2727.

[32] C. Wang, Z. Xu, C. Lai, X. Sun, *Beyond the standard two-film theory: Computational fluid dynamics simulations for carbon dioxide capture in a wetted wall column*, Chemical Engineering Science 184 (2018) 103–110.

[33] B. Z. Uysal, Mass transfer-fundamentals and applications (in Turkish), 3th Edition, Gazi Kitabevi, Ankara, 2019.

[34] G. F.,Versteeg, W. P. Van Swaaij, *Solubility and diffusivity of acid gases (carbon dioxide, nitrous oxide) in aqueous alkanolamine solutions*, Journal of Chemical Engineering Data 33 (1988) 29–34.

[35] A. Poisson, A. Papaud, *Diffusion coefficients of major ions in seawater*, Marine Chemistry 13 (4) (1983) 265–280.

[36] A. P. Lamourelle, O. C. Sandall, *Gas absorption into a turbulent liquid*, Chemical Enginering Science 27 (5) (1972) 1035–1043.

[37] S-M. Yih, K. -Y. Chen, *Gas absorption into wavy and turbulent falling liquid films in a wetted-wall column*, Chemical Engineering Communications 17 (1-6) (1982) 123–136.

[38] H. -J. Cho, J. Choi, *Calculation of the mass transfer coefficient for the dissolution of multiple carbon dioxide bubbles in sea water under varying conditions*, Journal of Marine Science and Engineering 7 (12) (2019) 457 11 pages.

Çanakkale Onsekiz Mart University

Journal of Advanced Research in Natural and Applied Sciences

dergipark.org.tr/tr/pub/jarnas

Open Access

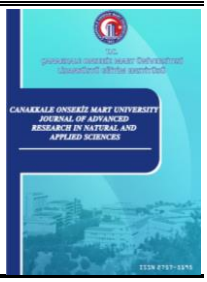

e-ISSN: 2757-5195 2024, Vol. 10, Issue 2, Pages: 415-425 doi.org/10.28979/jarnas.1418948

Synthesis of *E*-Isomer of *α*-Hydrazone Phosphonates via Nucleophilic Addition of Trialkyl Phosphite to Nitrile Imines (NIs) and DFT Calculations

Sıdıka Polat Çakır[1], Sinem Altınışık[2]

[1,2]Department of Chemical Engineering, Faculty of Engineering, Çanakkale Onsekiz Mart University, Çanakkale, Türkiye
[2]Department of Energy Resources and Management, School of Graduate Studies, Çanakkale Onsekiz Mart University, Çanakkale, Türkiye

Article History

Received: 12 Jan 2024

Accepted: 26 Mar 2024

Published: 25 Jun 2024

Research Article

Abstract − Nitrile imines (NIs) belong to the nitrilium betaine family of 1,3-dipoles. Due to their high reactivity, NI compounds cannot be isolated and must be generated *in situ* before undergoing the desired transformation. NI derivatives were prepared by the utilization of *N*-phenyl hydrazine chloride precursors in the presence of a base. The title compounds *α*-hydrazone phosphonates have the potential to be biologically active and may serve as a precursor compound for other biologically active substances like amino phosphonic acids. Shortly, they are highly significant compounds in medicinal and synthetic chemistry. The derivatives of *α*-hydrazone phosphonate are synthesized by the nucleophilic addition of trialkyl phosphite to *in situ* generated NI derivatives and obtained in 44-95% isolated chemical yields. It is worth noting that only the *E*-isomer of the *α*-hydrazone phosphonates was obtained. Structural analyses of the *α*-hydrazone phosphonates were conducted by using proton and carbon NMR analysis along with FTIR. The researchers also performed DFT calculations including structural parameters (bond length, bond angle, and dihedral angle), HOMO and LUMO energy levels, and the zero-point vibrational energy (ZPE) for both *E* and *Z* geometric isomers of unsubstituted phenyl *α*-hydrazone phosphonate.

Keywords − *Nitrile imines, nucleophilic addition, trialkyl phosphite, 1,3-dipole, α-hydrazone phosphonates*

1. Introduction

The Nitrile imines (NI) are members of the nitrilium betaine family, one of the 1,3-dipole varieties [1]. NIs are very reactive unstable compounds and are generated *in situ* rather than isolated as pure compounds. Since NIs are highly reactive, they cannot be isolated, and they are prepared in the reaction medium, and the relevant reaction is carried out. Here are some common methods for the generation of NI derivatives: Decomposition of tetrazole compounds [2], catalytic oxidation of hydrazine compounds [3], and N-phenyl hydrazine chloride/bromide precursors [4]. Currently, the most common method to generate NI is the dehalogenation of the *N*-phenyl hydrazine chloride/bromide precursors in the presence of a base. This procedure includes deprotonation followed by the removal of the halide ion. The formation of NIs from hydrazonyl chlorides was described first by Huisgen et al. [2]. Huisgen contributed valuable insights to NI chemistry through numerous publications [5-7].

Although the most prevalent application of NIs involves their use as 1,3-dipoles in cycloaddition reactions to have access to *N*-based heterocyclic compounds, their utilization in nucleophilic addition reactions with substances such as alcohols, amines, thiols, carboxylic acids, and triphenylphosphine is seldom documented

[1]spcakir@comu.edu.tr (Corresponding Author); [2]sinemaltinisik@comu.edu.tr

in existing literature [8-11]. Surprisingly, there is no detailed research concerning the nucleophilic addition reaction of trialkyl phosphite reagents (triethyl phosphite/trimethyl phosphite) to NI derivatives. (Scheme 1). *α*-Hydrazone phosphonates serve as precursors to *α*-amino phosphonates. The asymmetric synthesis of *α*-amino phosphonates is still a challenging process. *α*-Amino phosphonates are the close analogs of *α*-amino acids. Having phosphonate groups in its structure gives them unique properties and makes them valuable in various chemical and biological applications. *α*-Hydrazone phosphonate derivatives are of significant value in organic chemistry due to their role in accessing biologically active compounds containing phosphonate groups.

In the existing literature, one of the synthetic approaches for the synthesis of *α*-hydrazone phosphonates [12] is reacting phenylhydrazine with aroylphosphonate in pyridine as the solvent. Only the *Z* isomer of *α*-hydrazone phosphonate was isolated in 81% yield. The equilibrium between *Z* and *E* isomers was achieved by heating in acetic acid. Aroylphosphonates are not readily available and are prepared from benzoyl chloride. While the preparation of aroylphosphonate itself proceeds smoothly, the purification process demands high temperatures under vacuum conditions. The other work in the literature reported by Baccolini et al. [13] involves direct nucleophilic addition of triethyl phosphite/trimethyl phosphite to only diphenylnitrilimines. The reaction was carried out in benzene and the compound **2a** was isolated in 70% yields as a mixture of *E* and *Z* isomers with the 2:3 ratios. We have provided a detailed investigation of simple nucleophilic addition of trialkyl phosphite to NI derivatives to obtain *α*-hydrazone phosphonate derivatives to give solely *E* isomer. Although the *Z*-isomer is stable due to H-bonding, *E* configuration is less hindered.

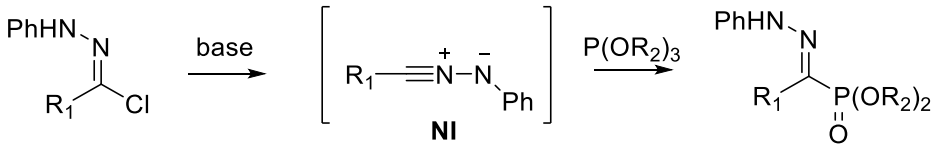

Scheme 1. General method for the nucleophilic addition of trialkyl phosphite to NI

2. Materials and Methods

All solvents used in the reaction are commercially available and of sufficient purity. Reaction stages were monitored under UV light using TLC (Thin-Layer Chromatography). Both proton and carbon spectra were recorded in $CDCl_3$ solution; at 400 MHz and 100 MHz, respectively. In these spectra, the TMS (tetramethylsilane) peak was used as the reference solvent. All *J* values in the spectrum are in Hz; s, singlet; d, doublet; t, triplet; q, quartet; m, multiplet, indicating multiple peaks. Both trialkyl phosphites are commercially available and used without any purification. The information regarding the known compounds aligns with the values documented in the report by Kaushik et al. [12] and Baccolini et al. [13].

Commercially unavailable *N*-phenyl arylhydrazonoyl chloride compounds were prepared in two steps by following the literature procedure starting from the corresponding aldehydes [14]. Aldehyde (1 equivalent) and phenylhydrazine (1 equivalent) reagents were dissolved in 50 mL of ethanol. The mixture was stirred at room temperature for approximately 2 hours until the aldehyde reagent was completely consumed which was monitored by TLC. Afterward, the reaction mixture was concentrated under a vacuum, and the expected product aryl aryl-substituted *N*-phenyl hydrazone was obtained as a solid and used for the next step. In the chlorination step, NCS (3 equivalents) was dissolved in DCM (100 mL) by stirring at 0°C for 5 minutes. Subsequently, $S(CH_3)_2$ (6 equivalents) was introduced drop by drop, and the mixture was stirred for 15 minutes. After the formation of a white solid product, the *N*-phenyl arylhydrazone compound (1 equivalent, 20 mL DCM) was added dropwise to the reaction medium. The reaction was stirred for 2 hours at 0°C, and then cold distilled water was added to quench the reaction. Following the extraction, the organic phase was

isolated, and the joined organic phase underwent washing with a saturated salt solution. The acquired organic phase was subsequently dried over sodium sulfate, filtered, and ultimately concentrated using a rotary evaporator. The resulting solid product, *N*-phenyl arylhydrazonoyl chloride, was used in the nucleophilic addition reaction without the need for any purification process.

3. Results and Discussion

3.1. Synthesis of Compounds 2a-j

There are no detailed studies in the literature that explore the addition reaction of trialkyl phosphites to NI derivatives. For this purpose, the optimization reaction has been carried out by using unsubstituted *N*-phenyl arylhydrazonoyl chloride **1a** and triethyl phosphite as shown in Table 1. *N*-Cl hydrazone compounds **1a-e** were easily prepared by following the literature procedure [14]. The generation of NI has been tested by using different bases such as triethyl amine, isopropyl amine, Ag_2CO_3, and Na_2CO_3. We have found that when the reaction was carried out in toluene and triethyl amine (entry 2) as the choice of base, the anticipated adduct **2a** was obtained in 72% yield. Isopropyl amine also gave the expected product **2a** (entry 6) albeit in low yield (55%). Inorganic bases such as Ag_2CO_3 and Na_2CO_3 were also tested in nucleophilic addition reaction of triethyl phosphite to NI **1a**. The former base did not give the product, but the later base gave the compound **2a** in acceptable chemical yield (entry 5, 63%). In all cases, we have isolated the ***E***-isomer of compound **2a**.

Table 1. Optimization reactions

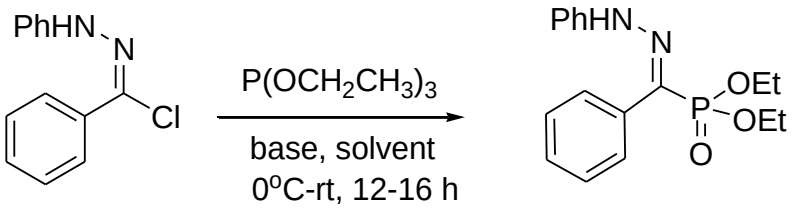

1a **2a**

Entry	Base[a]	Solvent	Yield (%)[b]
1	NEt_3	dichloromethane	67
2	NEt_3	toluene	72
3	NEt_3	asetonitrile	50
4	Ag_2CO_3	toluene[c]	-
5	Na_2CO_3	EtOAc	63
6	$NH(CHCH_3)_2$	toluene	55

[a]NI (1 equiv.), triethyl phosphite (1.2 equiv), and base (1.5 equiv.) [b]Isolated chemical yields. [c]No formation of product.

We have investigated the addition of triethyl phosphite/trimethyl phosphite to NI derivatives in the presence of triethyl amine as a choice of base. All NI derivatives were prepared *in situ* first and then trialkyl phosphite was introduced into the reaction mixture. In all cases, the expected compounds **2a-j** were obtained in good yields of 44%-95% as shown in Table 2. In the nucleophilic addition of trimethyl phosphite to NI both toluene and DCM were tested. Better chemical yields were obtained in the case of DCM (77%) and in the case of nucleophilic addition of trimethyl phosphite, DCM is the choice of solvent. It's worth noting that only the *E*-isomer of the *α*-hydrazone phosphonate compounds was obtained. We have tried to choose the different substituents at *para* position (CH_3, Br, and Cl and NO_2) in the aryl group. At *para* position, there is a direct effect on electrophilic properties of the *in situ* generated NI derivatives via resonance.

Table 2. Synthesis of α-hydrazone phosphonates **2a-j**

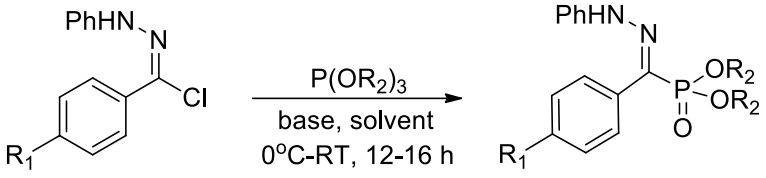

1 **2**

R_1= H (**1a**), CH_3 (**1b**), Br (**1c**), Cl (**1d**), NO_2(**1e**)

R_2= CH_2CH_3 (**2a-e**) and CH_3(**2f-j**)

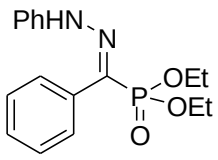

2a, 72%[a]

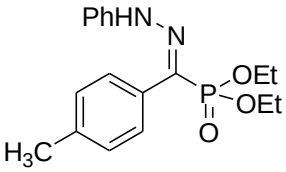

2b, 95%

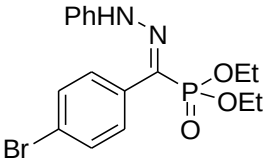

2c, 74%

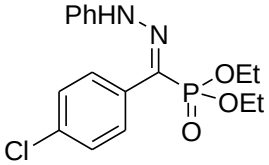

2d, 82%

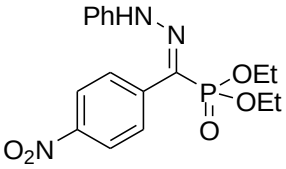

2e, 62%

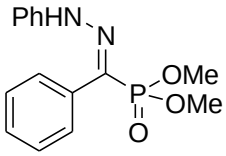

2f, 77% (DCM)[b]

61% (toluene)

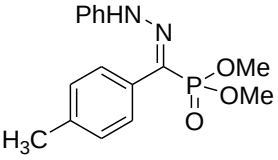

2g, 82%

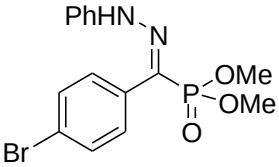

2h, 44%

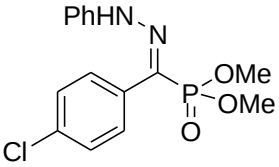

2i, 47%

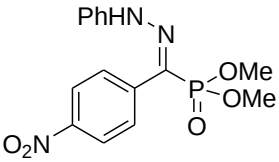

2j, 78%

[a]The reaction was carried out in toluene in the case of triethyl phosphite addition. [b] The reaction carried out in DCM in the case of trimethyl phosphite addition

The synthesized compounds **2a-j** were analyzed by using spectroscopic methods. In the FT-IR spectrum compound **2a** the signal around 3200 cm^{-1} corresponds to the NH group, the signal around 1600 cm^{-1} is attributed to the C=N bond, the broad signal at 1200 cm^{-1} is related to the P=O bond, and finally, the signal at 970 cm^{-1} is due to the vibration of the P-O bond. In the proton NMR spectrum of compound **2a**, the signals corresponding to the -OCH_2 moiety attached to the phosphonate group, -$P(OCH_2CH_3)_2$, were observed in the range of 4.23-4.14 ppm, while the signal attributed to the -CH_3 group appeared at 1.31 ppm. The existence of a signal for the H atom attached to the -NHPh indicated the formation of the *E*-isomer of α-hydrazone phosphonate (Table 3). In the *Z*-isomer, this H-atom is involved in hydrogen bonding and does not give any signals in proton NMR [12,13]. When examining the carbon NMR spectra of this compound **2a** the quaternary C-atom of C=N attached to the phosphonate group exhibited a doublet due to the coupling with the P-atom, and a large coupling constant was observed and summarized in Table 3. In compound **2a**, the quaternary C-atom (C=N) attached to the phosphonate group showed a signal at 136 ppm as a doublet with splitting by the neighboring P-atom, with a coupling constant of 239.9 Hz.

Table 3. ^{1}H NMR data for signal -NHPh and ^{13}C NMR data for quaternary carbon C=N in compounds **2a-j**

Compound **2**	^{1}H NMR of -NHPh (in ppm)	^{13}C NMR chemical shifts (in ppm) and coupling constant values (*J* in Hz)
2a	8.15	136.0 (d, *J* = 239.9 Hz)
2b	8.22	136.3 (d, *J* = 237.9 Hz)
2c	8.15	134.8 (d, *J* = 242.3 Hz)
2d	8.15	134.6 (d, *J* = 242.1 Hz)
2e	12.4	124.8 (d, *J* = 236.7 Hz)
2f	8.23	135.2 (d, *J* = 240.1 Hz)
2g	8.15	135.6 (d, *J* = 240.0 Hz)
2h	8.15	133.9 (d, *J* = 242.2 Hz)
2i	8.20	133.9 (d, *J* = 242.2 Hz)
2j	12.3	124.9 (d, *J* = 234.0 Hz)

3.1.1. Experimental Part

General Procedure for the synthesis of compound **2**: To a solution of N-chloroaroylhydrazine (1 equiv.) in toluene or DCM (0.5 M) triethyl amine (1.5 equiv.) was added at 0 ºC. After five minutes at this temperature, trialkyl phosphite (1.2 equiv.) was added drop by drop. The reaction mixture was stirred at ambient temperature for about 12-16 hours and then subjected to purification. The raw product underwent purification on silica gel utilizing hexane:EtOAc mixture as the eluting solvent.

- *(E)-diethyl (2-phenylhydrazono) (phenyl) methylphosphonate* 2a: Yellow oil, R_f=0.25 (1:1, hexane:EtOAc. ^{1}H ($CDCl_3$, 400 MHz, ppm): δ 8.15 (s, 1H, NHPh), 7.51 (t, *J* = 7.3 Hz, 2H), 7.42 (t, *J* = 7.6 Hz, 3H), 7.19 – 7.27 (m, 2H), 7.03 (d, *J* = 8.1 Hz, 2H), 6.91 (t, *J* = 7.4 Hz, 1H), 4.23 – 4.14 (m, 4H, $PO(OCH_2CH_3)_2$), 1.31 (t, *J* = 7.0 Hz, 6H, $PO(OCH_2CH_3)_2$). ^{13}C NMR (101 MHz, $CDCl_3$, ppm): δ 142.7 (C), 136.0 (d, *J* = 239.9 Hz, C=N), 129.9 (d, *J* = 22.6 Hz, C), 129.5, 129.4 (x2), 129.0 (x2), 128.50, 128.46, 121.6, 113.4 (x2), 62.8 (d, *J* = 6.1 Hz, $P(OCH_2CH_3)_2$), 16.2 (t, *J* = 6.7 Hz, $P(OCH_2CH_3)_2$). FT-IR (cm^{-1}): 3220, 2981, 1600, 1548, 1502, 1228, 1019, 970, 752, 695.
- *(E)-diethyl (2-phenylhydrazono) (p-tolyl) methylphosphonate* 2b: Yellow oil, R_f= 0.46 (1:1, hexane:EtOAc). ^{1}H ($CDCl_3$, 400 MHz, ppm): δ 8.22 (s, 1H, NHPh), 7.31 (s, 4H), 7.23 (dd, *J* = 8.5, 7.2 Hz, 2H), 7.04 (d, *J* = 7.5 Hz, 2H), 6.90 (t, *J* = 7.4 Hz, 1H), 4.24 – 4.08 (m, 4H, $PO(OCH_2CH_3)_2$), 2.34 (s, CH_3), 1.33 (dt, *J* = 11.0, 7.1 Hz, 6H, $PO(OCH_2CH_3)_2$). ^{13}C NMR (101 MHz, *$CDCl_3$*, ppm): δ 142.8 (C), 139.6 (C), 136.3 (d, *J* = 237.9 Hz, C=N), 130.1 (x2), 128.4 (x2), 128.37, 128.32, 126.8 (d, *J* = 22.8 Hz, C), 121.4, 113.3 (x2), 62.8 (d, *J* = 6.1 Hz, $P(OCH_2CH_3)$), 61.6 (d, *J* = 5.8 Hz, $P(OCH_2CH_3)_2$), 21.3 (CH_3), 16.2 (t, *J* = 6.5 Hz, $P(OCH_2CH_3)_2$). FT-IR (cm^{-1}): 3224, 2981, 1604, 1546, 1502, 1228, 1027, 970, 752, 662.
- *(E)-diethyl (2-phenylhydrazono) (4-bromophenyl) methylphosphonate* 2c: Yellow oil, R_f= 0.58 (1:1 hexane:EtOAc). ^{1}H ($CDCl_3$, 400 MHz, ppm): δ 8.15 (s, 1H, NHPh), 7.46 (d, *J* = 8.2 Hz, 2H), 7.35 (d, *J* = 7.9 Hz, 2H), 7.21 (d, *J* = 7.8 Hz, 2H), 7.03 (d, *J* = 7.8 Hz, 2H), 6.90 (t, *J* = 7.3 Hz, 1H), 4.19–4.05 (m, 4H, $PO(OCH_2CH_3)_2$), 1.30 (t, *J* = 8.0 Hz, 6H, $PO(OCH_2CH_3)_2$). ^{13}C NMR (101 MHz, $CDCl_3$, ppm): δ 142.6 (C), 135.6 (C-Cl), 134.8 (d, *J* = 242.3 Hz, C=N), 130.15, 130.11, 129.8 (x2), 129.1 (x2), 128.4 (d, *J* = 21.8 Hz, C), 121.9, 113.5 (x2), 62.9 (d, *J* = 6.1 Hz, $P(OCH_2CH_3)_2$), 61.7 (d, *J* = 5.6 Hz, $P(OCH_2CH_3)_2$), 16.2 (t, *J* = 6.8 Hz, $P(OCH_2CH_3)_2$). FT-IR (cm^{-1}): 3221, 2982, 1604, 1548, 1496, 1229, 1025, 972, 751, 656.

- *(E)-diethyl (2-phenylhydrazono) (4-chlorophenyl) methylphosphonate* 2d: Yellow oil, R_f= 0.46 (1:1 hexane:EtOAc). ^{1}H ($CDCl_3$, 400 MHz, ppm): δ 8.15 (s, 1H, NHPh), 7.54 (d, J = 8.3 Hz, 2H), 7.21 (d, J = 8.4 Hz, 2H), 7.13 (t, J = 8.0 Hz, 2H), 6.96 (d, J = 7.5 Hz, 2H), 6.82 (t, J = 7.3 Hz, 1H), 4.12–3.97 (m, 4H, $PO(OCH_2CH_3)_2$), 1.24 (t, J = 7.8 Hz, 6H, $PO(OCH_2CH_3)_2$). ^{13}C NMR (101 MHz, $CDCl_3$, ppm): δ 142.6 (C), 134.6 (d, J = 242.1 Hz, C=N), 132.7 (x2), 130.34, 130.30, 129.1 (x2), 128.8 (d, J = 23.0 Hz, C), 123.9 (C-Br), 121.8, 113.5 (x2), 62.9 (d, J = 6.2 Hz, $P(OCH_2CH_3)_2$), 61.7 (d, J = 5.6 Hz, $P(OCH_2CH_3)_2$), 16.1 (t, J = 6.7 Hz, $P(OCH_2CH_3)_2$). FT-IR (cm^{-1}): 3217, 2981, 1605, 1548, 1236, 1024, 972, 755, 696.

- *(E)-diethyl (2-phenylhydrazono) (4-nitrophenyl) methylphosphonate* 2e: Light brown oil, R_f= 0.62 (2:1 hexane:EtOAc). ^{1}H ($CDCl_3$, 400 MHz, ppm): δ 12.4 (s, 1H, NHPh), 8.11 (d, J = 8.5 Hz, 2H), 7.87 (d, J = 8.7 Hz, 2H), 7.30–7.15 (m, 4H), 6.94 (d, J = 7.1 Hz, 1H), 4.18–3.99 (m, 4H, $PO(OCH_2CH_3)_2$), 1.25 (t, J = 6.4 Hz, 6H, $PO(OCH_2CH_3)_2$). ^{13}C NMR (101 MHz, $CDCl_3$, ppm): δ 146.3, 143.1 (d, J = 26.8 Hz), 142.7, 129.7, 128.9, 126.1, 124.8 (d, J = 236.7 Hz, C=N), 123.4, 114.8, 113.8, 62.9 (d, J = 4.4 Hz, $P(OCH_2CH_3)_2$), 16.1 (t, J = 5.4 Hz, $P(OCH_2CH_3)_2$). FT-IR (cm^{-1}): 3162, 2963, 1594, 1466, 1330, 1264, 1013, 964.

- *(E)-dimethyl (2-phenylhydrazono) (phenyl) methylphosphonate* 2f: Yellow oil, R_f= 0.38 (2:1 Hexane:EtOAc). ^{1}H ($CDCl_3$, 400 MHz, ppm): δ 8.23 (s, 1H, NHPh), 7.49 (d, J = 7.1 Hz, 2H), 7.41 (t, J = 8.1 Hz, 3H), 7.21 (t, J = 8.0 Hz, 2H), 7.02 (d, J = 8.6 Hz, 2H), 6.89 (t, J = 7.3 Hz, 1H), 3.80 (d, J = 11.0 Hz, $PO(OCH_3)_2$, 6H). ^{13}C NMR (101 MHz, $CDCl_3$, ppm): δ 142.6, 135.2 (d, J = 240.1 Hz, C=N), 129.8, 129.6, 129.5 (x2), 129.1 (x2), 128.4 (d, J = 4.0 Hz, x2), 121.7, 113.4 (x2), 53.4 (d, J = 4.0 Hz, $P(OCH_3)_2$). FT-IR (cm^{-1}): 3197, 2952, 1702, 1546, 1226, 1179, 1017, 831, 753, 692.

- *(E)-dimethyl (2-phenylhydrazono) (p-tolyl) methylphosphonate* 2g: Yellow oil, R_f= 0.25 (1:1 hexane:EtOAc). ^{1}H ($CDCl_3$, 400 MHz, ppm): δ 8.15 (s, 1H, NHPh), 7.26 (s, 4H), 7.18 (dd, J = 8.6, 7.3 Hz, 2H), 6.98 (d, J = 7.5 Hz, 2H), 6.86 (t, J = 7.4 Hz, 1H), 3.77 (d, J = 11.0 Hz, 6H, $PO(OCH_3)_2$), 2.34 (s, CH_3). ^{13}C NMR (101 MHz, $CDCl_3$, ppm): δ 142.8 (C), 139.9 (C), 135.6 (d, J = 240.0 Hz, C=N), 130.6, 130.2, 129.4, 129.0, 128.6 (d, J = 4.0 Hz), 128.3 (d, J = 4.0 Hz), 126.7 (d, J = 22.7 Hz, C), 121.8 (d, J = 59.4 Hz), 113.5 (d, J = 60.2 Hz), 53.7 (d, J = 6.9 Hz, $P(OCH_3)_2$), 53.4 (d, J = 5.4 Hz, $P(OCH_3)_2$), 21.4 (CH_3). FT-IR (cm^{-1}): 3208, 2950, 1600, 1501, 1502, 1233, 1025, 834, 753.

- *(E)-dimethyl (2-phenylhydrazono) (4-bromophenyl) methylphosphonate* 2h: Yellow oil, R_f= 0.38 (1:1 hexane:EtOAc). ^{1}H ($CDCl_3$, 400 MHz, ppm): δ 8.15 (s, 1H, NHPh), 7.59 (t, J = 8.5 Hz, 2H), 7.26 (d, J = 8.4 Hz, 2H), 7.18 (d, J = 8.0 Hz, 2H), 7.00 (d, J = 8.1 Hz, 2H), 6.88 (t, J = 7.3 Hz, 1H), 3.78 (d, J = 11.0 Hz, 3H, $P(OCH_3)_2$), 3.71 (d, J = 11.6 Hz, 3H, $P(OCH_3)_2$). ^{13}C NMR (101 MHz, $CDCl_3$, ppm): δ 142.6 (C), 133.9 (d, J = 242.2 Hz, C=N), 132.9, 130.5, 130.1, 129.5, 129.0, 128.8, 128.6, 124.2, 122.1 (d, J = 56.4 Hz), 113.7 (d, J = 57.4 Hz), 53.7 (d, J = 6.8 Hz, $P(OCH_3)_2$), 53.4 (d, J = 5.8 Hz, $P(OCH_3)_2$). FT-IR (cm^{-1}): 3200, 2953, 1599, 1478, 1260, 1023, 791.

- *(E)-dimethyl (2-phenylhydrazono) (4-chlorophenyl) methylphosphonate* 2i: Yellow oil, R_f=0.39 (1:1 hexane:EtOAc). ^{1}H ($CDCl_3$, 400 MHz, ppm): δ 8.20 (s, 1H, NHPh), 7.48 (d, J = 8.5 Hz, 2H), 7.37 (d, J = 8.7 Hz, 2H), 7.28 – 7.18 (m, 2H), 7.05 (d, J = 7.5 Hz, 2H), 6.93 (t, J = 7.3 Hz, 1H), 3.82 (d, J = 11.0 Hz, 6H, $PO(OCH_3)_2$). ^{13}C NMR (101 MHz, $CDCl_3$, ppm): δ 142.6 (s, C), 135.8, 133.9 (d, J = 242.2 Hz, C=N), 130.5, 130.3, 130.1, 129.8, 129.71, 129.66, 128.7, 128.2 (d, J = 23.2 Hz), 122.1 (d, J = 56 Hz), 113.1 (d, J = 22.5 Hz), 53.4 (d, J = 3.7 Hz, $P(OCH_3)_2$). FT-IR (cm^{-1}): 3174, 2946, 1603, 1528, 1478, 1260, 1013, 792.

- *(E)-dimethyl (2-phenylhydrazono) (4-nitrophenyl) methylphosphonate* 2j: Light brown oil, R_f= 0.38 (2:1 hexane:EtOAc). ^{1}H ($CDCl_3$, 400 MHz, ppm): δ 12.3 (s, 1H, NHPh), 8.11 (d, J = 9.0 Hz, 2H), 7.84 (d, J = 9.2 Hz, 2H), 7.27 (t, J = 7.4 Hz, 2H), 7.23–7.17 (m, 2H), 6.96 (t, J = 7.2 Hz, 1H), 3.72 (d, J = 11.5 Hz, 6H,

$PO(OCH_3)_2$). ^{13}C NMR (101 MHz, $CDCl_3$, ppm): δ 146.6, 143.1 (d, J = 26.9 Hz), 142.8, 130.0, 129.2, 126.2, 124.9 (d, J = 234.0 Hz, C=N), 124.0, 115.1, 114.2, 53.1 (d, J = 7.4 Hz, $P(OCH_3)_2$). FT-IR (cm^{-1}): 3179, 2958, 1595, 1466, 1330, 1265, 1013, 851.

3.2. DFT Calculation of E/Z Form of Compounds 2a and 2f

Theoretical calculations utilized Gaussian 09, and visualization was conducted with GaussView 5.0 [15]. Geometry optimization for the *E* form of **2a** and **2f** and Z form of **2a** and **2f** molecules was carried out using the 6-31+G(d,p) basis set functional integrated with B3LYP in the DFT method. Molecules were determined by three structural parameters: bond length, bond angle and dihedral angle. In Figure S1 and Table S1-S4 (the data is given in the supporting information), the numbered arrangement of atoms in the molecules after geometric optimization, and the corresponding data for angles and bond lengths between these atoms are provided. The isomers can transform by rotating the nitrogen group 180°. The potential for hydrogen bonding between the hydrogen on nitrogen in the trans position and phosphorus results in the fixation of the nitrogen group and resistant to rotate (Figure 1). Therefore, the zero-point vibrational energy (ZPE) is approximately 0.21 kcal/mol and 0.10 kcal/mol higher for *Z*-configurations in *Z*-**2f** and *Z*-**2a**, respectively. These energy differences may be significant in terms of molecular stability and reactivity, as small energy changes in specific conformations can dictate the preferred pathway of chemical reactions.

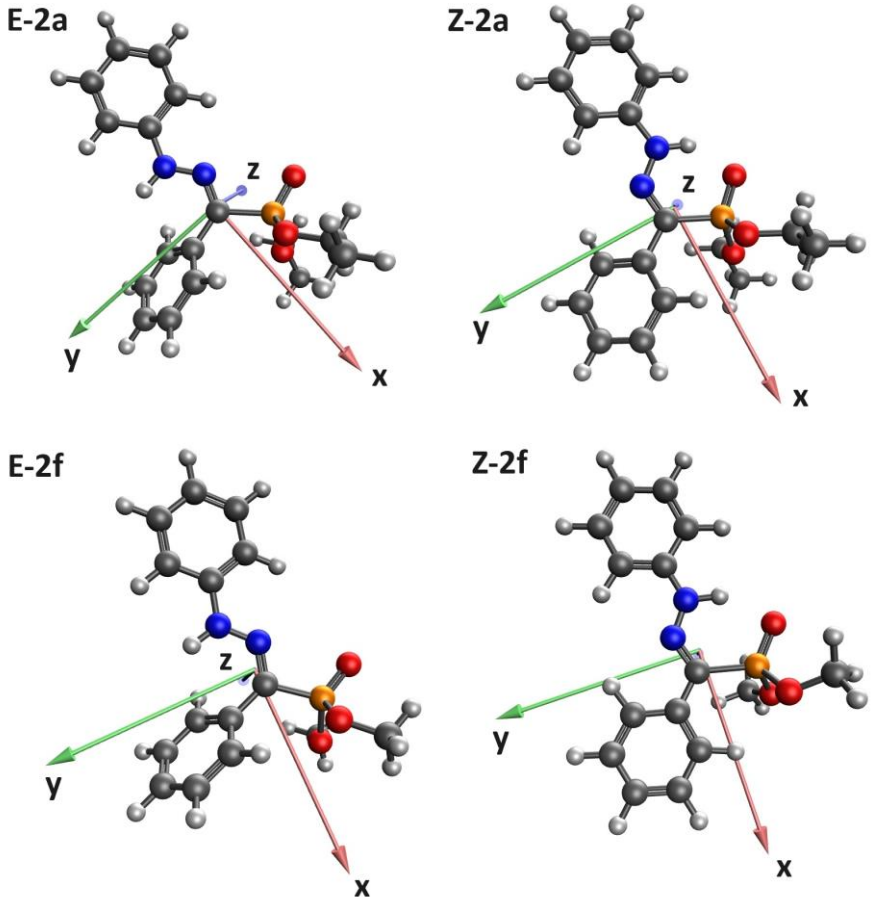

Figure 1. Images of molecules *E*-**2a** and *Z*-**2a**; *E*-**2f** and *Z*-**2f** from different perspectives after geometric optimization

The DFT analysis reveals that in the examined molecular structures, the Highest Occupied Molecular Orbital (HOMO) and Lowest Unoccupied Molecular Orbital (LUMO) exhibit charge distribution patterns along the entire molecular structure (Figure 2). Specifically, in *E*- configurations such as *E*-**2f** and *E*-**2a**, the phenyl units

are positioned in closer proximity, influencing the charge distribution. On the other hand, *Z*- configurations like *Z*-**2f** and *Z*-**2a** show phenyl units that are more distant from each other and adopt a planar arrangement. Despite these structural variations, the charge distribution appears to be consistently and homogeneously delocalized across the entirety of the systems studied. In addition, it has been observed that the band gap values of *Z*- configurations in both molecules are lower compared to the *E*- configurations. The fact that the LUMO level of the *Z*- configuration is lower than that of the *E*- configuration implies that the energy levels, and consequently, electron behavior, are more accessible in the *Z*- configuration. It is considered that the positions of the phenyl groups in the *E*-configuration create steric hindrance, while the planarity of the phenyl groups in the *Z*-configuration facilitates charge movement. Additionally, the interaction between the hydrogen attached to nitrogen in the *Z*-configuration and the electrophilic phosphorus atom in the phosphonate group has supported this situation. As a result, *Z*- configurations are energetically more stable for both molecules. The lower LUMO level in the *Z*- configuration suggests that the molecule can accept electrons at a lower energy, potentially making it more efficient in electron transfer processes.

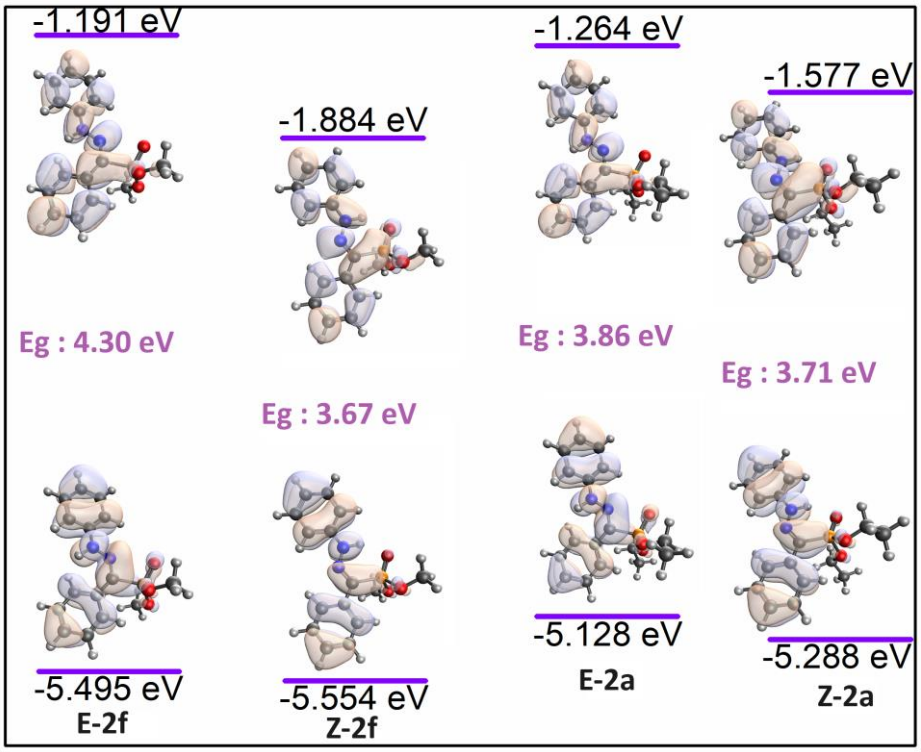

Figure 2. Theoretical charge distribution of HOMO-LUMO in *E*-**2f** and *Z*-**2f**; *E*-**2a** and *Z*-**2a** structures at the B3LYP/6-31G(d,p) level

In addition, the interaction between nucleophilic and electrophilic groups plays a vital role in chemical reactions, and understanding their contributions to factors like HOMO-LUMO and band structures is important [16]. According to the total density calculation, electrophilic phosphonates, a common group in structures, contribute directly to the LUMO of molecules since they tend to accept electrons (act as acceptors). The color scale of the phosphonate groups in trans configurations indicates their higher electronegativity, providing evidence for their lower energy levels (Figure 3).

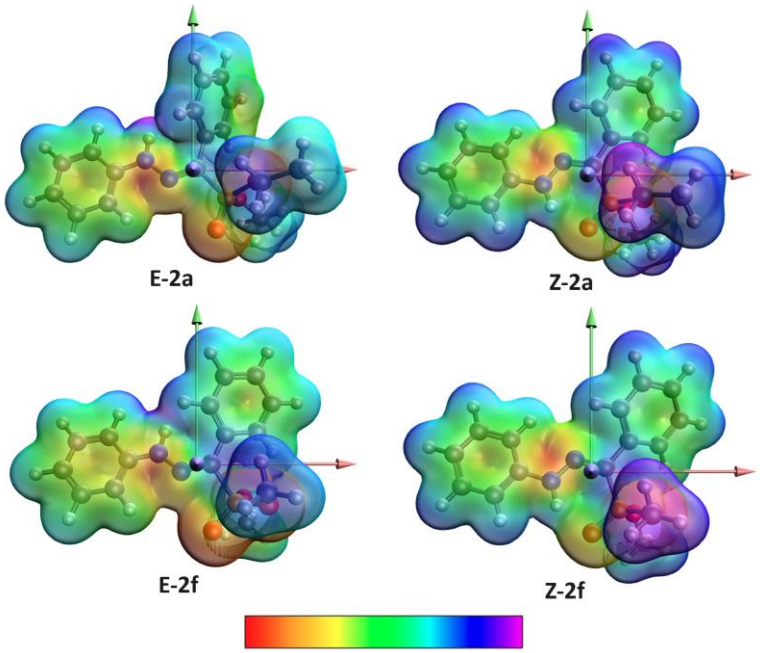

Figure 3. Electron density of *E*-**2a**/*Z*-**2a** and *E*-**2f**/*Z*-**2f**

4. Conclusion

The synthesis of exclusively the *E*-isomer of *α*-hydrazone phosphonates has been achieved in good yields through the nucleophilic addition of triethyl phosphite and trimethyl phosphite to NI derivatives. The dechlorination of compound **1** to form the corresponding NI's *in situ* was achieved by using triethylamine. The *α*-hydrazone phosphonates were obtained exclusively in *E* form rather than *Z* form. Nucleophilic addition of trialkyl phosphite prefers to attack NI derivatives from the less hindered site to give exclusively *E*-isomer of *α*-hydrazone phosphonate derivatives. *Z*-isomer of *α*-hydrazone phosphonate is stable due to H-bonding, but *E* configuration *α*-hydrazone phosphonate is sterically less hindered. We have also performed the DFT calculation for compounds **2a** and **2f** for both *E* and *Z* forms. After the geometric optimization, we have determined the three structural parameters bond length and angle along with the dihedral angle provided in supporting information. There is a potential H-bonding between the hydrogen atom connected to the *N*-atom and the *O*-atom in the phosphonate group in the *Z* geometry of compounds **2a** and **2f**. This makes the compounds **2a** and **2f** resistant to rotation (Fig. 1). This results in a higher zero-point vibrational energy (ZPE) and the value is about 0.21 kcal/mol and 0.10 kcal/mol higher for *Z*-configurations in compounds **2f** and **2a**, respectively. We have also determined the HOMO-LUMO energy levels for both *E* and *Z* isomer of compounds **2a** and **2f**. In *E* isomers of compound **2f** (Figure 2) and **2a** the phenyl groups are closely positioned affecting the charge distribution. However, in *Z*- isomer of compounds **2a** and **2f** phenyl units are spaced farther apart and adopt a planar arrangement. Due to H-bonding *Z*-configurations of both compounds **2a** and **2f** are found to be energetically more stable. To that end, the titled compounds *α*-hydrazone phosphonates will be converted into their *α*-hydrazone phosphonic acid forms and the investigation for the biological activity tests in due course.

Author Contributions

The first author designed and performed the synthesis and wrote the paper. The second author performed the DFT calculation of the titled compounds. They all read and approved the final version of the paper.

Conflicts of Interest

All the authors declare no conflict of interest.

References

[1] C. Jamieson, K. Livingstone, The nitrile imine 1,3-dipole: Properties, reactivity, and applications, 1st Edition, Springer, Cham, 2020.

[2] R. Huisgen, M. Seidel, J. Sauer, J. McFarland, G. Wallbillich, *The formation of nitrile imines in the thermal breakdown of 2,5-disubstituted tetrazoles*, Journal of Organic Chemistry 24 (1959) 892–893.

[3] S. Ningaiah, S.D. Doddaramappa, Chandra, M. Madegowda, S. Keshavamurthy, U. K. Bhadraiah, *One-pot tandem synthesis of tetrasubstituted pyrazoles via 1,3-dipolar cycloaddition between aryl hydrazones and ethyl but-2-ynoate*, Synthetic Communication 44 (2014) 2222–2231.

[4] A. S. Shawali, M. A. N. Mosselhi, *Hydrazonoyl halides: useful building blocks for the synthesis of arylazoheterocycles*, Journal of Heterocyclic Chemistry 40 (2003) 725–746.

[5] R. Huisgen, H. J. Sturm, M. Seidel, *Ringöffnungen der Azole, V. Weitere Reaktionen der Tetrazole mit elektrophilen Agenzien*, Chemische Berichte 94 (1961) 1555–1562.

[6] R. Huisgen, R. Grashey, M. Seidel, H. Knupfer, R. Schmidt, *1.3-Dipolare additionen, III. umsetzungen des diphenylnitrilimins mit carbonyl und thiocarbonyl-verbindungen*, Justus Liebigs Annalen der Chemie 658 (1962) 169–180.

[7] R. Huisgen, M. Seidel, G. Wallbillich, H. Knupfer, *Diphenyl-nitrilimin und seine 1.3-dipolaren additionen an alkene und alkine*, Tetrahedron 17 (1962) 3–29.

[8] Y. Zhang, W. Liu, Z. Zhao, *Nucleophilic trapping nitrilimine generated by photolysis of diaryltetrazole in aqueous phase*, Molecules 19 (2013) 306–315.

[9] C. Csongár, L. Grubert, G. Tomaschewski, *Photochemistry of Aryl-Substituted Sydnone IV. and 2H-Tetrazole VIII. Reaction of nitrilimines with phenols*, Zeitschrift für Chemie 28 (1988) 24–25.

[10] Z. Li, L. Qian, L. Li, J.C. Bernhammer, H. V. Huynh, J. S. Lee, S. Q. Yao, *Tetrazole photo click chemistry: reinvestigating its suitability as a bioorthogonal reaction and potential applications*, Angewandte Chemie International Edition 55 (2016) 2002–2006.

[11] P. D. Croce, P. Del Buttero, E. Licandro, S. Maiorana, *Synthesis of Arylazomethylenetriphenylphosphoranes from Arylhydrazonoyl chlorides (via Nitrilimines in situ) and Triphenylphosphine*, Synthesis 4 (1979) 299–300.

[12] M. P. Kaushik, B. Lal, C. D. Raghuveeran, R. Vaidyanathaswamy, *Stereochemistry of aroylphosphonate phenylhydrazones and their conversion to 1H-indazole-3-phosphonates*, The Journal of Organic Chemistry 47 (18) (1982) 3503-3505.

[13] G. Baccolini, M. Faggiano, P. E. Todesco, *Reactions of Diphenyl nitrilimine with Phosphites and Diazaphospholenes*, Journal of the Chemical Society, Perkin Transactions 1 0 (1979) 2329–2333.

[14] K. Paulvannan, T. Chen, R. Hale, *An improved synthesis of 1,2,4-triazoles using Ag_2CO_3*, Tetrahedron 56 (2000) 8071–8076.

[15] M. J. Frisch, G. W. Trucks, H. B. Schlegel, G. E. Scuseria, M. A. Robb, J. R. Cheeseman, G. Scalmani, V. Barone, G. A. Petersson, H. Nakatsuji, X. Li, M. Caricato, A. Marenich, J. Bloino, B. G. Janesko, R. Gomperts, B. Mennucci, H. P. Hratchian, J. V. Ortiz, A. F. Izmaylov, J. L. Sonnenberg, D. Williams-Young, F. Ding, F. Lipparini, F. Egidi, J. Goings, B. Peng, A. Petrone, T. Henderson, D. Ranasinghe, V. G. Zakrzewski, J. Gao, N. Rega, G. Zheng, W. Liang, M. Hada, M. Ehara, K. Toyota, R. Fukuda, J.

Hasegawa, M. Ishida, T. Nakajima, Y. Honda, O. Kitao, H. Nakai, T. Vreven, K. Throssell, J. A. Montgomery, Jr., J. E. Peralta, F. Ogliaro, M. Bearpark, J. J. Heyd, E. Brothers, K. N. Kudin, V. N. Staroverov, T. Keith, R. Kobayashi, J. Normand, K. Raghavachari, A. Rendell, J. C. Burant, S. S. Iyengar, J. Tomasi, M. Cossi, J. M. Millam, M. Klene, C. Adamo, R. Cammi, J. W. Ochterski, R. L. Martin, K. Morokuma, O. Farkas, J. B. Foresman, D. J. Fox, Gaussian 09 – Revision A.02 (2016), https://gaussian.com/g09citation/, Accessed 1 Jan 2024.

[16] M. Ríos-Gutiérrez, A. S. Sousa, L. R. Domingo, *Electrophilicity and nucleophilicity scales at different DFT computational levels*, The Journal of Physical Organic Chemistry 36 (7) (2023) e4503 14 pages.

Çanakkale Onsekiz Mart University

Journal of Advanced Research in Natural and Applied Sciences

dergipark.org.tr/tr/pub/jarnas

Open Access

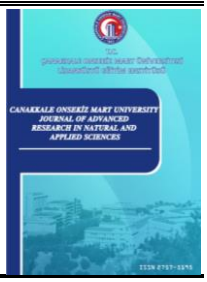

e-ISSN: 2757-5195 2024, Vol. 10, Issue 2, Pages: 426-434 doi.org/10.28979/jarnas.1428996

First Trials of Genome Analyses in Some *Onobrychis* Species using Dot-Blot and Genomic *in situ* Hybridization Techniques

Gülru Yücel[1], Bozena Kolano[2], Evren Cabi[3], Metin Tuna[4]

[1]Department of Agricultural Biotechnology, Faculty of Agriculture, Ondokuz Mayıs University, Samsun, Türkiye
[1]Department of Biology, Institute of Natural and Applied Sciences, Tekirdağ Namık Kemal University, Tekirdağ, Türkiye
[2]Plant Cytogenetics and Molecular Biology Group, Faculty of Natural Sciences, Institute of Biology, Biotechnology and Environmental Protection, University of Silesia, Katowice, Poland
[3]Department of Biology, Faculty of Arts and Sciences, Tekirdağ Namık Kemal University, Tekirdağ, Türkiye
[4]Department of Field Crops, Faculty of Agriculture, Tekirdağ Namık Kemal University, Tekirdağ, Türkiye

Article History
Received: 31 Jan 2024
Accepted: 26 Mar 2024
Published: 25 Jun 2024

Research Article

Abstract − The origin and genome composition of tetraploid cultivated *Onobrychis viciifolia* ($2n = 4x = 28$) were analyzed using dot-blot and genomic *in situ* hybridization (GISH) techniques. Dot-blot hybridization was used to find a genomic affinity between *O. viciifolia* and 16 diploid *Onobrychis* species. The hypothesis on the origin of the *O. viciifolia* was tested using GISH. Dot-blot analyses suggested a genomic affinity between *O. viciifolia* and four diploid *Onobrychis* species (*O. kachetica*, *O. supina*, *O. pallasii*, and *O. vaginalis*). Hybridization signals were observed on *O. viciifolia* chromosomes when gDNA of O. *kachetica*, *O. supina*, *O. pallasi*, and *O. hypargyrea* were used as probes. However, the observed chromosomal distribution of hybridization signals did not resemble GISH results. The observed signals colocalized with 35S rDNA or dispearse signals on all chromosomes were observed depending on the probe. Further investigations using more comprehensive and comparative analysis with both coding and repetitive DNA regions may provide a better understanding of the genome composition and evolution of *O. viciifolia*.

Keywords − *Onobrychis, Dot-blot hybridization, GISH, FISH*

1. Introduction

Onobrychis genus is a member of subfamily Faboidae of Fabaceae within the tribe Hedysareae. *Onobrychis* Mill. includes about 170 mostly perennial species distributed through temperate regions of North America, the Middle East and Europe [1-3]. Most *Onobrychis* species exist, especially in Anatolia, Caucasus, and Iran [4]. Based on floral characteristics this genus was classified into two subgenera: (i) *Onobrychis* Mill (consist of four sections *Dendrobrychis* DC., *Onobrychis,* Lophobrychis Hand.-Mazt., *Hemicyclobrychis* (Širj.) Rech.f.) and (ii) *Sisyrosema* Bunge (including sections *Hymenobrychis* DC., *Heliobrychis* Bunge ex Boiss., *Anthyllium* Nab., *Afghanicae* Širj.,) [5].

The most commonly cultivated species of the genus is *O. viciifolia*, used mainly as a forage crop with many valuable agronomic, environmental, and nutritional properties [1, 3, 6]. It is resistant to drought, pests, and diseases, palatability and is an important source for pollinators [1, 7]. Although the genus *Onobrychis* has potential agronomic importance, the genomic structure of *Onobrychis* species remains less studied [1, 8]. Detailed comprehensive analysis of its species in genetic and breeding research are necessary.

[1]gulru.yucel@omu.edu.tr (Corresponding Author); [2]bozena.kolano@us.edu.pl; [3]ecabi@nku.edu.tr; [4]mtuna@nku.edu.tr

Molecular phylogenetic analyses have shown that within the genus *Onobrychis* two main evolutionary lineages can be distinguished, which correspond to the redefined subgenus *Sisyrosema* and *Onobrychis* [8]. The nuclear genome size of *O. viciifolia* was reported as 2.5 pg/2C [9]. In this genus, two different basic chromosome numbers (x = 7 and 8) were reported with two different ploidy levels, diploids with ($2n = 2x$ = 14 or 16 and tetraploids with $2n = 4x$ = 28 or 32 chromosome number [10-14]. The ancestral basic chromosome number was determined as x = 8 in the nrITS phylogenetic context. Chromosomal organization of rDNA loci was analyzed by fluorescent *in situ* hybridization to provide more comprehensive information on karyotype structure of *Onobrychis* [15]. The genes encoding 5S rRNA and 35S rRNA (18S-5.8S-25S rRNA) consist of evolutionary highly conserved coding sequences [16] which are utilized as chromosomal markers [17, 18]. Several gains and repositioning of rDNA locus repatterning especially among diploids were suggested to explain their organisation in *Onobrychis*. Chromosome number and the organization of rDNA loci showed different patterns in both analysed *Onobrychis* subgenera. Two different basic chromosome numbers (x = 7 and 8) seem to be a result of several events of descending dysploidy (changes in chromosome number due to structural chromosomal rearrangements e.g., translocation or chromosome fusion [15, 19]. Dysploidy and polyploidy are important forces of evolution and diversification in *Onobrychis* genus and many of them are of polyploid origin [15]. Polyploids which derive from a genome doubling which happens in a species are called autopolyploids whereas, allopolyploid genome formation includes an interspecific hybridisation followed by a doubling of genome [20].

Different hybridization methods e.g. dot-blot and genomic *in situ* hybridization (GISH), might be useful in studying the genomic relationship among species. Dot-blot hybridization which is a nucleic acid hybridization technique where complementary single-stranded sequences of DNA probe hybridize with single-stranded sequences of the sample genome on a membrane under suitable conditions [21]. Dot-blot hybridizaiton was successfully used to analyse genome affinity in different genera for example *Arachis* species [22]. On the other hand, GISH is widely used to find the origin of numerous allopolyploids [23]. Molecular phylogenetic and GISH were used to identify the parental taxa of *Chenopodium quinoa* and *C. berlandieri* [24]. In *Passiflora* hybrid species, GISH was successfully used to confirm parental genomes [25].

The specific aims of this study were as: (i) to study genomic affinities of *O. viciifolia* with wild diploid taxa using dot-blot hybridization; (ii) to test the hypothetical parentage by mapping parental genomes in the polyploid using GISH.

2. Materials and Methods

2.1. Plant Material

Cultivated accession of tetraploid *O. viciifolia* and 16 diploid *Onobrychis* species were studied (Table 1). Seeds were grown in a greenhouse facility of University of Silesia in Katowice, Poland.

Table 1. Information of the analyzed taxa

Species name	USDA* Collection Number
O. viciifolia Scop.	PI 170583
O. vaginalis C.A. Mey.	PI 325444
O. megataphros	PI 301107
O. caput- galli (L.) Lam.	PI 205304
O. iberica Grossh.	PI219602
O. kachetica Boiss. & Buhse	PI 314469

*USDA North Central Regional Plant Introduction Station of the US National Plant Germplasm System

Table 1. (Continued) Information of the analyzed taxa

Species name	USDA* Collection Number
O. gaubae Boiss. & Buhse	PI 380931
O. radiata (Desf.) M. Bieb.	W6 24111
O. chorossanica Bunge ex Boiss.	PI 314160
O. sternorhiza D.C	PI 319056
O. vassilczenkoi Grossh.	PI 678913
O. gracilis Besser	W6 19496
O. pallasii	PI 325448
O. alba (Waldst. & Kit.) Desv. subsp. *laconica* (Boiss.) Hayek	W6 19337
O. supina (Vill.) DC.	PI 383721
O. ptolemaica (Delile) DC.	PI 215344
O. grandis Lipsky	PI 440568

*USDA North Central Regional Plant Introduction Station of the US National Plant Germplasm System

2.2. Genomic DNA Isolation

Total genomic DNA (gDNA) was extracted from healthy and fresh leaf tissue following the modified CTAB extraction method [26]. Genomic DNA concentration and quality were checked using Nano drop (ND-1000, peqLab, Erlangen, Germany). The quality of the DNA was verified by electrophoresis in 1% agarose gel.

2.3. Dot-Blot Hybridization

The genomic affinity between cultivated *O. viciifolia* and 16 wild diploid *Onobrychis* species (*O. vaginalis*, *O. caput-galli*, *O. iberica*, *O. kachetica*, *O. gaubae*, *O. radiata*, *O. chorossanica*, *O. sternorhiza*, *O. vassilczenkoi*, *O. gracilis*, *O. pallasii*, *O. alba* subp. *laconica*, *O. supina*, *O. ptolemaica*, *O. grandis*) was analyzed using dot-blot hybridization using as a probe gDNA of *O. viciifolia*. The total genomic DNA of tetraploid *O. viciifolia* was labelled with alkali-labile digoxigenin-11-dUTP using DIG Nick Translation Kit (Roche) according to the manufacturer protocol. The 1 µg of genomic DNA isolated from analysed diploid species were denatured at 95 ºC for 10 min and genomic DNA of the species were transferred onto a positively charged nylon membrane using the Dot-Blot 96 System (Biometra, Germany). gDNAs of the analysed samples were fixed to the positively charged nylon membrane by UV treatment (UVP, CL-1000 Ultraviolet Crosslinker), washed with distilled sterile water and then air dried. Hybridization process was performed at 37 ºC using the DIG High Prime DNA Labelling and Detection Starter Kit II (Roche) following to the manufacturer's protocol with 75% stringency washes. The signal detection process was accomplished using anti-DIG antibody conjugated with alkaline phosphatase and chemiluminescence visualization was used. The hybridisatiton signals were captured and quantified using ChemiDocXRS (BioRad, USA).

2.4. Genomic *in situ* Hybridization and Fluorescence *in situ* Hybridization

Seeds of the species were germinated in Petri dishes on moist filter paper at room temperature. Roots approximately 2.0 cm long were immersed in ice-cold water for approximately 24 h then fixed in methanol/glacial acetic acid (3:1). The fixed materials stored at 4 ºC until use. Fixed roots were washed in 0.01 citrate buffer for approximately 20 min and then digested in a mixture of enzymes, 20 % (v/v) pectinase (Sigma), 1% (w/v) cellulase 'Onozuka R-10' (Serva) and 1% (w/v) cellulase (Calbiochem) for 1.5 h at 37ºC. Dissected meristems from root tips were transferred on a microscope slide into a drop of 45% acetic acid and then squashed. The coverslips were removed from microscope slide following the freezing, the chromosome slides were air dried. The prepared chromosome slides stored at 4˚C [27].

The probe labelling and GISH followed the Kolano et al. [28]. The genomic DNA of *O. kachetica*, *O. supina*, *O. pallasii*, and *O. hypargyrea* were labelled with digoxygenin-11-dUTP using nick translation mix (Roche, Switzerland). gDNA isolated from *O. hypargyerea*, species which seems to be distantly related with *O.viciifolia* [13], was used as a control in GISH. The hybridization mixture containing 10% dextran sulphate, 50% deionised formamide, 0.5% SDS (sodium dodecyl sulphate), 2x SSC (Saline sodium citrate) and labelled gDNA, was denatured approximately 10 minutes at 75 ºC and applied to somatic chromosome slides. The chromosome preparations with the hybridization mixture were denatured together at 72 ºC approximately for 5 min in an *in situ* Thermal Cycler (ThermoHybaid, Franklin, USA). Hybridization was conducted about 48 h at 37 ºC in a humid chamber. FITC-conjugated primary anti-digoxigenin antibody (Roche, Switzerland) was used to detect digoxygenin following post-hybridization washes and signal amplification with FITC-conjugated antisheep secondary antibodies (Jackson ImmunoResearch, USA).

A 2.3-kb fragment of the 35S rDNA coding region of *Arabidopsis thaliana* [29] labelled with tetramethyl-rhodamine5-dUTP (Roche) was used to detect the 35S rDNA loci. The probe labelling process and FISH were performed according to the protocol of the Jenkins and Hasterok [30].

The chromosome slides were stained in Vectashield containing 2.5 ng/µL of DAPI (4′,6-diamidino-2-phenylindole dihydrochloride). All analyzed images were collected using a fluorescent microscope (Zeiss AxioImager.Z.2, Oberkochen, Germany). The somatic chromosome images were processed using ZEN 2. blue edition (Zeiss). Two individuals were analyzed for each species.

3. Results and Discussion

The affinity between the genome of cultivated tetraploid *O. viciifolia* (2*n* = 4*x* = 28) and 16 diploid *Onobrychis* species (2*n* = 2*x* = 14 or 16) was analysed using dot-blot hybridization (Figure 1). After dot-blot hybridization with labelled gDNA of *O. viciifolia*; relatively strong hybridization signals were observed for *O. kachetica, O. supina, O. pallasii* and *O. vaginalis* suggesting a relatively high genomic affinity between the tetraploid and these four diploids. Rest of the analyzed diploid *Onobrychis* species revealed weak or no signals after dot-blot hybridization with genomic DNA of *O. viciifolia* (Figure 1).

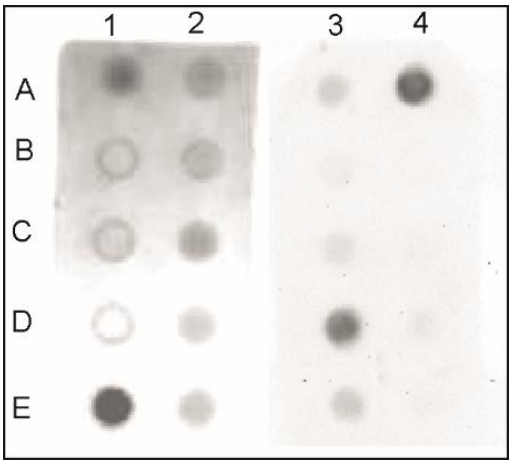

Figure 1. Dot-blot hybridization revealing the genome affinities of *O. viciifolia* with representative diploid *Onobrychis* species from two subgenera which are *Onobryhcis* and *Sisyrosema*: *O. vaginalis*, (A1), *O. megataphros (*B1), *O. caput-galli* (C1), *O. iberica* (D1), *O. kachetica* (E1), *O. gaubae* (A2), *O. radiata* (B2), *O. chorossanica* (C2), *O. sternohiza* (A3), *O. vassilczenkoi* (B3), *O. gracilis* (C3), *O. pallasi* (D3), *O. alba* subp. *laconica* (E3), *O. supina* (A4), *O. ptolemaica* (B4), *O. grandis* (C4).

Because *O. supina* belongs to the subgenus *Onobrychis* while three other diploids (*O. kachetica*, *O. pallasii* and *O. vaginalis*) belong to the subgenus *Sisyrosema* the obtained result suggested that the hybridization between species that belong to two different subgenera might have given rise of *O. viciifolia*. Its allotetraploid origin was also supported by analyses of repetitive sequences showing that two different centromeric satellite repeats interact with CENH3 in *O. viciifolia* also supports the allotetraploid origin of *O. viciifolia* [31, 32]. The origin of *O. viciifolia* and its genome composition was unknown [15, 32-36]. However recently analyses based on EST-SSRs markers and relatively complete chromosome level genome assemble supported rather autotetraploid origin of *O. viciifolia* [37, 38].

GISH is a valuable method to study the origin of polyploid species and enables the identification of two sets of parental chromosomes [24, 39-41]. gDNA of four diploid species, *O. kachetica*, *O. supina*, *O. pallasi* and *O. hypargyrea* were used as a probe in GISH to *O. viciifolia* chromosomes. Recent molecular phylogenetic analyses of nrITS and combined plastid markers (trnL- F, rpl32/rpl32-trnL-F(UAG), ndhFrpl32) have supported the close relationship between *O. viciifolia* and *O. supina* placed them in the same clade within the subgenus *Onobrychis* [8,15]. On the other hand, two other species, *O. kachetica* and *O. pallasi*, were recovered in a different clade and subgenus than *O. viciifolia* [2, 15].

After GISH with gDNA of *O. kachetica* as a probe, intense hybridisation signals were detected on four chromosomes of O. *viciifolia* while the remaining chromosomes showed much weaker and dispersed hybridization signals mainly located at pericentromeric region of *O. viciifolia* chromosomes (Fig. 2. A, C). After GISH using gDNA of *O. supina* as a probe, weak hybridization signals were observed mostly in subtelomeric regions of all chromosomes of the tetraploid (Fig. 2. B, C). The application of GISH with gDNA of *O. pallasi* as a probe allowed to observe four major and several minor hybridization signals on eight chromosomes of *O. viciifolia* (Fig. 2. D). When gDNA of *O. hypargyrea*, was used as a probe, hybridization signals were observed on four chromosomes of *O. viciifolia* (Fig. 2. E). Reprobing of the same metaphase plates with 35S rDNA revealed that four intense hybridization signals observed after GISH with *O. hypargyrea* colocalized with the hybridization signals of 35S rDNA (Fig. 2. F). The coding sequences of 35S rDNA are evolutionary conserved and very similar in all land plant [16]. Additionally, the four major hybridization signals observed with gDNA of *O. pallasii* resemble the results of FISH with 35S rDNA to *O. viciifolia* chromosomes which were obtained earlier by Yucel et al. [15].

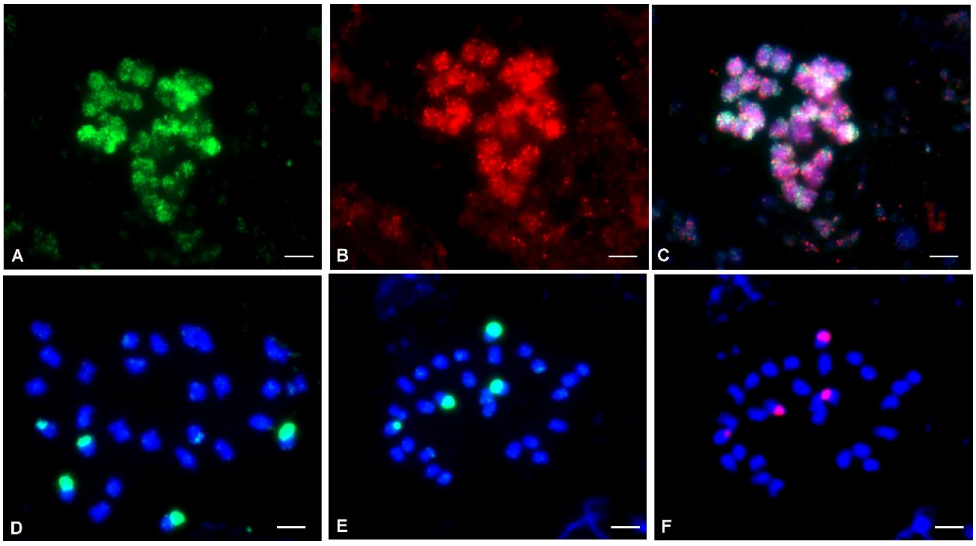

Figure 2. Somatic metaphases of *O. vicifolia* after GISH with gDNA isolated from **A.** *O. kachetica* **B**. *O. supina* gDNA on chromosomes of *O. viciifolia*, **C**. *O. supina* (red) and *O. kachetica* (green) **D**. *O. pallasi*. **E**. *O. hypargyrea* **F.** Reprobing with 35S rDNA on same metaphase plate of *O. viciifolia* chromosome plate.

GISH is a very useful method for the identification of an ancestor genome in hybrids and allopolyploid plants since it usually obtains clear and unambiguous distinction between two parental subgenomes e.g. GISH was successfully used to verify the origin of *Lilium* hybrids [39]. However, after GISH with tested gDNAs to *O. viciifolia* chromosomes observed patterns of hybridization signals did not allow to distinguish the parental subgenome. Obtained results showed that *O. viciifolia* and analysed diploids share similar repetitive sequences but they did not allow to identify parental species of the tetraploid. The coding sequences of 35S rRNA genes are evolutionary highly conserved and very similar in plant genome as it was shown by comparative GISH (cGISH) [42]. Except rDNA, the other hybridization signals were observed mainly in the pericentromeric region of *O. viciifolia* chromosomes (Fig. 2). This heterochromatic region of chromosomes contains many different repeats e.g. retrotransposons which might be similar in related species [43]. The obtained results may suggest several hypotheses: (i) tested diploids are not parental species of *O. viciifolia*; (ii) the parental species of analysed tetraploid were very closely related, and their genomes consist of similar repetitive sequences and (iii) the *O. viciifolia* is a relatively old allotetraploid which underwent extensive diploidization. This post-polyploidyzation evolution, which involve many different mechanisms e.g. homogenization, elimination and gene conversion [44], have made the parental subgenomes extremely difficult to distinguished [44-46].

4. Conclusion

The origin and evolutionary history of *O. viciifolia* is complex, and there is no exact data about progenitor or progenitors. A more global and comparative analyses combining molecular phylogenetic approached and cytogenetic studies should be applied to better understand the evolutionary and origin of *O. viciifolia*. For example, molecular markers such as chloroplast DNA (cpDNA) or methods based on new generation sequencing (NGS) e.g. RAD-seq should be used.

Author Contributions

The first author performed investigation, methodology, experiments, writing original draft preparation. The second, third, and fourth authors planned conceptualization, writing, review, and editing. The second author also planned methodology. All authors read and approved the final version of the paper. This paper is derived from the first author's doctoral dissertation supervised by the third and fourth authors.

Conflicts of Interest

All the authors declare no conflict of interest.

Acknowledgement

The study was supported by the Scientific and Technological Research Council of Turkey, Grant number: 215O526.

References

[1] C. H. Carbonero, I. Mueller-Harvey, T. A. Brown, L. Smith, *Sainfoin (Onobrychis viciifolia): A beneficial forage legume*, Plant Genetic Resources: Characterization and Utilization 9 (1) (2011) 70–85.

[2] C. H. Carbonero, F. Carbonero, L. M. J. Smith, T. A. Brown, *Phylogenetic characterisation of Onobrychis species with special focus on the forage crop Onobrychis viciifolia Scop*, Genetic Resources and Crop Evolution 59 (2012) 1777–1788.

[3] T. Sutcu, B. B. Bilgen, M. Tuna, *Analysis of genetic diversity among Onobrychis accessions with high agronomic performance by simple sequence repeat (SSR) markers*, Molecular Biology Reports 49 (2022) 5659–5668.

[4] B. Yıldız, B. Çıplak, E. Aktoklu, *Fruit morphology of sections of the genus Onobrychis Miller (Fabaceae) and its phylogenetic implications*, Israel Journal of Plant Sciences 47 (4) (1999) 269–282.

[5] G. I. Sirjaev, Onobrychis Generis Revisio Critica, Pars Prima; Faculte' des Sciences de I'Universite Masaryk: Brno, Brno, 1925.

[6] E. C. Yilmaz, B. B. Bilgen, M. Tuna, *Evaluation of the genetic structure of some accessions belonging to Onobrychis spp. using microsatellite DNA markers*, Journal of Tekirdag Agricultural Faculty 20 (2) (2023) 399-409.

[7] M. Mora-Ortiz, L. Smith, *Onobrychis viciifolia; a comprehensive literature review of its history, etymology, taxonomy, genetics, agronomy and botany*, Plant Genetic Resources 16 (5) (2018) 403–418.

[8] A. Amirahmadi, S. Kazempour-Osaloo, A. Kaveh, A. A Maassoumi, R. Naderi, *The phylogeny and new classification of the genus Onobrychis (Fabaceae-Hedysareae): Evidence from molecular data*, Plant Systematics and Evolution 302 (2016). 1445–1456.

[9] C. H. Carbonero, F. Carbonero, L. M. J. Smith, T. A. Brown, *Cytological characterisation of the underutilized forage crop Onobrychis viciifolia Scop. and other members of the Onobrychis genus*, Genetic Resources and Crop Evolution 60 (7) (2013) 1987–1996.

[10] M. M. Abou-El-Enain, *Chromosomal criteria and their phylogenetic implications in the genus Onobrychis Mill. sect. Lophobrychis (Leguminosae), with special reference to Egyptian species*, Botanical Journal of Linnean Society 139 (4) (2002) 409–414.

[11] H. Hoşgören, *Total numbers of chromosome numbers in species of Onobrychis Miller (Fabaceae) in Southeastern Anatolia region*, Biotechnology Biotechnoligal Equipment 20 (2) (2006) 57–61.

[12] H. H. S. Mohsen, M. Z. Nasab, *Cytotaxonomy of some Onobrychis (Fabaceae) species and populations in Iran*, Caryologia 63 (2010) 18–31.

[13] S. E. Akçelik, S. Avcı, S. Uzun, C. Sancak, *Karyotype analysis of some Onobrychis (sainfoin) species in Turkey*, Archieves of Biological Sciences 64 (2012) 567–571.

[14] M. Ranjbar, F. Hajmoradi, R. Karamian, *An overview on cytogenetics of the genus Onobrychis (Fabaceae) with special reference to O. sect. Hymenobrychis from Iran*, Caryologia 65 (2012) 187–198.

[15] G. Yücel, A. Betekhtin, E. Cabi, M. Tuna, R Hasterok, B. Kolano, *The chromosome number and rDNA loci evolution in Onobrychis (Fabaceae)*, International Journal of Molecular Sciences 23 (19) (2022) 11033 17 pages.

[16] R. Volkov, F. Medina, U. Zentgraf, V. Hemleben, Molecular Cell Biology: Organization and molecular evolution of rDNA, nucleolar dominance and nucleolus structure, Progress in Botany, Springer-Verlag, Berlin, 2004, Ch. 4 pp. 106–146.

[17] I. Alvarez, J. F. Wendel, *Ribosomal ITS sequences and plant phylogenetic inference*, Molecular Phylogenetics and Evolution 29 (3) (2003) 417–434.

[18] G. N. Feliner, J. A. Rossello, *Better the devil you know? Guidelines for insightful utilization of nrDNA ITS in species-level evolutionary studies in plants*, Molecular Phylogenetics and Evolution 44 (2) (2007) 911–919.

[19] M. A. Lysak, I. Schubert, Mechanisms of chromosome rearrangements, Plant Genome Diversity Volume 2, Springer, Vienna, 2013, Ch. 9, pp. 137–147.

[20] M. Te Beest, J. J. Le Roux, D. M. Richardson, A. K. Brysting, J. Suda, M. Kubesova, P. Pysek, *The more*

the better? The role of polyploidy in facilitating plant invasions, Annals of Botany 109 (1) (2012) 19–45.

[21] A. I. Bhat, G. P. Rao, Dot-Blot hybridization technique, Characterization of Plant Viruses, Springer Protocols Handbooks, New York, 2020, Ch. 34, pp. 303–321.

[22] G. Robledo, G. Seijo, *Characterization of the Arachis (Leguminosae) D genome using Fluorescence in situ Hybridization (FISH) chromosome markers and total genome DNA hybridization*, Genetics and Molecular Biology 31(3) (2008) 717–724.

[23] M. Markova, B. Vyskot, *New horizons of genomic in situ hybridization*, Cytogenetic and Genome Research 126 (4) (2009) 368–375.

[24] B. Kolano, J. McCann, M. Orzechowska, D. Siwinska, E. Temsch, H. Weiss-Schneeweiss, *Molecular and cytogenetic evidence for an allotetraploid origin of Chenopodium quinoa and C. berlandieri (Amaranthaceae)*, Molecular Phylogenetics and Evolution 100 (2016) 109–123.

[25] C. A. Melo, G. S. Silva, M. M. *Souza Establishment of the genomic in situ hybridization (GISH) technique for analysis in interspecific hybrids of Passiflora*, Genetics and Molecular Research: GMR 14 (1) (2015) 2176–2188.

[26] K. Emadzade, T.-S. Jang, J. Macas, A. Kovařík, P. Novák, J. Parker, H. Weiss-Schneeweiss, *Differential amplification of satellite PaB6 in chromosomally hypervariable Prospero autumnale complex (Hyacinthaceae)*, Annal of Botany 114 (8) (2014) 1597–1608.

[27] R. Hasterok, J. Draper, G. Jenkins, *Laying the cytotaxonomic foundations of a new model grass, Brachypodium distachyon (L.) Beauv*, Chromosome Research, 12 (2004) 397–403.

[28] B. Kolano, J. McCann, M. Oskedra, M. Chrapek, M. Rojek, A. Nobis, H. Weiss-Schneeweiss, *Parental origin and genome evolution of several Eurasian hexaploid species of Chenopodium (Chenopodiaceae)*, Phytotaxa 392 (3) (2019) 163–185.

[29] I. Unfried, P. Gruendler, *Nucleotide sequence of the 5.8S and 25S rRNA genes and of the internal transcribed spacers from Arabidopsis thaliana*, Nucleic Acids Researches 18 (13) (1990) 4011 1 pages.

[30] G. Jenkins, R. Hasterok, *BAC "landing" on chromosomes of Brachypodium distachyon for comparative genome alignment*, Nature Protocols 2 (2007) 88–98.

[31] A. L. Tek, S. D. Kara Öztürk, *High allelic diversity of the centromere-specific histone H3 (CENH3) in the legume sainfoin (Onobrychis viciifolia)*, Molecular Biology Reports 47 (2020) 8789–8795.

[32] S. D. Kara Öztürk, *Analysis of centromeric heterochromatin components by bioinformatics, molecular and cytogenetics methods in sainfoin (Onobrychis viciifolia scop.)*, Master Thesis Niğde Ömer Halisdemir University (2022) Niğde.

[33] M. D. Sacristan, Estudios citotaxonómicos sobre el género Onobrychis (L). Adanson conreferencia especial a la citogenética de la esparceta (*O. viciifolia* Scop.), Zaragoza, Spain, 1965.

[34] M. C. De Vicente, P. Arus, *Tetrasomic inheritance of isozymes in sainfoin (Onobrychis viciaefolia Scop.)*, Journal of Heredity 87 (1996) 54–62.

[35] M. Zarrabian, M. M. Majidi, M. H. Ehtemam, *Genetic diversity in a worldwide collection of sainfoin using morphological, anatomical, and molecular markers*, Crop Science 53 (6) (2013) 2483–2496.

[36] K. Kempf, *Self-fertilization and marker-trait associations in Sainfoin (Onobrychis viciifolia)*, Doctoral Dissertation ETH (2016) Zurich.

[37] S. Shen, X. Chai, Q. Zhou, D. Luo, Y. Wang, Z. Liu, *Development of polymorphic EST-SSR markers and characterization of the autotetraploid genome of sainfoin (Onobrychis viciifolia)*, PeerJ, 7:e6542 19 pages.

[38] J. He, D. Tian, X. Li, X. Wang, T. Wang, Z. Wang, H. Zang, X. He, T. Zhang, Q. Yun, R. Zhang, R. Jiang., S. Jia, Y. Zhang, *A chromosome-level genome assembly for Onobrychis viciifolia reveals gene copy number gain underlying enhanced proanthocyanidin biosynthesis*, Communicaitions Biology 7 19 (2024).

[39] A. Marasek, R. Hasterok, K. Wiejacha, T. Orlikowska, *Determination by GISH and FISH of hybrid status in Lilium*, Hereditas 140 (1) (2004) 1–7.

[40] G. Seijo, G.I. Lavia, A. Fernandez, A. Krapovickas, D.A. Ducasse, D. J. Bertioli, E. A. Moscone, *Genomic relationships between the cultivated peanut (Arachis hypogaea, Leguminosae) and its close relatives revealed by double GISH*, American Journal of Botany 94 (2007) 1963–1971.

[41] Z. Fredotovic, I. Samanic, H. Weiss-Schneeweiss, J. Kamenjarin, T. S. Jang, J. Puizina, *Triparental origin of triploid onion, Allium x cornutum (Clementi exVisiani, 1842), as evidenced by molecular, phylogenetic and cytogenetic analyses*, BMC Plant Biology 14 (2014) Article Number 24 14 pages.

[42] J. F. Zoller, Y. Yang, R. G. Herrmann, U. Hohmann, *Comparative genomic in situ hybridization (cGISH) analysis on plant chromosomes revealed by labelled Arabidopsis DNA*, Chromosome Research 9 (2001) 357–375.

[43] H. B. Ali, M. A. Lysak, I. Schubert, *Genomic in situ hybridization in plants with small genomes is feasible and elucidates the chromosomal parentage in interspecific Arabidopsis hybrids*, Genome 47 (5) (2004) 954–960.

[44] K. Wolfe, *Yesterday's polyploids and the mystery of diploidization*, Nature Reviews Genetics 2 (2001) 333–341.

[45] I. J. Leitch, L. Hanson, K. Y. Lim, A. Kovarik, M. W. Chase, J. J. Clarkson, A. R. Leitch, *The ups and downs of genome size evolution in polyploid species of Nicotiana (Solanaceae)*, Annals of Botany 101 (6) (2008) 805–814.

[46] T. S. Jang, H. Weiss-Schneeweiss, *Formamide-free genomic in situ hybridization allows unambiguous discrimination of highly similar parental genomes in diploid hybrids and allopolyploids*, Cytogenetic and Genome Research 146 (4) (2015) 325–331.

Çanakkale Onsekiz Mart University

Journal of Advanced Research in Natural and Applied Sciences

dergipark.org.tr/tr/pub/jarnas

Open Access

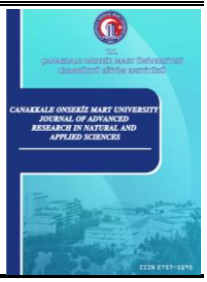

e-ISSN: 2757-5195 2024, Vol. 10, Issue 2, Pages: 435-445 doi.org/10.28979/jarnas.1440709

Merchant Fleet Performance of Türkiye: A CRITIC-based TOPSIS Approach

Ersin Firat Akgul[1], Emrah Akdamar[2], Maruf Gögebakan[3]

[1,2,3]Department of Maritime Business Administration, Maritime Faculty, Bandırma Onyedi Eylul University, Balıkesir, Türkiye

Article History

Received: 21 Feb 2024

Accepted: 01 Apr 2024

Published: 25 Jun 2024

Research Article

Abstract − The study focuses on assessing the merchant fleet performance of Türkiye, a country surrounded by seas on three sides and holding a pivotal position in global logistics networks. It considers mean age of vessels, total carrying capacity in dead weight tons, and the number of ships as indicators influencing Türkiye's merchant fleet performance, with the importance weights of these indicators determined using the CRITIC method. Based on the determined weights, Türkiye's merchant fleet performance for the years 2011-2023 is evaluated using the TOPSIS method. The findings reveal that mean age of vessels emerges as the indicator with the highest importance weight. The analysis indicates an improvement in Türkiye's fleet performance between 2011 and 2013, followed by a subsequent decline from 2013 onwards. Notably, there is a significant shift observed in 2016 across all three indicators. Given Türkiye's aging fleet, the study suggests a focus on acquiring young and high-capacity vessels to enhance fleet performance. This strategic approach can help Türkiye optimize its maritime trade capability and maintain competitiveness in the global shipping industry.

Keywords − *Merchant fleet performance, Türkiye, CRITIC, TOPSIS*

1. Introduction

Türkiye is situated at the intersection of Europe and Asia and its advantageous location along important trade routes has shaped its current prominence in international business. Türkiye's merchant fleet is an essential component of the global maritime network, with a varied fleet composition that meets a range of cargo demands and trade routes [1]. Erdogan and Cetin [2] highlights the crucial role of maritime transport in Turkish economy, particularly in facilitating trade with Asia, Africa, and Europe. This is further emphasized by Cerit [3], who identifies maritime transport as a key factor in the competitive advantage of Turkish exporters. The sector's contribution to Türkiye's industrial development, employment, and trade balance emphasizes economic significance. Nevertheless, despite these advantages, problems like complicated regulations, inadequate infrastructure, and environmental issues still exist, calling for a sophisticated approach to fleet management. The maritime transportation sector in Türkiye has gained substantial significance since the 1980s, with its importance only being recognized in more recent times [4].

Identifying the distinctive features of Türkiye's merchant fleet performance in the geopolitical, economic, and environmental context can enable the formulation of specific policy recommendations tailored to its needs. From a geopolitical perspective, Türkiye's unique geopolitical position as a bridge between Europe and Asia and its access to key waterways such as the Bosphorus make the performance of its merchant fleet critical for global trade [5]. Understanding how Türkiye's fleet competes in this strategic location can contribute to a

[1]eakgul@bandirma.edu.tr (Corresponding Author); [2]eakdamar@bandirma.edu.tr; [3]mgogebakan@bandirma.edu.tr

broader understanding of international maritime dynamics. From an economic perspective, analyzing the performance of Türkiye's merchant fleet, a large emerging market with a diverse economy, can provide insights into the economic factors affecting the efficiency and competitiveness of the maritime sector [6]. From an environmental perspective, analyzing the performance of Türkiye's merchant fleet, which like many other countries is subject to various environmental regulations and international standards in the maritime sector, can provide insight into the extent to which the country complies with these regulations and address environmental sustainability concerns [7]. In this study, we aim to analyze the performance of the merchant fleet of Türkiye in more depth. In this context, we seek answers to the questions, specifically (i) what are the strengths and weaknesses of Türkiye's merchant fleet performance using multi-criteria decision-making methods and how do they compare to global benchmarks? (ii) how has Türkiye's merchant fleet performance changed over the years?

This paper is structured as follows: Section two presents the literature review. Section three describes the dataset and methods used. Section four presents the findings and offers a detailed overview. Finally, the study concludes with a discussion of the findings in relation to the existing literature, as well as an exploration of limitations, implications, and directions for future research.

2. Literature Review

Studies on maritime competition and the search for policies to promote national shipping emphasize this situation and offer various policy recommendations. For instance, Gardner et al. [8], Leggate and McConville [9] and Brownrigg et al. [10] on the UK, Morris [11] on Australia, Coto-Millan [12] on Spain, Yercan [13] on Türkiye, Damachi and Zhaoshen [14] on Nigeria, [15] and Iheduru [16] on West and Central Africa, Sawiczewska [17] on Poland, Song [18], and Chiu [19] on China. In terms of cross-country comparisons, Marlow and Mitroussi [20] comparatively examined the tonnage tax regimes of the United Kingdom, Netherlands, Liberia, Panama and Greece and found that Panama is the most favorable regime and the United Kingdom is the least favorable regime under the scenario considered and that some of Greece's international rankings deteriorate as the age of the ship increases.

The performance of Türkiye's merchant fleet is subject to a range of influencing factors, as indicated by various studies. Cetin et al. [6] underscores the significance of competitiveness within the coaster market, while Yilmaz [21] evaluates the Port State Control (PSC) performance of Turkish-flagged ships, reporting favorable PSC performance. Karahan and Kirval [22] quantitatively assessed and visually map the primary attributes of the Turkish maritime transportation sector by employing a cluster approach and emphasized the potential of Istanbul county, also Karahan and Kirval [23] asserted that the maritime sector in Istanbul possesses substantial potential to evolve into a prominent maritime cluster, not only within its regional context but also on a global scale. While the observed statistical significance of clustering on firm performance is notable, the magnitude of this impact was found to be moderate rather than high. According to Ciftci [24], maritime merchant fleet are generally at or below the expected minimum levels relative to income levels in high-income countries with institutionalized market economies. Even in countries with effective maritime policies, the industry is adversely affected by high international competition. Furthermore, due to the extremely low GDP per capita levels in countries such as Russia, India, Indonesia and China, including Türkiye, it is only possible to maintain the existing capacities in merchant fleet formation, which requires high investment expenditures. Cetin et al. [6] emphasized that one of the most important factors hindering the competitiveness of the Turkish owned merchant fleet is the operation of old and outdated small sized general cargo vessels. As mentioned by Kaya and Erginer [25], the mean age of vessels owned by Turkish shipowners exceeds the global fleet average by

5.2 years. Another implications of Cetin et al. [6] is that In instances where funding is required, equity is predominantly utilized, although it frequently proves inadequate. Access to financial resources for modernization or the establishment of new fleets remains insufficient, prompting the pursuit of public support. Moreover, employment of inexperienced and mostly unqualified seafarers on small sized vessels leads to significant risks, and that a business model far from institutionalization is adopted, with family-owned companies dominating the sector.

Baser [4] examined the evolution of the Turkish merchant fleet since 1980, specifically focusing on the selection of technology and the overall productivity of the fleet. Accordingly, a critical issue within the Turkish merchant fleet is the aging of shipbuilding technology, representing a significant challenge in the industry. In addition, it was identified that the productivity of merchant fleet of Türkiye lags behind that of the global merchant fleet. Yercan [13] provided an overview of policy decisions made by Turkish authorities on both international and national fronts. Erdogan and Kara [26] employed a SWOT-AHP integrated method to determine the optimal approach for Türkiye's maritime transportation policy, highlighting the utilization of strengths to exploit opportunities as the most effective strategy in the former study. Kadioglu [27] traced the progression of Türkiye's maritime sector from an inward-oriented strategy to a partially liberal policy, followed by a planned development period, while also assessing the attainment of stated targets. Together, these studies provide a comprehensive insight into Türkiye's maritime transportation policy.

Celik et al. [28] developed a practical decision support mechanism aimed at facilitating a comprehensive multiple criteria analysis for the selection of ship registries using fuzzy AHP methodology and utilized with a case investigation on Turkish maritime industry. Results suggest that ship registries of Türkiye, Panama, and Malta have been selected for evaluation as potential alternatives for Turkish ship owners. Çelik and Topçu [29] conducted a quantitative decision analysis to address the flagging out issue within the Turkish shipping fleet. They evaluated shipowners' decision-making preferences among the Turkish National Shipping Registry (TNSR), Turkish International Shipping Registry (TISR), and Open Registries (ORs) as potential alternatives. The findings of this case study highlight a notable inclination among Turkish shipowners to register with ORs. Consequently, the study suggests that implementing significant changes in TNSR procedures could enhance competitiveness in the international shipping market. One of the model proposals concerning the flagging out issue in the Turkish maritime sector is a fuzzy quantified Strengths, Weaknesses, Opportunities, and Threats (SWOT) analysis developed by Çelik and Kandakoğlu [30]. An original model, the 'flagging out strategy development and evaluation matrix' (FODEM), holds promise in offering a structured decision-making tool for addressing the flagging out dilemma consistently.

Existing literature on maritime transport of Türkiye predominantly focuses on flagging out [29,30], market structure [6, 22, 23], and maritime policies [13, 26, 27]. Within the scope of merchant fleet performance, as far as we found out the studies are limited with fleet productivity [4] and PSC performance [21], and there is no comprehensive study on the factors affecting merchant fleet performance. Consequently, this study is anticipated to make a substantial contribution by addressing this gap and providing insights into the performance of merchant fleet of Türkiye.

3. Data and Methodology

The UNCTADstat database offers a variety of sub-indicators under the category of “Maritime Transport” [31]. However, when examining Türkiye’s data based on beneficial ownership, only two indicators are available: "deadweight tons in thousands" and "number of ships." In contrast, a broader range of indicators is accessible based on the flag of registration. In this study, Türkiye’s data has been meticulously reviewed to provide a

comprehensive analysis. The study spans the years 2011 to 2023 and encompasses key indicators such as "deadweight tons," "number of ships," and "mean age of vessels." By focusing on these indicators, the study aims to offer a thorough examination of Türkiye's merchant fleet performance over the specified timeframe, shedding light on trends, patterns, and potential areas for improvement within the country's maritime industry. The CRITIC method has been employed to assign weights to the indicators used in the study. With these weights determined, the TOPSIS method was then applied to measure performance and rank Türkiye's merchant fleet performance by year. This approach allows for a comprehensive evaluation of Türkiye's maritime industry over the analyzed period, offering insights into its relative performance and potential areas for enhancement.

3.1. CRITIC Weighting Method

CRITIC (Criteria Importance Through Intercriteria Correlation) method is used to determine the importance levels of the criteria in the data based on correlation [32].

The CRITIC method offers a superior approach for determining the importance levels of criteria in data based on correlation due to its ability to account for interdependence between criteria, robustness to data variability, reduction of subjectivity through objective measures, handling of multicollinearity, provision of decision support, and adaptability to diverse contexts. By considering the complex relationships between criteria, CRITIC provides more accurate and reliable importance rankings, making it a valuable tool for decision-making in various fields. The steps of probability weights with the CRITIC method are shown in Table 1 as follows.

Table 1. Algorithm of CRITIC weighting method

1.Step: Decision Matrix	$A = [a_{ij}]_{mxn}$
2.Step: Normalized benefit-cost matrix	$\bar{a}_{ij} = \frac{a_{ij} - {a_j}^{ideal^-}}{{a_j}^{ideal^+} - {a_j}^{ideal^-}}$, where ${a_j}^{ideal^-}$ and ${a_j}^{ideal^+}$ represents negative and possitive ideal solutions, respectively.
3.Step: Symmetric matrix	$r_{ij} = \frac{a_{ij}}{\sum_{i=1}^{m} a_{ij}}$, where $a_{ij} \in A$
4.Step: Information load	$c_j = \sigma_j \sum_{i=1}^{m}(1 - r_{ij})$, where standart deviation and measure of conflict calculated by $\sigma_j = \sqrt{\frac{1}{k-1}\sum_{i=1}^{m}(r_{ij} - r_j)^2}$ and $\sum_{i=1}^{m}(1 - r_{ij})$ equations, respectively.
5.Step: Probability weight	$w_j = \frac{c_j}{\sum_{i=1}^{m} c_j}$, where c_j correspon to each elemnt of information load.

3.2. TOPSIS Sorting Method

TOPSIS (Technique for Order Preference by Similarity to Ideal Solution) method was used to investigate the change and ranking of the number of ships, mean age of vessels and DWT variables by years [33]. It was proposed by Hwang and Yoon [33] to determine the best alternative based on a consensus solution. The method of determining the solutions that are closest to the ideal solution and farthest from the negative ideal solution is called consensus (optimum) solution [34].

The TOPSIS technique was selected due to its alignment with the data and research goals, assessing the performance of Turkey's merchant fleet using specific metrics such as the average age of vessels, cargo capacity, and number of ships. Its ability to facilitate precise, quantitative decision-making renders it well-suited for ranking options based on their proximity to the optimal solution. In comparison to other methods, such as Intuitionistic Fuzzy TOPSIS, conventional TOPSIS is more straightforward and computationally efficient, making it the preferred choice for evaluating Turkey's fleet performance from 2011 to 2023 with defined metrics and minimal uncertainty. TOPSIS ranking steps are shown in Table 2 as follows.

Table 2. Algorithm of TOPSIS sorting method

1. Step: Decision Matrix	$A = [a_{ij}]_{mxn}$, where a_{ij}correspond to each element of criteria
2. Step: Normalized Matrix	$r_{ij} = \frac{a_{ij}}{\sqrt{\sum_{i=1}^{m} a_{ij}^2}}$, where r_{ij} denotes the elements of the normalized matrix $N = [r_{ij}]_{mxn}$.
3.Step: Weighted Normalized Matrix	It consists of the elements $v_{ij} = w_j r_{ij}$ and is denoted as $V = [v_{ij}]_{mxn}$, where $\sum_{j=1}^{n} w_j = 1$ and $r_{ij} \in N$.
4. Step: Ideal and Non-Ideal Solutions	Ideal and negative ideal separation measures are calculated with weighted matrix elements as $S_i^+ = \sqrt{\sum_{j=1}^{n} (v_{ij} - v_j^+)^2}$ and $S_i^- = \sqrt{\sum_{j=1}^{n} (v_{ij} - v_j^-)^2}$, respectively.
5. Step: Similarity to Ideal Solution measure	The optimum solution is determined by the $C_i^+ = S_i^- / (S_i^- + S_i^+)$ ratio, where $0 \leq C_i^+ \leq 1$.

4. Findings

In this section, first the importance weights of performance indicators were determined for each year between 2011 and 2023 by employing the CRITIC method, which assigns weights to the indicators based on their relative importance. Subsequently, the TOPSIS approach is utilized to measure the merchant fleet performance and compare the years. The weights derived from the CRITIC method are applied to the TOPSIS method to evaluate and rank the performance of each year, allowing for a comprehensive analysis of Türkiye's merchant fleet performance over the specified timeframe. Table 3 presents the mean age of vessels, total carrying capacity in dead weight tons, and the number of ships, which serve as indicators of the merchant fleet performance of Turkish flagged ships from 2011 to 2023.

Since each of the indicators used to measure merchant fleet performance has a different unit of measurement, it would not be useful to show the trend of each indicator over the years on a single figure. Therefore, all three indicators are normalized with the 0-1 normalization method and the movement of the indicators between 2011 and 2023 is shown in Figure 1. This visual representation offers insights into the trends and patterns observed in Türkiye's merchant fleet over the specified period.

Table 3. Raw Data and Normalized Data

Years	Indicators			Normalized Indicators		
	Mean Age of Vessels	**Dead weight tons (in thousands)**	**Number of Ships**	**Mean Age of Vessels**	**Dead weight tons (in thousands)**	**Number of Ships**
2011	25	8753	1315	0,50	0,66	0,89
2012	24	9680	1333	1,00	0,89	1,00
2013	24	10132	1325	1,00	1,00	0,95
2014	25	8738	1254	0,50	0,65	0,53
2015	25	8557	1241	0,50	0,61	0,46
2016	26	8629	1267	0,00	0,62	0,61
2017	26	8241	1266	0,00	0,53	0,60
2018	26	7975	1256	0,00	0,46	0,54
2019	26	7559	1242	0,00	0,36	0,46
2020	26	7064	1241	0,00	0,23	0,46
2021	26	6301	1184	0,00	0,04	0,12
2022	26	6129	1164	0,00	0,00	0,00
2023	26	6651	1170	0,00	0,13	0,04
Mean	25,46	8031,46	1250,62	0,27	0,48	0,51
Median	0,78	1241,93	54,55	0,39	0,31	0,32
S.Dev	26,00	8241,00	1254,00	0,00	0,53	0,53
Min	24,00	6129,00	1164,00	0,00	0,00	0,00
Max	26,00	10132,00	1333,00	1,00	1,00	1,00
Coef. Var	0,03	0,15	0,04	1,44	0,65	0,63

In the normalization step, two distinct perspectives were taken into account: cost and benefit. Each criterion was approached differently to ensure a comprehensive evaluation. For the cost-oriented age criterion, the formula (xmax-x)/(xmax-xmin) was applied. This formula efficiently scales the data, allowing for a clear comparison of the costs associated with different age values. On the other hand, for the benefit-oriented criteria such as dwt (deadweight tonnage) and the number of ships, a different normalization formula was utilized. Here, (x-xmin)/(xmax-xmin) was employed. By using this formula, the focus shifts to the benefits derived from these criteria, enabling a fair assessment of their contributions relative to the entire range of data. These distinct approaches ensure that both the costs and benefits associated with each criterion are effectively considered during the normalization process, leading to a more balanced and insightful evaluation of the decision-making factors.

According to the findings, the mean age of vessels has remained constant since 2016. This indicates that there have been some attempts to keep the mean age of vessels constant or reduce it since this year. According to UNCTAD Review of Maritime Transport [35], 87.9% of bulk carriers, 78.7% of container ships, 65.1% of oil tankers and 42.8% of general cargo ships in the world merchant fleet are 19 years old or younger. When analyzed on the basis of total carrying capacity and number of vessels, it is observed that the indicator values reached a peak in 2013 but have been on a downward trend since then. Especially in 2016, it can be stated that a breakthrough was experienced in terms of all three indicators. Finally, there is also a downward trend in the number of vessels. The fact that the mean age of vessels has remained constant over the years suggests two scenarios. The first one is the inclusion of younger vessels in the fleet and the second one is the disposal of older vessels by directing them to the second-hand or demolition markets. However, the downward trends in total carrying capacity and the number of vessels imply that the latter scenario is more probable.

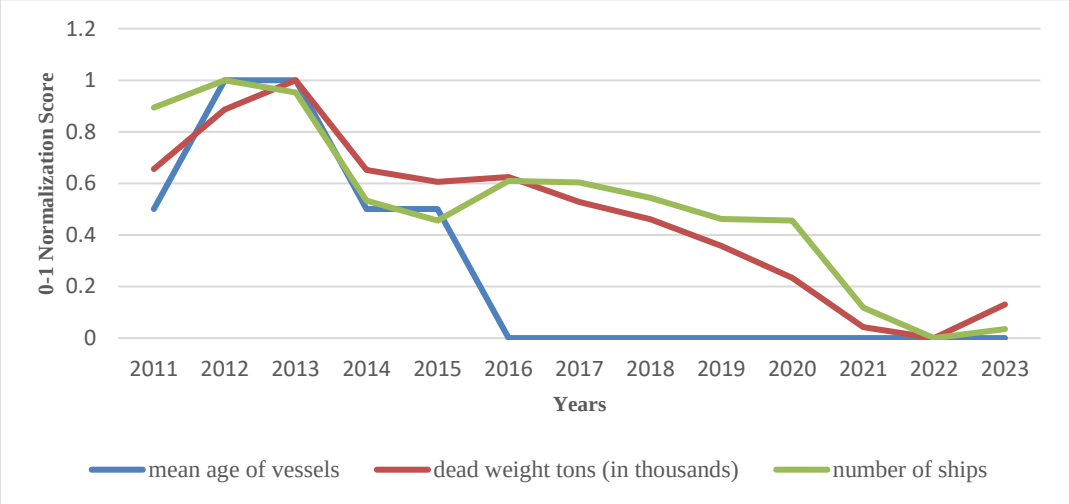

Figure 1. Visualization of the indicators based on 0-1 normalization scores by years

CRITIC method, one of the objective weighting methods, was used to determine the extent to which indicators are effective in Türkiye's merchant fleet performance, and the findings are given in Table 4.

Table 4. Weights and rankings of indicators

	Mean Age of Vessels	Dead weight tons	Number of Ships
σ	0.388125	0.310251017	0.322784
Cj	0.17524	0.07955129	0.1103753
Wj	47.99%	21.78%	30.23%
Rank	1	3	2

The most determinant indicator in Türkiye's merchant fleet performance is the mean age of vessels with a weight of 47.99%. This indicator is followed by the number of ships with a weight of 30.23% and total dwt with a weight of 21.78%. Türkiye's merchant fleet performance score between 2011 and 2023 is calculated by TOPSIS method using the weights obtained from the CRITIC method and the yearly change in the performance score is visualized with a line graph as shown in Figure 2.

Years	Score	Rank
2013	0.753464	1
2012	0.726215	2
2011	0.664766	3
2016	0.65016	4
2014	0.620122	5
2017	0.576564	6
2015	0.575698	7
2018	0.52126	8
2019	0.440594	9
2020	0.366133	10
2023	0.281591	11
2021	0.258525	12
2022	0.245006	13

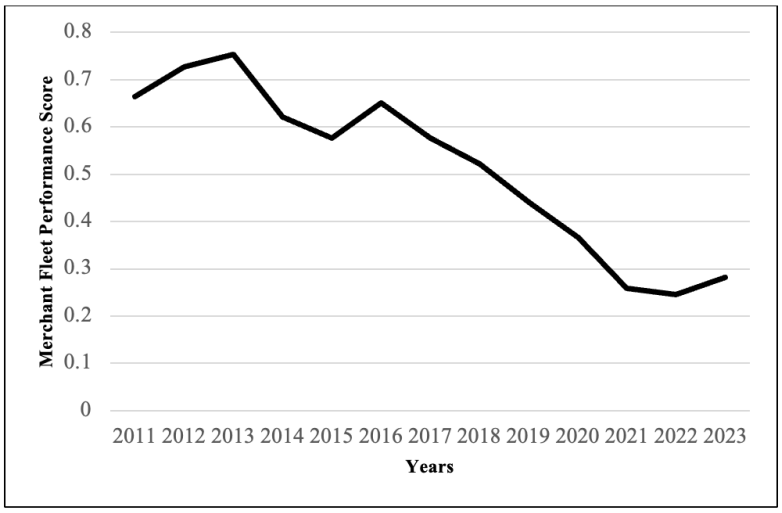

Figure 2. Merchant fleet performance score and rankings

Accordingly, Türkiye's merchant fleet performance score between 2011 and 2023 is on a downward trend and the most important reason for this is the aging of the fleet based on the findings of the CRITIC method. In addition to the aging of the fleet, the decline in the number of ships and total carrying capacity has made the decline in fleet performance inevitable. In line with the changes in the indicators, Türkiye's fleet performance showed a negative break in 2016.

Finally, the box plot in Figure 3 shows some descriptive statistics on Türkiye's merchant fleet performance score between 2011 and 2023.

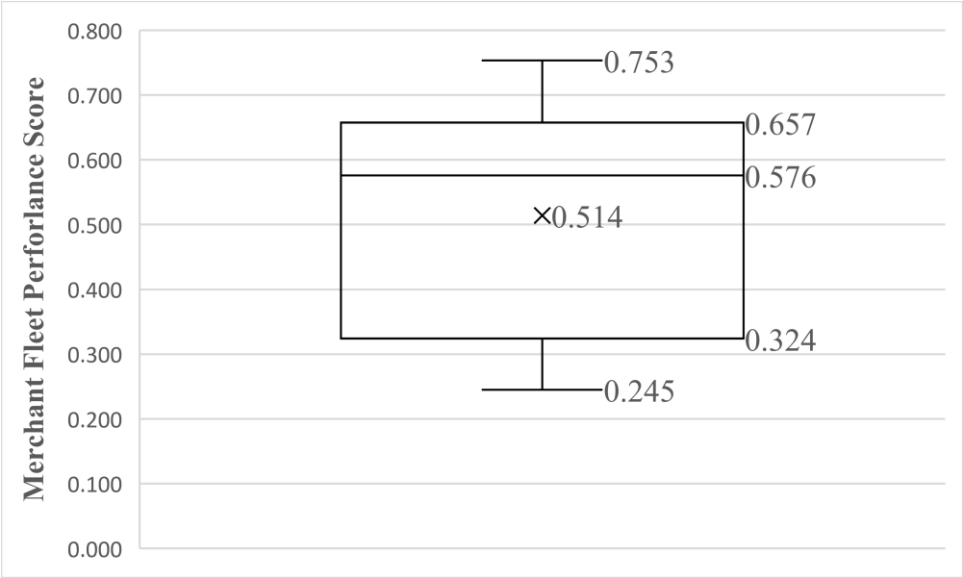

Figure 3. Merchant fleet performance score box plot

Accordingly, Türkiye's average merchant fleet performance for the years analyzed is 0.514. The lowest score among these years was 0.245, while the highest score was 0.753. When the third quartile value is taken into account, it is observed that the performance score is below 0.657 in 75% of the analyzed time period, and

according to the first quartile value, it is below 0.324 in 25% of the analyzed time period. The median merchant fleet performance score for Türkiye in the years analyzed was 0.576. In other words, fleet performance was below 0.576 in half of the time period and above 0.576 in the other half.

5. Discussion and Conclusion

In today's global economy, where services outweigh goods, maritime transportation stands out as the key for international movement and in this study, it is intended to evaluate the performance of merchant fleet of Türkiye that plays a crucial role in global logistics networks. Türkiye needs to boost its merchant fleet's competitiveness, but high costs pose challenges. Findings implies that incentive mechanisms are vital to spur development in maritime capabilities. Accordingly, to boost the Turkish merchant fleet, focus should shift to fleet rejuvenation as also depicted by Cetin et al. [6]. Since 2013, the fleet has aged, remaining at 26 since 2016. In line with Baser [4], prioritizing the replacement of older vessels with newer ones will enhance fleet efficiency. This means disposing older ships through the second-hand market or scrapping and acquiring younger ones. The study suggests efforts to rejuvenate the fleet, but they are insufficient. As asserted by Kaya and Erginer [25], the average age of Turkish fleet exceeds that of the world merchant fleet. Older vessels in Türkiye's fleet are being sold or scrapped to prevent the fleet's average age from rising. However, there is a lack of action to introduce new or younger ships, which would lower or at least maintain the average age. As the total carrying capacity declines due to limited acquisition of younger vessels, industry players should prioritize investing in vessels with significant carrying capacity. This strategic shift will improve all key fleet performance indicators: age, carrying capacity, and number of vessels, leading to overall enhancement in Türkiye's merchant fleet performance. At this point, it would be appropriate to emphasize the average vessel size. The implications of average vessel size can be evaluated from two different perspectives. A larger average ship size may suggest a fleet composed of fewer but more capacious vessels, potentially indicating economies of scale and operational efficiency as supported by Cullinane and Khanna [36]. Conversely, as also asserted by Mulligan and Lombardo [37], a smaller average ship size may reflect a more diversified fleet with smaller vessels catering to specific routes or cargo types.

The analysis underscores the need for Türkiye to invest in young and large commercial vessels, offering two distinct approaches. Firstly, neglecting investment in younger, high-capacity vessels could escalate operating expenses, notably in insurance and maintenance, due to Türkiye's fleet being older than the global average. In fact, as asserted by Tran and Haasis [38] investing in new capacity will result in higher total revenue for operators, albeit at lower unit revenue. Moreover, older vessels may struggle to meet international maritime standards, limiting charterer options and market reputation. An aging fleet also hampers competitiveness during intense market competition. As implied by Alexandridis et al. [39] continuous investment in the maritime sector is vital to tackle these challenges effectively. Secondly, the regional nature of trade in the Mediterranean-Black Sea region, with smaller parcels, may hinder investment in large tonnage vessels. Introducing newer, larger ships requires a review of existing business models to align with market demands. Diversifying business models to engage in global trade beyond local regions could significantly enhance fleet performance. As outlined by Lorange and Fjeldstad [40], expanding operations geographically enables access to new opportunities and boosts efficiency. Indeed, Saya [41] emphasized that the development of Greek shipping was greatly influenced by the fact that Greek shipowners gained the ability to develop business by opening offices in maritime centers such as New York and London. This shows the significance of market access, which Türkiye also needs to prioritize.

The study's limitations include its reliance on data spanning from 2011 to 2023, the utilization of CRITIC and

TOPSIS methodologies among numerous multi-criteria decision-making methods, and the adoption of mean age, deadweight tons, and number of vessels as merchant fleet performance indicators. Future research could explore varying time frames and employ diverse methods and indicators for comparative performance assessment.

Author Contributions

All the authors equally contributed to this work. They all read and approved the final version of the paper.

Conflicts of Interest

All the authors declare no conflict of interest.

References

[1] S. Suluk, *Colors of the economy: An evaluation of turkey in the context of the sustainable blue economy*, Dumlupınar University Journal of Social Sciences (74) (2022) 132–150.

[2] O. Erdogan, O. Cetin, *The effects of maritime transport on the Turkish economy* (2021), https://ssrn.com/abstract=3880804, Accessed 10 Feb 2024.

[3] A. G. Cerit, *Maritime transport as an area of competitive advantage in international marketing*, International Journal of Maritime Economics 2 (1) (2000) 49–67.

[4] S. O. Baser, *Technology Choice and Productivity in the Turkish merchant fleet in the last two decades*, Maritime Policy & Management 25 (4) (1998) 391–396.

[5] L. Berkoz, D. Tekba, *The role of ports in the economic development of Turkey*, in: European Regional Science Association (ERSA), Louvain-la-Neuve, Dublin, 1999.

[6] İ. B. Çetin, E. F. Akgül, E. Koçak, *Competitiveness of Turkish coaster merchant fleet: A qualitative analysis by short sea shipping perspective*, TransNav 12 (2) (2018) 389–396.

[7] O. Konur, M. Bayraktar, M. Pamik, B. Kuleyin, M. Nuran, *The energy efficiency gap in Turkish maritime transportation*, Polish Maritime Research 26 (3) (2019) 98–106.

[8] B. M. Gardner, S. J. Pettit, H. A. Thanopoulou, *Shifting challenges for British maritime policy*, Marine Policy 20 (6) (1996) 517–524.

[9] H. Leggate, J. McConville, *Tonnage tax: Is it working?*, Maritime Policy & Management 32 (2) (2005) 177–186.

[10] M. Brownrigg, G. Dawe, M. Mann, P. Weston, *Developments in UK shipping: the tonnage tax*, Maritime Policy & Management 28 (3) (2001) 213–223.

[11] R. Morris, *De-manning the fleet: federal government reforms and Australia's shipping debate*, Maritime Policy & Management 20 (1) (1993) 67–75.

[12] P. Coto-millán, *Maritime transport policy in Spain (1974–1995)*, Transport Policy 3 (1-2) (1996) 37–41.

[13] F. Yercan, *Maritime transport policy of Turkey*, Transport Policy 5 (4) (1998) 259–266.

[14] B. B. Damachi, Y. Zhaosheng, *The Nigerian shipping industry and indigenous shipping companies*, Maritime Policy & Management 32 (1) (2005) 31–38.

[15] M. G. Chasomeris, *South Africa's maritime policy and transformation of the shipping industry*, Journal of Interdisciplinary Economics 17 (3) (2006) 269–288.

[16] O. C. Iheduru, *Merchant fleet development by legislation: lessons from West and Central Africa*, Maritime Policy & Management 19 (4) (1992) 297–317.

[17] Z. Sawiczewska, *Reconstructing Polish ports and shipping*, Maritime Policy & Management 19 (1) (1992) 69–76.

[18] Y. B. Song, S*hipping and shipbuilding policies in PR China*, Marine Policy 14 (1) (1990) 53–70.

[19] R.-H. Chiu, *The liberalization of shipping in Taiwan*, Marine Policy 31 (3) (2007) 258–265.

[20] P. Marlow, K. Mitroussi, *EU shipping taxation: The comparative position of Greek shipping*, Maritime Economics & Logistics 10 (1-2) (2008) 185–207.

[21] F. Yılmaz, *Evaluation of port state control (PSC) performance of Turkish flagged merchant ships in Paris memorandum of understanding (MoU) on PSC*, Turkish Journal of Maritime and Marine Sciences 6 (1) (2020) 111–119.

[22] C. B. Karahan, L. Kırval, *Clustering analysis of Turkish maritime transportation sector*, Journal of Transportation and Logistics 3 (2) (2018) 63–80.

[23] C. B. Karahan, L. Kirval, *Clustering potential of Istanbul maritime sector*, Maritime Business Review 3 (3) (2018) 314–336.

[24] M. Çiftçi, *Global comparative position of Turkish maritime sector as a national wealth*, International Journal of Alanya Faculty of Business 4 (3) (2012) 1–9.

[25] A. Y. Kaya, K.E. Erginer, *An analysis of decision-making process of shipowners for implementing energy efficiency measures on existing ships: The case of Turkish maritime industry*, Ocean Engineering 241 (2021) 110001.

[26] A. Erdoğan, G. Kara, *Determining the maritime transportation policy of Turkey*, International Journal of Maritime Engineering 161 (A4) (2019) 437–448.

[27] M. Kadioglu, *Turkish maritime transport policy (1960-2008)*, TransNav 4 (2) (2010) 243–250.

[28] M. Celik, I. Deha Er, A. F. Ozok, *Application of fuzzy extended AHP methodology on shipping registry selection: The case of Turkish maritime industry*, Expert Systems with Applications 36 (1) (2009) 190–198

[29] M. Celik, Y. I. Topcu, *A decision-making solution to ship flagging out via administrative maritime strategies*, Maritime Policy & Management 41 (1) (2014) 112–127.

[30] M. Celik, A. Kandakoglu, *Maritime policy development against ship flagging out dilemma using a fuzzy quantified SWOT analysis*, Maritime Policy & Management 39 (4) (2012) 401–421.

[31] UNCTADStat, *UNCTAD Data Centre* (2023), https://unctadstat.unctad.org/wds/TableViewer/summary.aspx, Accessed 20 Dec 2023.

[32] D. Diakoulaki, G. Mavrotas, L. Papayannakis, *Determining objective weights in multiple criteria problems: The critic method*, Computers & Operations Research 22 (7) (1995) 763–770.

[33] C. -L. Hwang, K. Yoon, Multiple attribute decision making: methods and applications, Springer Berlin, Heidelberg, 1981.

[34] G. -H. Tzeng, J.-J. Huang, Multiple attribute decision making: methods and applications, CRC Press, New York, 2011.

[35] UNCTAD, *Review of Maritime Transport 2023, 2023.* https://unctad.org/system/files/official-document/rmt2023_en.pdf, Accessed 4 Oct 2023.

[36] N.K. Tran, HD. Haasis, *An empirical study of fleet expansion and growth of ship size in container liner shipping*, International Journal of Production Economics 159 (2015) 241–253.

[37] K. Cullinane, M. Khanna, *Economies of scale in large containerships: optimal size and geographical implications*, Journal of Transport Geography 8 (3) (2000) 181–195.

[38] R. F. Mulligan, G. A. Lombardo, Short sea shipping: — Alleviating the environmental impact of economic growth, WMU Journal of Maritime Affairs 5 (2) (2006) 181–194.

[39] G. Alexandridis, M. G. Kavussanos, C. Y. Kim, D. A. Tsouknidis, I. D. Visvikis, *A survey of shipping finance research: Setting the future research agenda*, Transportation Research Part E: Logistics and Transportation Review 115 (2018) 164–212.

[40] P. Lorange, O. D. Fjeldstad, New Business Models and Strategies in Shipping, in: W. K. Talley (Ed.), The Blackwell Companion to Maritime Economics, West Sussex, Wiley, 2012, pp. 263–280

[41] M. Saya, Examination of dynamics upgrading Greek shipping, Dokuz Eylul University Maritime Faculty Journal 15 (1) (2023) 35–51.

Çanakkale Onsekiz Mart University

Journal of Advanced Research in Natural and Applied Sciences

dergipark.org.tr/tr/pub/jarnas

Open Access

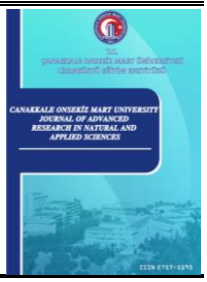

e-ISSN: 2757-5195 2024, Vol. 10, Issue 2, Pages: 446-463 doi.org/10.28979/jarnas.1416814

Hazardous Solid Waste Landfill Site Selection for İstanbul, Türkiye using Multi-Criteria Decision-Making Methods and GIS Data

Elif Elçin Günay[1], Sena Dere[2]

[1,2]Department of Industrial Engineering, Faculty of Engineering, Sakarya University, Sakarya, Türkiye
[1]School of Engineering, University of Dayton, Dayton, USA

Article History

Received: 11 Jan 2024

Accepted: 08 Apr 2024

Published: 25 Jun 2024

Research Article

Abstract − The high toxicity of materials in disaster waste poses a significant risk to the environment, including the air, water, soil, and all living beings. One of the commonly used disposal methods for hazardous solid waste is landfilling. The selection of sites for hazardous solid waste disposal requires extreme care and attention to multiple factors from environmental, social, and economic points of view. Considering the anticipated earthquake in Istanbul and the city's excessive population and urbanization, experts estimate that debris waste will be approximately 25 million tons. In this study, we propose a Geographic Information System (GIS) based fuzzy Multi-Criteria Decision Making (MCDM) approach to select hazardous solid waste landfill (HSWL) locations within the scope of disaster waste management for Istanbul. First, the evaluation criteria were identified through a literature review and expert opinions. Next, criteria are prioritized using the Fuzzy Analytic Hierarchy Process (FAHP). Then, GIS data for the criteria are gathered from multiple resources and entered into ArcGIS 10.8 for spatial analysis. Last, the suitability map of Istanbul for the HSWL construction is built. Considering five candidates, the Analytic Hierarchy Process (AHP) is applied to select the most suitable locations for Asian and European sites in the city. Accordingly, Fevzipaşa/Silivri for the European side and Hasanlı/Şile for the Asian side were selected as the most suitable two options. Last, a sensitivity analysis was performed to investigate the impact of the highest weight criterion on the final solution.

Keywords − *Disaster waste management, fuzzy analytic hierarchy process, geographic information system, hazardous solid waste management, multi-criteria decision making*

1. Introduction

Disasters can cause significant harm to society, damage residential areas and infrastructure, and produce extensive amounts of debris. Debris includes numerous hazardous materials, including heavy metals like lead, organic and inorganic substances with high toxicity, and asbestos. The release of asbestos-containing materials during a disaster pollutes water sources, soil, and air. It can pose serious health risks, such as lung cancer, mesothelioma, larynx, and asbestosis [1]. For instance, on February 6, 2023, two earthquakes measuring 7.7 and 7.6 magnitudes hit Kahramanmaraş, affecting 11 provinces deeply and resulting in the loss of 50,500 lives. At least 35,000 buildings were destroyed, while hundreds of thousands suffered severe and moderate damages. The disaster caused approximately 350 to 580 million tons of construction and demolition waste including around 1.5 million tons of hazardous waste, which threatened the health of people residing in the affected cities (around 13 million people) and the environment due to the emission of asbestos-containing materials [2, 3]. This unfortunate earthquake exhibits the importance of effective disaster waste management to prevent severe negative impacts on health and the environment.

[1]ekabeloglu@sakarya.edu.tr (Corresponding Author); [2]senadere33@gmail.com

The most critical objective of disaster management is appropriately managing the waste generated by the disaster [4]. This involves selecting locations for the storage and subsequent disposal of disaster waste and removing the hazardous debris and harmful waste immediately after the disaster to minimize the damage. Due to its complex geological structure and tectonic position, numerous active faults exist in Türkiye, leading to countless earthquakes throughout history. Therefore, utmost attention should be paid to disaster waste management to mitigate its negative impacts on the community and the environment. In this regard, this study aims to support experts in selecting hazardous solid waste landfill (HSWL) sites for the anticipated earthquake in Istanbul.

According to a Kandilli Observatory and Earthquake Research Institute report, Istanbul comprises 18.7% of Türkiye's total population, with more than 4.75 million households and 15.9 million people. It is estimated that around 70% of the buildings constructed before 2006 in Istanbul do not comply with seismic regulations, corresponding to more than 3.1 million dwellings. The anticipated Istanbul earthquake, estimated by experts to be between 7.5 and 7.6 magnitudes, will also affect eight neighboring provinces, impacting 7,870,806 households and 25,590,594 people, accounting for approximately 30% of Türkiye's population. Taking into account the region that the potential Istanbul earthquake will affect and the number of non-seismic code-compliant structures, it is expected that nearly 25 million tons of debris will be generated after the destructive earthquake [5]. Therefore, action plans to manage the disaster waste should be taken urgently.

This study contributes to the literature by integrating Geographic Information System (GIS) data with the Fuzzy Analytic Hierarchy Process (FAHP) method to decide optimal landfill sites for the Istanbul region for hazardous solid waste, specifically disaster waste. To decide on HSWL sites for Istanbul, we developed a fuzzy Multi-Criteria Decision Making (MCDM) model that utilizes GIS data and the FAHP method. First, essential criteria that impact the location selection are collected from literature and experts' opinions. Next, criteria are prioritized by FAHP, considering the former studies and experts' judgments. Then, geographical information for each criterion for the Istanbul region is mapped using ArcGIS 10.8 software. Using GIS data and criteria weights, the suitability map, which demonstrates the map of zones suitable for HSWL for Istanbul, is created. Last, alternative locations are ranked using Analytic Hierarchy Process (AHP), and the best locations for Asian and European sites in Istanbul are selected. Last, sensitivity analysis is performed to examine the impact of criteria weights on the solution. The organization of the paper is as follows. The studies in the literature are presented and discussed in Section 2. The methodology that utilizes GIS data and the FAHP method is outlined in Section 3. The case study and sensitivity analysis undertaken to explore the prioritization of criteria in decision-making are detailed in Section 4. Finally, Section 5 concludes the paper.

2. Literature Review

The selection of a location for the storage and disposal of hazardous solid waste is evaluated under the name "location selection problem" in the literature. The location selection problem, first introduced by the German economist Alfred Weber in 1909, focuses on selecting a depot that provides the most suitable raw materials, labor, logistics, and unit costs for all customers. Although Weber's work was initially conducted in the industrial field, his theory of "Location Selection" has significant importance not only in the industrial field but also in economics, mathematics, natural sciences, and many other disciplines [6].

An analysis of research related to the selection of locations for waste management and disaster waste management is outlined in Table 1. Most of these studies primarily concentrate on selecting locations for municipal solid waste landfills, with comparatively fewer investigations addressing disaster waste

management. Consequently, we have incorporated studies that specifically delve into selecting sites for hazardous waste disposal. Additionally, because GIS enables the inclusion of spatial data in the solution, we considered the studies utilizing GIS. GIS is a decision support system that allows us to collect, store, update, control, analyze, and visualize information related to the Earth's surface [7]. GIS allows us to comprehensively analyze the geographic and topographic characteristics of a specific area, such as land use, accessibility, proximity to settlement areas, and slope, which are essential in the selection of hazardous solid waste disposal sites.

Table 1. Summary studies for waste disposal selection problem that utilizes GIS

Problem	Methodology	Study
Disaster waste management: Istanbul, Türkiye	GIS – Multi-objective optimization (NSGA-II)	[8]
Disaster waste management site selection Victoria, Australia	GIS – Boolean logic	[9]
Disaster waste management site selection South Korea	GIS – MCDM (WSA)	[10]
Disaster waste management site selection Wenchuan, China	GIS – MCDM (TOPSIS)	[11, 12]
Disaster waste management site selection Egyptian Mediterranean Coast	GIS – MCDM (N-OPA)	[12]
Hazardous waste disposal site selection Zanjan province, Iran	GIS – MCDM (SAW)	[13]
Hazardous waste disposal site selection Avellino in Campania region	GIS – MCDM (SAW)	[14]
Hazardous waste disposal site selection Qom Province, Iran.	GIS – MCDM (AHP)	[15]
Hazardous waste disposal site selection Western Ghana	GIS – MCDM (AHP)	[16]
Municipal solid waste landfill location selection Kupang, Indonesia	GIS – MCDM (AHP-SAW)	[17]
Municipal solid waste landfill location selection Maharashtra, India	GIS – MCDM (AHP)	[18]
Municipal solid waste landfill location selection (Peshawar district) in Pakistan	GIS – MCDM (AHP)	[19]
Municipal solid waste landfill location selection Bandar Bushehr, Iran	GIS – MCDM (FAHP)	[20]
Municipal solid waste landfill location selection Najran, Saudi Arabia	GIS – MCDM (FAHP)	[21]
Municipal solid waste landfill location selection: Dhanbad, India	GIS – MCDM (FAHP)	[22]
Waste disposal site selection Dejen town, Ethiopia	GIS – MCDM (AHP)	[23]
Waste disposal site selection Fez province, Morocco	GIS – MCDM (AHP)	[24]
Landfill site selection: Istanbul, Türkiye	GIS – MCDM (AHP)	[7]
Landfill site selection: Javanrood, Iran	GIS – MCDM (AHP-TOPSIS)	[25]
Landfill site selection: Edirne, Türkiye	GIS – MCDM	[26]
Solid waste sanitary landfill site selection: Denizli, Türkiye	GIS – MCDM (AHP)	[27]

ANP - Analytic Network Process; TOPSIS - Technique for Order Preference by Similarity to Ideal Solutions, SAW - Simple Additive Weighting, Elitist Evolutionary Multi-Objective Optimization Technique (NSGA-II); WSA: Weighted Sum Analysis; N-OPA: Neutrosophic Ordinal Priority Approach

As seen in Table 1, MCDM methods are commonly used in solving the landfill site selection problem. MCDM is a useful tool for quickly obtaining the most effective result for problems that require considering multiple criteria, such as location selection. MCDM helps determine the best alternative by considering various criteria and their importance. Among the MCDM methods, AHP is most preferred. AHP decomposes a decision-making problem into criteria and sub-criteria; it defines and evaluates each criterion's relative importance through pairwise comparisons. Then, it ranks the available alternatives based on the importance of the criteria and leads to a conclusion [28]. However, classic AHP falls short of covering the uncertain judgments and opinions of the experts in decision-making. Therefore, AHP has been extended to FAHP to include the uncertainty associated with individual assessments. Studies incorporating FAHP or other fuzzy approaches are relatively fewer than crisp MCDM approaches [29].

Studies focus on selecting disaster waste management sites are as follows: Onan et al. [8] propose a multi-objective optimization framework that employs NSGA-II and GIS data to decide on temporary disaster waste management sites and incorporate the planning for collecting and transporting disaster waste. Cheng and Thompson [9] employed GIS to generate a suitability map in Victoria, Australia, employing Boolean logic to derive map layers. In another study, Lee et al. [10] applied the WSA with GIS data to address the challenge of selecting temporary disaster waste management sites. Liu [11] utilized TOPSIS to select the most suitable

location for disaster waste management in Wenchuan, China. AbdelAziz et al. [12] incorporated a fuzzy N-OPA approach for disaster waste management in the Egyptian Mediterranean Coast for flood-prone areas.

Our research stands out by integrating GIS data with FAHP methods to select optimal landfill sites for the Istanbul region for hazardous solid waste, particularly those originating from disasters. In this context, GIS accurately captures reliable spatial data, while FAHP models imprecise and uncertain expert opinions. Combining these two data types enhances decision-making processes and facilitates the efficient deployment of disaster waste management sites. This paper contributes to the existing literature in two keyways. Firstly, it introduces a three-step framework for HSWL location selection, where GIS analyses spatial data, FAHP prioritizes criteria, and AHP ranks the candidate sites. Secondly, it demonstrates the practical application of this framework through a case study in Istanbul, determining the optimal location for hazardous solid waste management.

3. Methodology

The methodology in deciding on the potential HSWL locations for Istanbul includes four steps, as presented in Figure 1. Each step is elaborated under subsections 3.1-3.4, respectively.

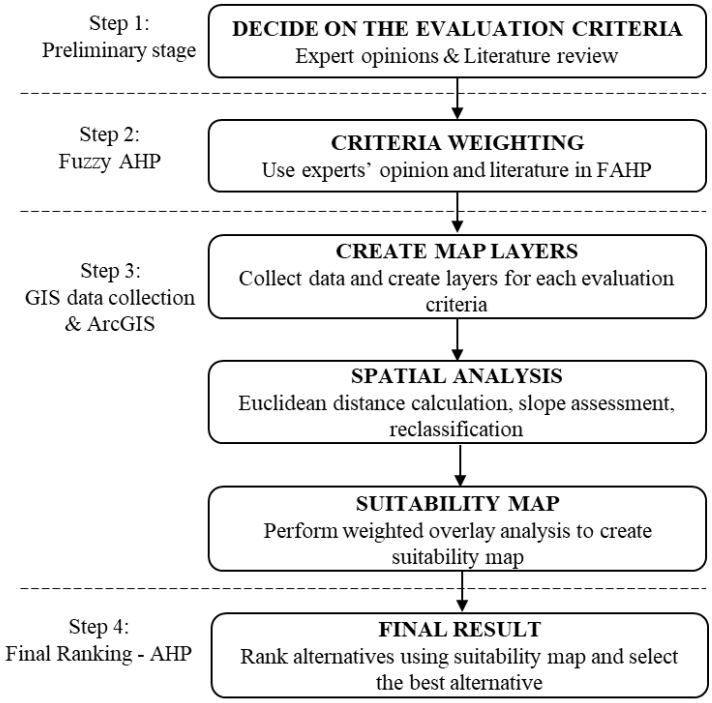

Figure 1. Methodology

3.1. Identification of Evaluation Criteria

In the scope of the research, a search was conducted on the Google Scholar search engine using specific keywords related to the study content, including "hazardous solid waste landfill" and "hazardous solid waste disposal", in addition to the terms "GIS" and "MCDM". Next, those articles are filtered to select potential evaluation criteria for HSWL site selection. Two experts with more than ten years of experience in environmental engineering with a geography background supported us in verifying the evaluation criteria gathered from the literature search. The evaluation criteria selected are described as follows.

Land cover (C1): Land cover refers to the physical or biophysical material covering the land, such as urban areas, forests, or grassland, and is essential for determining the disaster waste disposal location. For instance,

forests, urban areas, agricultural lands, natural reserves, or parks cannot be selected as HSWL locations. The storage site should be as far away as possible from those areas. Additionally, population density is also a crucial factor. The greater amount of debris is expected from the regions with higher populations. Therefore, debris storage locations should not be too far from residential areas, which may create transportation challenges and increase transportation costs. Soil and rock structure (C2): Geological maps provide valuable information about the region, including soil types, rocks, and other structural features. When selecting HSWL sites, areas where the soil types have a low permeability structure are preferred. Additionally, the ground should not be soft or prone to waterlogging; it should be firm and stable. Surface (C3) and ground (C4) waters: HSWL areas should be located far from water sources to prevent the leakage of toxic materials such as asbestos, which may be released from debris. However, to reduce the emission of toxic gases by irrigating the debris, the storage areas should be relatively close to water sources. Slope (C5): The slope of the areas where debris will be piled should be as low as possible. Areas with a slope greater than 20% are excluded from the analysis. Aspect (C6): To prevent the dispersion of harmful material dust by the wind, storage areas should not be constructed in the direction of prevailing winds. Fault line (C7): The suitability of an area increases proportionally with the distance from the fault line. Roadways (C8): The proximity of waste storage sites to roads is crucial for ease of transportation and cost-effectiveness. Wind speed (C9): Wind speed can facilitate the transport of toxic particles in the form of gas and dust clouds towards residential areas; therefore, it is beneficial to prefer areas with low annual average wind speeds. Land value (C10): It is more appropriate to select locations for HSWL in areas with relatively lower land values. Table 2 presents the relationship between evaluation criteria and the other studies in the literature.

Table 2. The relationship between identified evaluation criteria and literature

Literature Summary	Criteria									
	C1	C2	C3	C4	C5	C6	C7	C8	C9	C10
[7]	x	x	x		x			x		x
[25]	x	x	x	x	x	x	x	x	x	x
[26]	x	x	x		x	x		x	x	
[27]	x				x	x	x	x		
[30]		x	x	x				x		
[31]	x	x	x	x			x			
[8]			x	x			x		x	x
[19]	x	x	x	x	x	x		x		x
[23]	x	x	x		x	x		x	x	
[15]	x	x	x		x		x	x		
[17]		x		x	x					
[18]	x	x	x		x	x		x		
[14]	x		x	x			x	x	x	
[24]	x		x		x			x		
[16]	x	x	x		x	x	x	x		x
[9]	x		x		x			x		

3.2. Criteria Weighting - Fuzzy Analytical Hierarchy Process

The FAHP decision-making method incorporates uncertainty and ambiguity in subjective judgments for solving MCDM problems. It helps determine the relative importance of the criteria or alternatives through linguistic terms when judgments are difficult to quantify. By employing the FAHP, we aim to assign appropriate weights to each criterion to prioritize them based on their significance in the HSWL site selection process. In our study, we opted for triangular fuzzy numbers (TFN) to capture the vagueness related to the decision-maker due to its prominent applications. A TFN can be represented as $M = (l, m, u)$. These parameters represent the smallest possible (l), the most promising (m), and the largest possible value (u),

respectively. The FAHP, employing the geometric mean method, is implemented as described in [32] as follows:

Step 1: Make a pairwise comparison across evaluation criteria using linguistic terms [32] and create a fuzzy decision matrix, $\widetilde{\boldsymbol{M}}$.

$$\widetilde{M} = \begin{bmatrix} 1 & \widetilde{m}_{12} & \cdots & \widetilde{m}_{1n} \\ \widetilde{m}_{21} & 1 & \cdots & \widetilde{m}_{2n} \\ \vdots & \vdots & \ddots & \vdots \\ \widetilde{m}_{m1} & \widetilde{m}_{n2} & \cdots & 1 \end{bmatrix} = \begin{bmatrix} 1 & \widetilde{m}_{12} & \cdots & \widetilde{m}_{1n} \\ 1/\widetilde{m}_{12} & 1 & \cdots & \widetilde{m}_{2n} \\ \vdots & \vdots & \ddots & \vdots \\ 1/\widetilde{m}_{1n} & 1/\widetilde{m}_{2n} & \cdots & 1 \end{bmatrix}$$

$$\widetilde{m}_{ij} = \begin{cases} \tilde{9}^{-1}, \tilde{8}^{-1}, \tilde{7}^{-1}, \tilde{6}^{-1}, \tilde{5}^{-1}, \tilde{4}^{-1}, \tilde{3}^{-1}, \tilde{2}^{-1}, \tilde{1}^{-1}, \tilde{1}^{1}, \tilde{2}^{1}, \tilde{3}^{1}, \tilde{4}^{1}, \tilde{5}^{1}, \tilde{6}^{1}, \tilde{7}^{1}, \tilde{8}^{1}, \tilde{9}^{1}, 1, i \neq j \\ 1 \; i = j \end{cases}$$

Step 2: Calculate the fuzzy geometric mean and fuzzy weights for each criterion using (3.1) and (3.2).

$$\tilde{r}_i = \left(\widetilde{m}_{i1} \otimes \ldots \otimes \widetilde{m}_{ij} \otimes \ldots \widetilde{m}_{in}\right)^{1/n} \tag{3.1}$$

$$\widetilde{w}_i = (\tilde{r}_i \otimes [\tilde{r}_1 \oplus \ldots \oplus \tilde{r}_i \oplus \ldots \tilde{r}_n])^{-1} \tag{3.2}$$

In (3.1) and (3.2), $\widetilde{m}_{ij}$ shows the fuzzy comparison value of criterion i with respect to criterion j. The notation $\tilde{r}_i$ refers to the geometric mean of the fuzzy comparison value of $the\ i^{th}$ criterion, whereas $\widetilde{w}_i$ indicates the fuzzy weight of the criterion i, defined by TFN. Following, the center-of-area method is applied to defuzzify the weights using (3.3) [33].

$$T_i = \frac{l_{w_i} + m_{w_i} + u_{w_i}}{3} \tag{3.3}$$

Then, normalization in (3.4) is applied to non-fuzzy weights T_i to ensure the total sum of weights equals one [34]. (3.4) denotes the normalized crisp weight of criterion i.

$$N_i = \frac{T_i}{\sum_{i=1}^{n} T_i} \tag{3.4}$$

3.3. Creation of Map Layers and Spatial Analysis

Once the evaluation criteria have been identified, vector or raster data are acquired from multiple resources. The data collected from various sources has been entered to create relevant layers for each criterion in ArcGIS 10.8. The “Clip” tool is employed to cut all the layers according to the boundaries of Istanbul province. Next, spatial analysis, including slope calculation, Euclidean distance analysis, aspect identification, reclassification, and weighted overlay, are performed. In slope analysis, the slope of the area is calculated. Euclidean distance analysis calculates the closest distance between each point and its nearest source. The aspect of the area is determined by ArcToolBox – Spatial Analysis. Due to varying scales of input values for criteria, reclassification analysis is conducted to establish a uniform evaluation scale. The scale used ranges between “1” to “5”, where “1” refers to the lowest score and “5” denotes the highest score, based on the characteristic of the criterion, whether minimum or maximum better. Last, criteria weights determined by FAHP are incorporated, and weighted overlay analysis is executed. In weighted overlay analysis, the value of each cell within the map layers is multiplied by the corresponding criteria weights and then aggregated across all criteria

to generate a suitability map. The suitability map shows the suitable zones based on their scores from "1" to "5", ranging from unsuitable to very suitable.

3.4. Final Ranking – AHP

Considering the suitability scores of the regions and checking with the satellite images, candidate locations are determined to ensure that restricted areas, such as forests, residential areas, highways, or rivers, are not selected as candidate locations. Once the candidate locations are decided, the AHP method introduced by [35] is applied to select the best location for HSWL. In AHP, first, we constructed a pairwise comparison matrix, size mxm, where m refers to the alternatives (candidate HSWL sites) based on the reclassified values for each criterion. Then, each pairwise matrix is normalized by dividing each cell in the matrix into the sum of the associated columns. Last, the average of normalized values is computed for each alternative, which shows the weight of each alternative, preference vector, for the associated criteria.

4. Case Study

4.1. Data Set

Data for each evaluation criterion is presented in Table 3. Spatial analyses, including slope calculation, Euclidean distance analysis, and aspect identification, are conducted using the data in Figure 2. Next, reclassification analysis is performed using studies by [27] and [26] to ensure measurement integrity across evaluation criteria. Reclassification analysis for all evaluation criteria is presented in Tables 4 and 5.

Table 3. Data sources for evaluation criteria

Criteria	Source	Data Type	Scale	Analysis
C1	CORINE Land Cover (2018)	Raster	100m	Reclassification
C2	İstanbul ili Jeoloji Haritası (2023)			
C3	OpenStreetMap (2023)	Vector	1/25.000	Euclidean distance
C4	OpenStreetMap (2023)	Vector	1/25.000	Euclidean distance
C5	EarthExplorer USGS	Raster	25m	Slope
C6	EarthExplorer USGS	Raster	25m	Aspect
C7	MTA (2001)	Vector	1/25.000	Euclidean distance
C8	OpenStreetMap (2023)	Vector	1/25.000	Euclidean distance
C9	Global Wind Atlas (2018)	Raster	100m	Reclassification
C10	Gelir Dairesi Başkanlığı (2023)			

Table 4. Reclassification analysis for Criteria 1 and 2 (adopted from [27])

	Unsuitable (1)	Low suitable (2)	Moderately suitable (3)	Suitable (4)	Most suitable (5)
C1	Urban areas, Industrial or commercial units and public facilities, Mineral extraction sites, Non-irrigated arable land, Permanently irrigated arable land, Fruit trees and berry plantations, Broad-leaved forest, Coniferous forest, Mixed forest, Inland marshes, Water bodies	Complex cultivation, land principally occupied by agriculture, with significant areas of natural vegetation	Natural grasslands, Sclerophyllous vegetation, Transitional woodland-shrub	Pastures	Dumping ground, Bare rocks, Sparsely vegetated areas

Table 4. (Continued) Reclassification analysis for Criteria 1 and 2 (adopted from [27])

	Unsuitable (1)	Low suitable (2)	Moderately suitable (3)	Suitable (4)	Most suitable (5)
	Group A (Low Runoff Potential - Good Drainage)	Group B (Moderate Runoff Potential – Moderate Drainage)	Group C (High Runoff Potential - Restricted Drainage)	Group D (Very High Runoff Potential - Very Restricted Drainage)	Group D (Very High Runoff Potential - Very Restricted Drainage)
C2	Alluvial, Alluvial fan, Travertine	Olistostrome	Breccia, Conglomerate, Marble, Limestone, Metasandstone-Metaconglomerate-Metapelite, Quartzite-Quartz schist, Talus	Cherty limestone, Spilite Conglomerate-Sandstone-Mudstone, Dolomite, Limestone with clay, Melange, Sandstone-mudstone, Sandstone-Mudstone-limestone	Migmatite Gneiss, Peridotite, Schist, Schale

Table 5. Reclassification analysis for Criteria 3 and 9 (adopted from [26])

	Range	Value	Level of Suitability
C3	<2 km	1	Unsuitable
	2-3 km	2	Slightly suitable
	3-4 km	3	Moderately suitable
	4-5 km	4	Suitable
	>5 km	5	Very suitable
C4	<2.5 km	1	Unsuitable
	2.5-4 km	2	Slightly suitable
	4-5.5 km	3	Moderately suitable
	5.5-7 km	4	Suitable
	>7 km	5	Very suitable
C5	%0-5	5	Very suitable
	%5-10	4	Suitable
	%10-15	3	Moderately suitable
	%15-20	2	Slightly suitable
	>%20	1	Unsuitable
C6	Northwest - Southwest	3	Moderately suitable
	North - West	4	Suitable
	South – East – Southeast - Northeast	5	Very suitable
C7	0-0.5 km	1	Unsuitable
	0.5-0.75 km	2	Slightly suitable
	0.75-1.25 km	3	Moderately suitable
	1.25-2 km	4	Suitable
	>2 km	5	Very suitable
C8	0-0.1 km	1	Unsuitable
	0.1-1 km	3	Moderately suitable
	1-2 km	4	Suitable
	2-5 km	5	Very suitable
	> 5 km	1	Unsuitable
C9	0-5 km	5	Very suitable
	5-10 km	4	Suitable
	10-15 km	3	Moderately suitable
	15-20 km	2	Slightly suitable
	>20 km	1	Unsuitable

Figure 2 shows the GIS layers for each evaluation criteria after reclassification analysis. In these maps, for each particular criterion, unsuitable locations with a score of "1" are presented in light red color. In contrast, very suitable locations with a score of "5" are presented in dark red.

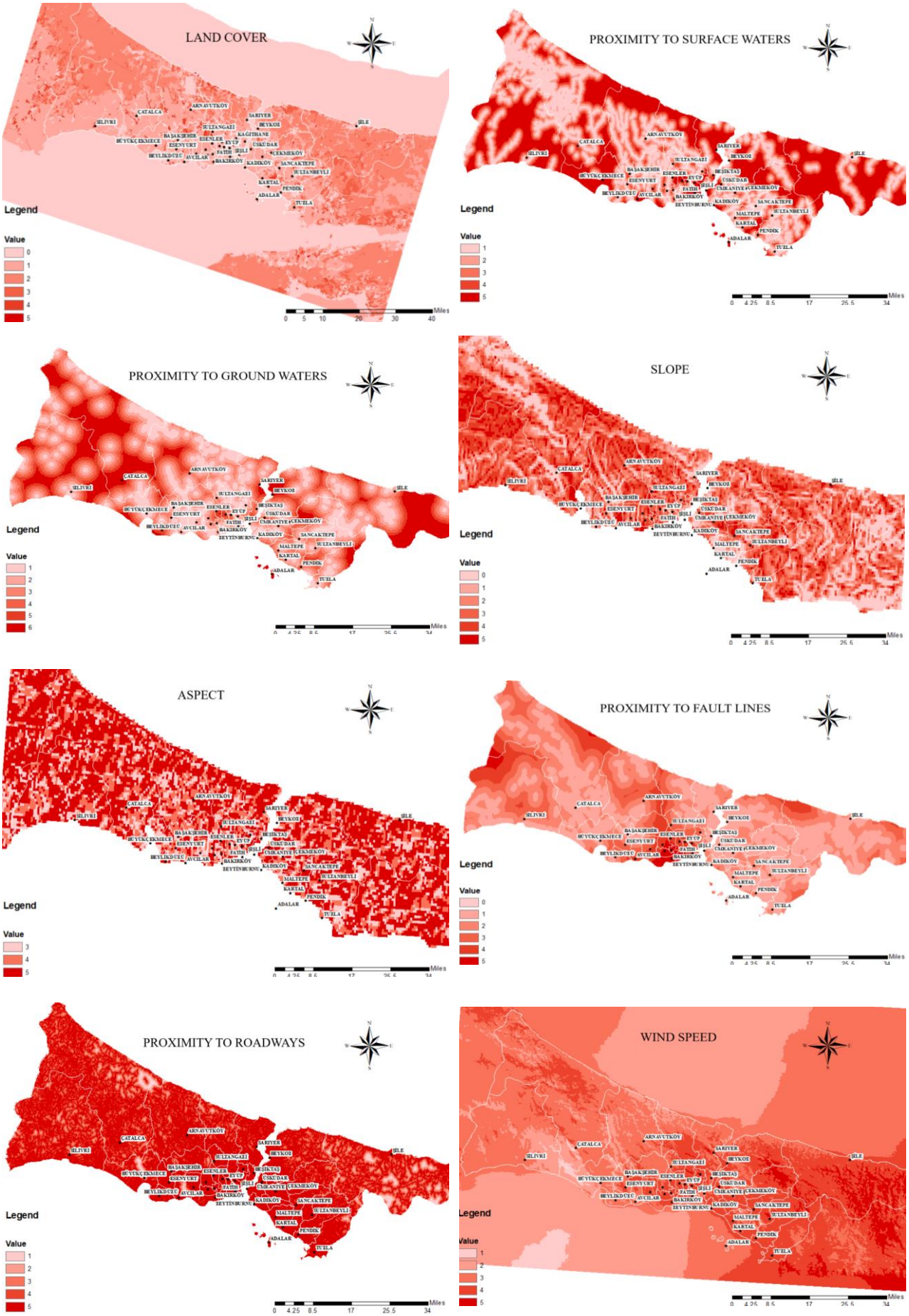

Figure 2. GIS layers for each evaluation criteria

4.2. Determination of Criteria Weights

We applied the FAHP method to prioritize the evaluation criteria. First, experts are asked to conduct a pairwise comparison using linguistic expressions. Specifically, experts are asked to evaluate the importance of each criterion against the rest of the criteria in the scale shown in Table 6. A common response from both experts for each comparison is used in the calculations.

Table 6. Linguistic terms used to define relative importance [32]

Linguistic variable	Fuzzy numbers
Extremely strong	(9,9,9)
Intermediate	(7,8,9)
Very strong	(6,7,8)
Intermediate	(5,6,7)
Strong	(4,5,6)
Intermediate	(3,4,5)
Moderately strong	(2,3,4)
Intermediate	(1,2,3)
Equally strong	(1,1,1)

The results of these comparisons are fuzzified, leading to a matrix consisting of TFN, as shown in Table 7. Table 7 shows a consistency ratio below 0.1, indicating high consistency and reliability in the experts' judgments. A consistency ratio below 0.1 ensures internal coherence in comparing criteria, allowing the matrix to be effectively utilized in subsequent stages of FAHP. Then, following the procedures outlined in Section 3.2 for FAHP, we have computed and displayed the crisp weights in Table 8. In Table 8, surface waters (0.273) followed by soil and rock structure (0.243) are determined as the two most essential criteria, whereas land value (0.009) is calculated as the least important criterion. The highest prioritized two criteria in our study, "surface waters" and "soil and rock structure" are also listed as the most frequently used criteria for landfill site selection in a review study by Donevska et al. [36] that investigates the landfill site selection methodologies and criteria. In another study Beskese et al. [37] determined soil conditions and topography as the most crucial criterion for the landfill site selection. Both studies in the literature verify the prioritization of the criteria for HSWL location selection.

4.3. Suitability Map and Final Ranking

Using the GIS layers presented in Figure 2 and criteria weights in Table 8, the "Weighted Overlay" analysis in ArcGIS 10.8 is performed to generate a suitability map. The most suitable HSWL sites have been identified based on the resulting output. Figure 3 presents the suitability map of Istanbul for HSWL construction. In Figure 3, locations with higher suitability scores are demonstrated in black color. In contrast, less suitable locations are in lighter red. According to the suitability map, five potential locations for storing solid and hazardous waste from west to east are determined as follows: Silivri, Çatalca, Arnavutköy, Beykoz, and Şile. Next, satellite images are used to select specific areas that are appropriate for the construction of the HSWL. For instance, the Riva neighborhood of Beykoz was selected as a candidate because the region is close to solid waste disposal facilities in İBB İstaç Kömürcüada. Additionally, considering the transportation cost, attention is paid to select areas not too far from residential locations [38]. Land value (C10) is also considered in alternative area determination. Specifically, Çatalca, Silivri, and Şile are included due to lower land values compared to Şişli or Beşiktaş [39]. Furthermore, the size of the candidate locations is adequate for the construction of HSWL. Figure 4 presents the satellite images for five candidate locations.

Table 7. Pairwise Comparison matrix of the criteria

		C1	C2	C3	C4	C5	C6	C7	C8	C9	C10
C1	***l***	1	4	6	5	0.25	0.13	0.33	0.17	0.11	0.11
	m	1	5	7	6	0.33	0.14	0.5	0.2	0.11	0.11
	u	1	6	8	7	0.5	0.17	1	0.25	0.11	0.11
C2	***l***	0.17	1	0.33	1	0.2	0.14	0.2	0.11	0.11	0.11
	m	0.2	1	0.5	1	0.25	0.17	0.25	0.13	0.13	0.11
	u	0.25	1	1	1	0.33	0.2	0.33	0.14	0.14	0.11
C3	***l***	0.13	1	1	0.25	0.14	0.11	0.2	0.11	0.11	0.11
	m	0.14	2	1	0.33	0.17	0.11	0.25	0.11	0.11	0.11
	u	0.17	3	1	1	0.2	0.11	0.33	0.11	0.11	0.11
C4	***l***	0.14	1	1	1	0.25	0.17	0.2	0.11	0.11	0.11
	m	0.17	1	3	1	0.33	0.2	0.25	0.11	0.13	0.11
	u	0.2	1	4	1	0.5	0.25	0.33	0.11	0.14	0.11
C5	***l***	2	3	5	2	1	0.33	0.33	0.2	0.25	0.11
	m	3	4	6	3	1	0.5	0.5	0.25	0.33	0.11
	u	4	5	7	4	1	1	1	0.33	0.5	0.11
C6	***l***	6	5	9	4	1	1	1	0.33	0.25	0.25
	m	7	6	9	5	2	1	2	0.5	0.33	0.33
	u	8	7	9	6	3	1	3	1	0.5	0.5
C7	***l***	1	3	3	3	1	0.33	1	0.2	0.33	0.11
	m	2	4	4	4	2	0.5	1	0.25	0.5	0.13
	u	3	5	5	5	3	1	1	0.33	1	0.14
C8	***l***	4	7	9	9	3	1	3	1	1	0.17
	m	5	8	9	9	4	2	4	1	2	0.2
	u	6	9	9	9	5	3	5	1	3	0.25
C9	***l***	9	7	9	7	2	2	1	0.33	1	0.25
	m	9	8	9	8	3	3	2	0.5	1	0.33
	u	9	9	9	9	4	4	3	1	1	0.5
C10	***l***	9	9	9	9	9	2	7	4	2	1
	m	9	9	9	9	9	3	8	5	3	1
	u	9	9	9	9	9	4	9	6	4	1

Table 8. Pairwise comparison matrix of the criteria

Criteria	Weights Crisp Values
C1. Land Cover	0.092
C2. Soil and Rock Structure	0.243
C3. Surface waters	0.273
C4. Groundwaters	0.203
C5. Slope	0.061
C6. Aspect	0.029
C7. Fault Line	0.053
C8. Roadways	0.018
C9. Wind	0.020
C10. Land Value	0.009

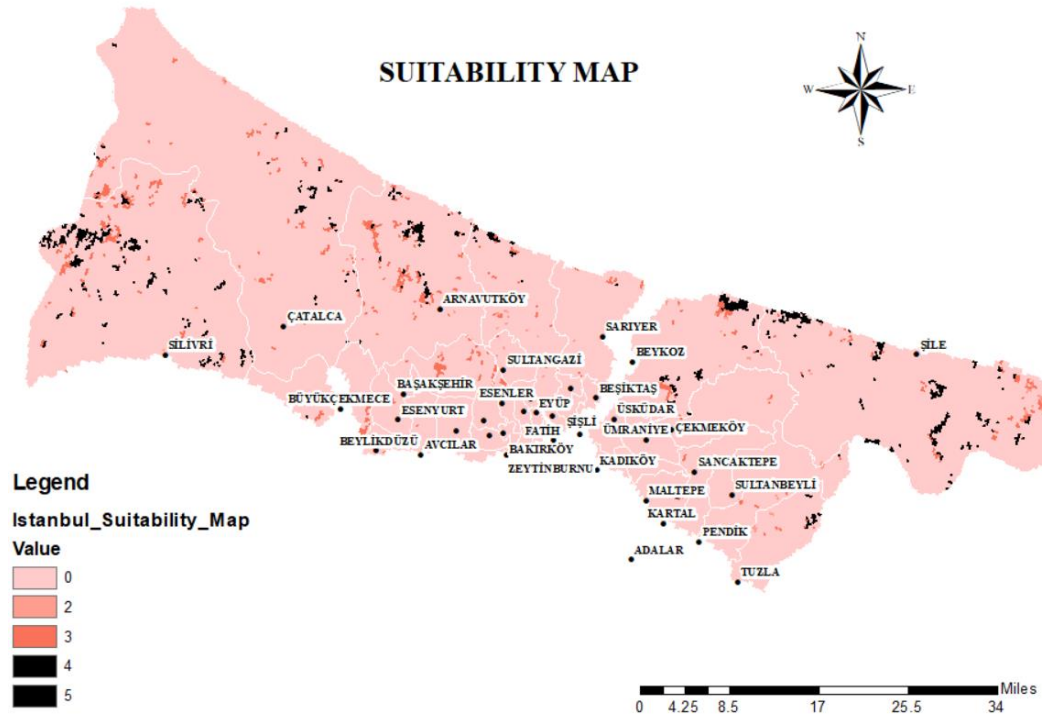

Figure 3. Suitability map

Fevzipaşa / Silivri (A1)

Örencik / Çatalca (A2)

Durusu / Arnavutköy (A3)

Riva / Beykoz (A4)

Hasanlı / Şile (A5)

Figure 4. Candidate locations for HSWL

Next, a pairwise matrix of candidates is created using the reclassified values for each criterion, as in Table 9.

Table 9. Pairwise comparison matrix of candidate locations for each criterion

C1	A1	A2	A3	A4	A5	**Weight**	**C6**	A1	A2	A3	A4	A5	**Weight**
A1	1	5	3	1	4	0.362	A1	1	2	5	4	3	0.425
A2	0.2	1	0.5	0.33	0.5	0.074	A2	0.5	1	3	3	2	0.253
A3	0.33	2	1	0.33	2	0.137	A3	0.2	0.33	1	1	0.5	0.083
A4	1	3	3	1	4	0.331	A4	0.25	0.33	1	1	0.5	0.087
A5	0.25	2	0.5	0.25	1	0.096	A5	0.33	0.5	2	2	1	0.151
C2	A1	A2	A3	A4	A5	**Weight**	**C7**	A1	A2	A3	A4	A5	**Weight**
A1	1	0.33	0.5	0.11	0.25	0.054	A1	1	3	4	2	1	0.321
A2	3	1	3	0.33	0.5	0.175	A2	0.33	1	2	0.5	0.33	0.112
A3	2	0.33	1	0.33	0.33	0.096	A3	0.25	0.5	1	0.5	0.25	0.075
A4	9	3	3	1	1	0.379	A4	0.5	2	2	1	0.5	0.171
A5	4	2	3	1	1	0.296	A5	1	3	4	2	1	0.321
C3	A1	A2	A3	A4	A5	**Weight**	**C8**	A1	A2	A3	A4	A5	**Weight**
A1	1	0.2	0.5	0.33	0.2	0.066	A1	1	1	1	1	1	0.200
A2	5	1	2	0.5	0.5	0.216	A2	1	1	1	1	1	0.200
A3	2	0.5	1	0.5	1	0.157	A3	1	1	1	1	1	0.200
A4	3	2	2	1	1	0.283	A4	1	1	1	1	1	0.200
A5	5	2	1	1	1	0.278	A5	1	1	1	1	1	0.200
C4	A1	A2	A3	A4	A5	**Weight**	**C9**	A1	A2	A3	A4	A5	**Weight**
A1	1	4	5	3	0.5	0.325	A1	1	0.5	2	0.33	0.25	0.104
A2	0.25	1	2	2	0.33	0.135	A2	2	1	3	0.5	0.33	0.169
A3	0.2	0.5	1	1	0.33	0.085	A3	0.5	0.33	1	0.33	0.33	0.079
A4	0.33	0.5	1	1	0.33	0.092	A4	3	2	3	1	0.5	0.255
A5	2	3	3	3	1	0.362	A5	4	3	3	2	1	0.393
C5	A1	A2	A3	A4	A5	**Weight**	**C10**	A1	A2	A3	A4	A5	**Weight**
A1	1	2	2	2	3	0.338	A1	1	0.5	3	2	2	0.246
A2	0.5	1	1	2	2	0.210	A2	2	1	5	3	2	0.385
A3	0.5	1	1	1	2	0.179	A3	0.33	0.2	1	0.5	0.5	0.075
A4	0.5	1	1	1	2	0.179	A4	0.5	0.33	2	1	0.5	0.120
A5	0.33	0.5	0.5	0.5	1	0.095	A5	0.5	0.5	2	2	1	0.174

The final ranking of the locations is shown in Figure 5. The ranking of candidate locations, from the highest to the lowest, is as follows: Hasanlı/Şile (A5), Riva/Beykoz (A4), Fevzipaşa/Silivri (A1), Örencik/Çatalca (A2), and Durusu/Arnavutköy (A3). Therefore, Hasanlı/Şile (A5) is the best location to construct HSWL, while Durusu/Arnavutköy (A3) is the worst candidate for HSWL construction.

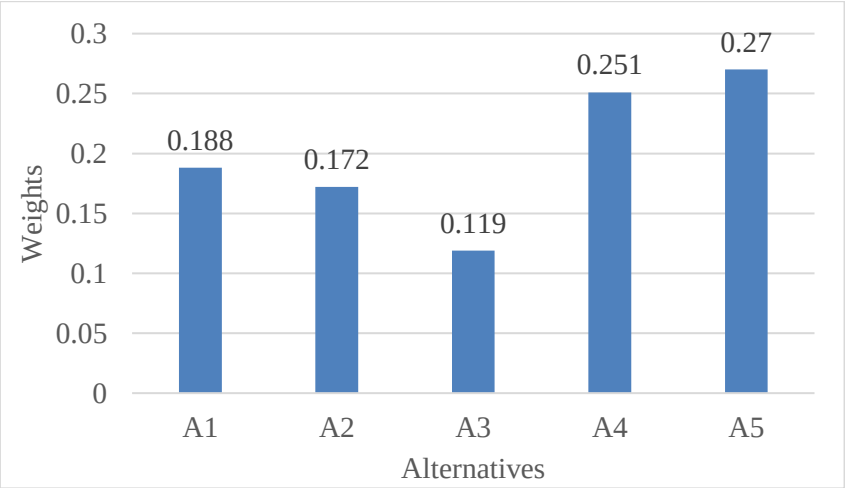

Figure 5. Ranking of alternative locations

Considering the AHP rankings, Fevzipaşa/Silivri (A1) for the European side and Hasanlı/Şile (A5) for the Asian side were chosen as the most suitable options. Silivri was also selected as a potential landfill site in studies by [37] and [7]. The total area of these two regions is 5,080,699 m^2. According to the regular waste disposal regulation published in the Official Gazette on March 26, 2010, hazardous solid waste facilities, classified as Class I, can stack waste up to 5 meters high. Therefore, the total capacity of the facilities is 25 million m^3, which is sufficient to handle the expected amount of debris.

4.4. Sensitivity Analysis

Sensitivity analysis is a common approach for methodically modifying criteria weighting and examining its influence on the solution. In this section, we explore how the final solution – the location of HSWL sites – changes in response to adjustments in the weights assigned to evaluation criteria. The percentage change in criterion i is presented in (4.4).

$$w_i = w_{i0} + w_{i0} \times YD \tag{4.4}$$

where w_{i0} presents the initial value of the i^{th} criterion, YD refers to a percentage, and w_i shows the updated value of the i^{th} criterion. For instance, when the surface water criterion was augmented by 5%, the resulting weight was computed to be 0.287. The weights of the remaining criteria must be modified to ensure that the total sum of all criteria weights equals "1". By applying (4.5), the rest of the parameters are updated. In (4.5), w_{j0} and w_j refer to the initial and final weights of the j^{th} criterion. For instance, the initial weight of the land cover is 0.092, with a 5% increase in the surface water; the new weight of the land cover is calculated as $0.090 = (1 - 0.287) \times \frac{(0.092)}{(1-0.273)}$. The weights of the rest of the criteria are calculated similarly.

$$w_j = (1 - w_i) \times \frac{w_{j0}}{(1 - w_{i0})} \tag{4.5}$$

Table 10 presents the corresponding shifts in weights for the remaining criteria based upon the change in the weight of the criterion "Surface water". Bold represents the baseline, a.k.a., initial weights.

Table 10. Change in criteria weights

Change in percentage	C1	C2	C3	C4	C5	C6	C7	C8	C9	C10
20%	0.085	0.225	0.328	0.188	0.056	0.027	0.049	0.017	0.018	0.008
15%	0.087	0.229	0.314	0.192	0.058	0.027	0.050	0.017	0.019	0.008
10%	0.089	0.234	0.300	0.195	0.059	0.028	0.051	0.017	0.019	0.009
5%	0.090	0.238	0.287	0.199	0.060	0.028	0.052	0.018	0.020	0.009
0%	**0.092**	**0.243**	**0.273**	**0.203**	**0.061**	**0.029**	**0.053**	**0.018**	**0.020**	**0.009**
-5%	0.094	0.248	0.259	0.207	0.062	0.030	0.054	0.018	0.020	0.009
-10%	0.095	0.252	0.246	0.211	0.063	0.030	0.055	0.019	0.021	0.009
-15%	0.097	0.257	0.232	0.214	0.064	0.031	0.056	0.019	0.021	0.010
-20%	0.099	0.261	0.218	0.218	0.066	0.031	0.057	0.019	0.022	0.010

Table 11 presents the solution with respect to the change in criteria weights. Accordingly, adjusting the surface water criterion weights in a range of 20% did not change the solution. The ranking of the candidates from most suitable to the least is as follows: Hasanlı/Şile (A5), Riva/Beykoz (A4), Fevzipaşa/Silivri (A1), Örencik/Çatalca (A2), and Durusu/Arnavutköy (A3).

Table 11. Results of the sensitivity analysis

Percentage change	Fevzipaşa/ Silivri	Örencik/ Çatalca	Durusu/ Arnavutköy	Riva/ Beykoz	Hasanlı/ Şile	Solution (best to the worst)
20%	0.179	0.176	0.122	0.253	**0.271**	A5-A4-A1-A2-A3
15%	0.181	0.175	0.121	0.253	**0.271**	A5-A4-A1-A2-A3
10%	0.184	0.174	0.121	0.252	**0.271**	A5-A4-A1-A2-A3
5%	0.186	0.173	0.120	0.251	**0.270**	A5-A4-A1-A2-A3
0%	0.188	0.172	0.119	0.251	**0.270**	A5-A4-A1-A2-A3
-5%	0.191	0.171	0.118	0.250	**0.270**	A5-A4-A1-A2-A3
-10%	0.193	0.171	0.118	0.250	**0.270**	A5-A4-A1-A2-A3
-15%	0.195	0.170	0.117	0.249	**0.270**	A5-A4-A1-A2-A3
-20%	0.197	0.169	0.116	0.248	**0.270**	A5-A4-A1-A2-A3

5. Conclusion

This study aims to select an optimal landfill site for hazardous solid waste resulting from a disaster in the Istanbul region so that harm to the environment and the health of individuals can be reduced. First, evaluation criteria for HSWL sites are determined by synthesizing studies in the literature and expert opinions. Next, those evaluation criteria are prioritized based on the experts' evaluation and judgment through the FAHP method. Then, to achieve more realistic and precise results in the site selection, spatial data analysis was performed in ArcGIS 10.8. A suitability map that demonstrates the appropriate locations for HSWL is identified. Appropriate locations in the suitability map and satellite images obtained from Google Earth are used to select the candidate locations to avoid the risk of defining residential areas as a candidate. AHP is performed to select the best location among five candidates. Accordingly, Hasanlı/Şile is the most suitable location, whereas Durusu/Arnavutköy is evaluated to be the least suitable region. However, to efficiently serve both the Asian and European sides, Fevzipaşa/Silivri for the European side and Hasanlı/Şile for the Asian side were chosen as the most suitable two options based on AHP rankings.

This research introduces a framework for determining optimal locations for HSWL in the Istanbul region, intending to mitigate the adverse effects of hazardous waste. Although the application is limited to Istanbul, the applicability of this framework extends beyond Istanbul. Decision makers can benefit from this framework for deciding on HSWL locations for different regions. The originality of the framework is integrating objective (spatial) and subjective data (expert opinions) using various techniques to assist decision-makers in selecting HSWL locations. One limitation of this study is that it does not fully cover the economic aspect of the problem. Only land prices and proximity to potential debris accumulation are considered when selecting candidate locations. However, disaster risk assessment for the areas where more debris is likely to occur [40,41] and the transportation cost to HSWL sites for cleaning up the debris [38] should be integrated in addition to land value. In a future study, we plan to analyze the region for the debris accumulation in depth and integrate transportation cost criteria in selecting the HSWL locations to address the cost, health, and environmental aspects.

Author Contributions

The first author devised the main conceptual ideas and developed the theoretical framework. The second author conducted the literature search and performed GIS analysis. The first author wrote the manuscript with support from the second author. They all read and approved the final version of the paper.

Conflicts of Interest

All the authors declare no conflict of interest.

References

[1] B. M. Demir, S. Ercan, M. Aktan, and H. Öztaşkin, *Turkey's asbestos profile and safety problem of asbestos*, The Journal of Geological Engineering 42 (2) (2018) 215–232.

[2] G. Doğdu, S. Nur Alkan, *Management of Post-earthquake Construction and Demolition Waste: 6 February, 2023 Kahramanmaraş Earthquake Disasters*, Artvin Coruh University Journal of Engineering and Sciences 1 (1) (2023) 38–50.

[3] T. C. Cumhurbaşkanlığı Strateji ve Bütçe Başkanlığı, Kahramanmaraş ve Hatay Depremleri Raporu (2023), https://www.sbb.gov.tr/2023-kahramanmaras-ve-hatay-depremleri-raporu/, Accessed 6 Apr 2024.

[4] M. S. Habib, M. H. Maqsood, N. Ahmed, M. Tayyab, M. Omair, *A multi-objective robust possibilistic programming approach for sustainable disaster waste management under disruptions and uncertainties*, International Journal of Disaster Risk Reduction 75 (2022) Article ID 102967 44 pages.

[5] E. Çaktı, E. Şafak, U. Hancılar, K. Şeşetyan, M. Baş, O. Kılıç, E. Y. Menteşe, Ö. Uzunkol, S. Kara, İstanbul İli Olasi Deprem Kayıp Tahminlerinin Güncellenmesi Projesi (2019), https://depremzemin.ibb.istanbul/calismalarimiz/tamamlanmis-calismalar/istanbul-ili-olasi-deprem-kayip-tahminlerinin-guncellenmesi-projesi/, Accessed 6 Apr 2024.

[6] D. Fearon, A. Weber, Theory of the location of industries, 1909. CSISS Classics, 2002.

[7] D. Güler, T. Yomralıoğlu, *Alternative suitable landfill site selection using analytic hierarchy process and geographic information systems: A case study in Istanbul*, Environmental Earth Sciences 76 (20) (2017) Article Number 678 13 pages.

[8] K. Onan, F. Ülengin, B. Sennaroglu, *An evolutionary multi-objective optimization approach to disaster waste management: A case study of Istanbul, Turkey*, Expert Systems with Applications 42 (22) (2015) 8850–8857.

[9] C. Cheng, R. G. Thompson, *Application of boolean logic and GIS for determining suitable locations for temporary disaster waste management sites*, International Journal of Disaster Risk Reduction 20 (2016) 78–92.

[10] Y. H. Lee, Y. C. Kim, H. Kyoung Lee, *Framework for selection of temporary disaster waste management sites for post-flood recovery in Seoul, South Korea*, International Journal of Disaster Risk Reduction 71 (2022) Article ID 102832 15 pages.

[11] K. Liu, *GIS-based MCDM framework combined with coupled multi-hazard assessment for site selection of post-earthquake emergency medical service facilities in Wenchuan, China*, International Journal of Disaster Risk Reduction 73 (2022) Article ID 102873 18 pages.

[12] N. M. AbdelAziz, K. A. Eldrandaly, S. Al-Saeed, A. Gamal, M. Abdel-Basset, *Application of GIS and IOT Technology-Based MCDM for disaster risk management: methods and case study*, Decision Making: Applications in Management and Engineering 7 (1) (2024) 1–36.

[13] M. Khamehchiyan, M. R. Nikoudel, M. Boroumandi, *Identification of hazardous waste landfill site: A case study from Zanjan province, Iran*, Environmental Earth Sciences 64 (7) (2011) 1763–1776.

[14] G. De Feo, S. De Gisi, *Using MCDA and GIS for hazardous waste landfill siting considering land scarcity for waste disposal*, Waste Management 34 (11) (2024) 2225–2238.

[15] M. Rezaeimahmoudi, A. Esmaeli, A. Gharegozlu, H. Shabanian, L. Rokni, *Application of geographical information system in disposal site selection for hazardous wastes*, Journal of Environmental Health Science and Engineering 12 (2014) Article ID 141 6 pages.

[16] E. Stemn, B. Kumi-Boateng, *Hazardous waste landfill site selection in Western Ghana: An integration*

of multi-criteria decision analysis and geographic information system, Waste Management and Research 37 (7) (2019) 723–736.

[17] A. Titu-Eki, H. Z. Kotta, *Environmental geology assessment on the regional Pitay landfill site: A case study in Kupang, Indonesia*, SN Applied Sciences 3 (2021) Article ID 35 13 pages.

[18] V. Ahire, D. K. Behera, M. R. Saxena, S. Patil, M. Endait, H. Poduri, *Potential landfill site suitability study for environmental sustainability using GIS-based multi-criteria techniques for nashik and environs*, Environmental Earth Sciences 81 (2022) Article ID 17815 pages.

[19] I. Ali, A. Islam, S. M. Ali, S. Adnan, *Identification and selection of suitable landfill sites using GIS-based multi-criteria decision analysis in the Peshawar District, Pakistan*, Waste Management and Research 41 (3) (2023) 608–619.

[20] F. Amiri, *Solid waste disposal site selection using geospatial information technologies and fuzzy analytic hierarchy process (FAHP): A case study in Bandar Bushehr, Iran*, GeoJournal 88 (3) (2023) 3347–3368.

[21] I. Elkhrachy, A. Alhamami, S. H. Alyami, *Landfill site selection using multi-criteria decision analysis, remote sensing data, and geographic information system tools in Najran City, Saudi Arabia*, Remote Sensing 15 (15) (2023) Article ID 3754 26 pages.

[22] V. Singh, P. Sardar, S. R. Samadder, *Landfill site selection in a mining dominated area using a fuzzy AHP and DRASTIC vulnerability based multicriteria decision analysis: A case study of Dhanbad, India*, Environmental Monitoring and Assessment 195 (2023) Article ID 1172 19 pages.

[23] M. M. Zewdie, S. M. Yeshanew, *GIS based MCDM for waste disposal site selection in Dejen town, Ethiopia,* Environmental and Sustainability Indicators 18 (2023) Article ID 100228 18 pages.

[24] T. Chafiq, M. Hmamou, I. Ouhammou, A. Labriki, M. ElHabchi, M. Raji, *Geographic analysis of landfill suitability in Fez, Morocco: A multi-criteria approach*, Discover Environment 1 (2023) Article ID 16 8 pages.

[25] H. Karimi, S. Amiri, J. Huang, and A. Karimi, *Integrating GIS and multi-criteria decision analysis for landfill site selection, case study: Javanrood County in Iran*, International Journal of Environmental Science and Technology 16 (11) (2019) 7305–7318.

[26] A. Kuru, E. Tok, M. Guroglu Aktas, H. H. Demir, H. K. Özcan, G. Demir, *GIS and multicriteria decision analysis for landfill site selection in Edirne province, Turkey*, Journal of the Institute of Science and Technology 11 (2) (2021) 969–981.

[27] C. Tekin Cure, M. Zengin, F. C. Yilmaz, *Site selection based on analytic hierarchy process in the planning process for solid waste sanitary landfills: The case of Denizli city, Turkey*, Journal of Bartin Faculty of Forestry 23 (2) (2021) 493–509.

[28] A. Abdulvahitoğlu, İ. Macit, M. Koyuncu, *Selecting the facility location of the gendarmerie station with an AHP-TOPSIS based mathematical model and analysis using GAS/GIS; A case study in a city*, The Journal of Security Sciences 10 (2) (2021) 305–338.

[29] M. T. El-Saadony et al., *Hazardous wastes and management strategies of landfill leachates: A comprehensive review*, Environmental Technology and Innovation 31 (2023) Article ID 103150 26 pages.

[30] E. Gidarakos, K. Anastasiadou, E. Koumantakis, S. Nikolaos, *Investigative studies for the use of an inactive asbestos mine as a disposal site for asbestos wastes*, Journal of Hazardous Materials 153 (3) (2008) 955–965.

[31] F. Gabrielli, A. Amato, S. Balducci, L. Magi Galluzzi, F. Beolchini, *Disaster waste management in Italy: Analysis of recent case studies*, Waste Management 71 (2018) 542–555.

[32] D. Kannan, R. Khodaverdi, L. Olfat, A. Jafarian, A. Diabat, *Integrated fuzzy multi criteria decision*

making method and multiobjective programming approach for supplier selection and order allocation in a green supply chain, Journal of Cleaner Production 47 (2013) 355–367.

[33] S. W. Chou and Y. C. Chang, *The implementation factors that influence the ERP (enterprise resource planning) benefits*, Decision Support Systems 46 (1) (2008) 149–157.

[34] M. B. Ayhan, *A fuzzy AHP approach for supplier selection problem: A case study in a gearmotor company*, International Journal of Managing Value and Supply Chains 4 (3) (2013) 11–23.

[35] T. L. Saaty, The analytic hierarchy process, McGraw-Hill, New York, 1980.

[36] K. Donevska, J. Jovanovski, L. Gligorova, *Comprehensive review of the landfill site selection methodologies and criteria*, Journal of the Indian Institute of Science 101 (4) (2021) 509–521.

[37] A. Beskese, H. H. Demir, H. K. Ozcan, H. E. Okten, *Landfill site selection using fuzzy AHP and fuzzy TOPSIS: A case study for Istanbul*, Environmental Earth Sciences 73 (7) (2015) 3513–3521.

[38] C. Cheng, J. W. Lu, R. Zhu, Z. Xiao, A. M. Costa, R. G. Thompson, *An integrated multi-objective model for disaster waste clean-up systems optimization*, Transportation Research Part E: Logistics and Transportation Review 165 (2022) Article ID 102867 19 pages.

[39] Gelir Dairesi Baskanligi, *Arsa ve Arazi Asgari Metrekare Birim Değerleri, İstanbul İl* (2023), https://ivdb.gib.gov.tr/, Accessed 8 Apr 2023.

[40] M. Erdik, *Earthquake risk assessment*, Bulletin of Earthquake Engineering 15 (2017) 5055–5092.

[41] M. Battarra, B. Balcik, H. Xu, *Disaster preparedness using risk-assessment methods from earthquake engineering*, European Journal of Operational Research 269 (2) (2018) 423–435.

Çanakkale Onsekiz Mart University

Journal of Advanced Research in Natural and Applied Sciences

dergipark.org.tr/tr/pub/jarnas

Open Access

e-ISSN: 2757-5195 2024, Vol. 10, Issue 2, Pages: 464-475 doi.org/10.28979/jarnas.1409809

Potasyum Borhidrürün Formik Asit Katalizörü Varlığındaki Hidrolizi

Mehmet Emre Kenar[1], Ömer Şahin[2], Fatma Elif Genceli Güner[3]

[1]İstanbul Teknik Üniversitesi, Kimya Metalurji Fakültesi, Kimya Mühendisliği Bölümü, İstanbul, Türkiye

Makale Tarihçesi

Gönderim: 25 Aralık 2023

Kabul: 29 Nisan 2024

Yayım: 25 Haziran 2024

Araştırma Makalesi

Öz – Günümüzde artan enerji ihtiyacına paralel olarak özellikle fosil yakıtların tükenmesiyle birlikte alternatif yenilenebilir enerji kaynaklarına yönelim hızla artmaktadır. Artan bu eğilim ile birlikte, önemli bir enerji taşıyıcı kaynağı olan hidrojen öne çıkmaktadır. Hidroliz ile kolay, güvenilir ve hızlı bir şekilde hidrojen elde edebilme imkânı sağlayan borhidrürler bu kaynakların başında gelir. Ancak borhidrürlerin sulu ortamdaki hidrolizleri oldukça yavaş olduğundan reaksiyonu hızlandırmak amacıyla katalizörlerin kullanılması gerekir. Bu katalizörler homojen veya heterojen olabilirken, homojen katalizörlerin endüstriyel uygulamalarda daha fazla avantajı bulunur. Bu çalışma kapsamında potasyum borhidrürün (KBH_4) asit bazlı homojen bir katalizör olan formik asit varlığında hidroliz reaksiyonu ele alınmıştır. Reaksiyonun kinetik davranışı formik asit miktarı, sıcaklık ve potasyum borhidrür konsantrasyonu parametreleri incelenerek belirlenmiştir. Farklı sıcaklık verilerinden yola çıkılıp reaksiyon hız eşitlikleri kullanılarak potasyum borhidrürün formik asit varlığında hidroliz reaksiyonunun hızı 5 litre $H_2/g_{kat}dk$ civarında, reaksiyon hız derecesi 1.1, aktivasyon enerjisi 57.92 kJ/mol, reaksiyon entalpisi 55.32 kJ/mol, entropi azalışı 58.11 J/molK olarak bulunmuştur. Hidroliz reaksiyonuna ait Gibbs serbest enerjileri ise 20, 30, 40 ve 60 °C için sırasıyla 72.35, 72.93, 73.51, 74.67 kJ/mol olarak hesaplanmıştır. Sonuç olarak potasyum borhidrürün hidrolizi sonucu elde edilen hidrojenin, küçük ölçekli PEM yakıt hücrelerinin ihtiyacını karşılamak için yeterli seviyede olduğu, hidroliz reaksiyonunun hız değerlerinden anlaşılmaktadır.

Anahtar Kelimeler – *Formik asit, hidroliz, homojen katalizör, kinetik, potasyum borhidrür*

Hydrolysis of Potassium Borohydride using Formic Acid Catalyst

[1] Department of Chemical Engineering, Faculty of Chemical-Metallurgical Engineering, İstanbul Technical University, İstanbul, Türkiye

Article History

Received: 25 Dec 2023

Accepted: 29 Apr 2024

Published: 25 Jun 2024

Research Article

Abstract – Nowadays, in parallel with the increasing energy requirements, especially with the depletion of fossil fuels, the trend towards alternative renewable energy sources is rapidly increasing. With this increasing trend, hydrogen, an important energy carrier source, comes to the fore. Borohydrides provide the opportunity to obtain hydrogen easily, reliably and quickly by hydrolysis. However, since the hydrolysis of borohydrides in aqueous solutions is slow, catalysts have to be used to accelerate the reaction. While these catalysts can be homogeneous or heterogeneous, homogeneous catalysts have more advantages in industrial applications. In this study, in the presence of formic acid, an acid-based homogeneous catalyst, the hydrolysis reaction of potassium borohydride (KBH_4) was investigated. The kinetic behavior of the examined reaction was determined depending on formic acid amount, temperature, and potassium borohydride concentration. Based on different temperature data and reaction rate equations, the hydrolysis reaction rate is found as around 5 liters of $H_2/g_{cat}min$, the reaction rate is 1.1, the activation energy is 57.92 kJ/mol, the reaction enthalpy is 55.32 kJ/mol, and the entropy decrease is 58.11 J/molK. The Gibbs free energies of the hydrolysis reaction were calculated as 72.35, 72.93, 73.51, 74.67 kJ/mol for 20, 30, 40 and 60 °C, respectively. As a result, it is understood from the hydrolysis reaction rate that the hydrogen obtained at the end of potassium borohydride hydrolysis is sufficient to meet the needs of small-scale PEM fuel cells.

Keywords – *Formic acid, homogeneous catalyst, hydrolysis, kinetics, potassium borohydride*

[1]kenarme@itu.edu.tr; [2]omersahinr@itu.edu.tr; [3]gencelie@itu.edu.tr (Corresponding Author)

1. Giriş

Son yıllarda artan nüfusla birlikte kullanılan enerji miktarlarında hızlı bir artış meydana gelmiştir. Dünya üzerinde enerji ihtiyacı ağırlıklı olarak fosil yakıtlardan karşılanmaktadır. Ancak fosil yakıtların yol açtığı çevre kirliliği ve rezervlerinin yıllar içinde azalması ile birlikte meydana gelen sürdürülemez durum, yakın gelecekte alternatif enerji kaynaklarına yönelmeyi zorunlu hale getirmektedir. Günümüzde gelecek vadeden en önemli temiz enerji kaynaklarından biri hidrojendir. Hidrojen doğada en çok bulunan element olmakla birlikte, hidrojenin uygulama alanı geniştir. Hidrojen; kokusuz, tatsız, renksiz, hafif ve yanıcı bir gazdır. Temiz enerji taşıyıcısı olan hidrojen, kütle bazında yüksek enerji içeriğine sahiptir. Hidrojenin yanma ısısı yüksektir ve zehirli etkisi yoktur. Hidrojendeki kimyasal enerji, yakıt pilleri kullanılarak elektrik enerjisine çevrilir. Sonuç olarak, enerji verimliliği ve çevresel etkiler açısından değerlendirildiğinde hidrojenin, fosil yakıtlara kıyasla avantajları oldukça fazladır. Bu sebeple hidrojen, gelecekte kullanılabilecek en önemli temiz enerji taşıyıcılarından biridir [1, 2].

Tüm avantajlarına rağmen, hafif bir element olduğu için hidrojenin üretildikten sonra depolanma sorunu ortaya çıkmaktadır. Günümüzde hidrojen, sıkıştırılmış gaz şeklinde basınçlı tanklarda, çok düşük sıcaklıklarda sıvı halde, metal hidrürlerde ve karbon nanotüplerde olmak üzere dört temel yöntemle depolanabilmektedir. Bunlar içerisinde en güvenilir yöntemlerden biri olarak, hidrojenin metal hidrürlerde depolanması görülür [3-5]. Metal hidrürlerden biri olan borhidrürler kolay taşınabilir ve hidrojen depolama kapasiteleri yüksektir. Hidrojen depolamada, amonyum borhidrür, sodyum borhidrür, potasyum borhidrür ve lityum borhidrür öne çıkmaktadır. Borhidrürlerin yüksek pH'lardaki çözeltileri zehirsiz ve kararlı olup bu çözeltilerin alev alma, yanma ve patlama riskleri yoktur. Borhidrürlerin hidroliziyle, hızlı bir şekilde hidrojen elde edilebilmesi için reaksiyonları hızlandıran katalizörlere ihtiyaç duyulmaktadır. Bu amaçla literatürde, farklı borhidrür çeşitleriyle -özellikle metal bazlı- katalizörler kullanılarak, çeşitli çalışmalar gerçekleştirilmiştir [6-9].

Literatürde, hidroliz edilecek çözeltiyle aynı fazda bulunmayıp genellikle katı olarak sentezlenen metal bazlı kobalt, nikel gibi heterojen katalizörler ve asetik asit, fosforik asit, sülfürik asit, formik asit gibi asit bazlı homojen katalizörler ile çalışmalar yapılıp, hidrojen oluşum hızları hesaplanmıştır [10].

Homojen katalizlemede, katalizör gaz veya sıvı formda olup reaktanlar ile aynı fazdadır. Homojen katalizörler, reaksiyon ortamında çözünebilen kimyasal türlerdir ve ortama katı madde olarak eklenmezler. Bu tip katalizörler, reaksiyon başlamadan önce reaktiflerle birleşerek aktif merkezleri oluştururlar. Bu aktif merkezler, reaksiyon mekanizmalarına etki edip geçici ara ürünlerin oluşmasını sağlayarak reaksiyon hızını artırırlar. Katalizör, reaksiyonun hızını artırmak için sürekli kendini tekrarlar ve yüksek miktarda ürün oluşmasına yardımcı olur. Homojen katalizörlerin etkinliği, aktif merkezlerin doğru biçimde oluşması, reaktiflerle verimli etkileşim, reaksiyon koşulları ve çözücünün türü gibi parametrelere bağlıdır. Heterojen katalizörlerde ise homojen katalizörlerin aksine yüzey alanının sınırlı olması, katalitik aktiviteyi azaltan önemli bir faktördür [11].

Literatürde genellikle sodyum borhidrür ile çalışmalar gerçekleştirilmiştir. $NaBH_4$ hidrolizi ile hidrojen üretiminde kullanılan homojen kataliz türleri asitler (örneğin H_3PO_4, H_2SO_4, HCl ve CH_3COOH) ve metal kompleksleri (örneğin Co, Ni, Pd kompleksleri) olarak iki grup altında kategorize edilebilir [7, 12-17].

Sodyum borhidrürün hidrolizinde homojen katalizör olarak kullanılan farklı türdeki asitlerin hidrojen oluşum hızlarına etkisinin kontrol edildiği araştırmalar belgelenmiştir [18, 19]. Ayrıca potasyum borhidrürün (KBH_4) hidrolizinde homojen katalizör olarak fosforik asidin kullanıldığı ve hidrojen oluşum hızlarından yararlanılarak hidroliz reaksiyonuna ait kinetik modelin çıkarıldığı ve ilgili bu hidroliz reaksiyonu sonucunda en fazla 4296 $ml \cdot dak^{-1} \cdot g^{-1}_{kat}$. hidrojen üretme hızı olduğu raporlanmıştır [14].

Hidroliz reaksiyonunda homojen katalizör olarak asit kullanımı i) optimum koşullarda yüksek reaktivite, ii) minimum yan reaksiyon, iii) ucuzluk, iv) enjeksiyon ve kullanım kolaylığı, v) yüksek kontrol edilebilirlik gibi avantajlara sahiptir [7, 20].

Araştırmalarda genellikle stabilitesi yüksek, hidrojen depolama kapasitesi %10.8 olan, toksik ve yanıcı olmayan sodyum borhidrür kullanılmaktadır. Bu çalışmada ise hidroliz reaksiyonunun entalpi ve aktivasyon enerjisini düşürebilmek amacıyla potasyum borhidrür kullanılmış olup [21], homojen bir katalizör olan formik asitin potasyum borhidrürün hidrolizinde kullanılması ilk kez araştırılmıştır.

Potasyum borhidrürün hidrolizi sıcaklık, potasyum borhidrür konsantrasyonu ve formik asit konsantrasyonu parametrelerine bağlı olarak yürütülmüştür. Potasyum borhidrürün formik asit varlığındaki hidrolizi, açığa çıkan hidrojen hacimlerinin zamanla değişimine bağlı olarak incelenip ilgili tepkimeye ait reaksiyon mertebesi, aktivasyon enerjisi ile Gibbs enerjisi değerlerinin belirlenmesi hedeflenmiştir.

2. Materyal ve Yöntem

2.1. Materyal ve Kimyasallar

Bu deneysel çalışmada, potasyum hidroksit (KOH, saflık derecesi >%99, Merck), potasyum borhidrür (KBH_4, saflık derecesi >=%98, Sigma-Aldrich), formik asit (HCOOH, saflık derecesi %98-100, Merck) kimyasalları kullanılmıştır.

2.2. Deney Yürütülüşü

Deneysel çalışmalarda kullanılan ağırlıkça KBH_4 kütlesinin, hacimce KBH_4 sulu karışımına oranı $\left(\frac{m_{KBH_4}}{V_{(KBH_4+H_2O)}}\left[\frac{g}{ml}\right]\right)$ %1.5 olarak hazırlanan çözeltinin kendi kendine bozunmasını önlemek için %2.5 ağ/hacim oranında potasyum hidroksit çözelti ortamında çalışılmıştır. Elde edilen bu potasyum borhidrür çözeltisi 30 °C' ye ısıtılıp karıştırılarak, termal dengeye gelince üzerine belirlenen miktarda formik asit (HCOOH) eklenip, reaksiyon başlatılmıştır. Deney düzeneği Şekil 1'de sunulmaktadır. Reaksiyon sırasında çıkan hidrojenin hacmi, dereceli bir mezür yardımıyla zamana göre kaydedilmiştir. Değişen formik asit miktarı (150, 350, 450 µl) ile bu deney tekrarlanmış ve asit miktarının reaksiyon üzerindeki etkisi araştırılmıştır. Daha sonraki deneylerde, sabit tutulan asit miktarı (250 µl) ile reaksiyon farklı sıcaklıklarda (20, 40, 60 °C) gerçekleştirilerek, sıcaklığın etkisi araştırılmıştır. Deneylerin son kısmında, %1.5'luk olan potasyum borhidrür çözelti konsantrasyon yüzdesi değiştirilerek (%0.25, %0.5, %1), sabit miktarda formik asit (250 µl) ile sabit sıcaklıkta (30 °C) çalışmalar yürütülmüştür. Tüm deneyler, %2.5'luk potasyum hidroksit (KOH) çözeltisi ile gerçekleştirilmiştir. Deneylerde formik asit, mikropipet yardımıyla çekilmiştir. Reaksiyon için hazırlanan potasyum borhidrür çözeltisi, her bir deneyde 10 ml'dir. Çalışma boyunca çözeltiler için % ifadesi, ağ/hacim oranı cinsinden kullanılmıştır.

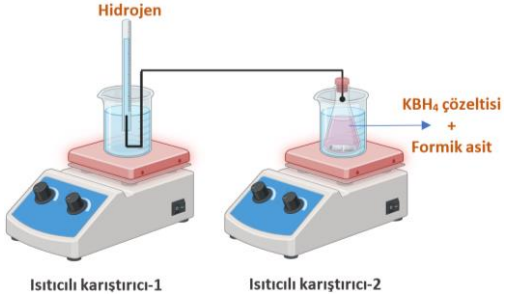

Şekil 1. Deney düzeneği

3. Bulgular ve Tartışma

Bu çalışmada potasyum borhidrürün hidrolizi formik asit varlığında katalizör miktarı, sıcaklık, potasyum borhidrür konsantrasyonu gibi parametrelere bağlı olarak incelenmiş olup kinetik davranış çıkarılmıştır. Bu parametrelerden elde edilen veriler ayrı ayrı ele alınarak aşağıda verilmiştir.

3.1. Potasyum Borhidrürün Hidrolizine Farklı Katalizör Miktarlarının Etkisi

Katalitik bir reaksiyon olan potasyum borhidrürün hidrolizi, 30 °C'ye getirilen 10 ml %1.5'luk KBH_4 çözeltisine homojen bir katalizör olan formik asidin farklı miktarları eklenerek, 400 rpm hızla karıştırılmıştır. Hidrolizin başlatılmasıyla elde edilen hidrojen hacimlerinin zamanla değişimi Şekil 2a'da verilmiştir. Grafiğe göre 150 µl formik asit katalizörü varlığında, KBH_4'ün tamamının bozunmasıyla elde edilecek H_2 gazı ideal gaz denklemi ile 276 ml hesaplanmıştır. Deneysel çalışmada kazanılmış olan 150 ml H_2 miktarının bu %100 teorik dönüşüm miktarına oranı %54'tür ve bu nedenle reaksiyonun tamamlanmadığı söylenebilir. 250 µl ve üzerindeki asit katalizörü varlığında dönüşüm %100 civarındadır. 350 ve 450 µl katalizör varlığında hidroliz eğrilerinin çoğunlukla üst üste çakıştığı görülebilir. Şekil 2a'da ve daha sonraki grafiklerde bu gibi eğrilerin elde edilmesinde, reaksiyonun 100 saniye gibi kısa bir zaman sürecinde sonlanmasının etkili olduğu düşünülmektedir. %1.5 KBH_4 için en uygun katalizör miktarının hangi değer olduğunu belirlemek amacıyla, her bir katalizör miktarı için, Şekil 2a'da verilen davranışa ait başlangıç reaksiyon hızları çıkarılmıştır.

Şekil 2b'de katalizör miktarı arttıkça başlangıç reaksiyon hızları süratle düşmektedir. Başlangıç reaksiyon hızları dikkate alındığında, bu grafiğe göre en uygun katalizör miktarının 150 µl formik asit olduğu görülmektedir. Bu şartlar uygulandığında gram katalizör başına dakikada yaklaşık 5 litre H_2 gazı elde edilmektedir. Hidroliz reaksiyonunda 150 µl formik asit katalizörü varlığında hidrojen salınımının, teorik değerin %54'ünde kaldığı bulunmuştur (Şekil 2a). Bu sebeple deneysel çalışmaların bundan sonraki parametreleri incelenirken, en uygun katalizör miktarı olarak 250 µl seçilmiştir.

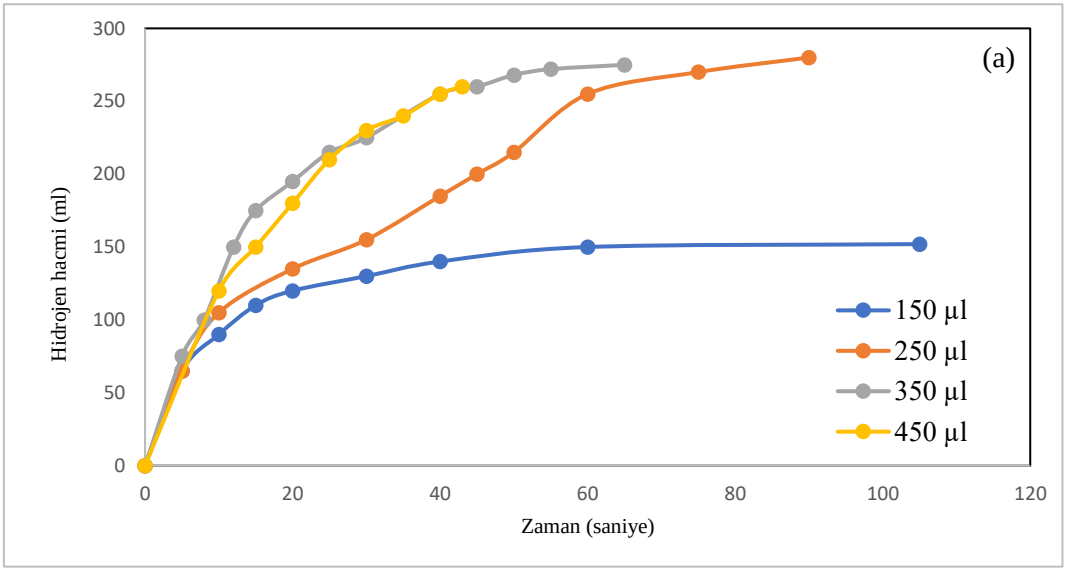

Şekil 2. (a) Potasyum borhidrürün hidrolizinde formik asit katalizör miktarı-elde edilen hidrojen hacimlerinin zamanla değişim grafiği (10 ml çözelti, %1.5 KBH_4, %2.5 KOH) (b) Başlangıç hızlarının katalizör miktarıyla değişim grafiği (Başlangıç reaksiyon hızının maksimum seviyede olduğu kabulünden yola çıkarak, Şekil 2a'daki verilere uyan polinom denklemlerinin x katsayısının katalizör kütlesine oranı, başlangıç reaksiyon hızını vermektedir)

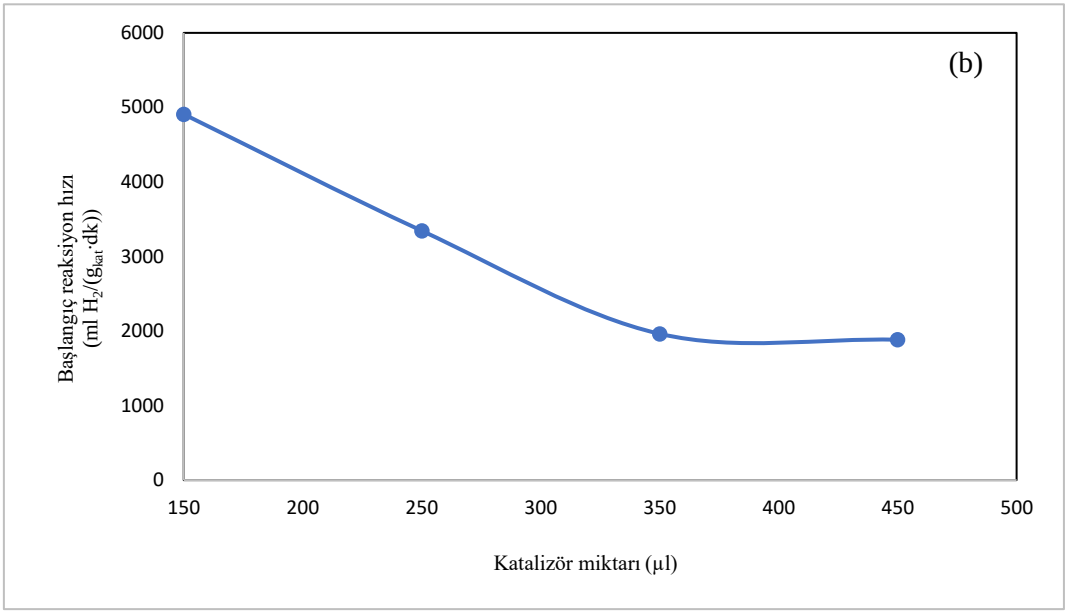

Şekil 2. (Continued) (a) Potasyum borhidrürün hidrolizinde formik asit katalizör miktarı-elde edilen hidrojen hacimlerinin zamanla değişim grafiği (10 ml çözelti, %1.5 KBH_4, %2.5 KOH) (b) Başlangıç hızlarının katalizör miktarıyla değişim grafiği (Başlangıç reaksiyon hızının maksimum seviyede olduğu kabulünden yola çıkarak, Şekil 2a'daki verilere uyan polinom denklemlerinin x katsayısının katalizör kütlesine oranı, başlangıç reaksiyon hızını vermektedir)

3.2. Potasyum Borhidrürün Hidrolizine Farklı Sıcaklıkların Etkisi

Potasyum borhidrürün 20-60 °C arasındaki hidrolizi formik asit katalizörü varlığında 4 farklı sıcaklık için incelenmiş olup elde edilen hidrojen hacimlerinin zamanla değişim grafiği Şekil 3a'da verilmiştir. Burada görüleceği gibi hidroliz hızı, sıcaklığın yükselmesi ile birlikte artmaktadır. Şahin vd. [22]'nin katalizör katkısız KBH_4 hidrolizi araştırmasında, 20-60 ºC sıcaklık aralığında hidrojen salınım oranının 5 saat sonunda bile en fazla %60 mertebelerine ulaşabildiği raporlanmıştır. Bu bulgu, katalizör varlığının reaksiyon hızının yüksek, dönüşümün fazla olması için elzem olduğunu gösterir.

Şekil 3a'da hidrolizin kinetik davranışı incelendiğinde, 30-60 °C aralığında açığa çıkan hidrojen hacmi, 20 °C' dekinden farklılık gösterir (bknz. Şekil 3a). Bu davranışın muhtemel nedeni, sıcaklığın artmasıyla birlikte hidroliz reaksiyonunun daha kısa sürede tamamlanmasıdır. 30 °C' de ve üstündeki sıcaklıklarda hidroliz reaksiyonu 90 saniyeden daha kısa bir sürede sonlanmaktadır. Şekil 3a'daki formik asit katalizörü varlığında potasyum borhidrürün hidrolizi, 30 ve 40 °C sıcaklıklarda, ilk 10 saniyedeki başlangıç bölgesinde bir adım, sonrasında başka bir adım olmak üzere iki aşamada gerçekleşir. Aynı adımlar 60 °C'de görülememektedir. Bunun nedeni, hidrolizin 10 saniyeden kısa sürede tamamlanması ve bu basamakların üst üste çakışmasıdır.

Şekil 3b'de ise farklı sıcaklıklardaki başlangıç reaksiyon hızları verilmektedir. Bu grafik incelendiğinde sıcaklık artışıyla birlikte başlangıç hızlarında da artış olduğu görülmektedir. Katalizör miktarı artışı parametresi incelenirken, katalizör miktarı ve başlangıç reaksiyon hızının ters orantılı olarak değiştiği gözlenmiştir (Şekil 2b). Çalışmanın bu kısmında ise artan sıcaklık etkisiyle başlangıç reaksiyon hızının sürekli olarak arttığı hesaplanmıştır.

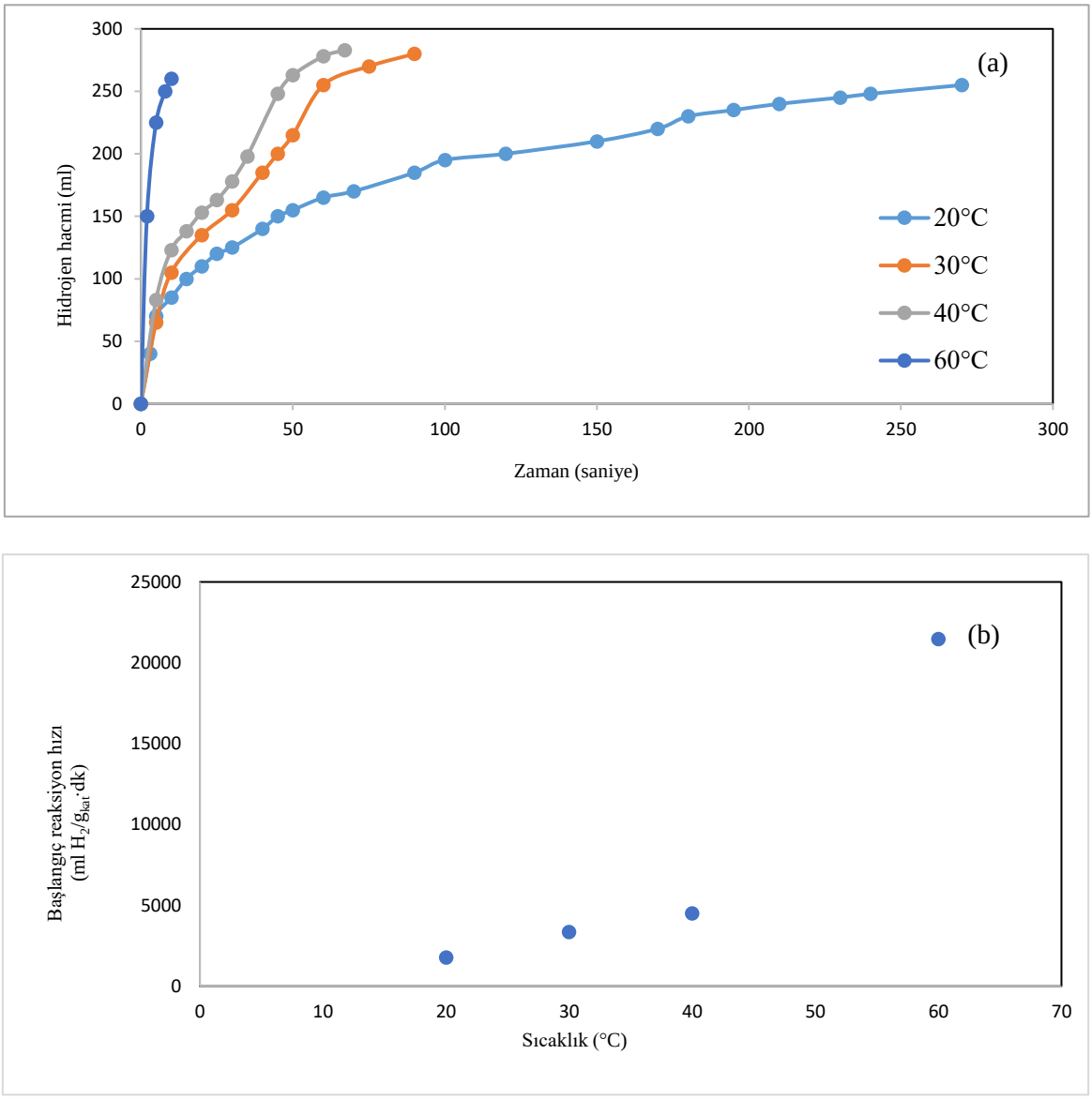

Şekil 3. (a) Formik asit katalizörü ile potasyum borhidrür hidrolizinde sıcaklık-elde edilen hidrojen hacimlerinin zamanla değişim grafiği (250 µl formik asit, 10 ml çözelti, %1.5 KBH_4, %2.5 KOH) (b) Başlangıç hızlarının farklı sıcaklıklarla değişim grafiği

3.3. Potasyum Borhidrür Konsantrasyonunun Hidrolizine Etkisi

Potasyum borhidrürün hidrolizi 30 °C'de farklı konsantrasyondaki çözeltilerin varlığında 250 µl formik asit katalizörü ilave edilerek gerçekleştirilmiş, elde edilen hidrojen hacimlerinin zamanla değişimi Şekil 4'te verilmiştir. Bu grafikte görüleceği gibi, çözeltiye eklenen potasyum borhidrür miktarı azaldıkça, çıkan hidrojen hacmi azalmıştır. 0.15 g, 0.1 g, 0.05 g ve 0.025 g KBH_4 miktarları için hidrojen salınım teorik değerleri sırasıyla 276 ml, 184 ml, 92 ml ve 46 ml hesaplanmıştır. Bu KBH_4 başlangıç miktarları için deneylerde %100'e yakın hidrojen çıkışı olduğundan (Şekil 4) reaksiyonların tamamlandığı söylenebilir. Bu çalışmayla paralel olarak, literatürde borik asit konsantrasyonu sabitken, $NaBH_4$ konsantrasyonu artırıldığında, H_2 gazı çıkışında artış gözlenmiştir [23].

Heterojen katalizörler kullanıldığında, potasyum borhidrür çözeltilerinin hidrolizi sonucu açığa çıkan potasyum metaboratın katalizörün aktif bölgelerine çökerek katalizörü bloke edebilmesi veya viskozitenin artmasıyla birlikte heterojen katalizörlerin etkinliğini belirleyen kütle transfer adımında hidroliz reaksiyonunun yavaşlayabilmesi mümkündür. Sodyum borhidrür ve potasyum borhidrürlerin hidroliziyle

hidrojen üretiminde en önemli sorun, çözeltideki konsantrasyon arttıkça katalizörün etkin yüzey alanının azalmasından dolayı katalizör etkinliğinin düşmesidir [24]. Fakat formik asit gibi homojen katalizörler, çözeltinin içerisinde tamamen dağılmış olduğu için hidroliz sonucu oluşan potasyum metaboratın aktiviteyi düşürmesi söz konusu değildir. Bu davranış sebebiyle homojen katalizörler heterojen katalizörlere nazaran uygulamada üstünlük sağlar. Diğer taraftan şunu da ifade etmekte fayda vardır; formik asit gibi homojen katalizörlerin en büyük dezavantajı tüm katalizör yüzey alanının etkin olmasından dolayı çözelti ilave edildikten sonra hidroliz reaksiyonunun sonuna kadar devam etmesi, yani istenilen bir ara kademede durdurulamamasıdır [11].

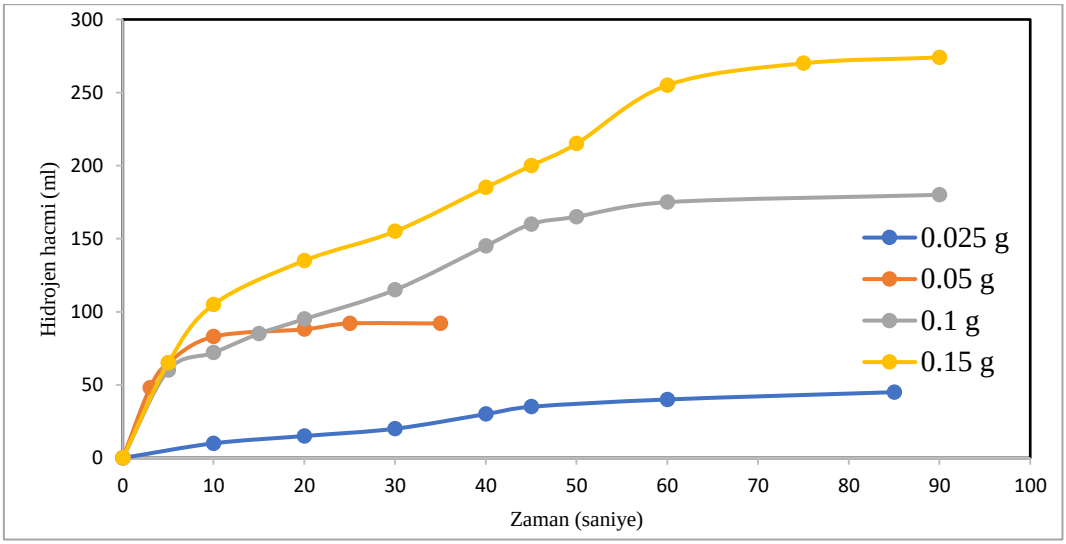

Şekil 4. Formik asit katalizörü ile potasyum borhidrür hidrolizinde potasyum borhidrür konsatrasyonu-elde edilen hidrojen hacimlerinin zamanla değişim grafiği (250 µl formik asit, 10 ml çözelti, %2.5 KOH)

3.4. Formik Asit Varlığında Potasyum Borhidrürün Hidroliz Kinetik Çalışmaları

Potasyum borhidrürün formik asit varlığındaki hidrolizine ait kinetik davranışını belirlemek üzere Şekil 3a'da verilen farklı sıcaklıklardaki hidrojen hacimlerinin zamanla değişim değerlerinden yararlanılmıştır. Bu amaçla n. dereceden reaksiyon hızı eşitliği kullanılmıştır. Potasyum borhidrürün hidroliz reaksiyonuna ait reaksiyon (3.1)'de verilmiştir [22].

$$KBH_{4(suda)} + 2H_2O \xrightarrow{formik\ asit} KBO_{2\,(suda)} + 4H_{2(g)} \tag{3.1}$$

(3.1)'e ait n. derece hız eşitliği aşağıda verilmektedir:

$$-\frac{dC_{KBH_4}}{dt} = k_{reak} C_{KBH_4}^{n}\, C_{H_2O}^{m} \tag{3.2}$$

$C_{H_2O} \gg C_{KBH_4}$ olduğu için $k_{reak} C_{H2O}^{m} = k$ denilebilir. Bu durumda (3.2),

$$-\frac{dC_{KBH_4}}{dt} = k C_{KBH_4}^{n} \tag{3.3}$$

denklemine dönüşür. (3.3)'ün reaksiyon şartlarına göre integrali alınırsa,

$$\int_{C_{KBH_{4_o}}}^{C_{KBH_4}} \frac{-dC_{KBH_4}}{C_{KBH_4}^n} = \int_0^t kdt \tag{3.4}$$

İntegral alınıp sınırlar yerine yazıldığında,

$$\frac{1}{C_{KBH_4}^{n-1}} = (n-1)kt + \frac{1}{C_{KBH_{4_o}}^{n-1}} \tag{3.5}$$

denklemi elde edilir. (3.5)'ten $\frac{1}{C_{KBH_4}^{n-1}}$'e karşı t çizildiğinde Şekil 5'te görüldüğü gibi elde edilen doğruların eğimlerinden hidroliz reaksiyonuna ait farklı sıcaklıklardaki reaksiyon hız sabitleri olan k değerleri bulunur. Şekil 5'teki reaksiyon hız derecesi ise her bir sıcaklık davranışı için aynı olmak üzere iterasyon yoluyla (regresyon katsayısı takip edilerek) n=1.1 olarak bulunmuştur. Şekil 5'te bulunan farklı sıcaklıklardaki hız sabitleri kullanılarak Arrhenius eşitliği uygulanmıştır. Arrhenius eşitliği (3.6)'da verilmiştir.

$$k = A\, e^{-\frac{Ea}{RT}} \tag{3.6}$$

(3.6) lineerleştirilirse,

$$\ln k = \ln A - \frac{Ea}{RT} \tag{3.7}$$

denklemi elde edilir. (3.7) denklemine göre Ink'ya karşı 1/T grafiği Şekil 6'da verildiği gibi çizildiğinde elde edilen doğrunun eğiminden potasyum borhidrürün formik asit varlığındaki hidrolizi için gerekli olan aktivasyon enerjisi, Ea= 57.92 kJ/mol olarak bulunur.

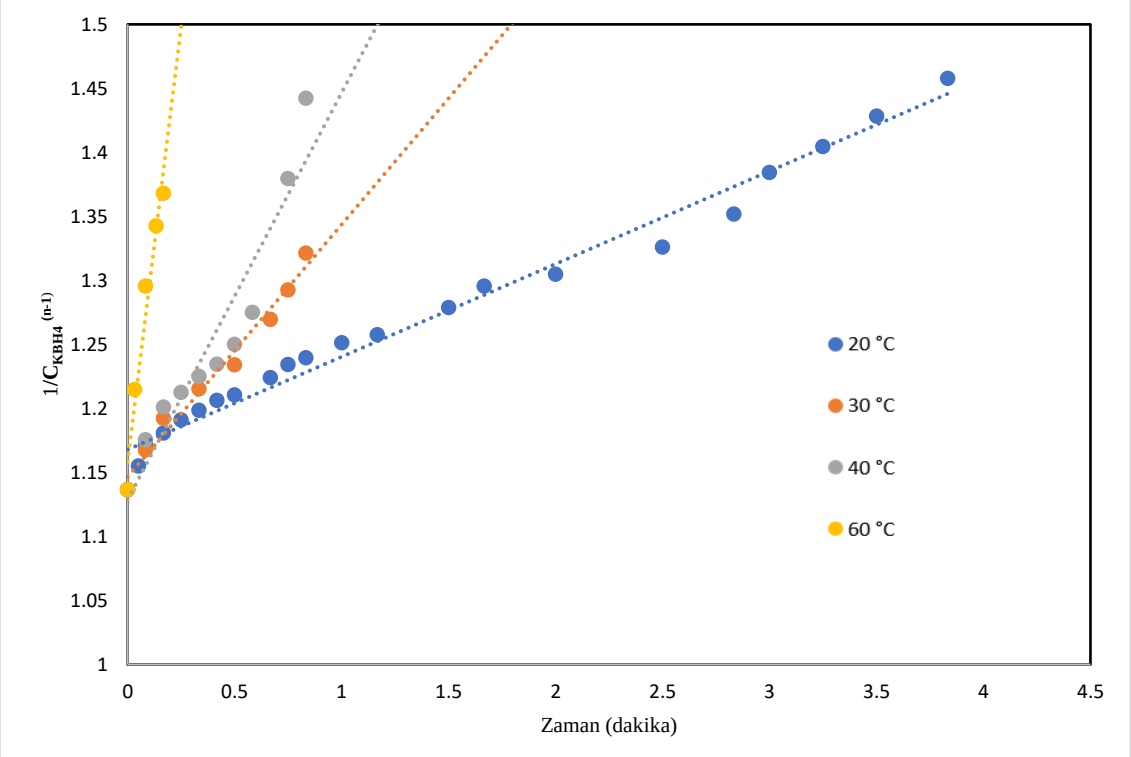

Şekil 5. Farklı sıcaklıklarda formik asit homojen katalizörü varlığında KBH_4'ün hidrolizinin n. derece kimyasal denkleme göre davranışı (n=1.1'de en iyi uyum sağlamıştır.)

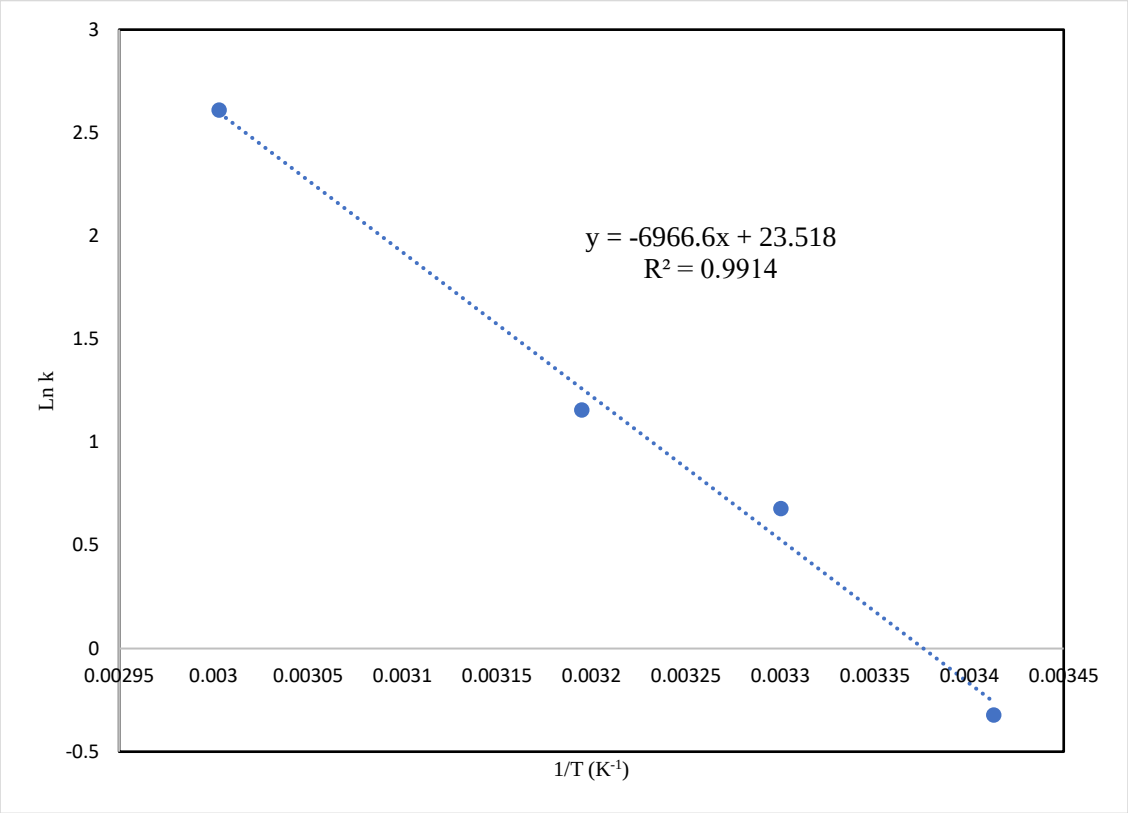

Şekil 6. Potasyum borhidrürün formik asit katalizörü varlığında hidrolizinin Arrhenius eşitliğine göre değerlendirilmesi

3.5. Termodinamik Değerlerin Hesaplanması

(3.5)'ten hesaplanan farklı sıcaklıklardaki hız sabitleri kullanılarak Eyring eşitliğinden termodinamik değerler hesaplanmıştır. Eyring Eşitliği (3.8)'de verilmiştir. Denklemde k_B ve h sırasıyla Boltzman ve Planck sabitleridir.

$$k = \frac{k_B T}{h} e^{\frac{-\Delta G}{RT}} \tag{3.8}$$

$$\Delta G = \Delta H - T\Delta S \tag{3.9}$$

olduğundan

$$k = \frac{k_B T}{h} e^{\frac{-\Delta H + T\Delta S}{RT}} \tag{3.10}$$

(3.10), T'ye bölünüp lineerleştirilirse,

$$\ln\frac{k}{T} = -\frac{\Delta H}{RT} + \left(\ln\frac{k_B}{h} + \frac{\Delta S}{R}\right) \tag{3.11}$$

$\ln\frac{k}{T}$ 'ye karşı $\frac{1}{T}$ çizildiğinde, grafiğin eğiminden ΔH değeri, kayımdan da ΔS değeri Tablo 1'de verildiği gibi bulunmuştur $\left(\ln\frac{k_B}{h} = 27.85\right)$. ΔG değerleri ise her sıcaklık için hesaplanmıştır.

Tablo 1'de formik asit katalizörü varlığında potasyum borhidrürün hidroliz reaksiyonuna ait aktivasyon

enerjisi (Ea), reaksiyon entalpi (ΔH) ve entropi (ΔS) değerleri ile farklı sıcaklıklardaki reaksiyon hız sabitleri (k) ve Gibbs serbest enerjileri (ΔG) verilmektedir.

Tablo 1. Formik asit katalizörü varlığında potasyum borhidrür hidrolizine ait kinetik ve termodinamik parametreler

T (°C)	$k \frac{1}{\left(\frac{mol}{l}\right)^{n-1} dk}$	Ea (kJ/mol)	ΔH (kJ/mol)	ΔS (J/molK)	ΔG (kJ/mol)
20	0.725	57.92	55.32	-92.11	82.31
30	1.971	57.92	55.32	-92.11	83.23
40	3.178	57.92	55.32	-92.11	84.15
60	13.60	57.92	55.32	-92.11	85.99

Şekil 6'da sunulan veriler ışığında KBH_4 hidrolizi için gereken aktivasyon enerjisi 57.92 kJ/mol olarak hesaplanmış olup bu değer literatürde $NaBH_4$ hidrolizi için gerekli olan takriben 50 kJ/mol değeri civarı ile paraleldir [7, 25, 26]. Tablo 1'de hesaplanarak verilmiş olan ΔG değerleri pozitif bulunduğundan, hidroliz reaksiyonunun ürünler yönünde kendiliğinden gerçekleşemeyeceği, aksine reaktanlar yönüne hareket etme eğiliminin olduğu anlaşılmaktadır.

4. Sonuçlar

Bu çalışmada potasyum borhidrürün hidrolizi homojen bir katalizör olan formik asit varlığında gerçekleştirildiğinde hidroliz reaksiyon hızı 5 litre $H_2/g_{kat}dk$ civarında bulunmuştur. Bu değer küçük ölçekli PEM yakıt hücrelerinin ihtiyacını karşılamak [27, 28] için yeterli olduğundan, formik asitin katalizör olarak kullanımının endüstriyel anlamda uygulanabilir seviyede olduğu söylenebilir.

Formik asit varlığında potasyum borhidrürün hidrolizine ait aktivasyon enerjisinin 57.92 kJ/mol olduğu, reaksiyona ait hız derecesinin ise 1.1 olduğu bu çalışmada ulaşılan sonuçlardandır. Ayrıca heterojen katalizörler kullanıldığında görülen KBH_4 konsantrasyonunun artmasıyla birlikte reaksiyon hızında yaşanan düşüşlerin formik asit gibi homojen katalizörler kullanıldığında görülmediği ve bu tip homojen katalizörlerin sodyum borhidrür, lityum borhidrür, amonyum borhidrür gibi diğer borhidrürlerde de kullanılabileceği düşünülmektedir.

Yazar Katkıları

İlk Yazar literatür araştırmış, veri toplamış ve analizini yapmıştır. İkinci Yazar analizi planlamış, tasarlamış ve hesaplamaları yapmıştır. Üçüncü yazar araştırmayı kurgulamış, koordine etmiş ve makaleyi yazmıştır. Tüm yazarlar çalışmanın son hâlini okuyup onaylamıştır.

Çıkar Çatışması

Yazarlar hiçbir çıkar çatışması olmadığını beyan etmektedir.

Kaynaklar

[1] Z. Ö. Özdemir, H. Mutlubaş, *Enerji taşıyıcısı olarak hidrojen ve hidrojen üretim yöntemleri*, Bartın University International Journal of Natural and Applied Sciences 2 (1) (2019) 16–34.

[2] A. L. Kübra, E. B. Ateş, *Sürdürülebilir hidrojen üretim teknolojileri: biyokütle temelli yaklaşımlar*, Bartın University International Journal of Natural and Applied Sciences 5 (1) (2022) 18–37.

[3] EnerjiEtüt (2023), https://www.enerjietutraporu.com/hidrojen-depolama-teknolojileri-nelerdir.html, Accessed 25 Dec 2023.

[4] Tesisat (2016), https://www.tesisat.org/hidrojen-enerjisi-uretimi-ve-depolanmasi.html, Accessed 25 Dec 2023.

[5] B. Sakintuna, F. Lamari-Darkrim, M. Hirscher, *Metal hydride materials for solid hydrogen storage: a review*, International Journal of Hydrogen Energy 32 (9) (2007) 1121–1140.

[6] M. Paskevicius, L. H. Jepsen, P. Schouwink, R. Černý, D. B. Ravnsbæk, Y. Filinchuk, M. Dornheim, F. Besenbacher, T. R. Jensen, *Metal borohydrides and derivatives–synthesis, structure and properties*, Chemical Society Reviews 46 (5) (2017) 1565–1634.

[7] H. N. Abdelhamid, *A review on hydrogen generation from the hydrolysis of sodium borohydride*, International Journal of Hydrogen Energy 46 (1) (2021) 726–765.

[8] J. Liu, Y. Ma, J. Yang, L. Sun, D. Guo, P. Xiao, *Recent advance of metal borohydrides for hydrogen storage*, Frontiers in Chemistry 10 (2022) 945208.

[9] F. Xu, J. Ren, J. Ma, Y. Wang, K. Zhang, Z. Cao, Q. Sun, S. Wu, G. Li, S. Bai, *A review of hydrogen production kinetics from the hydrolysis of $NaBH_4$ solution catalyzed by Co-based catalysts*, International Journal of Hydrogen Energy 50 (D) (2024) 827–844.

[10] P. Brack, S. E. Dann, K. U. Wijayantha, *Heterogeneous and homogenous catalysts for hydrogen generation by hydrolysis of aqueous sodium borohydride ($NaBH_4$) solutions*, Energy Science & Engineering 3 (3) (2015) 174–188.

[11] M. Masjedi, *Homogeneous catalysts for the hydrolysis of Sodium Borohydride: synthesis, characterization and catalytic use*, Doctoral Dissertation Orta Doğu Technical University (2010) Ankara.

[12] S. Murugesan, V. Subramanian, *Effects of acid accelerators on hydrogen generation from solid sodium borohydride using small scale devices*, Journal of Power Sources 187 (2009) 216–223.

[13] O Akdim, U. B. Demirci, P. Miele, *Acetic acid, a relatively green single-use catalyst for hydrogen generation from sodium borohydride*, International Journal of Hydrogen Energy 34 (2009) 7231–7238.

[14] C. Saka, A. Balbay, *Fast and effective hydrogen production from ethanolysis and hydrolysis reactions of potassium borohydride using phosphoric acid*, International Journal of Hydrogen Energy 43 (43) (2018) 19976–19983.

[15] C. Saka, A. Balbay, *Influence of process parameters on enhanced hydrogen generation via semi-methanolysis and semi-ethanolysis reactions of sodium borohydride using phosphoric acid*, International Journal of Hydrogen Energy 44 (2019) 30119–3011926.

[16] A. Balbay, C. Saka, *The effect of the concentration of hydrochloric acid and acetic acid aqueous solution for fast hydrogen production from methanol solution of $NaBH_4$*, International Journal of Hydrogen Energy 43 (2018) 14265–14272.

[17] A. Balbay, C. Saka, *Semi-methanolysis reaction of potassium borohydride with phosphoric acid for effective hydrogen production*, International Journal of Hydrogen Energy 43 (2018) 21299–21306.

[18] H. J. Kim, K. J. Shin, H. J. Kim, M. K. Han, H. Kim, Y. G. Shul, K. T. Jung, *Hydrogen generation from aqueous acid-catalyzed hydrolysis of sodium borohydride*, International Journal of Hydrogen Energy 35 (22) (2010) 12239–12245.

[19] E. Fangaj, A. A. Ceyhan, *Apricot Kernel shell waste treated with phosphoric acid used as a green, metal-free catalyst for hydrogen generation from hydrolysis of sodium borohydride*, International Journal of Hydrogen Energy 45 (35) (2020) 17104–17117.

[20] S. Kwon, M. J. Kim, S. Kang, T. Kim, *Development of a high storage-density hydrogen generator using solid-state $NaBH_4$ as a hydrogen source for unmanned aerial vehicles*, Applied Energy 251 (2019) 113331.

[21] D. Kilinc, O. Sahin, *High volume hydrogen evolution from KBH4 hydrolysis with palladium complex catalyst*, Renewable Energy 161 (2020) 257–264.

[22] Ö. Şahin, H. Dolaş, M. Özdemir, *The effect of various factors on the hydrogen generation by hydrolysis reaction of potassium borohydride*, International Journal of Hydrogen Energy 32 (13) (2007) 2330–2336.

[23] A. Balbay, Ö. Şahin, *Hydrogen production from sodium borohydride in boric acid-water mixtures*, Energy Sources, Part A: Recovery, Utilization, and Environmental Effects 36 (11) (2014) 1166–1174.

[24] S. Özkar, *Enhancement of catalytic activity by increasing surface area in heterogeneous catalysis*, Applied Surface Science 256 (5) (2009) 1272–1277.

[25] C. T. F. Lo, K. Karan, B. R. Davis, *Kinetic studies of reaction between sodium borohydride and methanol, water, and their mixtures*, Industrial & Engineering Chemistry Research 46 (17) (2007) 5478–5484.

[26] A. J. Hung, S. F. Tsai, Y. Y. Hsu, J. R. Ku, Y. H. Chen, C. C. Yu, *Kinetics of sodium borohydride hydrolysis reaction for hydrogen generation*, International Journal of Hydrogen Energy 33 (21) (2008) 6205–6215.

[27] M. T. Gencoglu, Z. Ural, *Design of a PEM fuel cell system for residential application*, International Journal of Hydrogen Energy 34 (12) (2009) 5242–5248.

[28] Y. Wang, Y. Pang, H. Xu, A. Martinez, K. S. Chen, *PEM Fuel cell and electrolysis cell technologies and hydrogen infrastructure development–A review*, Energy & Environmental Science 15 (6) (2022) 2288–2328.

Çanakkale Onsekiz Mart University

Journal of Advanced Research in Natural and Applied Sciences

dergipark.org.tr/tr/pub/jarnas

Open Access

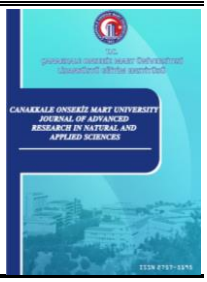

e-ISSN: 2757-5195 2024, Vol. 10, Issue 2, Pages: 476-492 doi.org/10.28979/jarnas.1440658

Transversal Lightlike Submersions

Esra Karataş[1], Cumali Yıldırım[2]

[1,2]Department of Mathematics, Faculty of Arts and Sciences, İnönü University, Malatya, Türkiye

Article History

Received: 21 Feb 2024

Accepted: 29 Apr 2024

Published: 25 Jun 2024

Research Article

Abstract − In this paper, we introduce the concept of transversal lightlike submersions from semi-Riemannian manifolds onto semi-Riemannian manifolds. Specifically, we present the concepts of transversal *r*-lightlike and isotropic transversal lightlike submersions and examine the geometry of foliations formed by these submersions through various examples. In this way, we demonstrate certain points where transversal *r*-lightlike submersions differ from semi-Riemannian submersions. Furthermore, we investigate O'Neill's tensors for transversal *r*-lightlike submersions and examine the integrability of certain distributions by employing these tensor fields. Thus, valuable information regarding such submersions' geometric structures and properties can be provided, paving the way for new research avenues. We finally discuss the need for further research.

Keywords − *Transversal submersion, Riemannian submersion, lightlike manifold, lightlike submersion*

1. Introduction

Riemannian submersions are foundational mappings within the realm of differential geometry, serving as potent instruments for unraveling the geometric properties of Riemannian manifolds. These submersions allow for methodically examining the interactions between several manifolds. Their importance spans several fields in pure mathematics and theoretical physics, providing a detailed framework for examining the complex interactions between different geometries and providing deep insights into the structure of the physical universe.

O'Neill [1] and Gray [2] introduced the theory of Riemannian submersion, which has subsequently become the subject of numerous studies [3-12]. Consequently, it has become a useful tool for clarifying the structure of Riemannian manifolds. It is well known that when M_1 and M_2 are Riemannian manifolds, the fibers become Riemannian manifolds; however, it has been noted that the fibers of f may not be semi-Riemannian when the manifolds are semi-Riemannian [13].

Şahin has recently introduced and studied the concept of submersion from lightlike manifolds onto semi-Riemannian manifolds in [14], along with the submersion from semi-Riemannian manifolds onto lightlike manifolds in [13], providing significant insights into the geometric relationship between these disparate manifold types.

Hereinafter, we will initially provide an overview of a lightlike manifold and subsequently introduce the concept of transversal submersion from semi-Riemannian manifolds to semi-Riemannian manifolds. We will investigate specific examples to assess the possibility of constructing such a submersion and draw conclusions based on our analysis. Thus, the concept of transversal lightlike submersion will pave the way for innovative

[1]esrakrts4422@gmail.com (Corresponding Author); [2]cumali.yildirim@inonu.edu.tr

geometric inquiries.

2. Lightlike Manifolds

Let V be a real vector space and g_1 be a bilinear form on V. If there exists a non-zero vector ξ in V such that $g_1(\xi, v) = 0$, for every $v \in V$, then g_1 is considered degenerate on V; otherwise, it is termed as non-degenerate. On the other hand, if $g_1(v, v) > 0$, then g_1 is said to be positively defined on V; conversely, $g_1(v, v) < 0$, then g_1 is said to be negatively defined on V. Consequently, a positive or negative defined g_1 is deemed to be non-degenerate [15].

Consider V as a vector space and suppose that there exists a symmetric bilinear form g_1 on V. In this case, there exist bases $\{e_i\}$ on V that

$$\begin{pmatrix} 1 \le i \le r & ; & g_1(e_i, e_i) & = & 0 \\ 1 \le j \le q & ; & g_1(e_j, e_j) & = & -1 \\ 1 \le k \le p & ; & g_1(e_k, e_k) & = & 1 \\ i \ne j & ; & g_1(e_i, e_j) & = & 0 \end{pmatrix}$$

These bases are referred to as orthonormal bases, and the triplet (r, q, p) is the type of the bilinear form g_1 [16]. Let (M_1, g_1) denote a real differentiable n dimensional manifold, where g_1 is a symmetric tensor field of type $(0,2)$. Assume that M_1 is paracompact. The radical space of T_xM_1 denoted by Rad T_xM_1 and given as

$$\text{Rad } T_xM_1 = \{\xi \in T_xM_1 : g_1(\xi, X) = 0, X \in T_xM_1\}$$

The nullity degree of g_1 corresponds to the dimension of T_xM_1. Suppose Rad TM_1 corresponds to the radical subspace of Rad T_xM_1 for every $x \in M_1$. In this case, Rad TM_1 becomes the radical distribution of M_1, and if $0 < r \le n$, this manifold M_1 is called a lightlike manifold [13]. The non-degenerate symmetric bilinear form g_1 on V is referred to as a semi-Euclidean metric, in this case, V is termed as a semi-Euclidean space [15].

We note that $g_1(v, v)>0$ or $v = 0$, then v is defined as spacelike. Similarly, if $g_1(v, v)<0$, then v is defined as timelike. Moreover, if $g_1(v, v)=0$ and $v \ne 0$, then v is defined as lightlike (null, isotropic), where $v \in V$, V is a semi-Euclidean space [15].

Afterward, we present the concepts of Riemannian and lightlike submersions, necessary for providing transversal lightlike submersions.

3. Riemannian Submersions

In this section, the definition of Riemann submersions is provided, along with some significant information concerning these submersions.

Let (M_1, g_1) and (M_2, g_2) be m and n dimensional Riemannian manifolds, respectively, and $f: M_1 \to M_2$ be a submersion. In this case, $\text{rank } f = \dim M_2 < \dim M_1$. For any $x \in M_2$, the fiber $F_x = f^{-1}(x)$ is a submanifold of M_1 with dimension $r = (m - n)$. Submanifolds $f^{-1}(x)$ are called submersion fibers.

The integrable distribution $\mathcal{V}$ of the submersion $f: M_1 \to M_2$ in (M_1, g_1) is defined by $\mathcal{V}_p = \ker f_{*\text{p}}$, where $p \in M_1$. $\mathcal{V}_p$ is called the vertical distribution of submersion. Furthermore, $\mathcal{H}_p = (\mathcal{V}_p)^{\perp}$ is orthogonal to and complements the vertical distribution. We refer to the $\mathcal{H}$ distribution as the horizontal distribution of the submersion [17, 18].

Consider (M_1, g_1) and (M_2, g_2) as Riemannian manifolds. A differentiable mapping f is referred to as a Riemannian submersion if it satisfies the following conditions:

i. f has maximal rank.

ii. For any $p \in M_1$, f_{*_p} preserves the length of $X_p \in \Gamma(\mathcal{H}_p)$, where $\mathcal{H}_p$ represents the horizontal vectors [1].

The first condition in the definition ensures that the mapping is a submersion. The second condition states that the f_* derivative transformation at the point $p \in M_1$ is a linear isometry from the horizontal space $\mathcal{H}_{\mathrm{p}}$ to the tangent space $T_{f(p)}M_2$. Therefore, $g_{1_p}(u, v) = g_{2f(p)}(f_{*p}u, f_{*p}v)$, holds for $u, v \in \mathcal{H}_p$, $p \in M_1$ [17]. Furthermore, given that X is horizontal and f–related to a vector field $\tilde{X}$ on M_2, that is, $f_*(X) = \tilde{X}_f(p)$ for any $p \in M_1$ a vector field X on M_1 is considered basic [1].

Proposition 3.1 Let (M_1, g_1) and (M_2, g_2) be Riemannian manifolds, where $f: (M_1, g_1) \to (M_2, g_2)$ is a Riemannian submersion, and let ∇ and ∇' denote the Levi-Civita connections of M_1 and M_2, respectively. Suppose the basic vector fields X and Y on M_1 are f −related to the vector fields X' and Y'. In this case, the following equations are obtained [18]:

1. $g_1(X, Y) = g_2(X', Y') \circ f$

2. The basic vector field $h[X, Y]$ corresponds to $[\tilde{X}, \tilde{Y}]$

3. The basic vector field $h(\nabla_X Y)$ corresponds to $\nabla_{X,} Y'$

4. Lightlike Submersions

Sahin and Gündüzalp previously introduced several concepts related to lightlike submersions in [13]. Let (M_1, g_1) be a semi-Riemannian manifold, (M_2, g_2) be an r-lightlike manifold. Consider a differentiable submersion $f: M_1 \to M_2$, where f_* denotes the derivative transformation. The kernel of f_* at the point $p \in M_2$, denotes as $\ker f_*$, is defined as [13]:

$$\ker f_* = \{X \in T_p(M_1): f_*(X) = 0\}$$

Case 4.1 $0 < \dim \Delta < \min\{\dim(\ker f_*), \dim(\ker f_*)^{\perp}\}$: In this case, Δ is the radical subspace of T_pM_1. Thus, a quasi-orthonormal basis of M_1 along $\ker f_*$ is constructed as described in [15]. Since $\ker f_*$ is a real lightlike vector space, there exists a non-degenerate subspace that complements Δ [15]. Then,

$$\ker f_* = \Delta \perp S(\ker f_*)$$

and similarly,

$$(\ker f_*)^{\perp} = \Delta \perp S(\ker f_*)^{\perp}$$

where $S(\ker f_*)^{\perp}$ denotes the complementary subspace of Δ in $(\ker f_*)^{\perp}$. Given the expression $T_pM_1 = S(\ker f_*) \perp (S(\ker f_*))^{\perp}$, since $S(\ker f_*)$ is non-degenerate in T_pM_1, it can be observed that $(S(\ker f_*))^{\perp}$ is the complementary subspace of $S(\ker f_*)$ in T_pM_1. Additionally, since $S(\ker f_*)$ and $(S(\ker f_*))^{\perp}$ are non-degenerate, we can observe that

$$(S(\ker f_*))^{\perp} = S(\ker f_*)^{\perp} \perp (S(\ker f_*)^{\perp})^{\perp}$$

Then, according to Proposition 2.4 in [15], it is known that "There exists a quasi-orthonormal basis of $\ker f_*$". Therefore, we have the following expressions:

$$\begin{pmatrix} g_1(\xi_i,\xi_j)=g_1(N_i,N_j)=0 & ; & g_1(\xi_i,N_j)=\delta_{ij} \\ g_1(W_\alpha,\xi_j)=g_1(W_\alpha,N_j)=0 & ; & g_1(W_\alpha,W_\alpha)=\varepsilon_\alpha\delta_{\alpha\beta} \end{pmatrix}$$

where $i,j\in\{1,\dots,r\}$ and $\alpha,\beta\in\{1,\dots,t\}$. Here $\{N_i\}$ represents differentiable null vector fields of $(S(\ker f_*)^\perp)^\perp$, $\{\xi_i\}$ is the basis of Δ, and $\{W_\alpha\}$ is the basis of $S(\ker f_*)^\perp$. The set of vector fields $\{N_i\}$ is denoted by $\mathrm{ltr}(\ker f_*)$, and consider the following subspace:

$$\mathrm{tr}(\ker f_*)=\mathrm{ltr}(\ker f_*)\perp S(\ker f_*)^\perp$$

It should be noted that $\mathrm{ltr}(\ker f_*)$ and $(\ker f_*)$ are not orthogonal to each other. The space $\ker f_*$, denoted as $\mathcal{V}$, is referred to as the vertical space of T_pM_1, while $\mathrm{tr}(\ker f_*)$, denoted as $\mathcal{H}$, is called the horizontal space of T_pM_1, as is usual in the theory of Riemannian submersions. Thus, we have the decomposition:

$$T_pM_1=\mathcal{V}_p\oplus\mathcal{H}_p$$

We notice that $\mathcal{V}$ and $\mathcal{H}$ are not orthogonal [13].

Definition 4.2 [13] Let (M_1,g_1) be a semi-Riemannian manifold and (M_2,g_2) be an r-lightlike manifold. Consider a submersion $f:M_1\to M_2$ satisfying the following conditions:

i. $\dim\Delta=\dim\{(\ker f_*)\cap(\ker f_*)^\perp\}=r$, $0<r<\min\{\dim(\ker f_*),\dim(\ker f_*)^\perp\}$.

ii. f_* preserves the length of horizontal vectors, i.e. $g_1(X,Y)=g_2(f_*X,f_*Y)$ *for* $X,Y\in\Gamma(\mathcal{H})$. In this case, we can say that f is an r-lightlike submersion.

Case 4.3. [13] $\dim\Delta=\dim(\ker f_*)<\dim(\ker f_*)^\perp$. Then, $\mathcal{V}=\Delta$ and $\mathcal{H}=\mathcal{S}(\ker f_*)^\perp\perp\mathrm{ltr}(\ker f_*)$. Thus, we name f an isotropic submersion.

Case 4.4. [13] $\dim\Delta=\dim(\ker f_*)^\perp<\dim(\ker f_*)$. Then, $\mathcal{V}=\mathcal{S}(\ker f_*)\perp\Delta$ and $\mathcal{H}=\mathrm{ltr}(\ker f_*)$. Thus, we name f co-isotropic submersion.

Case 4.5. [13] $\dim\Delta=\dim(\ker f_*)^\perp=\dim(\ker f_*)$. Then, $\mathcal{V}=\Delta$ and $\mathcal{H}=\mathrm{ltr}(\ker f_*)$. Thus, we name f totally lightlike submersion.

Therefore, in conjunction with this information, we present a new concept.

5. Transversal Lightlike Submersions

In this section, we will introduce the concept of transversal submersion and provide four related examples. Through these examples, we will explore the existence of various types of submersions. Additionally, we will introduce O'Neill tensors for transversal submersions, which will lead to different results regarding their overall properties.

Firstly we note that a basic vector field on M_1 is a horizontal vector field X that is f-related to vector field $\tilde{X}$ on M_2, meaning that $f_*(X_p)=\tilde{X}_{f(p)}$ for all $p\in M_1$ (Where f_* is a derivative map). Every vector field $\tilde{X}$ on M_2 has a unique horizontal lift X to M_1, and X is basic. Therefore, the correspondence $X\leftrightarrow\tilde{X}$ establishes a one-to-one relationship between fundamental vector fields on M_1 and arbitrary vector fields on M_2 [13]. Thus, we can give the following definition.

Definition 5.1 Consider (M_1,g_1) and (M_2,g_2) be a semi-Riemannian manifold and let $f:M_1\to M_2$ be a submersion. If the condition

$$g_1(X,Y) = g_2(f_*(X), f_*(Y)) \tag{5.1}$$

holds for all $X, Y \in \Gamma(S(\ker f_*)^{\perp})$, we call the mapping f as a transversal submersion.

Therefore,

- f has maximal rank,
- At each point p in M_1, the f_{*p} mapping preserves the lengths of horizontal vectors; that is, $g_{1p}(X,Y) = g_{2f(p)}(f_{*p}X, f_{*p}Y)$. This implies that at a point p in M_1, the f_* derivative transformation states a linear isometry from $\Gamma(S(\ker f_*)^{\perp})$ space onto $T_{f(p)}M_2$.

Note that for $p \in M_2$, $f^{-1}(p)$ is a submanifold with $\dim M_1$-$\dim M_2$.

Definition 5.2 Consider (M_1, g_1) and (M_2, g_2) as semi-Riemannian manifolds and let $f: M_1 \to M_2$ be a transversal submersion. According to Definition 4.2 in Case 4.1, f is characterized as a transversal r-lightlike submersion. Furthermore, as per Definition 4.2 in Case 4.3, f is denoted as an isotropic transversal lightlike submersion.

We will give examples of transversal r-lightlike and isotropic transversal lightlike submersions.

Example 5.3 Consider $\mathbb{R}_1^6$ and $\mathbb{R}_1^3$ to be $\mathbb{R}^6$ and $\mathbb{R}^3$endowed with semi-Riemannian metrics. Define these metrics as follows:

$$g_1 = -(dx_1)^2 + (dx_2)^2 + (dx_3)^2 + (dx_4)^2 + (dx_5)^2 + (dx_6)^2$$

and

$$g_2 = -(dy_1)^2 + \frac{1}{2}(dy_2)^2 + \frac{1}{2}(dy_3)^2$$

where $\{x_1, x_2, x_3, x_4, x_5, x_6\}$ and $\{y_1, y_2, y_3\}$ are the canonical coordinates on $\mathbb{R}^6$ and $\mathbb{R}^3$, respectively. Moreover, we define the following map:

$$\begin{array}{rccc} f: & \mathbb{R}_1^6 & \to & \mathbb{R}_1^3 \\ & (x_1, x_2, x_3, x_4, x_5, x_6) & \to & (x_1 - x_5, x_2 + x_6, x_3 + x_4) \end{array}$$

The kernel of f_* is then given by

$$\ker f_* = \mathrm{Span}\left\{W_1 = \frac{\partial}{\partial x_1} + \frac{\partial}{\partial x_5},\ W_2 = -\frac{\partial}{\partial x_2} + \frac{\partial}{\partial x_6}, W_3 = -\frac{\partial}{\partial x_3} + \frac{\partial}{\partial x_4}\right\}$$

Thus,

$$(\ker f_*)^{\perp} = \mathrm{Span}\left\{T_1 = \frac{\partial}{\partial x_1} + \frac{\partial}{\partial x_5}, T_2 = \frac{\partial}{\partial x_2} + \frac{\partial}{\partial x_6}, T_3 = \frac{\partial}{\partial x_3} + \frac{\partial}{\partial x_4}\right\}$$

Therefore,

$$W_1 = T_1, \qquad \Delta = \ker f_* \cap (\ker f_*)^{\perp} = \mathrm{Span}\{W_1\}$$

Then,

$$\mathrm{ltr}(\ker f_*) = \mathrm{Span}\left\{N = \frac{1}{2}\left(-\frac{\partial}{\partial x_1} + \frac{\partial}{\partial x_5}\right)\right\}$$

Using $N = \frac{1}{g_1(\xi,V)}\left\{V - \frac{g_1(V,V)}{2g_1(\xi,V)}\xi\right\}$ from Equation (1.5) in [15], it is easy to check that $g_1(N,W_1) = 1$, $g_1(N,W_2) = 0$, and $g_1(N,W_3) = 0$. Thus, we give the vertical and horizontal spaces as:

$$\mathcal{V} = \text{Span}\{W_1, W_2, W_3\}, \mathcal{H} = \text{Span}\{T_2, T_3, N\}$$

Furthermore, since $f_*(T_2) = 2\frac{\partial}{\partial y_2}$, $f_*(T_3) = 2\frac{\partial}{\partial y_3}$, and $f_*(N) = -\frac{\partial}{\partial y_1}$, we obtain that

$$g_1(T_2,T_2) = g_2\big(f_*(T_2), f_*(T_2)\big) = 2, g_1(T_3,T_3) = g_2(f_*(T_3), f_*(T_3)) = 2$$

$$g_1(N,N) = 0, g_2(f_*(N), f_*(N)) = -1$$

Here, we state that the lengths of the vectors in $S(\ker f_*)^{\perp}$ are conserved, but we cannot say the same for $\text{ltr}(\ker f_*)$. In this case, the mapping f is a transversal $1-$lightlike submersion.

Example 5.4 Consider $\mathbb{R}_2^6$ and $\mathbb{R}_2^3$ be $\mathbb{R}^6$ and $\mathbb{R}^3$endowed with semi-Riemannian metrics. Define these metrics as follows:

$$g_1 = -(dx_1)^2 - (dx_2)^2 + (dx_3)^2 + (dx_4)^2 + (dx_5)^2 + (dx_6)^2$$

and

$$g_2 = -(dy_1)^2 - (dy_2)^2 + \frac{1}{2}(dy_3)^2$$

where $\{x_1, x_2, x_3, x_4, x_5, x_6\}$ and $\{y_1, y_2, y_3\}$ are the canonical coordinates on $\mathbb{R}^6$ and $\mathbb{R}^3$, respectively. We define the following map:

$$\begin{array}{rccc} f: & \mathbb{R}_2^6 & \to & \mathbb{R}_2^3 \\ & (x_1,x_2,x_3,x_4,x_5,x_6) & \to & (x_1+x_4, x_2+x_5, x_3+x_6) \end{array}$$

The kernel of f_* is then

$$\ker f_* = \text{Span}\left\{W_1 = -\frac{\partial}{\partial x_1} + \frac{\partial}{\partial x_4}, W_2 = -\frac{\partial}{\partial x_2} + \frac{\partial}{\partial x_5}, W_3 = -\frac{\partial}{\partial x_3} + \frac{\partial}{\partial x_6}\right\}$$

Thus,

$$(\ker f_*)^{\perp} = \text{Span}\left\{T_1 = -\frac{\partial}{\partial x_1} + \frac{\partial}{\partial x_4}, T_2 = -\frac{\partial}{\partial x_2} + \frac{\partial}{\partial x_5}, T_3 = \frac{\partial}{\partial x_3} + \frac{\partial}{\partial x_6}\right\}$$

Therefore, we have $W_1 = T_1$ and $W_2 = T_2$,

$$\Delta = (\ker f_*) \cap (\ker f_*)^{\perp} = \text{Span}\{W_1 = T_1,\ W_2 = T_2\}$$

Then,

$$\text{ltr}(\ker f_*) = \text{Span}\left\{N_1 = \frac{1}{2}\left(\frac{\partial}{\partial x_1} + \frac{\partial}{\partial x_4}\right), N_2 = \frac{1}{2}\left(\frac{\partial}{\partial x_2} + \frac{\partial}{\partial x_5}\right)\right\}$$

Moreover, we have

$$f_*(T_3) = 2\frac{\partial}{\partial y_3}, f_*(N_1) = \frac{\partial}{\partial y_1}, f_*(N_2) = \frac{\partial}{\partial y_2}$$

Then, we obtain that

$$g_1(T_3,T_3) = g_2(f_*(T_3), f_*(T_3)) = 2$$

$$g_1(N_1,N_1) = 0, g_2(f_*(N_1), f_*(N_1)) = -1, g_1(N_2,N_2) = 0, g_2(f_*(N_2), f_*(N_2)) = -1$$

Thus, f is a transversal 2-lightlike submersion.

Example 5.5 Let $\mathbb{R}_1^4$ and $\mathbb{R}_1^3$ be $\mathbb{R}^4$ and $\mathbb{R}^3$endowed with semi-Riemannian metrics. Define these metrics as follows:

$$g_1 = -(dx_1)^2 + (dx_2)^2 + (dx_3)^2 + (dx_4)^2$$

and

$$g_2 = -(dy_1)^2 + (dy_2)^2 + (dy_3)^2$$

where $\{x_1, x_2, x_3, x_4\}$ and $\{y_1, y_2, y_3\}$ are the canonical coordinates on $\mathbb{R}^4$ and $\mathbb{R}^3$, respectively. We define the following map:

$$\begin{array}{rccc} f & : & \mathbb{R}_1^4 & \to & \mathbb{R}_1^3 \\ & & (x_1, x_2, x_3, x_4) & \to & (x_1 + x_2, x_3, x_4) \end{array}$$

The kernel of f_* is then

$$\ker f_* = Span\left\{W_1 = -\frac{\partial}{\partial x_1} + \frac{\partial}{\partial x_2}\right\}$$

Thus,

$$(\ker f_*)^{\perp} = \mathrm{Span}\left\{T_1 = -\frac{\partial}{\partial x_1} + \frac{\partial}{\partial x_2}, T_2 = \frac{\partial}{\partial x_3}, T_3 = \frac{\partial}{\partial x_4}\right\}$$

Hence, we have

$$\Delta = \ker f_* \cap (\ker f_*)^{\perp} = \mathrm{Span}\{W_1\}$$

Then,

$$\mathrm{ltr}(\ker f_*) = \mathrm{Span}\left\{N = \frac{1}{2}\left(\frac{\partial}{\partial x_1} + \frac{\partial}{\partial x_2}\right)\right\}$$

Moreover,

$$f_*(N) = \frac{\partial}{\partial y_1}, f_*(T_2) = \frac{\partial}{\partial y_2}, f_*(T_3) = \frac{\partial}{\partial y_3}$$

Thus, we obtain that

$$g_1(T_2, T_2) = 1, g_2\big(f_*(T_2), f_*(T_2)\big) = 1, g_1(T_3, T_3) = 1, g_2(f_*(T_3), f_*(T_3)) = 1$$

$$g_1(N, N) = 0, g_2(f_*(N), f_*(N))) = -1$$

Hence, f is isotropic transversal 1-lightlike submersion.

Example 5.6 Let $\mathbb{R}_2^6$ and $\mathbb{R}_2^4$ be $\mathbb{R}^6$ and $\mathbb{R}^4$endowed with semi-Riemannian metrics. Define these metrics as follows:

$$g_1 = -(dx_1)^2 - (dx_2)^2 + (dx_3)^2 + (dx_4)^2 + (dx_5)^2 + (dx_6)^2$$

and

$$g_2 = -(dy_1)^2 - (dy_2)^2 + (dy_3)^2 + (dy_4)^2$$

where $\{x_1, x_2, x_3, x_4, x_5, x_6\}$ and $\{y_1, y_2, y_3, y_4\}$ are the canonical coordinates on $\mathbb{R}^6$ and $\mathbb{R}^4$, respectively. We define the following map:

$$f : \mathbb{R}_2^6 \to \mathbb{R}_2^4$$
$$(x_1, x_2, x_3, x_4, x_5, x_6) \to \left(\frac{x_1 + x_5}{\sqrt{2}}, \frac{x_2 + x_6}{\sqrt{2}}, x_3, x_4\right)$$

The kernel of f_* is then

$$\ker f_* = \text{Span}\left\{W_1 = -\frac{\partial}{\partial x_1} + \frac{\partial}{\partial x_5}, W_2 = -\frac{\partial}{\partial x_2} + \frac{\partial}{\partial x_6}\right\}$$

Thus,

$$(\ker f_*)^{\perp} = \text{Span}\left\{T_1 = -\frac{\partial}{\partial x_1} + \frac{\partial}{\partial x_5}, T_2 = -\frac{\partial}{\partial x_2} + \frac{\partial}{\partial x_6}, T_3 = \frac{\partial}{\partial x_3}, T_4 = \frac{\partial}{\partial x_4}\right\}$$

Hence, we have $W_1 = T_1$, $W_2 = T_2$,and

$$\Delta = \ker f_* \cap (\ker f_*)^{\perp} = \text{Span}\{W_1 = T_1, W_2 = T_2\}$$

Then,

$$\text{ltr}(\ker f_*) = \text{Span}\left\{N_1 = \frac{1}{2}\frac{\partial}{\partial x_1} + \frac{1}{2}\frac{\partial}{\partial x_5}, N_2 = \frac{1}{2}\frac{\partial}{\partial x_2} + \frac{1}{2}\frac{\partial}{\partial x_6}\right\}$$

Moreover, we have

$$f_*(N_1) = \frac{1}{\sqrt{2}}\frac{\partial}{\partial y_1}, f_*(N_2) = \frac{1}{\sqrt{2}}\frac{\partial}{\partial y_2}, f_*(T_3) = \frac{\partial}{\partial y_3}, f_*(T_4) = \frac{\partial}{\partial y_4}$$

Then,

$$g_1(T_3, T_3) = g_2(f_*(T_3), f_*(T_3)) = 1, g_1(T_4, T_4) = g_2(f_*(T_4), f_*(T_4)) = 1$$

$$g_1(N_1, N_1) = 0, g_2\big(f_*(N_1), f_*(N_1)\big) = -\frac{1}{2}, g_1(N_2, N_2) = 0, g_2\big(f_*(N_2), f_*(N_2)\big) = -\frac{1}{2}$$

Thus, f is isotropic transversal $2-$lightlike submersion.

Corollary 5.7 From Definition 5.1 and the examples provided above for a transversal submersion with degenerate fibers, we can introduce the concepts of transversal *r*-lightlike and isotropic transversal submersion. However, it is important to note that the notions of co-isotropic and totally lightlike submersion are not applicable in this context.

Lemma 5.8 Let $f: (M_1, g_1) \to (M_2, g_2)$ be a transversal $r-$lightlike submersion between semi-Riemannian manifolds (M_1, g_1) and (M_2, g_2). Then, for all $X, Y \in \Gamma(S(\ker f_*)^{\perp})$

$$g_1(X, Y) = g_2(\tilde{X}, \tilde{Y}) \circ f$$

Proof. The proof can be made easily from the isometry condition in Definition 5.1 using (5.1).

Theorem 5.9 Let $f: (M_1, g_1) \to (M_2, g_2)$ be a transversal $r-$lightlike submersion between semi-Riemannian manifolds (M_1, g_1) and (M_2, g_2). Then $h\nabla_X Y$ is the fundamental vector field corresponding to $\overset{M_2}{\nabla}_{\tilde{X}}\tilde{Y}$, for X, $Y \in \Gamma(S(\ker f_*)^{\perp})$.

Proof. Since M_1 is a semi-Riemannian manifold with the Levi-Civita connection, the Koszul equality holds, leading to

$$2g_1(\nabla_X Y, Z) = X\big(g_1(Y, Z)\big) + Y\big(g_1(X, Z)\big) - Z\big(g_1(X, Y)\big) + g_1([X, Y], Z) + g_1([Z, X], Y) - g_1([Y, Z], X)$$

where $X, Y, Z \in \Gamma(S(\ker f_*)^{\perp})$. By utilizing Lemma 5.8, we obtain $(g_1(Y,Z)) = \tilde{X}g_2(\tilde{Y},\tilde{Z}) \circ f$. Similarly, if we generalize this equality, we have

$$2g_1(\nabla_X Y, Z) = \tilde{X}g_2(\tilde{Y},\tilde{Z}) \circ f + \tilde{Y}g_2(\tilde{Z},\tilde{X}) \circ f - \tilde{Z}g_2(\tilde{Y},\tilde{X}) \circ f + g_2([\tilde{X},\tilde{Y}],\tilde{Z}) \circ f + g_2([\tilde{Z},\tilde{X}],\tilde{Y}) \circ f - g_2([\tilde{Y},\tilde{Z}],\tilde{X}) \circ f$$

Considering that M_2 is a semi-Riemannian manifold, it has a Levi-Civita connection. From here, we can state that $\overset{M_2}{\nabla}$ satisfies Koszul's equality. Then,

$$g_1(\nabla_X Y, Z) = g_2(\overset{M_2}{\nabla}_{\tilde{X}}\tilde{Y}, \tilde{Z}) \circ f$$

Therefore, we deduce that $h\nabla_X Y$ represents the fundamental vector field associated with $\overset{M_2}{\nabla}_{\tilde{X}}\tilde{Y}$.

Remark 5.10 *Let* $f\colon (M_1, g_1) \to (M_2, g_2)$ be a transversal r −lightlike submersion between semi-Riemannian manifolds (M_1, g_1) and (M_2, g_2), in this case, the expression in Theorem 5.9 does not apply to $N_1, N_2 \in \Gamma(\mathrm{ltr}(\ker f_*))$.

Remark 5.11 Let $f\colon (M_1, g_1) \to (M_2, g_2)$ be a transversal r −lightlike submersion between semi-Riemannian manifolds (M_1, g_1) and (M_2, g_2). In this case, for any $U \in \Gamma(S(\ker f_*))$ and $X \in \Gamma(S(\ker f_*)^{\perp})$, $[X, U]$ is a vertical vector field.

Theorem 5.12 Consider the semi-Riemannian manifolds, M_1 and M_2, equipped with the metrics g_1 and g_2, respectively. Let $f\colon M_1 \to M_2$ be a transversal r-lightlike submersion. In this case, we have $g_1(\nabla_{N_1} N_2, N_3) = -g_1(N_2, \nabla_{N_1} N_3)$ for all N_1, N_2, N_3 in $\Gamma(\mathrm{ltr}(\ker f_*))$, where ∇ represents the Levi-Civita connection.

Proof. Since ∇ is the Levi-Civita connection for N_1, N_2, N_3 in $\Gamma(\mathrm{ltr}(\ker f_*))$, we have

$$(\nabla_{N_1} g_1)(N_2, N_3) = N_1\big(g_1(N_2, N_3)\big) - g_1\big(\nabla_{N_1} N_2, N_3\big) - g_1\big(N_2, \nabla_{N_1} N_3\big)$$

$$g_1\big(\nabla_{N_1} N_2, N_3\big) = -g_1\big(N_2, \nabla_{N_1} N_3\big)$$

□

Let M_1 and M_2 be semi-Riemannian manifolds, $f\colon M_1 \to M_2$ be transversal submersion and E, F arbitrary vector fields on M_1. Also, let the projections $h\colon TM_1 \to \mathcal{H}$ and $v\colon TM_1 \to \mathcal{V}$ denote the natural projections associated with the decomposition of $TM_1 = \mathcal{H} \oplus \mathcal{V}$. Moreover, ∇ represents the Levi-Civita connection of (M_1, g_1). We define the fundamental tensor field T of type (1,2);

$$T_E F = h\nabla_{vE} vF + v\nabla_{vE} hF \tag{5.2}$$

has the following properties:

i. T exchances the role of horizontal and vertical subspaces

ii. T is vertical: $T_E = T_{vE}$

The tensor field A;

$$A_E F = v\nabla_{hE} hF + h\nabla_{hE} vF \tag{5.3}$$

has the following properties:

i. A exchances the role of horizontal and vertical subspaces

ii. A is horizontal: $A_X = A_{hX}$

Lemma 5.13 Let $f:(M_1,g_1)\to(M_2,g_2)$ be a transversal r −lightlike submersion between semi-Riemannian manifolds (M_1,g_1) and (M_2,g_2). In this case, we obtain the followings:

i. $T_UV=h\nabla_UV$ (5.4)

ii. $T_U\xi=h\nabla_U\xi$ (5.5)

iii. $T_\xi V=h\nabla_\xi V$ (5.6)

iv. $T_{\xi_1}\xi_2=h\nabla_{\xi_1}\xi_2$ (5.7)

where $U,V\in\Gamma(S(\ker f_*))$, $\xi,\xi_1,\xi_2\in\Gamma(\Delta)$.

Proof. Here, we will consider two situations:

i. If we use (5.2) for transversal r-lightlike submersion, we can express it as

$$T_UV=h\nabla_UV \tag{5.8}$$

ii. Considering elements for which the multiplication equations by T_UV is non-zero, examine the following equations:

$$\begin{gathered}Ug_1(V,\xi)=g_1(\nabla_UV,\xi)+g_1(V,\nabla_U\xi)\\ g_1(\nabla_UV,\xi)=-g_1(V,\nabla_U\xi)\\ g_1(h\nabla_UV,\xi)=-g_1(V,v\nabla_U\xi)-g_1(V,h\nabla_U\xi)\\ g_1(T_UV,\xi)=\underbrace{-g_1(V,v\nabla_U\xi)}_{\neq0}\end{gathered} \tag{5.9}$$

where $U,V\in\Gamma(S(\ker f_*))$, $\xi\in\Gamma(\Delta)$. In this case, $T_UV\neq0$.

$$\begin{gathered}Ug_1(V,X)=g_1(\nabla_UV,X)+g_1(V,\nabla_UX)\\ g_1(\nabla_UV,X)=-g_1(V,\nabla_UX)\\ g_1(h\nabla_UV,X)=-g_1(V,v\nabla_UX)-g_1(V,h\nabla_UX)\\ g_1(T_UV,X)=\underbrace{-g_1(V,v\nabla_UX)}_{\neq0}\end{gathered} \tag{5.10}$$

In this case, $T_UV\neq0$ where $U,V\in\Gamma(S(\ker f_*))$, $X\in\Gamma(S(\ker f_*)^\perp)$. Consequently, from (5.9) and (5.10), we derive the non-zero equality expressed as $T_UV=h\nabla_UV$. Similarly, we can establish the proofs for (5.5)-(5.7).

Corollary 5.14 Let $f:(M_1,g_1)\to(M_2,g_2)$ be a transversal r-lightlike submersion between semi-Riemannian manifolds (M_1,g_1) and (M_2,g_2). In this case, utilizing Lemma 5.13, we can deduce the expression:

$$T_{W_1}W_2=h\nabla_{W_1}W_2 \tag{5.11}$$

where $W_1,W_2\in\Gamma(\ker f_*)$.

Lemma 5.15 Let $f:(M_1,g_1)\to(M_2,g_2)$ be a transversal r-lightlike submersion between semi-Riemannian manifolds (M_1,g_1) and (M_2,g_2). In this case, we have the following equations:

i. $T_UX=v\nabla_UX$

ii. $T_UN=v\nabla_UN$

iii. $T_\xi X = v\nabla_\xi X$

iv. $T_\xi N = v\nabla_\xi N$

where $U \in \Gamma(S(\ker f_*))$, $\xi \in \Gamma(\Delta)$, $X \in \Gamma(S(\ker f_*)^\perp)$, $N \in \Gamma(\mathrm{ltr}(\ker f_*))$.

Proof. The proof of the first equation is done in a similar way to the proof of Lemma 5.13, using (5.2) and the Levi-Civita connection. Other equations can be obtained similarly easily.

Corollary 5.16 Let $f:(M_1, g_1) \to (M_2, g_2)$ be a transversal r −lightlike submersion between semi-Riemannian manifolds (M_1, g_1) and (M_2, g_2). In this case, by using Lemma 5.15, we obtain

$$T_W F = v\nabla_W F$$

where $W \in \Gamma(\ker f_*)$, $F \in \Gamma(\mathrm{tr}(\ker f_*))$.

Lemma 5.17 Let $f:(M_1, g_1) \to (M_2, g_2)$ be a transversal r −lightlike submersion between semi-Riemannian manifolds (M_1, g_1) and (M_2, g_2). In this case, we have

i. $A_X U = h\nabla_X U$

ii. $A_X \xi = h\nabla_X \xi$

iii. $A_N U = h\nabla_N U$

iv. $A_N \xi = h\nabla_N \xi$

where $U \in \Gamma(S(\ker f_*))$, $\xi \in \Gamma(\Delta)$, $X \in \Gamma(S(\ker f_*)^\perp)$, $N \in \Gamma(\mathrm{ltr}(\ker f_*))$.

Proof. The proof of the first equation is done in a similar way to the proof of Lemma 5.13, using (5.3) and the Levi-Civita connection. Other equations can be obtained similarly easily.

Corollary 5.18 Let (M_1, g_1), (M_2, g_2) be semi-Riemannian manifold and $f:(M_1, g_1) \to (M_2, g_2)$ be a transversal r −lightlike submersion. In this case, based on Lemma 5.17, we obtain $A_F W = h\nabla_F W$, where $F \in \Gamma(\mathrm{tr}(\ker f_*))$, $W \in \Gamma(\ker f_*)$.

Lemma 5.19 Let $f:(M_1, g_1) \to (M_2, g_2)$ be a transversal r-lightlike submersion between semi-Riemannian manifolds (M_1, g_1) and (M_2, g_2). In this case, we have

i. $A_X Y = v\nabla_X Y$ (5.12)

ii. $A_X N = v\nabla_X N$ (5.13)

iii. $A_N X = v\nabla_N X$ (5.14)

iv. $A_{N_1} N_2 = v\nabla_{N_1} N_2$ (5.15)

where $X, Y \in \Gamma(S(\ker f_*)^\perp)$, $N, N_1, N_2 \in \Gamma(\mathrm{ltr}(\ker f_*))$.

Proof: The proof of (5.12) is done in a similar way to the proof of Lemma 5.13, using (5.3) and the Levi-Civita connection. Other equations can be obtained similarly easily.

Corollary 5.20 Let $f:(M_1, g_1) \to (M_2, g_2)$ be a transversal r −lightlike submersion between semi-Riemannian manifolds (M_1, g_1) and (M_2, g_2). In this case, utilizing Lemma 5.19, we derive $A_{F_1} F_2 = v\nabla_{F_1} F_2$, where $F_1, F_2 \in \Gamma(\mathrm{tr}(\ker f_*))$.

Lemma 5.21 Let (M_1, g_1), (M_2, g_2) be semi-Riemannian manifolds, ∇ be Levi-Civita connection in M_1, T and A be tensor fields, $f:(M_1, g_1) \to (M_2, g_2)$ be a transversal r-lightlike submersion. In this case,

i. $\nabla_{W_1} W_2 = T_{W_1} W_2 + v\nabla_{W_1} W_2$ (5.16)

ii. $\nabla_W \xi = T_W \xi + v\nabla_W \xi$ (5.17)

iii. $\nabla_U W = T_U W + v\nabla_U W$ (5.18)

iv. $\nabla_U V = T_U V + v\nabla_U V$ (5.19)

v. $\nabla_U \xi = T_U \xi + v\nabla_U \xi$ (5.20)

vi. $\nabla_\xi W = T_\xi W + v\nabla_\xi W$ (5.21)

vii. $\nabla_{\xi_1} \xi_2 = T_{\xi_1} \xi_2 + v\nabla_{\xi_1} \xi_2$ (5.22)

viii. $\nabla_\xi V = T_\xi V + v\nabla_\xi V$ (5.23)

where $W, W_1, W_2, \in \Gamma(\ker f_*)$, $\xi, \xi_1, \xi_2 \in \Gamma(\nabla)$, $U, V \in \Gamma(S(\ker f_*))$.

Proof. Here, we will prove only (5.16). For any vector fields $W_1, W_2 \in \Gamma(\ker f_*)$, we can establish the equation $\nabla_{W_1} W_2 = v\nabla_{W_1} W_2 + h\nabla_{W_1} W_2$. Using Lemma 5.13 and Corollary 5.14, we obtain the equation $\nabla_{W_1} W_2 = v\nabla_{W_1} W_2 + T_{W_1} W_2$. The proof of the remaining equations can also be carried out similarly. □

Lemma 5.22 Let (M_1, g_1), (M_2, g_2) be semi-Riemannian manifolds, ∇ be Levi-Civita connection in M_1, T and A be tensor fields, $f: (M_1, g_1) \to (M_2, g_2)$ be a transversal r −lightlike submersion. In this case, we obtain the following equations:

i. $\nabla_W N = T_W N + h\nabla_W N$

ii. $\nabla_U N = T_U N + h\nabla_U N$

iii. $\nabla_\xi N = T_\xi N + h\nabla_\xi N$

iv. $\nabla_U F = T_U F + h\nabla_U F$

v. $\nabla_\xi F = T_\xi F + h\nabla_\xi F$

vi. $\nabla_W F = T_W F + h\nabla_W F$

where $W \in \Gamma(\ker f_*)$, $U, V \in \Gamma(S(\ker f_*))$, $N \in \Gamma(\mathrm{ltr}(\ker f_*))$, $F \in \Gamma(\mathrm{tr}(\ker f_*))$.

Proof. Here, we will prove only second equation. For any vector fields $U \in \Gamma(S(\ker f_*))$, and $N \in \Gamma(\mathrm{ltr}(\ker f_*))$, we can establish the equation $\nabla_U N = v\nabla_U N + h\nabla_U N$. Using Lemma 5.15, we can establish $\nabla_U N = T_U N + h\nabla_U N$. Other equations can be obtained in a similar way.

Lemma 5.23 Let (M_1, g_1), (M_2, g_2) be semi-Riemannian manifolds, ∇ be Levi-Civita connection in M_1, T and A be tensor fields, $f: (M_1, g_1) \to (M_2, g_2)$ be a transversal r-lightlike submersion. In this case, we obtain the following equations:

i. $\nabla_X W = A_X W + v\nabla_X W$

ii. $\nabla_X \xi = A_X \xi + v\nabla_X \xi$

iii. $\nabla_N W = A_N W + v\nabla_N W$

iv. $\nabla_N U = A_N U + v\nabla_N U$

v. $\nabla_N \xi = A_N \xi + v\nabla_N \xi$

vi. $\nabla_F W = A_F W + v\nabla_F W$

vii. $\nabla_F U = A_F U + v\nabla_F U$

viii. $\nabla_F\xi = A_F\xi + v\nabla_F\xi$

where $U \in \Gamma(S(\ker f_*))$, $\xi \in \Gamma(\Delta)$, $W \in \Gamma(\ker f_*)$, $X \in \Gamma(S(\ker f_*)^{\perp})$, $N \in \Gamma(\mathrm{ltr}(\ker f_*))$, $F \in \Gamma(\mathrm{tr}(\ker f_*))$.

Proof. Here we will prove only fourth equation. For any vector fields $N \in \Gamma(\mathrm{ltr}(\ker f_*))$ and $U \in \Gamma(S(\ker f_*))$, we can establish the equation $\nabla_N U = v\nabla_N U + h\nabla_N U$. Using Lemma 5.17, we can establish the equation $\nabla_N U = A_N U + v\nabla_N U$. Other equations can be obtained in a similar way.

Lemma 5.24 Let (M_1, g_1), (M_2, g_2) be semi-Riemannian manifolds, ∇ be Levi-Civita connection in M_1, T and A be basic tensor fields, $f: (M_1, g_1) \to (M_2, g_2)$ be a transversal r-lightlike submersion. In this instance, we obtain the following equations:

i. $\nabla_X N = A_X N + h\nabla_X N$ (5.24)

ii. $\nabla_{N_1} N_2 = A_{N_1} N_2 + h\nabla_{N_1} N_2$ (5.25)

iii. $\nabla_{F_1} F_2 = A_{F_1} F_2 + h\nabla_{F_1} F_2$ (5.26)

iv. $\nabla_X F = A_X F + h\nabla_X F$ (5.27)

v. $\nabla_N F = A_N F + h\nabla_N F$ (5.28)

vi. $\nabla_F N = A_F N + h\nabla_F N$ (5.29)

vii. $\nabla_X Y = A_X Y + h\nabla_X Y$ (5.30)

where $X, Y \in \Gamma(S(\ker f_*)^{\perp})$, $N, N_1, N_2 \in \Gamma(\mathrm{ltr}(\ker f_*))$, $F, F_1, F_2 \in \Gamma(\mathrm{tr}(\ker f_*))$.

Proof. Here we will prove only first equation. For any vector fields $X \in \Gamma(S(\ker f_*)^{\perp})$ and $N \in \Gamma(\mathrm{ltr}(\ker f_*))$, we can establish the equation $\nabla_X N = v\nabla_X N + h\nabla_X N$. Using Lemma 5.19, we can establish $\nabla_X N = A_X N + h\nabla_X N$. Other equations can be obtained in a similar way.

Corollary 5.25. Let $f: (M_1, g_1) \to (M_2, g_2)$ be a transversal $r-$lightlike submersion between semi-Riemannian manifolds (M_1, g_1) and (M_2, g_2). Then,

i. $g_1(T_U N_1, N_2) = -g_1(N_1, T_U N_2)$

ii. $g_1(T_\xi N_1, N_2) = -g_1(N_1, T_\xi N_2)$

iii. $g_1(A_N\xi_1, \xi_2) = -g_1(\xi_1, A_N\xi_2)$

iv. $g_1(A_X N_1, N_2) = -g_1(N_1, A_X N_2)$

where $U \in \Gamma(S(\ker f_*))$, $\xi_1, \xi_2 \in \Gamma(\Delta)$, $X \in \Gamma(S(\ker f_*)^{\perp})$, $N_1, N_2 \in \Gamma(\mathrm{ltr}(\ker f_*))$.

Proof. Provide the proof solely for the first equality.

Since (M_1, g_1) is a semi-Riemannian manifold the torsion-free metric connection used here is the Levi-Civita connection. For $U \in \Gamma(S(\ker f_*))$, $N_1, N_2 \in \Gamma(\mathrm{ltr}(\ker f_*))$, we have

$$U g_1(N_1, N_2) = g_1(\nabla_U N_1, N_2) + g_1(N_1, \nabla_U N_2)$$

$$g_1(v\nabla_U N_1, N_2) = -g_1(N_1, v\nabla_U N_2)$$

By using Lemma 5.15 and Lemma 5.22, we can derive the expression $g_1(T_U N_1, N_2) = -g_1(N_1, T_U N_2)$. Similarly, by using Lemma 5.23 and Lemma 5.24, we can obtain other equations.

Theorem 5.26. Let $f:(M_1,g_1)\to(M_2,g_2)$ be a transversal $r-$lightlike submersion between semi-Riemannian manifolds (M_1,g_1) and (M_2,g_2). In this case, $\ker f_*$ integrable for $W_1, W_2 \in \Gamma(\ker f_*)$.

Proof. Since W_{1p}, W_{2p} are elements of $\Gamma(\ker f_{*p})$, we have $f_*(W_1)=\widetilde{W_1}=0$ and $f_*(W_2)=\widetilde{W_2}=0$. From equation in Definition 20 [1], we obtain $[\widetilde{W}_1,\widetilde{W}_2]g_2=f_*([W_1,W_2])\circ g_2$. Therefore, $[W_1,W_2]$ belongs to $\Gamma(\ker f_*)$, then $\ker f_*$ is integrable. □

Remark 5.27 Let $f:(\widetilde{M}_1,\tilde{g}_1)\to(\widetilde{M}_2,\tilde{g}_2)$ be a transversal $r-$ lightlike submersion between semi-Riemannian manifolds $(\widetilde{M}_1,\tilde{g}_1)$ and $(\widetilde{M}_2,\tilde{g}_2)$, where ∇ is the Levi-Civita connection corresponding to $\tilde{g}_1$ on the manifold M_1. $S(\ker f_*)$ and $\mathrm{tr}(\ker f_*)$ denote the corresponding screen distribution and transversal lightlike vector bundle of M_1, respectively. By utilizing the expression $T\widetilde{M}_1=\ker f_*\oplus\mathrm{tr}(\ker f_*)$, we can derive $\nabla_U V=v\nabla_U V+h\nabla_U V$, where $U,V\in\Gamma(\ker f_*)$. Furthermore, using (5.4), we obtain $\tilde{\nabla}_U V=\hat{\nabla}_U V+T_U V$, where $T_U V$ is associated with $\Gamma(\mathrm{tr}(\ker f_*))$ and $\tilde{\nabla}_U V$ is associated with $\Gamma(\ker f_*)$.

Remark 5.28 Let P denote the projection morphism of $(\ker f_*)$ onto $S(\ker f_*)$ based on the decomposition of V. By utilizing the equation $\nabla_U PV=v\overset{*}{\nabla}_U PV+h\overset{*}{\nabla}_U PV$, we get the following equation:

$$\nabla_U PV=\overset{\widehat{*}}{\nabla}_U PV+\overset{*}{T}_U PV \tag{5.31}$$

where $\overset{*}{T}_U PV$ is associated with $\Gamma(\Delta)$, while $\overset{\widehat{*}}{\nabla}_U PV$ is associated with $\Gamma(\ker f_*)$.

Theorem 5.29 Let $f:(\widetilde{M}_1,\tilde{g}_1)\to(\widetilde{M}_2,\tilde{g}_2)$ be a transversal r-lightlike submersion between semi-Riemannian manifolds $(\widetilde{M}_1,\tilde{g}_1)$ and $(\widetilde{M}_2,\tilde{g}_2)$. In this case, the necessary and sufficient condition for the integrability $S(\ker f_*)$ is that $\overset{*}{T}_U PV=\overset{*}{T}_V PU$.

Proof. Let $U,\ V\in\Gamma(\ker f_*),\ N\in\Gamma(\mathrm{ltr}(\ker f_*))$. Since ∇ is torsion-free, we have $\tilde{g}_1([U,V],N)=\tilde{g}_1(\nabla_U V,N)-\tilde{g}_1(\nabla_V U,N)$. From (5.31), it is easy to see that $\tilde{g}_1([U,V],N)=\tilde{g}_1(\overset{\widehat{*}}{\nabla}_U PV+\overset{*}{T}_U PV,N)-\tilde{g}_1(\overset{\widehat{*}}{\nabla}_V PU+\overset{*}{T}_V PU,N)$. Then, since $\tilde{g}_1(\overset{\widehat{*}}{\nabla}_U PV,N)=0$ and $\tilde{g}_1(\overset{\widehat{*}}{\nabla}_V PU,N)=0$, we have

$$\tilde{g}_1([U,V],N)=\tilde{g}_1\left(\overset{*}{T}_U PV,N\right)-\tilde{g}_1\left(\overset{*}{T}_V PU,N\right)$$

□

Theorem 5.30 Let $f:(M_1,g_1)\to(M_2,g_2)$ be a transversal r-lightlike submersion between semi-Riemannian manifolds (M_1,g_1) and (M_2,g_2). In this case, for $W_1,W_2\in\Gamma(\ker f_*)$, we have,

$$T_{W_1}W_2=T_{W_2}W_1$$

Proof. Utilizing equation (5.11) for $W_1,W_2\in\Gamma(\ker f_*)$, we observe $T_{W_1}W_2-T_{W_2}W_1=h[W_1,W_2]$. By employing Theorem 5.26, as $[W_1,W_2]\in\Gamma(\ker f_*)$, we deduce $h[W_1,W_2]=0$. Consequently, this completes proof.

Theorem 5.31 Let $f:(M_1,g_1)\to(M_2,g_2)$ be a transversal r-lightlike submersion between semi-Riemannian manifolds (M_1,g_1) and (M_2,g_2). In this case, if $S(\ker f_*)^{\perp}$ is integrable, we obtain $A_X Y=A_Y X$ for $X,Y\in\Gamma(S(\ker f_*)^{\perp})$. Conversely, if $A_X Y=A_Y X$, we have $[X,Y]\in\mathcal{H}$.

Proof. We will prove this theorem by considering two situations together.

i. Since ∇ is the Levi-Civita connection, the following equation holds:

$$g_1([X,Y],U) = g_1(\nabla_X Y,U) - g_1(\nabla_Y X,U)$$

where $X,Y \in \Gamma(S(\ker f_*)^{\perp})$, $U \in \Gamma(S(\ker f_*))$. By using (5.30), we can derive the following expression.

$$g_1([X,Y],U) = g_1(A_X Y,U) - g_1(A_Y X,U)$$

If $S(\ker f_*)^{\perp}$ is integrable, we can further simplify the equation and obtain:

$$g_1(A_X Y,U) = g_1(A_Y X,U) \tag{5.32}$$

ii. From the equation $g_1([X,Y],N) = g_1(\nabla_X Y,N) - g_1(\nabla_Y X,N)$ and the integrability of $S(\ker f_*)^{\perp}$, we obtain the following equation:

$$g_1(A_X Y,N) = g_1(A_Y X,N) \tag{5.33}$$

If we consider (5.32) and (5.33) together, it follows that $A_X Y = A_Y X$. We can easily show that if $A_X Y = A_Y X$, then $[X,Y] \in \mathcal{H}$.

We also note that A has the alternation property $A_X Y = -A_Y X$ for a Riemannian submersion. However, this situation differs for transversal r-lightlike submersions.

Theorem 5.32 Let $f\colon (M_1,g_1) \to (M_2,g_2)$ be a transversal r-lightlike submersion between semi-Riemannian manifolds (M_1,g_1) and (M_2,g_2). In this case, if the $\mathrm{ltr}(\ker f_*)$ distribution is parallel in the direction of the $S(\ker f_*)^{\perp}$ distribution, we obtain the equality $A_X Y = -A_Y X$, where $X,Y \in \Gamma(S(\ker f_*)^{\perp})$, $N \in \Gamma(\mathrm{ltr}(\ker f_*))$.

Proof. We first establish $A_X X = 0$ for any X $\in \Gamma(S(\ker f_*)^{\perp})$. Let X,$Y \in \Gamma(S(\ker f_*)^{\perp})$, then we derive $V g_1(X,X) = 2g_1(\nabla_V X,X)$, where $V \in \Gamma(S(\ker f_*))$. By utilizing Remark 5.11, we then have $2g_1(\nabla_V X,X) = 2g_1(\nabla_X V,X)$. Subsequently, it becomes apparent that $2g_1(\nabla_X V,X) = -2g_1(\nabla_X X,V)$. Furthermore, in accordance with (5.30), we conclude that

$$2g_1(\nabla_X V,X) = -2g_1(A_X X,V) \tag{5.34}$$

On the other hand, since M_1 is a semi-Riemannian manifold, $g_1(X,X)$ is constant on each fiber, and thus $V g_1(X,X) = 0$. From this, we conclude that $g_1(A_X X,V) = 0$. However, the condition for the result to be zero relies on two possibilities: either $A_X X \in \Gamma(\Delta)$ or $A_X X = 0$. It can be observed that if $A_X X = 0$, then $A_X Y = -A_Y X$. If we consider the expression $g_1(A_X X,N)$ for $N \in \Gamma(\mathrm{ltr}(\ker f_*))$, using (5.12), we obtain

$$g_1(A_X X,N) = g_1(\nabla_X X,N) = X g_1(X,N) - g_1(\nabla_X N,X)$$

$$g_1(A_X X,N) = -g_1(\nabla_X N,X)$$

Then, if the $\mathrm{ltr}(\ker f_*)$ distribution for $N \in \Gamma(\mathrm{ltr}(\ker f_*))$ is parallel in the direction of the $S(\ker f_*)^{\perp}$ distribution, then, $\nabla_X N \in \Gamma(\mathrm{ltr}(\ker f_*))$, we have

$$g_1(A_X X,N) = 0 \tag{5.35}$$

Thus, from (5.34) and (5.35), we obtain the expression

$$A_X Y = -A_Y X$$

6. Conclusion

In this study, we introduced the concept of transversal lightlike submersions, and to illustrate the existence of such a structure, we offer illustrative examples. Our research delves into significant geometric analyses by

examining O'Neill tensors for submersion, which we have defined as transversal lightlike submersions. In this way, various connections were obtained according to vector fields selected from certain fibers by utilizing these tensor fields, and meaningful results were obtained by investigating the integrability of certain distributions.

Thus, meaningful outcomes can be derived by computing various curvatures on the structure established for transversal submersions. Moreover, examining these submersions from two perspectives, transversal r-lightlike and isotropic transversal lightlike submersions, facilitates a geometric comparison. These investigations offer valuable insights into the intrinsic geometric properties of such mappings, potentially paving the way for new avenues of research.

Author Contributions

All the authors equally contributed to this work. They all read and approved the final version of the paper.

Conflicts of Interest

All the authors declare no conflict of interest.

References

[1] B. O'Neill, *The fundamental equations of a submersion*, Michigan Mathematical Journal 13 (4) (1966) 459–469.

[2] A. Gray, *Pseudo-Riemannian almost product manifolds and submersions*, Journal of Mathematics and Mechanics 16 (7) (1967) 715–737.

[3] R. H. Escobales Jr, *Riemannian submersions with totally geodesic fibers*, Journal of Differential Geometry 10 (2) (1975) 253–276.

[4] S. Ianuş, R. Mazzocco, G. E. Vilcu, *Riemannian submersions from quaternionic manifolds*, Acta Applicandae Mathematicae 104 (2008) 83–89.

[5] V. N. Beretovskii, L. Guijarro, *A metric characterization of Riemannian submersions*, Annals of Global Analysis and Geometry 18 (6) (2000) 577–588.

[6] Ş. Eken Meriç, M. Gülbahar, E. Kılıç, *Some inequalities for Riemannian submersions*, Analele Stiintifice Ale Universitatii Al I Cuza Din Iasi-Serie Noua-Matematica 63 (3) (2017) 1–12.

[7] B. Şahin, *Riemannian submersions from almost Hermitian manifolds*, Taiwanese Journal of Mathematics 17 (2) (2013) 629–659.

[8] F. Narita, *Riemannian submersion with isometric reflections with respect to the fibers*, Kodai Mathematical Journal 16 (3) (1993) 416–427.

[9] M. A. Akyol, S. Beyendi, *Riemannian submersions endowed with a semi-symmetric non-metric connection*, Konuralp Journal of Mathematics 6 (1) (2018) 188–193.

[10] H. Demir, R. Sarı, *Riemannian submersions with quarter-symmetric non-metric connection*, Journal of Engineering Technology and Applied Sciences 6 (1) (2021) 1–8.

[11] E. Karataş, S. Zeren, M. Altin, *Riemannian submersions endowed with a new type of semisymmetric non-metric connection*, Thermal Science 27 (4B) (2023) 3393–3403.

[12] Y. Gündüzalp, *On the geometry of Riemannian submersions*, Master's Thesis İnönü University (2007) Malatya.

[13] B. Şahin, Y. Gündüzalp, *Submersion from semi-Riemannian manifolds onto lightlike manifolds*, Hacettepe Journal of Mathematics and Statistics 39 (1) (2010), 41–53.

[14] B. Şahin, *On a submersion between Reinhart lightlike manifolds and semi-Riemannian manifolds*, Mediterranean Journal of Mathematics 5 (3) (2008) 273–284.

[15] K. L. Duggal, A. Bejancu, Lightlike submanifolds of semi-Riemannian manifolds and applications, Kluwer Academic, Dordrecht, 1996.

[16] K. Nomizu, Fundamentals of linear algebra, McGraw-Hill, New York, 1966.

[17] B. Sahin, Riemannian submersions, Riemannian maps in Hermitian geometry, and their applications, Academic Press, 2017.

[18] M. Falcitelli, S. Ianus, A. M. Pastore, Riemannian submersions and related topics, World Scientific, 2004.